Durham E-Theses

A numerical study of the dynamics of subduction

Whittaker, A.

A Numerical Study Of The

Dynamics Of Subduction

by

A. Whittaker

A thesis submitted to the University

of Durham for the degree of

Doctor of Philosophy

Graduate Society

September 1988

2 3 MAR 1989

Abstract

The mechanics and dynamics of subduction have been studied using 2-D finite element analysis. Two finite element formulations have been employed; one formulation for Newtonian viscous flow and one formulation for linear elasticity and viscoelasticity. Quadratic isoparametric quadrilateral and triangular elements are used for both formulations.

Models of flow in the mantle driven by oblique subduction produce an asymmetric depression of the surface above the slab. The width and depth of this depression are dependent on the value of the viscosity of the lower mantle, the length and mechanical strength of the slab. Analysis of the flow patterns suggests that the viscosity contrast at the 670 km sesmic discontinuity is likely to be of the order $\times 10$.

The stress regime at an island arc margin with a subducting slab dipping at $45°$ has been modelled using an elastic-viscoelastic rheology. The body forces of the slab produce an asymmetric depression of the surface above the slab which generates horizontal deviatoric compression in the plates. Unlocking the thrust zone between the subducting and overriding plates eliminates the shear stress in the fault plane resulting in regional horizontal tension in both plates, uplift of the leading edge of the overriding plate and depression of the subducting plate. The regional tension is interpreted as the source of the plate driving forces of slab pull and trench suction. Local horizontal compression in the arc-forearc region produced by the surface depression exceeds the regional tension and this may be the source of lateral variation in stress that is observed across the strike of convergent margins. It may also be the source of backarc compression for low angle slabs at Chilean type margins.

Depression of the surface provides partial compensation of the slab body forces. Thus the downdip force is reduced and the resulting stress regime in the slab is controlled by the isostatic upthrust at the trench and the viscosity contrast at 670 km depth. A low pressure zone above and high pressure zone below the slab may act against the body forces which rotate the slab towards vertical subduction. Anomalous pressures in the mantle are created and sustained by continuous subduction and rollback, and may behave in a self-regulating mechanism. A low viscosity zone in the mantle wedge above the slab leads to the development of double seismic zones as suggested by Sleep (1979).

Acknowledgements

I would like to thank Professor M.H.P. Bott for his guidance and encouragement throughout the 3 years of my research at Durham University.

Contents

CHAPTER 1

Introduction

The world-wide distribution of earthquake epicentres is shown in figure 1.1. It is a striking pattern (Isacks et al. 1968). Nearly all of the seismic energy release is concentrated in narrow, continuous belts outside of which seismic activity is almost absent. This observation was a major contribution to the formulation of plate tectonic theory (McKenzie and Parker 1967, Morgan 1968), which postulates that the relatively aseismic regions of the surface of the Earth are thin. rigid plates of lithosphere which interact at their boundaries, defined by the belts of seismicity. The mobility and integrity of the plates serves to explain phenomena such as continental drift and sea-floor spreading which had become popular explanations of the palaeo-reconstructions made from the present-day positions of the continents.

The earlier discovery by Raff and Mason (1961) of the magnetic lineations parallel to. and symmetric about the spreading centres (ocean ridges), and the realisation that these abrupt changes in magnetic intensity could be related to reversals in the Earth's magnetic field (Vine and Matthews 1963), lead to the theory of plate tectonics. The magnetic stripes thus 'date' the ocean floor and indicate how the plates are moving. Plate boundaries can be classified into three possible categories; divergent margins, the site of plate creation where the plates move apart. convergent margins where the plates move toward one another, and transform faults where the plates slip by one another.

The oldest parts of the ocean floor are found at convergent margins, and generally the stripes are not parallel to the plate boundary. Also at convergent margins the earthquakes occur at much greater depths and they lie along a plane descending into the Earth and dipping away from the ocean with a fairly smooth trajectory (Sykes 1966, Oliver and Isacks 1967). This plane, the Wadati-Benioff zone, was proposed to define the descent of the surface lithospheric plate underneath its neighbour, a process called subduction, which conveniently accounts for the oblique disappearance of the magnetic stripes at the margin. Subduction zones are thus the site of consumption of the oceanic parts of the system of plates, and this thesis will attempt to provide some insight into
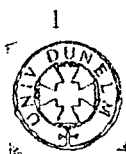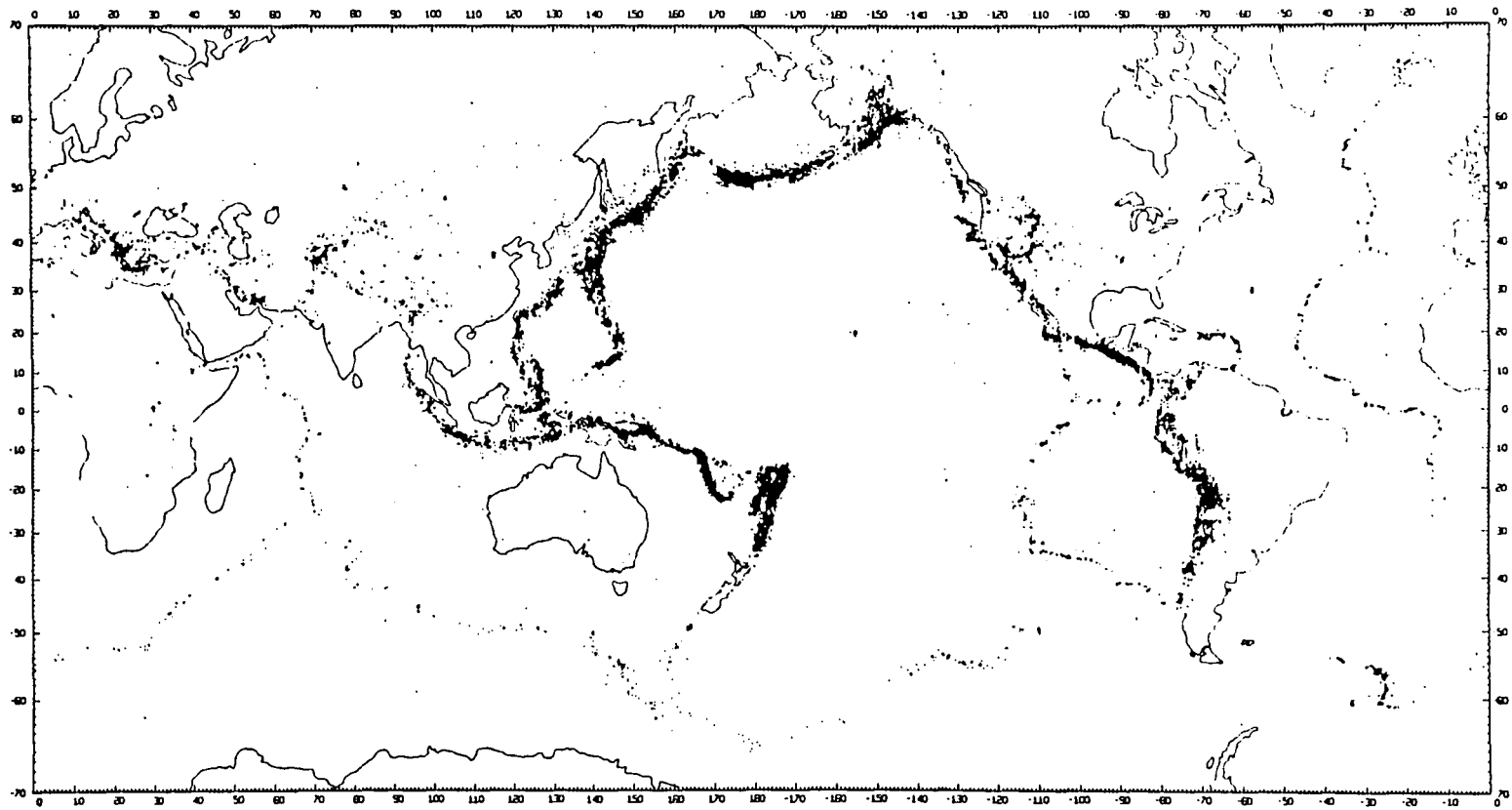
Figure 1.1   Distribution of the epicentres of earthquakes recorded between 1961 and 1967.
From Bott (1984), originally Barazangi and Dorman (1969).

the dynamics of this process.

1.1 The Structure of Subduction Zones

Subduction zones are of two types; the island arc margin in which the overriding plate is oceanic, and the active continental margin in which the overriding plate at the boundary carries continental crust. Whilst the differences are essential, the similarities allow us to discuss a 'typical convergent margin', and I will concentrate on the island arcs.

The morphological and structural units of the Lesser Antilles island arc margin are shown in figure 1.2. This particular margin exhibits most features commonly associated with subduction and so it is a convenient reference. The term island arc arises from the arcuate segments of exposed, and submarine, volcanics and volcanoes which form an almost continuous line about 100 km from the plate boundary on the overriding plate. The arcuate nature is one example of the 3-dimensionality of subduction zones which will be discussed later. Meanwhile it is convenient to remain in two dimensions to describe the surface features of the margin.

The outer rise is a low up-arching of the oceanic plate seaward of the trench, rising about 200 − 400 m over a distance of about 200 km. It is generally accepted to be the flexural response of the plate to the downbending at the trench (Parsons and Molnar 1976). The outer trench slope is generally low-angled dipping at 2° − 5° into the trench and exhibits extensional tectonics attributable to the flexure stresses. The ocean trench is the surface bounding line between the subducting and overriding plates. Most trenches have a thin sedimentary cover, and they are recognised as the deepest features of the ocean floor.

Landwards of the trench line is a highly deformed, and possibly metamorphosed, sedimentary accumulation called the accretionary prism. The width and depth of the prism varies greatly, from near zero in the Marianas to the great extent of the Lesser Antilles (as shown in figure 1.2) which covers the trench and part of the outer rise. The sediments are derived from turbidites and slumps, often reworkings, and from 'scraping off' the top layer of the descending oceanic plate as it passes the trench line. As the prism grows it gives birth to an outer sedimentary rise which can breach the

2
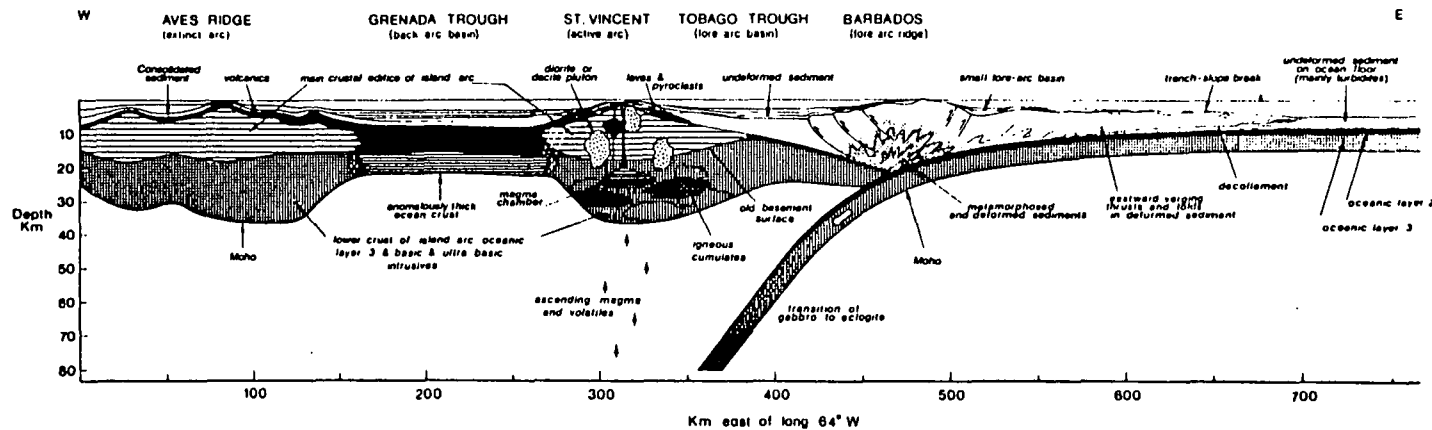
Figure 1.2 The major morphological units of the Lesser Antilles subduction zone (vertical exaggeration ×2) portraying from left to right: remnant arc, backarc basin, arc, forearc basin, forearc ridge, accretionary prism, and oceanic crust of the subducting plate. Accretion of the forearc complex has swamped the trench in this example, obscuring the inner- and outer- trench slopes and the outer rise. From Westbrook and McCann (1986).

ocean surface, in this case generating the island of Barbados. For margins with a more diminutive accretionary prism the inner trench slope rises at $10° - 20°$ from the trench which is considerably steeper than the outer slope. The intimate structure of the accretionary prism is complex and will not be pursued further. A forearc basin may develop behind this sedimentary ridge, in the case of the Lesser Antilles it is the Tobago Trough. Unconformably overlying the prism, it consists of undeformed, mainly terrigenous sediments derived from the volcanic arc.

The arc itself begins abruptly $150 - 250$ km landward of the trench. It is the site of intense, dominantly andesitic volcanicity of calc-alkaline type which, coupled with the observed uplift, is evidence of considerable magmatism at depth. The backarc region shows great variety among the subduction zones of the world. Commonly a backarc basin is characterised by thin sedimentary cover and high heat flow. Marginal seas evolve when active spreading occurs and magnetic lineations become identifiable. The Lesser Antilles margin is a good example of a remnant arc at the far side of the backarc sea. This inactive volcanic island is recognised as an extinct arc.

Earthquake hypocentre location has clearly defined the intermediate and deep earthquakes that are clustered along Wadati-Benioff zones. Isacks and Barazangi (1977) interpreted the position of the upper surface of the descending slab in vertical cross-section through Wadati-Benioff zones, and a selection of these interpretations is shown in figure 1.3. The angle of descent of the slab varies but one common feature of deep seismicity is that none has been observed deeper than 720 km (Stark and Frohlich 1985). This correlates well with the known seismic discontinuity at 670 - 700 km depth, the nature of which is still the subject of debate. Initially this cut-off point was taken to be the termination of the descending plate but recently Creager and Jordan (1984, 1986) have used teleseismic residuals to show that the slabs of at least the Western Pacific extend, albeit aseismically, to depths of at least 1000 km and probably 1400 km.

The cross-section in figure 1.2 provides a useful description of the subduction process, but out-of-plane effects are also important. As already mentioned, the trench and arc are linear but arcuate features. This can be understood in terms of the ping-pong ball analogy (Frank 1968). Indenting the surface of the ping-pong ball creates a depression with a curvature equal to that of the ball and so the dip of the slab can be related to the curvature of the arc. Although this is an oversimplification applied to trenches,

3
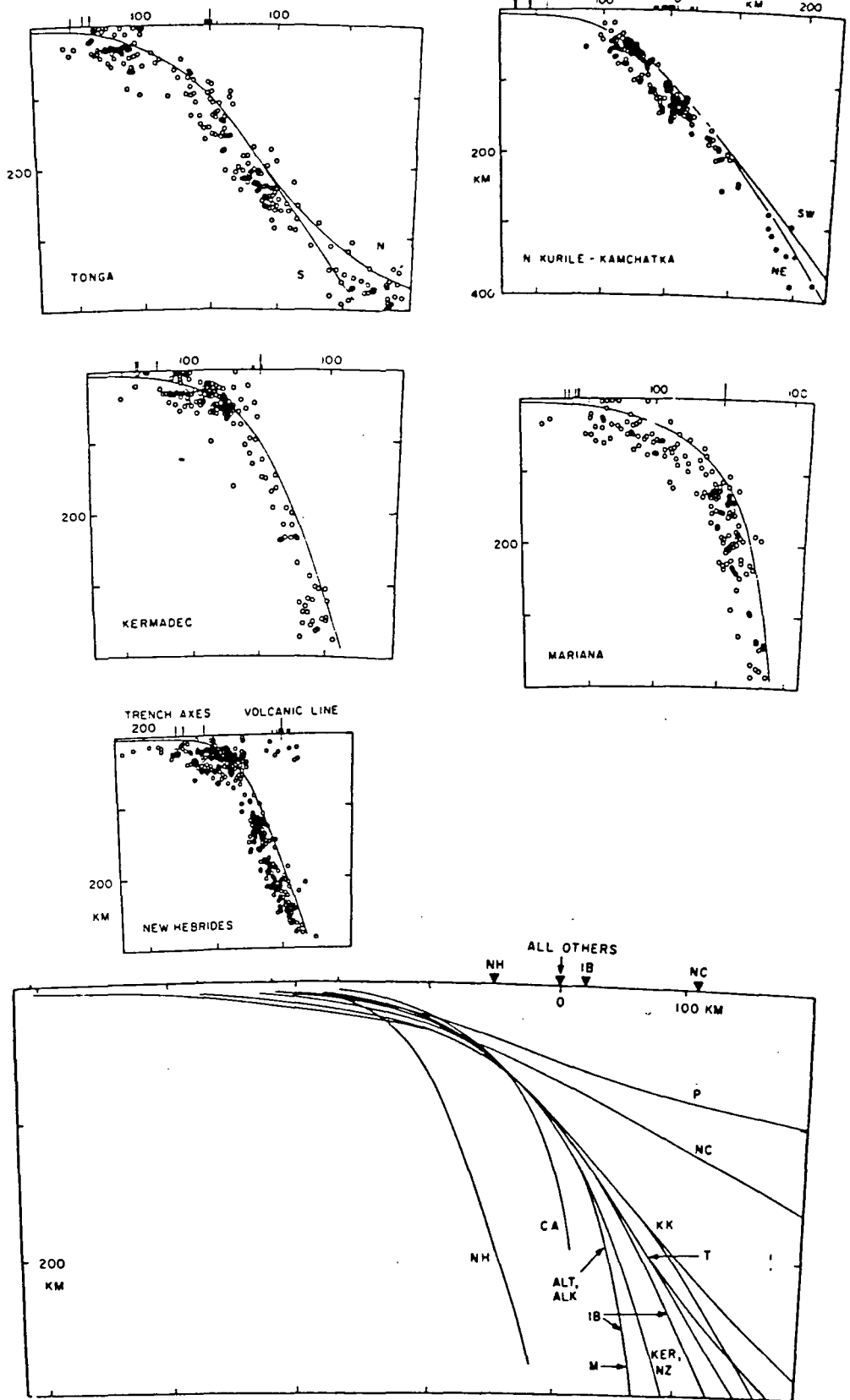
Figure 1.3   Earthquake hypocentre distributions at a selection of convergent margins. The solid line is the best estimate of the upper surface of the subducting lithosphere. Below, a compilation of the interpretations of slab surfaces with the position of the volcanic arc denoted by a black triangle (NH = New Hebrides, CA = Central America, ALT = Aleutian, ALK = Alaska, M = Mariana, IB = Izu-Bonin, KER = Kermedec, NZ = New Zealand, T = Tonga, KK = Kurile-Kamchatka, NC = North Chile, P = Peru). From Isacks and Barazangi (1977).

the concept is valid and the associated stress system must exist (Fukao et al. 1987). The relative motion of the plates is rarely perpendicular to the trench, and this oblique convergence is responsible for the strike-slip tectonics of the forearc and the resulting terrane motion. This further complicates the stress/strain regime of the overlying plate and may jeopardise any predictions from 2-D modelling.

The preceding description of a typical convergent margin obviously precludes one of the major observations concerning subduction zones: they are not all the same. Much literature has been devoted to investigating the correlation between the properties such as convergence rate and age of subducting slab, with the observations of slab dip, seismicity etc. A recent extensive analysis by Jarrard (1986) using a multiple linear regression has convincingly catalogued some significant correlations. While correlation is not direct proof of causality, it is a useful indication of the relative effect of the fundamental parameters of subduction. Jarrard considered slab length, earthquake magnitude, strain regime, slab dip, arc-trench gap and trench depth and found that they can all be accounted for by a combination of slab age, convergence rate and intermediate dip. The Benioff zone length is correlated with the product of convergence and slab age, in line with conducting heating models. The maximum earthquake magnitude is correlated with convergence and slab age, supporting the theories of seismic coupling, and trench depth correlates with age and dip which supports the notion of slab pull. However there are a few inconsistencies, notably that the slab dip correlates negatively with duration of subduction, implying that subduction shallows with age. Also Jarrard found that strain regime of the overriding plate is affected by the slab dip and presumed that this is due to its effect on the seismic coupling.

1.2 Rheology

This section is a short discussion of rheology of the Earth with a view to modelling this behaviour numerically. Consequently this is a somewhat simplified perspective considering the recent advances in understanding (e.g. Braun and Beaumont 1987, Kirby and Kronenberg 1987, Hager and Gurnis 1987) but it is adequate for the purposes of this thesis.

Plate tectonic theory requires that the outer shell of the Earth, the lithosphere,

4

retains its rigidity over geological time scales. The vertical extent of the lithosphere can be defined by the depth to a characteristic isotherm, typically 1550 K, above which the rock is cool enough to behave rigidly, and below which the rock deforms by solid state creep, behaving as a viscous fluid. The asthenosphere is a weak zone underlying the lithosphere which flows laterally in response to lithospheric movement allowing isostatic adjustment to occur on a time scale of the order 10^4 years (Robinson et al. 1987, Ceuleneer et al. 1988).

The lithosphere is composed of the crust and the top of the mantle. These are chemically distinct and meet at the Mohorovičić Discontinuity (Moho). Oceanic lithosphere is created at ocean ridges, it cools and thickens as it migrates and isostatically subsides away from the ridge (Sclater and Francheteau 1970). At subduction zones the oldest oceanic lithosphere is about 100 km thick with about 5 km of oceanic crust at the top. Continental lithosphere is typically twice as thick as oceanic and the Moho is observed at about 40 km depth on average. The relatively low density crust lowers the average density of continental lithosphere sufficiently to inhibit subduction and this creates an important distinction between the two types of lithosphere. Continental lithosphere is thus much older, and also its integrated strength is much less since crustal rocks are much weaker than those of the mantle, and the lower lithosphere rock is much hotter and weaker because of its greater depth.

The exact rheology of the lithosphere is uncertain. Many possibilities have been proposed as models for the long term lithospheric behaviour. Simple models of an elastic plate overlying a fluid substratum were reasonably successful for early flexural studies and led to the concepts of flexural rigidity and corresponding effective elastic thickness (EET) for the lithosphere. This elastic thickness was found to be about half the seismic or thermal thickness for the oceanic lithosphere (e.g. Walcott 1970, Watts and Cochran 1974, Watts et al. 1980) and so it can be concluded that only the upper, cooler part of the lithosphere can support long term elastic stresses. The lower lithosphere is expected to relax viscously over geological time, and Kusznir and Bott (1977) demonstrated that this relaxation leads to amplification of the stresses in the upper elastic layer. These observations have led to many other more complex models using viscoelastic (Nakada and Lambeck 1986), elastic-plastic (Turcotte et al. 1978) or other thermo-mechanical rheologies for the plates. However Lui et al. (1982) and

5

Karner (1984, 1985) have shown that a simple elastic model, combined with thermal effects, can produce behaviour normally associated with the more complex rheologies, and so the representation of lithospheric behaviour by flexure of an elastic plate remains a very useful approximation.

Flexure of the lithosphere is strongly dependent on the load. Short wavelength ($\leq$ 50 km) loads will be almost entirely supported by the rigidity, but to long wavelength ($\geq$ 1000 km) loads the lithosphere is virtually transparent and then the load is supported in effect by local isostasy. In conjunction with the elastic flexure the lithosphere suffers a great deal of non-elastic deformation. At shallow depth rocks may suffer brittle fracture when their strength is exceeded, generally described by modified Griffith theory (Jaeger and Cook 1976). Under tension the yield values of upper and lower crustal rocks are about 10 and 50 MPa respectively.

The overall seismic structure of the mantle is shown in figure 1.4. The S-wave velocity reaches a minimum between the base of the lithosphere and 220 km depth. This is the low velocity zone, probably the region where the mantle comes closest to melting, which is often regarded as the asthenosphere. The transition zone is marked by sharp increases in P- and S-wave velocities at 400 km and at 700 km. The lower mantle is relatively unstructured except for a slight flattening of the velocity curves near the core-mantle boundary (CMB). The seismic discontinuity at 400 km is a density discontinuity caused mainly by a solid state phase change. This has been reproduced in laboratory experiments recreating the discontinuous reaction from olivine + γ-spinel to β-phase spinel at 14 GPa pressure and a temperature of 1700 ($\pm$300) K (Jeanloz and Thompson 1983). This phase change is sufficiently sharp i.e. occurs over a narrow pressure and temperature range, to account for the observed sharpness of the seismic discontinuity.

The diamond-anvil cell experiments have also shown that the dominant minerals of the upper mantle (olivine, pyroxene and garnet) all transform to a silicate perovskite at lower mantle temperatures and pressures (Jeanloz and Morris 1986). Sufficient quantities of perovskite have been retrieved to allow its zero pressure density-temperature behaviour to be determined (Knittle et al. 1986). The perovskite cannot match the decompressed value of lower mantle density derived from seismological studies. Thus it has been suggested that the lower mantle is rich in iron or silica to account for the
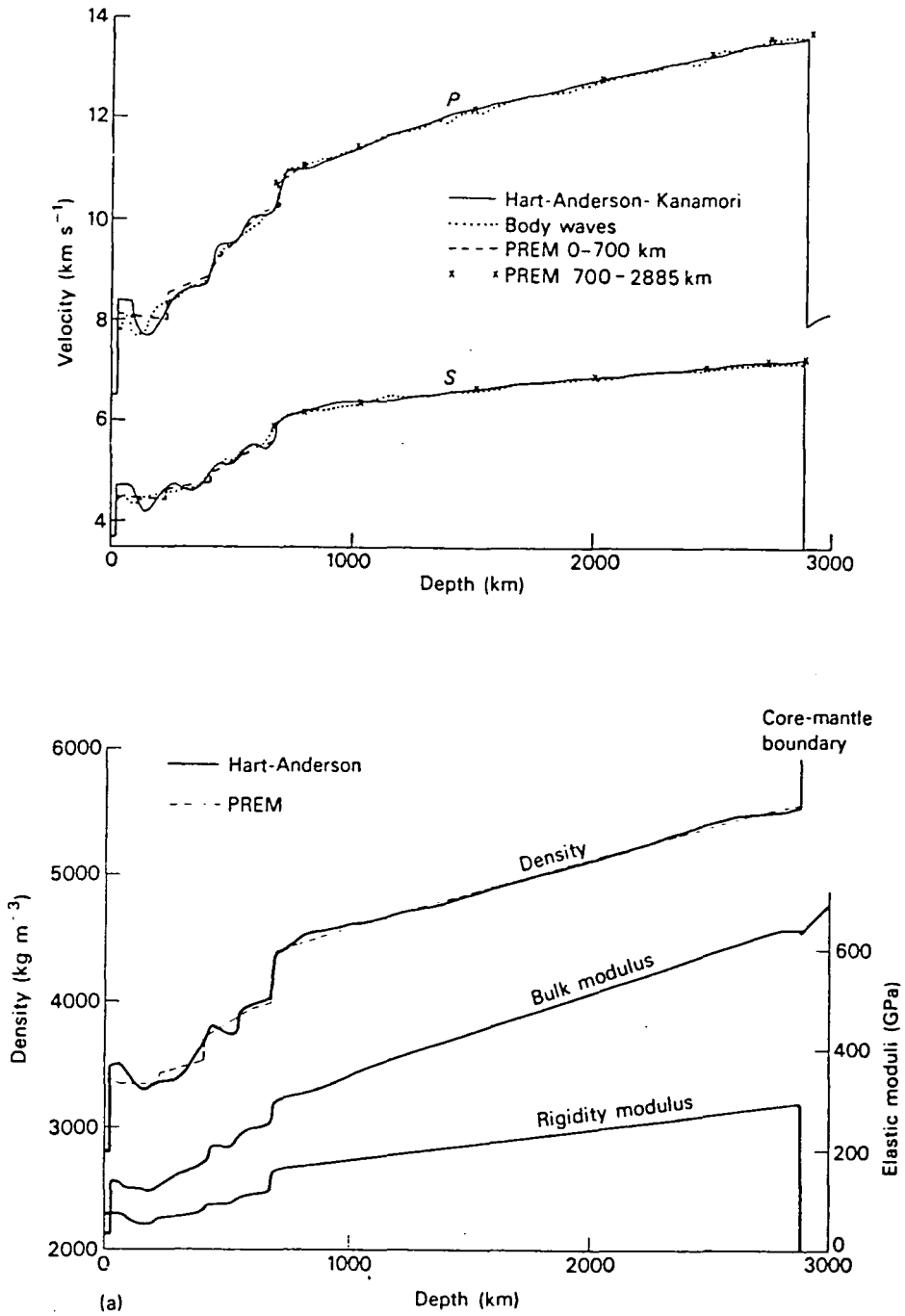
Figure 1.4 Global average seismologically determined properties of the Earth's mantle showing P and S velocities, and below density, bulk and rigidity moduli. From Bott (1984), original data compiled from Hart et al. (1977), Dziewonski and Anderson (1981), Burdick and Helmburger (1978), Helmburger and Engan (1974), Sengupta and Julian (1978), Anderson and Hart (1976).

density discrepancy.

There are many deviations from this average mantle structure, in particular in the vicinity of the subducting slab. The slab is cooler, and hence denser, than the surrounding mantle but additional body forces are generated by the elevated phase changes in the slab. shown in figure 1.5. The Clapeyron curve. which defines the phase change in $p - T$ space. has a positive slope $\gamma = 4$ MPa K^{-1} for the olivine-spinel transition. Since the slab is cooler the transition will occur at lower pressures and hence at a shallower depth. Schubert et al. (1975) estimated a maximum elevation of 115 km in the cool core of the slab, giving a fourfold increase in the body force for a density contrast of 240 kg m^{-3}. The elevated olivine-spinel phase boundary is probably a very significant factor in the mechanism of sinking lithosphere.

The deeper phase change to perovskite is predicted to have a small negative Clapeyron slope (Jeanloz and Morris 1986). At the phase boundary at 400 km depth the co-ordination number of Si remains at 4, but this deeper transition raises the coordination number to 6. The reorganisation of the oxygen nuclei could result in significant stress relief and thus explain the lack of seismic activity below this depth in the slab (Liu 1979).

Seismic probing of the deep interior yields the instantaneous. elastic properties of the Earth. However, over geological time the mantle undergoes solid state creep at extremely small strain rates. The dominant mechanisms at low stresses are probably diffusion creep or Coble creep. Diffusion creep describes the migration of atoms through the crystal's interior, but for Coble creep the diffusion takes place along the grain boundary. Macrophysically this is described by a Newtonian fluid, where strain rate $\dot{\varepsilon}$ is proportional to the stress σ and the constant of proportionality is the pressure-temperature dependent viscosity μ.

$$\dot{\varepsilon} = \mu \sigma$$

Crystal lattices are not perfect structures and the imperfections, the dislocations, facilitate creep. Two mechanisms are dislocation glide and dislocation climb, and they involve the diffusion of the additional nuclei, or holes. through the lattice. In the macrophysical model of dislocation creep the strain rate is proportional to a power n of the stress, this is non-Newtonian flow,

$$\dot{\varepsilon} \propto \sigma^n$$

7
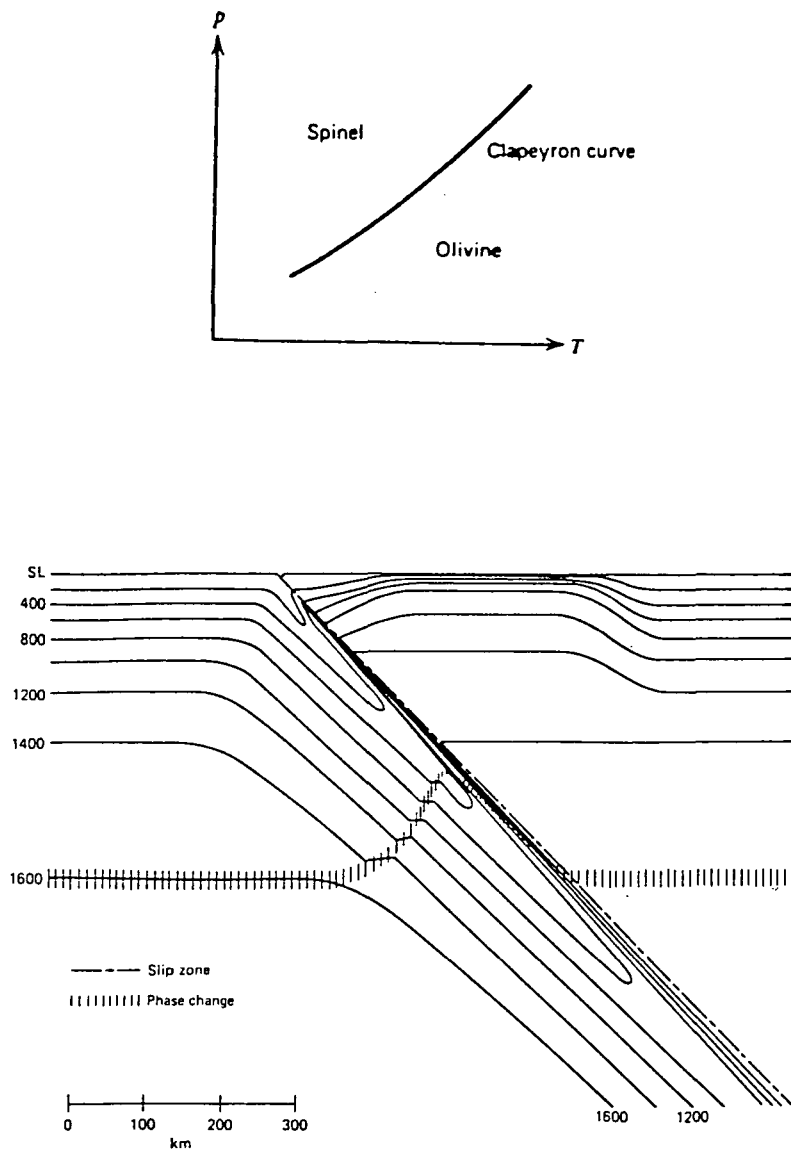
Figure 1.5   The Clapeyron curve delineates the phase change in $p - T$ space, and below, a typical isotherm distribution in descending lithosphere showing the elevated phase change in the cool slab. From Turcotte and Schubert (1982).

where commonly $n = 3$. The effective viscosity is defined by the ratio of stress to strain rate, which now becomes dependent on the stress aswell as being exponentially dependent on the pressure and temperature.

Flow in the hot, underlying mantle can be suitably represented by diffusion creep, but the deviatoric stresses in the lower lithosphere generate a highly non-Newtonian response. The exact rheology of the mantle is not known and for mathematical simplicity it is often modelled as a Newtonian fluid, and with considerable success (e.g. Cathles 1975, Peltier et al. 1978).

In order to investigate the long term response of the mantle the study of post-glacial rebound has become popular. Glaciation provided a significant long term load on the Earth which depressed the surface, but on relief of the load by glacial retreat the surface has been rising and recovering its pre-glacial configuration. Cathles (1975) made a world-wide study of post-glacial rebound and discussed at length the applicability of the self-gravitating Newtonian viscous sphere as a whole Earth model. The resulting viscosity-depth profile is shown in figure 1.6. However, the time-scale of post-glacial rebound, about 20000 yrs. is still considerably less than that characteristic of subduction, about 10^6 yrs. Peltier et al. (1986) attempted to reconcile the relatively low viscosity lower mantle inferred from rebound studies with the much higher viscosities required by microphysical models of solid state creep. They interpreted the low viscosity as a transient value, since in their Burgers body representation the elastic moduli become frequency dependent.

Further support for a higher viscosity lower mantle comes from Richards and Hager (1984) and Hager (1984) who studied the geoid anomalies due to mass anomalies in a self-gravitating Newtonian viscous body. The relative high in the geoid at subduction zones was well documented (e.g. Crough and Jurdy 1980. Chapman and Talwani 1982, Chase and McNutt 1982). Hager (1984) proposed that the lower mantle should be at least 30 times, and probably as much as 100 times, more viscous than the upper mantle in order to support the observed geoid.

In the subsequent 2-D mantle-wide subduction zone simulations the long term behaviour of the lithosphere will be modelled as an elastic upper layer overlying a viscoelastic lower layer. The mantle will be treated as a layered Newtonian body.

MANTLE DIVISIONS	η [poise]	$\Delta\rho_{NA}$ $\nabla\rho_{NA}$ [gm/cc]	ELASTIC PROPERTIES [dyne cm^{-2}]
LITHOSPHERE	∞	.6λ	D = 50 × 10^{23} N·m
Low Viscosity Channel	$04 × 10^{22}$		
UPPER MANTLE			
Phase Change Region	$1.0 \pm .1 × 10^{22}$	$\sim$0 ?	
LOWER MANTLE	$0.9 \pm .2 × 10^{22}$	0	Same as Haddon & Bullen HB$_1$ Model
		4.4	
CORE			

Depth into mantle [km]: ~70-150, 0, ~75, ~335, ~635, ~1000, ~2848
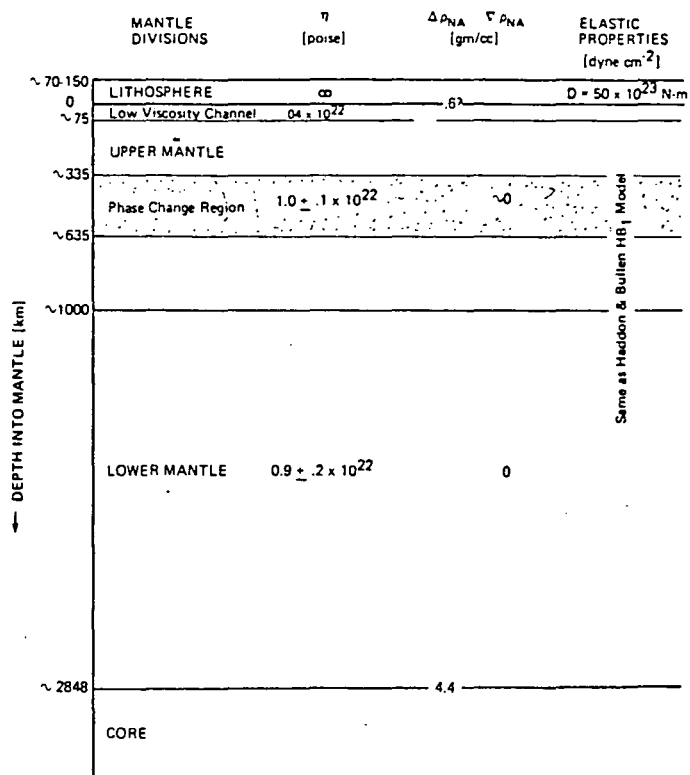
Figure 1.6   Schematic diagram of the varation of viscosity with depth in the mantle, derived from post-glacial rebound studies (10 poise = 1 Pa s). From Cathles (1975).

1.3 Driving Forces of Plate Motion

The driving mechanism of the motion of the lithosphere has frequently been attributed to forces acting at the plate boundaries. Plates are rigid and act as stress guides so that edge forces result in motion rather than deformation. Forsyth and Uyeda (1975) summarised the forces acting on a plate, see figure 1.7. The ridge push force arises from the gravitational energy generated by the thermal upwelling at mid-ocean ridges. Lister (1975) and Hager (1978) demonstrated that this force exists throughout the oceanic lithosphere that is continuously cooling and subsiding (Crough 1975). The slab pull force is the component of negative buoyancy of the cool descending slab which is transmitted to the surface. Other effects include the trench suction force which pulls the overriding plate towards the trench, asthenospheric drag. and continental collision. Forsyth and Uyeda presumed that the torques on the plate sum to zero, and the resulting analysis showed the slab pull contribution to be an order of magnitude greater than the ridge push. demonstrating the dominance of slab pull. Among the forces resisting plate motion. asthenospheric drag is greater under continental lithosphere than oceanic.

Carlson (1981, 1983) expanded on this idea: if plate motion is due to boundary forces then its speed is predictable from the known boundary elements. Using linear regression he produced an empirical equation successfully predicting the plate speeds (in cm yr^{-1}) from the proportion of ridge push (RP), slab pull (SP), trench suction (TS) and excess continental drag (CD) present in each.

$$v = (2.6 \pm 0.4) + (4.8 \pm 1.8)\text{RP} + (14.3 \pm 1.7)\text{SP} + (3.5 \pm 2.5)\text{TS} - (5.1 \pm 0.7)\text{CD}$$

The slab pull contribution is three times that of the ridge push. which is almost balanced by the excess continental drag, in line with Forsyth and Uyeda (1975). The trench suction force is small and not statistically significant. Carlson noted that the large positive constant term in the equation implies that lithospheric forces omitted from the regression all contribute a similar amount to each plate. The major omission is the non-continental asthenospheric drag (or pull), and Harper (1986) concluded that this is an important effect. As Carlson pointed out, correlation is not proof of causality and regression analysis is a somewhat circular argument. However, the success of the model encourages the notion of the driving mechanism as a system of boundary forces which are intimately dependent on the plate itself.
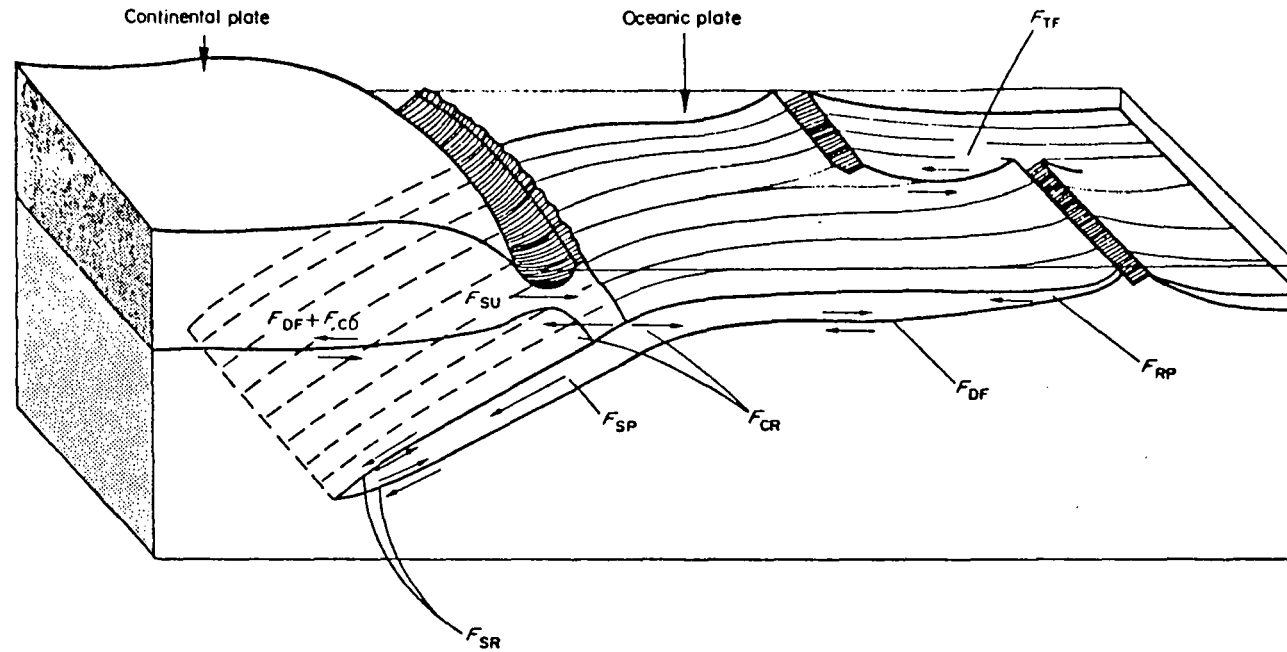
Figure 1.7   A summary of the forces acting on a plate. Briefly, F_{RP} is the ridge push force, F_{DF} is a drag force from the underlying asthenosphere, F_{SP} is the slab pull force, F_{SR} is the mantle resistance to slab motion, F_{SU} is the trench suction force. From Forsyth and Uyeda (1975).

The forces acting on the lithosphere generate stresses within it and the origin of the stresses was recently reviewed by Bott and Kusznir (1984). Stress systems are catalogued as renewable or non-renewable. Plate boundary forces and isostatically compensated loads are renewable stress sources since the forces, and stresses, persist over geological time. Bending, membrane, and thermally induced stresses can be dissipated by fracture and creep, will then no longer exist, and are thus non-renewable. Non-renewable stresses may dominate locally but it is the renewable stresses that are subject to stress amplification and control most of the tectonics. Wiens and Stein (1985) presented a small dataset (57 earthquakes) of intraplate seismicity, half of the data was taken from the Central Indian Ocean. The principal stresses derived from the focal mechanisms show that oceanic lithosphere > 35 Ma is in deviatoric compression. Wiens and Okal (1987) described additional tensional intraplate events but Haxby and Parmentier (1988) demonstrated that thermal stresses probably dominate the stress regime of oceanic lithosphere in ocean basins, and thus it is difficult to derive the tectonic stresses from the seismic evidence.

1.4 Convection in the Mantle

Sustaining the plate motion requires a great deal of energy. It is generally believed that the only viable source is the interior heat generated by radioactive decay combined with a gradual cooling of the Earth. A simple thermal convection model of the mantle is shown in figure 1.8. The efficiency of these thermodynamic engines for driving lithospheric plates is maximised for whole mantle convection but the exact mode that operates converting heat to work is not clear. The Rayleigh number of the mantle ranges between 10^2 and 10^4 times the critical Rayleigh number (e.g. Jarvis and Peltier 1982) and under these conditions the heat transport is dominated by thin boundary layers of the convection cell. The direct inference is that the lithosphere is a passive upper boundary layer.

Numerous numerical simulations of this type of thermal convection, the Rayleigh-Bénard cell, permeate the literature (e.g. McKenzie et al. 1974, Hansen and Ebel 1984a, 1984b, Boss and Sacks 1986, Jarvis and Peltier 1986) attempting to reconcile the geological and geophysical evidence. Recent work has concentrated on the question

10
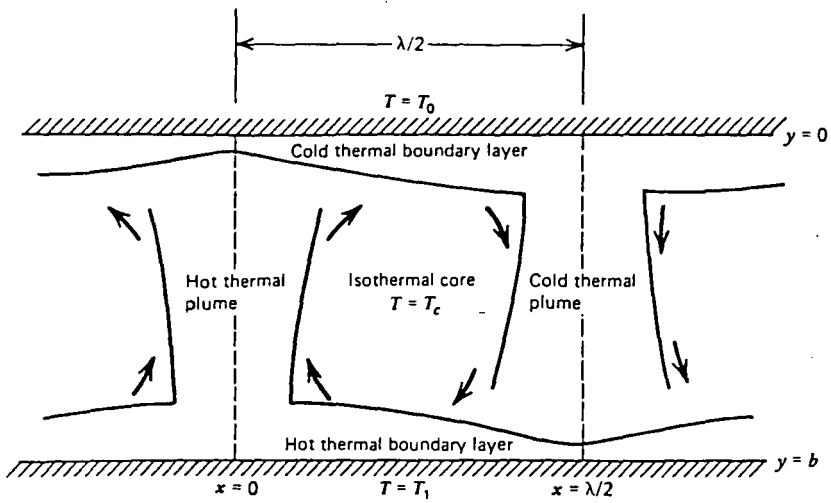
Figure 1.8   The simple two dimensional thermal convection cells generated in a
fluid heated from below and cooled from above. The high Rayleigh number
causes the boundary layers to develop and dominate the heat transfer. From
Turcotte and Schubert (1982).

of whether the present-day convection is mantle-wide or is layered. Christensen and Yuen (1984, 1985) showed that a compositional density contrast of 5% at 670 km depth is sufficient to deflect the slab, but this would produce observable topography at the boundary. A density contrast < 2 % allows complete slab penetration of the lower mantle. Only a highly endothermic phase transition $\gamma = -6$ MPa K^{-1} could enforce a 'leaky' two layer convection system.

The descending oceanic lithosphere is widely believed to penetrate the lower mantle from the seismic studies of high velocity regions immediately beneath subduction zones (e.g. Engdahl 1975, Jordan 1977, Creager and Jordan 1984, 1986, Silver and Chan 1986, Grand 1987) which are interpreted as aseismic extensions of the slab. Dziewonski (1984) and Woodhouse and Dziewonski (1984) presented a tomographic inversion of velocity heterogeneity in the mantle which shows fast regions of the lower mantle (in the depth range 1000 km to core-mantle boundary) that correspond to deep extrapolations of present-day subduction (Chase 1979, Hager et al. 1985). The calculations of slab assimilation by Wortel (1982, 1986) predict that the slab retains an elastic core down to the upper-lower mantle boundary. Shoino and Sugi (1985) also estimated assimilation time for subduction, assuming that it is related to cooling time for oceanic lithosphere. It is clear in the results that older lithosphere requires a much longer slab than indicated by the Wadati-Benioff zone, a further validation of slab extension into the lower mantle.

The geophysical evidence weighs in favour of whole mantle convection, but not of the simple Rayleigh-Bénard cell type. Loper (1985) presented a quite comprehensive discussion of the evidence, arguments and suppositions concerning mantle convection. He offered a solution in terms of two modes of convection, the primary mode is driven by the negative buoyancy of the slab at subduction zones, and the secondary mode takes the form of narrow, axisymmetric plumes rising from the core-mantle boundary (CMB). The primary mode flow is controlled by the viscosity-depth distribution. The cool, wide slab is strongly coupled to the viscous mantle and excites considerable flow in the surrounding mantle. The exact flow patterns will be decided by the 3-D interaction of flow created by subduction and other density heterogeneities such as ocean ridges and plumes.

Stacey and Loper (1983), Loper and Stacey (1983) and Loper (1984) provided the analytical framework of the D'' thermal boundary layer at the base of the mantle,

11

and the lower mantle plume. More recently Sleep (1987) added a simple analytical plume model in the same vein. Plumes are envisaged as narrow, about 20 km in diameter, axisymmetric vertical channels which carry hot, low viscosity material up to the surface with little or no coupling to the surrounding mantle. The plumes are fed from the D'' layer which itself is sustained by a bulk sinking of the lower mantle. The ascent of the plume material is terminated by the rigid lithosphere. At the surface the underlying plumes are evidenced by hot spots, and these are generally active volcanic islands centred on a topographic swell. The hot, low density plume material feeds the volcanicity. The mass deficit associated with the hot upper mantle supplemented by a positive fluid pressure at the top of the plume causes the up-arching of the lithosphere (Richards et al. 1987). The observed hot spot volcanics can only account for a few percent of the estimated mass flux of the plumes and so it is presumed that the material flows laterally in the asthenosphere. Loper (1985) estimated a layer 140 km thick would accumulate over the lifetime of the Earth assuming present day rates, and perhaps this is the source of the low velocity zone. This surface layer would originate from the bottom 280 km of the lower mantle leaving shallower material in the vicinity of the plume potentially untouched.

However, the mineral physics experiments discussed earlier suggest a slight compositional difference between the upper and lower mantle. This may cause some separation of the circulation at the 670 km discontinuity and the consequent formation of thin thermal boundary layers, but not strictly layered convection with a chemical boundary layer. This has implications for the mantle geotherm (Jeanloz and Morris 1986) causing the lower mantle to be hotter and the upper mantle colder than for whole mantle convection. This increases the thermal response time of the Earth. Kenyon and Turcotte (1983) modelled the development of thermal boundary layers due to two layer convection with no mass flux across the 670 km discontinuity. This analysis showed that the relatively hot lower mantle would possess an unacceptably low viscosity. In this respect the thermal arguments favour whole mantle convection.

The geochemical evidence is another important constraint on the evolution of the mantle (Davies 1984). Using isotopic and trace element data Hofmann et al. (1986) described the chemical history of the mantle in terms of two depletion events. The first event generated continental crust, depleting at least half of the primitive mantle.

The residual mantle may or may not be remixed and homogenised. The second event involves the formation of oceanic crust in the form of present-day plate tectonics. The isotopic character of mid-ocean ridge basalts (MORB) is unique and fairly constant over the Earth (Zindler and Hart 1986), and the MORB source region is generally considered to be the uppermost upper mantle. Subduction returns the oceanic lithosphere, that is the enriched oceanic crust and its depleted mantle component. back into the mantle. It is generally believed (e.g. Davies et al. 1988) that subducted crust forms the main source of ocean island basalts (OIB) at hot spots, since OIB has distinct isotopic and trace element characteristics that are most readily explained this way.

At first glance the geophysical, geochemical and mineral physics evidence are not compatible. However, if all are accepted at face value, there emerges the possibility of partial decoupling of the thermal and chemical systems involved in mantle evolution. Subduction must take oceanic crust down to the chemical boundary layer at the CMB, which then rises as narrow plumes to form hot spots. However, the volume of material produced by the plumes must be much less than that estimated by Loper (1985) to prevent contamination of the MORB source region. At the 670 km discontinuity the cold, dense. rigid slab will plunge through into the lower mantle. but the induced flow will be partially decoupled. The induced flow will create some mass flux across the upper - lower mantle boundary but it will be inhibited by the compositional difference (which may occur at a much greater depth). Thus thin thermal boundary layers may form about the discontinuity.

These are very tentative assertions about the mode of present-day convection in the mantle. In the context of this thesis subduction assumes the role of principal driving force of plate motion and flow in the mantle, with deep mantle penetration controlled by the viscosity-depth distribution. The next section discusses the cause-and-effect relationships which help to determine the dynamics of subduction. an understanding of which is crucial to the understanding of mantle evolution.

1.5   Aspects of Subduction Zone Dynamics

The mechanics and dynamics of subduction will be discussed with reference to a 2-D cross-section since the numerical models of this thesis are two dimensional. Where

appropriate, the 3-D influences will be included as an acknowledgement of the need to include sphericity when discussing subduction tectonics. Despite the assertions of Uyeda (1982) that 'comparative subductology' is the only useful analysis of subduction, it is apparent that 2-D generalisations can provide an important description of the behaviour and development of convergent margins. So, following a brief account of the overall mechanism of subduction, each feature typical of subduction will be described in more detail, incorporating some of the relevant previous numerical analyses.

1.5.1   The Mechanism of Subduction

The highly simplified cross-section in figure 1.9 portrays the more significant properties of subduction zones. The slab, defined here as the lithosphere below 90 km depth, carries a mass anomaly which generates a body force acting in the direction of the gravitational field. This can be resolved into two components, one acting downdip and one acting perpendicular to the slab.

The downdip component of slab motion has received a considerable amount of attention in the literature. Davies (1980, 1981, 1983) assessed the downdip force balance to determine the relative magnitude of forces opposing subduction and the net stress distribution in the slab. The force balance occurs in the mantle: the downdip slab force is opposed by in-plate tension at the top of the slab, viscous shear resistance at the slab sides, and resistance to penetration at the leading edge. The viscous shear is the dominant reactive force. Davies (1983) modelled shear resistance in an isoviscous mantle ($\mu = 10^{21}$ Pa s) and argued that the resulting compression (1 GPa) in the lower sections of the slab would exceed slab strength and thus the system of resistive forces was untenable. The estimated large compressions may arise because the calculations assume that the slab tip reaches an impenetrable boundary at depth, which the overburden rests on. The slab tip is likely to be ductile after a long residence time in the mantle and thus the overburden pressure will cause deformation flow of the leading edge (Fischer et al. 1988) which may transmit much less compression back up the slab. Davies (1983) demonstrated that increasing shear resistance from a more viscous mantle ($\mu = 4 \times 10^{21}$ Pa s) reduces the slab stresses to a more acceptable value (300 MPa), and so perhaps simple shear resistance in an isoviscous mantle is not adequate. These presumptions require some detailed modelling to determine the precise effects.
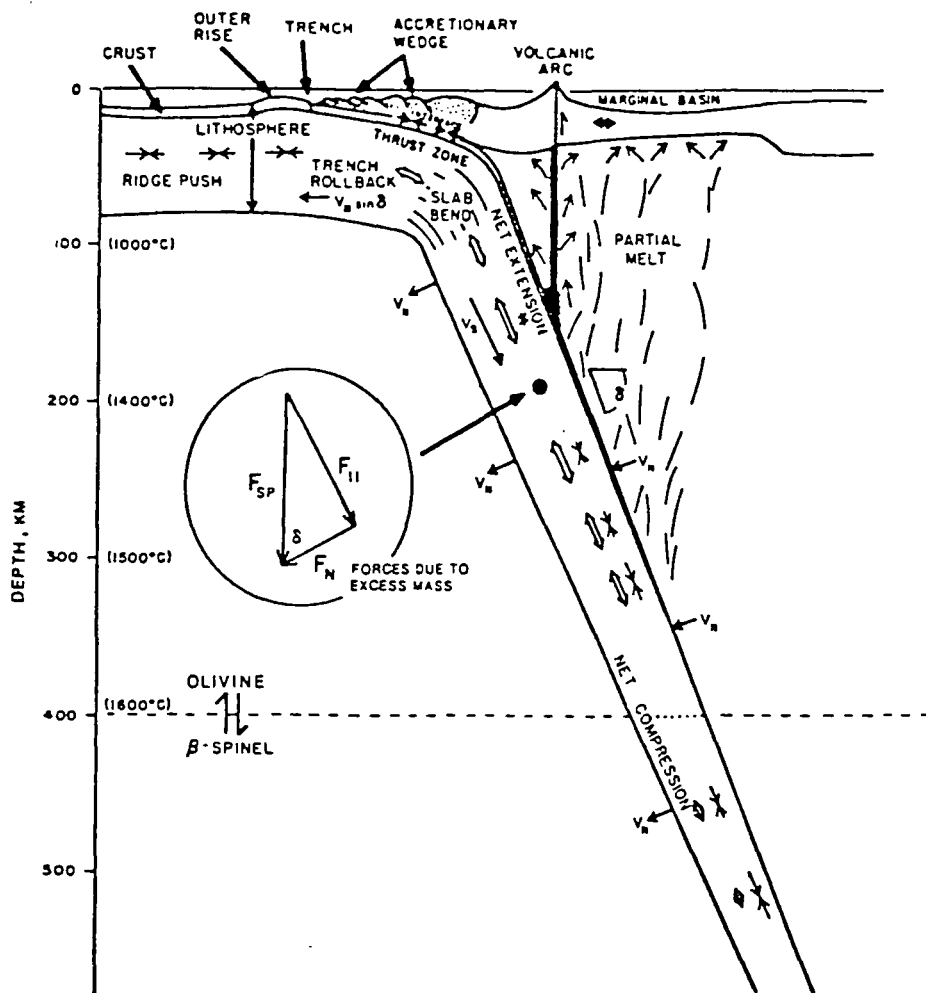
Figure 1.9 A cross-section through a typical subduction zone defining the main
system of forces and major features of the subduction process. The body force
of the excess density of the slab is resolved downdip and perpendicular to the
slab. From Spence (1987).

The in-plate tension at the top of the slab is coupled to the surface subducting plate through the slab bend region. The vertical component of this tension holds the trench down out of isostatic equilibrium, and creates the flexural response of the outer rise. Horizontal tension is transmitted along the subducting plate, dragging it into the trench. This is a major contribution to the slab pull force of the plate driving mechanism. The numerical models of the stress regime at subduction zones in this thesis will attempt to elucidate the origin of the plate driving forces. The large mass deficit of the trench creates an isostatic reaction to the downpull. This is spatially offset from the in-plate tension, generating an enormous bending couple at the top of the slab. This is the origin of the large increase in curvature of the subducting plate at the slab bend region.

The component of negative buoyancy perpendicular to the slab causes rollback, a retrograde motion in which the slab and trench migrate seawards e.g. Carlson and Melia 1984). Garfunkel et al. (1986) proposed that slab migration is the major control of the time and space dependence of mantle flow and estimated the average rollback velocity to be 20 mm yr^{-1}. Over the vast surface area of subducted slabs this motion will cause a considerable mass flux, comparable to that at the ocean ridges. Davies (1981, 1983) noted that this motion will be coupled to the overriding plate through the viscous mantle, inducing a broad downwarping about 1 km deep. This correlates well with observations of depth anomalies in the Western Pacific marginal basins (Louden 1980). Around 70-90% of the magnitude of observed geoid anomalies in the backarc could be explained by this depression.

The negative buoyancy of the slab tends to rotate the descending lithosphere towards the vertical. This is contradictory to the present-day data of slab dips, displayed in figure 1.10. As Jarrard (1986) pointed out, subducting slabs appear to show a general shallowing of dip with duration of subduction. The concept of corner flow was originally applied by McKenzie (1969) to provide a mechanism of maintaining slab dip. In the mantle wedge above the slab the downdip motion drags away material which cannot be replaced because the overriding plate is stationary relative to the trench. This creates a pressure difference across the slab counteracting the gravitational forces. This mechanism was restated by Stephenson and Turner (1977) and extended to include non-linear rheology by Tovish et al. (1978). There is a relative geoid high at the
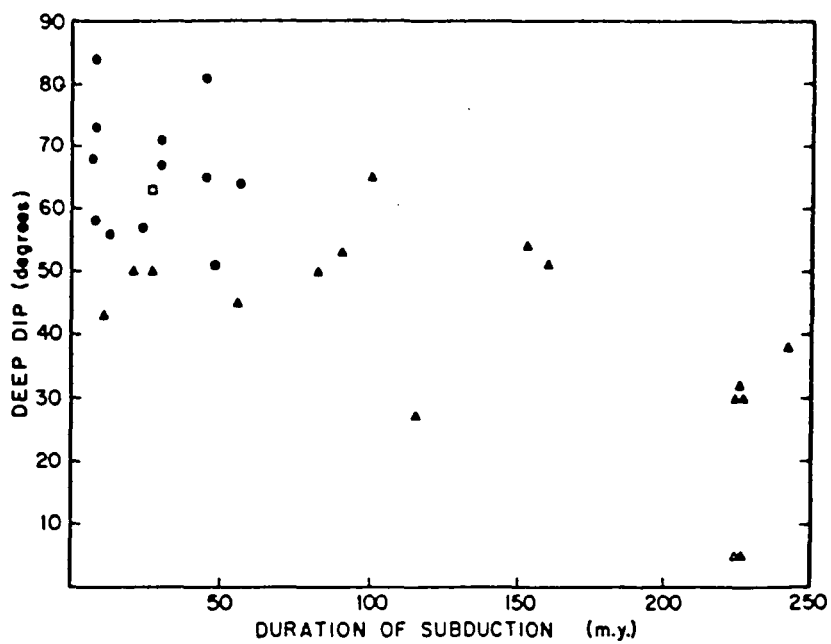
Figure 1.10   A cross-plot of slab dip in the depth range 100 → 400 km against
duration of subduction. The slab dip tends to shallow with duration of sub-
duction. From Jarrard (1986).

trench (Crough and Jurdy 1980, McAdoo 1981) and McAdoo (1982) managed to generate correct geoid slopes using highly non-linear corner flow. Hager 1984) has since demonstrated the origin of geoid highs at convergent margins due to the viscosity-depth variation, and Willemann and Anderson (1987) successfully modelled geoid slopes due to vertical subduction of an inextensible slab in a layered Newtonian mantle.

The pressure difference across the slab produced by corner flow falls off with distance downdip. Willeman and Davies (1982) compared this corner flow support with the integrated slab force normal to the dip. These calculations showed that different variation downdip (of the two opposing mechanisms) creates large torques which the slab could not endure. Corner flow support is proportional to the effective viscosity which is predicted to be low in the mantle wedge. So, the evidence weighs against corner flow as the dominant mechanism of slab support.

Bott (1988) calculated that a pressure deficit of 10 MPa in the mantle wedge would provide significant support to the descending slab against the rotational forces. This pressure low could be produced and dynamically sustained by continuous rollback causing lateral flow in the asthenosphere. Global flow will probably locally modify the specific effect of the basic mechanism. Whilst the dynamic flow pressure may maintain a particular slab dip, it is rather more unlikely to cause shallowing. A possible mechanism for shallowing involves slab penetration of a high viscosity lower mantle. The slab tip will move more slowly through the lower mantle than the upper mantle rollback, and thus the longest subducting slabs may tend to shallow.

The numerical models of Gurnis and Hager (1988) predict vertical subduction until the slab tip collides with the top of the lower mantle. Ongoing subduction then causes a shallowing of dip as the slab tip interacts with the more viscous lower mantle. This cannot explain the observed variation of dip among the shallowest Benioff zones except by aseismic extension of the slab in the upper mantle.

1.5.2 Controlling Factors of the Subduction Process

Conductive cooling models of the oceanic lithosphere (Crough 1975), as it migrates away from the ridge and isostatically subsides, show that it is cooler and denser than the underlying asthenosphere. Numerical predictions of slab isotherms, combined with estimates of the coefficient of thermal expansion, yield an average thermal density

anomaly of approximately $\Delta\rho = 50 \ \text{kg} \ \text{m}^{-3}$ for the descending lithosphere at subduction zones. As subduction progresses, conductive heating spreads the thermal anomaly and so the effective density anomaly may be reduced with distance downdip, but this is slow compared to the time constant of convection. Hence as a good approximation for numerical models (Willemann and Anderson 1987) the density anomaly will generally persist throughout the length of the slab. Kincaid and Olsen (1987) suggested that the ratio of density anomalies in the upper and lower mantle is an important control.

The low temperature of the slab will cause mineral phase changes to occur at different depths relative to the surrounding mantle. The discontinuities at 400 km and 670 km depth were discussed previously (see section 1.3). In numerical implementations the olivine-spinel transition is represented by additional body forces above 400 km depth in the slab. Anderson (1987) proposed that the lateral temperature anomaly of the slab causes isobaric phase changes, increasing the density anomaly further (figure 1.11). The increased mass anomaly and velocity of the slab may then negate the requirement of slab extension into the lower mantle.

Isacks and Molnar (1971) completed the first global study of earthquake generating stresses deduced from focal mechanism solutions of intermediate and deep focus earthquakes. That survey has been updated recently by Vassiliou (1984) and Apperson and Frohlich (1987) using the newly available moment tensor inversion data, resulting in very little alteration to the initial conclusions. The diagram in figure 1.12 portrays the variation of number of earthquakes with depth. The histogram has a distinct minimum at 250-300 km depth, many more earthquakes occur at a shallow depth than below 300 km. The deep focus earthquakes are predominantly downdip compression, with 50% of P-axes lying within 28° of slab dip. The intermediate depth earthquakes, in the range 90 — 300 km, have a regional variation and the principal stress axis is not well aligned downdip, but in general terms downdip tension prevails in both deep and shallow penetrating slabs. However, Apperson and Frohlich (1987) calculated that, in a global sense, less than 30% of focal mechanisms fit this general pattern.

The longest subducting slabs roughly follow the average earthquake distribution but a notable exception is the Tonga slab which is almost entirely compressional throughout its length (Giardini and Woodhouse 1984). Double seismic zones are the best documented departure from the average earthquake profile (Fujita and Kanamori

ρ_o, g/cm^3

3.0 3.2 3.4 3.6 3.8 4.0 4.2

Pressure, kbar

100

—400 km

β + mj s.s.
—+cpx

200

2 pv + gt + mw

—670 km

3 pv + mw

300

a + opx + cpx + gt

2β + st + gt
+ cpx

2γ + st + gt
+ cpx

ilm s.s.+
gt + mw
+ Ca–pv

$\overline{T}$ $\overline{T}$– 800 °C
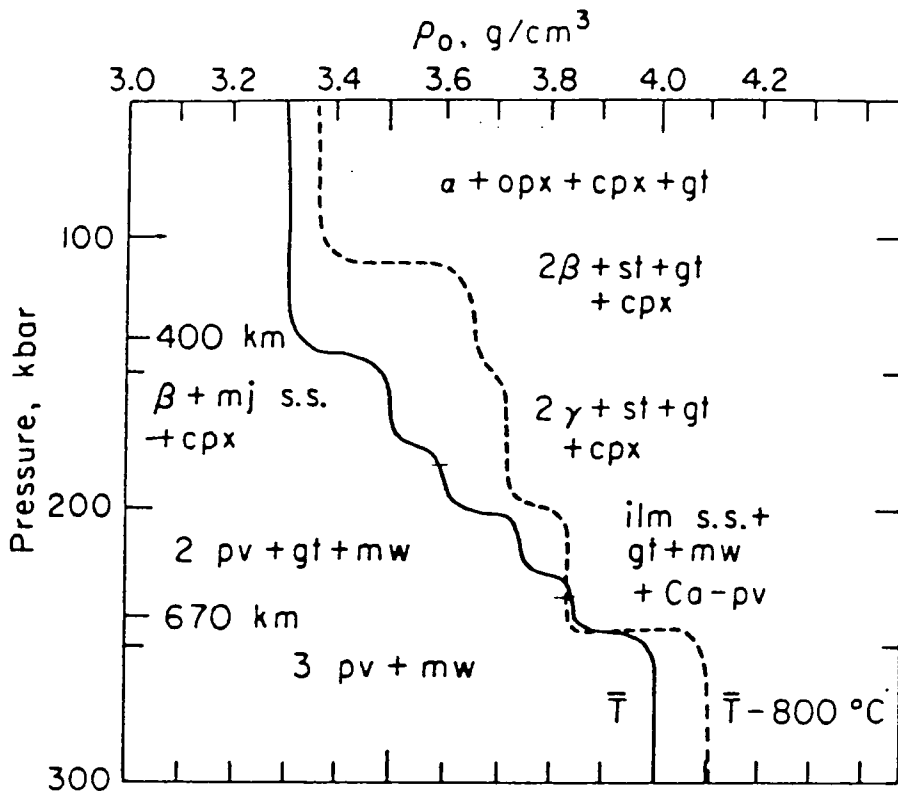
Figure 1.11   The density-depth distribution in a descending slab produced by the isobaric phase changes proposed by Anderson (1987).
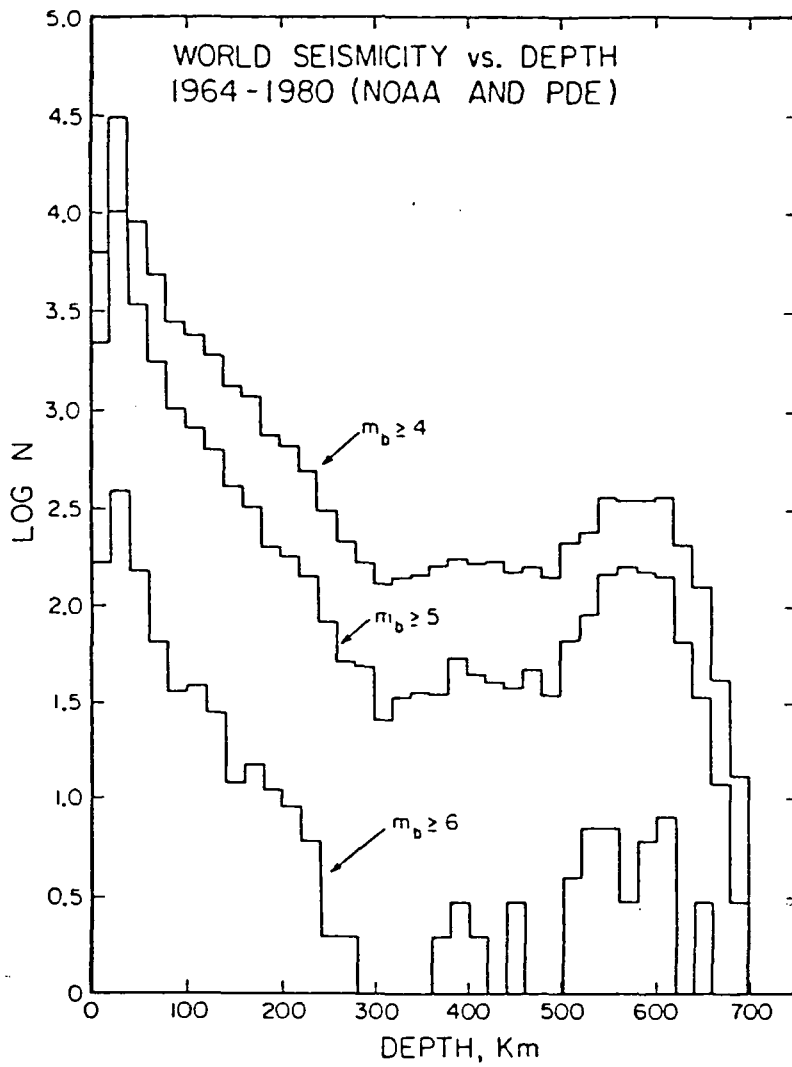
Figure 1.12   A histogram of the logarithm of number of earthquakes plotted
against depth of hypocentre. The linear portion of the curve is evidence of an
exponential decrease in number of earthquakes with depth. From Vassiliou et
al. (1984).

1981) but the recent surge in discoveries (e.g. Samowitz and Forsyth 1981, Reyners and Coles 1982, House and Jacob 1983, Suzuki et al. 1983, Kawakatsu 1986a) suggests that the double seismic zone might well be the normal mode of intermediate earthquake distribution (Kawakatsu 1986b). The most convincing double seismic zones are observed in the depth range 60 — 200 km in slabs with dips 30° − 45° and are characterised by two layers of seismicity. Compressional mechanisms dominate the top layer near the surface of the slab, and tensional earthquakes make up the lower layer about 30 km further into the slab. Fujita and Kanamori (1981) note that double seismic zones persist over a large depth range, and hence a long time, and thus discount unbending stresses and phase changes as the sole mechanisms. Sleep (1979) suggested a model of a slab sagging under its own weight, the low viscosity mantle above the slab relaxes quickly allowing compressive stresses to develop in the upper surface. The lower layer of in-plate tension persists as it is near the neutral fibre of the bending moment. A displacement of 2 km is probably sufficient sagging to create the required stresses and this would be indistinguishable for current earthquake location accuracies (± 5 km).

The physical mechanism of deep earthquakes is not well understood. The volume change in high pressure polymorphic phase transitions would not produce the observed double-couple mechanisms, but a variation on this theme by Kirby (1987) has again lent credence to this notion. The earthquake generating stresses in the slab can be of mechanical or thermal origin. Phase changes serve to magnify both of these effects with an increase in buoyancy and the latent heat release. Hamaguchi et al. (1983) and Goto et al. (1985) used a finite element method to evaluate the thermal stresses induced by conductive heating of the slab, including the latent heat release of the olivine-spinel transition (using a non-linear Clapeyron curve). The thermal stresses dominated the mechanical stress field, but did not correlate well with the stress distribution derived from the average earthquake profile. Vassiliou et al. (1984) studied the mechanical stress distribution generated by a viscous slab sinking under its own weight into a layered Newtonian mantle. A viscosity increase of ×25 at 670 km depth approximately reproduces the observed stress field. However, this is indistinguishable from the stress regime generated by higher viscosity contrasts or an impenetrable boundary. The inclusion of the body forces of the elevated olivine-spinel transition in the slab was discovered to be incompatible with the observed stresses. Neither study could account for double

seismic zones. Spherical shell tectonics analysed by Yamaoka et al. (1986) and Yamaoka (1988) are an important addition to the stress field.

The slab bend region connects the descending slab to the surface plate (Spence 1986, 1987). It is characterised by a marked increase in curvature of the lithosphere with little associated seismicity. This occurs at about 40 km depth, roughly coinciding with the basalt-eclogite phase change in the oceanic crust of the descending plate. This transforms the initially buoyant crust to a high density phase. Bending will thin the crust and the phase change leads to a volume reduction and more plastic behaviour which may aid any possible decoupling from the overriding plate. Thus the onset of the slab bend region could define the end of the brittle fracture zone and help to explain the lack of large magnitude thrust earthquakes below 40 km depth. The descending lithosphere must pass through the slab bend and potentially is severely fractured and deformed. This could influence the mechanical and chemical interaction with the asthenosphere.

The thrust zone is the site of the largest magnitude thrust earthquakes. It does not contribute directly to the force balance in the mantle, but it serves to redistribute the stresses in the surface plates. The nature of the contact across the thrust zone is not well understood. Ruff and Kanamori (1980, 1983) suggested a distribution of large asperities in the fault zone to account for the large magnitude earthquakes and the nature of aftershocks. The asperities could be due to surface features of the subducting plate or due to variations in contact length and angle along the fault line. However, it is difficult to predict the amount of sediment subduction and the behaviour of the crust which may contribute to the properties of the thrust zone (Peterson and Seno 1984, Kostoglodov 1988).

Ridges and seamounts are the largest topography of the seafloor and attempted subduction will generate a very large asperity which may temporarily halt subduction in that region. Locking-up one segment of a subduction zone will have a dramatic effect on the stress regime, with a large component of regional horizontal compression being transmitted across the fault (Waghorn 1984). For an elastic plate the compression would be transmitted throughout the plate length causing considerable vertical motion. Wortel and Cloetingh (1986) showed that flexural basins in the centre of the plates will suffer significant uplift as the regional stress field becomes compressive.

Free-air gravity anomalies seaward of convergent margins follow the seafloor topography indicating that the trench and outer rise are held out of isostatic equilibrium. The flexure can be modelled to a first approximation by an elastic layer of age-dependent thickness, 100 Ma lithosphere has an effective elastic thickness (EET) of 30 km (Watts and Talwani 1974, Watts 1982). However, some outer trench slopes have high curvatures which are best described by flexure of a lithosphere with an elastic core and an outer plastic layer (Turcotte et al. 1978). The bending stresses fracture the crust under tension to form graben blocks which trap sediment for subsequent subduction (Hilde and Sharman 1978, Wortel and Cloetingh 1986). The weight of the accretionary prism, and possibly the forearc, are additional loads on the subducting plate which will modify the surface flexure.

The dominant features of the forearc are the accretionary prism, the structural high and forearc basin, which may or may not be present at a particular margin. In the nomenclature of Seely (1979), the residual forearc basin is considered to be typical of major forearc basins. The evolution is shown in figure 1.13. The basement and the initiation of the structural high is remnant oceanic or transitional lithosphere (Kiechefer et al. 1980, Lewis and Hayes 1984), and its inception must have some flexural control. Subsequent evolution is dependent on accretion, understuffing and compressional failure. The forearc is controlled by compressional tectonics. The Lesser Antilles is an example of a non-typical structural high. Since the basement spur is small the Barbados Ridge has developed by growth of a huge accretionary prism (Westbrook and Brown 1986). The isostatic gravity anomaly over the Lesser Antilles forearc complex is strongly negative showing that the system is depressed by the action of subduction (Westbrook and McCann 1980, Westbrook et al. 1984).

Tharp (1985) modelled shallow subduction to investigate forearc basin evolution using finite element methods. This produced 5 km structural highs and forearc basins a few kms deep, which are greatly in excess of the observed. This discrepancy in magnitude is attributed to the method used; viscous strain rate was defined as an elastic strain distributed over a small time period.

The volcanic front of arc volcanism always lies above the point where the Wadati-Benioff zone reaches 100-150 km depth. There is no volcanism seaward of this. Uyeda (1986) reviewed two possible sources of arc volcanism, diapiric rise due to melting, and

RESIDUAL FOREARC BASIN SEDIMENTS

ABYSSAL PLAIN, TRENCH, AND SLOPE
SEDIMENTS, DISMEMBERED OPHIOLITES
AND LOW-T, HIGH-P METAMORPHICS

TRENCH WEDGE SEDIMENTS

ABYSSAL PLAIN SEDIMENTS

OCEANIC BASEMENT &
"BASALTIC CONTINENTAL"
SUBSTRATUM

ARC MASSIF & SED. COVER
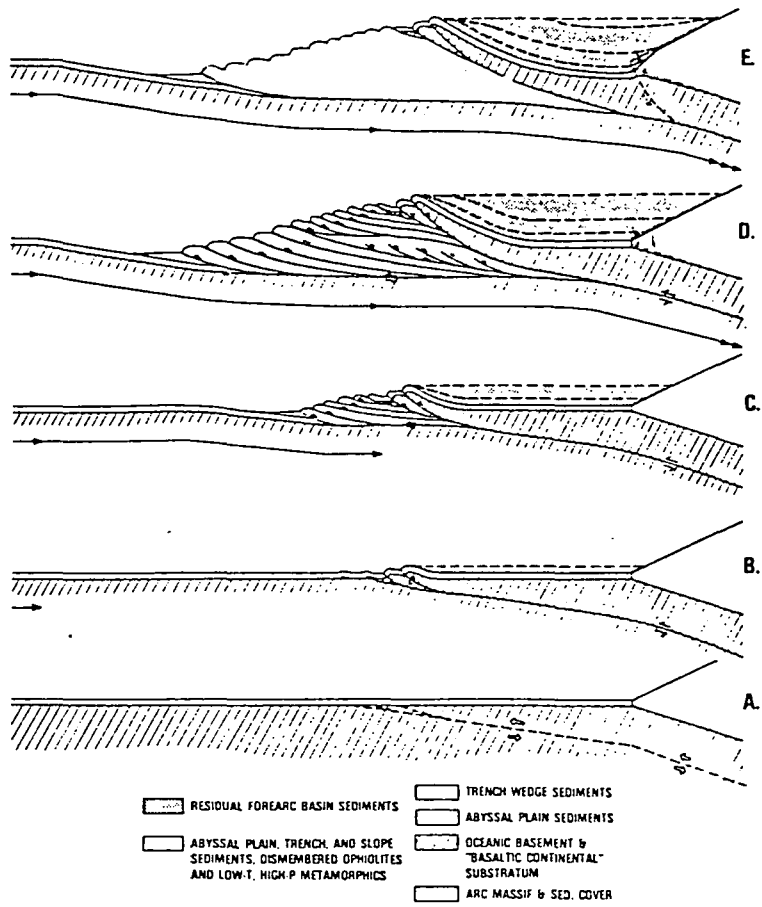
Figure 1.13   The evolution with time of a typical residual forearc basin. From
Seely (1979).

induced flow above the slab (Andrews and Sleep 1974, Achayra 1981, Honda 1985). The downdip motion induces convection in the mantle wedge, the material rises adiabatically and partially melts in response to the drop in pressure. The melt is buoyant and is released at the highest point of the flow, where the surface lithosphere is ablated and intruded by the melt. Experimental evidence implies that high temperatures (1400 °C) are necessary in the mantle wedge (Tatsumi et al. 1983). This induced flow model is supported by the absence of volcanism in the South American Cordillera where there is no underlying mantle wedge.

The backarc of convergent margins has been catalogued by Taylor and Karner (1983) and Brookes et al. (1984), among others, and classified by strain regime by Jarrard (1986) and by stress-gradient by Nakamura and Uyeda (1980). There is a complete gradation of strain regimes from the highly extensional with active backarc spreading e.g. Marianas, through the neutral regimes e.g. Lesser Antilles. to the highly compressive of North and South Chile.

Dewey (1980) presented a vector analysis of absolute horizontal motion of the plates. relating backarc and forearc tectonics to the resultant of trench rollback and overriding plate motion. Extensional backarcs occur when rollback is faster than the advance of the overriding plate, neutral backarcs arise when both move at a similar rate. and compressional backarcs are created when the overriding plate advances faster than the trench rollback. Oblique motion creates strike-slip features and terrane motion. Thus the model requires a change in overriding plate motion or rollback velocity to affect the tectonics. For instance, a decrease in rollback velocity due to younger lithosphere at the trench can transform an extensional to a compressional backarc. This absolute motion model can explain most, but not all, of the variation in the tectonics of the overriding plate.

Backarc spreading appears to have a limited lifetime < 17 Ma. a change in plate motions can cause an immediate cessation of spreading but there is a time lag of 6-10 Ma before spreading resumes elsewhere (Jurdy and Stefanick 1983). Proposals for the mechanism of backarc spreading can be divided into either active or passive groups (Uyeda 1986). Active mechanisms include the induced flow driving spreading (e.g. Andrews and Sleep 1974, Toksoz and Hsui 1978, Hsui and Toksoz 1981, Ida 1983, Jurdy and Stefanick 1983, Vanpé 1984). Induced convection in the mantle wedge above

the slab produces hot, buoyant rising material about 300-400 km from the trench. The buoyancy forces create small tensions of about 20 MPa in the surface plate (Jurdy and Stefanick 1983) and these would be expected at all backarcs unless the induced convection is modified by global flow. Passive mechanisms of backarc spreading include the absolute motion model of Dewey (1980) and the 3-D buckling hypothesis of Yamaoka et al. (1986) and Fukao et al. (1987). As rollback progresses the arc grows, and backarc opening initiates to accommodate the increasing area enclosed by the evolving arc. This buckling mechanism can account for the limited size of the backarc basins, but again it inherently implies that this should happen at all convergent margins.

Sclater (1972), Sclater et al. (1976), Watanabe et al. (1977) and Louden (1980) noted that the marginal basins of the western Pacific have a negative depth anomaly of approximately 1 km relative to the Pacific Ocean. The free-air gravity anomalies are generally small and positive (< 50 mgal).

The existence of remnant arcs at the far side of the backarc spreading centres implies that spreading was initiated at the arc. This is the hottest, weakest part of the overriding plate, intruded and fractured by magma injection. The loading of the volcanic arc and the underlying compensatory hot, buoyant magma will generate horizontal deviatoric tensions in the lithosphere. In combination with the absolute motion of the overriding plate this could overcome the local compression in the forearc to induce a split. This accounts for the time lag to initiate spreading after subduction begins. Once initiated, spreading can propagate by a number of mechanisms discussed above, and can be terminated also.

Throughout the whole of the preceding discussion subduction has been treated as a continuous phenomenon. One of the major problems of tectonics is the initiation of subduction, the rupture process which permits oceanic lithosphere to re-enter the mantle is not well understood. Cloetingh et al. (1982) investigated the evolution of passive margins and found that ageing alone is not sufficient to initiate subduction without a pre-existing zone of weakness. The most suitable condition was sediment loading of a young passive margin. Transform faults, separating lithosphere of differing ages, are possible sites for inducing subduction in oceanic lithosphere. Fujimoto and Tomoda (1985) used finite element models of viscous flow to model the development of subduction at a transform fault, and showed the older lithosphere thickening and

descending under the fault line.

1.6   Aims of the Study

The 2-D finite element simulations of this thesis use a highly simplified model of subduction. Varying the parameters of the models will give a quantitative assessment of the effect of the parameter on each of the features of subduction zones described above. From this a generalised picture of the mechanics and dynamics of a subduction zone and its role in global tectonics can be constructed.

CHAPTER 2

The Finite Element Method

The finite element method has been widely used for stress analysis in engineering applications but it is a highly versatile numerical tool and can also be applied to fluid flow, heat conduction and convection, and electric and magnetic potential problems. The basis of the method is to divide a continuum into a number of finite elements which are defined by nodes on the element boundary. Each element is assigned the relevant properties such as Lamé parameters, viscosity, conductivity, to approximate the real body. Under a given set of conditions we can solve for the unknown variable such as displacement, velocity, temperature, at the nodes which approximates the continuum response. Solution accuracy increases as the element mesh is refined and with higher order elements we can define how the variable field behaves across the element, whether it is linear, quadratic, cubic etc. This study uses the 2-dimensional, quadratic, isoparametric Serendipity element, in the form of 8-node quadrilaterals and 6-node triangles. The elements have 2 degrees-of-freedom (dof) at each node which define the variable field: for elasticity problems these are the x and y displacements and for fluid flow problems these are the x and y velocities, in Cartesian space. Serendipity elements ensure that the unknown variable is continuous across the element boundaries, but any derivatives will be discontinuous; this is C_o continuity.

The following two sections are essentially a summary of the techniques developed by Waghorn (1984) for elastic and viscoelastic behaviour where further details may be found. The final section is an extension of the previous work to produce a finite element code for viscous, incompressible flow. The purpose of this chapter is solely to present the theory of finite element analysis, as it is applicable to studies of global geodynamics, and in particular the subduction process. A full discussion of the implementation of this theory is given in the next chapter, where the previous problems of faulting and thermal anomalies are addressed, and benchmark studies of fluid flow analyses are used to determine the accuracy of the viscous flow finite element program.

24

2.1 The Quadratic Isoparametric Formulation

2.1.1 Shape Functions

The element nodes define the two basic qualities of an element,

- nodal coordinates $\{c\}$ define the global coordinates of a point in the element interior through the interpolating shape functions $[\tilde{N}]$.

$$\{x\} = [\tilde{N}]\{c\} \tag{2.1}$$

- nodal dof $\{d\}$ define the vector of the domain variable at a point in the element interior through the interpolating shape functions $[N]$,

$$\{u\} = [N]\{d\} \tag{2.2}$$

An element is isoparametric if the nodes defining $\{c\}$ and $\{d\}$ are identical and the shape functions $[\tilde{N}]$ and $[N]$ are also identical. The quadratic Serendipity elements are shown in figure 2.1. In the local coordinate space (ξ, η) the elements are straight-sided of unit dimension. The mapping into the global Cartesian space (x, y) allows curve-sided elements to be used to model the complex body geometries whilst the calculations are performed in the local coordinate space. Considerable distortion of the elements is possible as long as the one-to-one correspondence of the transformation from Cartesian to curvilinear space is maintained.

The mapping is contained within the element shape functions. The quadratic polynomial interpolation in the triangular element which defines the global coordinates of a point from the local coordinates of that point can be written.

$$x(\xi, \eta) = a_1 + a_2\xi + a_3\eta + a_4\xi^2 - a_5\eta^2 + a_6\xi\eta \tag{2.3}$$

$$y(\xi, \eta) = b_1 + b_2\xi + b_3\eta + b_4\xi^2 - b_5\eta^2 + b_6\xi\eta \tag{2.4}$$

where a_i, b_i are the nodal coefficients. This can be written as,

$$x = [C]\{a\}, \qquad y = [C]\{b\}$$

where,

$$[C] = [1 \quad \xi \quad \eta \quad \xi^2 \quad \eta^2 \quad \xi\eta]$$

25
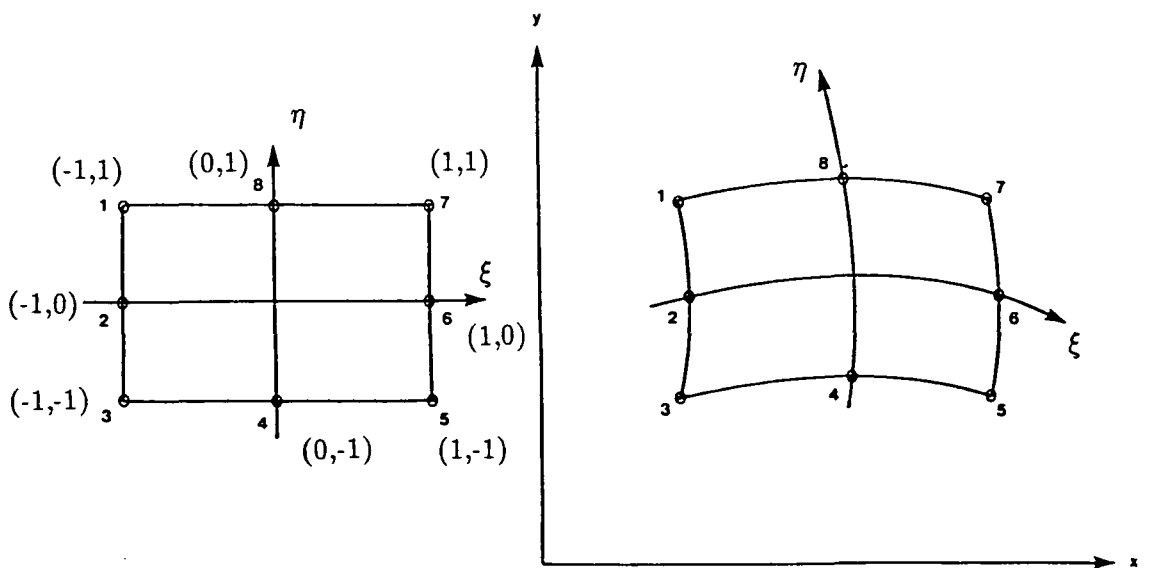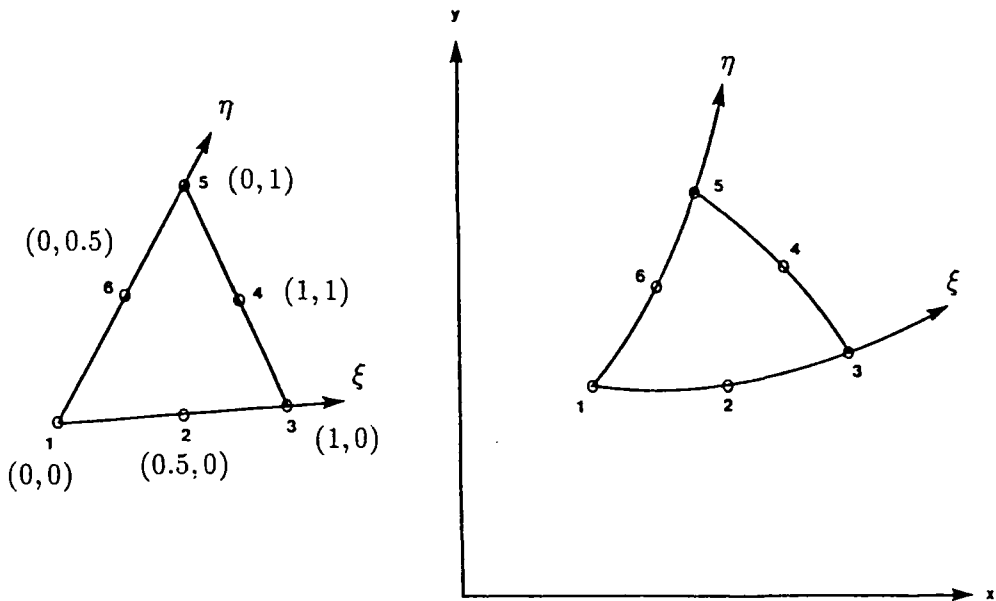
Figure 2.1   The six-node triangular element in local (ξ, η) and global (x, y) co-ordinate space, and below, the eight-node quadrilateral element in local (ξ, η) and global (x, y) coordinate space.

$$\{a\}^T = \{a_1 \quad a_2 \quad a_3 \quad a_4 \quad a_5 \quad a_6\}, \quad \{b\}^T = \{b_1 \quad b_2 \quad b_3 \quad b_4 \quad b_5 \quad b_6\}$$

The local coordinates are known so then substituting the values for the x-coordinate gives,

$$x_1(0,0) = a_1$$

$$x_2\left(\frac{1}{2},0\right) = a_1 + \frac{a_2}{2} + \frac{a_4}{4})$$

$$x_3(1,0) = a_1 + a_2 + a_4$$

$$x_4\left(\frac{1}{2},\frac{1}{2}\right) = a_1 + \frac{a_2}{2} + \frac{a_3}{2} + \frac{a_4}{4} - \frac{a_5}{4} + \frac{a_6}{4}$$

$$x_5(0,1) = a_1 + a_3 + a_5$$

$$x_6\left(0,\frac{1}{2}\right) = a_1 + \frac{a_3}{2} + \frac{a_5}{4}$$

which can be written,

$$\{c\} = [A]\{a\}$$

and inverting this,

$$\{a\} = [A]^{-1}\{c\}$$

Hence the x-coordinate of a general point can be written,

$$x = [C][A]^{-1}\{c\}$$

thus the shape functions which define a coordinate from the nodal values are,

$$[N] = [C][A]^{-1} \tag{2.5}$$

in full,

$$N_1 = 1 - 3\xi - 3\eta + 2\xi^2 - 2\eta^2 - 4\xi\eta$$

$$N_2 = 4\xi - 4\xi^2 - 4\xi\eta$$

$$N_3 = 2\xi^2 - \xi$$

$$N_4 = 4\xi\eta$$

$$N_5 = 2\eta^2 - \eta$$

$$N_6 = 4\eta - 4\eta^2 - 4\xi\eta$$

The y-coordinates yield an identical result, and by definition the shape functions for the field variable are identical. Local derivatives are obtained by differentiating the shape functions. then evaluating the derivative at the point in the element, for example,

$$\frac{\partial x}{\partial \eta} = \sum_{i=1}^{6} \frac{\partial N_i}{\partial \eta} x_i \tag{2.6}$$

26

The process outlined above will generate the shape functions for a quadrilateral element using the following quadratic polynomial,

$$x(\xi, \eta) = a_1 + a_2\xi + a_3\eta + a_4\xi^2 + a_5\eta^2 + a_6\xi\eta - a_7\xi^2\eta + a_8\xi\eta^2 \qquad (2.7)$$

$$y(\xi, \eta) = b_1 + b_2\xi + b_3\eta + b_4\xi^2 + b_5\eta^2 + b_6\xi\eta - a_7\xi^2\eta + a_8\xi\eta^2 \qquad (2.8)$$

and the resulting shape functions are,

$$N_1 = \frac{1}{4}\left(-1 + \xi^2 + \eta^2 - \xi\eta + \xi^2\eta - \xi\eta^2\right)$$

$$N_2 = \frac{1}{2}\left(1 - \xi - \eta^2 + \xi\eta^2\right)$$

$$N_3 = \frac{1}{4}\left(-1 + \xi^2 + \eta^2 + \xi\eta - \xi^2\eta - \xi\eta^2\right)$$

$$N_4 = \frac{1}{2}\left(1 - \eta - \xi^2 + \xi^2\eta\right)$$

$$N_5 = \frac{1}{4}\left(-1 + \xi^2 - \eta^2 - \xi\eta - \xi^2\eta - \xi\eta^2\right)$$

$$N_6 = \frac{1}{2}\left(1 + \xi - \eta^2 - \xi\eta^2\right)$$

$$N_7 = \frac{1}{4}\left(-1 + \xi^2 + \eta^2 + \xi\eta + \xi^2\eta - \xi\eta^2\right)$$

$$N_8 = \frac{1}{2}\left(1 + \eta - \xi^2 - \xi^2\eta\right)$$

2.1.2   The Jacobian Matrix

The global derivatives of the variable field defined over the finite element domain are required. The chain rule gives the local differential operators.

$$\frac{\partial}{\partial\xi} = \frac{\partial x}{\partial\xi}\frac{\partial}{\partial x} + \frac{\partial y}{\partial\xi}\frac{\partial}{\partial y}$$

$$\frac{\partial}{\partial\eta} = \frac{\partial x}{\partial\eta}\frac{\partial}{\partial x} + \frac{\partial y}{\partial\eta}\frac{\partial}{\partial y}$$

which can be written in matrix form and inverted to give the global derivatives,

$$\begin{bmatrix} \dfrac{\partial}{\partial x} \\ \dfrac{\partial}{\partial y} \end{bmatrix} = [J]^{-1} \begin{bmatrix} \dfrac{\partial}{\partial\xi} \\ \dfrac{\partial}{\partial\eta} \end{bmatrix}$$

where the inverse Jacobian operator,

$$[J]^{-1} = \begin{bmatrix} \Gamma_{11} & \Gamma_{12} \\ \Gamma_{21} & \Gamma_{22} \end{bmatrix} = \frac{1}{\det J} \begin{bmatrix} \dfrac{\partial y}{\partial\eta} & -\dfrac{\partial y}{\partial\xi} \\ \dfrac{\partial x}{\partial\eta} & \dfrac{\partial x}{\partial\xi} \end{bmatrix} \qquad (2.9)$$

and detJ is the determinant of the Jacobian.

2.1.3 Numerical Integration

Global integrations over distorted elements are simplified by the transformation into local coordinate space. The integral of the function f over the specified area can be calculated from,

$$I = \int\int f \, dx\,dy = \int\int f \, \det J \, d\xi\, d\eta \qquad (2.10)$$

Integrals must be evaluated numerically and the Gauss-Legendre quadrature of the function f in 2-dimensions is given by,

$$I = \sum_{i=1}^{m} \sum_{j=1}^{n} W_i W_j \, f(\xi_i, \eta_j) \det J \qquad (2.11)$$

where ξ_i, η_j are the local integration points in the elements and W_i, W_j are the associated weighting functions. It is most common for $m = n$. In one-dimensional Gauss-Legendre quadrature, if the function f is a polynomial then n sampling points will exactly integrate a polynomial of degree $2n - 1$. However the order of integration and the location of Gauss points which yields the best results for a particular element is not immediately obvious. Barlow (1976) discussed the optimal stress locations for some popular finite elements in elasticity and discussions in Cook (1981), Zienkiewicz (1977) and Segerlind (1976) show that 4-pt integration in quadrilaterals and 6-pt integration in triangles is sufficiently accurate.

2.2 The Variational Method for Elasticity

2.2.1 The Strain Matrix

In an elastic continuum the strain is the first spatial derivative of the displacement and for 2-D analysis the in-plane strain at a point can be written,

$$\begin{pmatrix} \varepsilon_x \\ \varepsilon_y \\ \gamma_{xy} \end{pmatrix} = \begin{pmatrix} \dfrac{\partial u}{\partial x} \\[2mm] \dfrac{\partial v}{\partial y} \\[2mm] \dfrac{\partial u}{\partial y} + \dfrac{\partial v}{\partial x} \end{pmatrix}$$

where u, v are the x, y components of displacement interpolated from the nodal values using the shape functions, $[N]\{d\}$. The differential operators have been derived,

equation 2.9, so the strain can be defined by,

$$\{\varepsilon\} = [B]\{d\}$$ (2.12)

where,

$$[B] = \begin{bmatrix} \Gamma_{11} & \Gamma_{12} & 0 & 0 \\ 0 & 0 & \Gamma_{12} & \Gamma_{22} \\ \Gamma_{21} & \Gamma_{22} & \Gamma_{11} & \Gamma_{12} \end{bmatrix} \begin{bmatrix} \dfrac{\partial}{\partial \xi} & 0 \\ \dfrac{\partial}{\partial \eta} & 0 \\ 0 & \dfrac{\partial}{\partial \xi} \\ 0 & \dfrac{\partial}{\partial \eta} \end{bmatrix} [N]$$ (2.13)

2.2.2 The Elasticity Matrix

In linear elastic solids the stress is proportional to the strain giving the general stress-strain relation.

$$\{\sigma\} = \begin{Bmatrix} \sigma_x \\ \sigma_y \\ \tau_{xy} \end{Bmatrix} = [C](\{\varepsilon\} - \{\varepsilon_0\}) - \{\sigma_0\}$$ (2.14)

where $[C]$ is the elasticity matrix, $\{\varepsilon_0\}$ are the initial strains, and $\{\sigma_0\}$ the initial stresses.

Hookes' law in two dimensions for the case of plane strain in which $\{\varepsilon_z\} = 0$ is,

$$\varepsilon_x = \frac{(\sigma_x - \nu\sigma_y - \nu\sigma_z)}{E} + \varepsilon_{x_0}$$

$$\varepsilon_y = \frac{(-\nu\sigma_x + \sigma_y - \nu\sigma_z)}{E} + \varepsilon_{y_0}$$

$$\gamma_{xy} = \frac{2(1 + \nu)}{E} \tau_{xy} + \gamma_{xy_0}$$

where the elasticity constants ν is Poisson's ratio, E is Young's modulus. Rearranging these equations into the form of equation 2.14 gives the elasticity matrix,

$$[C] = \frac{E}{(1 + \nu)(1 - 2\nu)} \begin{bmatrix} 1 - \nu & \nu & 0 \\ \nu & 1 - \nu & 0 \\ 0 & 0 & \dfrac{(1 - 2\nu)}{2} \end{bmatrix}$$ (2.15)

with initial strains.

$$\{\varepsilon_0\} = \begin{Bmatrix} \varepsilon_{x_0} + \nu\varepsilon_{z_0} \\ \varepsilon_{y_0} + \nu\varepsilon_{z_0} \\ \gamma_{xy_0} \end{Bmatrix}$$

and the out-of-plane stress,

$$\sigma_z = \nu(\sigma_x + \sigma_y) - E\sigma_{z_0}$$

29

Other formulations which could be used are plane stress $\sigma_z = 0$, or a lithostatic z-stress. This latter formulation allows both stress and strain in the out-of-plane z-direction, but constrains the stress to be lithostatic by,

$$\sigma_z = \frac{\sigma_x + \sigma_y}{2}$$

The elasticity matrix can be evaluated by substituting into the constitutive relations above to give,

$$[C] = \frac{E}{(1+\nu)(1-2\nu)} \begin{bmatrix} 1 - \dfrac{\nu}{2} & \dfrac{3\nu}{2} & 0 \\ \dfrac{3\nu}{2} & 1 - \dfrac{\nu}{2} & 0 \\ 0 & 0 & \dfrac{(1-2\nu)}{2} \end{bmatrix} \tag{2.16}$$

The advantage of this formulation is that the deviatoric stresses in the z-direction are identically zero.

2.2.3 The Stiffness Matrix

The equations controlling the elastic response of a body are derived using the variational method, which is possibly the simplest and most physically meaningful approach. The method entails summing the potential energy of the body, due to the body forces $\{b\}$, surface forces $\{q\}$, and the accumulated strain energy, and minimising this with respect to the displacements. The approximation of the finite element method is that the variations are restricted to a finite number of parameters i.e. the number of nodes in the body (see Zienkiewicz 1977).

Let the total potential energy of the volume of the continuum be,

$$\Pi = W + U$$

where the work done by the applied loads in response to the virtual displacements $\{u\}$ is,

$$
\begin{aligned}
W &= \int \{u\}^T \{b\}\, dV \;+\; \int \{u\}^T \{q\}\, dA \\
&= \int \{d\}^T [N]^T \{b\}\, dV \;+\; \int \{d\}^T [N]^T \{q\}\, dA
\end{aligned} \tag{2.17}
$$

and the strain energy is,

$$
\begin{aligned}
U &= \frac{1}{2} \int \{\varepsilon\}^T \{\sigma\}\, dV \\
&= \frac{1}{2} \int \{d\}^T [B]^T [C][B]\{d\}\, dV \;-\; \int \{d\}^T [B]^T [C]\{\varepsilon_0\}\, dV \\
&\quad + \int \{d\}^T [B]^T \{\sigma_0\}\, dV
\end{aligned} \tag{2.18}
$$

30

Using matrix and tensor calculus the minimisation of,

$$\frac{\partial \Pi}{\partial \{d\}} = 0$$

gives,

$$[K]\{d\} = \{F\} \qquad (2.19)$$

where $[K]$ is the stiffness matrix and $\{F\}$ is the global force vector. For a unit thickness in the z-direction the stiffness matrix becomes,

$$[K] = \int [B]^T [C][B] \; dx \, dy \qquad (2.20)$$

and the force vector is.

$$\{F\} = \{f_{\varepsilon_0}\} - \{f_{\sigma_0}\} - \{f_b\} - \{f_q\} \qquad (2.21)$$

where,

$$\{f_{\varepsilon_0}\} = \int [B]^T [C]\{\varepsilon_0\} \; dx \, dy \qquad (2.22)$$

$$\{f_{\sigma_0}\} = \int [B]^T \{\sigma_0\} \; dx \, dy \qquad (2.23)$$

$$\{f_b\} = \int [N]^T \{b\} \; dx \, dy \qquad (2.24)$$

$$\{f_q\} = \int [N]^T \{q\} \; dS \qquad (2.25)$$

The stiffnesses are evaluated element-by-element and assembled into the global stiffness matrix. The assembly process is a simple summation of element contributions at each node, and the resulting global matrix is symmetric. A comprehensive and rigorous discussion of this derivation can be found in most finite element texts (e.g. Zienkiewicz 1977).

2.2.4 Dirichlet Boundary Conditions

The previous finite element analyses of Mithen (1980), Park (1981) and Waghorn (1984) used the Payne-Irons approximation to apply Dirichlet boundary conditions. The nodal displacement has a prescribed value $u_i = \bar{u}$ which is imposed as follows: replace the diagonal term of the stiffness matrix K_{ii} by $K_{ii} X$ and the row of the force vector F_i by $K_{ii} X \bar{u}$ where X is a large positive constant. This approximation simply weights the equation to the value $u_i = \bar{u}$. It is a useful method since it preserves the

symmetry of the global stiffness. However, a more exact representation of boundary conditions may be required and an alternative method is outlined in section 2.3.5.

2.2.5 Nodal Forces

The gravitational field g acting on a volume element of density ρ generates the body force vector.

$$\{b\} = \begin{Bmatrix} \rho g_x \\ \rho g_y \end{Bmatrix}$$

where g_x, g_y are the components of g acting in the x- and y-directions. The body force vector is directly substituted into equation 2.24.

Surface loads act only on an element edge and it is convenient to re-define the three edge nodes as a one-dimensional isoparametric edge element with a separate local coordinate system, as shown in figure 2.2. As before, the global coordinates of a general point are interpolated from the nodal values using the local coordinate shape functions $[\bar{N}]$,

$$\{x\} = [\bar{N}]\{c\} \tag{2.26}$$

where the shape functions written in full are,

$$\bar{N}_1 = \frac{\xi}{l}\left(\frac{2\xi}{l} - 1\right)$$

$$\bar{N}_2 = 1 - \frac{4\xi^2}{l^2}$$

$$\bar{N}_3 = \frac{\xi}{l}\left(\frac{2\xi}{l} + 1\right)$$

Surface loads will generally be prescribed in the form of normal and shear stresses, $\{q_{sn}\}$. Resolving these at a point in Cartesian space,

$$\begin{Bmatrix} q_x \\ q_y \end{Bmatrix} = \begin{bmatrix} \cos\alpha & -\sin\alpha \\ \sin\alpha & \cos\alpha \end{bmatrix} \begin{Bmatrix} q_s \\ q_n \end{Bmatrix} = R' \begin{Bmatrix} q_s \\ q_n \end{Bmatrix}$$

where from figure 2.2,

$$[R'] = \begin{bmatrix} \dfrac{\partial x}{\partial \xi} & -\dfrac{\partial y}{\partial \xi} \\ \dfrac{\partial y}{\partial \eta} & \dfrac{\partial x}{\partial \eta} \end{bmatrix} \tag{2.27}$$

the matrix components are the local derivatives obtained from the shape functions.

Hence, for the complete edge element,

$$\{q\} = [R]\{q_{sn}\}$$

32
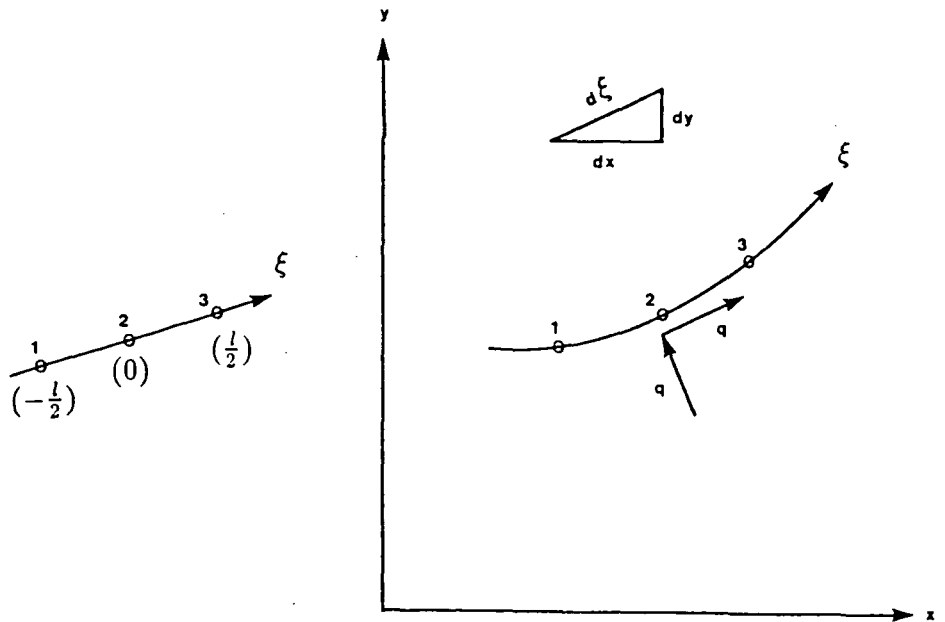
Figure 2.2   The three-node isoparametric edge element in local and global coordinate space. The normal q_n and shear q_s surface tractions act perpendicular or tangential to the element in both coordinate systems. The insert at the top shows the relationship between ξ and (x, y) space required to evaluate the rotational transformation.

where,

$$[R] = \begin{bmatrix} R' & 0 & 0 \\ 0 & R' & 0 \\ 0 & 0 & R' \end{bmatrix}$$

$$\{q_{sn}\}^T = \{q_{s_1} \quad q_{n_1} \quad q_{s_2} \quad q_{n_2} \quad q_{s_3} \quad \ldots\}$$

and so the elemental contribution to the force vector evaluated in the local coordinate space is,

$$\{f_q\} = \int [\bar{N}]^T [R]\{q_{sn}\}\, d\xi \tag{2.28}$$

since the determinant of the rotation is one. This integral is evaluated numerically using three-pt one-dimensional Gauss-Legendre quadrature.

2.2.6 Isostatic Compensation

Boundaries which represent density discontinuities will generate a reaction to any perturbation, or displacement across them, in the direction of the gravitational field. Lithospheric behaviour is often modelled as a thin, elastic layer overlying an inviscid, fluid substratum. An inviscid fluid reacts instantly to deformation and supports no viscous stresses, so the reaction to the deformation will be the buoyancy of the displaced fluid,

$$\rho_{fluid}\mathbf{g}U'$$

where U' is the displacement in the direction of the gravitational field $\mathbf{g}$. The buoyancy forces will act normal to the element edge and can be written,

$$\{q_{sn}\} = \rho_{fluid}[g][\bar{N}]\{d\} \tag{2.29}$$

where $\{d\}$ is the displacement and the gravitational field matrix $[g]$ is,

$$[g] = \begin{bmatrix} 0 & 0 & 0 & 0 & 0 & 0 \\ g_x & g_y & 0 & 0 & 0 & 0 \\ 0 & 0 & 0 & 0 & 0 & 0 \\ 0 & 0 & g_x & g_y & 0 & 0 \\ 0 & 0 & 0 & 0 & 0 & 0 \\ 0 & 0 & 0 & 0 & g_x & g_y \end{bmatrix}$$

Substituting in equation 2.25 using the results from the previous evaluation of surface tractions gives,

$$\{f\} = [K_I]\{d\} \tag{2.30}$$

where the isostatic stiffness matrix is,

$$[K_I] = \int \rho_{fluid}[\bar{N}]^T [R][g][\bar{N}]\, d\xi \tag{2.31}$$

33

The isostatic stiffness matrix is assembled element-by-element and then subtracted from the global stiffness matrix. This destroys the symmetry of the global stiffness.

2.2.7 Thermal Stresses

The thermal anomaly of an element produces an anomalous temperature field which generates a non-renewable stress system. This is incorporated in the finite element method as an initial strain. In 2-D, the thermal strain is.

$$\{\varepsilon_0\} = (1 + \nu) \left\{ \begin{array}{c} \alpha\,\Delta T \\ \alpha\,\Delta T \\ 0 \end{array} \right\} \tag{2.32}$$

where α is the thermal expansion coefficient, ΔT is the temperature anomaly. This is included in the global force vector by substitution in equation 2.22. The final stress field is then calculated from,

$$\{\sigma\} = [C]\,(\,\{\varepsilon\} - \{\varepsilon_0\}\,) \;+\; \{\sigma_0\}$$

where, for plane strain the z-stress is,

$$\sigma_z = \nu(\sigma_x + \sigma_y) - E\,\alpha\,\Delta T$$

A full discussion of the effects of a thermal anomaly in an elastic-viscoelastic body can be found in the next chapter.

2.2.8 Viscoelasticity

A viscoelastic material subject to a force field undergoes instantaneous elastic deformation followed by viscous relaxation of the deviatoric stresses. The relaxation rate is controlled by the Maxwell time.

$$t_m = \frac{2\mu}{E} \tag{2.33}$$

where μ is the viscosity and E is the Young's modulus.

The strain rate at a point in a Maxwell body depends on the deviatoric stresses which can be written.

$$\{\dot\varepsilon\} = \left\{ \begin{array}{c} \dot\varepsilon_x \\ \dot\varepsilon_y \\ \dot\gamma_{xy} \\ \dot\varepsilon_z \end{array} \right\} = \frac{1}{2\mu} \left\{ \begin{array}{c} \sigma_x - \sigma_r \\ \sigma_y - \sigma_r \\ 2\tau_{xy} \\ \sigma_z - \sigma_r \end{array} \right\} \tag{2.34}$$

34

where σ_h is the hydrostatic pressure, defined by,

$$\sigma_h = \frac{1}{3}(\sigma_x + \sigma_y + \sigma_z)$$

For the case of plane strain the z-strain must be zero, but deviatoric z-stresses may exist. To overcome this, a fictitious elastic z-strain is introduced which is equal and opposite to the calculated viscous z-strain.

Viscoelastic behaviour is modelled by the initial strain approach (Zienkiewicz 1968). Over a small time increment Δt the strain can be approximated by,

$$\{\varepsilon_0\} = \{\dot{\varepsilon}\}\Delta t$$

which is considered to be an initial strain. Substitution in equation 2.22 yields an additional component to the force vector, and thus the equations can be resolved for the next time increment.

The final stress system at the end of the time-marching relaxation is given by,

$$\{\sigma\} = [C](\{\varepsilon\} - \{\varepsilon_0\}) + \{\tau_0\}$$

The detailed algorithm can be found in Park (1981) and Mithen (1980).

2.2.9 Fault Elements

Fault elements are introduced into the mesh via the dual node approach. The mesh is divided into two bodies whose contact nodes are spatially coincident along the fault section. The stiffnesses of the two halves of the mesh are assembled into the global stiffness and then the elastic properties of the one dimensional fault elements which join the halves are added.

The local coordinate system of a fault element of length l is given in figure 2.3. The shape functions are defined identically for the nodes either side of the fault line (as equ. 2.26).

$$\bar{N}_1 = \bar{N}_4 = \frac{s}{l}\left(\frac{2s}{l} - 1\right)$$

$$\bar{N}_2 = \bar{N}_5 = 1 - \frac{4s^2}{l^2}$$

$$\bar{N}_3 = \bar{N}_6 = \frac{s}{l}\left(\frac{2s}{l} + 1\right)$$

35
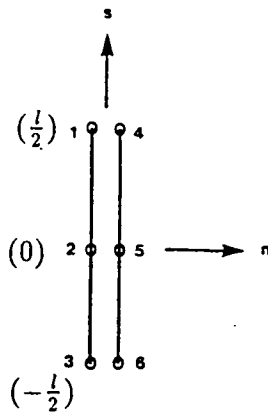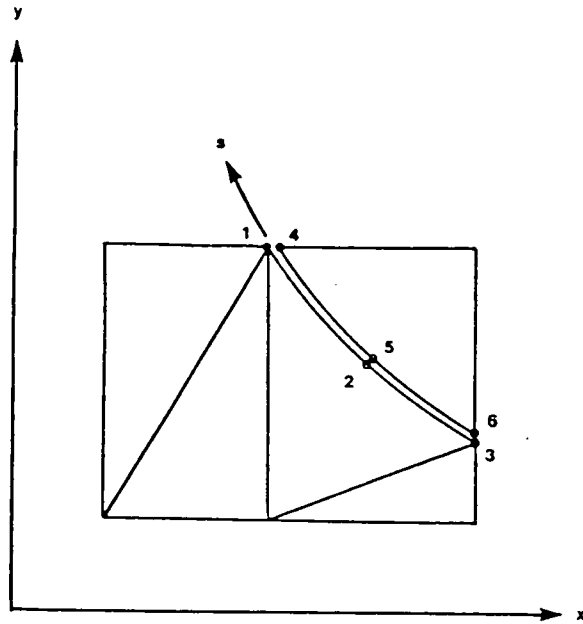
Figure 2.3   The fault element in local (s, n) and global (x, y) coordinate space. The top diagram shows the fault dividing the mesh into two bodies, the adjoining nodes of the fault element are spatially coincident. Below, the coordinates of the nodes in (s, n) space showing the order of the node numbering for the fault element.

Define the relative displacement at a general point $\{w\}$ along the fault section using the shape function interpolation of the local parallel and normal displacements at a node,

$$\{w\} = [\bar{L}]\{\bar{d}\}$$

where,

$$[\bar{L}] = \begin{bmatrix} -\bar{N}_1 & 0 & -\bar{N}_2 & \ldots & \bar{N}_4 & 0 & \bar{N}_5 & \ldots \\ 0 & -\bar{N}_1 & 0 & \ldots & 0 & \bar{N}_4 & & \ldots \end{bmatrix}$$

$$\{\bar{d}\}^T = \{u_{s_1} \quad u_{n_1} \quad u_{s_2} \quad u_{n_2} \quad u_{s_3} \quad \ldots\}$$

Then the local displacement is related to the global displacement by,

$$\begin{Bmatrix} u_s \\ u_n \end{Bmatrix} = \begin{bmatrix} \dfrac{dx}{ds} & \dfrac{dy}{ds} \\ -\dfrac{dy}{ds} & \dfrac{dx}{ds} \end{bmatrix} \begin{Bmatrix} u \\ v \end{Bmatrix}$$

so the local nodal displacements can be written,

$$\{\bar{d}\} = [R]\{d\}$$

Define the force per unit length at a general point along the fault section,

$$\{p\} = \begin{Bmatrix} p_s \\ p_n \end{Bmatrix} = \frac{1}{l}[\bar{K}]\{w\} \tag{2.35}$$

where,

$$[\bar{K}] = \begin{bmatrix} k_s & 0 \\ 0 & k_n \end{bmatrix} \tag{2.36}$$

k_s, k_n are the shear and normal stiffnesses respectively, which define the elastic properties of the fault.

The variational method requires the stored energy of the fault element which is defined as,

$$W = \frac{1}{2} \int_{-\frac{l}{2}}^{\frac{l}{2}} \{w\}^T \{p\}\, ds$$

substitute the relations evaluated above gives,

$$W = \frac{1}{2} \int_{-\frac{l}{2}}^{\frac{l}{2}} \{d\}^T [R]^T [\bar{L}]^T \frac{1}{l} [\bar{K}][\bar{L}][R]\{d\}\, ds$$

and the minimisation yields,

$$\frac{\partial W}{\partial \{d\}} = [K_F]\{d\}$$

where the fault stiffness matrix is,

$$[K_F] = \frac{1}{l} \int_{-\frac{l}{2}}^{\frac{l}{2}} [R]^T [\bar{L}]^T [\bar{K}][\bar{L}][R]\, ds \tag{2.37}$$

36

The fault stiffness matrix is added into the global stiffness matrix at the relevant nodal positions. The behaviour of fault elements is discussed in detail in the next chapter.

2.3 The RIP Method for Incompressible Fluids

In this section the finite element solution of the Navier-Stokes equations for incompressible, viscous flow using the reduced integration penalty (RIP) method will be presented. Zienkiewicz and Godbole (1975) demonstrated the direct analogy with incompressible elasticity. Thus it becomes obvious to convert existing elasticity programs to solve fluid flow problems with very little alteration necessary.

2.3.1 The Eulerian Description

In the preceding Lagrangian description of an elastic body the forces produce an immediate displacement. which is the minimum energy configuration of the body. Lagrangian space represents the reference frame of the material and so the displacement represents the actual particle motion of the points in the body referenced to its current equilibrium position. The Eulerian description defines the reference points in space, the initial position in space of the fluid body. The equations of motion yield the velocity at a point in space which defines the instantaneous response of the fluid to the applied force field. However, for a finite body, as soon as the fluid begins to move the equations are invalidated and so the velocities and stresses recovered are relevant only to the onset of motion. Thus the main difference from the Lagrangian representation is that the acceleration contains both spatial and temporal derivatives. Cathles (1975) provided a good illustration of this point. Consider a one-dimensional bar carrying a temperature gradient and moving rapidly along axis, as shown figure 2.4. Over a small time increment a point on the bar will maintain the same temperature, but the spatial reference point S will record a change in temperature. So, returning to the equations of fluid flow the 'convective' acceleration operator can be defined by,

$$\frac{d}{dt} = \frac{\partial}{\partial t} + \vec{u}.\nabla \qquad (2.38)$$

where $\vec{u}$ is the velocity vector at a point, and ∇ is the gradient operator. Thus even steady state flow can have an accelerative component.
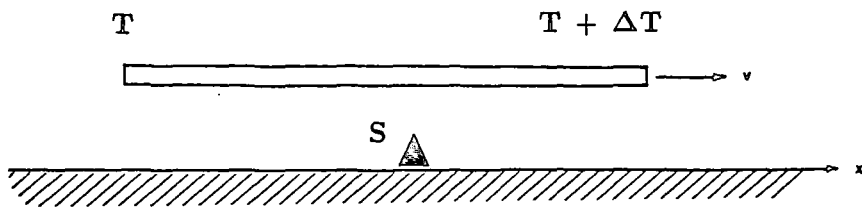
Figure 2.4   Schematic representation of a 1-dimensional bar of length l carrying a temperature gradient $\Delta T/l$ and travelling rapidly along the x-axis at velocity v. Over a small time increment, the temperature distribution in the bar is unaltered, but the spatial reference point S which is fixed with respect to the x-axis, records a change in temperature.

In a fluid the motion is driven by the deviatoric stresses. and for a 2-D linear, isotropic, incompressible fluid of viscosity μ the deviatoric stresses are,

$$\{\sigma\} = [D_\mu]\{\varepsilon\} \tag{2.39}$$

where,

$$[D_\mu] = \mu \begin{bmatrix} 2 & 0 & 0 \\ 0 & 2 & 0 \\ 0 & 0 & 1 \end{bmatrix} \tag{2.40}$$

and the strain rate tensor is,

$$\dot{\varepsilon}_{ij} = \frac{1}{2} \left(\frac{\partial u_i}{\partial x_j} + \frac{\partial u_j}{\partial x_i} \right)$$

for the Cartesian coordinates x_i, and so for a finite element this can be written,

$$\{\dot{\varepsilon}\} = [B]\{d\}$$

where $\{d\}$ are now the nodal velocities, and therefore the analogy to the constitutive relations of elasticity. with displacement replaced by velocity. is obvious.

Incompressibility is a constraint on the fluid behaviour and is defined by a zero rate of volumetric straining,

$$\dot{\varepsilon}_v = \nabla.\vec{u} = 0 \tag{2.41}$$

This condition may be imposed in a variety of ways. Using velocity and pressure as nodal variables yields a set of coupled equations incorporating the incompressibility as part of the formulation. but it introduces the extra dof of the pressure variable. Alternatively the stream function formulation defines the velocity field in terms of auxiliary functions which automatically satisfy the incompressibility requirement exactly. The disadvantage of this method is that second order derivatives appear in the stiffnesses and this requires elements with C_1 continuity shape functions. The approach taken in this thesis is to generate a near incompressibility condition via a penalty function, as used for incompressible elasticity studies. The conceptual difference to compressible elasticity is that 'compressibility' in fluid flow represents net fluid loss or gain.

2.3.2   The Variational Statement of the Navier-Stokes Equations

By analogy with the previous variational derivation we can construct the rate of work functional,

$$\Pi = \frac{1}{2} \int \{\dot{\varepsilon}\}^T [D_\mu]\{\dot{\varepsilon}\} \, dV \quad - \quad \int \{u\}^T \{b\} \, dV \quad - \quad \int \{u\}^T \{q\} \, dA \tag{2.42}$$

and require stationarity with respect to small variations of the velocity, subject to the constraint,

$$\dot{\varepsilon}_v = [m]^T \{\dot{\varepsilon}\} = 0$$

where,

$$[m] = [1 \quad 1 \quad 0]$$

The incompressibility constraint is incorporated via a penalty function approach. The dilatational strain energy is given by the product of hydrostatic pressure p and dilatational strain rate.

$$\int p \dot{\varepsilon}_v \, dV$$

For a large, positive constant λ, make the substitution for the pressure dof,

$$p = \lambda \dot{\varepsilon}_v \tag{2.43}$$

and then the complete functional becomes,

$$\bar{\Pi} = \frac{1}{2} \int \{\dot{\varepsilon}\}^T [D_{..}]\{\dot{\varepsilon}\} \, dV \quad - \int \{u\}^T \{b\} \, dV \quad - \int \{u\}^T \{q\} \, dA \quad + \lambda \int \dot{\varepsilon}_v^2 \, dV$$

$$= \frac{1}{2} \int \{\dot{\varepsilon}\}^T [D]\{\dot{\varepsilon}\} \, dV \quad - \int \{u\}^T \{b\} \, dV \quad - \int \{u\}^T \{q\} \, dA$$

where,

$$[D] = [D_{..}] \quad + \quad \lambda [m][m]^T$$

Thus we have recovered the equations analogous to the functional for elasticity with two contributions to the global stiffness, denoted $[K_u]$ and K respectively.

However, as previously mentioned, the acceleration in Eulerian space differs from the Lagrangian, and so by d'Alembert's Principle the body forces in a body of density ρ are,

$$\{b\} = \{b_0\} + \rho\{a\} \tag{2.44}$$

where the acceleration.

$$\{a\} = \frac{d}{dt}\{u\}$$

and so the Eulerian finite element representation of the body forces at a general point becomes,

$$\{b\} = \{b_0\} + \rho \frac{\partial}{\partial t}\{u\} + \rho [J']\{u\} \tag{2.45}$$

39

where,

$$[J'] = \begin{bmatrix} u_x & u_y \\ v_x & v_y \end{bmatrix}$$

and the subscripts denote differentiation with respect to x and y.

The minimisation of the complete functional yields the Navier-Stokes equations,

$$[M]\frac{\partial}{\partial t}\{d\} + [K]\{d\} + \{H\} = \{F\} \tag{2.46}$$

which is similar to the equations for elasticity, but with two additional terms. These terms are defined by,

$$[M]\frac{\partial}{\partial t}\{d\} = \left[\int [N]^T \rho [N]\, dV\right] \frac{\partial}{\partial t}\{d\} \qquad \text{inertial} \tag{2.47}$$

$$\{H\} = \left[\int [N]^T \rho [J'][N]\, dV\right] \{d\} \qquad \text{convective} \tag{2.48}$$

and so the full equations are time-dependent, non-linear and non-symmetric.

Fortunately the Earth's mantle exhibits creeping flow, and so the inertial and convective terms are negligible and the problem is reduced to Stokes flow. Temam (1977) has proved the convergence of the penalty function method for Stokes flow, but the crucial factor remains the invoking of the incompressibility constraint. In order to maintain a sensible pressure field (equation 2.43), as $\dot{\varepsilon}_v \to 0$ then $\lambda \to \infty$. Consequently to avoid the infinity, the penalty term $[K_\lambda]$ must be singular. This is achieved by underintegrating the penalty term, but retaining sufficiently accurate integration for the viscosity term $[K_\mu]$ so that the summed global stiffness matrix is non-singular. This is called selective integration. Zienkiewicz (1977) pointed out that sufficiently accurate integration for 8-node Serendipity quadrilaterals is in fact reduced integration, and thus the two stiffnesses can be assembled together which greatly simplifies the computing. In this study the triangular elements use 3-point reduced integration on the penalty term.

Hughes et al. (1979) presented a simple criterion for the selection of the penalty parameter for Stokes flow,

$$\lambda = c\mu \tag{2.49}$$

where c is a constant that is dependent on the computer word length and is problem independent. Oden (1982) discussed in full the RIP method in view of the order of selective integration required to retrieve meaningful velocities and pressures. The method

will often work without reduced integration but at the expense of stability and accuracy. Often it is the pressure which shows the greatest divergence and instability (being a derivative) particularly the 'checkerboard' mode of the bilinear elements. This may require a pressure filter or some sort of smoothing. The pressure will not be required in this study, and the velocities will be shown to be stable in a numerical evaluation in the next chapter.

2.3.3   Axisymmetric Analysis

The 2-D analysis can also be applied to the cross-section through an axisymmetric body, requiring very little alteration to the finite element code. The major difference is that an axisymmetric deformation involves four strain components and not just the three components of plane strain.

The cylindrical coordinate system can be related to the Cartesian system by,

$$x = r \cos \theta, \quad y = y, \quad z = r \sin \theta$$

so that on the plane $\theta = 0°$,

$$x = r, \quad y = y$$

and hence the Jacobian used in the isoparametric formulation, to transform from local to global coordinates, will be identical for cylindrical (r, y) and Cartesian (x, y) coordinates. However, in cylindrical coordinates the volume element becomes,

$$dV = r \, dr \, d\theta \, dy$$

and integrating around θ gives,

$$dV = 2\pi r \, dr \, dy \tag{2.50}$$

and so to generate the element stiffness the integral becomes,

$$\int [B^T \, D \, B] \, 2\pi r \, dr \, dy \quad = \quad \int [B]^T [D][B] \, 2\pi r \, \det J \, d\xi \, d\eta$$

Also the strain operator will differ from the 2-D Cartesian analysis because now any radial strain rate will create a circumferential component. Thus the operator matrices become,

$$[D_\lambda] = \lambda \begin{bmatrix} 1 & 1 & 0 & 1 \\ 1 & 1 & 0 & 1 \\ 0 & 0 & 0 & 0 \\ 1 & 1 & 0 & 1 \end{bmatrix} \qquad [D_\mu] = \mu \begin{bmatrix} 2 & 0 & 0 & 0 \\ 0 & 2 & 0 & 0 \\ 0 & 0 & 1 & 0 \\ 0 & 0 & 0 & 2 \end{bmatrix}$$

$$[B] = \begin{bmatrix} \dfrac{\partial N}{\partial r} & 0 \\[2mm] 0 & \dfrac{\partial N}{\partial y} \\[2mm] \dfrac{\partial N}{\partial y} & \dfrac{\partial N}{\partial r} \\[2mm] \dfrac{N}{r} & 0 \end{bmatrix}$$

The nodal components now depend on the radial position r and so the stiffness matrix is no longer symmetric. Similarly, the strain operator $[B]$ will be non-symmetric across an element as the element varies with r.

Finally the external forces at a node $\{\bar{F}\}$ now represent a force per unit length applied over the whole circumference and are effected as,

$$2\pi r \, \{\bar{F}\}$$

2.3.4 Solving for Unsteady Fluid Flow

The time-dependent linear equations have been derived as,

$$[M]\frac{\partial}{\partial t}\{d\} - [K]\{d\} = \{F\} \tag{2.51}$$

Hughes et al. (1979) presented an algorithm for the solution of the full Navier-Stokes equations which is adopted and adapted here.

The mass matrix $[M]$ which is the inertial control over the time-developing flow is diagonalised to form the 'lumped' mass matrix. Cook (1981) discussed lumping methods and the advantages and disadvantages over the consistent mass matrix. Conceptually, lumping replaces the element mass by effective nodal masses (which may be positive or negative). This operation to diagonalise considerably simplifies the calculations. The solution algorithm is a one-step, linearly implicit, predictor-corrector. Given the solution at time-step n, the solution at time-step $n + 1$ is summarised as,

$$\{\tilde{d}\}_{n+1} = \{d\}_n + (1 - \gamma)\Delta t \{a\}_n \tag{2.52}$$

$$([M] - \gamma\Delta t [K])\{d\}_{n+1} = [M]\{\tilde{d}\}_{n+1} - \gamma\Delta t \{F\}_{n+1} \tag{2.53}$$

$$\{a\}_{n+1} = \frac{(\{d\}_{n+1} - \{\tilde{d}\}_{n+1})}{\gamma\Delta t} \tag{2.54}$$

where γ is a stability constant $\frac{1}{2} \le \gamma \le 1$, Δt is the time-step, and $\{a\}$ is the vector of nodal accelerations. So, for a constant time step Δt the system matrix need only be factorised once which greatly reduces the computational cost and time.

42

2.3.5 Nodal Forces and Boundary Conditions

Body forces and surface tractions will act similarly to those previously discussed for elasticity, and the subroutines developed for the elastic finite element code can be used for the viscous case.

Dirichlet boundary conditions are not applied by the Payne-Irons approximation and instead are applied 'exactly'. Each prescribed dof is incorporated by substituting the given value $u = \bar{u}$ into each equation, and then adding all known values into the global force vector. Then the row and column of the stiffness matrix are zeroed and the trivial solution $u = \bar{u}$ is written in lieu.

Standard Dirichlet conditions suffice if the model boundaries are aligned along the global axes, but it is quite likely that curved boundaries will exist in which case the 2 dof at a node become linearly dependent. This is a coupled equivalent Dirichlet condition (see Norrie and DeVries 1978) where we can write for a node n,

$$u_n = u(v_n)$$

and so the functional has one less dependent variable,

$$\bar{\Pi} = \bar{\Pi}(\ldots u(v_n), v_n, \ldots)$$

and the two minimisation conditions,

$$\frac{\partial \bar{\Pi}}{\partial u} = 0 \quad , \quad \frac{\partial \bar{\Pi}}{\partial v_n} = 0$$

can be accomplished by the single condition,

$$\frac{\partial \bar{\Pi}}{\partial v}\bigg|_n = \frac{\partial \bar{\Pi}}{\partial v_n} + \frac{\partial \bar{\Pi}}{\partial u} \left(\frac{\partial u_n}{\partial v_n} \right) = 0$$

This is applied as follows: multiply the row and column corresponding to u_n by the derivative, and add to the row and column corresponding to v_n. Then zero the u_n row and column and insert the coupled condition in the vacant row. On solution this will automatically give the correct value of u_n and v_n but the method renders the global stiffness unsymmetric.

Density discontinuities such as the surface of the Earth have been accounted for in the elasticity formulation by isostatic compensation. In the fluid mechanics models

43

the free surface at the top of the mantle is a most taxing problem which may be handled by one of a number of approximations. Firstly we could assign a thin, high viscosity layer at the surface and assume that this approximates an elastic lithosphere. Then the existing isostatic compensation can be applied, by assuming that the surface displacement can be approximated by $v\Delta t$, where Δt is a small time increment (e.g. Tharp 1985). Alternatively we can evaluate the boundary conditions at the free surface of a viscous fluid (see Cathles 1975) which specify that a traction-free surface must develop. One approach is to prescribe zero vertical motion at the surface (e.g. Richter 1973, Sleep 1979). This eliminates shear stress but generates large normal stresses at the surface. Another method involves integrating the velocities to redefine the free surface until the velocity vector is tangential to the surface at all points. This is the more satisfactory, but more time-consuming and expensive method, and it is only applicable to steady state problems when the initial boundary is close to the steady state free surface (Zienkiewicz 1977). Subduction zone models will include regions of the free surface that have velocity vectors near perpendicular rather than parallel and to this end it is necessary to adopt a more formal approach to the problem.

2.3.6 The ALE Formulation

The difficulties engendered by the motion of the free surface of an unsteady fluid can be overcome by the arbitrary Lagrange-Eulerian (ALE) formulation presented by Hughes et al. (1978). This is a generalisation of the Eulerian solution of the Navier-Stokes equations in Hughes et al. (1979) which was discussed in previous sections. This section will outline the fundamentals of the formulation but will not attempt to derive formally the finite element equations. The notation in this section will follow the preceding as far as possible but unfortunately some symbols must change their meaning.

Consider the three closed domains Ω_x, Ω_y, Ω_z in figure 2.5.

- Ω_x is the reference domain and is 'fixed' in time and space

- Ω_y is the image of Ω_x at a particular time t and this is the 'Eulerian space' normally associated with the fluid body under consideration

- Ω_z is the domain of the material that would exist at $t = 0$ given that the fluid occupies Ω_z at time t

44
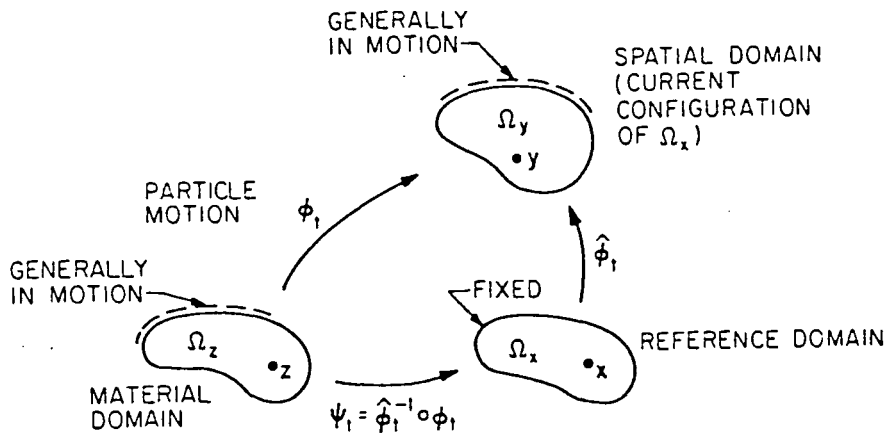
Figure 2.5   The three closed domains Ω_x, Ω_y, Ω_z describing the properties and relationships between them. From Hughes et al. (1978).

Let the Cartesian coordinates of the domains be respectively,

$$\underline{x} = (x_1, x_2), \quad \underline{y} = (y_1, y_2), \quad \underline{z} = (z_1, z_2) \tag{2.55}$$

The domains are interdependent and are related by the coordinate mappings; by definition we have,

$$\underline{y} = \underline{\phi}(\underline{z}, t) \qquad \text{particle motion} \tag{2.56}$$

$$\underline{y} = \underline{\hat{\phi}}(\underline{x}, t) \qquad \text{mesh motion} \tag{2.57}$$

and define the third mapping,

$$\underline{x} = \underline{\psi}(\underline{z}, t) \tag{2.58}$$

to be representable by a function of the first two mappings. Hence we can solve a fluid mechanics problem in the domain Ω_y and relate this, through the mappings, to the actual particle motion and consequently follow the free surface.

Firstly we must derive the exact relationship that defines a variable field in each domain. Define the displacements for each dof i,

$$u_i = y_i - z_i \quad \text{for} \quad \phi_i$$

$$\hat{u}_i = y_i - x_i \quad \text{for} \quad \hat{\phi}_i$$

$$w_i = x_i - z_i \quad \text{for} \quad \psi_i$$

note that the symbol u was a velocity and is now a displacement at a general point.

To relate this to the finite element method, the reference domain Ω_z is the initially specified mesh coordinates. The mapping $\hat{\phi}$ thus defines the motion of the mesh as the domain Ω_y, and this motion can be followed by evaluating the velocity with respect to the reference domain.

$$\left. \frac{\partial \hat{u}_i}{\partial t} \right|_{x_i} \qquad \text{for} \quad t > 0$$

Consider the simple example element in figure 2.6, where the free surface is to be modelled by the line $\eta = +1$ in local coordinate space. The two components of mesh velocity which define that lines of constant η move with the free surface can be derived as,

$$\frac{\partial \hat{u}_1}{\partial t} = 0$$

$$\frac{\partial \hat{u}_2}{\partial t} = \frac{\partial u_2}{\partial t} - \left. \frac{\partial (\hat{u}_2 + x_2)}{\partial x_1} \right|_\eta \frac{\partial u_1}{\partial t}$$

45
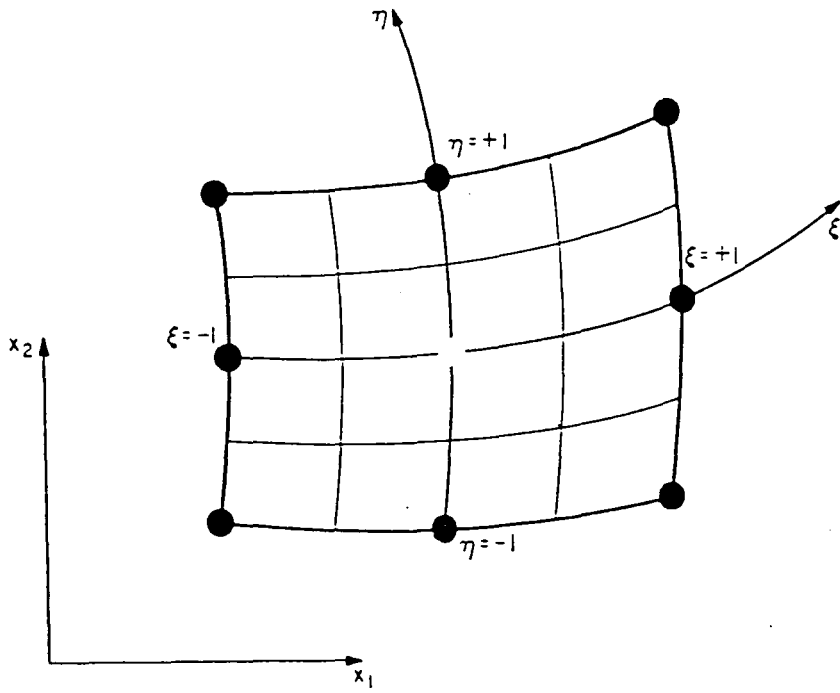
Figure 2.6   The quadrilateral element in global space (x, y). The line $\eta = +1$ is chosen to follow the free-surface.

where $\hat{u}_2 + x_2$ is simply the coordinate y_2 of the domain Ω_y and is a function of x_1 and η. This can be generalised to relate each dof to it's specific representation by introducing the parameter α and the velocities become,

$$\frac{\partial \hat{u}_1}{\partial t} = \alpha_1 \frac{\partial u_1}{\partial t} - \alpha_1 \left.\frac{\partial(\hat{u}_1 + x_1)}{\partial x_2}\right|_{\eta} (1 - \alpha_2) \frac{\partial u_2}{\partial t} \qquad (2.59)$$

$$\frac{\partial \hat{u}_2}{\partial t} = \alpha_2 \frac{\partial u_2}{\partial t} - \alpha_2 \left.\frac{\partial(\hat{u}_2 + x_2)}{\partial x_1}\right|_{\eta} (1 - \alpha_1) \frac{\partial u_1}{\partial t} \qquad (2.60)$$

A Eulerian dof is defined as stationary with respect to particle motion and a Lagrangian dof follows particle motion and so,

$$\alpha = 0 \qquad \text{Eulerian} \quad \text{dof} \qquad (2.61)$$

$$\alpha = 1 \qquad \text{Lagrangian} \quad \text{dof} \qquad (2.62)$$

These equations allow lines of constant η to move with the free surface, and it is now the parameter α which is used to define the surface.

The finite element discretisation of equations 2.59, 2.60 yields,

$$\{\hat{v}\} = [A]\{v\} - [L]^{-1}\{S\} \qquad (2.63)$$

where $\{\hat{v}\}$ is the vector of nodal values of the mesh velocity. $[A]$ is the diagonal matrix of nodal values of the parameter α, $\{v\}$ is the vector of nodal values of the particle velocity. The transform matrix $[L]$ is defined by,

$$[L] = \int [N]^T [N] \, dV \qquad (2.64)$$

however the vector $\{S\}$ cannot be written in the notation used so far. Instead each node a will contribute to the element integration as follows.

$$\int N_a \alpha_i \left.\frac{\partial(\hat{u}_i + x_i)}{\partial x_j}\right|_{\eta} (1 - \alpha_j) \frac{\partial u_j}{\partial t} \, dV \qquad (2.65)$$

The calculations are simplified and stability ensured by lumping $[L]$, in an identical procedure to that used for the mass matrix $[M]$. Now the inverse $[L]^{-1}$ is trivial. Hughes et al. (1978) present an approximation for $\{S\}$ but the differential in the integrand can be evaluated numerically. Consider the function $f = f(\xi, \eta)$ then,

$$\frac{\partial f}{\partial x_2} = \frac{\partial f}{\partial \xi}\frac{\partial \xi}{\partial x_2} + \frac{\partial f}{\partial \eta}\frac{\partial \eta}{\partial x_2}$$

46

but for a constant η,

$$\frac{\partial f}{\partial x_2}\bigg|_\eta = \frac{\partial f}{\partial \xi}\frac{\partial \xi}{\partial x_2}$$

and the derivatives on the right hand side are available from the shape functions and the inverse Jacobian. Hence the integrand in equation 2.65 can be evaluated and the integral evaluated numerically.

So given a solution to the fluid mechanics problem $\{v\}$ in domain Ω_y we can now evaluate the mesh velocity $\{\hat{v}\}$ and update the domain to follow the free surface. The previous algorithm to solve the Navier-Stokes equations can thus be generalised to give the full solution at time step $n+1$, note that $\{d\}$ are nodal displacements, $\{v\}$ are nodal velocities, $\{a\}$ are nodal accelerations of the particular mappings.

First, initialise this time step of the solution (for $n = 1$ the quiescent state is a good approximation).

$$\{\hat{d}\}_{n+1}^{(0)} = \{\hat{d}\}_n + \Delta t\{\hat{v}\}_n + \frac{\Delta t^2}{2}(1 - 2\beta)\{\hat{a}\}_n$$

$$\{\hat{v}\}_{n+1}^{(0)} = \{\hat{v}\}_n + \Delta t(1 - \gamma)\{\hat{a}\}_n$$

$$\{v\}_{n+1}^{(0)} = \{v\}_n + \Delta t(1 - \gamma)\{a\}_n$$

solve the equations for the time step $n+1$,

$$\left([M] + \gamma\Delta t[K]\right)\{v\}_{n+1}^{(i+1)} = [M]\{v\}_{n+1}^{(0)} + \gamma\Delta t\left[\{F\}_{i-1} - \{H\}_{n+1}^{(i)}\right]$$

Now iterate the non-linear term, and for each iteration reassemble the system matrix from the updated domain Ω_y,

$$\{\hat{v}\}_{n+1}^{(i+1)} = [A]\{v\}_{n+1}^{(i+1)} - [L]^{-1}\{S\}_{i-1}^{(i-1)}$$

$$\{\hat{a}\}_{n+1}^{(i+1)} = \left(\{\hat{v}\}_{n+1}^{(i+1)} - \{\hat{v}\}_{n+1}^{(0)}\right)/(\gamma\Delta t)$$

$$\{\hat{d}\}_{n+1}^{(i+1)} = \{\hat{d}\}_{n+1}^{(0)} + \Delta t^2\beta\{\hat{a}\}_{n+1}^{(i+1)}$$

Finally assign the nodal values at the end of the time increment.

$$\{\hat{d}\}_{n+1} = \{\hat{d}\}_{n+1}^{(i+1)}$$

$$\{\hat{v}\}_{n+1} = \{\hat{v}\}_{n+1}^{(i+1)}$$

$$\{\hat{a}\}_{n+1} = \{\hat{a}\}_{n+1}^{(i+1)}$$

$$\{v\}_{n+1} = \{v\}_{n+1}^{(i+1)}$$

$$\{a\}_{n+1} = \left(\{v\}_{n+1} - \{v\}_{n+1}^{(0)}\right)/(\gamma\Delta t)$$

thus, given the solution vectors at the end of the time step, the next time step can be intialised. The displacement vector of the mesh $\{\hat{d}\}$ maps the evolution of the free surface.

47

CHAPTER 3

Implementation Of The Finite Element Theory

The numerical analysis of Waghorn (1984) has demonstrated that the elastic-viscoelastic finite element code performs satisfactorily. This short chapter is devoted firstly to a validation of the method of evaluating fault slip and thermal stresses in the structural mechanics problems. Mithen (1980) used fault elements to study stress-controlled graben formation and subsidence in continental lithosphere, following the energy budget calculations of Bott (1976). Horizontal tension causes normal faulting in the brittle upper crust and graben subsidence is accompanied by flow in the ductile lower crust. The graben models of Mithen (1980) proved to be unstable as the stresses in the ductile layer under the fault increased dramatically with time. Waghorn (1984) studied the surface lithosphere at subduction zones and used fault elements to represent the thrust zone between the plates. However, this analysis of faulting was restricted to elastic behaviour only. The first section of this chapter demonstrates that fault elements can usefully represent a fault zone in both brittle and ductile regimes. The stresses generated by the thermal anomaly in the backarc of subduction zones are an important contribution to the stress regime. Waghorn (1984) studied the elastic response to a temperature anomaly and the second section of this chapter demonstrates how the thermal anomaly can be more fully applied to the elastic-viscoelastic rheology.

The second half of this chapter is devoted to a numerical evaluation of the conversion of the existing finite element code to solve the viscous flow problems. The simple entry flow problem is used to evaluate the machine constant required for $\lambda = c\mu$ (see equation 2.49) using the results published by Zienkiewicz and Godbole (1975) as a benchmark. The subsequent tests are designed to show that the finite element method will accurately reproduce the features of incompressible flow that are required.

3.1   The Fault Elements

The ability of the finite element method to incorporate adequately the thrust zone

of subduction is a most important feature of the numerical models. In this section the previous method of controlling fault slip is briefly reviewed and then an alternative approach is discussed and tested on a simple model.

The elastic properties of the fault element are the normal and shear stiffnesses k_n, k_s and these control the instantaneous elastic displacement along the fault zone. The nodal displacements of the elements adjacent to the fault element are used to calculate the normal σ and shear τ stress at the central nodes either side of the fault element. Stresses are discontinuous at element boundaries but average values of the stress along the fault section can be estimated. If μ is the coefficient of friction of the fault, then the frictional strength can be defined by $\tau_F = \mu\sigma$ (where σ includes the overburden pressure which may have been explicitly omitted from the initial calculation). Hence if $\tau > \tau_F$ frictional sliding could occur, in addition to the initial elastic response. This can be modelled by calculating the excess shear stress $\tau_{xs} = \tau - \tau_F$ and applying it as fault-parallel nodal forces to the fault elements. The process is then repeated until τ_{xs} drops to an acceptable value. The previous studies of Mithen (1980) and Waghorn (1984) encountered major difficulties with this iterative technique.

It is useful to examine the role of the two stiffnesses k_n, k_s. A high value of stiffness means that a large amount of work must be done to create a displacement. Thus k_n is set to a high value $(10^{15}$ N m$^{-1})$ to ensure that the fault walls remain in contact. This is a physical necessity under the confining pressures at depths greater than a couple of kilometres. The shear stiffness controls the fault-parallel movement. If it is high then no movement occurs, but if it is an intermediate value, 10^{10} N m^{-1} (typical of the values used by Waghorn and Mithen), then the work done on the fault section will produce a small displacement. This can be envisaged as a fault resistance which prevents the adjacent elements from attaining the preferred equilibrium configurations and generates large resistive stresses at the interface. In the aforementioned iterative method these large shear stresses are relieved by 'forcing' the fault nodes to slip further. In this context it would seem reasonable to permit greater instantaneous fault slip, thereby reducing the resultant shear stress and so the need for iterative forcing is eliminated. So, what controls the amount of slip and how does this compare to the physical realities of fault movement? The degree of fault slip is quite simply dictated by the two halves of the mesh attaining equilibria under appropriate boundary conditions, whilst being

coupled normally at the fault line. Thus, in most models, isostasy at the surface (the largest density contrast) will be the principal control on the fault slip, other boundaries (such as the Moho) will have a lesser effect. Physically the shear strength of the fault does no work on the adjacent bodies and so does not establish any residual stresses in them. This may approximate to the situation after major slip on a fault zone when the large asperities have been overcome.

However, the discussion must not be limited to the behaviour of brittle fracture in which the adjacent elements are elastic. A ductile shear zone may be represented by a fault segment in which both adjacent elements are viscoelastic, and at a subduction zone the fault line defines the top surface of the subducting slab which separates elastic elements below from viscoelastic elements above. A typical model of stress controlled graben formation in the upper crust has an upper brittle fracture zone continuing down into a ductile shear zone. The simple mechanics of fault movement could be envisaged as initial elastic slip in the competent layer, followed by creep along the shear zone and accompanying flow in the incompetent layer. This creates considerable difficulties for the existing method. To prevent large instantaneous elastic displacements in the lower shear zone requires a high k_s to be assigned. This causes the layer to behave as a continuum or generates large shears which must be relieved as the layer as a whole relaxes. One method of overcoming this problem is to parameterise the shear zone with a finite width and viscosity, and then model the zone as viscous flow between parallel plates. Thus the shear stress on the fault sides will generate a fault-parallel velocity which is applied over a small time increment as a fault displacement. This is a more reasonable approach than 'forcing' the nodes to slip, but this still perturbs the bulk energy minimisation. The optimum method should not destroy the self-consistency of the viscoelasticity algorithm. It is quite probable that the shear zone is significantly weaker than the surrounding ductile layer and so fault movement is dominated by the relaxation time constant of the whole layer. Physically this is equivalent to stating that graben subside because the ductile layer flows laterally rather than because the shear zone creeps. If this is the case, then the whole fault zone can be modelled with a low shear stiffness. The proposals above will be tested by reproducing the graben models of Bott (1976) and Mithen (1980).

The brittle upper crust is modelled by a finite element mesh representing a 1210 ×

10 km cross-section. The right hand end is an axis of symmetry and the left hand end is subjected to a uniform tension T. The top surface and base are isostatically compensated with density contrasts of $\rho = 2750$ kg m^{-3} and $\rho = 50$ kg m^{-3} respectively, the flexural parameter $\alpha = 32.4$ km and the fault hade is $26.57°$. This model is almost identical to the elastic upbending models of Bott (1976) with no frictional dissipation of energy in the fault, and so the results are presented in a similar fashion in the table 3.1 below. The subsidence is given in kilometres for a range of graben surface widths and applied tensions. The figures in brackets show the percentage increase over Bott (1976).

Width / km	$T = 50$ MPa	$T = 100$ MPa
30	1.18 (53%)	2.35 (53%)
40	0.84 (35%)	1.68 (37%)
50	0.62 (19%)	1.24 (19%)

Table 3.1   Relative vertical displacements of the elastic graben model.

There are certain differences between the finite element models and the energy budget calculations. The finite element models include the downbending of the graben edge, and in general the bending does not follow the 1-D elastic flexure equation because of the contact across the fault zone. The crustal shortening caused by fault slip relieves only 70% of the tensile extension and Bott (1976) assumed complete readjustment of the brittle layer. The systematic gain in wedge subsidence with decreasing graben width is due to a 'constant' gain in gravitational energy in the layer for a particular tension T. This allows progressively greater subsidence for smaller graben. The subsidence is large compared to the thickness of the brittle layer (10 km) and so the analysis must be near the limit of the capability of this particular mesh.

This simple model is also a convenient demonstration of the effect of the shear stiffness as discussed earlier. Table 3.2 below shows the variation of average shear stress at the centre of the fault zone for a uniform tension.

Shear Stiffness / N m^{-1}	Shear Stress / MPa
10^{15}	80.0
10^{10}	78.5
10^9	68.0
10^8	41.0
0	4.0

Table 3.2   Variation of shear stress with shear stiffness

The preceding models inherently assume that the underlying ductile layer is inviscid and reacts instantaneously to the vertical motion of the brittle layer. The lower crust is likely to possess a high viscosity and thus graben subsidence will occur over a long time scale. The finite element mesh is simply an extension of the previous mesh to represent a 1210 × 100 km cross-section through the lithosphere, and the right hand portion is shown in figure 3.1. The right hand end is an axis of symmetry and its horizontal motion is prevented. The rheology is described in table 3.3 below, the omission of a value for viscosity denotes that the layer is elastic.

Depth / km	Young's Modulus / N m^{-2}	Poisson's Ratio	Viscosity / Pa s
0-10	0.85×10^{11}	0.25	
10-20	0.85×10^{11}	0.25	10^{23}
20-35	1.08×10^{11}	0.25	10^{23}
35-100	1.80×10^{11}	0.25	10^{23}

Table 3.3   Rheology of the graben model

The fault line (labelled F) dips at 63.43° and breaches the surface 25 km from the end of the mesh, thus representing a 50 km wide graben. So far, the mesh is identical to that used by Mithen(1980). Isostatic conditions are applied at the base of the crust, $\rho = 500$ kg m^{-3} and the surface, $\rho = 2750$ kg m^{-3}, and at the base of the brittle layer $\rho = 50$ kg m^{-3}. The left hand end is subjected to a uniform 50 MPa tension. Initially the fault was completely locked and the lithosphere allowed to relax for 5 Ma. The right hand edge subsided by 25 m due to stretching flow in the ductile layers.

Then the fault shear stiffness in the upper crust (0-20 km) was set to zero, leaving the remaining mesh parameters untouched, and the model was rerun. The principal stress regime and surface displacement profile after 5 Ma relaxation are shown in figure
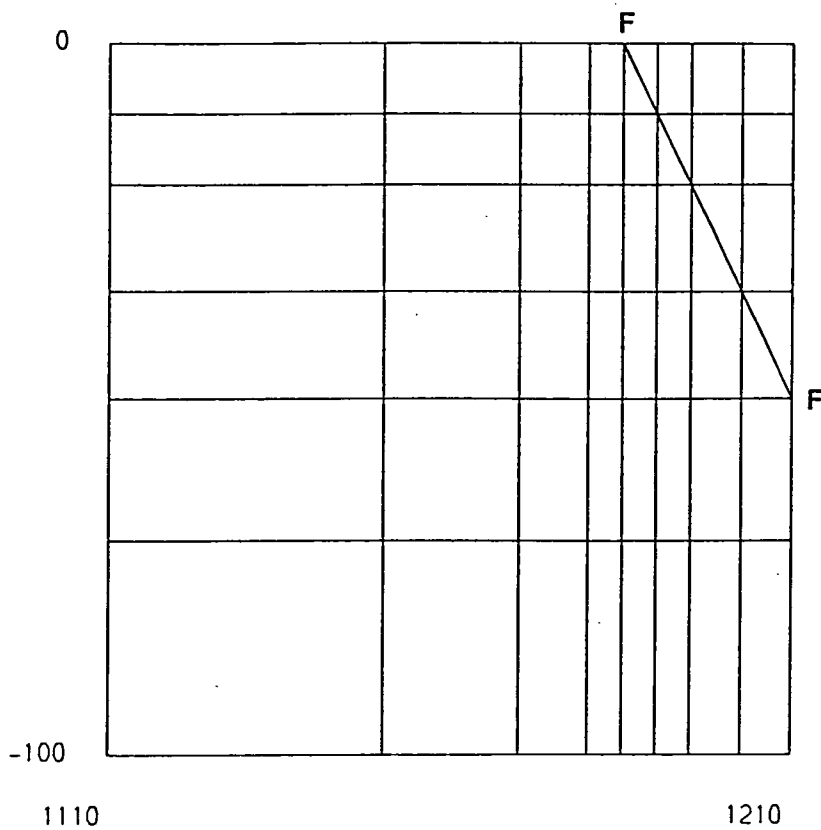
Figure 3.1 The right hand section of the finite element mesh for the graben subsidence model (no vertical exaggeration). The top three rows of elements represent the 35 km of crust, the uppermost 10 km thick layer is elastic. The lower three rows are the viscoelastic mantle layer of the lower lithosphere. The right hand edge is an axis of symmetry. The fault line is marked F and divides the mesh into two bodies, producing a graben of surface width 50 km.

STRESS VECTORS

(DOTTED LINES TENSIONAL)
- 100 MPA

0

-60

1160   1210
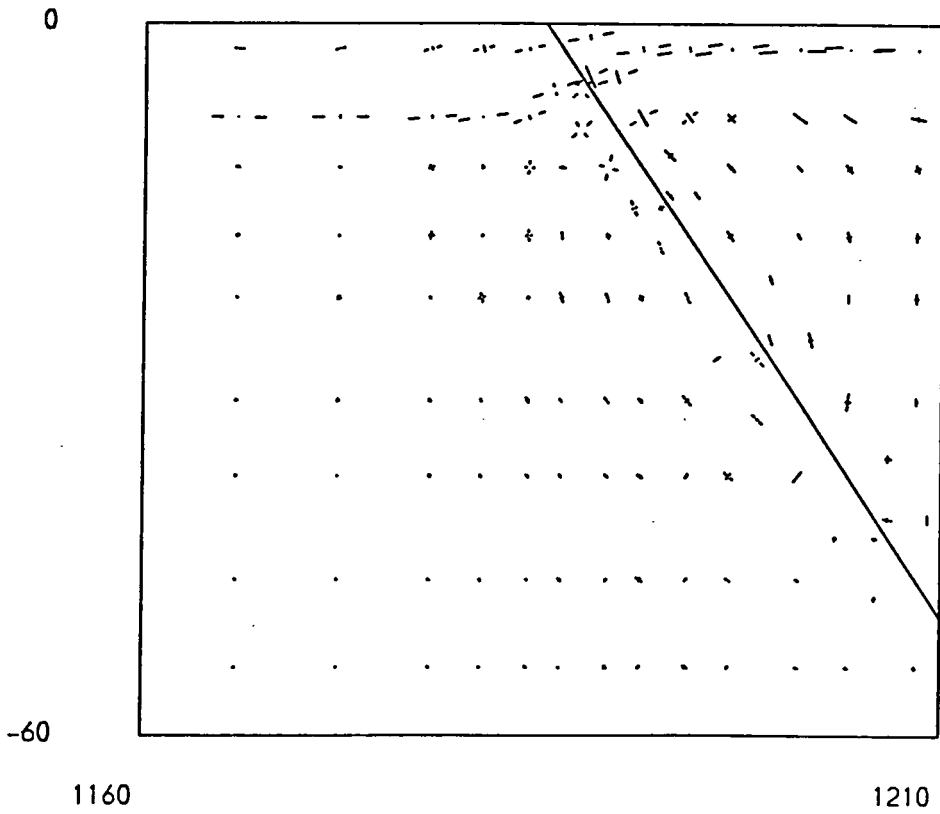
Figure 3.2   The stress regime of the upper 60 km of lithosphere (vertical exag-
geration ×1.4) after 5 Ma relaxation. This shows the large principal stresses
mostly confined to the upper 10 km elastic layer. The fault line is denoted by
the solid diagonal.

(DOTTED LINES TENSIONAL)
- 100 MPA

0

-60

1160   1210
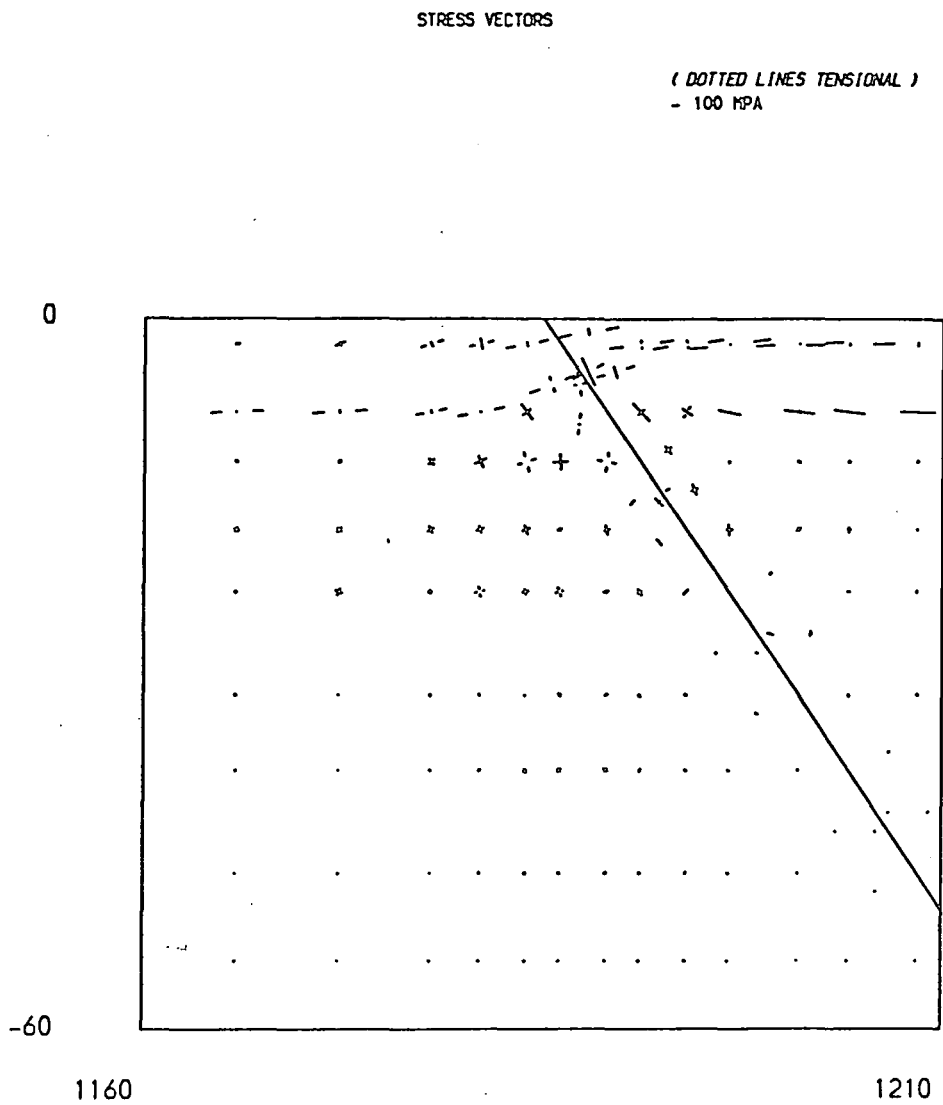
Figure 3.3   The stress regime of the upper 60 km of lithosphere (vertical exaggeration ×1.4) after 25 Ma relaxation. This shows the large principal stresses completely confined to the upper elastic layer. The fault line is denoted by the solid diagonal.

Creep Flow Vectors

———10.8 metres

0

-60

1160   1210
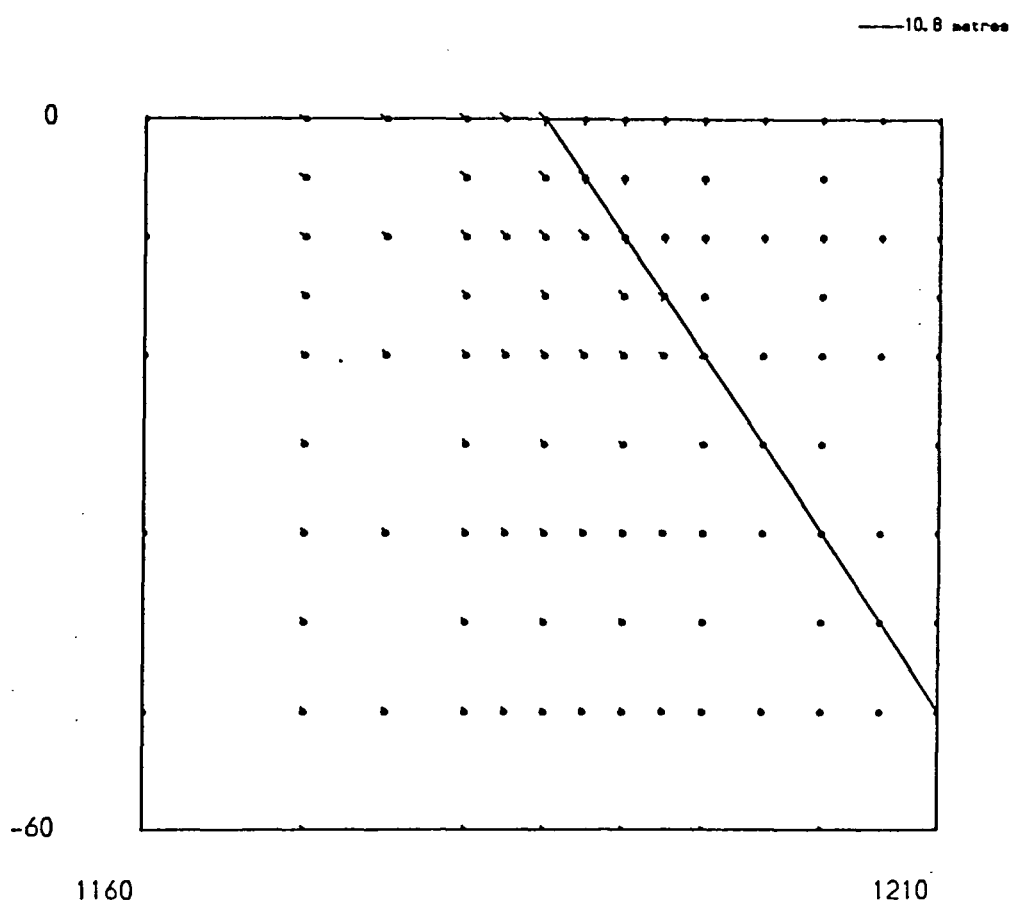
Figure 3.4   The flow vectors of the upper 60 km of the lithosphere (vertical ex-
    aggeration ×1.4) after 5 Ma relaxation represent the actual flow field over the
    final time increment. Each node is denoted by a circle and the associated flow
    vector has a length proportional to its magnitude. This shows the graben is
    still subsiding after 5 Ma but further relaxation shows the graben has virtually
    stopped subsiding after 25 Ma.

3.2. Stress is concentrated in the upper 10 km and well relaxed throughout the lower 90 km. The surface displacement shows a relative subsidence (ignoring edge flexure) of 525 m, which is less than the equivalent elastic model. This solution is in distinct contrast to the results of Mithen (1980, figure 8.17). Failure to extend the fault throughout the mesh created a singularity at the fault bottom as evidenced by the excessively large principal stresses (1250 MPa) generated in the ductile region underlying the fault which restrict the relative subsidence to 440 m. The surface stresses in the elastic layer are larger (400 MPa) in this model than those of Mithen (200 MPa), this is because the elastic layer is half the thickness and thus the stress amplification is doubled. Allowing the model to relax further results in subsidence of 1450 m at 20 Ma and 1750 m at 25 Ma. The stress regime in figure 3.3 shows the very large principal stresses (bending superposed on the amplified applied tension) restricted to the elastic layer only. The surface displacement profile shows roughly equal upbending of the rim and sinking of the graben. In practice, fracture, erosion of the uplift and deposition in the trough will greatly modify these models.

Within the confines of these models our best representation of graben subsidence permits the elastic layer to sink into the viscous layer along a pre-defined zone of weakness. The particular limitation of this model is that the compensating flow occurs on a local, rather than regional, scale; this is shown by the creep flow vectors in figure 3.4. The creep vectors also show that the graben is continuing to subside at 5 Ma but has almost stopped by 25 Ma.

The fault configuration at subduction zones will be discussed in more detail in the later chapters. Briefly, the surface lithosphere is decoupled at the thrust zone, but at depth the descending slab is expected to be strongly coupled to the mantle.

3.2 Thermal Stresses

The backarc region of subduction zones is often characterised by high surface heat flow (100mW m^{-2}) implying the existence of a thermal anomaly at depth. The thermal anomaly generated by raising the isotherms creates a temperature anomaly. In the finite element method this temperature anomaly is implemented by the initial strain $\{\varepsilon_0\}$ (see section 2.5). In a constrained body, the displacements $\{d\}$ will be very small and the

stress field will be dominated by $\{\sigma_0\} = [C]\{\varepsilon_0\}$. However, in an unrestrained body both will contribute to the final stress field. Under these conditions the thermal gradient must not exceed the order of the strain field of the element (Cook 1980), and thus we are restricted to a linear temperature gradient across the element.

In linear, isotropic, elastic material the temperature anomaly produces a fractional change in volume.

$$\frac{\Delta V}{V} = \alpha_v \Delta T$$

where ΔT is the temperature anomaly and α_v is the volume coefficient of expansion. If this material is then allowed to behave viscoelastically, the thermal stresses are relaxed but the expansion will remain. In a gravitational field this volume change results in a buoyancy force. This body force is not included in the initial strain approach and so must be added explicitly. As Jurdy and Stefanick (1983) point out, it is the buoyancy force of the thermal anomaly which is responsible for the surface uplift and long term stresses.

Since the finite element implementations of these aspects of the thermal anomaly are quite different, it is necessary to investigate quantitatively the potential differences. The finite element mesh represents a cross-section through 90 km thick oceanic lithosphere. The rheology is shown in the table 3.4 below.

Depth / km	Young's Modulus / N m^{-2}	Poisson's Ratio	Viscosity / Pa s
0-7	0.85×10^{11}	0.25	
7-20	1.80×10^{11}	0.25	
20-90	1.80×10^{11}	0.25	10^{23}

Table 3.4 Rheology of the thermal anomaly model

The right hand portion of the mesh is shown in figure 3.5, the right hand end is an axis of symmetry. Isostatic conditions are imposed at the base of the crust (7 km depth) $\rho = 600$ kg m^{-3} and at the surface $\rho = 1670$ kg m^{-3}. The two manifestations of the thermal anomaly are depicted in figure 3.5, which shows the region of uniform 200 K increase in temperature at the base of the lithosphere surrounded by a linear gradient to zero over one element thickness. Assuming a linear coefficient of expansion $\alpha = 10^{-5}$ K^{-1}, then for lithosphere of density $\rho = 3300$ kg m^{-3}, the equivalent density
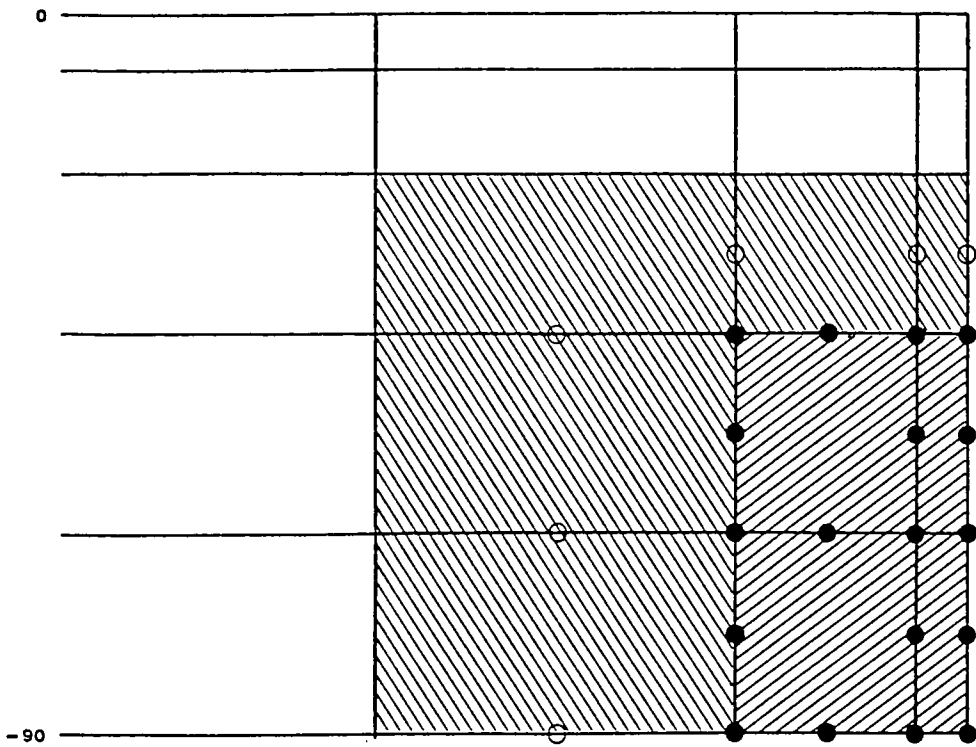
Figure 3.5   The right hand section of the finite element mesh (vertical exaggeration ×1.5) for the thermal anomaly model. The right hand edge is an axis of symmetry. The rheology is given in the text. The two manifestations of the thermal anomaly are superposed on the mesh. The open circles o represent a nodal temperature rise of 100 K, the full circles • represent a nodal temperature rise of 200 K. The left diagonal shading denotes a density anomaly $\rho = -6.6$ kg m^{-3} and the right diagonal shading a density anomaly $\rho = -13.2$ kg m^{-3}.

0

-90

500   675

0

-90

500   675
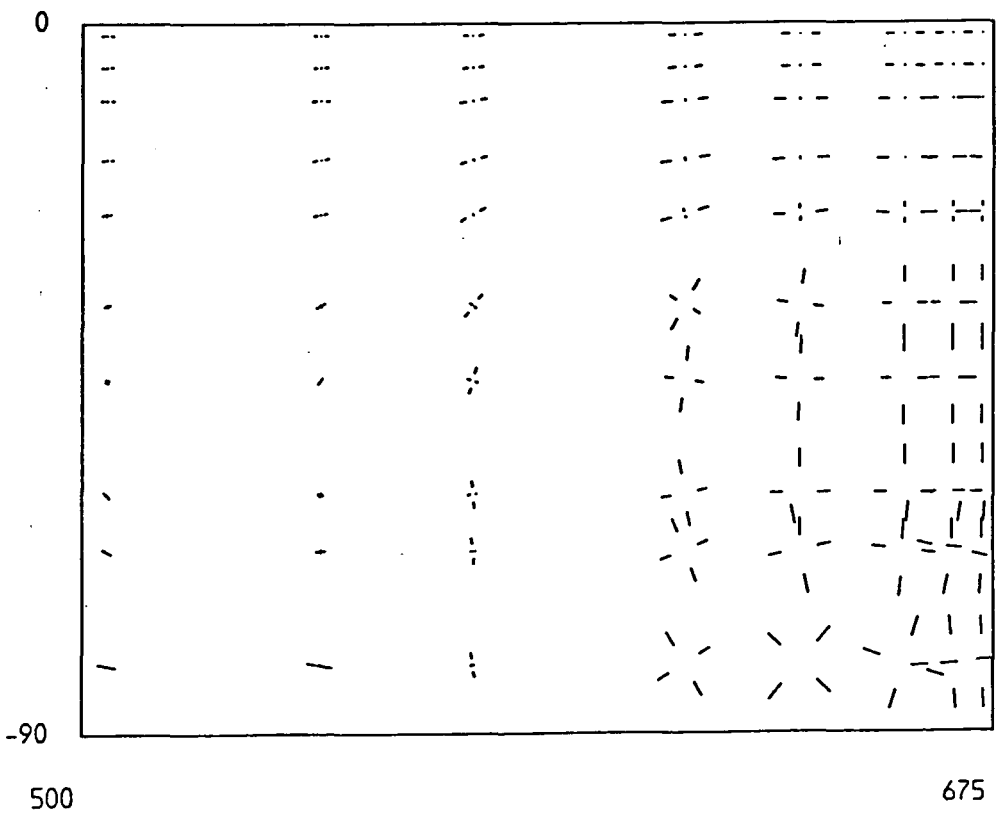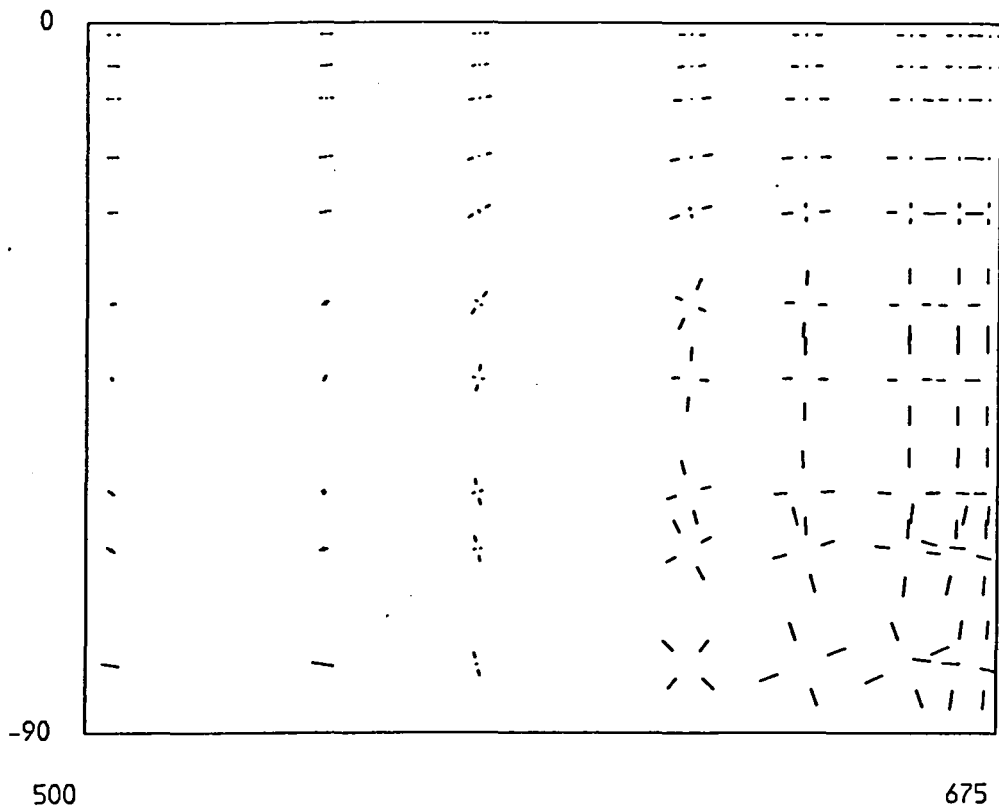
Figure 3.6   The stress regime for the initial elastic solution (vertical exaggeration
    ×1.5) for two models, a temperature anomaly only, and the combined thermal
    anomaly. The stresses produced by the density anomaly are so small as to have
    no significance in the wholly elastic models.
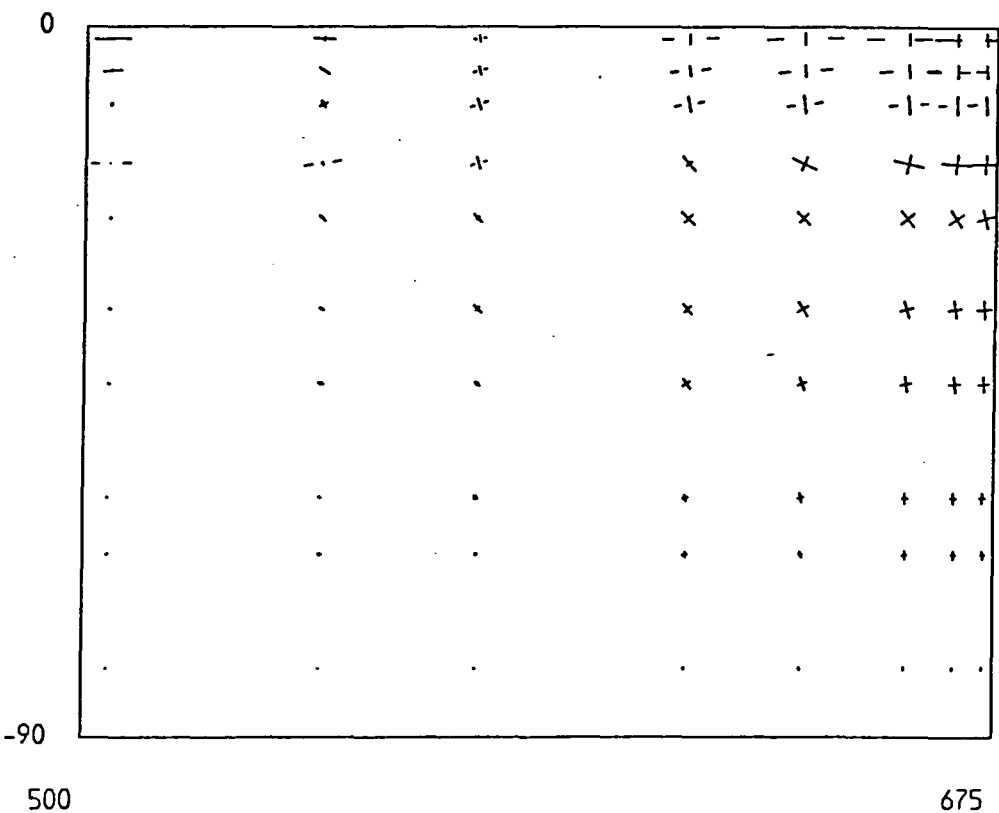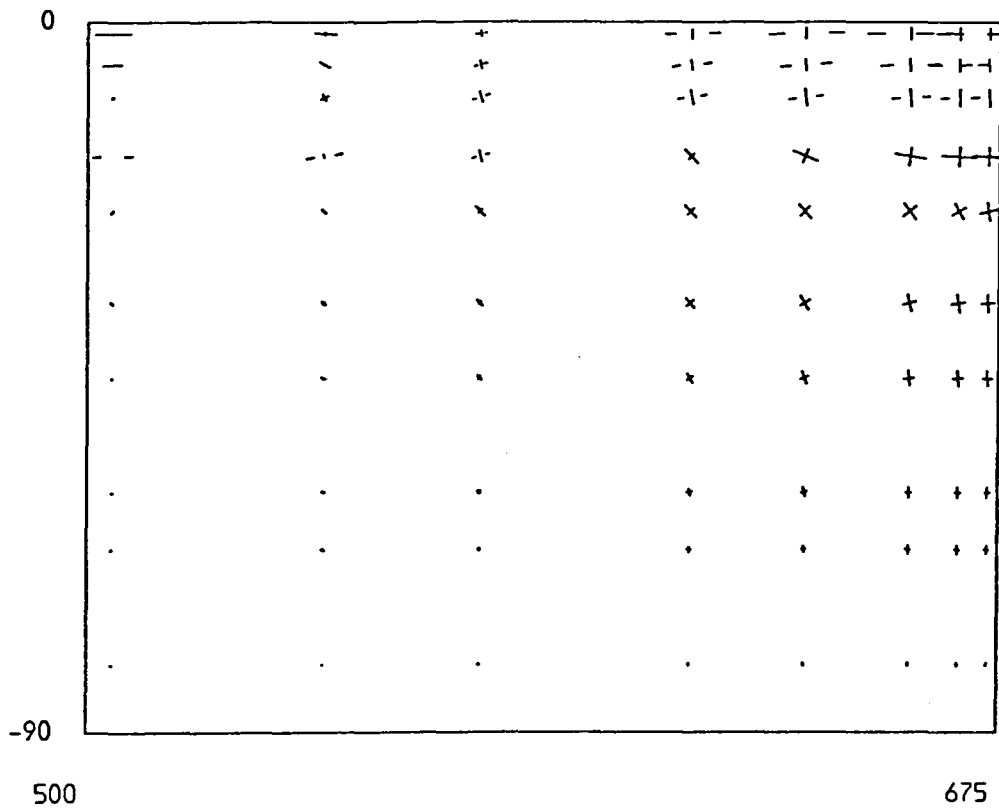
Figure 3.7   The stress regime after 5 Ma relaxation (vertical exaggeration ×1.5)
for two models, a density anomaly only, and the combined thermal anomaly.
The stresses produced by the temperature anomaly have been completely re-
laxed and now the density anomaly dominates the stress regime.

anomaly of a 200 K rise in temperature is,

$$\Delta\rho = -\rho \frac{\alpha_v \Delta T}{1 + \alpha_v \Delta T} = -13.2 \text{ kg m}^{-3}$$

The density distribution cannot mimic the temperature gradient and so an average value of $\Delta\rho = -6.2$ kg m^{-3} is used in the bordering elements.

Initial elastic solutions for the temperature anomaly and the combined thermal anomaly are shown in figure 3.6. The stress regime for the temperature anomaly utterly dominates the elastic response. The lower layer, in which the anomaly exists, was relaxed for 5 Ma and the stress regimes are shown in figure 3.7. This clearly demonstrates the dominance of the density anomaly in the long term response, the temperature stresses have been relaxed but the thermal expansion remains. This is shown in the table 3.5 below which catalogues the vertical displacement (in metres) of the surface (S) and the base (B) of the right hand edge at times 0 Ma and 5 Ma.

Time / Ma	Temperature	Density	Combined
0	S=-270	S=310	S=45
	B=-570	B=305	B=-265
5	S=-2	S=280	S=280
	B=-242	B=290	B=45

Table 3.5   Absolute vertical displacement (in m) of the right hand edge

The surface displacement of the temperature anomaly decreases to zero with time, whilst retaining the vertical expansion of the layer (the difference of the displacements). The sum of temperature displacement + density displacement gives the displacement of the combined thermal anomaly (to within a couple of metres), as would be expected.

In this example the thermal anomaly was confined to the ductile layer, which is probably not realistic. Stresses due to a temperature anomaly in the elastic layer will persist, and even a small change in temperature can swamp the stress field of the body forces. So, when incorporating a thermal anomaly in the finite element method the temperature anomaly will dominate the elastic response and the associated buoyancy forces will dominate the long term viscoelastic response.

3.3 Entry Flow

Entry flow is possibly the simplest of steady state Stokes flow problems, solving the set of linear equations,

$$[K]\{d\} = \{F\}$$

and this test model uses the axisymmetric formulation.

The model parameters are non-dimensional and the finite element meshes for quadrilateral and triangular elements, together with the boundary conditions are shown in figure 3.8. The mesh has a radial dimension of 1 unit and an axial dimension of 2 units. The left hand edge is the axis of symmetry and has the boundary condition $u = 0$, the right edge has a no-slip condition, the top edge has $u = 0$, and the bottom edge prescribes a constant inflow $u = 0$, $v = 1$. Thus the model represents the developement of axial flow along a cylinder given the uniform inflow velocity. A velocity singularity occurs at the bottom right hand corner and so a finer mesh subdivision is used to prevent the disturbance affecting the bulk flow. The fluid has a density $\rho = 1$, and a viscosity $\mu = 1$ yielding a Reynold's number of 1. The purpose of this test model is to establish the value of the penalty parameter c (see equation 2.49). For several values of the penalty parameter it was found that $c = 10^7$ gave the best results. Varying the penalty parameter by a factor of 10 had a negligible effect.

Comparison is taken from a study of finite elements in fluid flow by Zienkiewicz and Godbole (1975) and both sets of non-dimensional results are shown in figure 3.9 for the quadrilaterals and figure 3.10 for the triangles (benchmark study plotted as open circles). This shows velocity profiles along a radius taken at six points along the axis, and both the axial and radial velocity components are displayed. The two sets of results show reasonable agreement, particularly at the further axial distances for the mesh of quadrilateral elements. Increasing the penalty parameter ($c \geq 10^9$) only degrades the flow and does not improve the velocity fit. Thus we must suffer a small trade-off between accuracy and numerical stability which is essentially dependent on the computer word length.

3.4 Couette Flow

This is a simple time-dependent laminar flow problem in which the convection term

Axlsymmetric Entry Flow   Axlsymmetric Entry Flow
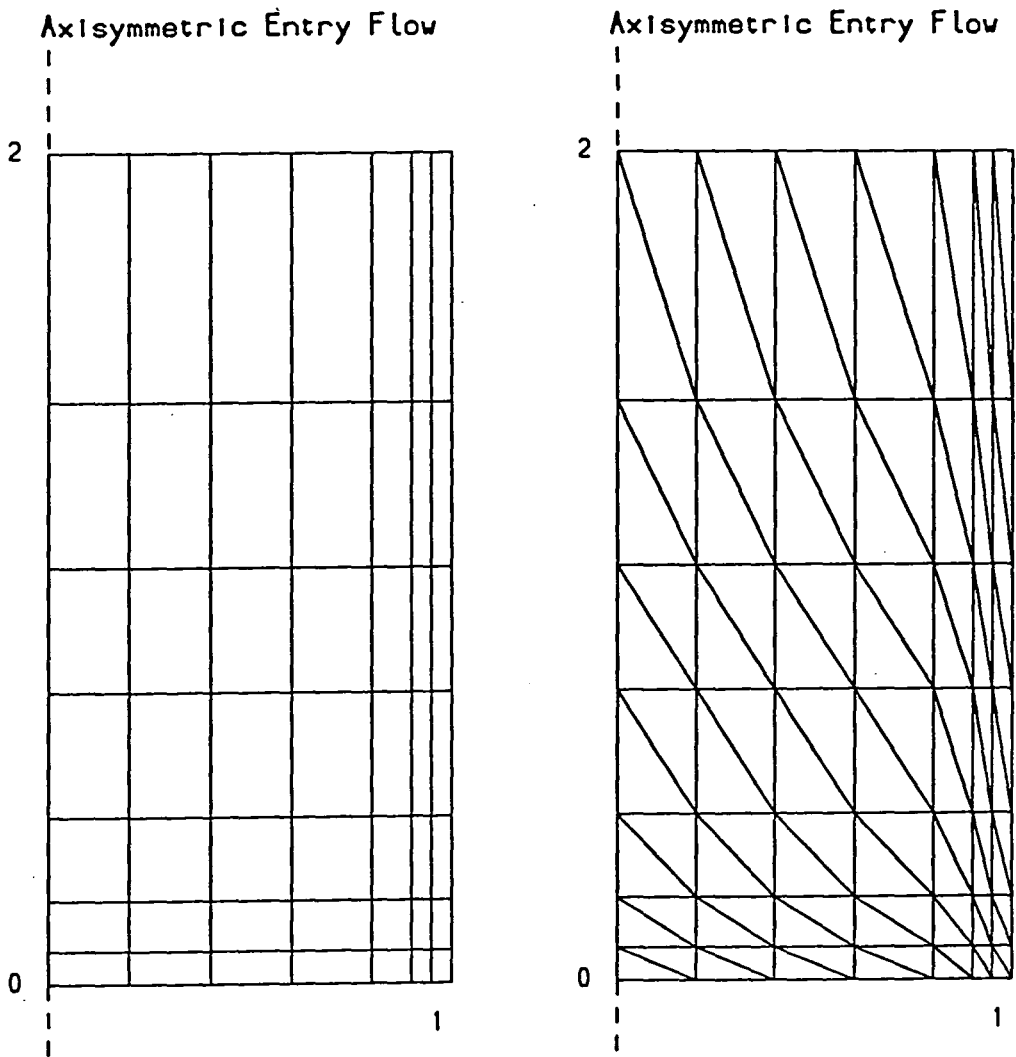
Figure 3.8   The finite element meshes for the entry flow problem, left a mesh
    wholly composed of quadrilaterals, and right a mesh wholly composed of tri-
    angles. The dashed line denotes the axis of symmetry. The base of the mesh
    has a prescribed uniform inflow of unit velocity, the right hand side has a
    no-slip condition.

Velocity Profiles at Specified Axial Distances
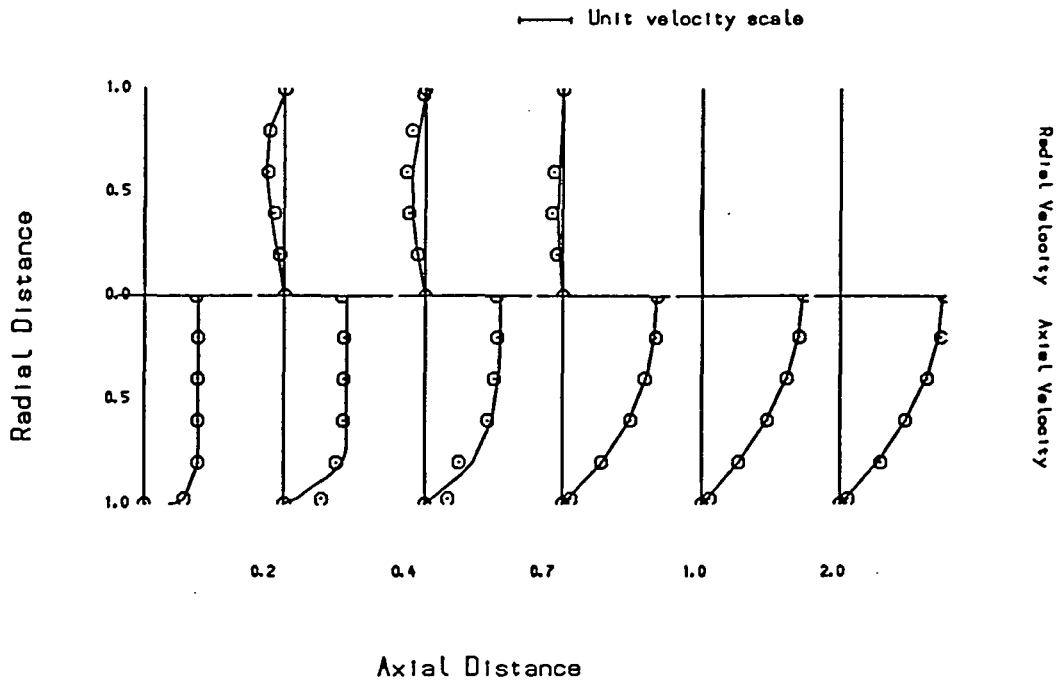
Figure 3.9   The velocity profiles for the mesh of quadrilateral elements. At six points along the axis 0, 0.2, 0.4, 0.7, 1.0, 2.0 the velocity profiles along the radius are plotted. The open circles denote the benchmark study of Zienkiewicz and Godbole (1975).

Velocity Profiles at Specified Axial Distances
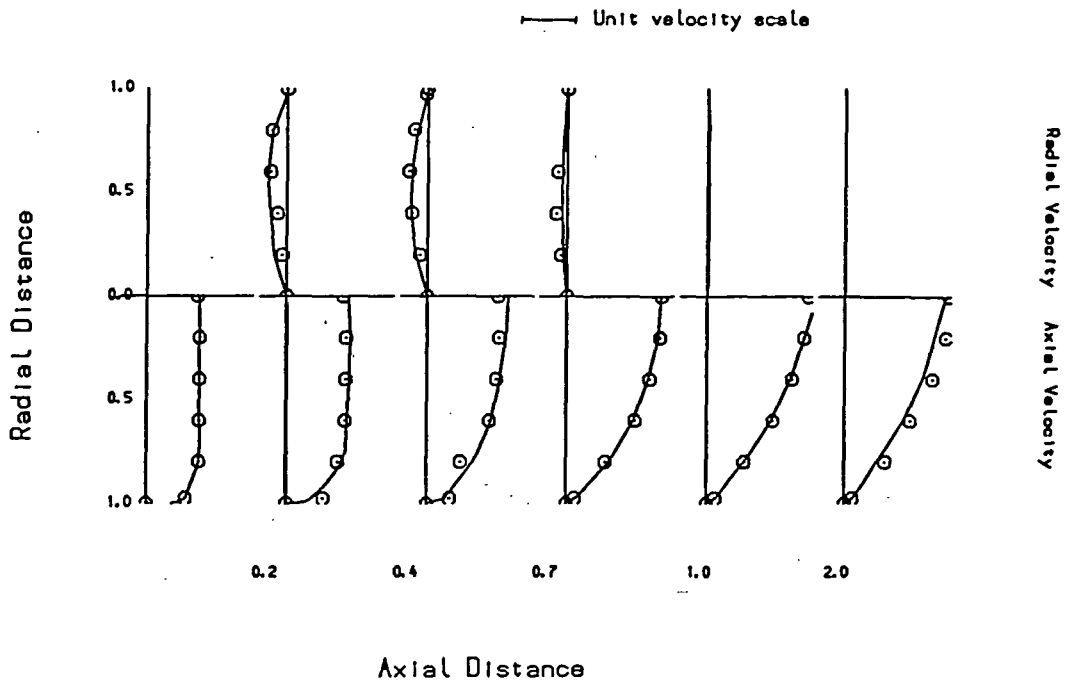
Figure 3.10   The velocity profiles for the mesh of triangular elements. At six points along the axis 0, 0.2, 0.4, 0.7, 1.0, 2.0 the velocity profiles along the radius are plotted. The open circles denote the benchmark study of Zienkiewicz and Godbole (1975).

Unsteady Couette Flow
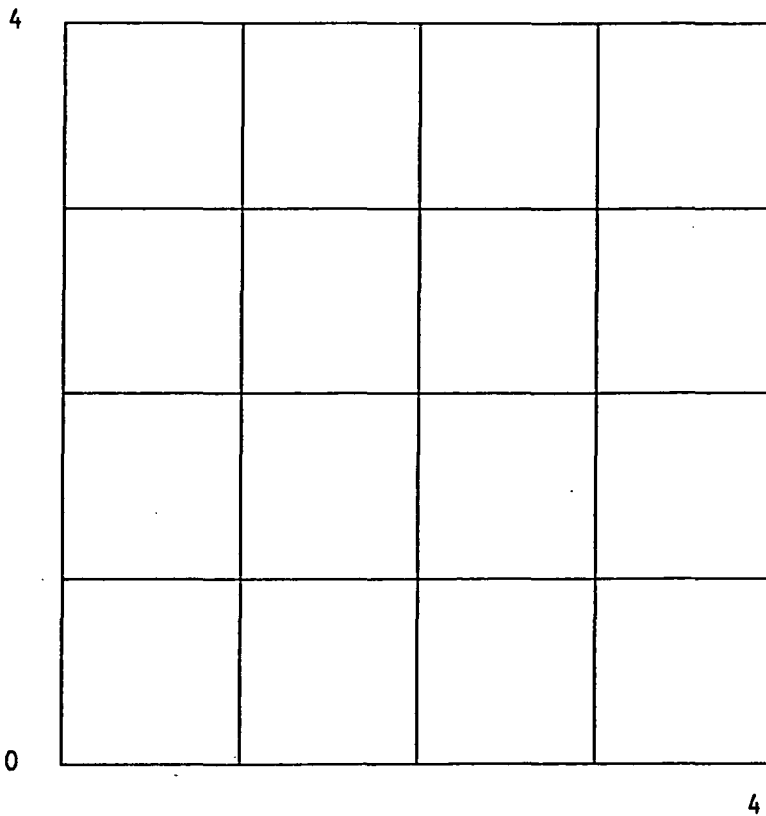
Figure 3.11   The simple finite element mesh of 16 quadrilaterals for the Couette flow problem. The top surface is held fixed and the base moves at unit velocity along axis.

Velocity Profiles For Couette Flow
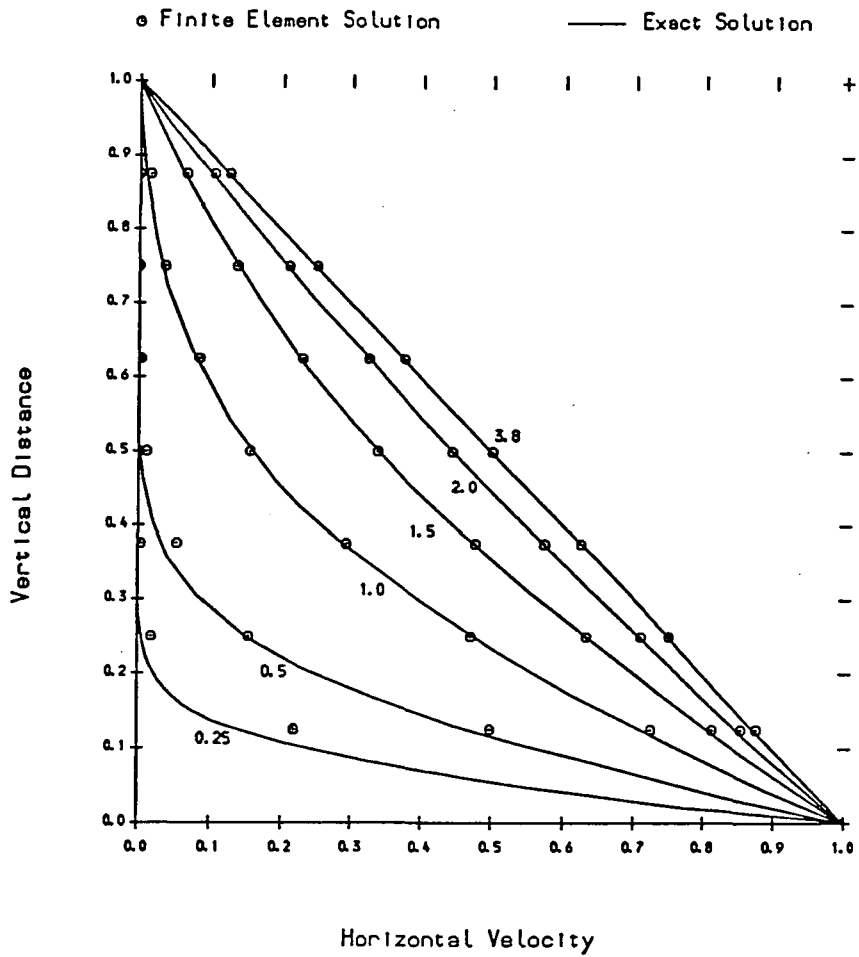
Figure 3.12   The velocity profiles at selected time intervals showing the developing Couette flow. The dimensionless parameter characterising the curves is defined in the text and represents increasing time.   The finite element solution is denoted by open circles, the exact solution is the solid lines. The first curve (labelled 0.25) is one time-step of the finite element solution.

of the Navier-Stokes equations is identically zero,

$$[M]\frac{\partial}{\partial t}\{d\} + [K]\{d\} = \{F\}$$

The solution to these equations was presented in section 2.3.4 and the implementation of the algorithm will be tested by the model of Couette flow. A viscous fluid exists between two parallel plates, the upper of which is held stationary. The lower plate moves along its axis at unit velocity for $t \geq 0$. A boundary layer forms along the lower edge and diffuses upward, developing a steady state linear velocity profile as time progresses. The mesh is shown in figure 3.11, and the non-dimensional parameters of this problem are $\mu = 1$, $\gamma = 0.5$, $\Delta t = 0.0625$. The results are compared to the theoretical flow profiles in figure 3.12 and show good agreement (open circles are the finite element solutions). The dimensionless parameter which characterises the curves is,

$$\frac{4\sqrt{\mu\,t}}{H}$$

where μ is the dynamic viscosity, t is the total time, and H is the plate separation. The x-axis defines the flow velocity and the y-axis defines the vertical distance between the plates. So, as time progresses the curves map the upward diffusion of velocity towards the steady state linear velocity profile.

3.5   Shear Stress Evaluation

The viscous flow finite element code is required to evaluate the amount of viscous shear stress produced by an 'elastic' slab moving through the mantle. The representation of an elastic slab must accurately support the shear stress generated along its edge. Melosh and Raefsky (1980) found that an effective viscosity of 2×10^{21} Pa s was suitable to support the outer arc bulge of a viscous lower lithosphere. Vassiliou et al. (1984) used a viscosity contrast of ×10 between mantle and slab. Hager et al. (1983) followed Melosh and Raefsky and used a viscosity of 10^{22} Pa s, which equates to a viscosity contrast of ×10. Intuitively the slab is significantly more rigid than the mantle, both upper and lower, and this is justified by the lack of divergent flow at the 670 km discontinuity (as evidenced by the stresses). Since lower mantle viscosities of 10^{23} Pa s have been proposed, my own rather arbitrary choice of slab viscosity is 10^{23}

Pa s. This is considered to be large enough to distinguish the lithosphere within the flow, without being so large that it decouples as a rigid intrusion.

The finite element mesh represents a long, thin channel of dimensions appropriate to the mantle. The lower surface is held stationary and the upper surface has a prescribed velocity of 10^{-8} m s^{-1} (300 mm yr^{-1}). The top 50 km of the mesh has a viscosity of 10^{23} Pa s and the lower 340 km a viscosity of 10^{21} Pa s. Assuming that the top layer retains its rigidity and transfers the motion of the upper surface to the top of the lower layer, then steady state Couette flow is induced in the lower layer. The analytical solution is well-known, the only non-zero stress components are horizontal shears,

$$\tau_{21} = \tau_{12} = \mu \frac{\partial u}{\partial y} = \mu \frac{U}{b}$$

where μ is the viscosity, U is the velocity of the upper surface, b is the width of the channel. Thus, substitute the parameters of the finite element mesh into the equation and the shear stress which would be generated by flow in the lower layer is,

$$\tau = \frac{10^{21} \times 10^{-8}}{340 \times 10^3} = 0.294 \times 10^8 \text{ Pa}$$

Apart from small edge effects, this shear stress is reproduced throughout the 50 km upper layer by the finite element model. The normal stress components exist but are small, being about $\times 10^{-4} \tau$.

In conclusion, a lithosphere of viscosity 10^{23} Pa s will accurately represent the shear stress induced by viscous flow along its boundaries.

3.6 Time-Dependent Free Surface Flow

The complete Navier-Stokes equations were derived in section 2.3 and can be written,

$$[M] \frac{\partial}{\partial t} \{d\} + [K]\{d\} + \{H\} = \{F\}$$

The theory of an algorithm formulated for free-surface flow was sketched in the previous chapter. In order to test the free-surface algorithm Hughes et al. (1978) provided details of an experimental wave-generation study and also supplied the finite element simulation of this wave propagation. It is appropriate to follow an identical simulation to examine the implementation of the free-surface algorithm in this thesis.

The finite element mesh in figure 3.13 depicts the left hand edge of a rectangular box of length L=949.095 units and depth D=10 units. The base nodes permit horizontal motion only, and the right hand edge nodes only permit vertical motion. The nodes along the top surface are assigned $\alpha_y = 1$ to designate motion with the free-surface, while all other dof are assigned $\alpha = 0$ (see equations 2.61, 2.62). A surface wave is generated by prescribing the displacement-time function of the left hand edge nodes as,

$$\hat{u}_x(t) = \frac{H}{\kappa} \left[1 + \tanh \left(\frac{c\kappa t}{D} - 4 \right) \right]$$

where,

$$c = \sqrt{gD \left(1 + \frac{H}{D} \right)} \qquad \kappa = \sqrt{\frac{3H}{4D}}$$

Differentiation yields the velocity at the left hand edge,

$$\frac{\partial \hat{u}_x}{\partial t} = \frac{Hc}{D} \left[1 - \tanh^2 \left(\frac{c\kappa t}{D} - 4 \right) \right]$$

where, $g = 1$, and H=0.86. The remaining parameters to be defined are $\mu = 0$, $\rho = 1$, $\Delta t = 1.7$ s, $\beta = 0.6$, and $\gamma = 0.5$. The wave-generation function is formulated such that non-linear and dispersive terms are balanced and the wave should propagate without distortion.

For each time increment the velocity of the left hand edge nodes is applied as a boundary condition, and the body forces of the fluid are calculated under a scaled gravitational field of $g = 1$. Two iterations of the non-linear term $\{H\}$ are applied, and for each iteration the system matrix is calculated from the updated mesh positions. To ensure solution stability, the displacements of the mid-side nodes are defined as the average of the displacements of the adjacent corner nodes.

The set of profiles in figure 3.14 describe the evolution of the surface of the fluid with time. The axes are scaled by the depth of the fluid. The profiles show the development of the surface wave and its subsequent propagation. Hughes et al. (1978) follow the wave over a solution duration of 286 secs (160 time steps at $\Delta t = 1.788$ s), it has an almost constant scaled amplitude of 0.095, propagates at a constant velocity of 3.31 units s^{-1}, and changes slightly in half-width from 6 — 6.2. By contrast, the wave in figure 3.15 has evolved over 170 secs; it has a scaled amplitude of 0.058 which is decaying with time, it propagates at 2.86 units s^{-1} and disperses with a half-width increase of 6.1 → 7.2. The details of the wave propagation differ quite markedly from the benchmark
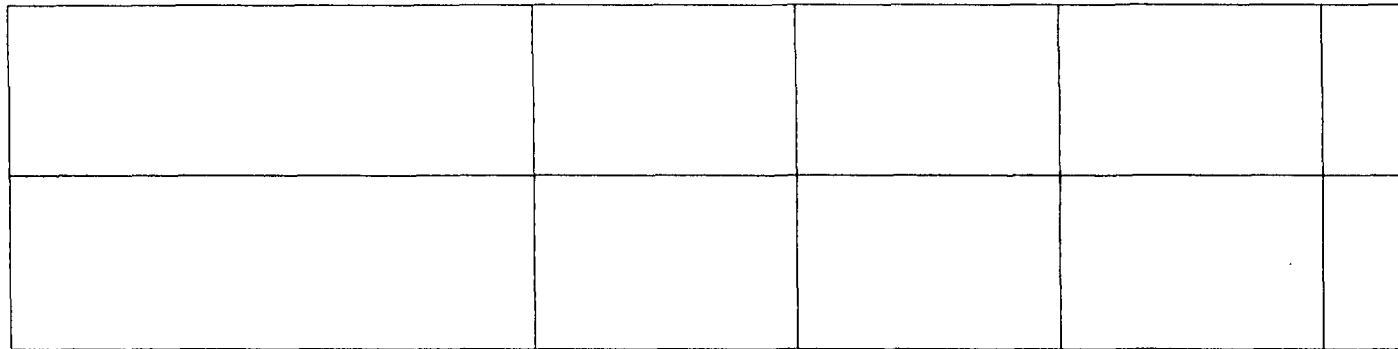
Figure 3.13   The left hand section of the simple finite element mesh for the wave
propagation problem. The displacement-time history of the left hand edge
decreases the volume of the box which generates a travelling surface wave.

Free-surface of the fluid at selected times

Scaled amplitude of position of free-surface

Scaled distance in reference frame
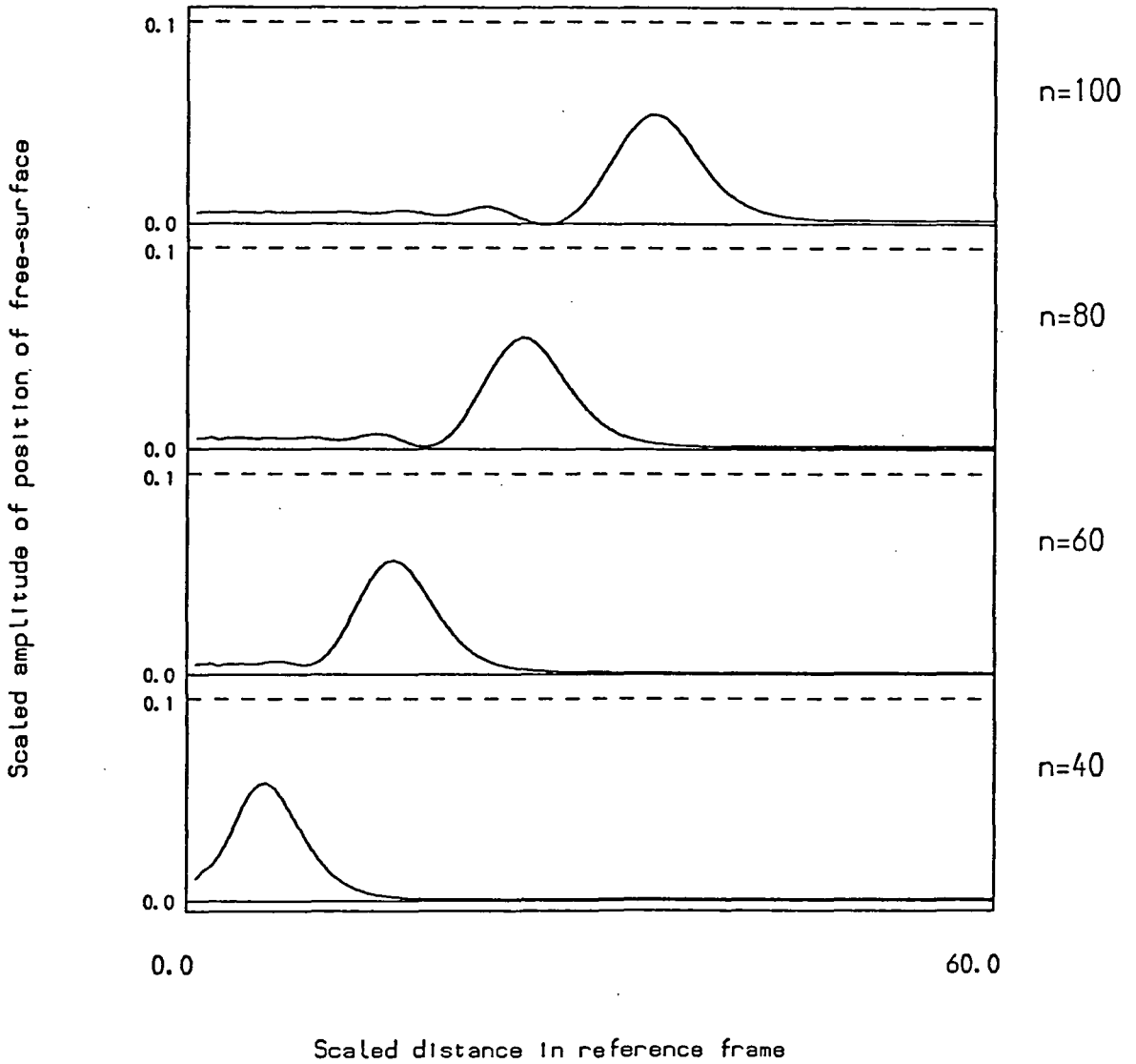
Figure 3.14   The scaled profiles of the free-surface at 4 stages in the propagation of the travelling wave corresponding to 40, 60, 80 and 100 time steps.

solution. The dispersive effects, i.e. decaying amplitude and increasing half-width, can be attributed to the smoothing (removing the high frequency components) and the inferior performance of the Serendipity elements in coping with the non-linear terms. This is evident in the low value of the stability constants γ, β necessary to achieve a stable solution. The cause of the low amplitude and low velocity is more difficult to pinpoint. The non-linear terms control the amplitude growth of the wave in the initial period of generation. The subsequent propagation is dependent on the developement of the wave, and hence the low velocity could be due to the formation of a small initial wave. Hence, if a wave of amplitude 0.095 had formed initially then it would probably propagate at 3.31 units s^{-1} in this model, but it would still be subject to dispersive effects. This problem with the non-linear terms can be removed by considering a very low Reynold's number test model, more appropriate to the subsequent simulations of flow in the mantle.

The algorithm outlined above has been adapted for low Reynold's number flow and the finite element code has been tested using a simple gravity slump problem. The mesh is shown in figure 3.15, it represents a 600×200 km cross-section with a 5 km high-standing 'mountain' at the centre. The topographic high is generated by a linear rise and fall over a distance of 120 km. The body of fluid has a uniform density $\rho = 3300$ kg m^{-3} and uniform viscosity $\mu = 10^{21}$ Pa s yielding an extremely small Reynold's number. The base and sides have free-slip boundary conditions. The free surface is defined by the parameter α (see equations 2.61, 2.62), and for the nodes of this mesh all $\alpha_x = 0$, $\alpha_y = 0$ except for the surface where $\alpha_x = 0$, $\alpha_y = 1$. This allows the nodes to move vertically and thus map the development of the surface. The stability constants $\gamma = \beta = 1.0$ and the time step employed is $\Delta t = 1000$ yrs.

Under the law of conservation of mass the high-standing mass at the centre should flow laterally under gravity and spread its volume as a uniform increase in surface height. The volume of the mountain is 300 km^2, which when completely relaxed will generate an overall rise in surface level of 0.5 km. The ability of the finite element method to model this redistribution of the surface is considered to be a good assessment of both the time-stepping algorithm and the incompressibilty constraint. The development of the surface with time is shown in figure 3.16 for a total solution duration of 2 Ma.

The perturbation at the centre dies sufficiently quickly and the overall rise in

20

-200

0

600
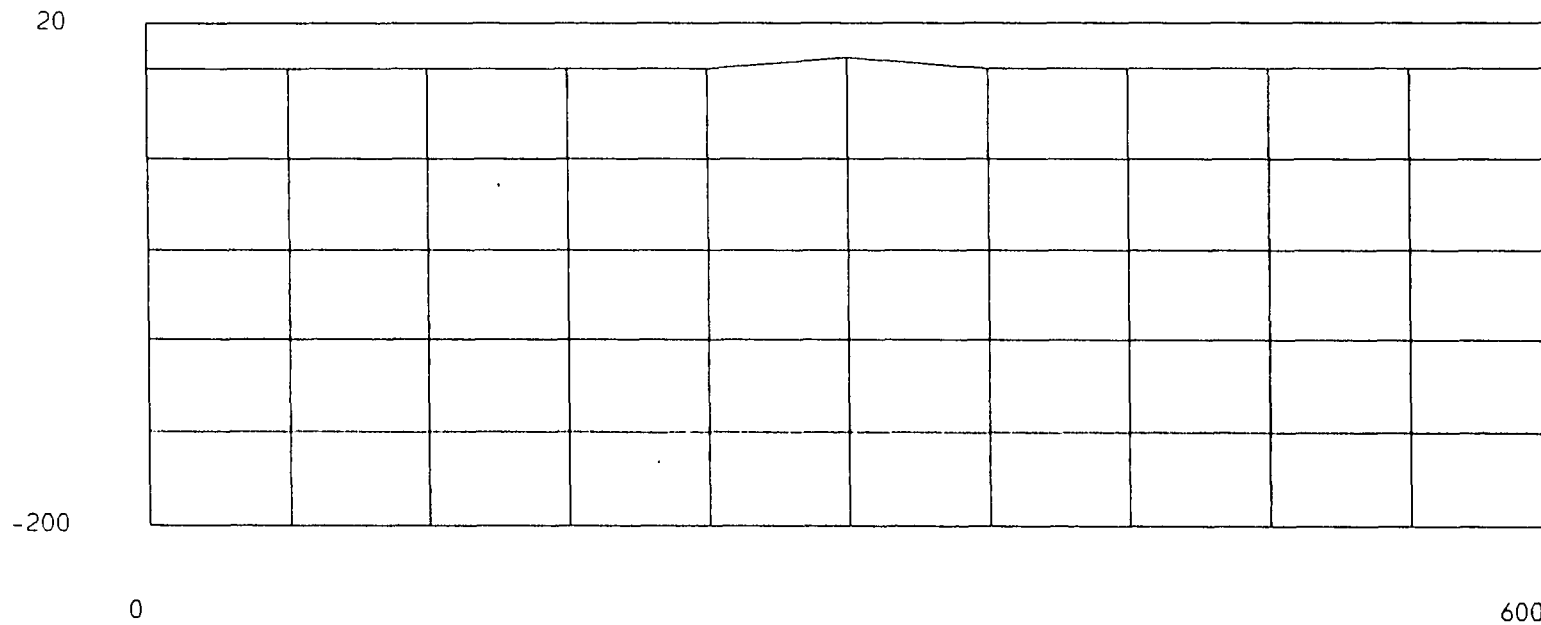
Figure 3.15   The simple finite element mesh for the gravity slump test problem.
The right hand edge is a 5 km topographic high.

Surface Motion
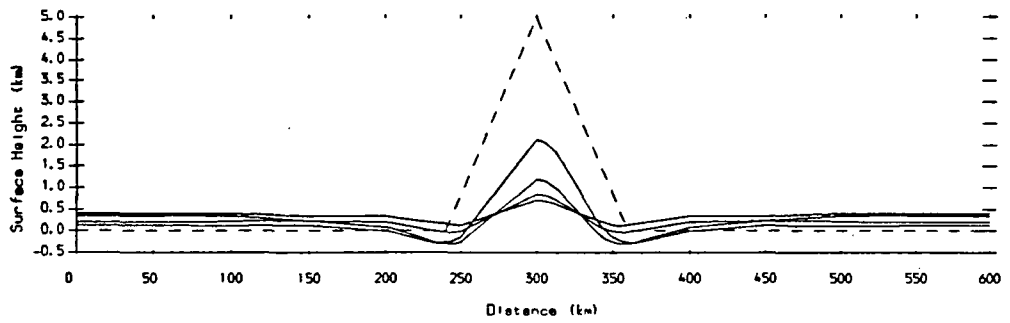
Figure 3.16   The evolution of the free-surface with time, the curves represent 0, 0.01, 0.05 and 0.2 Ma. The initial topography has almost completely relaxed and spread as an even increase in surface height.

surface level is exactly as predicted.

CHAPTER 4

Flow In A Viscous Earth

4.1 Introduction

Density heterogeneities at the surface or in the interior of the Earth persist over geological time and provide significant long-term loads. The lithosphere and the underlying mantle respond differently to these loads; lithospheric behaviour can be approximated by the flexure of an elastic plate, and mantle creep is best modelled by flow of a viscous fluid. Attempts to formulate a numerical method to couple directly both elastic and viscous rheologies (e.g. Tharp 1985, Ward 1985) have had only limited success. As a compromise in this chapter the Earth is modelled as a viscous, incompressible fluid body denoting the lithosphere as a high viscosity layer.

As a preface to the models of mantle flow driven by subduction a few examples of earlier numerical analyses will be reviewed. Since it is not possible to simulate accurately the entire Earth in a single model, the boundary conditions of a particular cross-section must be a good approximation to the response of the material outside the domain under consideration. The choice of boundary conditions originates from the work in the early 1970s, notably Richter (1973), where mantle convection was modelled by the 2-D Rayleigh-Bénard convection. Sleep (1975) studied the response to the anomalously high density slab using a viscous, incompressible fluid rheology. The 2-D cross-section through the asthenosphere included the slab as a high viscosity intrusion. He adopted the same surface boundary conditions as Richter (1973) and stated '*The free surface of the Earth was modelled as a vertically immovable, horizontally frictionless boundary and the inferred elevation of the surface computed from the vertical stress on that boundary...*' and he asserted that these assumptions will '*...contribute mainly geometrical distortion of the computed versus the actual flow field but do not significantly affect the dynamics.*' This is true for the classical Rayleigh-Bénard thermal convection cell, but some studies, such as Hager et al. (1983) and Vassiliou et al. (1984) for exam-

ple, incorporated these assumptions into models of subduction which depend critically on the flow pattern.

The subduction models of Vassiliou et al. (1984) used a penalty function finite element method for Stokes flow similar to that used in this thesis. Erroneous boundary conditions have two major effects which influence the dynamics of the model. The top surface is constrained to move horizontally, and so a high viscosity lithosphere would induce the top of the asthenosphere to move only horizontally also. While this motion could be real, the constraints are artificial. Secondly, the zero vertical motion at the top of the slab prescribes that its surface points are fixed with respect to the gravitational field. Thus slab motion is controlled by stretching under its own weight. This is highlighted by the note on slab viscosity (relative to the upper mantle viscosity of unity) from Vassiliou et al. (1984) '...*dimensionless slab viscosities of 10 yield reasonable flow velocities...*'. This is interpreted as stating that a viscosity contrast of ×10 between mantle and slab was required to allow the slab to flow downdip at velocities which have been observed for the subduction zones of the Earth. It is likely that the slab is significantly more rigid than the surrounding mantle and perhaps a viscosity contrast of ×100 is more appropriate.

Subduction is not a steady-state process. Time-dependence is controlled by the temporal variation of the boundary conditions. Over long time periods this variation is provided by the motion of the slab, but over short time periods it is the adjustment of the free surface. The 2-D models of a viscous fluid in a box require a suitable method for dealing with the free surface. Other boundaries, at the base and sides, can be approximated quite adequately with Dirichlet conditions or lithostatic pressure gradients and will have less influence on the dynamics. The previous chapter demonstrated that the free surface can be modelled numerically and the following simulations of flow in the mantle utilise this representation of the free surface of the Earth.

4.1.1   The Conceptual Basis of the Finite Element Models

Loper (1985) proposed that the viscosity-depth profile, rather than the density-depth profile, exerts a primary control over the structure of mantle convection. The 1-D exploratory model presented by Loper (1985) advocated an isoviscous mantle. Richards and Hager (1984) and Hager (1984) modelled the mantle as a layered, Newtonian sphere.

63

Density anomalies of the descending slab at convergent margins were employed to drive mantle convection and the geoid was calculated from the driving densities and the deformation of the surface and the core-mantle boundary (CMB). Hager (1984) demonstrated that a viscosity contrast of ×30 between the upper and lower mantle is required to produce a relative high in the geoid at subduction zones. Willemann and Anderson (1987) extended the analysis of Hager (1984) to investigate the geoid due to an inextensible vertical slab in 2-D finite element models of viscous flow. A relative geoid high was produced by a viscosity contrast of ×10 at the upper - lower mantle interface.

The numerical simulations of this chapter are based on the assumption that the viscosity-depth distribution controls subduction. The average density-depth variation of the mantle (e.g. figure 1.6) is not included. The anomalous density of the descending slab drives the motion. The major sophistication over previous analyses is that short period time-dependence is included by permitting motion of the free surface. Thus the pattern of the flow in the mantle may be studied with a greater degree of confidence. The surface deformation is essentially instantaneous compared to the time constant of subduction (Hager 1984). This is translated into the finite element models by allowing the free surface to evolve over a time interval of 50000 yrs (the time scale of post-glacial rebound). This time interval is instantaneous with respect to slab motion and so the nodal coordinates of the slab remain unchanged.

4.2   The Finite Element Mesh

The finite element mesh represents a rectangular cross-section throughout the mantle of dimensions 9130 × 2800 km and is shown in figure 4.1. The bulk of the mesh has a layered structure. The top 90 km is oceanic lithosphere and underlying this is the asthenosphere, 90 → 180 km depth. The rest of the upper mantle extends between 180 → 670 km depth and most of the mesh represents the lower mantle, 670 → 2800 km depth. The general rheology is given in Table 4.1 below.
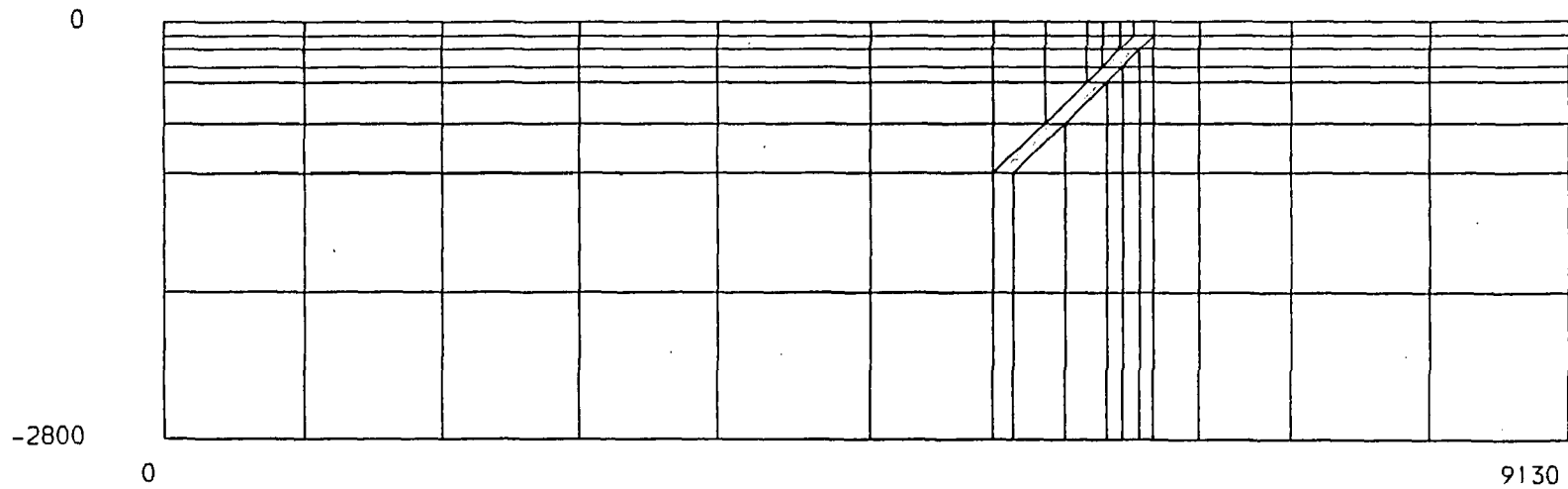
Figure 4.1   The mesh represents a 9130 × 2800 km cross-section through the mantle. The general rheology is given in the text. The slab is shaded; it dips at 45° and carries the anomalous density.

Depth (km)	Density (kg m^{-3})	Viscosity (Pa s)
0 – 90	3300	10^{23}
90 – 180	3200	$10^{19} \rightarrow 10^{21}$
180 – 670	3200	10^{21}
670 – 2800	3200	$10^{21} \rightarrow 10^{23}$

Table 4.1   General Rheology

Although the average viscosity-depth profile of the mantle is not well constrained, the best estimate available is an upper mantle viscosity of $\mu = 10^{21}$ Pa s (Cathles 1975). Estimates of the depth extent and viscosity of the asthenosphere vary widely (e.g. Cathles 1975, Robinson et al. 1987, Ceuleneer et al. 1988) and the model values of 90 km and $\mu = 10^{19} - 10^{21}$ Pa s are representative. Recently published estimates of lower mantle viscosity generally fall in the range $\mu = 10^{21} - 10^{23}$ Pa s (Peltier et al. 1986). The mantle is assigned a constant density of $\rho = 3200$ kg m^{-3} to remove the effects of the vertical density variation. The oceanic lithosphere is assigned a density of $\rho = 3300$ kg m^{-3} to represent the thermal density contrast.

The position of the slab is shown in figure 4.1. It is represented by oceanic lithosphere of viscosity $\mu = 10^{23}$ Pa s dipping at 45°. The slab tip is streamlined in the downdip direction. The elevated olivine-spinel phase change in the slab is included as a density anomaly of 150 kg m^{-3} over the depth range 300 $\rightarrow$ 400 km. The phase change is spread over a larger volume than predicted (Schubert et al. 1975) and so the density anomaly is reduced to maintain a consistent mass anomaly. The magnitude of the density anomalies may be considered a little high but this will only affect the magnitude of the flow velocities and should not seriously affect the dynamics.

Free slip boundary conditions are applied to the base and sides. Thus the base permits only horizontal flow and the sides permit only vertical flow. The boundary conditions contain the fluid within the domain of the mesh. The surface nodes are assigned $\alpha_y = 1$ to define the free surface, all other $\alpha = 0$ (see equations 2.61, 2.62).

The deflection of the CMB is not included in the finite element models. Willemann and Anderson (1987, figures 3 and 4) showed that this is a significant contribution to the geoid for long slabs (1400 km penetration) with a viscosity contrast at the 670

km discontinuity of at least $\times 10$. The CMB topography will generate a negative, long wavelength gravity anomaly. Deeply sourced gravity anomalies are attenuated at the surface and so the gravity profile will be dominated by the contributions from shallower loads.

The magnitude of the time increment for the time-stepping algorithm is a somewhat arbitrary choice since it only has a maximum value which is dependent on the flow velocity. The models were assigned a time increment of 1 000 yrs and evolve over 50 time steps.

The finite element models of this chapter investigate the effect of mantle viscosity and depth of slab penetration on the mantle flow patterns generated by subduction. Model limitations, such as lithospheric rheology and the thrust zone, are discussed in the final section.

4.3   The Influence of Lower Mantle Viscosity

One of the main concerns of geodynamical studies of mantle convection is the ability of the slab to penetrate the lower mantle. This chapter concentrates on the role of the viscosity structure in the control of slab motion and thus the viscosity of the lower mantle is a dominant theme. This opening section is devoted to a brief introduction to the action of the lower mantle viscosity using a model of slab penetration to 1000 km depth. Throughout the remainder of the chapter variations in lower mantle viscosity will be included in addition to the study of other parameters. The three models of this section have an asthenospheric and upper mantle viscosity of $\mu = 10^{21}$ Pa s, and lower mantle viscosities of 10^{21}, 10^{22} and 10^{23} Pa s respectively.

The flow fields and surface displacement profiles are given in figures 4.2 - 4.4 for the 10^{21}, 10^{22} and 10^{23} Pa s models respectively. The plots of flow vectors have a circle at each node and a vector denoting the velocity away from the node. The velocity scale at the top varies between models. The flow field is enclosed by a solid border. The surface displacement profile is shown above the flow field. The dashed line is the initial position of the surface at $t = 0$. The solid curve represents the vertical displacement of the surface at $t = 50\,000$ yrs. The vertical line at the left hand edge is a vertical scale denoting 5 km of displacement.

66

Figure 4.2   The flow field and surface displacement profile for the model of slab
penetration to 1000 km depth, with asthenosphere, upper mantle and lower
mantle viscosities of $\mu = 10^{21}$ Pa s. The flow field is depicted by a circle at
each node and a vector denoting velocity away from the node. The velocity
scale is given at the top. The flow field is enclosed by a solid border. At the
right hand edge the ratios of upper mantle viscosity : asthenosphere viscosity,
and lower mantle viscosity : upper mantle viscosity are given. The surface
displacement profile is shown above the flow field.

Figure 4.3   The flow field and surface displacement profile for the model of slab penetration to 1000 km depth, with asthenosphere viscosity 10^{21} Pa s, upper mantle $\mu = 10^{21}$ Pa s and lower mantle $\mu = 10^{22}$ Pa s.

Figure 4.4   The flow field and surface displacement profile for the model of slab penetration to 1000 km depth, with asthenosphere viscosity 10^{21} Pa s, upper mantle $\mu = 10^{21}$ Pa s and lower mantle $\mu = 10^{23}$ Pa s.

The constant viscosity mantle in figure 4.2 generates a continuous flow circulation about the slab. Under the slab the flow vectors are near vertical. The upper mantle material is being driven down into the lower mantle and this would cause the depression of the CMB (not present in these models because of the base boundary condition). The flow is circulating from under the subducting plate around the slab tip as noted by Garfunkel et al. (1986). The width of the circulation is about 3000 km, but this may be controlled by the depth of the mesh (2800 km), and also be influenced by the left hand boundary.

In the upper mantle above the slab the flow is roughly horizontal with a maximum (100 mm/yr) at about 400 km depth. The overriding plate is nearly stationary. Within the slab the flow is aligned roughly downdip (80 mm/yr) in the upper sections but inclined more towards vertical below 400 km depth. In the subducting plate, flow is nearly horizontal (30 mm/yr) and directed towards the trench, and the underlying mantle has a vertical velocity gradient with the lateral velocity dropping to zero at about 400 km depth.

The surface displacement profile shows a maximum depression at the top of the slab of 3.4 km. The right hand edge of the depression rises over a width of about 200 km, but the left hand edge rises at a lower angle, over a width of about 1100 km. The far left and right hand edges of the surface plates are elevated by about 0.5 km.

The flow field in figure 4.3 demonstrates the effect of a viscosity contrast of $\times 10$ at the 670 km discontinuity. The overall magnitude of the flow velocity is smaller but the general pattern is similar to figure 4.2. There is a circulation about the slab tip, with near vertical flow below the slab and horizontal flow above the slab. However, there is distinct partial decoupling of this circulation at 670 km depth.

The subducting plate flows towards the trench at 15 mm/yr with an underlying velocity gradient to zero at 670 km depth. The overriding plate is virtually stationary with an underlying velocity gradient to a maximum (10 mm/yr) at about 400 km depth. Within the slab the flow is fairly consistently aligned just vertical of downdip (50 mm/yr). The maximum depression of the surface is 2.1 km with an enhanced asymmetry to the uplift of the flanks.

Increasing the viscosity of the lower mantle further, figure 4.4 shows the flow field utilising a viscosity contrast of $\times 100$ at the 670 km discontinuity. There is almost

complete decoupling of the flow at the upper-lower mantle boundary. In the lower mantle there is a small downdip component of flow (10 mm/yr) due to the portion of slab in the lower mantle. In the upper mantle the flow is predominantly horizontal and directed seawards with a velocity maximum (25 mm/yr) at about 400 km depth. Thus the flow is 'channelled' through the upper mantle. The overriding plate has a small seawards velocity and the subducting plate is roughly stationary with an underlying velocity gradient now directed seawards. Flow within the slab varies along its length; it is roughly vertical in the upper section and downdip in the lower section. The surface depression is broader and reaches a maximum depth of about 1.9 km.

The surface depressions decrease in depth and increase in width as the lower mantle viscosity increases. This variation in depth, and its effect on the geoid, was noted by Hager (1984). The variation in width is partially due to the overall reduction in magnitude of the flow velocity. Thus, over a fixed time interval, the surface has not evolved as far. The shape of the depression is also affected by the mechanical strength of the slab. The flow field in figure 4.5 reproduces the model of figure 4.3 with the lower mantle viscosity 10^{22} Pa s, but there is no viscosity contrast between the slab and mantle. The overall magnitude of flow is much greater (as shown by the velocity scale at the top of the figures) and aligned downdip, and the surface depression is broader.

The asymmetry of the depression is due to the dip of the slab. The vertical motion of the sinking slab is coupled to the surface plates through the 'mechanical strength' of the high viscosity lithosphere, and by viscous coupling through the mantle overlying the slab. The uplift of about 0.5 km at the left and right hand edges of the surface plates is due to the boundary conditions. There is zero mass flux at the vertical sides and so depression of the surface at the top of the slab will cause uplift of the flanks. This is a limitation of the models that is further discussed in the final section. The depression of the surface is sustained by continuous slab motion. The models do not reach a steady state because slip at the thrust zone cannot be simulated.

These preliminary models demonstrate the ability of a viscosity contrast at the 670 km discontinuity to decouple the flow systems in the upper and lower mantle. This provokes a change of flow in the surface plates, flow within the slab, as well as the flow systems in the mantle.

4.4 The Influence of the Asthenosphere

The following sequence of models investigate the effect of varying the viscosity in the asthenospheric layer, 90 $\rightarrow$ 180 km depth. The flow fields in figures 4.6 - 4.8 employ an asthenospheric viscosity of $\mu = 10^{20}$ Pa s in models of slab penetration to 1000 km with lower mantle viscosities of $\mu = 10^{21}$, 10^{22} and 10^{23} Pa s.

Comparison with figures 4.2 - 4.4 shows that the decrease in asthenospheric viscosity has very little effect on the gross flow pattern. The main effect is to concentrate the lateral flow in the upper mantle into the asthenosphere and thus partially decouple the surface plates. This introduces a small landward component of velocity in the overriding plate above the slab.

The models in figures 4.9 - 4.11 further decrease the viscosity in the asthenosphere to 10^{19} Pa s. Comparison with the models described above shows an exactly similar effect. The low viscosity zone concentrates the lateral flow and produces a small landward component of velocity in the overriding plate.

4.5 Variation in Depth of Slab Penetration

The models in this section describe the influence of variations in slab length. Depths of slab penetration are set to 300, 400 and 670 km. The basic mesh parameters remain unchanged from the models of the previous section and variations in viscosity in the mantle layers are included.

The models in figures 4.12 - 4.14 represent slab penetration to 670 km and have a uniform viscosity asthenosphere and upper mantle $\mu = 10^{21}$ Pa s, with lower mantle viscosities of 10^{21}, 10^{22} and 10^{23} Pa s. Comparison with figures 4.2 - 4.8 shows that for a given mantle viscosity the gross flow structure is similar to the 1000 km penetration model. In more detail, the models in figures 4.2 and 4.12 for the constant viscosity mantle show that the 670 km penetration model has a slightly reduced width of circulation around the slab. Also, the flow vectors within the slab are rotated slightly anticlockwise. A similar situation occurs for the 10^{22} Pa s lower mantle model in figure 4.13. The width of circulation is reduced, relative to figure 4.3, and the flow within the slab is rotated anticlockwise from the vertical. The high viscosity 10^{23} Pa s lower mantle models in figures 4.4 and 4.14 are very similar with simply a reduction in the

Figure 4.5   The flow field and surface displacement profile for the model of slab penetration to 1000 km depth, with asthenosphere viscosity 10^{21} Pa s, upper mantle $\mu = 10^{21}$ Pa s and lower mantle $\mu = 10^{22}$ Pa s. There is no visocsity contrast between the slab and the mantle.

Figure 4.6   The flow field and surface displacement profile for the model of slab penetration to 1000 km depth, with asthenosphere viscosity 10^{20} Pa s, upper mantle $\mu = 10^{21}$ Pa s and lower mantle $\mu = 10^{21}$ Pa s.

Figure 4.7   The flow field and surface displacement profile for the model of slab
penetration to 1000 km depth, with asthenosphere viscosity 10^{20} Pa s, upper
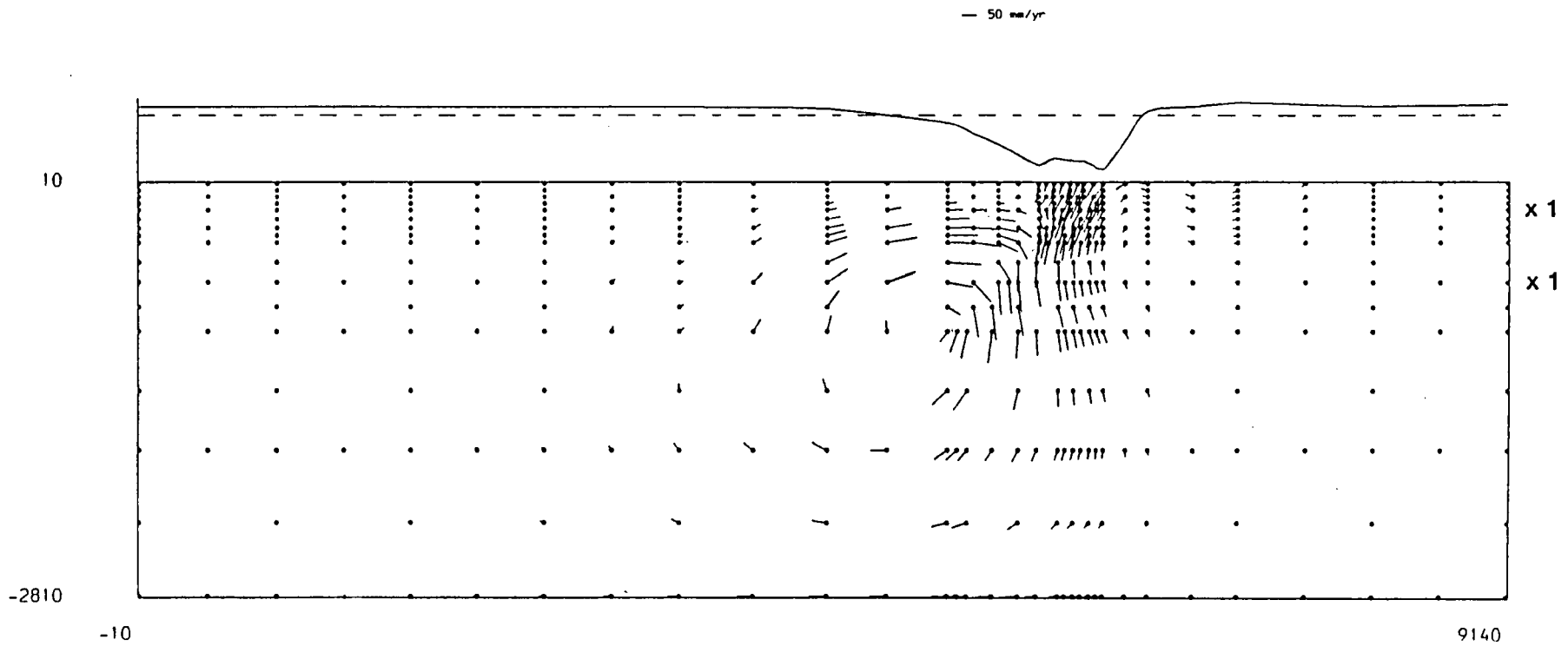mantle $\mu = 10^{21}$ Pa s and lower mantle $\mu = 10^{22}$ Pa s.

Figure 4.8   The flow field and surface displacement profile for the model of slab
penetration to 1000 km depth, with asthenosphere viscosity 10^{20} Pa s, upper
mantle $\mu = 10^{21}$ Pa s and lower mantle $\mu = 10^{23}$ Pa s.

Figure 4.9   The flow field and surface displacement profile for the model of slab
penetration to 1000 km depth, with asthenosphere viscosity 10^{19} Pa s, upper
mantle $\mu = 10^{21}$ Pa s and lower mantle $\mu = 10^{21}$ Pa s.

Figure 4.10   The flow field and surface displacement profile for the model of slab penetration to 1000 km depth, with asthenosphere viscosity 10^{19} Pa s, upper mantle $\mu = 10^{21}$ Pa s and lower mantle $\mu = 10^{22}$ Pa s.

Figure 4.11   The flow field and surface displacement profile for the model of slab
penetration to 1000 km depth, with asthenosphere viscosity 10^{19} Pa s, upper
mantle $\mu = 10^{21}$ Pa s and lower mantle $\mu = 10^{23}$ Pa s.
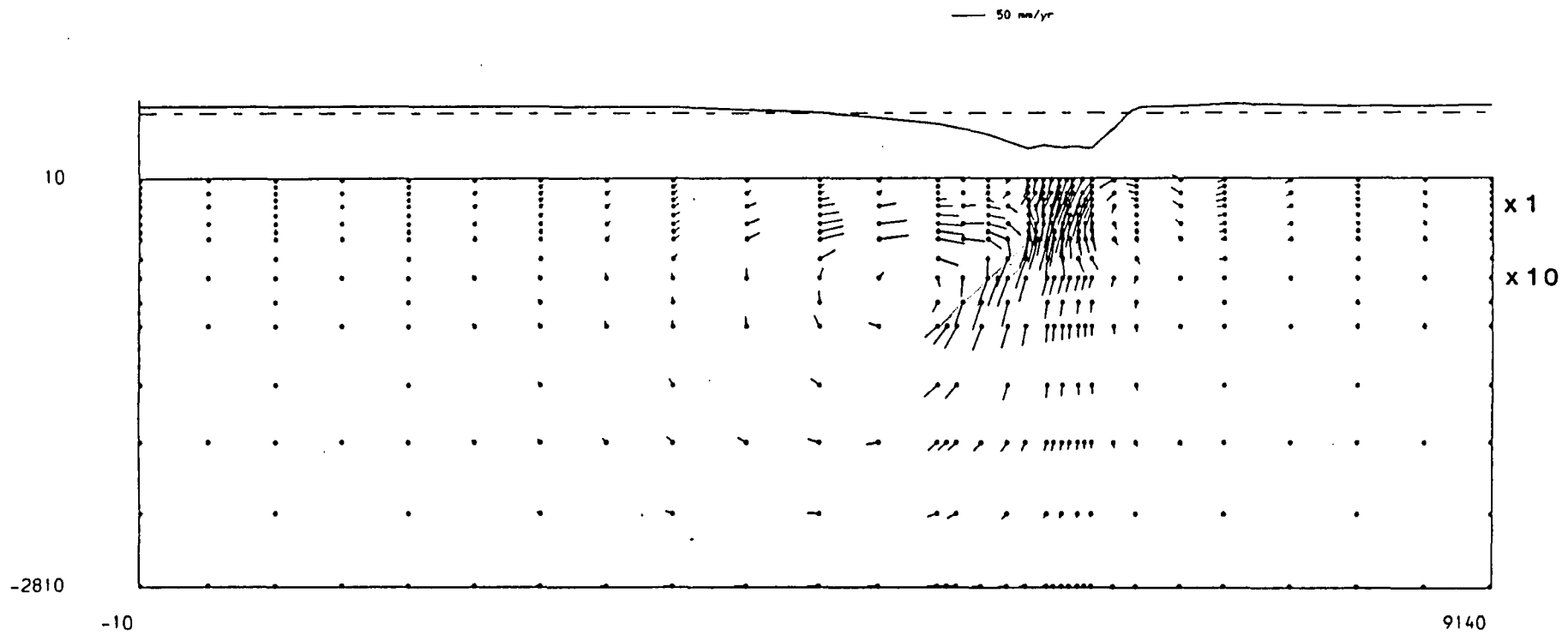
Figure 4.12   The flow field and surface displacement profile for the model of slab
penetration to 670 km depth, with asthenosphere viscosity 10^{21} Pa s, upper
mantle $\mu = 10^{21}$ Pa s and lower mantle $\mu = 10^{21}$ Pa s.

Figure 4.13   The flow field and surface displacement profile for the model of slab penetration to 670 km depth, with asthenosphere viscosity 10^{21} Pa s, upper mantle $\mu = 10^{21}$ Pa s and lower mantle $\mu = 10^{22}$ Pa s.
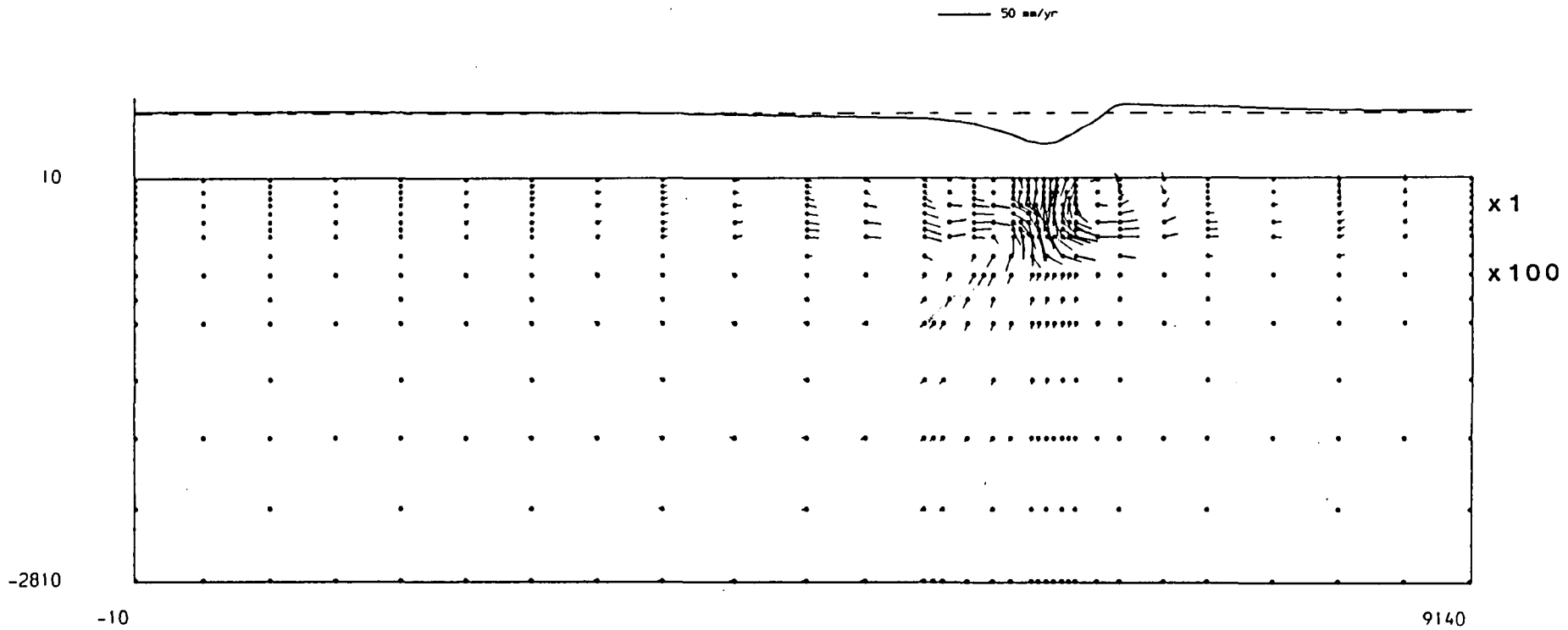
Figure 4.14   The flow field and surface displacement profile for the model of slab penetration to 670 km depth, with asthenosphere viscosity 10^{21} Pa s, upper mantle $\mu = 10^{21}$ Pa s and lower mantle $\mu = 10^{23}$ Pa s.

magnitude of the small velocities just below the slab tip. The surface depression in all three models has slightly decreased in width and depth.

The models in figures 4.15 - 4.17 represent the addition of a low viscosity asthenosphere with $\mu = 10^{20}$ Pa s to the preceding models of 670 km penetration. The asthenosphere has an identical effect to the description given in the previous section. Flow is concentrated into the asthenosphere, partially decoupling the surface plates. However, there is an additional complication for the 10^{22} Pa s lower mantle model in figure 4.16. The anticlockwise rotation of the flow vectors within the slab is amplified by the asthenosphere creating seawards lateral flow under the subducting plate.

The flow fields shown in figures 4.18 - 4.20 represent the models of slab penetration to 670 km depth with the asthenospheric viscosity further reduced to 10^{19} Pa s. The flow patterns are similar to figures 4.15 - 4.17 but the horizontal flow in the upper mantle has been further concentrated into the low viscosity zone.

The slab length is shortened and the flow fields for the models of 400 km penetration are shown in figures 4.21 - 4.23. The asthenosphere viscosity $\mu = 10^{20}$ Pa s, the upper mantle $\mu = 10^{21}$ Pa s, and the lower mantle viscosities are 10^{21} Pa s, 10^{22} Pa s or 10^{23} Pa s. The flow field in figure 4.21 represents no viscosity contrast at 670 km depth. There is a flow circulation about the slab tip but the cell width is less than the deeper penetrating models (figures 4.15, 4.6). Horizontal flow under the overriding plate is concentrated into the low viscosity zone. Within the slab the flow in the lower sections is rotated almost 45° anticlockwise of vertical. This creates a component of seaward horizontal flow under the subducting plate. The flow field in figure 4.22 represents the model with lower mantle viscosity of 10^{22} Pa s. There is decoupling of the flow in the mantle about the 670 km discontinuity, leaving only a small component of entrained flow in the lower mantle. The circulation about the slab tip now occurs in the upper mantle. Lateral flow under the overriding plate is concentrated into the asthenosphere and the overriding plate has a small landward component of velocity. Flow within the slab is nearly downdip in the upper sections and vertical in the lower sections. Increasing the lower mantle viscosity to 10^{23} Pa s, figure 4.23 shows that the flow is completely confined to the upper mantle. The circulation around the slab tip causes a small component of flow above the slab, but there is no flow under the bulk of the overriding plate. There is a large component of seawards horizontal flow under the subducting plate, and also
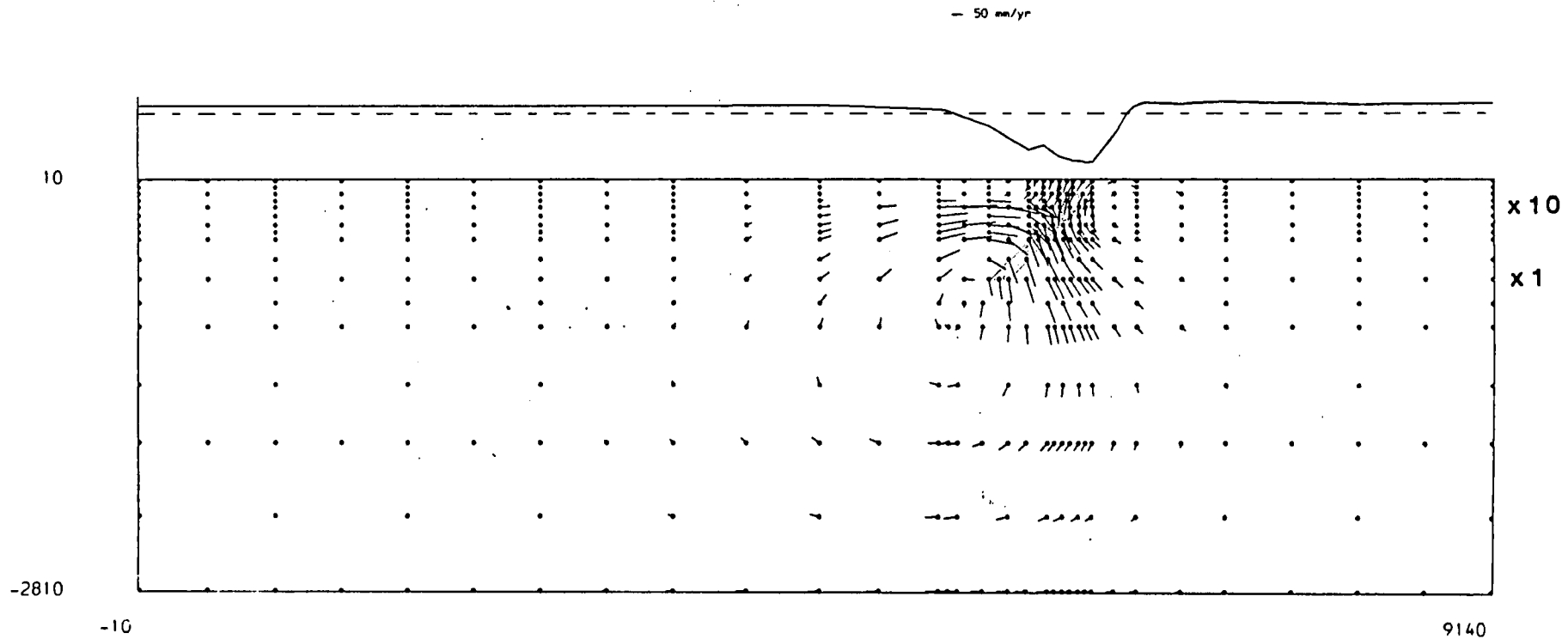
Figure 4.15 The flow field and surface displacement profile for the model of slab penetration to 670 km depth, with asthenosphere viscosity 10^{20} Pa s, upper mantle $\mu = 10^{21}$ Pa s and lower mantle $\mu = 10^{21}$ Pa s.
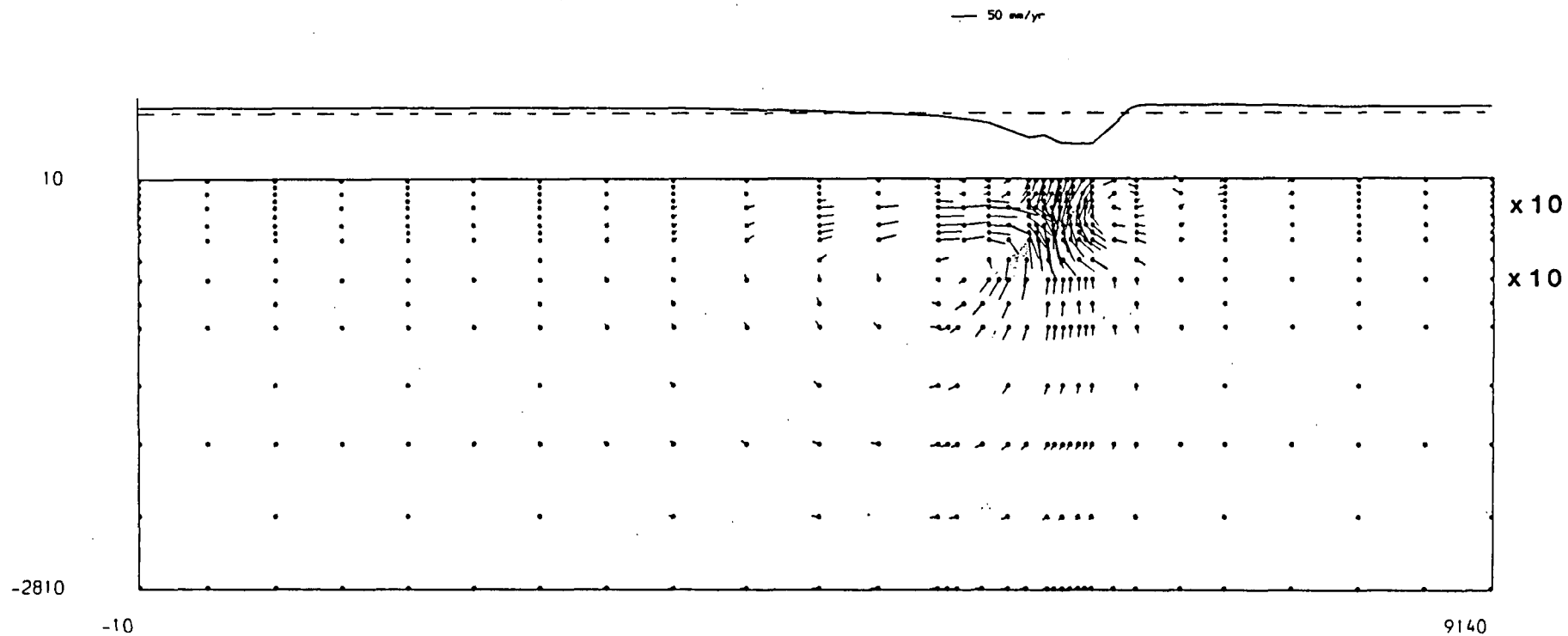
Figure 4.16   The flow field and surface displacement profile for the model of slab penetration to 670 km depth, with asthenosphere viscosity 10^{20} Pa s, upper mantle $\mu = 10^{21}$ Pa s and lower mantle $\mu = 10^{22}$ Pa s.
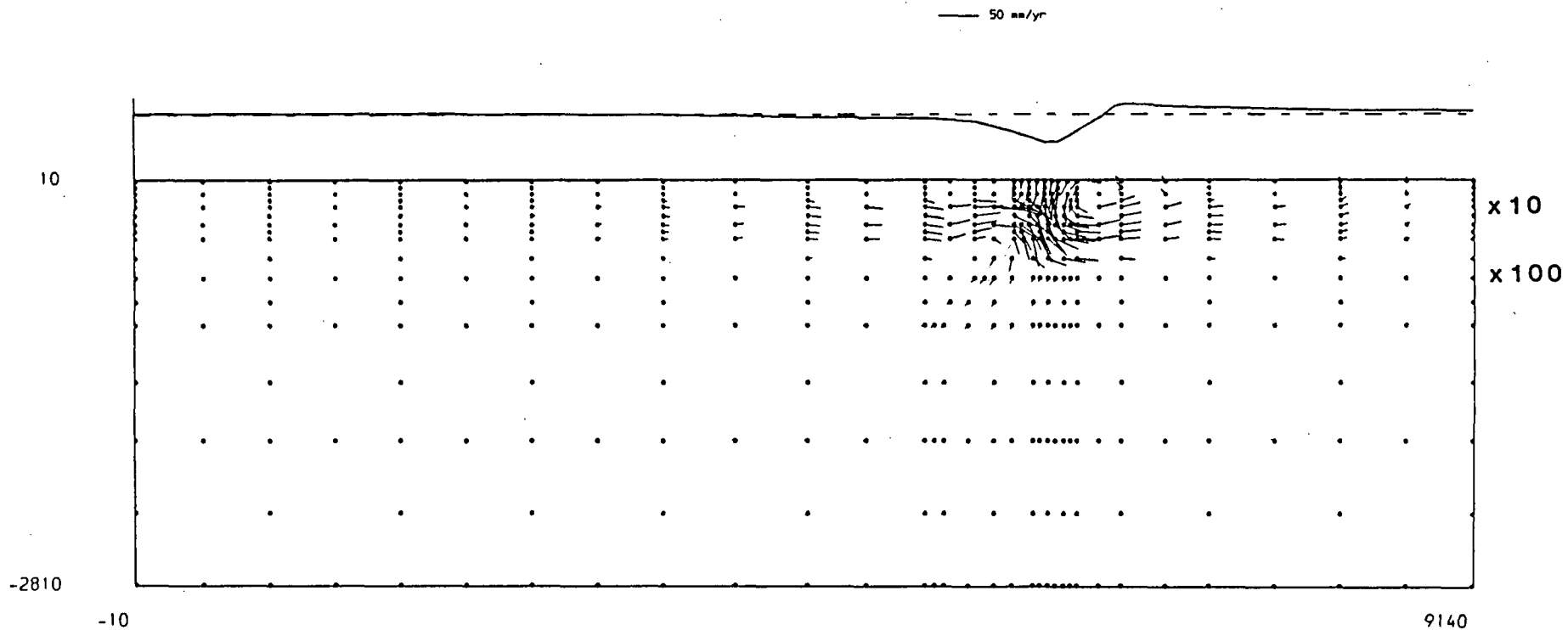
Figure 4.17   The flow field and surface displacement profile for the model of slab
    penetration to 670 km depth, with asthenosphere viscosity 10^{20} Pa s, upper
    mantle $\mu = 10^{21}$ Pa s and lower mantle $\mu = 10^{23}$ Pa s.
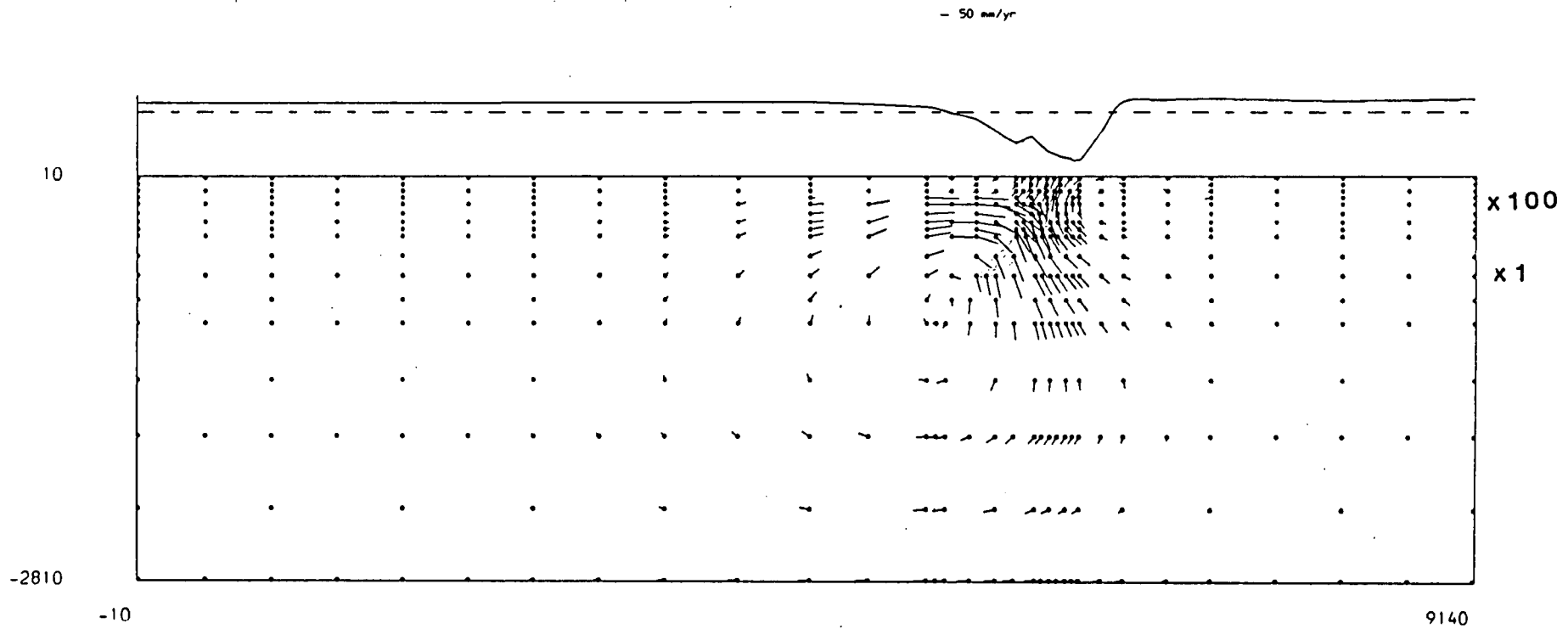
Figure 4.18 The flow field and surface displacement profile for the model of slab penetration to 670 km depth, with asthenosphere viscosity 10^{19} Pa s, upper mantle $\mu = 10^{21}$ Pa s and lower mantle $\mu = 10^{21}$ Pa s.
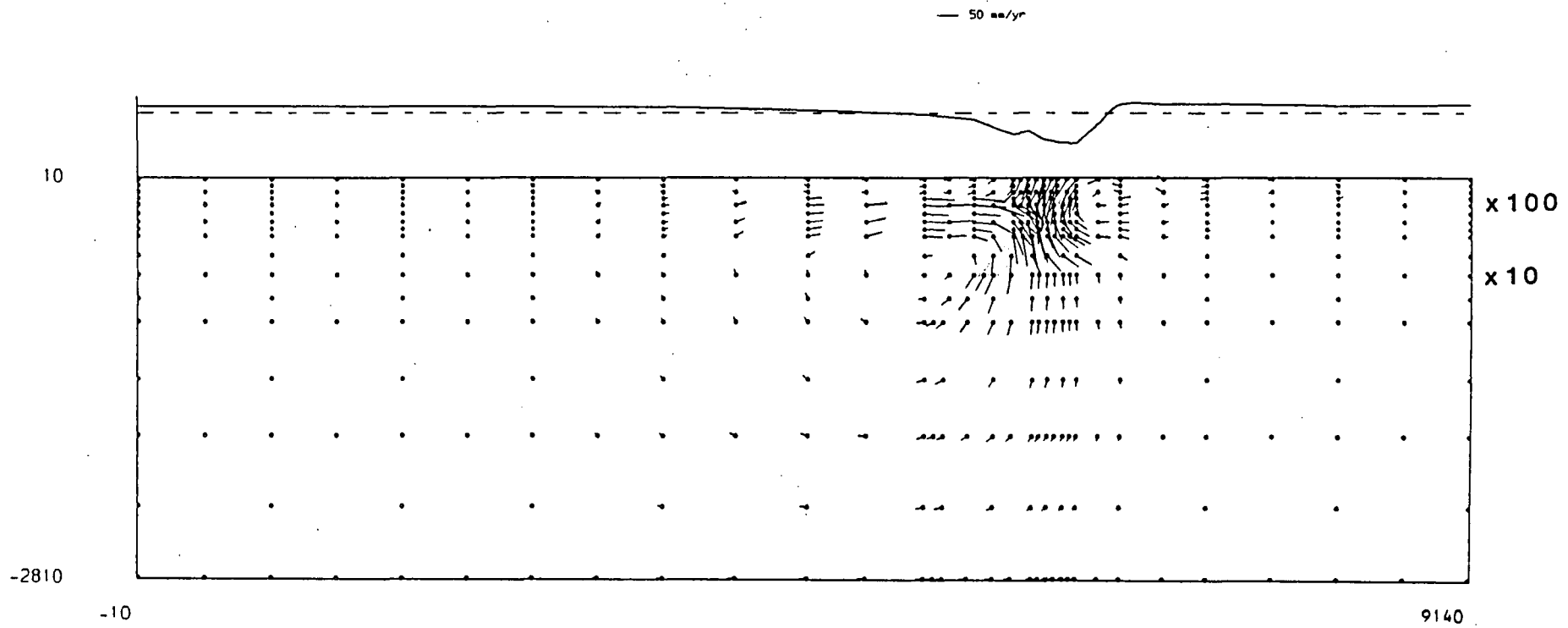
Figure 4.19   The flow field and surface displacement profile for the model of slab
penetration to 670 km depth, with asthenosphere viscosity 10^{19} Pa s, upper
mantle $\mu = 10^{21}$ Pa s and lower mantle $\mu = 10^{22}$ Pa s.
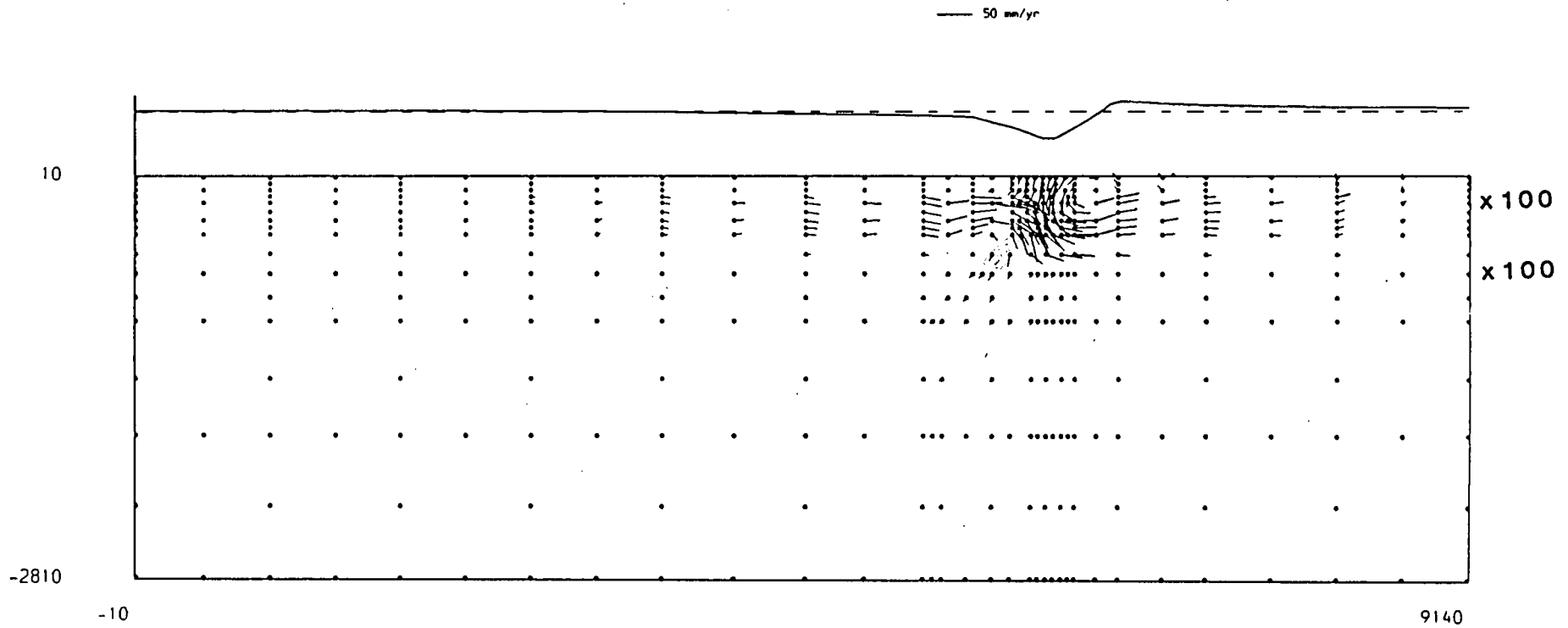
Figure 4.20   The flow field and surface displacement profile for the model of slab
penetration to 670 km depth, with asthenosphere viscosity 10^{19} Pa s, upper
mantle $\mu = 10^{21}$ Pa s and lower mantle $\mu = 10^{23}$ Pa s.
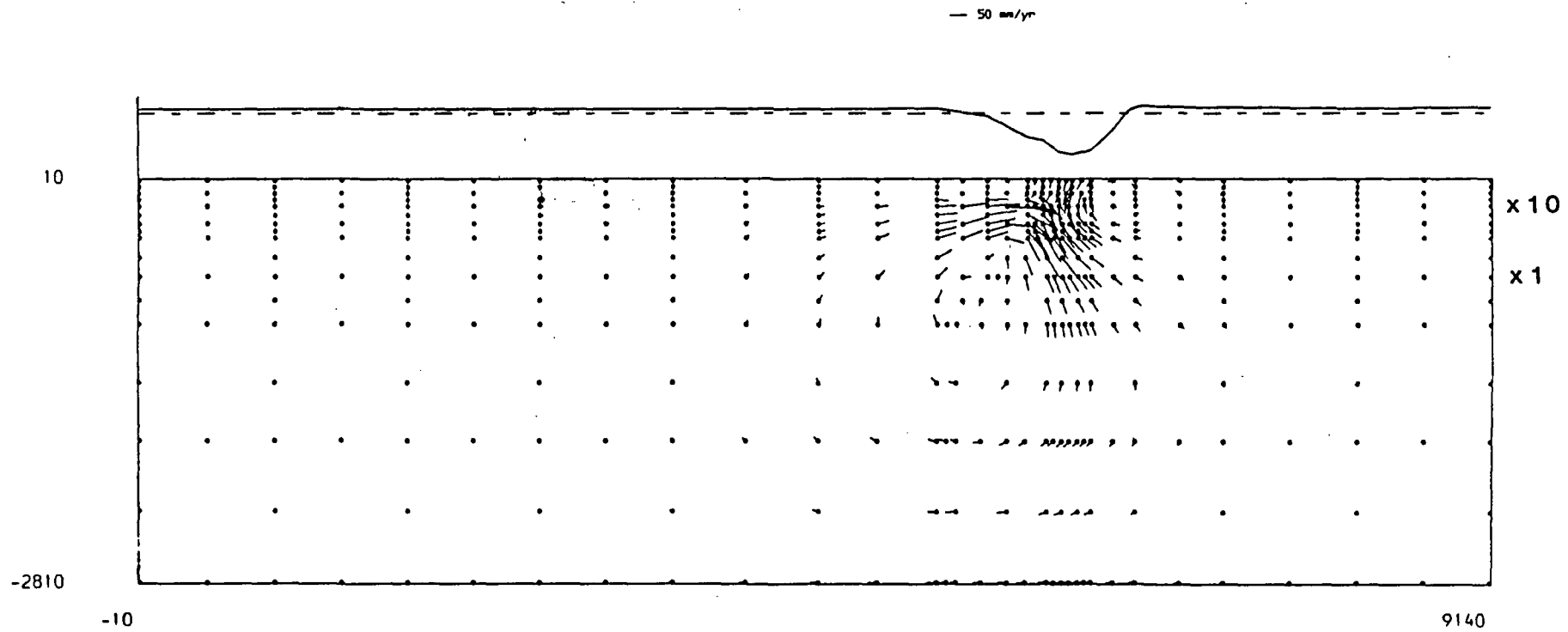
Figure 4.21   The flow field and surface displacement profile for the model of slab penetration to 400 km depth, with asthenosphere viscosity 10^{20} Pa s, upper mantle $\mu = 10^{21}$ Pa s and lower mantle $\mu = 10^{21}$ Pa s.
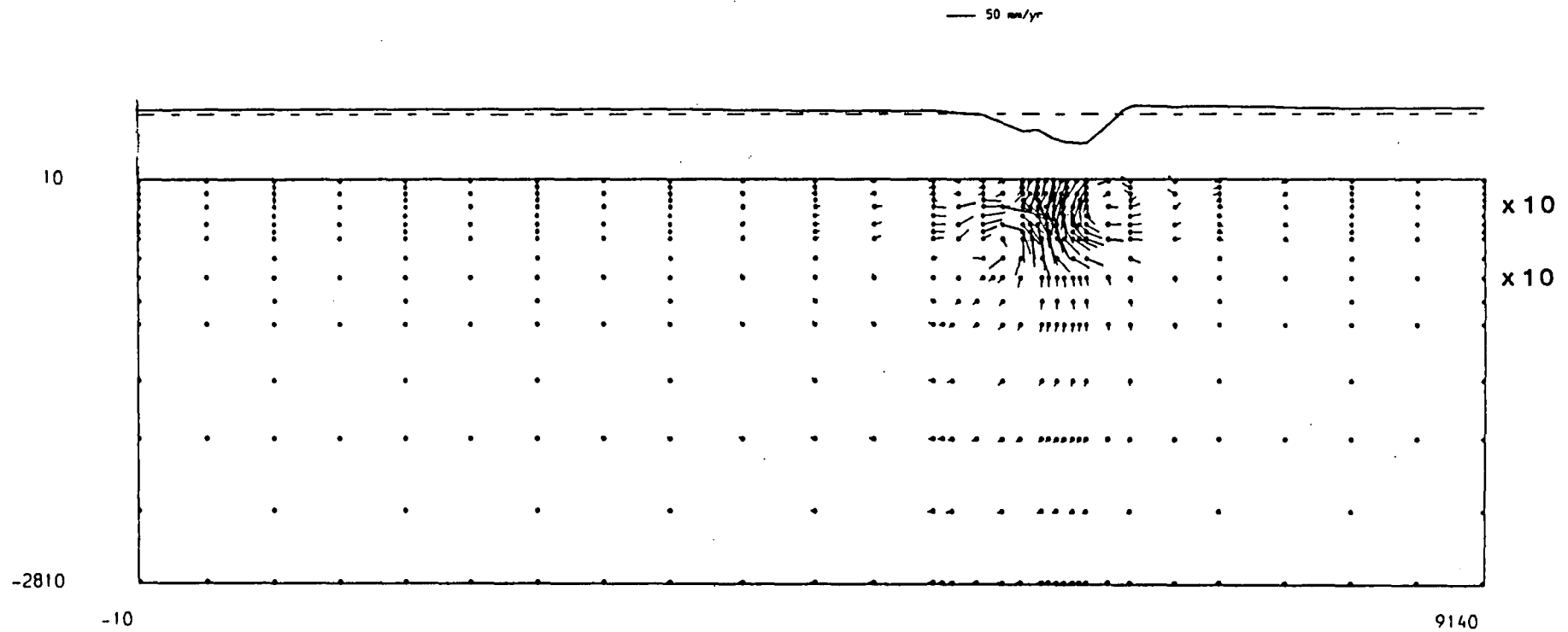
Figure 4.22   The flow field and surface displacement profile for the model of slab
penetration to 400 km depth, with asthenosphere viscosity 10^{20} Pa s, upper
mantle $\mu = 10^{21}$ Pa s and lower mantle $\mu = 10^{22}$ Pa s.
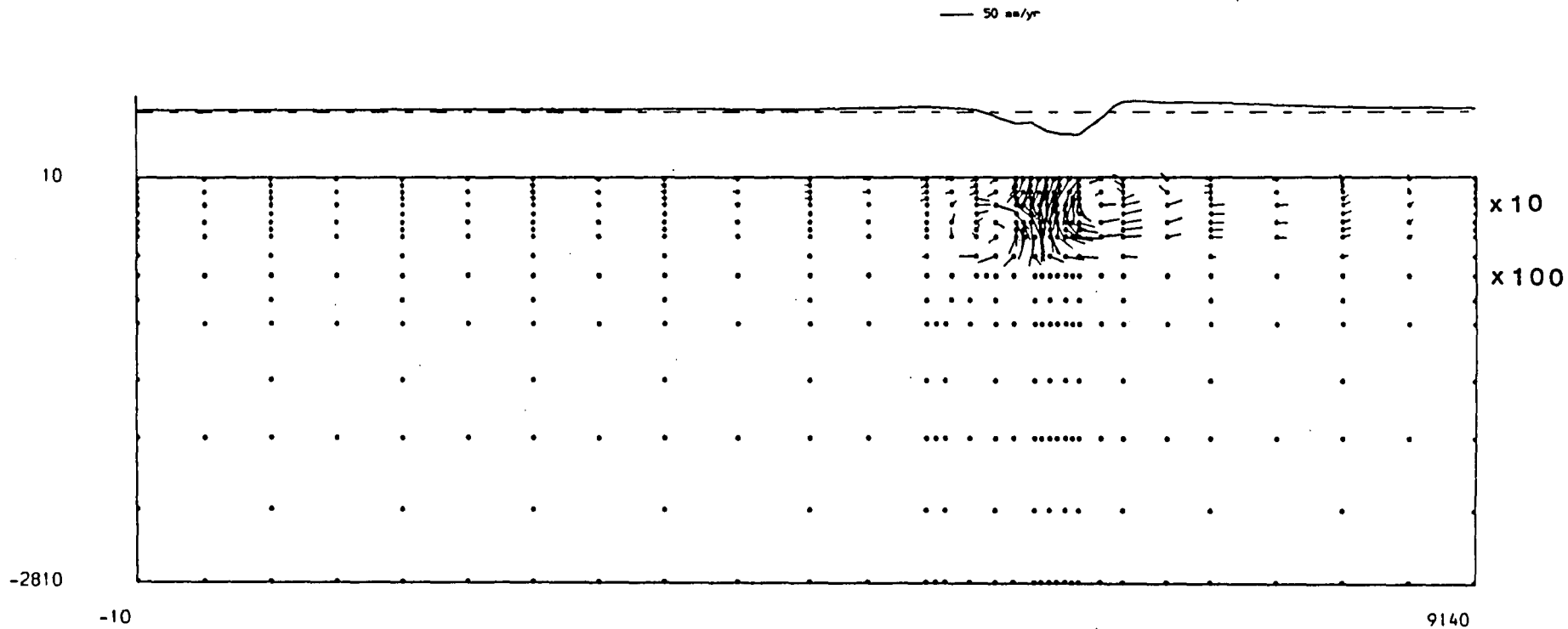
Figure 4.23   The flow field and surface displacement profile for the model of slab
penetration to 400 km depth, with asthenosphere viscosity 10^{20} Pa s, upper
mantle $\mu = 10^{21}$ Pa s and lower mantle $\mu = 10^{23}$ Pa s.
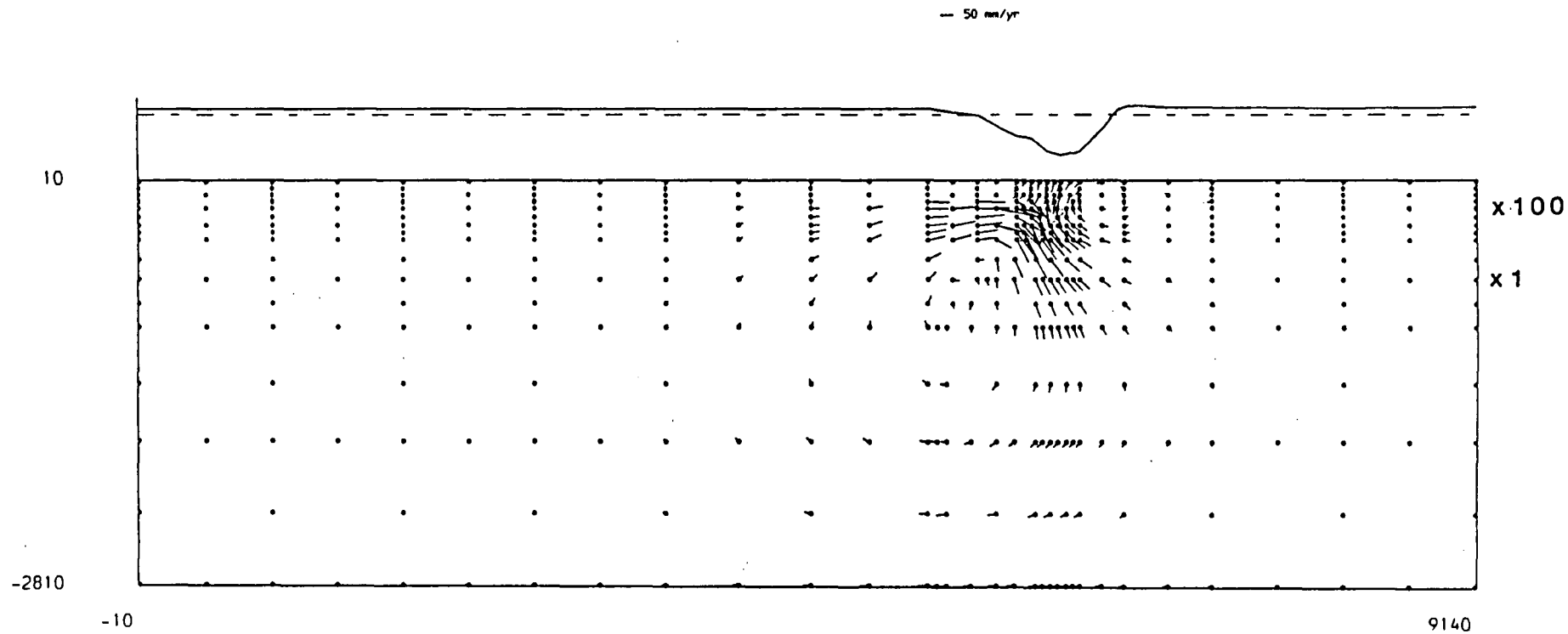
Figure 4.24 The flow field and surface displacement profile for the model of slab penetration to 400 km depth, with asthenosphere viscosity 10^{19} Pa s, upper mantle $\mu = 10^{21}$ Pa s and lower mantle $\mu = 10^{21}$ Pa s.
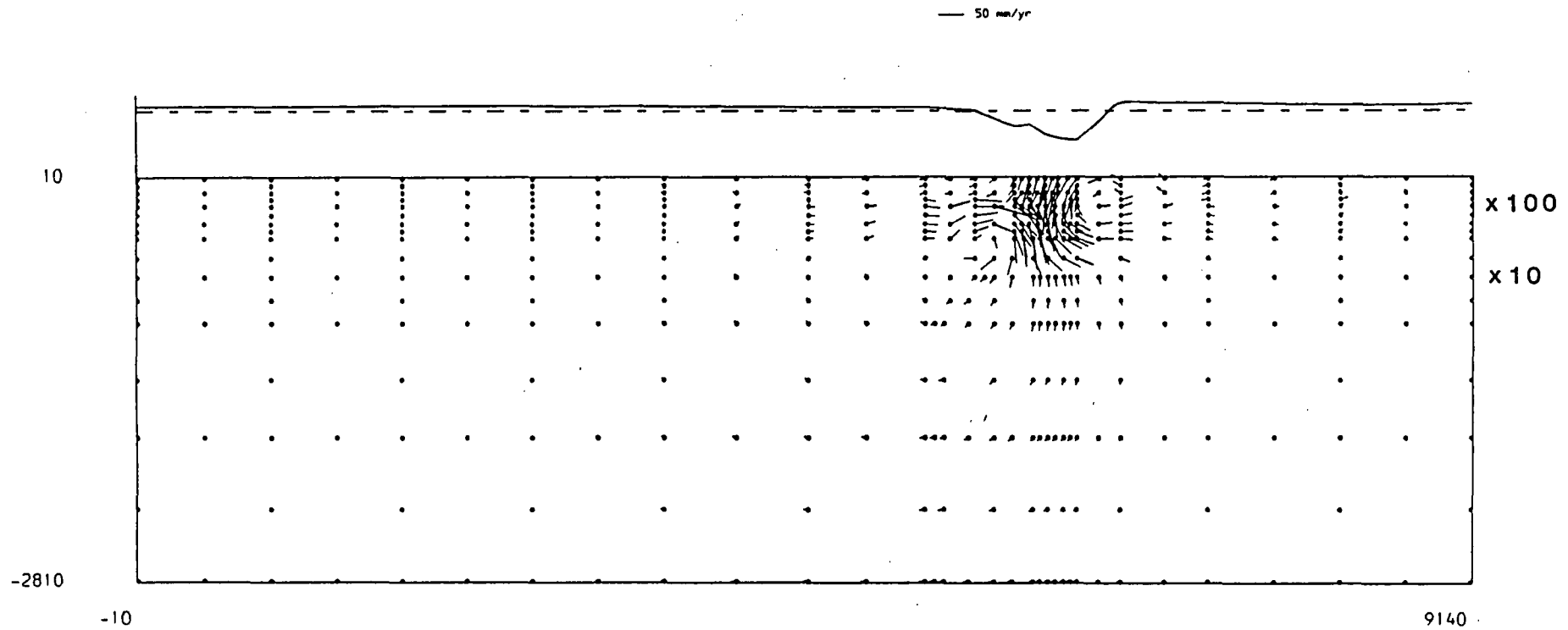
Figure 4.25   The flow field and surface displacement profile for the model of slab penetration to 400 km depth, with asthenosphere viscosity 10^{19} Pa s, upper mantle $\mu = 10^{21}$ Pa s and lower mantle $\mu = 10^{22}$ Pa s.
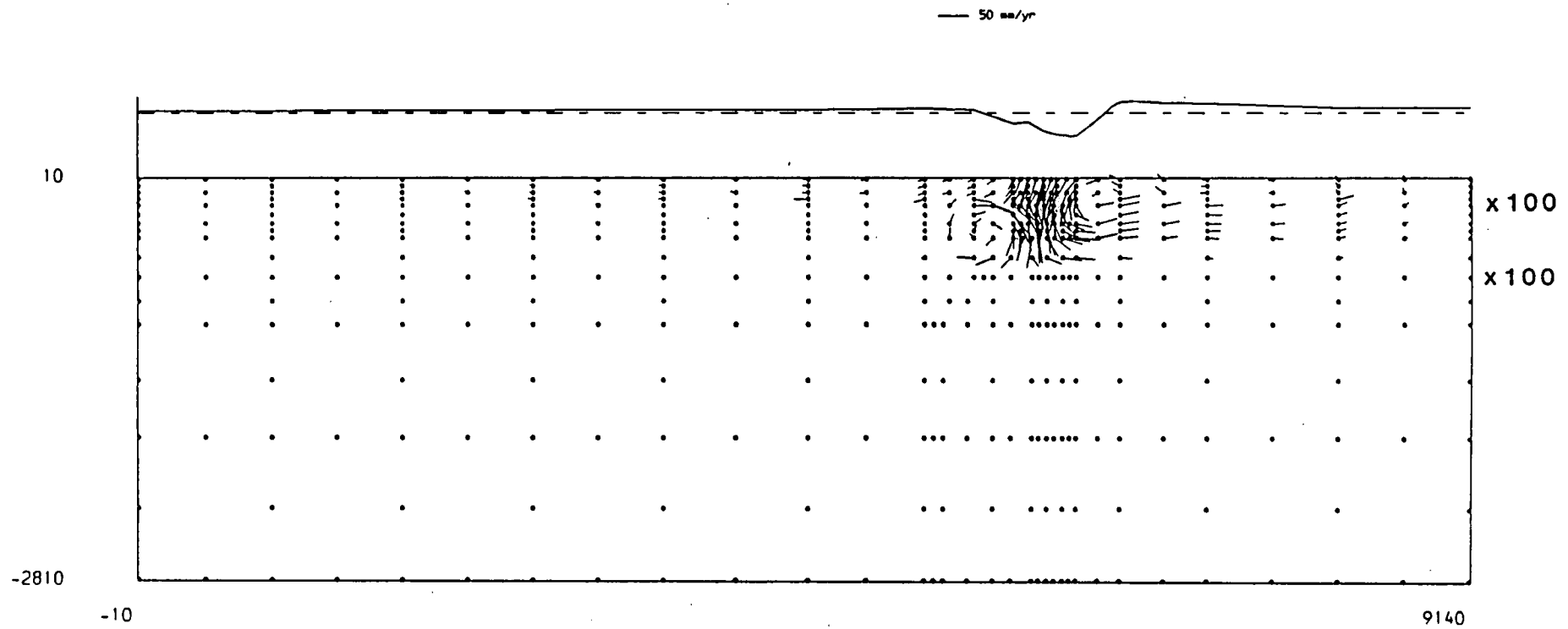
Figure 4.26   The flow field and surface displacement profile for the model of slab penetration to 400 km depth, with asthenosphere viscosity 10^{19} Pa s, upper mantle $\mu = 10^{21}$ Pa s and lower mantle $\mu = 10^{23}$ Pa s.
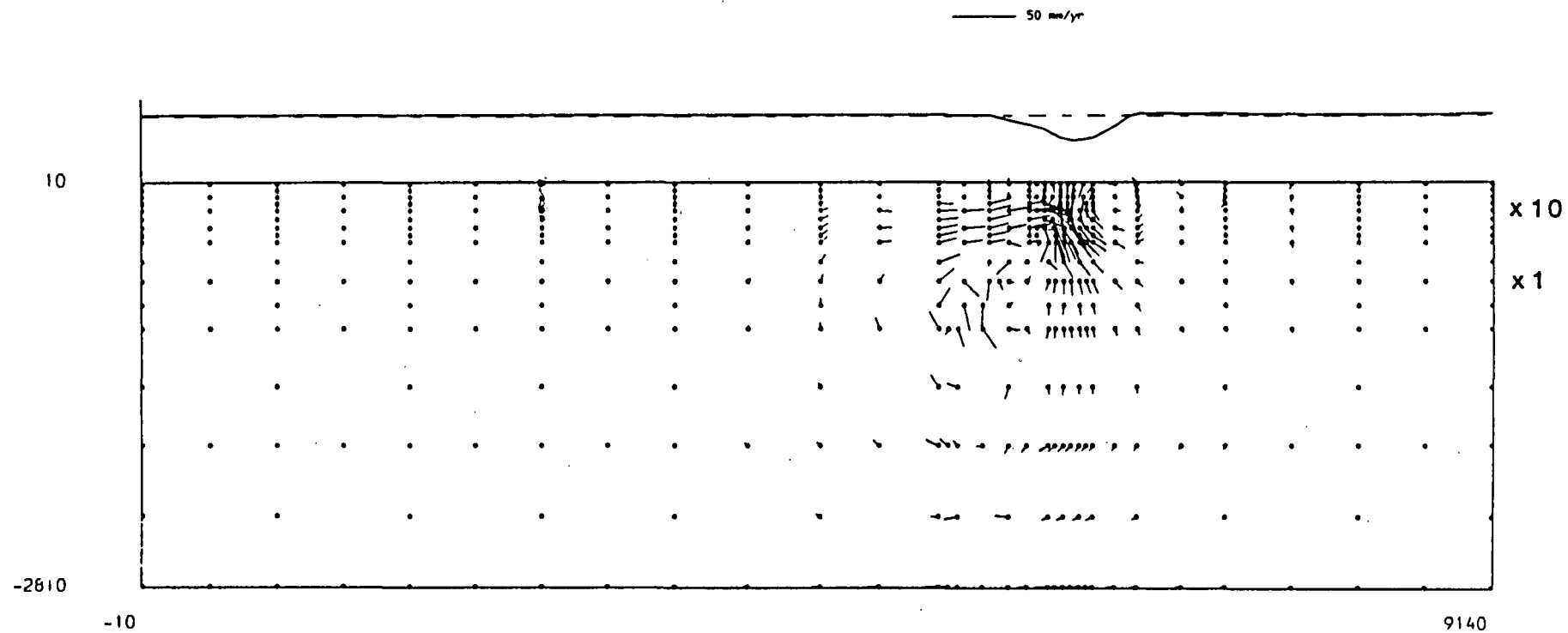
Figure 4.27 The flow field and surface displacement profile for the model of slab penetration to 300 km depth, with asthenosphere viscosity 10^{20} Pa s, upper mantle $\mu = 10^{21}$ Pa s and lower mantle $\mu = 10^{21}$ Pa s.
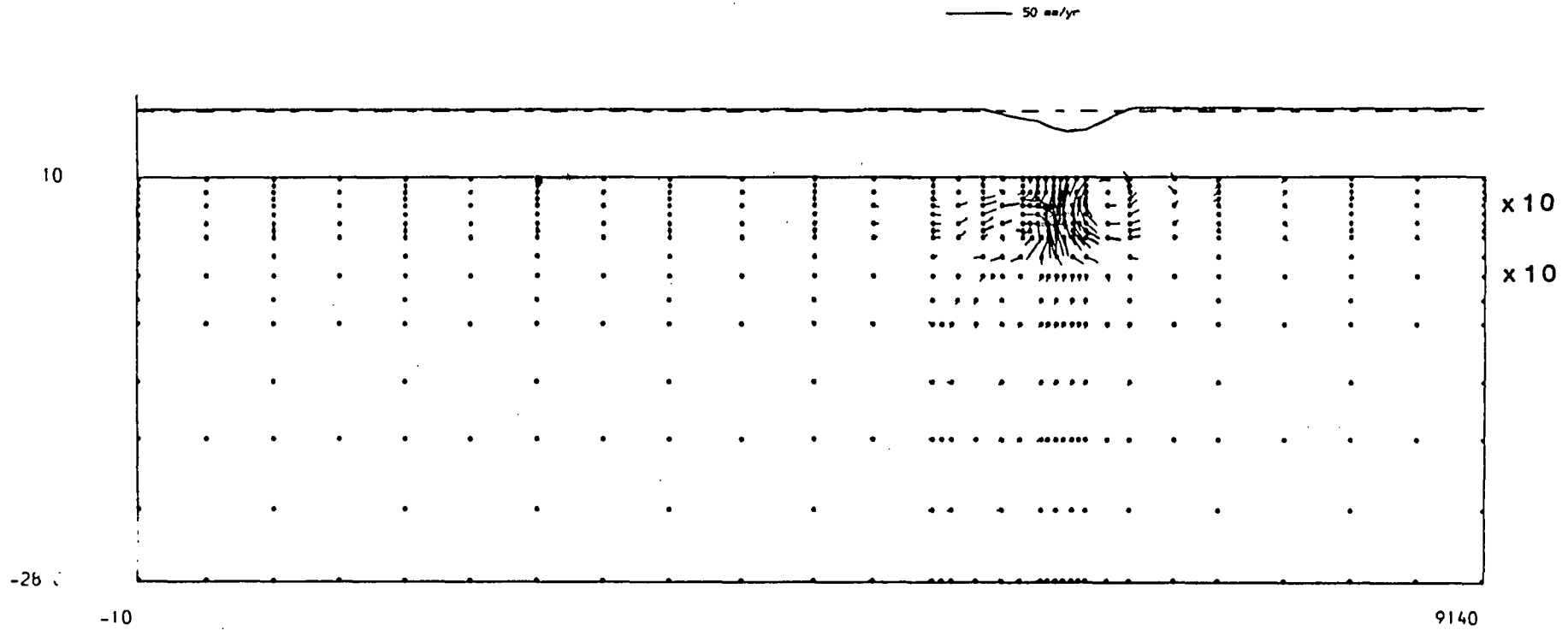
Figure 4.28 The flow field and surface displacement profile for the model of slab penetration to 300 km depth, with asthenosphere viscosity 10^{20} Pa s, upper mantle $\mu = 10^{21}$ Pa s and lower mantle $\mu = 10^{22}$ Pa s.
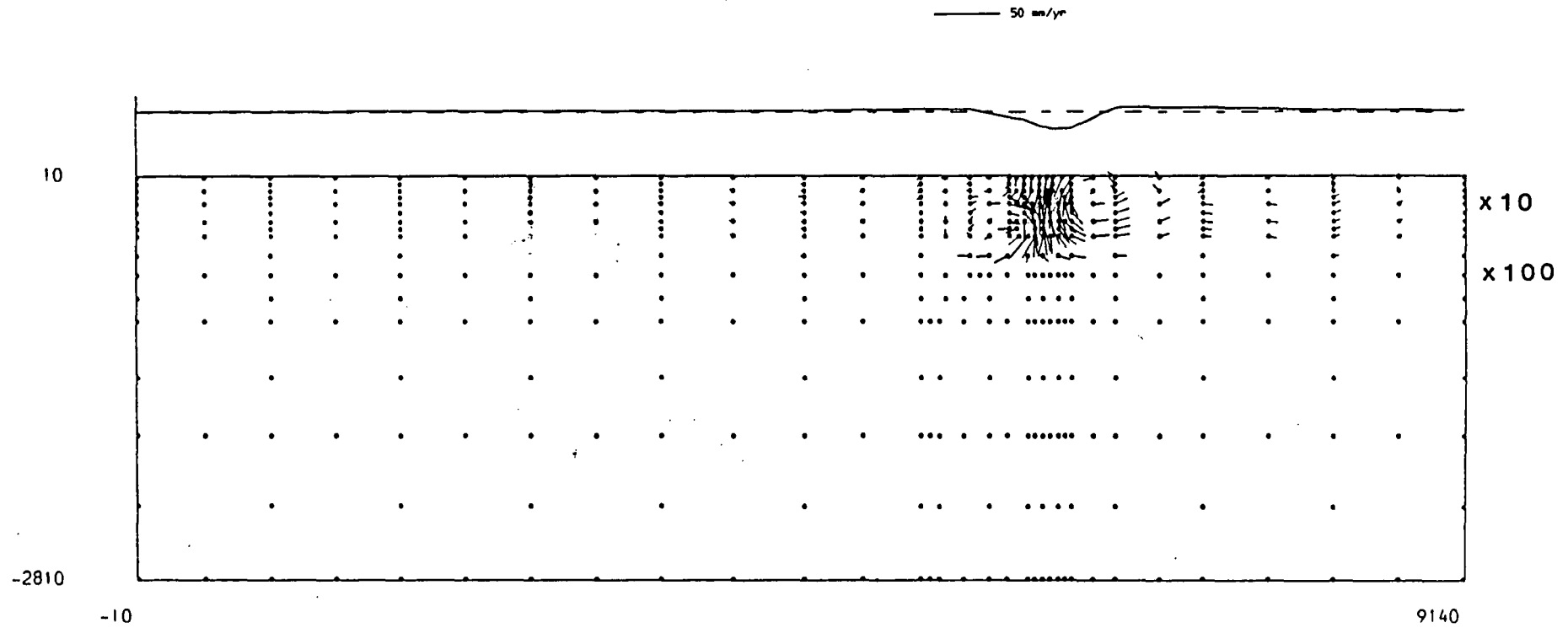
Figure 4.29   The flow field and surface displacement profile for the model of slab
penetration to 300 km depth, with asthenosphere viscosity 10^{20} Pa s, upper
mantle $\mu = 10^{21}$ Pa s and lower mantle $\mu = 10^{23}$ Pa s.
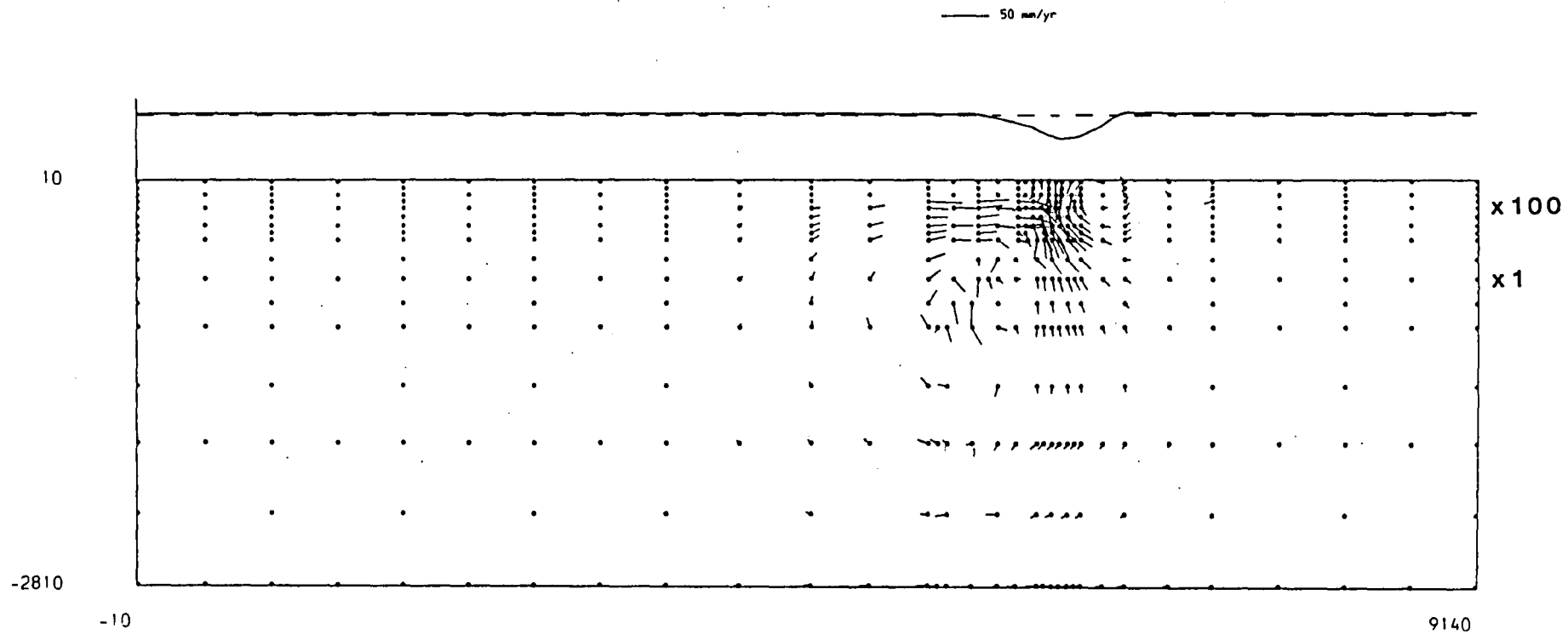
Figure 4.30 The flow field and surface displacement profile for the model of slab penetration to 300 km depth, with asthenosphere viscosity 10^{19} Pa s, upper mantle $\mu = 10^{21}$ Pa s and lower mantle $\mu = 10^{21}$ Pa s.
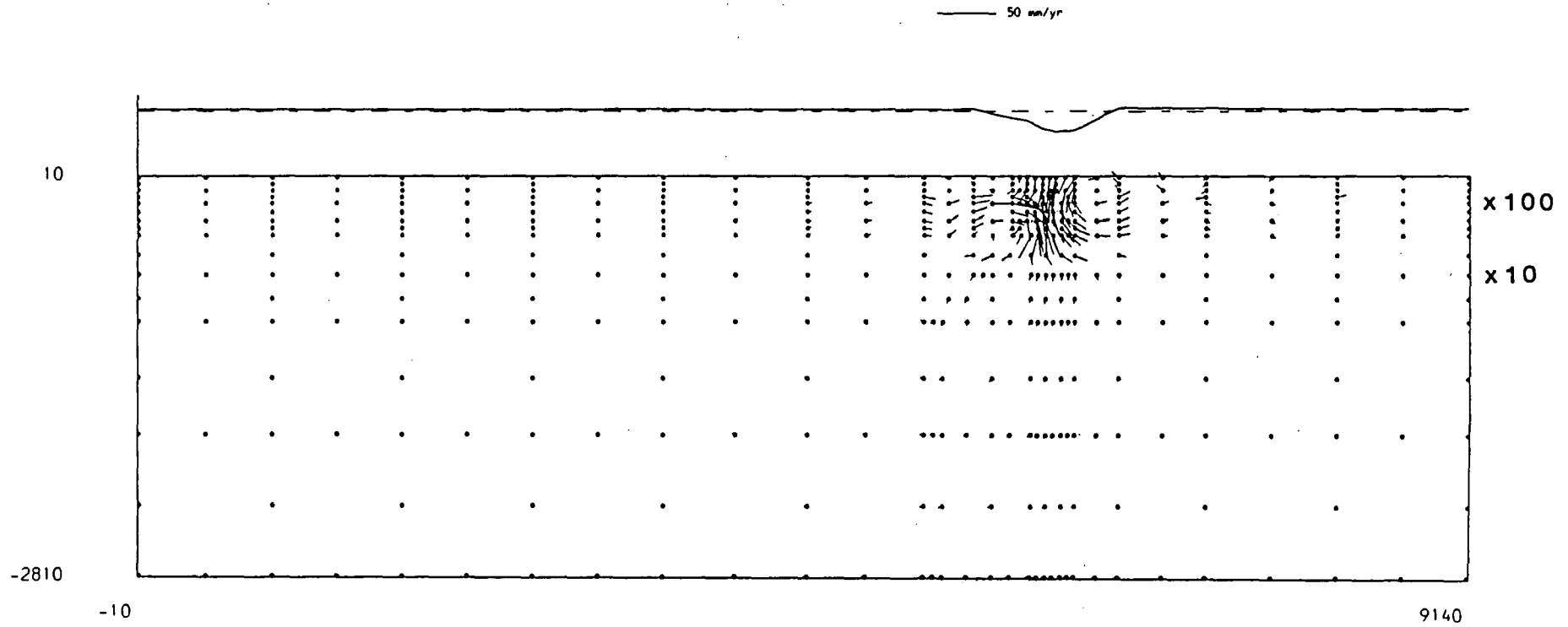
Figure 4.31   The flow field and surface displacement profile for the model of slab penetration to 300 km depth, with asthenosphere viscosity 10^{19} Pa s, upper mantle $\mu = 10^{21}$ Pa s and lower mantle $\mu = 10^{22}$ Pa s.
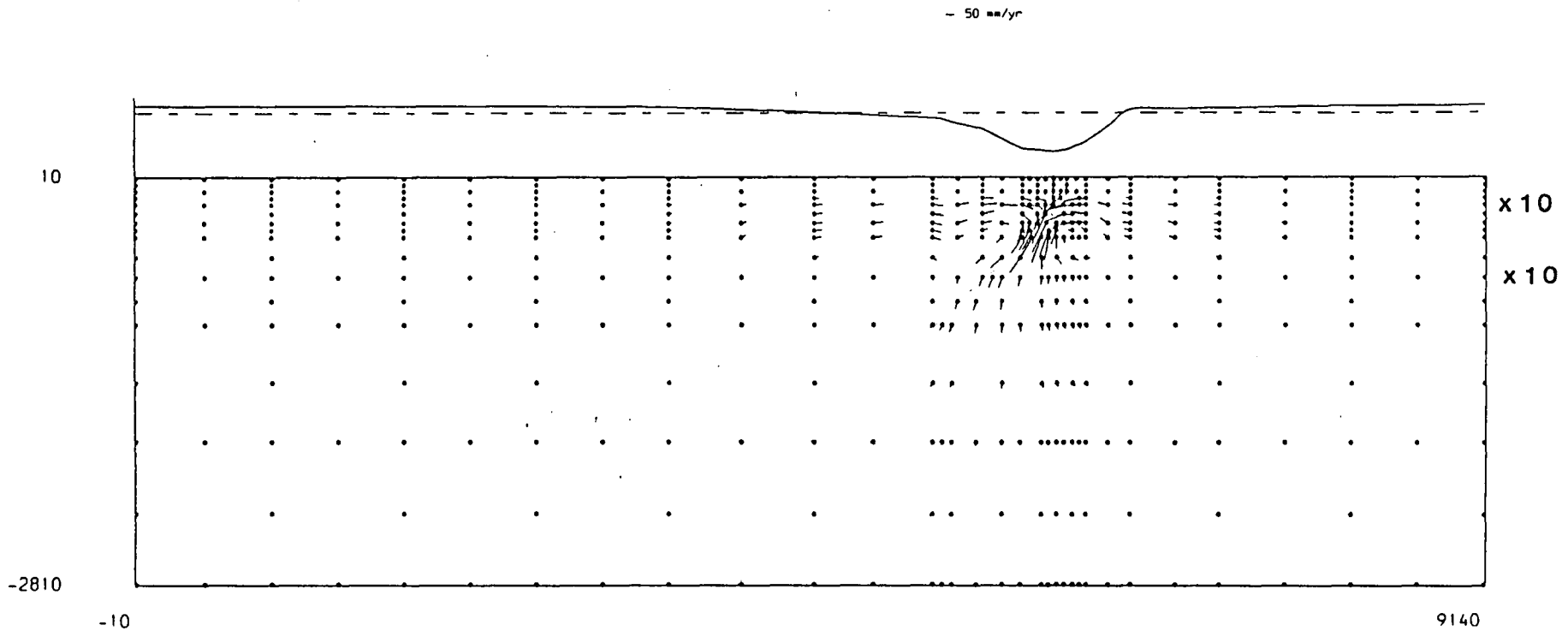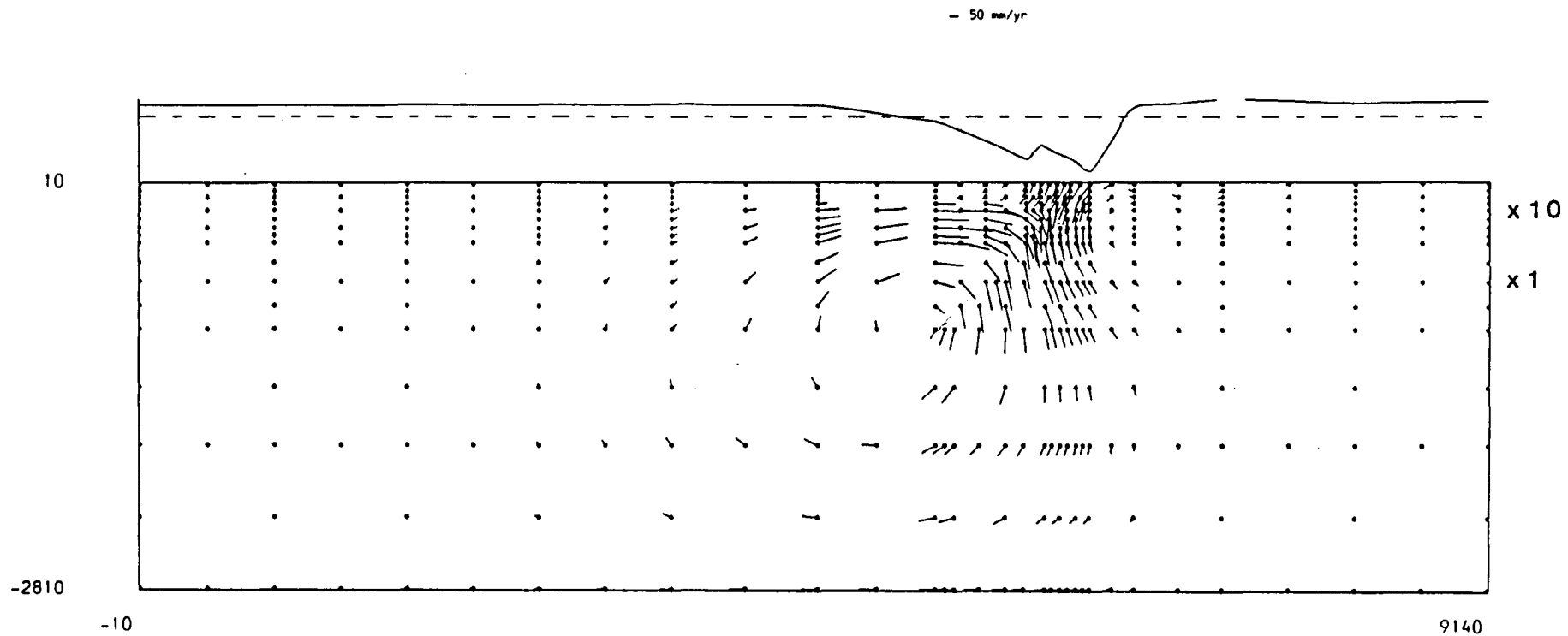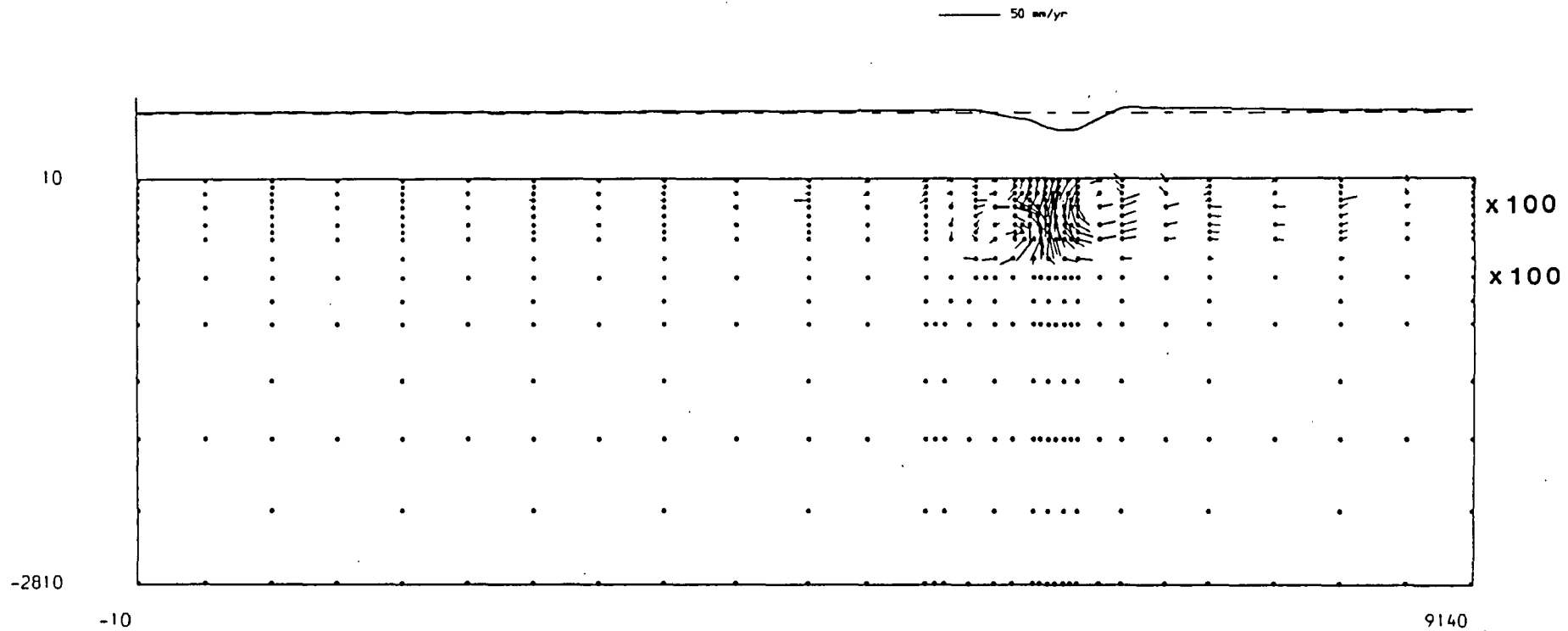
Figure 4.32   The flow field and surface displacement profile for the model of slab
penetration to 300 km depth, with asthenosphere viscosity 10^{19} Pa s, upper
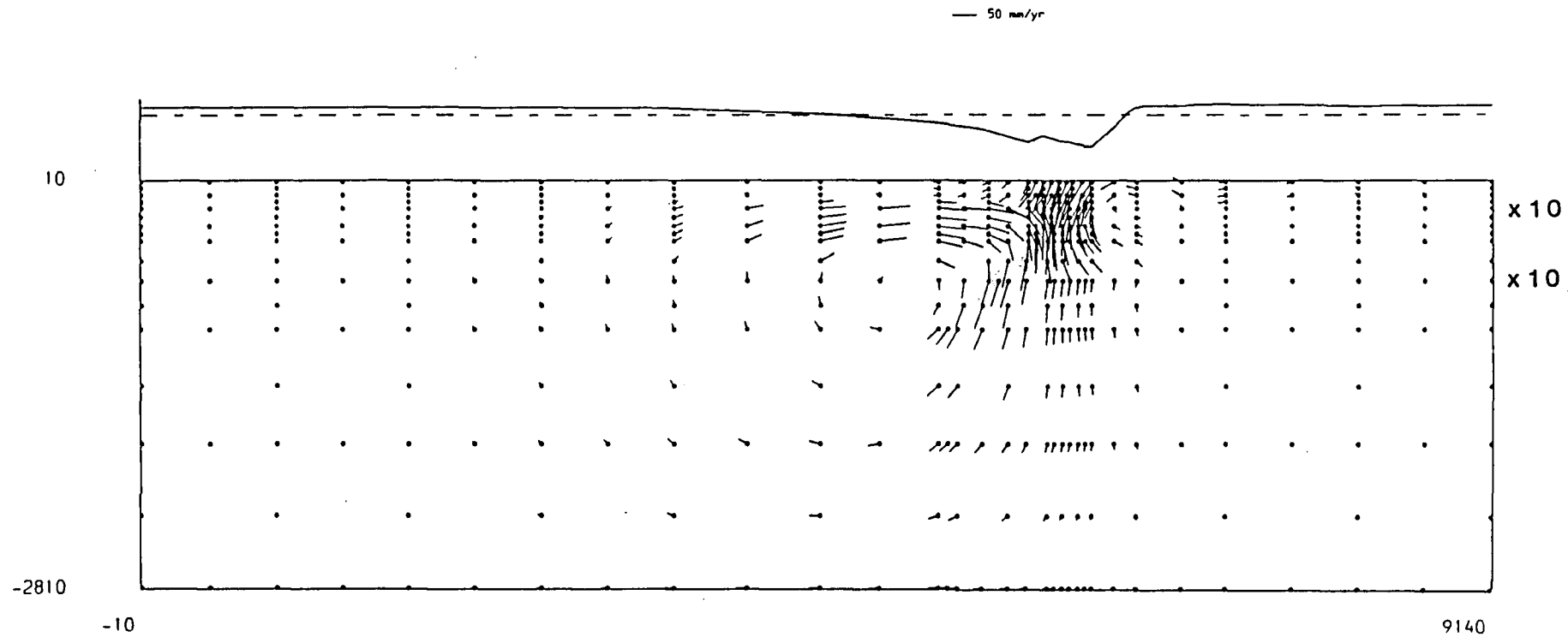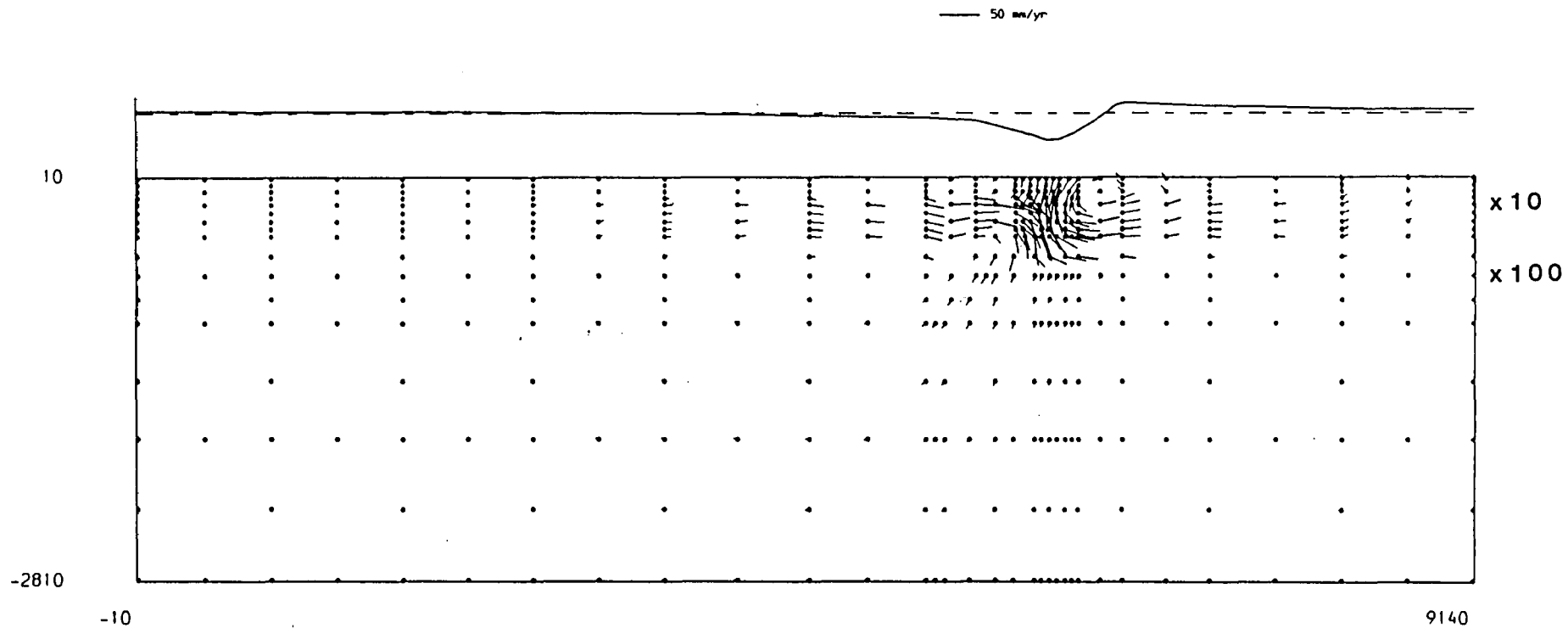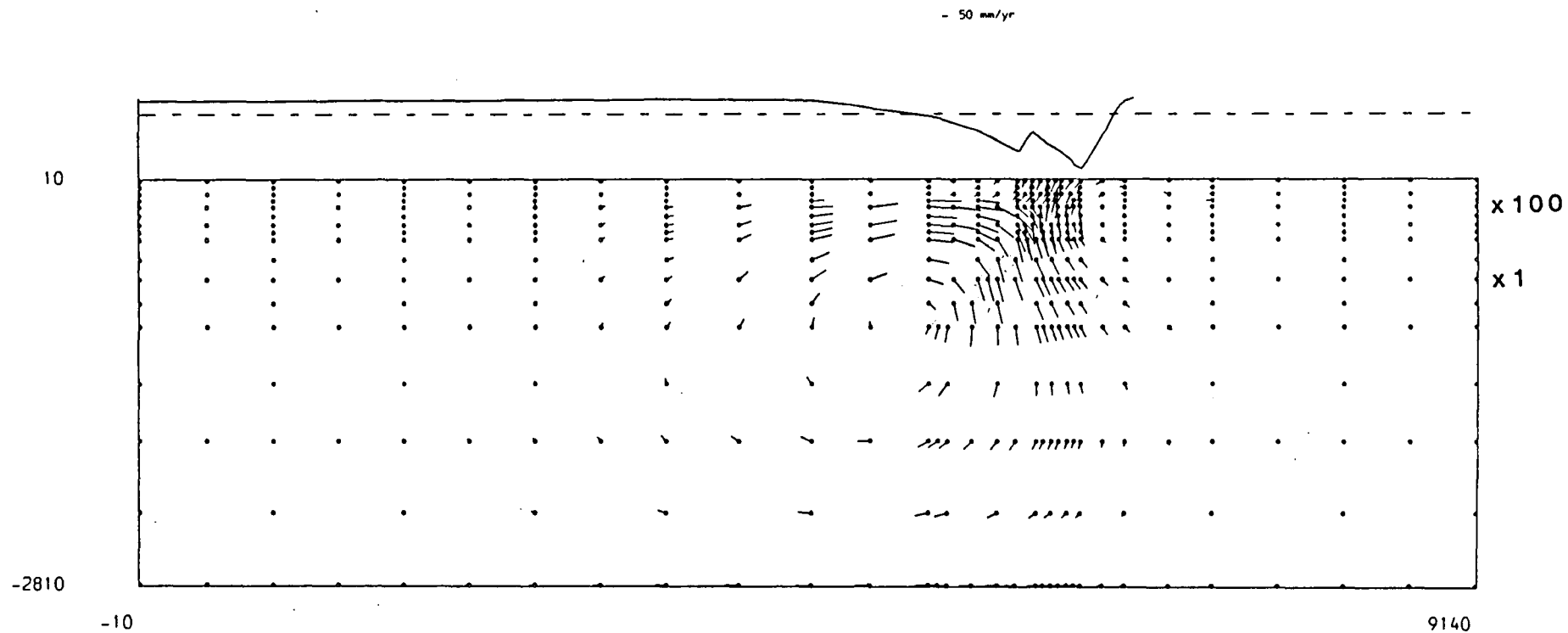mantle $\mu = 10^{21}$ Pa s and lower mantle $\mu = 10^{23}$ Pa s.

a reduction in the width and depth of the surface depression.

The flow fields shown in figures 4.24 - 4.26 represent the models of 400 km penetration with the viscosity of the asthenosphere reduced to 10^{19} Pa s. The flow patterns are similar to figures 4.21 - 4.23 but the horizontal flow under the subducting plate has been enhanced at the expense of the flow under the overriding plate.

Slab penetration to 300 km depth with an asthenospheric viscosity of 10^{20} Pa s are shown in figures 4.27 - 4.29. The lower mantle $\mu = 10^{21}$ Pa s model in figure 4.27 has a small circulation cell around the slab tip similar to the preceding 400 km penetration model (figure 4.21). Flow within the slab is slightly rotated anticlockwise of vertical. Horizontal flow under the overriding plate is concentrated into the low viscosity zone. The model of lower mantle $\mu = 10^{22}$ Pa s in figure 4.28 shows the circulation around the slab tip confined to the upper mantle. Very little flow is entrained in the lower mantle. Within the slab the flow is nearly downdip in the upper sections and roughly vertical in the lower sections. The overriding plate is nearly stationary and flow underneath is confined to the region above the slab. Increasing the lower mantle viscosity to 10^{23} Pa s confines the flow to the upper mantle (figure 4.29). The circulation around the slab tip generates a small flow under the overriding plate, but the low viscosity zone decouples the plate allowing a small landward component. There is large horizontal seawards flow under the subducting plate.

The final three models of 300 km penetration assign an asthenospheric viscosity of 10^{19} Pa s, figures 4.30 - 4.32. Comparison with figures 4.27 - 4.29 shows that decreasing the viscosity of the asthenosphere enhances the horizontal flow under the subducting plate at the expense of the flow under the overriding plate.

4.6 Discussion of Results

There are strong arguments for viscosity stratification of the mantle. Hager (1984) suggested a viscosity contrast of $\times 30 \rightarrow \times 100$ at the upper - lower mantle boundary, while Willemann and Anderson (1987) preferred a viscosity contrast of $\times 10$. The finite element models of flow due to oblique subduction in this chapter provide some constraints on the viscosity structure.

The principal observation taken from the preceding flow fields is that a viscosity

contrast of ×100 at 670 km depth is sufficient to effectively decouple the flow systems in the upper and lower mantle. This has the greatest influence on the longest slabs, in this case penetrating to 670 km and 1000 km depth. In addition to decoupling the induced flow, the viscosity contrast affects the flow within the slab. There is a large change in orientation of the flow vectors along the length of the slab (figures 4.4, 4.8, 4.11, 4.14. 4.17, 4.20) which implies differing motion along the length and thus contortion of the slab. There is no evidence for excessive slab bending among observations of Wadati-Benioff zones which are remarkably straight at depth (see compilation in Jarrard (1986) for example).

The flow fields of the model of slab penetration to 670 km depth (figures 4.14, 4.17, 4.20) show much higher velocities in the upper sections of the slab compared to the slab tip. This can be interpreted as resistance to penetration of the lower mantle causing rollback to layer the slab along the interface. There is no seismic evidence of substantial amounts of slab material at the 670 km discontinuity and the observed slab stresses are not consistent with the high degree of bending that this may entail (Vassiliou et al. 1984).

The flow fields of models with a viscosity contrast of ×10 (figures 4.3, 4.10, 4.13. 4.16. 4.19) do not show the problems discussed above. Penetration of the lower mantle is observed whilst flow within the slab is fairly consistent in velocity and orientation along the slab length. In this respect the viscosity contrast of ×10 is preferred.

The magnitude of viscosity in the asthenosphere does not affect the bulk flow pattern greatly (figures 4.6-4.11). The general influence of the low viscosity zone is to concentrate the upper mantle flow and decouple the motion of the surface plates. A viscosity of $\mu = 10^{19}$ Pa s is at the low end of the range of possible viscosities, so for a general model the value $\mu = 10^{20}$ Pa s is taken. However, these finite element models are relatively insensitive to the value of asthenospheric viscosity.

A general model of mantle stratification has been adopted, the asthenosphere $\mu = 10^{20}$ Pa s. upper mantle $\mu = 10^{21}$ Pa s and lower mantle $\mu = 10^{22}$ Pa s. The flow fields in figures 4.33 - 4.36 represent slab penetration to 300, 400, 670 and 1000 km in this general mantle model and are blow-ups of figures 4.28, 4.22, 4.16 and 4.7.

There are a few observations to make on these models of increasing slab penetration. The width of circulation in the mantle increases, as does the depth and width of
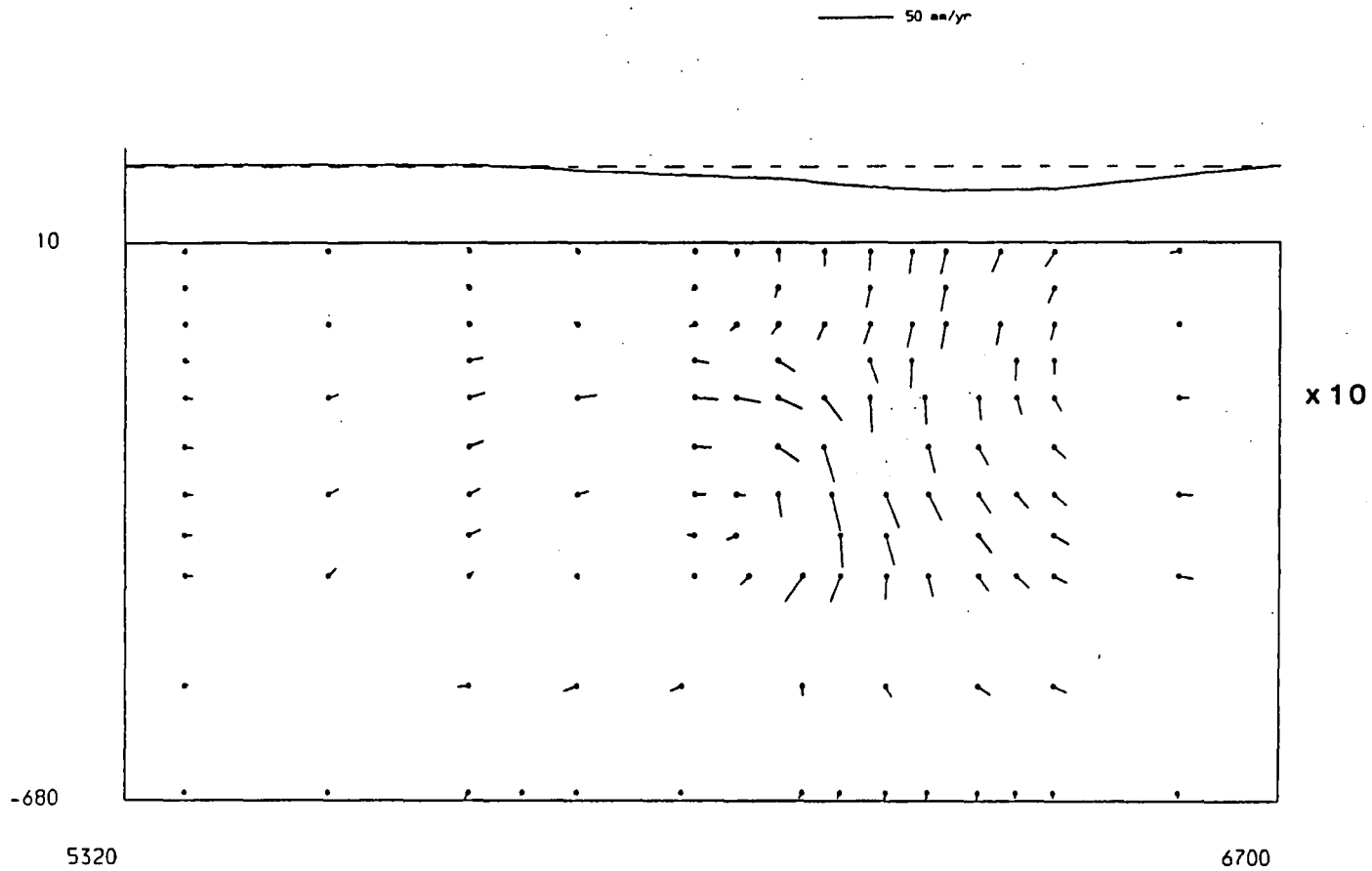
Figure 4.33   The flow field and surface displacement profile at the centre section
of the mesh for the model of slab penetration to 300 km depth, with astheno-
sphere viscosity 10^{20} Pa s, upper mantle $\mu = 10^{21}$ Pa s and lower mantle
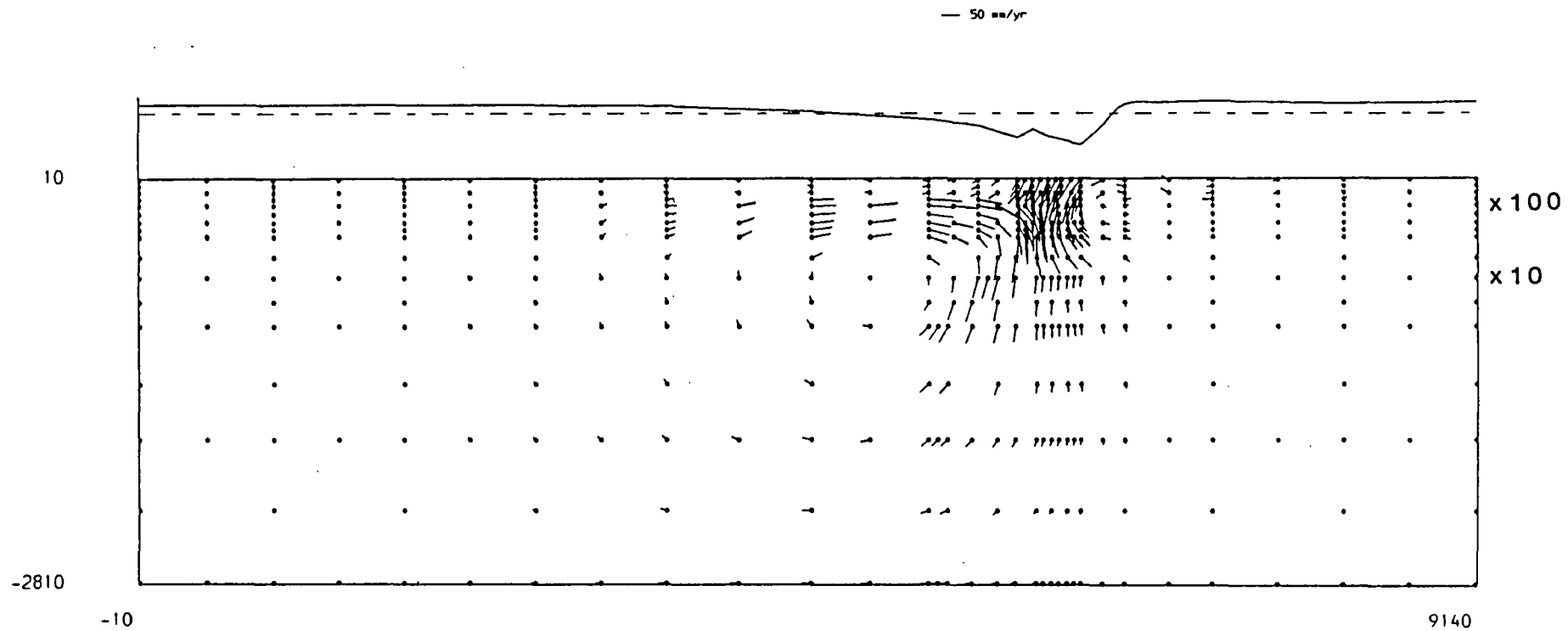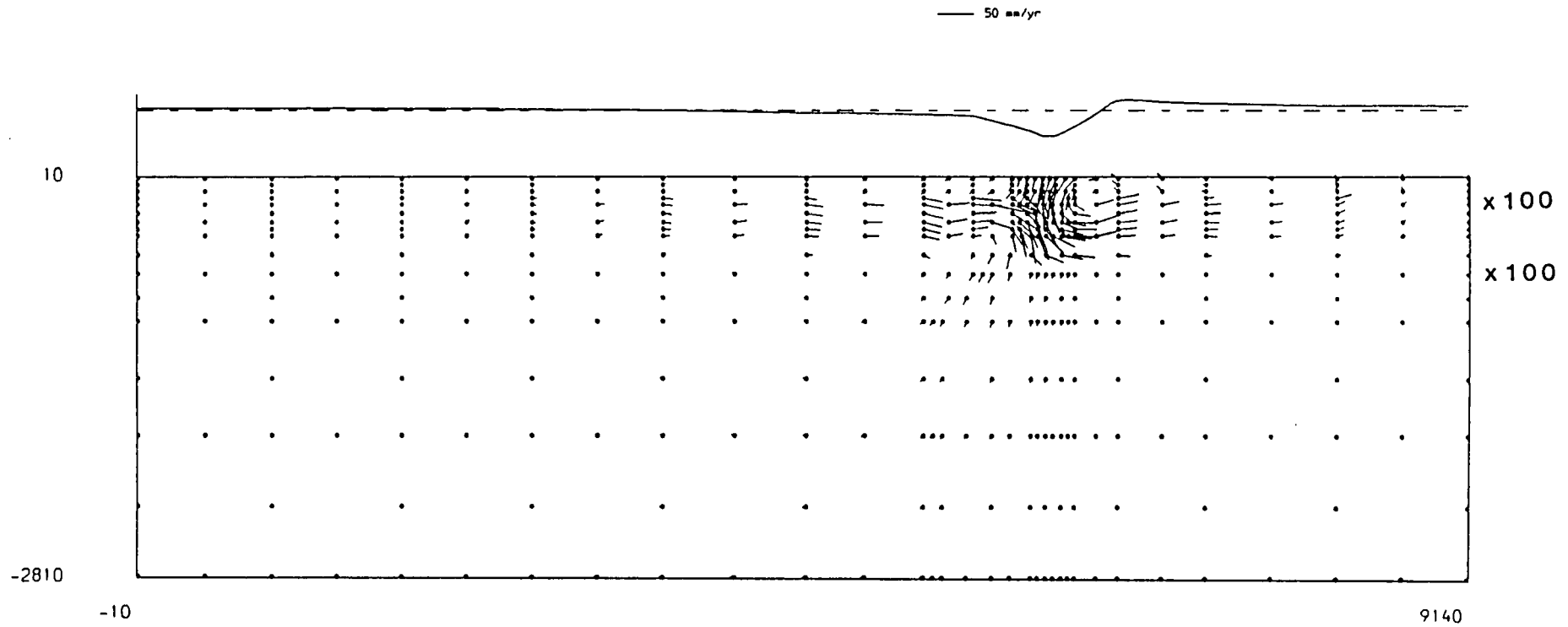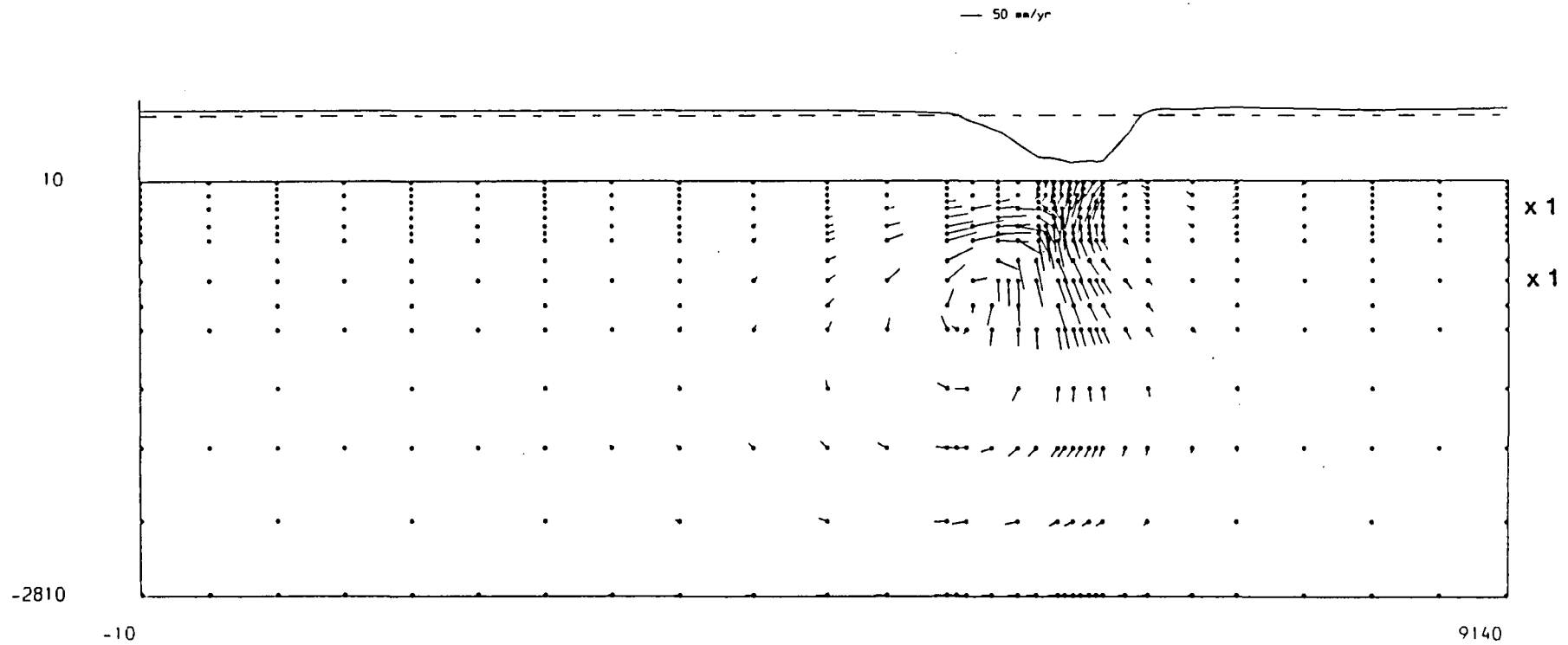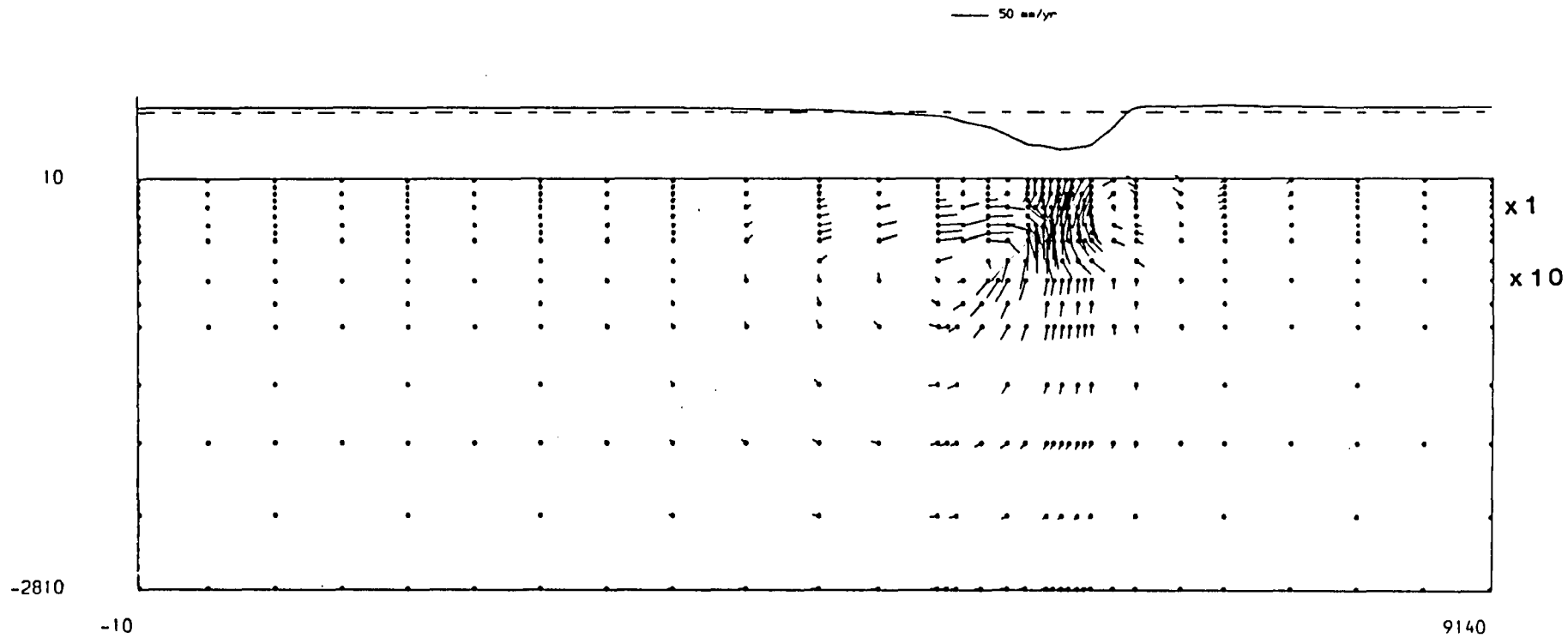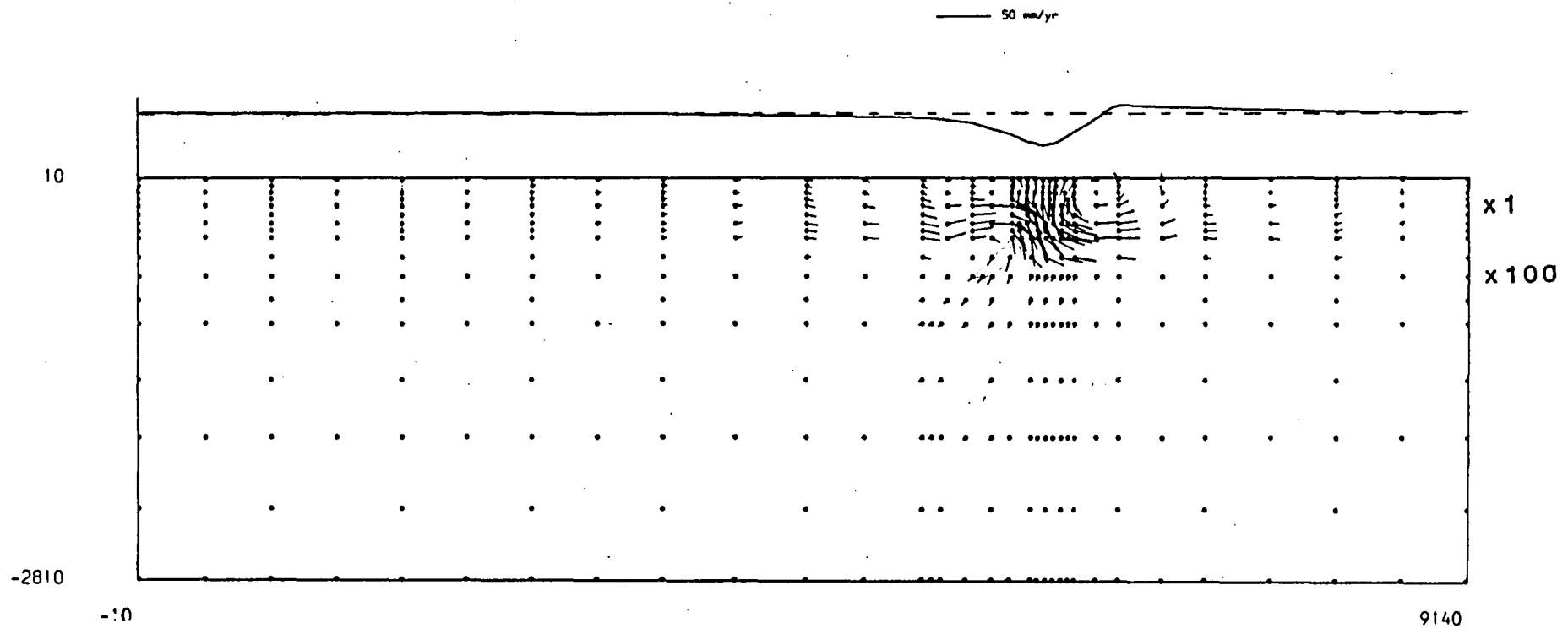$\mu = 10^{22}$ Pa s.
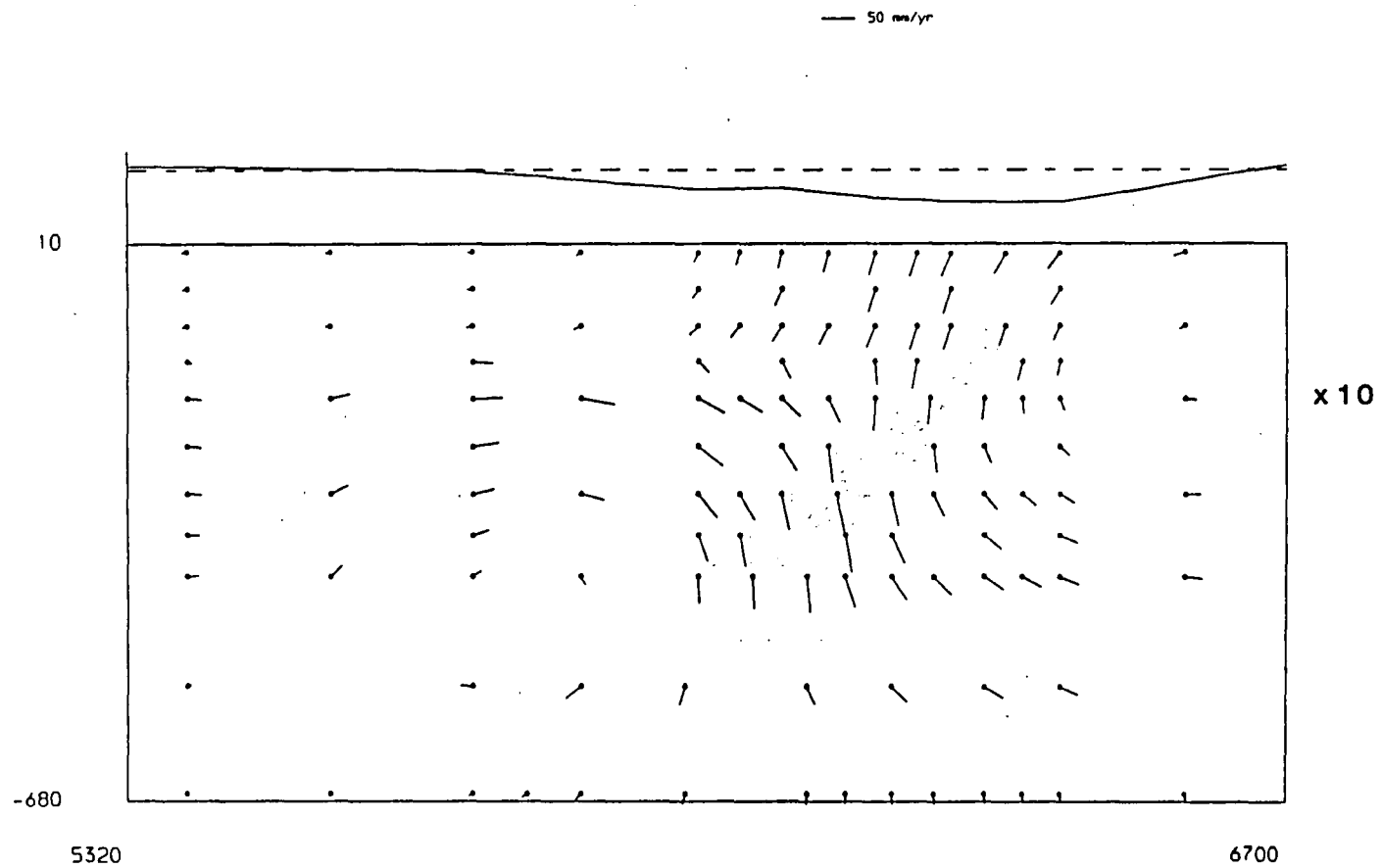
Figure 4.34 The flow field and surface displacement profile at the centre section of the mesh for the model of slab penetration to 400 km depth, with asthenosphere viscosity 10^{20} Pa s, upper mantle $\mu = 10^{21}$ Pa s and lower mantle $\mu = 10^{22}$ Pa s.
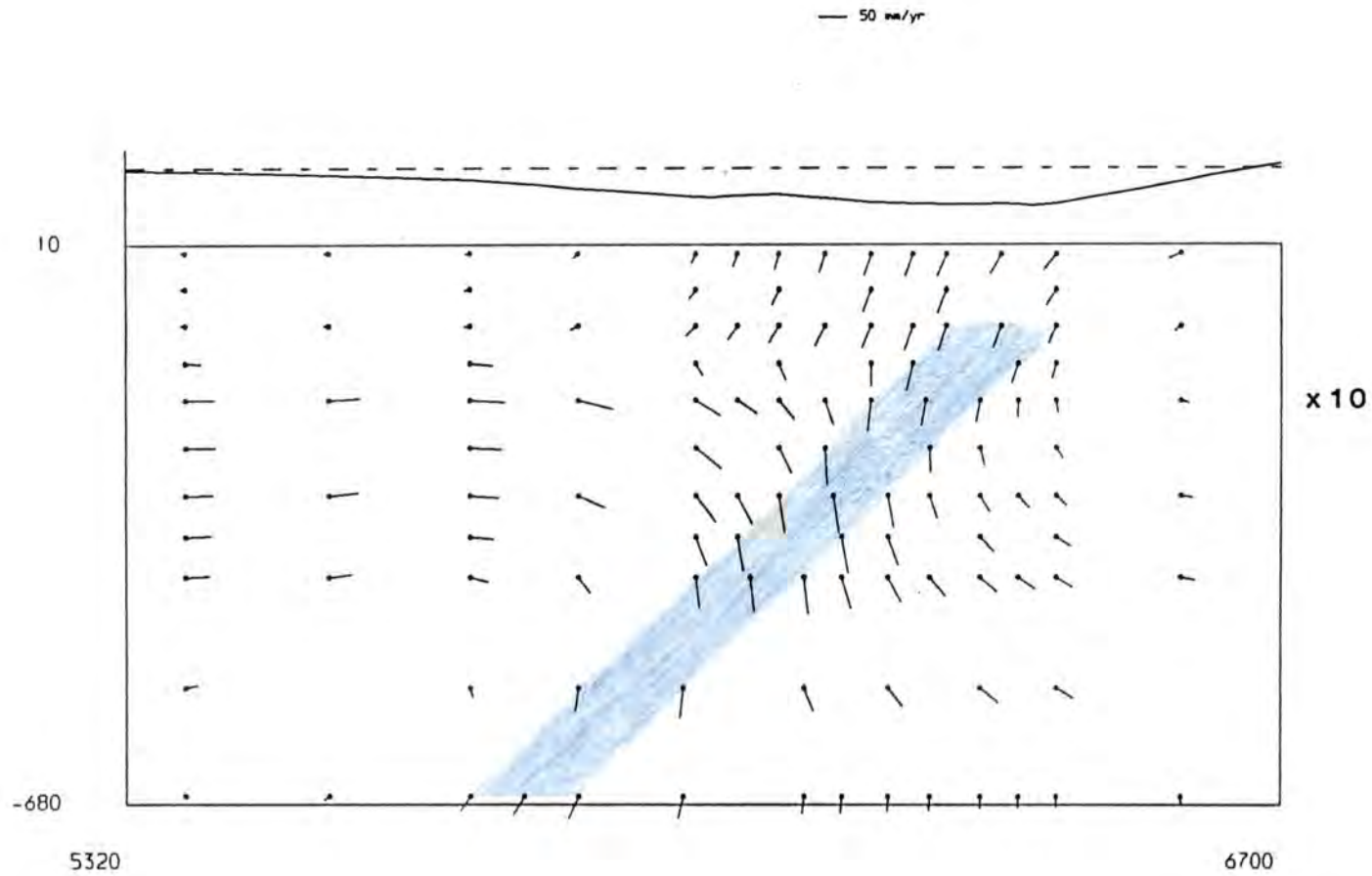
Figure 4.35   The flow field and surface displacement profile at the centre section
of the mesh for the model of slab penetration to 670 km depth, with astheno-
sphere viscosity 10^{20} Pa s, upper mantle $\mu = 10^{21}$ Pa s and lower mantle
$\mu = 10^{22}$ Pa s.
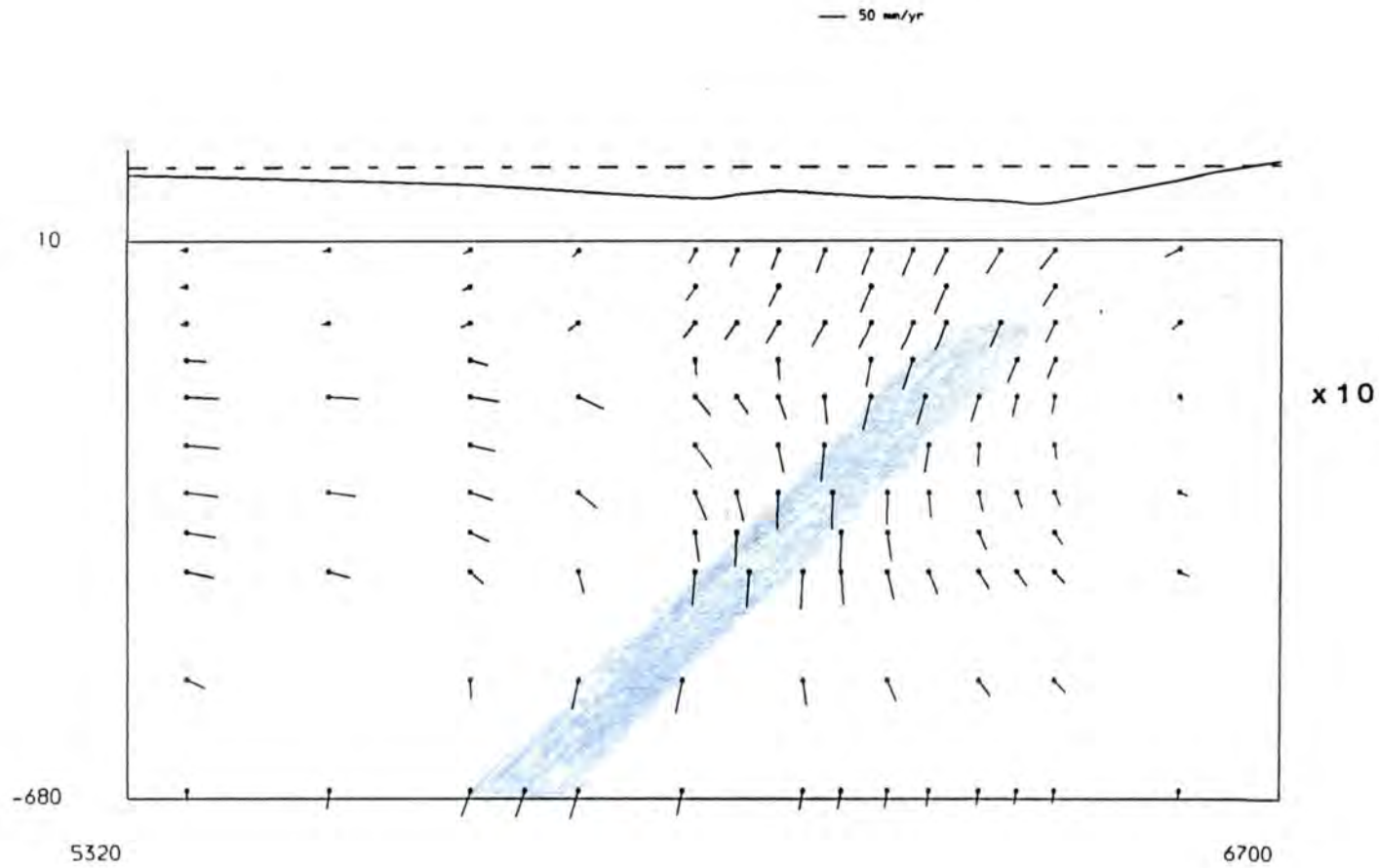
Figure 4.36 The flow field and surface displacement profile at the centre section of the mesh for the model of slab penetration to 1000 km depth, with asthenosphere viscosity 10^{20} Pa s, upper mantle $\mu = 10^{21}$ Pa s and lower mantle $\mu = 10^{22}$ Pa s.

the surface depression, with increasing slab depth. The significant change occurs when the elevated olivine-spinel transition is reached. Depression of the surface is caused by a combination of viscous and mechanical coupling of the vertical motion of the slab. The topography of the surface and the CMB serve to compensate the body force of the descending lithosphere and the relationship is controlled by the viscosity stratification (Hager 1984).

The flow field in figure 4.33 for the model of 300 km penetration has a relatively low magnitude of flow velocity. Flow within the slab (25 mm/yr) is roughly vertical in the upper section (200 km depth) but rotated anticlockwise of vertical in the lower section (300 km depth). The flow vectors do not represent particle trajectories but the general motion of the slab can be defined as sinking vertically and rotating towards vertical subduction. The 400 km penetration model (figure 4.34) shows flow in the upper section of the slab oriented roughly downdip of vertical (60 mm/yr) and flow in the lower sections is rotated anticlockwise of vertical. Thus the motion of the slab is vertical sinking combined with rotation towards vertical. At 670 km penetration the slab tip hits the top of the lower mantle (figure 4.35). In the upper slab the flow is oriented downdip of vertical, at 400 km depth the flow is rotated anticlockwise of vertical (70 mm/yr) and in the lower section the flow is aligned vertical of downdip. Thus the general motion is altered, the slab is sinking more obliquely and bending at mid-length. Deeper penetration into the lower mantle (figure 4.36) shows a similar pattern. flow in the upper and lower sections of the slab is aligned vertical of downdip. At about 400 km depth the flow is aligned vertically. Thus the general slab motion is oblique sinking accompanied by bending at mid-depth.

Thus, as subduction proceeds, the flow vectors within the slab rotate clockwise towards an orientation just vertical of downdip. Interaction with the lower mantle causes stagnation of the slab tip and the mechanical strength of the lithosphere transmits the resistance to motion along the length of the slab.

The flow field above the slab was aligned horizontally in all models, there was no evidence of 'backarc convection'. Omission of the thrust zone prevents shear slip between the plates at the surface and it is the relative motion which drives corner flow (McKenzie 1969).

4.7 Limitations of the Models

The viscous flow models of this chapter have not attempted to model a particular subduction zone but rather present a generalised simulation of the action of subduction. The aim of the study is to predict the overall flow field generated by a mechanically strong, oblique, sinking slab. Despite the simplistic approach of assuming only that the viscosity distribution has primary control over subduction, the models have many limitations.

The lithosphere was represented by a 90 km thick layer of viscosity 10^{23} Pa s. The mechanical strength of oceanic lithosphere is best modelled by an elastic component to the rheology. The high viscosity approximation cannot truly simulate the flexural strength of the elastic component. The long term time-dependence produced by slab motion was not considered and only slab dips of 45^c were included. The age-dependent thickness of the lithosphere was also ommitted.

Short term time-dependence was allowed for by the movement of the free surface. In the far field from the slab this allowed the topography to balance roughly the induced flow stresses, but at the top of the slab the surface will not reach equilibrium. The subducting plate is not detached from the overriding plate at the thrust zone, in the absence of shear slip between the plates the flow field at the top of the slab will not be realistic. Thus the models cannot simulate the subduction of one plate under the other and will not produce corner flow. The omission of the thrust zone also prevents an accurate simulation of the surface topography which compensates the underlying vertical forces.

The length of the mesh is almost one quarter of the circumference of the Earth and so the rectangular box is not a good approximation. Curvature will cause the base to be much shorter than the surface. The boundary conditions at the sides of the mesh contain the fluid within the domain of the mesh and do not permit a mass flux across the sides. This is an important omission. There is a circulation of mantle material due to thermal convection and subduction is only the descending limb. Material is removed from the mantle at ocean ridges to form the lithosphere of the surface plates and injected back again at subduction zones. A major component of flow in the mantle will probably be the lateral flow in the asthenosphere towards ocean ridges which replenishes the MOR source region. This flow is driven by the rollback of the slab (Garfunkel et al. 1986).

These finite element models do not simulate this circulation of material but simply depict the return flow of the lithosphere back into the mantle which is the dominant driving force of mantle flow (Loper 1985).

The mantle was assigned uniform Newtonian viscosities and the $p - T$ dependence was not included. However, over the short time periods considered the heat transport will be small and so this is not expected to have a great deal of effect. The seismic discontinuities at 400 km and 670 km depth were not included as horizontal mantle boundaries. The sharpness of the transitions and the lack of topography at the seismic discontinuities suggest that they are instantaneous phase changes. Lateral variations in the properties of the lithosphere and the mantle were not included and may be expected to play an important role.

An important omission is the out-of-plane flow. Subduction zones are arcuate and of a finite length and will drive a considerable component of flow in the z-direction. The 2-D finite element analysis cannot model this flow.

CHAPTER 5

The Stress Regime At Subduction Zones

The previous chapter dealt with flow in a viscous mantle and encountered certain problems with the surface of the Earth and the behaviour of the thrust zone. The models of this chapter describe the evolution of subduction zones with an elastic-viscoelastic rheology which provides a more precise description of the response of the surface and thrust zone. The limitations of the models are elaborated upon in the final section. A single, highly simplified basic model of an island arc convergent margin has been chosen as a suitable starting point. Oceanic lithosphere subducts beneath an adjacent plate which is also composed of oceanic lithosphere. Gradual complication of the model should enable us to discriminate the effect of each factor controlling the evolution of subduction. The models and results are presented and commented upon in this chapter, and a full discussion of the results is given in the next chapter.

There are several initial assumptions which form the basis for the numerical simulations of this chapter. The rheology of the lithosphere is represented by a 30 km thick elastic layer overlying 60 km of Newtonian viscoelastic material. The finite element meshes lack sufficient resolution to include the crust explicitly. Crustal thickness variations may locally dominate the stress regime. At subduction zones the isostatically compensated load of the volcanic arc is an important contribution to the crustal loads. The arc is incorporated as equivalent normal stresses about the elastic layer of the lithosphere to simulate the topographic load and the underlying upthrust. The absence of the oceanic crust excludes the basalt-eclogite phase change from the models. This is an important addition to the body forces as it converts buoyant crust to the denser phase of eclogite, which adds to the driving force of subduction. The mantle below the lithosphere is modelled as a three layer Newtonian, viscoelastic body. The asthenosphere exists between the base of the lithosphere (90 km) and 200 km depth, the upper mantle extends to 670 km depth, and the lower mantle layer constitutes the bottom layer from 670 km depth to the base of the model.

Slab dip was chosen to be a constant 45° throughout the mantle. This is the

highest dip at which double seismic zones have been observed (Fujita and Kanamori 1981). A specific slab profile of a particular subduction zone has not been modelled because of the difficulty of estimating the residual bending stresses that generate the shape. However, the contortion of an initially straight slab will provide information on the subduction dynamics.

The trench has been included as a geometrical effect only, and its mass deficit and the flexural response of the outer rise have been omitted. The mass deficit of the trench is a reaction to the slab pull and these two opposing forces generate an enormous couple at the slab bend region (see section 1.5). Stresses exceeding the failure criteria of the lithosphere cause significant anelastic deformation which cannot be modelled by this finite element method. The stress regime of the slab bend region of these models will not be realistic, however the trench - outer rise flexure system should develop as a consequence of slab pull, inducing a reactive upthrust at the top of the slab.

5.1   The Finite Element Meshes

The two finite element meshes that are used in this chapter possess very similar basic characteristics, differing only in dimension and resolution. The disadvantage of attempting to model these larger cross-sections is that the internal resolution is reduced as the element size increases. This constraint cannot be overcome by maintaining the resolution (smaller elements) only in the region of interest around the slab. Selective increased resolution need not significantly increase the total number of nodes (N) required for a particular mesh, but it does greatly increase the semibandwidth (KSBW) of the system matrix. The computation time (in CPU sec) to perform the LU decomposition of the unsymmetric, banded system matrix by Gaussian elimination is proportional to $N \times (2 \times KSBW - 1)^2$ (Greenough and Robinson 1981). Limitations in core storage and computing power thus preclude a large increase in KSBW.

Mesh (i) in figure 5.1 represents a 4600×1400 km cross-section through the top half of the mantle. Mesh (ii) represents a cross-section through the upper mantle only, of dimensions 3100×670 km and is shown in figure 5.2. The general rheology, pertaining to the left and right hand edges of the two meshes, is given in Table 5.1 below.

The Finite Element Mesh
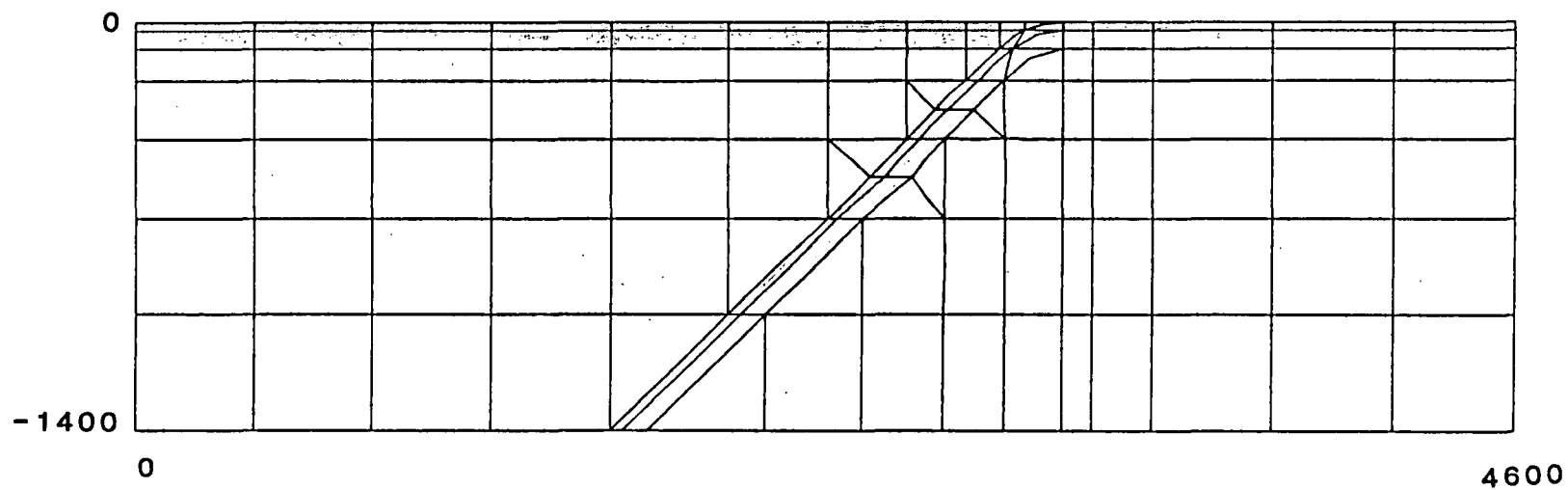
Figure 5.1   Mesh (1) represents a 4600 × 1400 km cross-section of the top of the mantle. The shading denotes the lithosphere.

The Finite Element Mesh
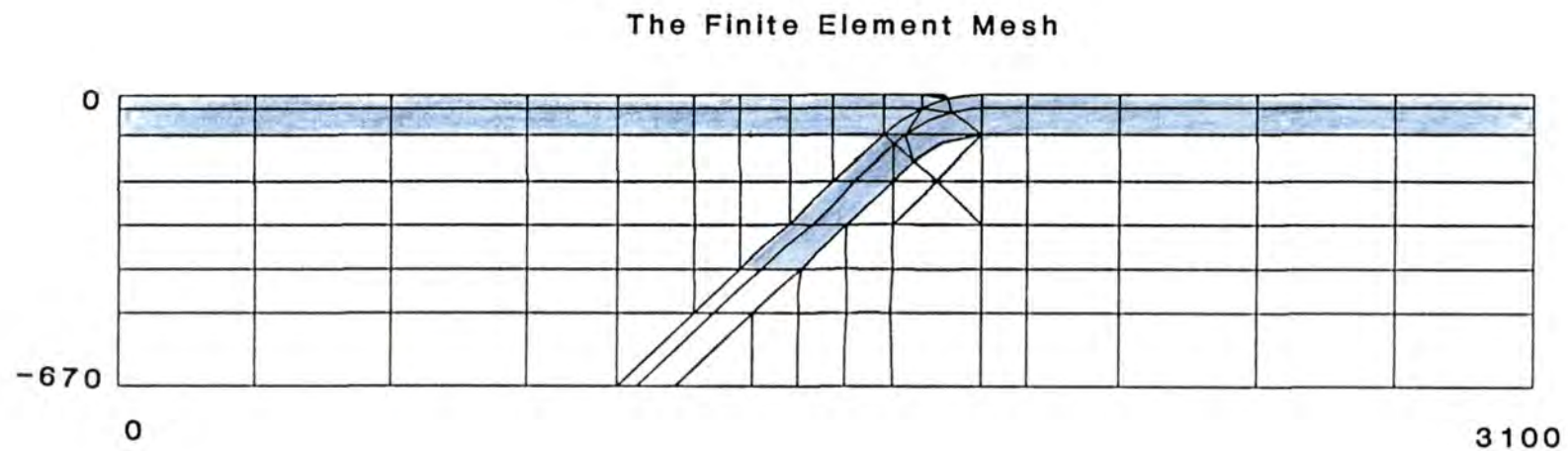
Figure 5.2   Mesh (ıı) represents a 3100×670 km cross-section of the upper mantle.
The shading denotes the lithosphere.

The Finite Element Mesh (Centre Section)
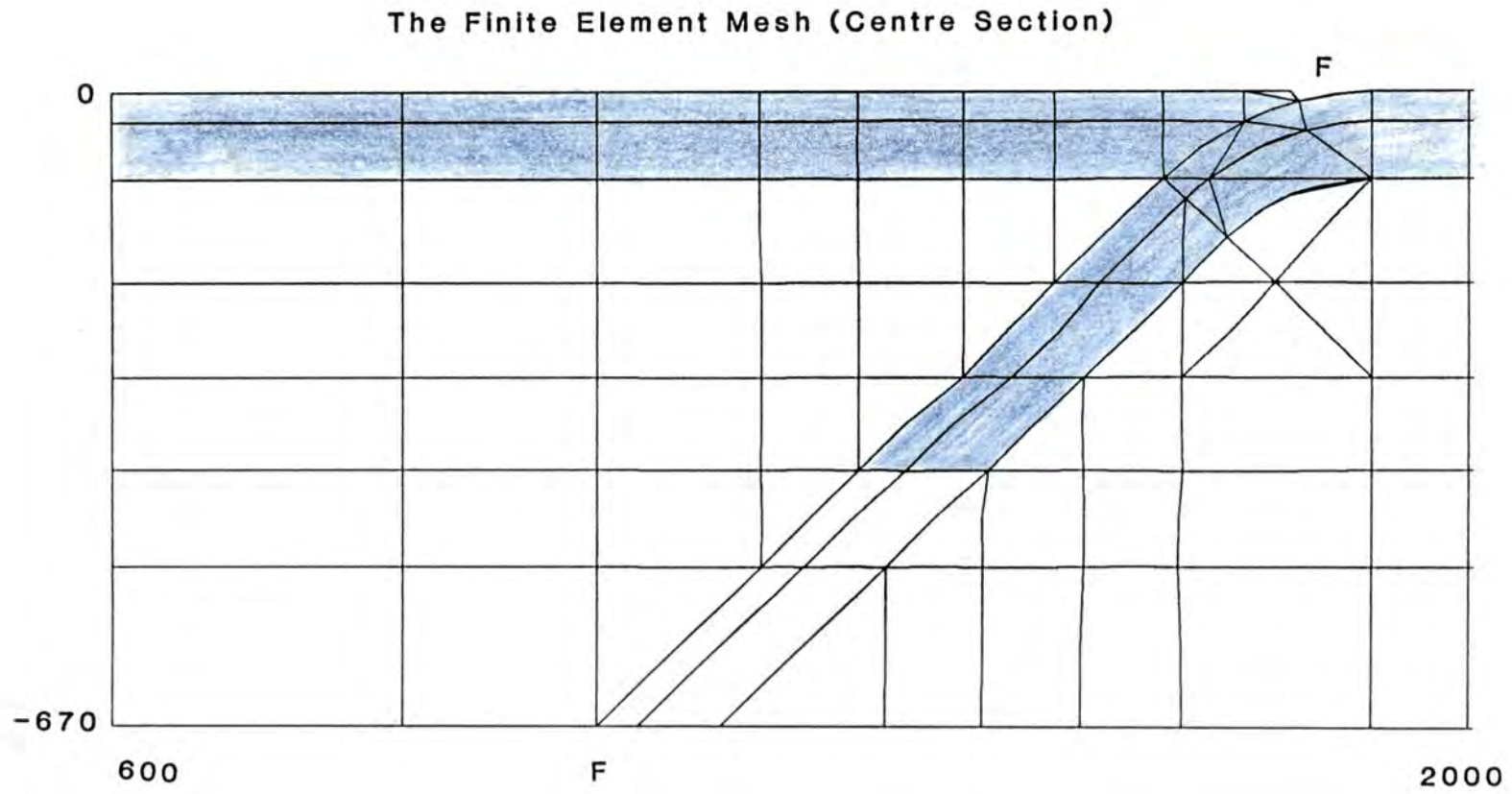
Figure 5.3   The mid-section of mesh (ɪɪ) of dimensions 1310 × 670 km. The
shading denotes the lithosphere and the fault line along the top surface of the
slab is marked by F.

Depth Range (km)	Young's Modulus (N m^{-2})	Poisson's Ratio	Viscosity (Pa s)
0 – 30	1.11×10^{11}	0.25	
30 – 90	1.11×10^{11}	0.25	10^{22}
90 – 200	1.11×10^{11}	0.25	$10^{20} \rightarrow 10^{21}$
200 – 670	1.11×10^{11}	0.25	10^{21}
670 – 1400	1.11×10^{11}	0.25	$10^{21} \rightarrow 10^{23}$

Table 5.1   General rheology

In the vicinity of the subduction zone this layered rheology is intruded by the descending slab and figure 5.3 shows a blow-up of this mid-section of mesh (ii), but the following description is equally applicable to mesh (i). This portion of the mesh represents a cross-section 1310 × 670 km. The fault line is marked by F and it divides the mesh into two bodies along the top surface of the subducting slab. The section of the fault line dividing the surface plates is the thrust zone. The lithosphere to the right of the thrust zone is the subducting plate and that to the left is the overriding plate. The forearc is the region of the overriding plate within about 200 km of the trench, the arc is the region under which the slab reaches about 100 – 150 km depth and the backarc is the area of the overriding plate approximately 300 – 700 km from the trench. The slab is the portion of lithosphere below 90 km depth and it carries the density anomaly. The base of the slab is horizontal which streamlines the slab tip in the downdip direction. The mesh is density stripped relative to the left hand edge (see Park 1981 for discussion), leaving the slab mass anomaly as the only surviving body force. This removes the large principal stresses due to the overburden and the resulting stress regime is interpreted relative to an unperturbed lithostatic stress field.

General mesh boundary conditions are straightforward. The sides are constrained by a lithostatic pressure gradient which becomes zero under the density stripping, and the surface is isostatically compensated using a rock - water density contrast of $\rho = 2270$ kg m^{-3}. This is the mantle - water contrast since the crust has been omitted from the models. Internal density contrasts such as the 400 km and 670 km seismic discontinuities have not been included because of the likelihood that they are phase changes that allow material to pass across the boundary. Isostatic conditions simulate the density jump at a compositional boundary which does not permit a mass flux, only an equilibrium

topography. All the models are calculated under the plane strain approximation.

Computing power limits the mesh sizes and so the full vertical extent of the mantle cannot be modelled. There are two possibilities for the mid-mantle basal boundary condition, a vertically immovable traction free base, or an isostatically compensated base. Preliminary tests have shown that altering the basal boundary condition provokes a negligible change in the stress regime but there is a small effect on the absolute motion. The flexural twist of the whole mesh is included in the absolute motion, an unwanted effect of the isostatic base, and so the fixed base condition is used. The most important boundary condition is the edge of the surface plates. One plate edge must be restrained to eliminate the rigid body motion mode, but the plate boundaries strongly influence the stress regime of the surface lithosphere and thus demand a careful analysis of these boundary conditions.

The magnitude of the time increment for the viscoelasticity algorithm must be less than the smallest Maxwell time in the mesh. For example, if $\mu = 10^{21}$ Pa s, and $E = 1.11 \times 10^{11}$ N m^{-2} then the Maxwell time will be,

$$\frac{2\mu}{E} = 570 \text{ yrs}$$

The initial strain method for viscoelastic relaxation gradually increases the magnitude of the force vector $\{F\}$ with time (see section 2.2.8). At the completion of the time stepping procedure the mesh suffers very large displacements, but the initial strain is subtracted from the calculated strain leaving only very small resulting stresses. Thus the algorithm becomes unstable as the force vector gets very large, and in practice one is limited to about 1000 time steps. If there are extremely large viscosity contrasts within the mesh the deviatoric stresses will only be relaxed in the elements with the smaller viscosities.

The relaxation period is defined as the number of time steps multiplied by the magnitude of the time increment. The models evolve for a variety of relaxation periods but all are small compared to the time constant of subduction. So the solutions correspond to the first motion from an initially quiescent state. The relatively short relaxation periods make it necessary to impose an abnormally low viscosity for the lower lithosphere, $\mu = 10^{22}$ Pa s instead of the more realistic estimate of $\mu = 10^{23}$ Pa s. This compromise viscosity allows a reasonable thermal thickness (90 km) combined with a reasonable flexural thickness (30 km) for the lithosphere.

The numerical solutions are displayed in five specific formats; the stress regime, the vertical displacement of the surface, the true motion of the surface of the slab, the displacement vectors and the gravity profile. The various properties of subduction to be investigated are: the thrust zone, the viscosity of the mantle, the duration of subduction, the thermal anomaly of the backarc, the slab mass anomaly, the slab rheology, and the plate boundary conditions. The sections of this chapter are presented as a progressive assembly of a subduction zone, so each subsequent section assumes the properties of all other preceding sections.

5.2   The Action of the Thrust Zone

5.2.1   Problem Statement

As the thrust zone could not be incorporated into the viscous flow models of the previous chapter, the first problem is to establish, and attempt to quantify, the effect of the thrust zone on subduction mechanics. It was suggested earlier (see section 1.5.2) that the thrust is responsible for redistribution of stress in the surface plates, not influencing the force balance in the mantle. A model of slab penetration to a depth of 1000 km in mesh (1) is used as the demonstration model, but the general conclusions apply universally. The slab is assigned a thermal density anomaly of $\rho = 50$ kg m^{-3} throughout its length. As discussed in section 1.5.2 conductive heating slowly spreads the anomaly, leading eventually to assimilation of the slab. For the purposes of modelling subduction the constant thermal density anomaly is a good approximation. The right hand edge of the subducting plate is held fixed in the x-direction, and the overriding plate is unrestrained. The viscosity of the asthenosphere and upper mantle is $\mu = 10^{21}$ Pa s, and below 670 km the lower mantle has a viscosity of $\mu = 10^{22}$ Pa s. The models evolve for a relaxation period of 50 000 yrs, this is 100 time steps at $\Delta t = 500$ yrs.

In the first model the thrust zone is locked and all fault stiffnesses are set to 10^{15} N m^{-1}. Shear slip at the thrust zone is allowed in the second model. The shear stiffness in the three shallowest fault elements is reset to $k_s = 0$ and this is the sole difference between the two models.

5.2.2   Discussion of Results

The stress regime of the centre section of the mesh for the model with a locked thrust zone is shown in figure 5.4, the vertical displacement of the surface is shown in figure 5.5, the slab motion in figure 5.6, and finally the gravity profile in figure 5.7. The solid line dividing figure 5.4 delineates the fault line joining the mesh halves. The principal stress vectors are depicted by solid lines for compression and by dashed lines for tension. A scale vector is given at the top which shows the considerable variation in stress magnitude in subsequent models. The slab stresses have a distinctive pattern. There is a stress minimum at about 300 km depth, below which the slab shows downdip compression (up to 180 MPa), and above which the slab is under downdip tension (up to 180 MPa). Above the stress minimum the tensions increase with distance updip, but below it the compressions have a local maximum at about 650 km depth. Thus the portion of the slab in the lower mantle is under reduced downdip compression. In general the slab stresses are not perfectly aligned downdip but are rotated slightly towards the vertical. The overriding plate has large horizontal compressions (up to 200 MPa) in the forearc which gradually diminish into the far backarc. Outside the immediate vicinity of the trench the subducting plate is under horizontal tension throughout, but only the edge of the plate adjacent to the trench is shown here. Small bending stresses are superimposed on these large tensions.

Away from the region around the slab the stresses throughout the upper and lower mantle are well relaxed. In contrast, above the slab there is a low pressure region denoted by the large principal tensions. The pressures in the mantle wedge vary from about 10 — 50 MPa. Below the slab is high pressure region evidenced by the principal compressions, and the pressures here vary from about 5 — 30 MPa. These pressure differences in the mantle adjacent to the slab are generated and sustained by slab motion and act to support the slab body force. This observation is quantified and discussed further in the next chapter.

The surface displacement profile in figure 5.5 is split into two halves representing the overriding and subducting plates and the lower box shows the relative position of the density anomalies. The overriding plate shows a broad asymmetric depression with the maximum amplitude of 1600 m centred close to the top of the slab. The right hand curve denoting the subducting plate shows the development of the trench and a 100 m

Figure 5.4   The principal stresses for the model of 1000 km penetration, lower mantle viscosity $\mu = 10^{22}$ Pa s and the thrust zone locked. The solid line denotes the position of the fault. The shading denotes the lithosphere. A scale length of vector magnitude is given above.

Surface displacement profile (in m)

Distance in km

Figure 5.5 The vertical displacement of the surface for the model of 1000 km penetration, lower mantle viscosity $\mu = 10^{22}$ Pa s and the thrust zone locked. The left hand curve denotes the overriding plate, the right hand curve denotes the subducting plate. The lower box shows the relative position of the density anomalies.
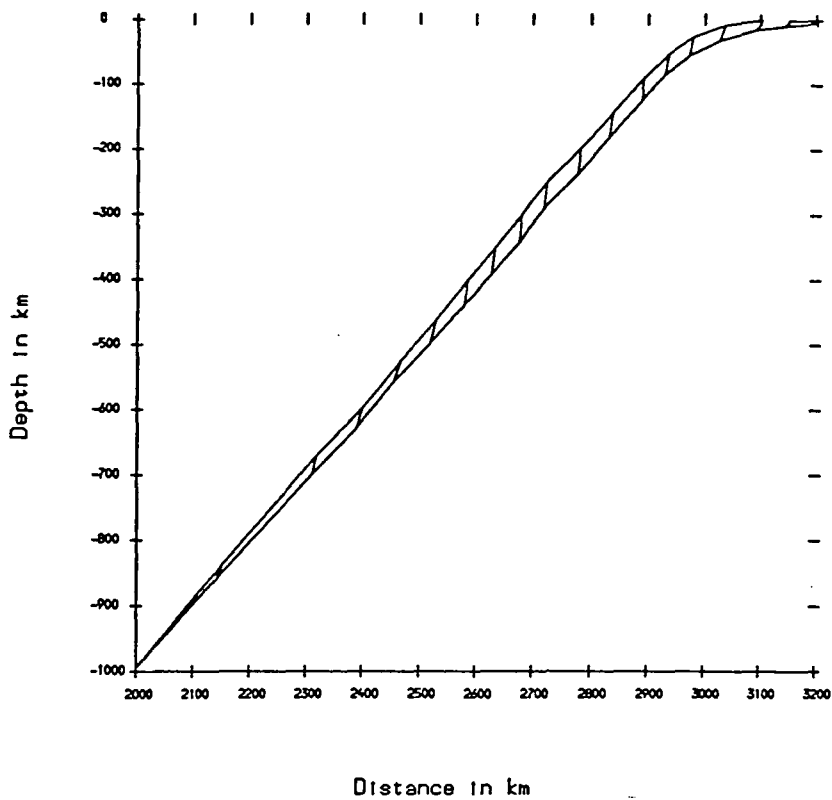
Figure 5.6   The absolute slab motion linearly extrapolated by a factor of 20 for the model of 1000 km penetration, lower mantle viscosity $\mu = 10^{22}$ Pa s and the thrust zone locked. The upper curve denotes the original position of the top surface of the slab and the lower curve denotes the final position of the top surface of the slab. The cross-lines represent displacement vectors of the nodes.

Gravity Profile

Figure 5.7   The gravity profile in mGal calculated on a plane 0.5 km above the surface of the overriding plate for the model of 1000 km penetration, lower mantle viscosity $\mu = 10^{22}$ Pa s and the thrust zone locked. The lower box shows the position of the density anomalies.

high outer rise. However, this feature is very broad because the stresses in the lower lithosphere are not fully relaxed (thereby increasing the effective flexural strength of the plate). From elastic beam theory, a 30 km thick elastic layer will produce an outer rise centred 170 km from the trench, and a 90 km elastic layer will produce an outer rise centred 400 km from the trench. In figure 5.5 the outer rise is centred about 300 km from the trench. The true slab motion in figure 5.6 plots the movement of the slab linearly extrapolated to 1 Ma (factor of 20). The top curve is the original position of the top surface of the slab, and the lower curve is the final position. The cross lines are displacement vectors of points (nodes). The slab in the upper mantle is sinking almost vertically but slab motion in the lower mantle is inhibited. At the surface the subducting plate is dragged into the trench, lateral displacement is greater than vertical despite the boundary condition on the right hand edge.

The gravity profile in figure 5.7 is calculated along a plane 0.5 km above the surface of the overriding plate (see Appendix for details of the calculation) and the lower box shows the relative position of the density anomalies. The density anomaly of the slab, and the deflection of the isostatic boundary at the surface are the only contributions to the gravity anomaly. The deflection of the core-mantle boundary would contribute a small, negative, long wavelength anomaly, but this will be attenuated and will probably be negligible at the surface. The profile shows a maximum of 35 mGal just landward of the trench, followed by gradual decline to a minimum about 2600 km from the trench.

The second model unlocks the thrust zone and the resulting stress regime, surface displacement, slab motion and gravity profile are shown in figures 5.8 - 5.11 respectively. The deep compressions in the slab (figure 5.8) are relatively unaffected compared to figure 5.4, but the stress minimum occurs at a slightly shallower depth. The upper sections of the slab show quite a variable orientation of tensions accompanied by a reduction in magnitude. Horizontal compression in the overriding plate is reduced, and the far backarc now exhibits small tensions (15 MPa). The subducting plate is again under horizontal tension but carries stresses of a higher magnitude and the region of the plate under the thrust is now under surface-parallel tension. The surface displacement in figure 5.9 is quite similar to the locked thrust zone model. The maximum depression of 1400 m is a slight reduction, and the trench - outer rise flexure is slightly sharper than figure 5.5. The slab motion and gravity profile show slight increases in magnitude.

Figure 5.8   The principal stresses for the model of 1000 km penetration, lower mantle viscosity $\mu = 10^{22}$ Pa s and the thrust zone unlocked. The solid line denotes the position of the fault. The shading denotes the lithosphere. A scale length of vector magnitude is given above.

Surface displacement profile (in m)

Figure 5.9

Figure 5.9   The vertical displacement of the surface for the model of 1000 km penetration, lower mantle viscosity $\mu = 10^{22}$ Pa s and the thrust zone unlocked. The left hand curve denotes the overriding plate, the right hand curve denotes the subducting plate. The lower box shows the relative position of the density anomalies.

Figure 5.10   The absolute slab motion linearly extrapolated by a factor of 20 for the model of 1000 km penetration, lower mantle viscosity $\mu = 10^{22}$ Pa s and the thrust zone unlocked. The upper curve denotes the original position of the top surface of the slab and the lower curve denotes the final position of the top surface of the slab. The cross-lines represent displacement vectors of the nodes.

Gravity Profile

Figure 5.11   The gravity profile in mGal calculated on a plane 0.5 km above the surface of the overriding plate for the model of 1000 km penetration, lower mantle viscosity $\mu = 10^{22}$ Pa s and the thrust zone unlocked. The lower box shows the position of the density anomalies.
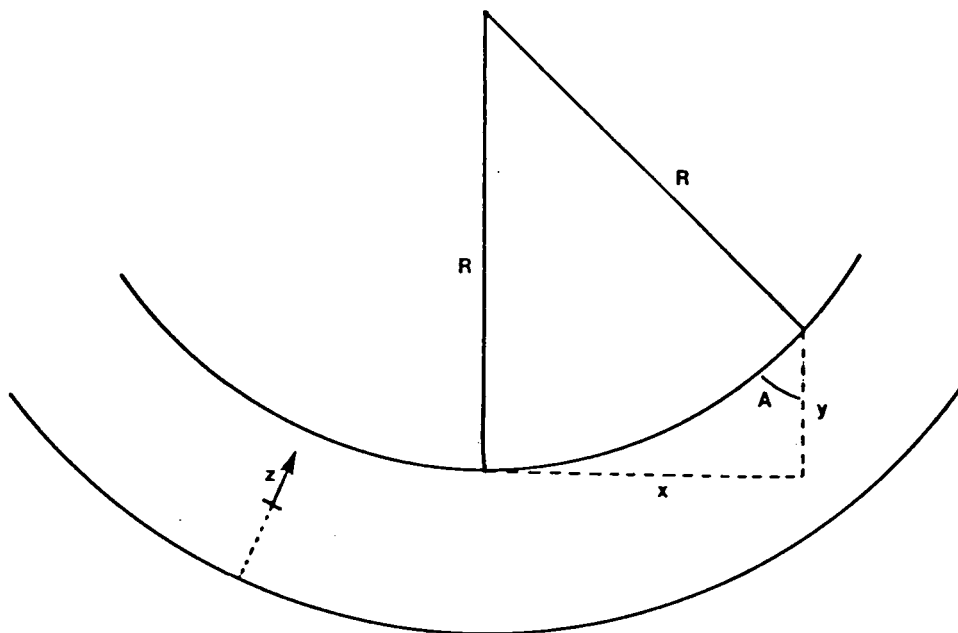
Two-Dimensional Plate Flexure

The bending stress at a distance z from the neutral fibre of an elastic plate of Young's modulus E, and Poisson's ratio ν bent with a radius of curvature R is given by,

$$\sigma_{xx} = \frac{E}{(1 - \nu^2)} \, \epsilon_{xx}$$

where,

$$\epsilon_{xx} = \frac{z}{R}$$

From the diagram above let,

$$\tan A = \frac{x}{y} \qquad \text{arc length} = x$$

since $x \gg y$.

Then the bending stress can be approximated by,

$$\sigma_{xx} = \frac{E}{(1 - \nu^2)} \, \frac{z \, (\pi - 2A)}{\text{arc}}$$

Figure 5.12   An estimate of the bending stresses produced in an elastic layer with a curvature R^{-1}.

Thus the thrust zone exerts strong control over the stress distribution in the surface plates without contributing greatly to the force balance in the mantle. In this particular model, unlocking the fault redistributes the stresses local to the thrust zone and generates a component of regional tension throughout the subducting and overriding plates of about 20 MPa. This agrees with the models of Waghorn (1984, figures 7.66, 7.77), which predicted this effect from purely elastic behaviour of the surface plates. In the final section of this chapter we will return to this behaviour of the thrust zone.

The broad band of horizontal compression in the overriding plate, a maximum in the arc gradually dying to leave tension in the far backarc and beyond, is controlled by viscous coupling through the mantle wedge. Vertical motion of the slab exerts normal stresses at the base of the surface lithosphere which create a broad depression of the overriding plate (Davies 1981, 1983) as shown in figures 5.5 and 5.9. This depression generates two contributions to the stress regime. Bending stresses are characterised by opposing compression and tension either side of the neutral fibre and these are not readily apparent in the overriding plate of figures 5.4 and 5.8. A method of estimating the bending stresses is given in figure 5.12. Taking values from the surface displacement profiles, let $x = 500$ km, $y = 1500$ m, and from the finite element mesh $z = 8.7$ km in the elastic layer. This yields bending stresses of about 13 MPa.

The normal stresses at the base of the lithosphere have an isostatic reaction at the surface which induces vertical tension in the lithosphere. The reduction in the vertical component of the overburden pressure creates horizontal deviatoric compression which will be amplified by stress relaxation in the lower lithosphere. The vertical tension can be estimated from the isostatic reaction to the surface displacement (h),

$$\rho gh = 2270 \times 9.81 \times 1500 = 33 \text{ MPa}$$

Stress amplification for a 30 km elastic layer in 90 km thick lithosphere yields horizontal compressions of 100 MPa. This is an order of magnitude higher than the bending stress but also it is less than the maximum stresses in figures 5.4 and 5.8. Much deeper stress relaxation, in the asthenosphere and below, may also contribute to the stress amplification. Thus deep loads may be able to produce very large horizontal stresses in the elastic portion of the surface lithosphere by stress relaxation. It is possible to discriminate the bending stresses superimposed onto the large compressions in the elastic layer of the overriding plate in figures 5.4 and 5.8. At the arc the plate is bent

down and the upper compression is greater than the lower, whilst in the backarc the lithosphere is convex upwards and the upper stress is then smaller than the lower.

The maximum surface depression above the top of the slab is 1600 m and this is approximately half of most estimates of the relative trench depth (Davies 1983). The reactive upthrust at the surface may be underestimated in these models and it is spread over a broad area of the surface plates. This may cause an overestimate of the forearc compressions and also an underestimate of the upper slab tensions and depth of the stress minimum. The enforcement of normal contact at the thrust zone causes the leading edge of the overriding plate to follow the slab rollback. If the asthenosphere exerts a basal drag on the overriding plate then the application of this edge force at the thrust zone will induce a regional tension in the plate. Boundary conditions at the right hand edge of the subducting plate cause it to be under horizontal tension.

Jarrard (1986) calculated a correlation coefficient of -0.67 between deep dip (in the depth range 100 → 400 km) and strain regime. As dip increases the strain regime becomes more tensional. This is consistent with the viscous coupling mechanism described above, but there are many other mechanisms through which slab dip can influence the strain regime and it is difficult to discriminate the relative importance of these effects.

5.3   The Olivine-Spinel Phase Change

5.3.1   Problem Statement

The olivine-spinel phase change at 400 km depth in the mantle occurs at a shallower depth in the cool slab. Schubert et al. (1975) estimated a maximum elevation of 115 km in the slab core with an associated density contrast of 280 kg m^{-3} across the boundary. The finite element mesh does not have sufficient resolution to accurately map the predicted distribution of the elevated phase transition (as shown earlier in figure 1.5). As a compromise a density of 150 kg m^{-3} is applied over the depth range 300 → 400 km in the slab. The increased body forces are distributed over a larger volume than predicted for subducting lithosphere and so the density anomaly is reduced accordingly to maintain the mass anomaly. All other mesh parameters are identical to the unlocked thrust zone model of the previous section. The model evolves for a

relaxation period of 50 000 yrs as before.

5.3.2 Discussion of Results

The model results are given in figures 5.13 - 5.16. There is an overall increase in magnitude in the stress regime of figure 5.13 compared to figure 5.8, as shown by the change in scale. Deep slab compressions are increased to 300 MPa from 180 MPa, and upper slab tensions to 180 MPa from 120 MPa. There is an increase of 80 MPa to give 200 MPa compressions in the forearc and an increase from 15 MPa to 30 MPa tension in the far backarc. The only significant alteration to the actual pattern of the stress distribution is the realignment of the slab tensions. The stresses in the upper slab now tend more nearly downdip. This result is in contrast to that of Vassiliou et al. (1984) who found that the addition of the body forces of the elevated phase change could not be reconciled with the stress regime derived from the study of earthquake distributions at Wadati-Benioff zones.

Davies (1983) modelled the downdip force in the slab due to shear resistance in an isoviscous mantle (as discussed in section 1.5.1). He concluded that an unreasonably large mantle viscosity of $\mu = 4 \times 10^{21}$ Pa s was required to generate sufficiently small (300 MPa) compressions in the lower slab. In this finite element model, an acceptable stress distribution is generated by a viscosity contrast ×10 at 670 km, including the elevated phase change and in the absence of an impenetrable boundary at the base of the slab. In particular the compression in the slab tip in the lower mantle is of much smaller magnitude. The mechanisms controlling the stress regime of the slab are discussed in the next chapter.

The surface displacement profile in figure 5.14 shows a significant increase in the maximum amplitude of depression to 1900 m. The slab motion curve in figure 5.15 shows a large increase in magnitude of displacement compared to figure 5.10, and a distinct change in sense of motion of the slab. The slab is moving quickest in the 300 → 400 km depth range which leads to an increase in dip of the upper slab and a decrease in dip of the lower slab due to the reactions of the trench and lower mantle. This general shape is observed in the Wadati-Benioff zones of Izu-Bonin and Tonga but other deeply penetrating slabs such as Mariana, Kamchatka, Kurile and Java do not show the shallowing of dip at the slab tip. The gravity profile in figure 5.16 shows a
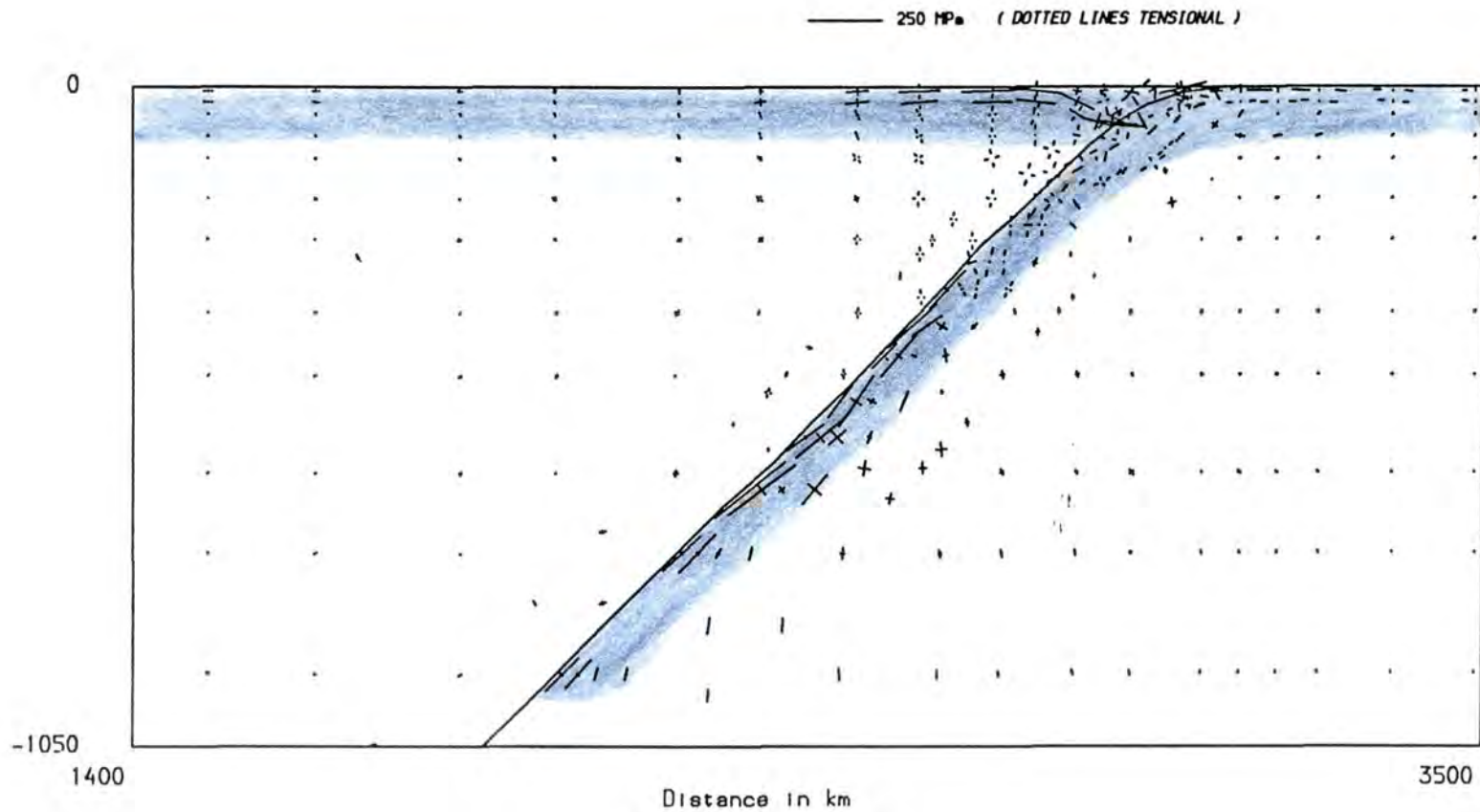
Figure 5.13   The principal stresses for the model of 1000 km penetration, lower mantle viscosity $\mu = 10^{22}$ Pa s including the olivine-spinel transition. The solid line denotes the position of the fault. The shading denotes the lithosphere. A scale length of vector magnitude is given above.

Surface displacement profile (in m)

Distance in km
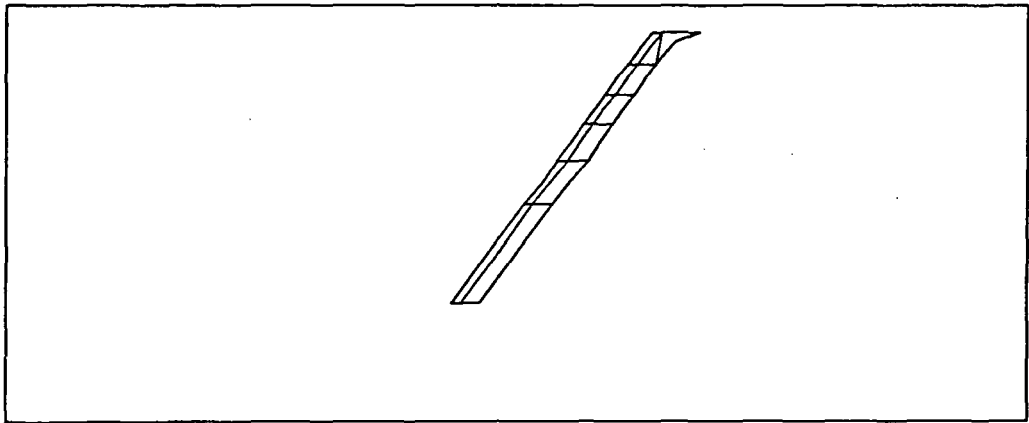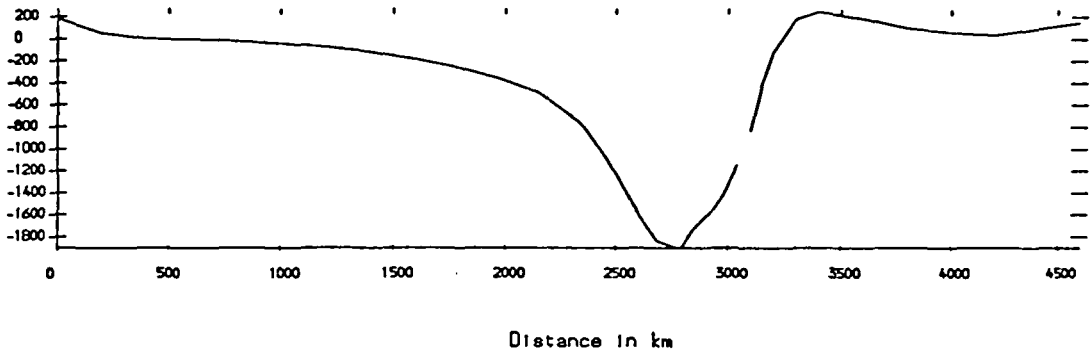
Figure 5.14   The vertical displacement of the surface for the model of 1000 km
penetration, lower mantle viscosity $\mu = 10^{22}$ Pa s including the olivine-spinel
transition. The left hand curve denotes the overriding plate, the right hand
curve denotes the subducting plate. The lower box shows the relative position
of the density anomalies.
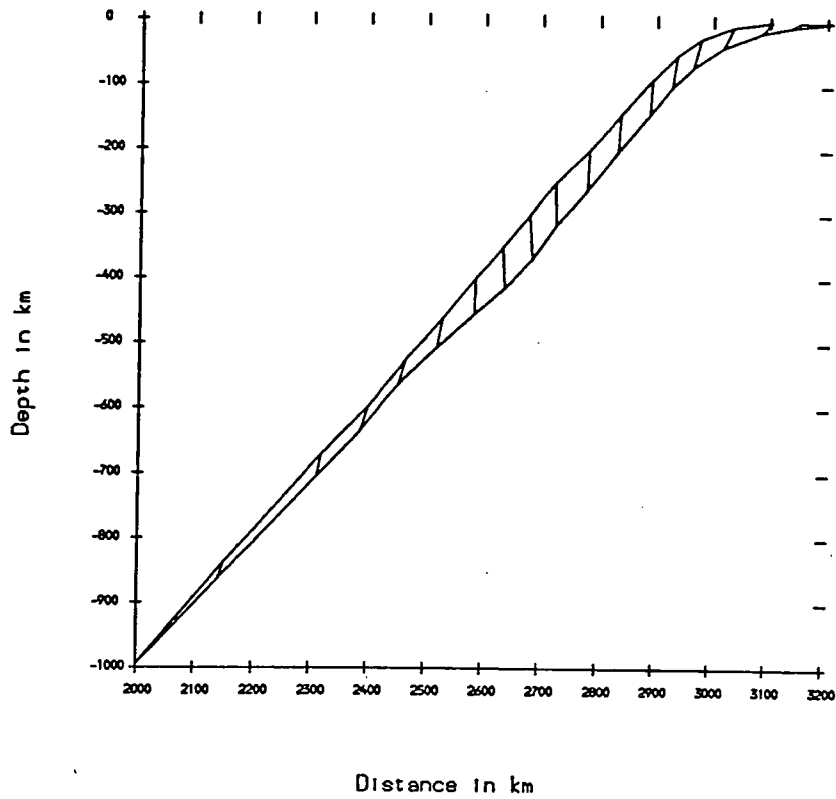
Figure 5.15   The absolute slab motion linearly extrapolated by a factor of 20 for the model of 1000 km penetration, lower mantle viscosity $\mu = 10^{22}$ Pa s including the olivine-spinel transition. The upper curve denotes the original position of the top surface of the slab and the lower curve denotes the final position of the top surface of the slab. The cross-lines represent displacement vectors of the nodes.
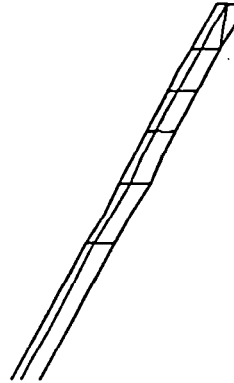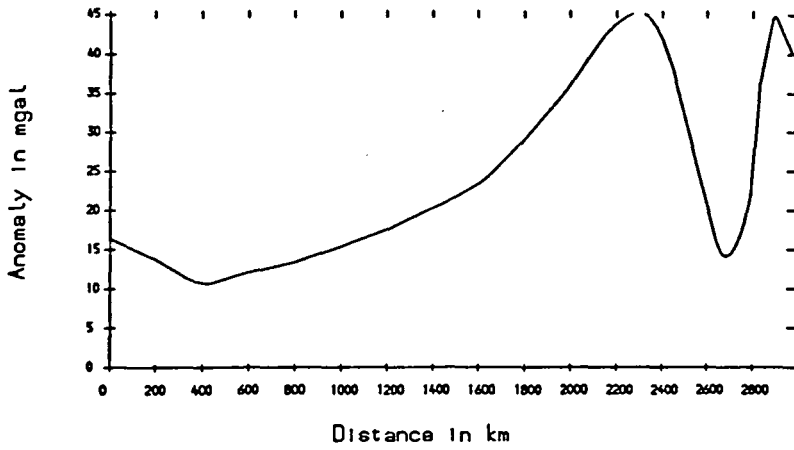
Gravity Profile

Figure 5.16   The gravity profile in mGal calculated on a plane 0.5 km above the surface of the overriding plate for the model of 1000 km penetration, lower mantle viscosity $\mu = 10^{22}$ Pa s including the olivine-spinel transition. The lower box shows the position of the density anomalies.

slight increase in the peak value, up to 40 mGal, but retains the same general shape. It is noted at this point that the profiles compare favourably with the compilations of average gravity profile landwards of the South American margins by Rabinowicz et al. (1984). The observed profiles have a high of about 50 mGal just landward of the trench with a gradual decrease to an absolute minimum about 3000 km from the trench.

5.4 Duration Of Subduction

5.4.1 Problem Statement

This finite element method cannot describe the continuous, dynamic evolution of subduction zones and so the following series of models are presented as 'snapshots' in time. The depth of slab penetration is used to define the duration of subduction without specifying any particular time scale. Five depths of penetration are used: 300, 400, 535, 670 and 1000 km. So, if the slab were assumed to be moving downdip with a velocity of 100 mm yr^{-1} then the 'snapshots' are at least 1 Ma apart. Apart from the alteration in slab length, all mesh parameters are identical to the model of the previous section and so the 1000 km penetration model is referred to the figures 5.13 - 5.16 of the previous section. The models have a relaxation period of 50 000 yrs which allows the upper mantle to flow but is only a small perturbation about the age of duration.

5.4.2 Discussion of Results

The stress regime, surface displacement, slab motion and gravity profile are shown in figures 5.17 - 5.20, 5.21 - 5.24, 5.25 - 5.28 and 5.29 - 5.32 for the 300, 400, 535 and 670 km penetration models respectively. The sequence shows that increasing duration of subduction extends compression into the backarc region, progressively eliminating the 40 MPa tensions of figure 5.17. The forearc is under horizontal compression in all models, regardless of duration of subduction. As slab length increases, viscous coupling through the mantle wedge penetrates further into the overriding plate. The surface displacement profiles in figures 5.18, 5.22, 5.26, 5.30 and 5.14 show the gradual increase in the width of concavity and the change in depth of the depression. As the olivine-spinel transition is reached the greatest change occurs. The depth of depression
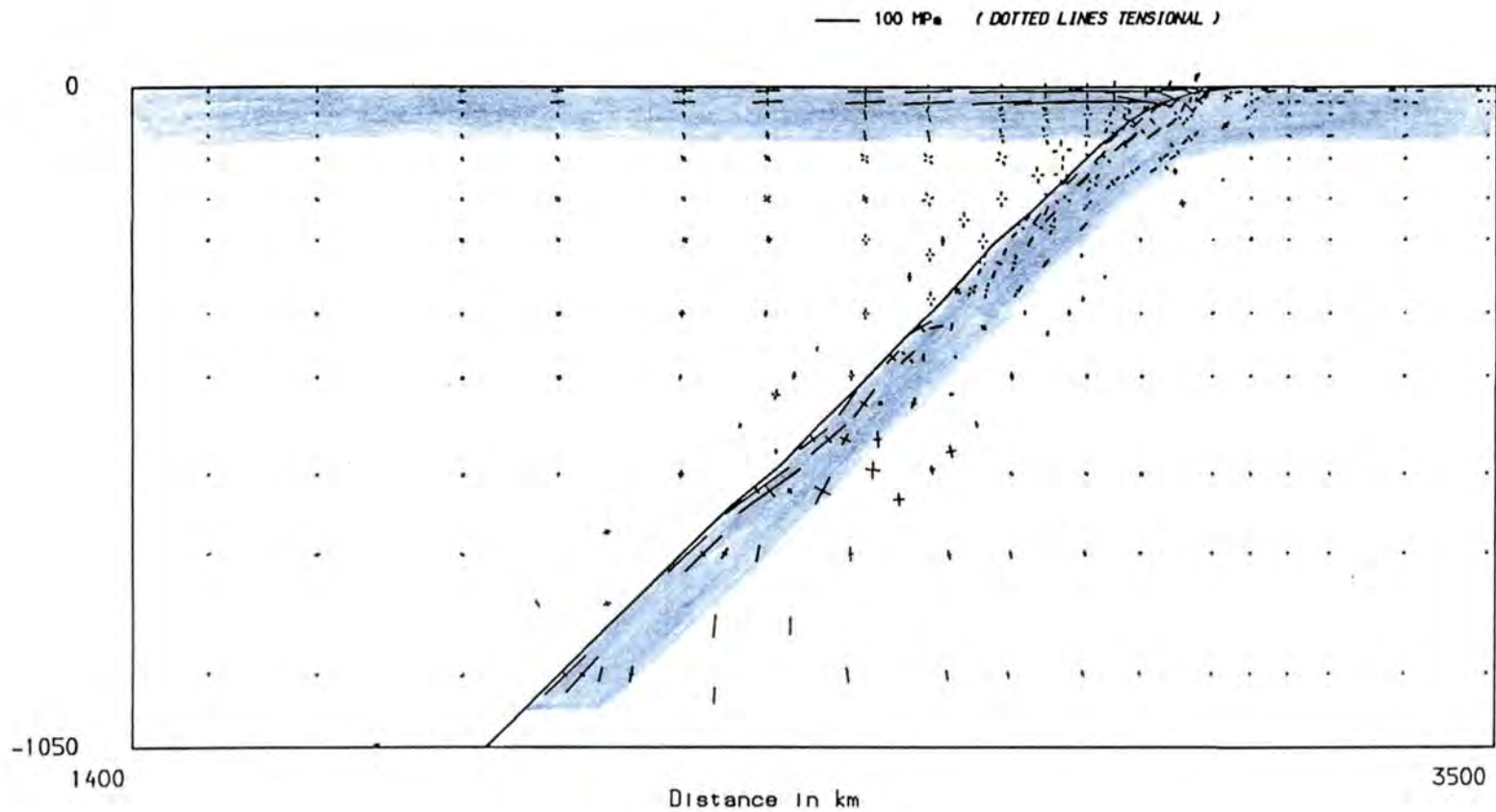
Figure 5.17 The principal stresses for the model of 300 km penetration and lower mantle viscosity $\mu = 10^{22}$ Pa s. The solid line denotes the position of the fault. The shading denotes the lithosphere. A scale length of vector magnitude is given above.
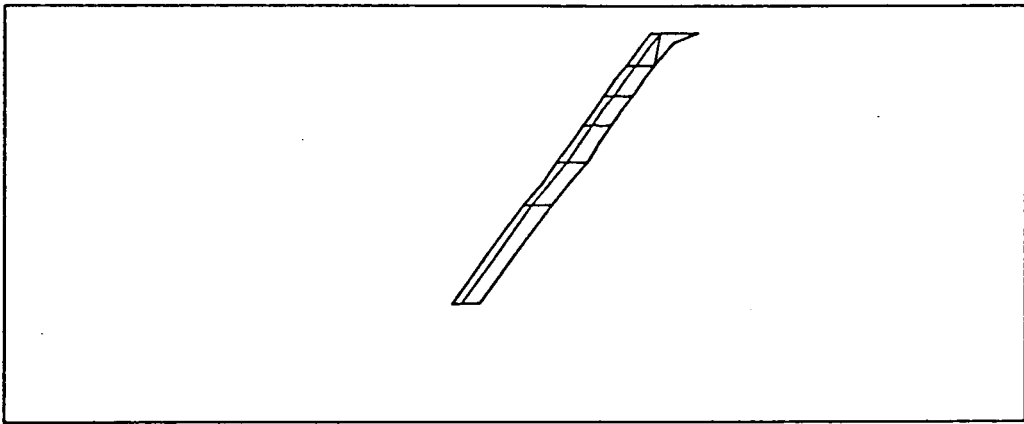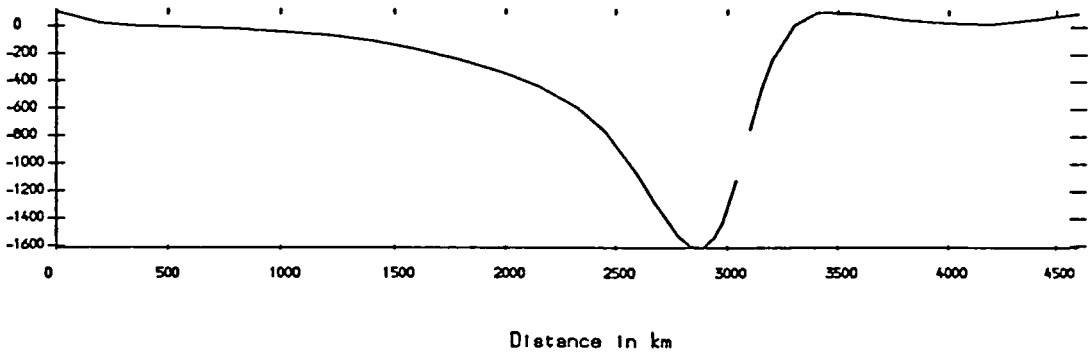
Surface displacement profile (in m)

Distance in km
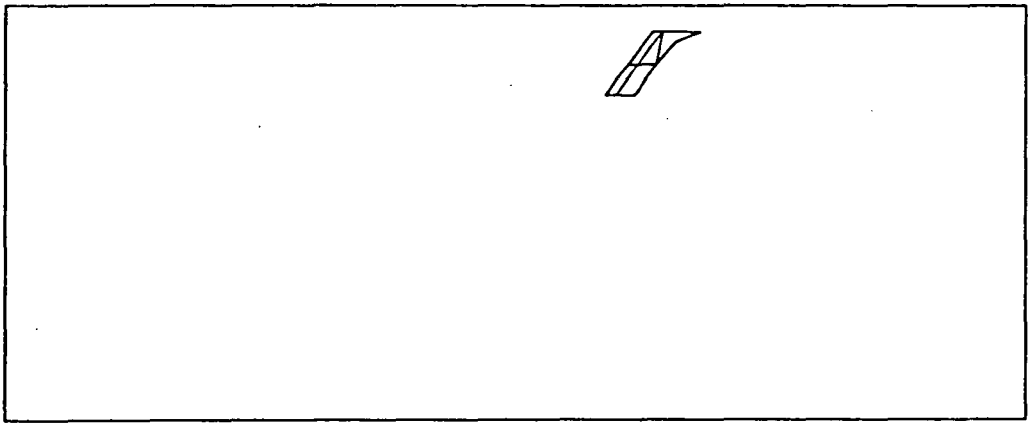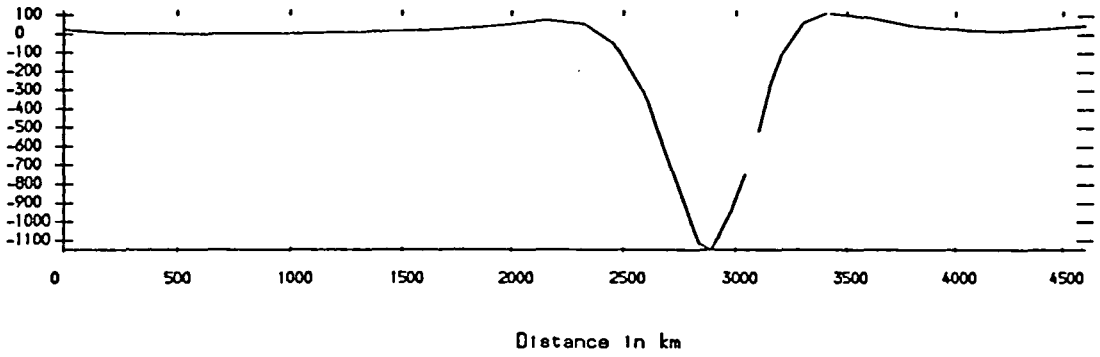
Figure 5.18   The vertical displacement of the surface for the model of 300 km penetration and lower mantle viscosity $\mu = 10^{22}$ Pa s. The left hand curve denotes the overriding plate, the right hand curve denotes the subducting plate. The lower box shows the relative position of the density anomalies.

Figure 5.19   The absolute slab motion linearly extrapolated by a factor of 20 for the model of 300 km penetration and lower mantle viscosity $\mu = 10^{22}$ Pa s. The upper curve denotes the original position of the top surface of the slab and the lower curve denotes the final position of the top surface of the slab. The cross-lines represent displacement vectors of the nodes.
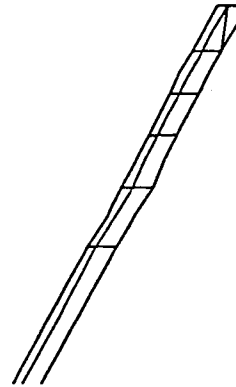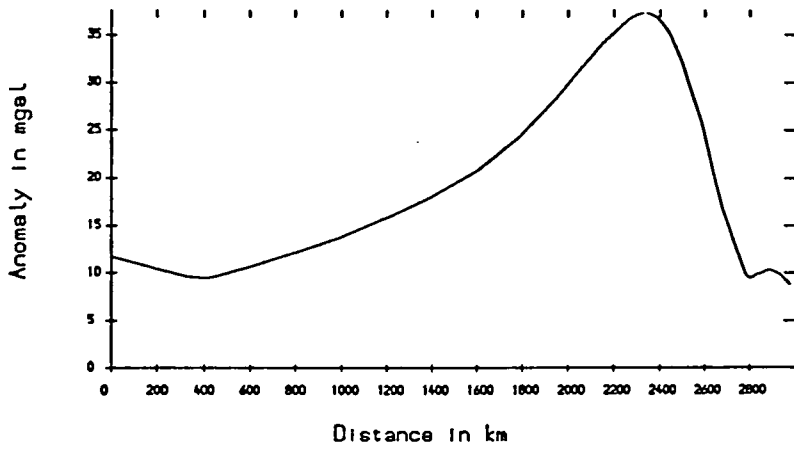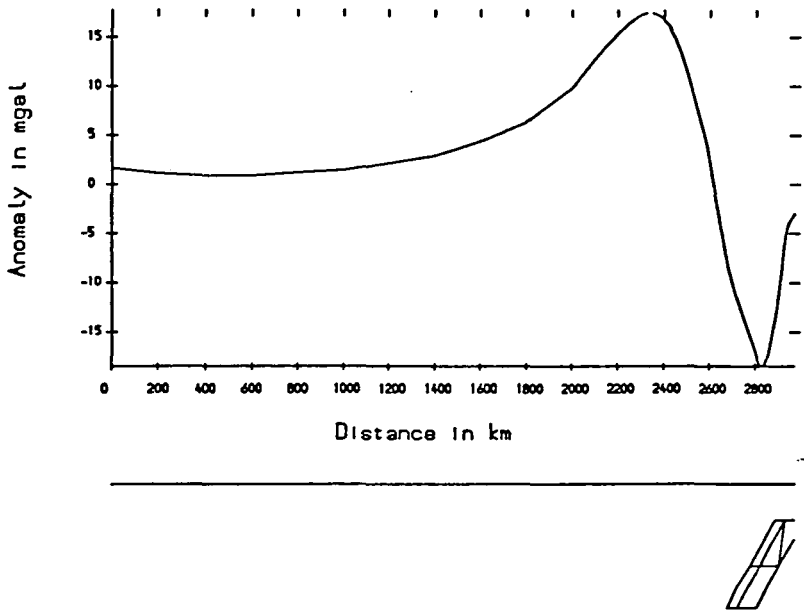
Gravity Profile

Figure 5.20   The gravity profile in mGal calculated on a plane 0.5 km above the surface of the overriding plate for the model of 300 km penetration and lower mantle viscosity $\mu = 10^{22}$ Pa s. The lower box shows the position of the density anomalies.

Figure 5.21 The principal stresses for the model of 400 km penetration, lower mantle viscosity $\mu = 10^{22}$ Pa s including the olivine-spinel transition. The solid line denotes the position of the fault. The shading denotes the lithosphere. A scale length of vector magnitude is given above.

Surface displacement profile (in m)

Distance in km
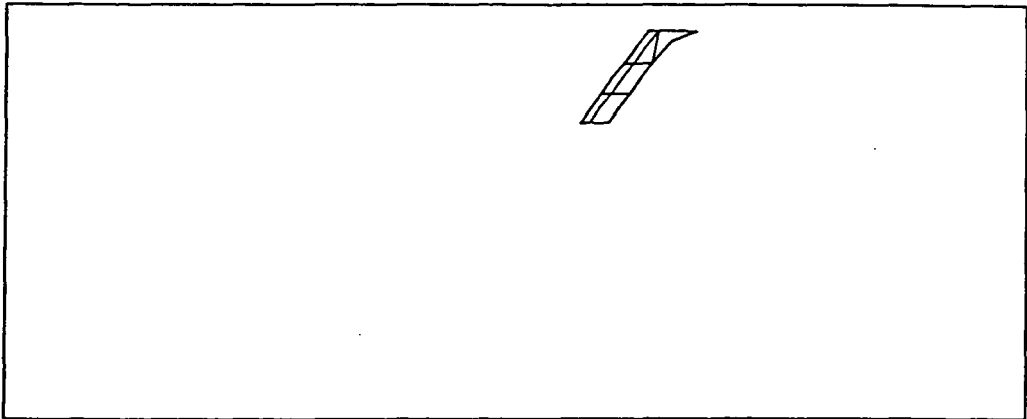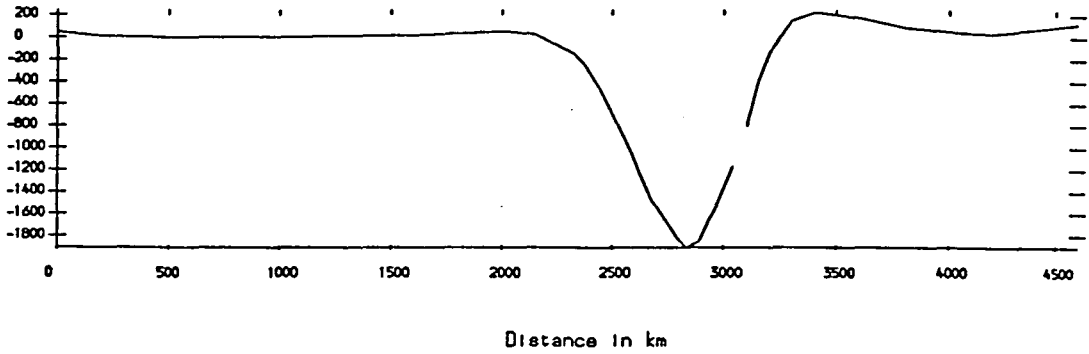
Figure 5.22   The vertical displacement of the surface for the model of 400 km penetration, lower mantle viscosity $\mu = 10^{22}$ Pa s including the olivine-spinel transition. The left hand curve denotes the overriding plate, the right hand curve denotes the subducting plate. The lower box shows the relative position of the density anomalies.
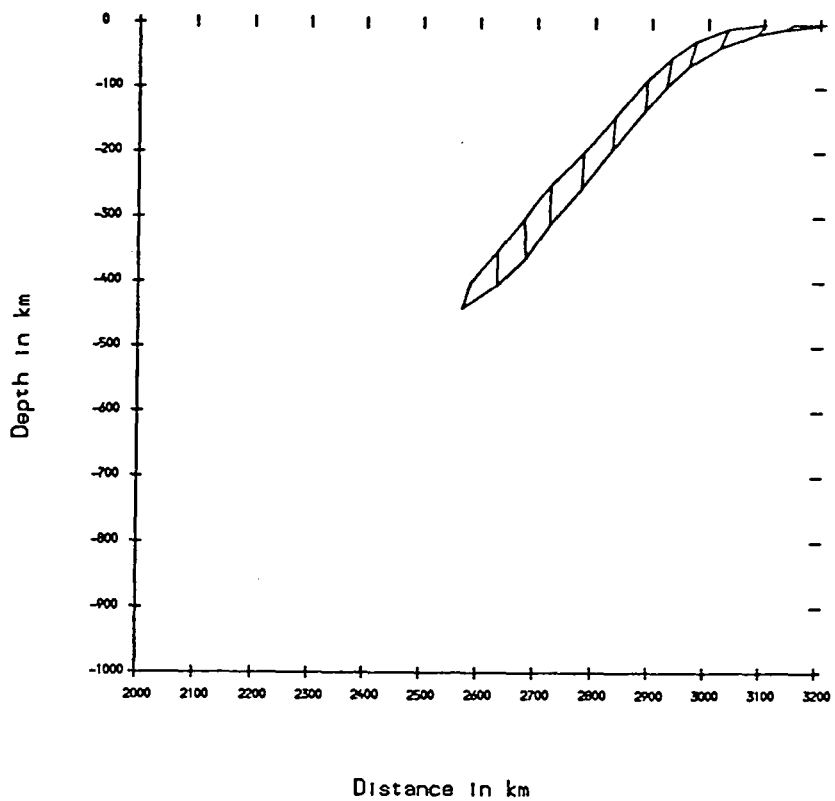
Figure 5.23 The absolute slab motion linearly extrapolated by a factor of 20
for the model of 400 km penetration, lower mantle viscosity $\mu = 10^{22}$ Pa s
including the olivine-spinel transition. The upper curve denotes the original
position of the top surface of the slab and the lower curve denotes the final
position of the top surface of the slab. The cross-lines represent displacement
vectors of the nodes.

Gravity Profile

Figure 5.24   The gravity profile in mGal calculated on a plane 0.5 km above the
surface of the overriding plate for the model of 400 km penetration, lower
mantle viscosity $\mu = 10^{22}$ Pa s including the olivine-spinel transition. The
lower box shows the position of the density anomalies.
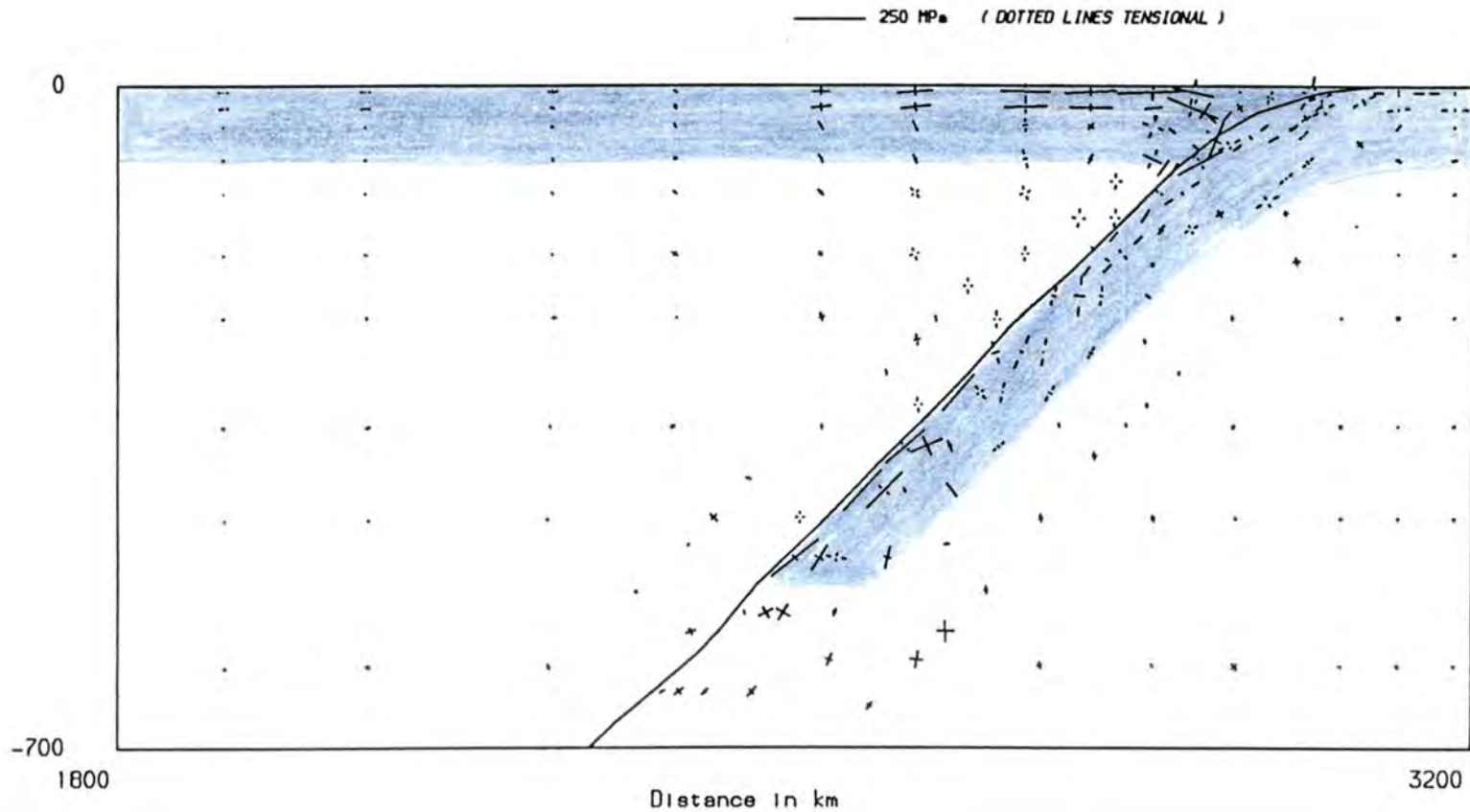
Figure 5.25 The principal stresses for the model of 535 km penetration, lower mantle viscosity $\mu = 10^{22}$ Pa s including the olivine-spinel transition. The solid line denotes the position of the fault. The shading denotes the lithosphere. A scale length of vector magnitude is given above.

Surface displacement profile (in m)
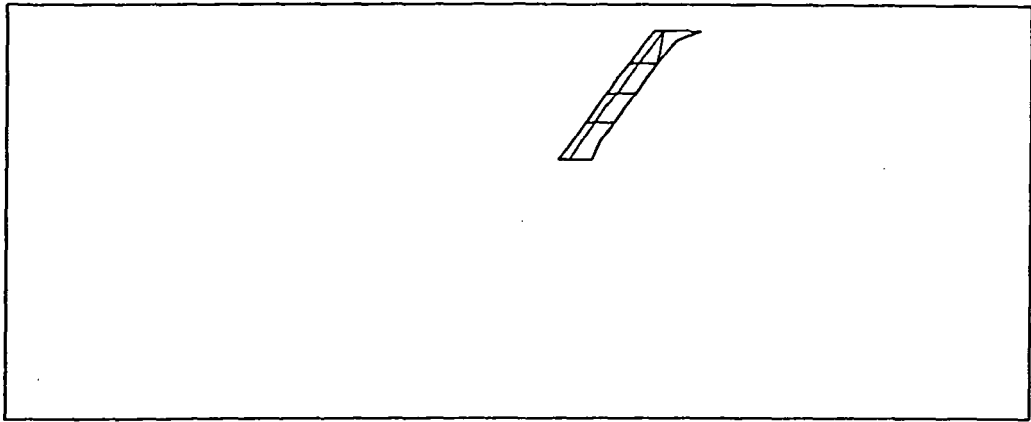
Figure 5.26   The vertical displacement of the surface for the model of 535 km
penetration, lower mantle viscosity $\mu = 10^{22}$ Pa s including the olivine-spinel
transition. The left hand curve denotes the overriding plate, the right hand
curve denotes the subducting plate. The lower box shows the relative position
of the density anomalies.

Figure 5.27   The absolute slab motion linearly extrapolated by a factor of 20
for the model of 535 km penetration, lower mantle viscosity $\mu = 10^{22}$ Pa s
including the olivine-spinel transition. The upper curve denotes the original
position of the top surface of the slab and the lower curve denotes the final
position of the top surface of the slab. The cross-lines represent displacement
vectors of the nodes.

Gravity Profile

Figure 5.28 The gravity profile in mGal calculated on a plane 0.5 km above the surface of the overriding plate for the model of 535 km penetration, lower mantle viscosity $\mu = 10^{22}$ Pa s including the olivine-spinel transition. The lower box shows the position of the density anomalies.
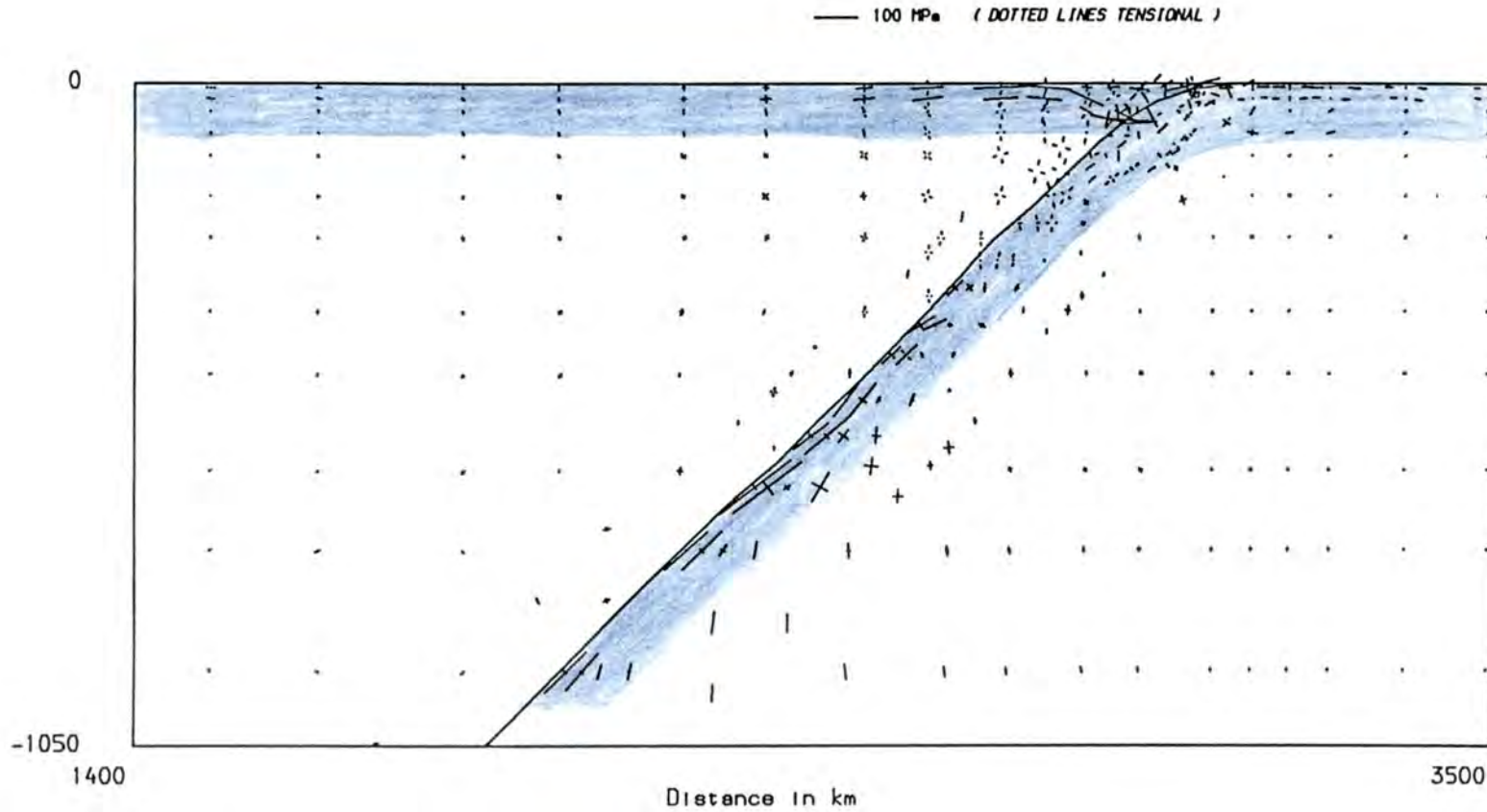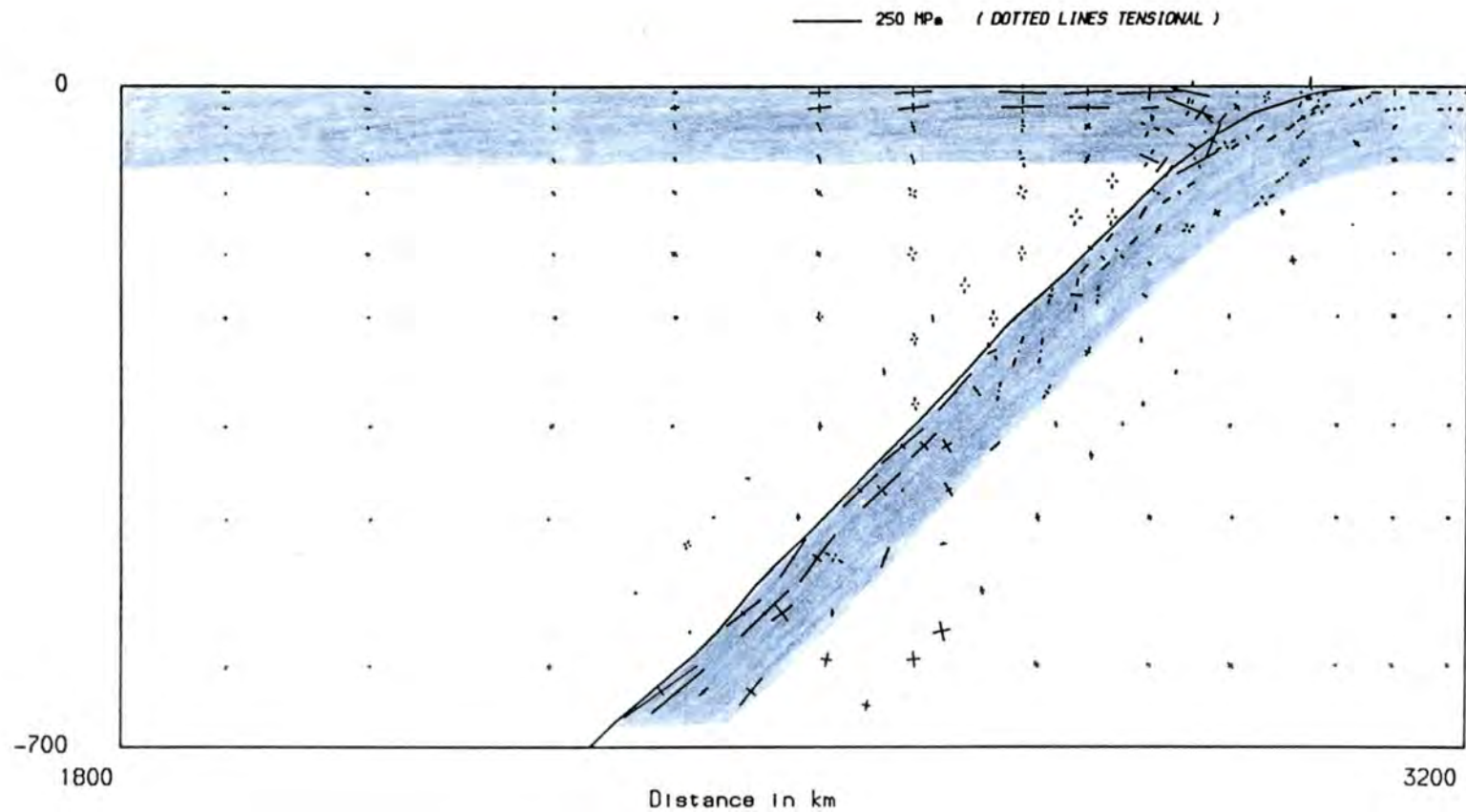
Figure 5.29 The principal stresses for the model of 670 km penetration, lower mantle viscosity $\mu = 10^{22}$ Pa s including the olivine-spinel transition. The solid line denotes the position of the fault. The shading denotes the lithosphere. A scale length of vector magnitude is given above.
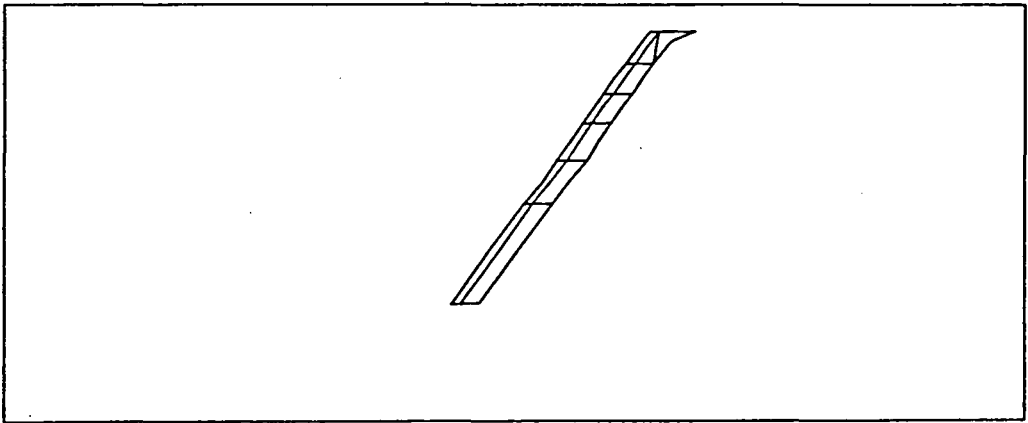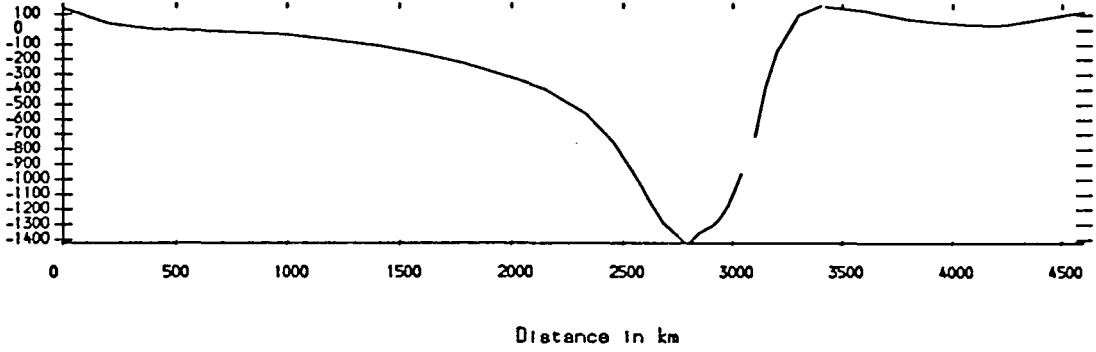
Surface displacement profile (In m)
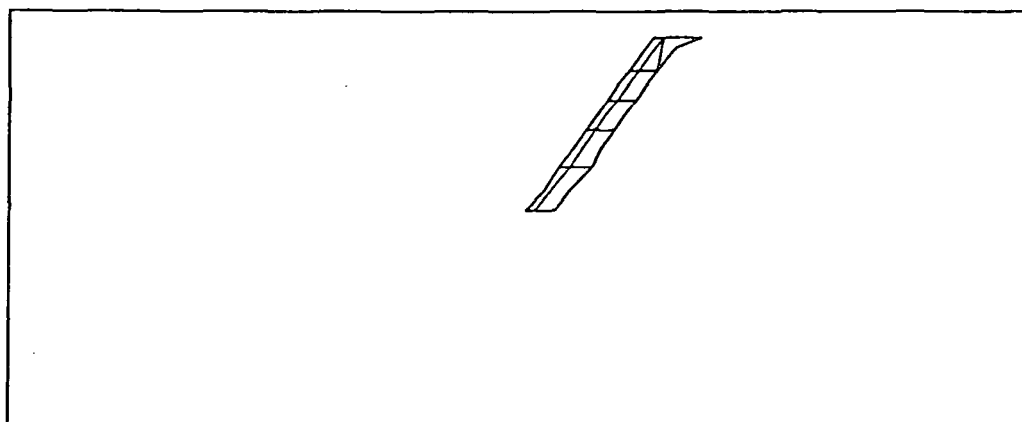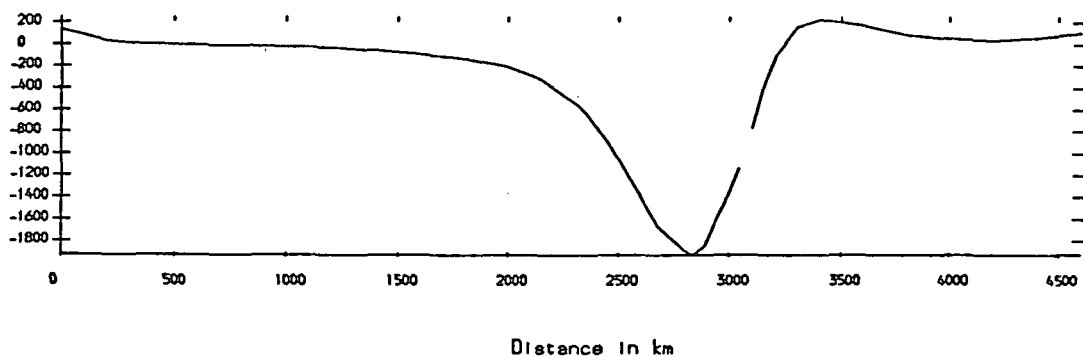
Figure 5.30   The vertical displacement of the surface for the model of 670 km penetration, lower mantle viscosity $\mu = 10^{22}$ Pa s including the olivine-spinel transition. The left hand curve denotes the overriding plate, the right hand curve denotes the subducting plate. The lower box shows the relative position of the density anomalies.
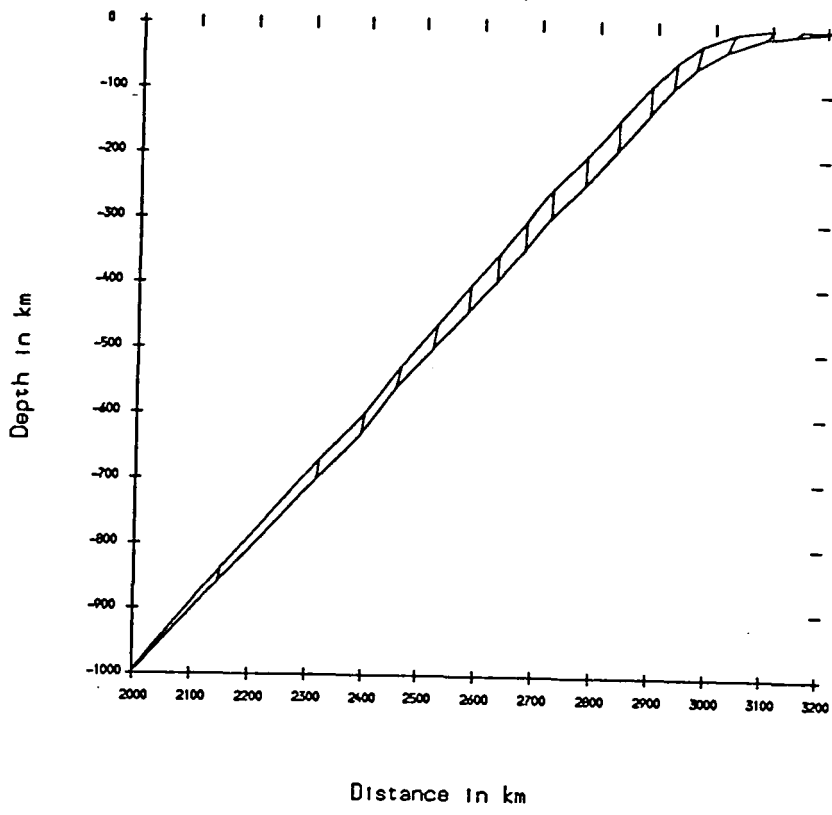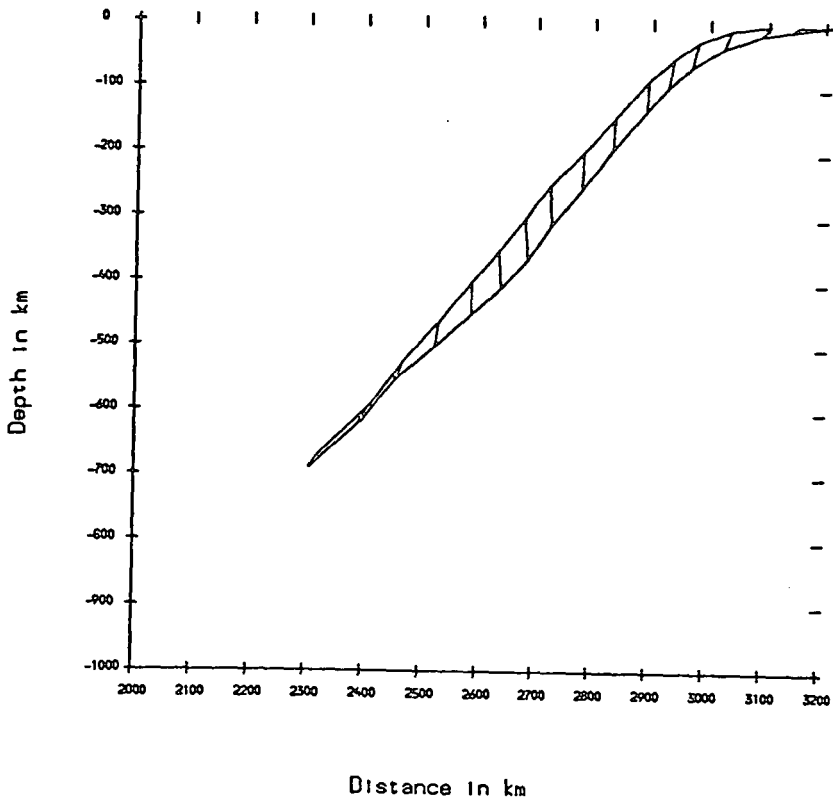
Figure 5.31 The absolute slab motion linearly extrapolated by a factor of 20 for the model of 670 km penetration, lower mantle viscosity $\mu = 10^{22}$ Pa s including the olivine-spinel transition. The upper curve denotes the original position of the top surface of the slab and the lower curve denotes the final position of the top surface of the slab. The cross-lines represent displacement vectors of the nodes.
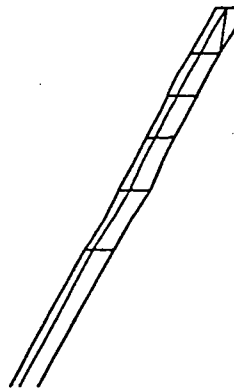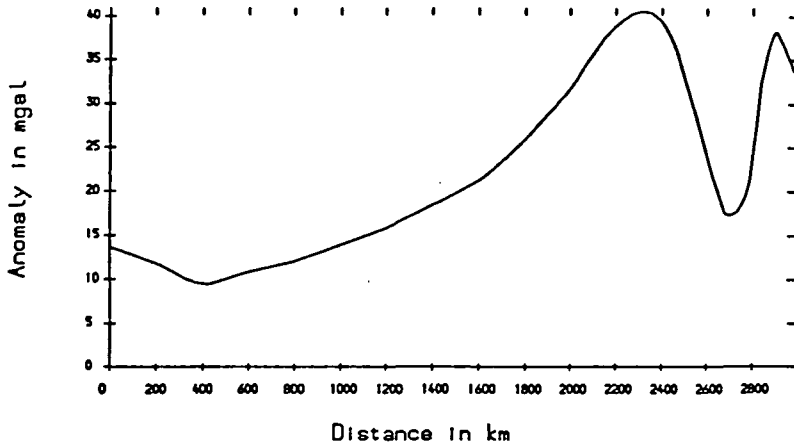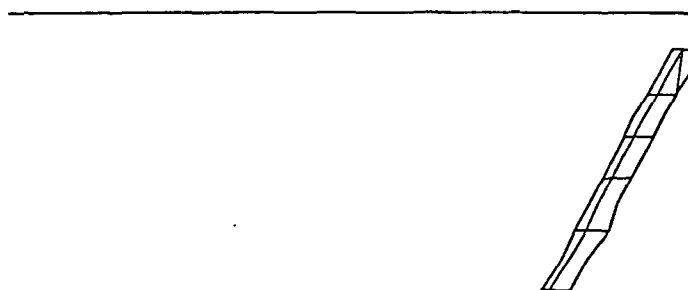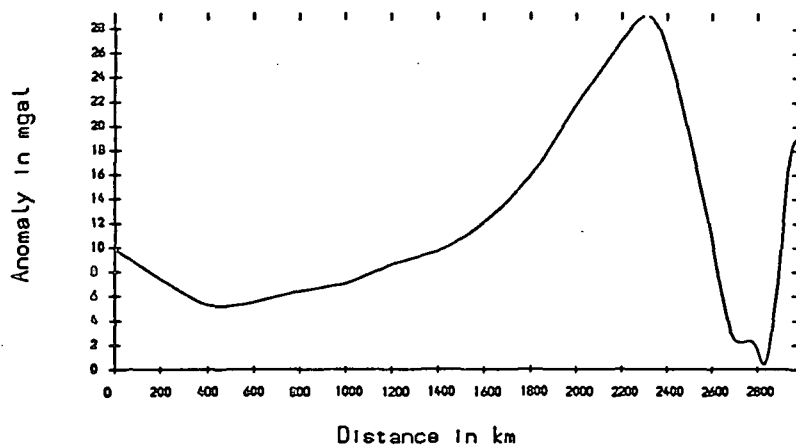
Gravity Profile

Figure 5.32 The gravity profile in mGal calculated on a plane 0.5 km above the surface of the overriding plate for the model of 670 km penetration, lower mantle viscosity $\mu = 10^{22}$ Pa s including the olivine-spinel transition. The lower box shows the position of the density anomalies.

increases from 1150 m at 300 km penetration, to 1900 m at 400 km penetration. Then there is a slight increase for the bigger slab at 535 km to 2000 m, but as the higher viscosity lower mantle is sensed at 670 km the depth of depression reduces slightly to 1900 m. Without the trench, the models tend to overestimate the magnitude of the horizontal compression and its lateral extent in the overriding plate.

The magnitude and spatial extent of the depression of the overriding plate is obviously dependent on the angle of slab dip as well as the length of the slab. Louden (1980) reported that the Phillipine Sea is approximately 1 km deeper than predictions from thermal subsidence models of ridge spreading (as discussed in section 1.5.2), and this depth anomaly occurs in many other marginal basins of the Western Pacific. The dips of the deeply penetrating Marianas and Izu-Bonin slabs underlying the eastern edge Phillipine Sea have been estimated at 81° and 65° respectively, (Jarrard 1986). Obviously it is not possible to compare directly with the model predictions, but these results support the suggestion of Davies (1983) that the slab-induced depression of the backarc is an important influence, and preferrable to the theory of Watanabe et al. (1977) that the mantle under the basin carries a density anomaly of $+10$ kg m^{-3} down to 300 km depth.

The horizontal tension in the subducting plate does not vary greatly with increasing duration of subduction. The general behaviour is a slight increase in horizontal tension as the slab length increases. This pattern is reflected in the increase in forearc compression and depth of depression which is significant only when the olivine-spinel transition is reached. This is also true for the slab motion in figures 5.19, 5.23, 5.27 and 5.31. The gravity profiles in figures 5.20, 5.24, 5.28 and 5.31 show a gradual increase in maximum $17 \rightarrow 40$ mGal as slab length increases reflecting the diminishing influence of the surface deformation relative to the slab.

The models with slab penetration to depths of 670 km and 1000 km have very similar stress distributions (figures 5.29 and 5.13). The single difference occurs at 75 km depth where the 670 km penetration model shows downdip compression in the upper surface of the slab and an opposing tension in the lower surface. This is probably an expression of unbending near the base of the slab bend region and it occurs in all other shallower penetrating models. However, since this is part of the slab bend region these stresses are not considered reliable.

The three shallowest penetrating models also display a systematic slab stress distribution (figures 5.17, 5.21 and 5.25). The lowest section of the slab is always in downdip compression regardless of depth of penetration. This is caused in part by a resistance to penetration but mostly by upbending of the slab tip as it sinks (a phenomenon which Harper (1984) observed in 3-D constant viscosity flow models of subducting lithosphere). Evidence for the upbending is provided by the balancing tensions in the lower surface of the slab and the shape of the slab profile in figures 5.19, 5.23 and 5.27. However, for the shallowest model the upbending causes compression throughout the upper surface of the slab. The majority of shallow Wadati-Benioff zones are tensional (Isacks and Molnar 1971, Apperson and Frohlich 1987) and this cannot be explained by these models.

The mesh is not fine enough to give very good resolution of the stresses, so it is desirable to repeat the models using identical parameters applied to mesh (ii). The fixed base condition inherently assumes that shallow penetrating slabs do not sense the lower mantle. The stress regime in figure 5.33 represents slab penetration to 400 km depth in a constant viscosity ($\mu = 10^{21}$ Pa s) mantle and this is very similar to figure 5.21 which used a lower mantle viscosity of $\mu = 10^{22}$ Pa s in an otherwise identical model. So it is appropriate to use the upper mantle mesh for models of shallow subduction. A more detailed analysis of the effect of mantle viscosity is taken up in the next section.

The stress regime, surface displacement, slab motion and gravity profile are shown in figures 5.34 - 5.37, 5.38 - 5.41 and 5.42 - 5.45 for slab penetration to 200, 300 and 400 km respectively. These are in very good agreement with the results obtained from the previous mesh (figures 5.17 - 5.24), and it is apparent that the stress regime in the slab is not a product of the possible 'stiffness' of a coarse mesh. The downdip compression is not typical of the observations of slab stresses and requires some investigation. It was suggested earlier (see section 1.5.1) that the leading edge of the slab contributed to the force balance in the mantle, and in all the preceding models the slab tip was streamlined in the downdip direction. A variety of shapes of slab tip were experimented with using the model of slab penetration to 200 km, with the conclusion that only addition of mass below 200 km reduces the compression in the top surface of the slab. This is because the centre of mass of the slab is lowered and thus the upbending of the slab tip is inhibited. So, in these models, downdip tension can be generated only by aseismic
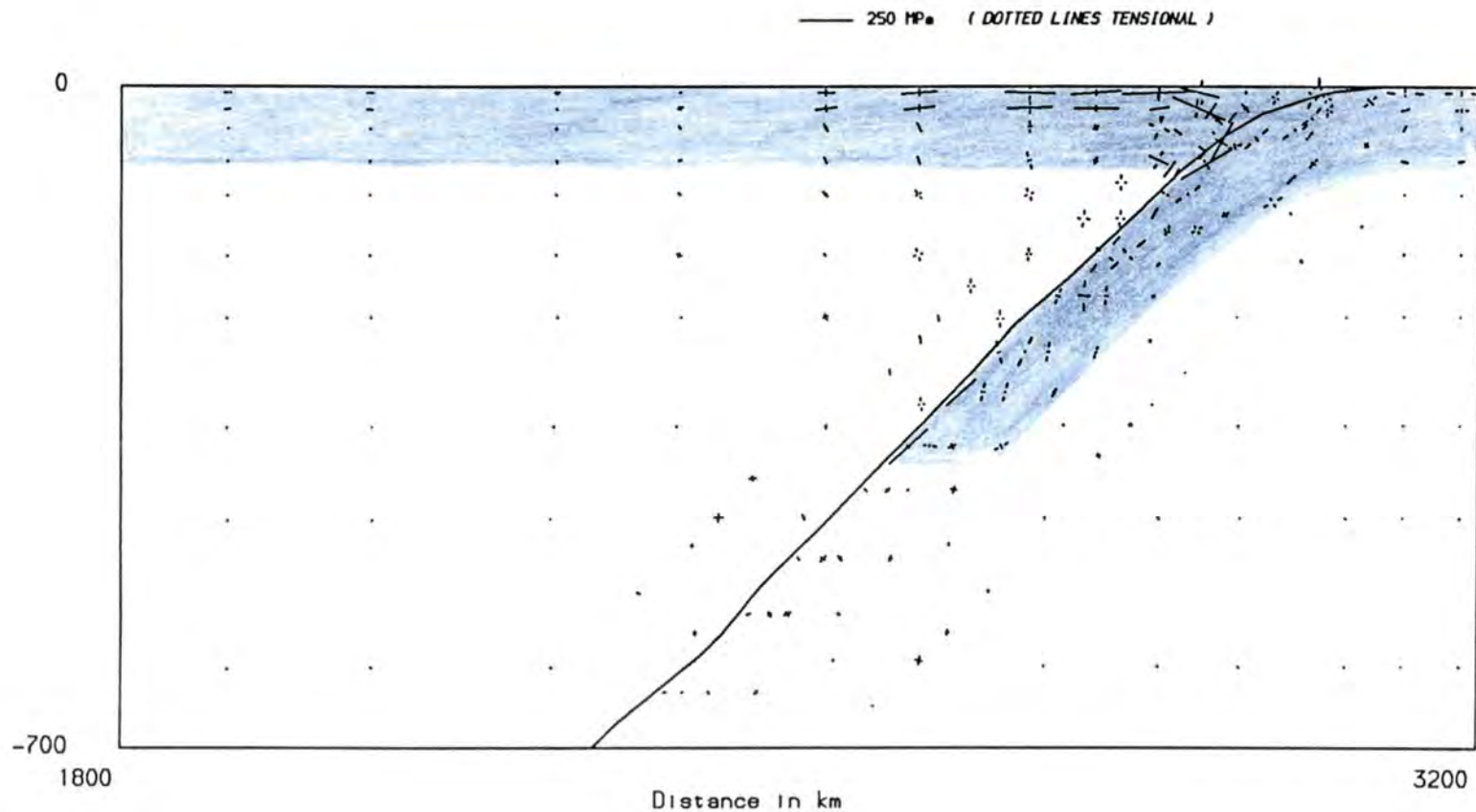
Figure 5.33   The principal stresses for the model of 400 km penetration, lower mantle viscosity $\mu = 10^{21}$ Pa s including the olivine-spinel transition. The solid line denotes the position of the fault. The shading denotes the lithosphere. A scale length of vector magnitude is given above.

Figure 5.34   The principal stresses for the model of 200 km penetration in mesh (ɪɪ). The solid line denotes the position of the fault. The shading denotes the lithosphere. A scale length of vector magnitude is given above.

Surface displacement profile (in m)

Distance in km
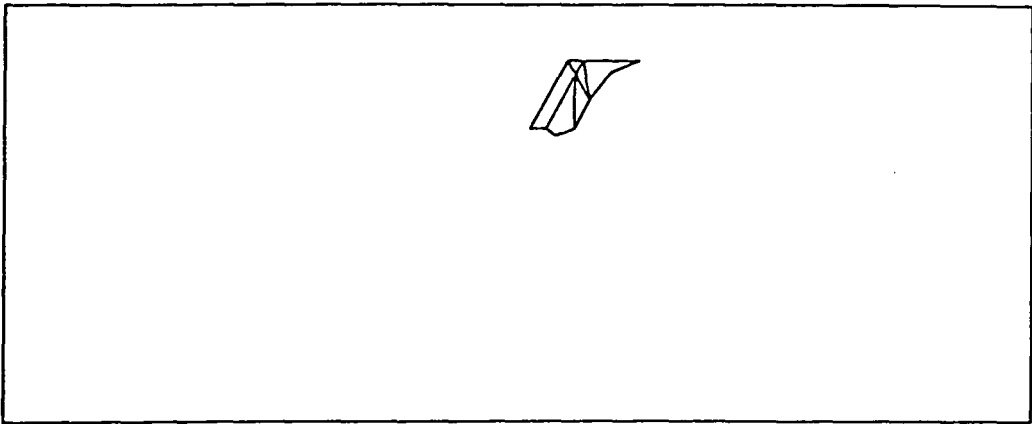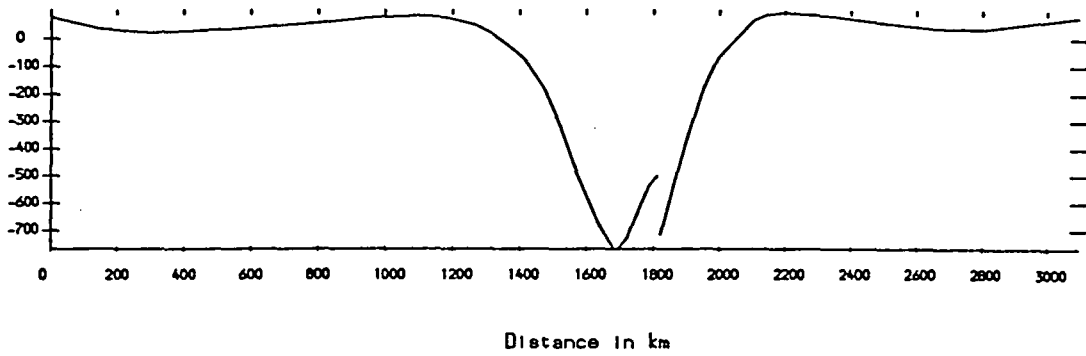
Figure 5.35   The vertical displacement of the surface for the model of 200 km
penetration in mesh(ıı). The left hand curve denotes the overriding plate,
the right hand curve denotes the subducting plate. The lower box shows the
relative position of the density anomalies.

Figure 5.36   The absolute slab motion linearly extrapolated by a factor of 20 for the model of 200 km penetration in mesh (II). The upper curve denotes the original position of the top surface of the slab and the lower curve denotes the final position of the top surface of the slab. The cross-lines represent displacement vectors of the nodes.

Gravity Profile

Figure 5.37   The gravity profile in mGal calculated on a plane 0.5 km above the surface of the overriding plate for the model of 200 km penetration in mesh (11). The lower box shows the position of the density anomalies.
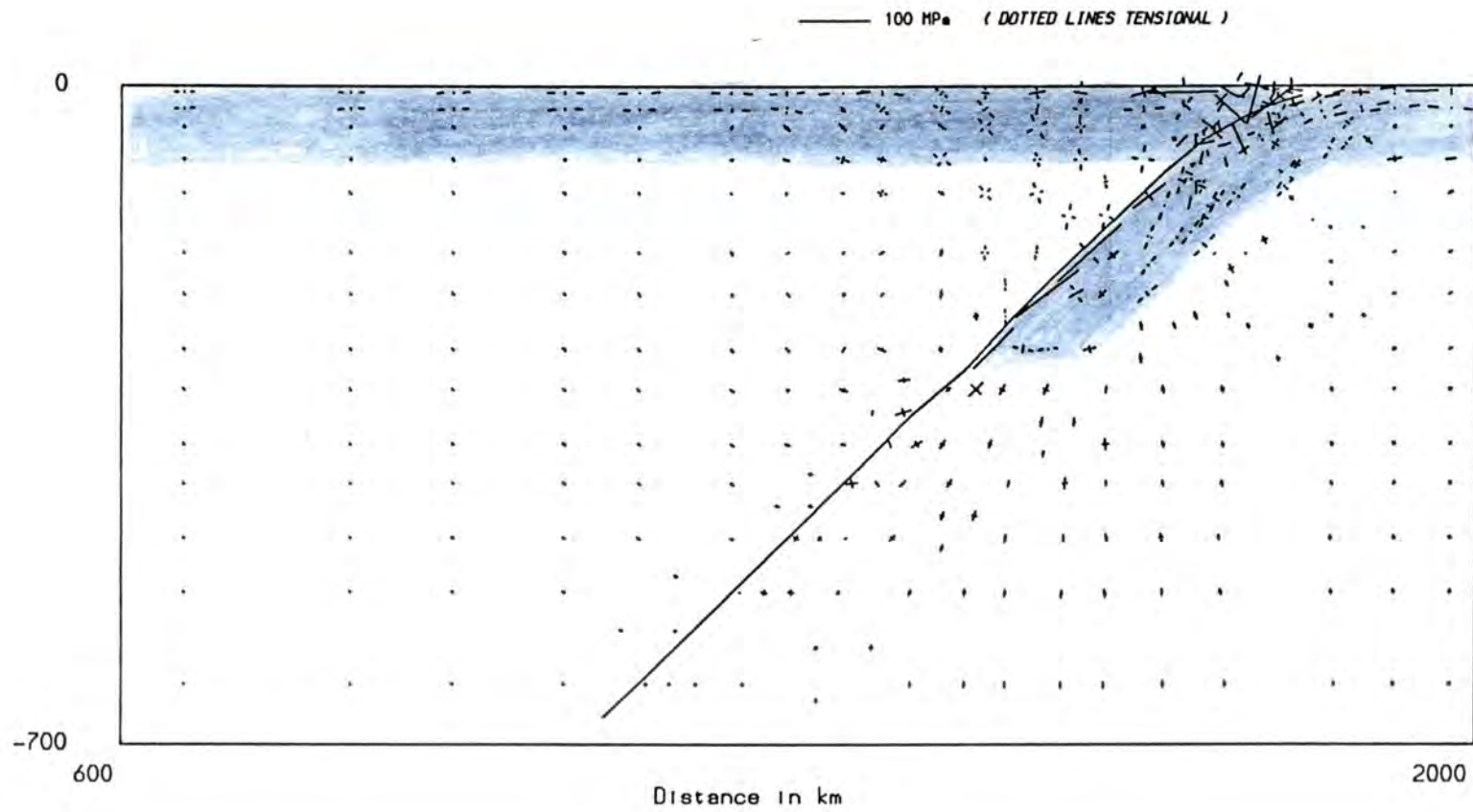
Figure 5.38   The principal stresses for the model of 300 km penetration in mesh (ii). The solid line denotes the position of the fault. The shading denotes the lithosphere. A scale length of vector magnitude is given above.

Surface displacement profile (in m)

Distance in km
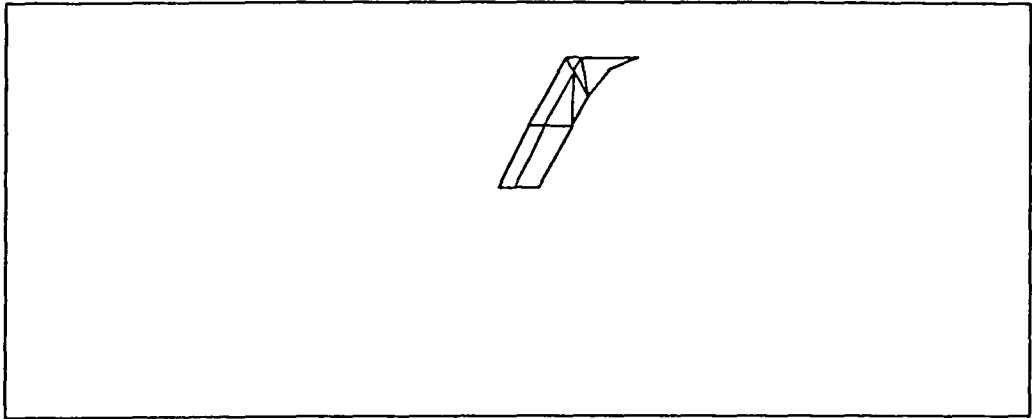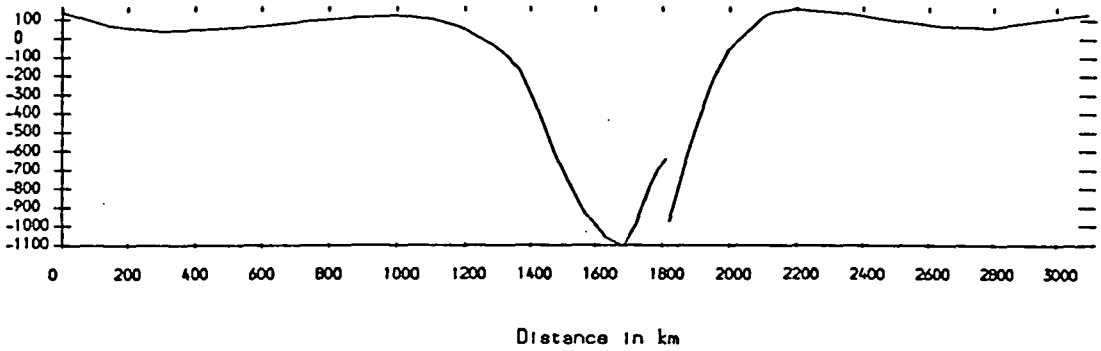
Figure 5.39 The vertical displacement of the surface for the model of 300 km penetration in mesh(n). The left hand curve denotes the overriding plate, the right hand curve denotes the subducting plate. The lower box shows the relative position of the density anomalies.

Figure 5.40   The absolute slab motion linearly extrapolated by a factor of 20 for
the model of 300 km penetration in mesh (11). The upper curve denotes the
original position of the top surface of the slab and the lower curve denotes
the final position of the top surface of the slab. The cross-lines represent
displacement vectors of the nodes.

Gravity Profile

Figure 5.41   The gravity profile in mGal calculated on a plane 0.5 km above the surface of the overriding plate for the model of 300 km penetration in mesh (11). The lower box shows the position of the density anomalies.
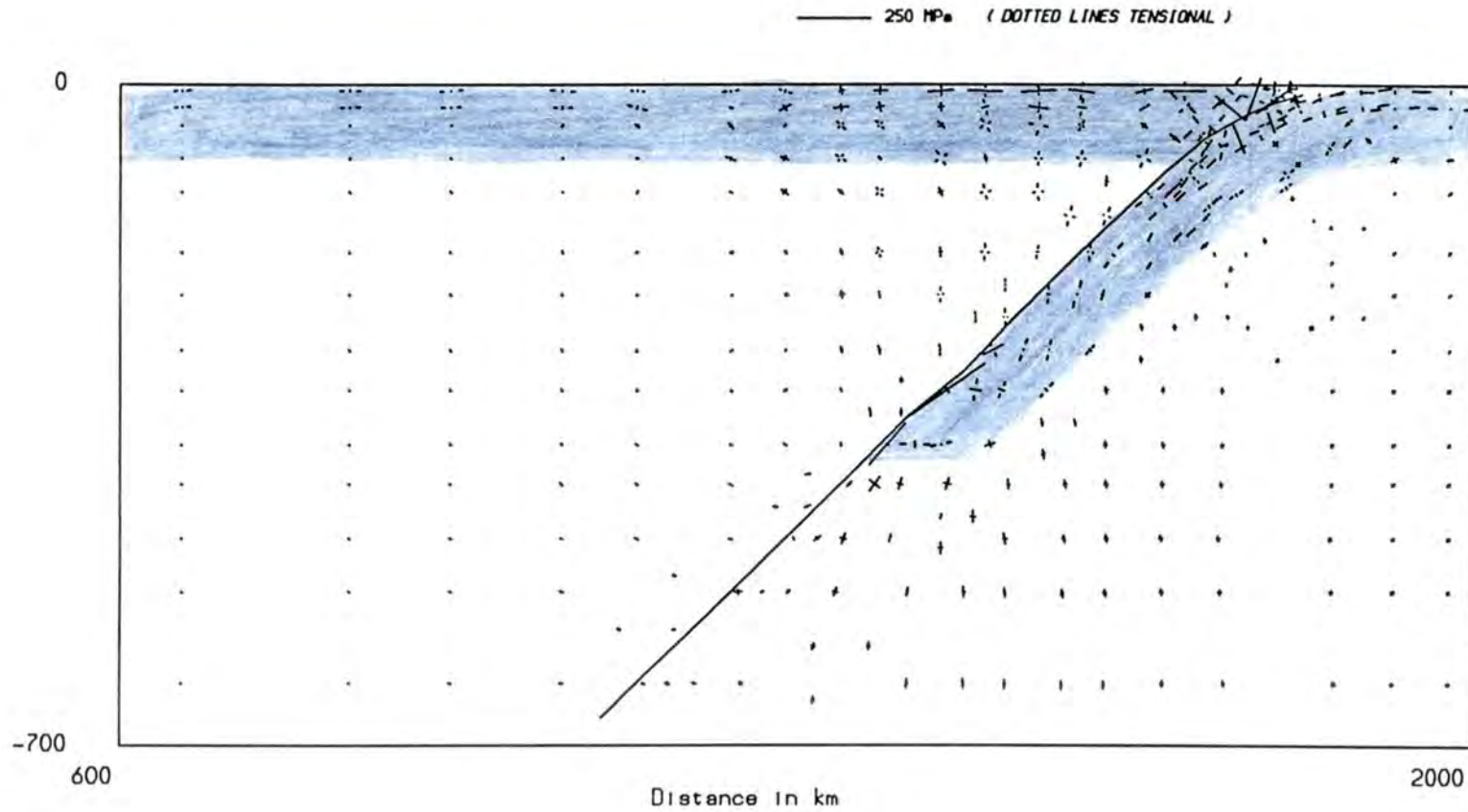
Figure 5.42   The principal stresses for the model of 400 km penetration including the olivine-spinel transition in mesh (II). The solid line denotes the position of the fault. The shading denotes the lithosphere. A scale length of vector magnitude is given above.

Surface displacement profile (in m)

Distance in km
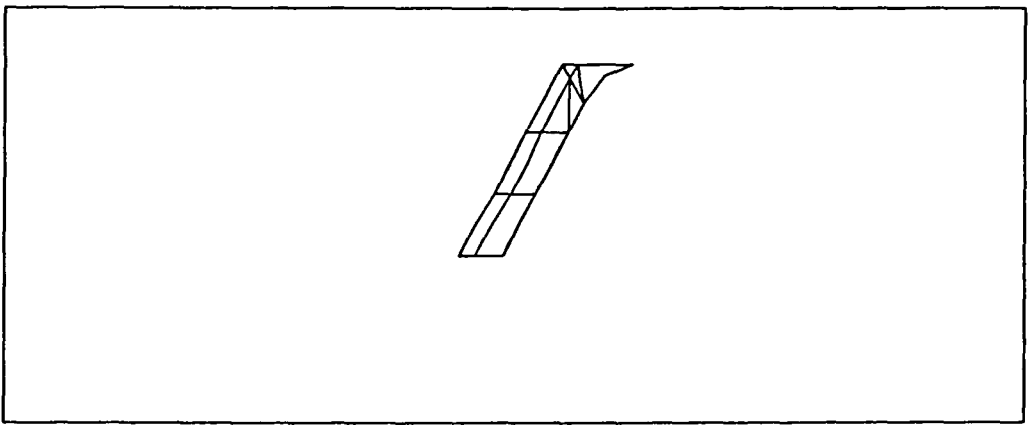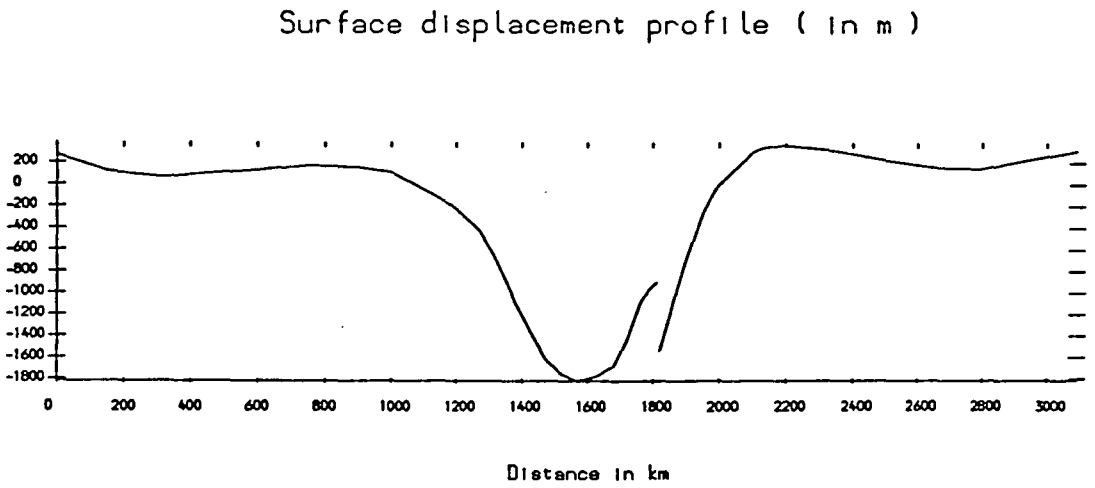
Figure 5.43   The vertical displacement of the surface for the model of 400 km
penetration including the olivine-spinel transition in mesh (11). The left hand
curve denotes the overriding plate, the right hand curve denotes the subducting
plate. The lower box shows the relative position of the density anomalies.
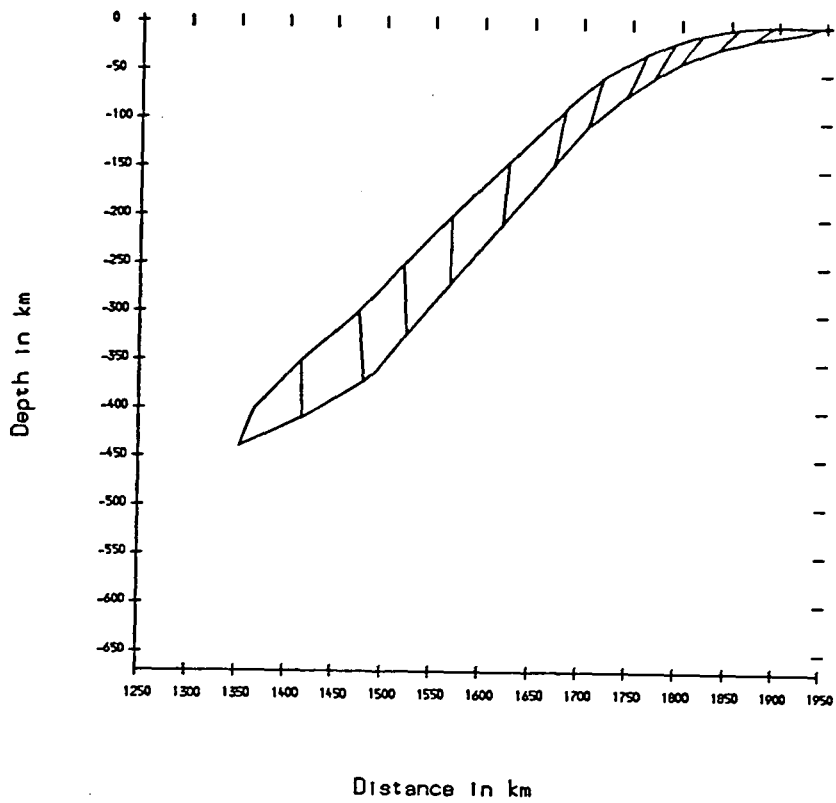
Figure 5.44   The absolute slab motion linearly extrapolated by a factor of 20
for the model of 400 km penetration including the olivine-spinel transition in
mesh (11). The upper curve denotes the original position of the top surface of
the slab and the lower curve denotes the final position of the top surface of
the slab. The cross-lines represent displacement vectors of the nodes.
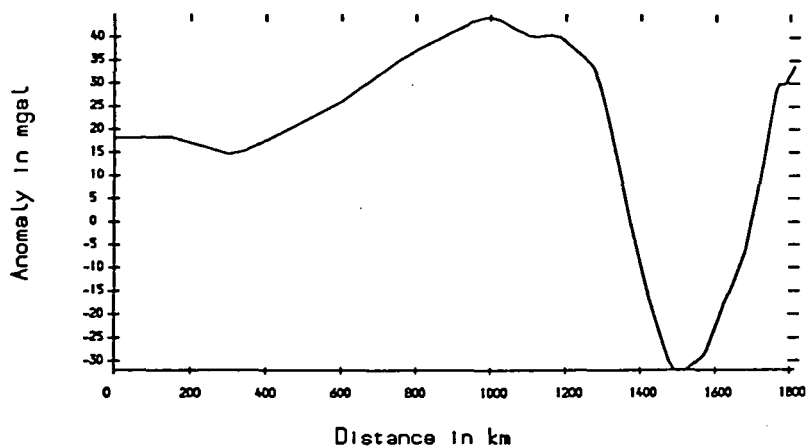
Gravity Profile

Figure 5.45   The gravity profile in mGal calculated on a plane 0.5 km above the surface of the overriding plate for the model of 400 km penetration including the olivine-spinel transition in mesh (ıı). The lower box shows the position of the density anomalies.

extension of the slab in the upper mantle. The surface displacement profiles in figures 5.35, 5.39 and 5.43 display trench depths of 700, 1000 and 1600 m for the 200, 300 and 400 km penetration models. Davies (1983) estimated the average trench depth to be 3 km, so perhaps these models underestimate the reactive upthrust at the top of the slab and overestimate the surface reaction within the overriding plate. Greater trench reaction may act to redistribute the slab stresses and thus reduce the compression in the upper slab of these models.

The large compressions in the top surface of the subducting slab accompanied by smaller tensions 20 km further into the slab are reminiscent of the stress regime required to generate double seismic zones. However, these stresses occur over a very large depth range (90 → 300 km) and are associated with the slab tip and so could only contribute to the double seismic zone in the shallowest penetrating slabs. The origin of double seismic zones in deeply subducting slabs will be discussed in a later section.

The short wavelength upflexing of the leading edge is a flexural reaction to the downpull, accentuated by the trench geometry and shear slip. This is similar to the results of Tharp (1985) except the effect occurs over much longer wavelengths (800 km width) and has a much smaller amplitude. The models of Tharp (1985) produced 5 km deep depressions and attendant 5 km structural highs over a width of 250 km. This was generated by coupling of slab pull across 70 km thick lithosphere, the mantle not being included. The consistency of this style of deformation suggests that this effect may contribute to the forearc tectonics and is discussed further in the next chapter.

5.5   An Assessment of Mantle Viscosity

5.5.1   Problem Statement - Lower Mantle

The models of the previous sections (except figure 5.33) used the same viscosity structure for the mantle, a uniform asthenosphere and upper mantle with $\mu = 10^{21}$ Pa s and a uniform lower mantle with $\mu = 10^{22}$ Pa s. The average radial viscosity profile of the mantle is not very well constrained but there is a general consensus that $\mu = 10^{21}$ Pa s is a realistic value for the upper mantle. The only direct observational constraint pertinent to this study is the earthquake distribution in the Wadati-Benioff zone and

89

its relationship to the slab stresses as discussed earlier (see section 1.5.2).

There have been many estimates of the viscosity of the lower mantle, most of which lie in the range $10^{21} - 10^{23}$ Pa s. The following set of models involves slab penetration to 1000 km and 670 km and employs a uniform viscosity $\mu = 10^{21}$ Pa s in the asthenosphere and upper mantle above 670 km depth with lower mantle viscosities of either $\mu = 10^{21}$, 10^{22}, or 10^{23} Pa s. All other parameters of mesh (1) are identical to the models of the previous section, and so the 10^{22} Pa s model is referred to the figures 5.13 - 5.16 for 1000 km penetration and figures 5.29 - 5.32 for 670 km penetration. The relaxation period is once again 50 000 yrs.

5.5.2 Discussion of Results

The stress regime and gravity profile for 1000 km penetration are displayed in figures 5.46 and 5.47 for the 10^{21} Pa s lower mantle model, and in figures 5.48 and 5.49 for the 10^{23} Pa s model. The constant viscosity mantle (figure 5.46) does not generate the compressive stresses in the depth range 400 $\rightarrow$ 670 km in the slab which is required for consistency with the observed earthquake distribution. Also the gravity profile (figure 5.47) gives a low of -80 mGal just landward of the trench. On these grounds it is discounted. Obviously this model may not include every aspect of the force balance and so it is unwise to exclude completely the possibility of an isoviscous mantle.

The slab stresses in the other two models (figures 5.13 and 5.48) are similar. The 10^{22} Pa s lower mantle gives a stress minimum at about 270 km depth, and the 10^{23} Pa s lower mantle gives the minimum at about 200 km depth. On this basis one would prefer a lower mantle viscosity of approximately 10^{22} Pa s but it is clear that the slab stresses are not very sensitive to the higher viscosity contrasts. This agrees with the conclusions of a similar study by Vassiliou et al. (1984). There is a small change in the stress distribution of the surface plates for the latter two models. The higher viscosity mantle generates more tension in the overriding plate and reduces the tension in the subducting plate. This is because the lower mantle severely inhibits slab motion, reducing the normal viscous coupling to the overriding plate and transmitting compression all the way back along the subducting plate.

As the stress regime is unable to distinguish between the higher viscosities, it is
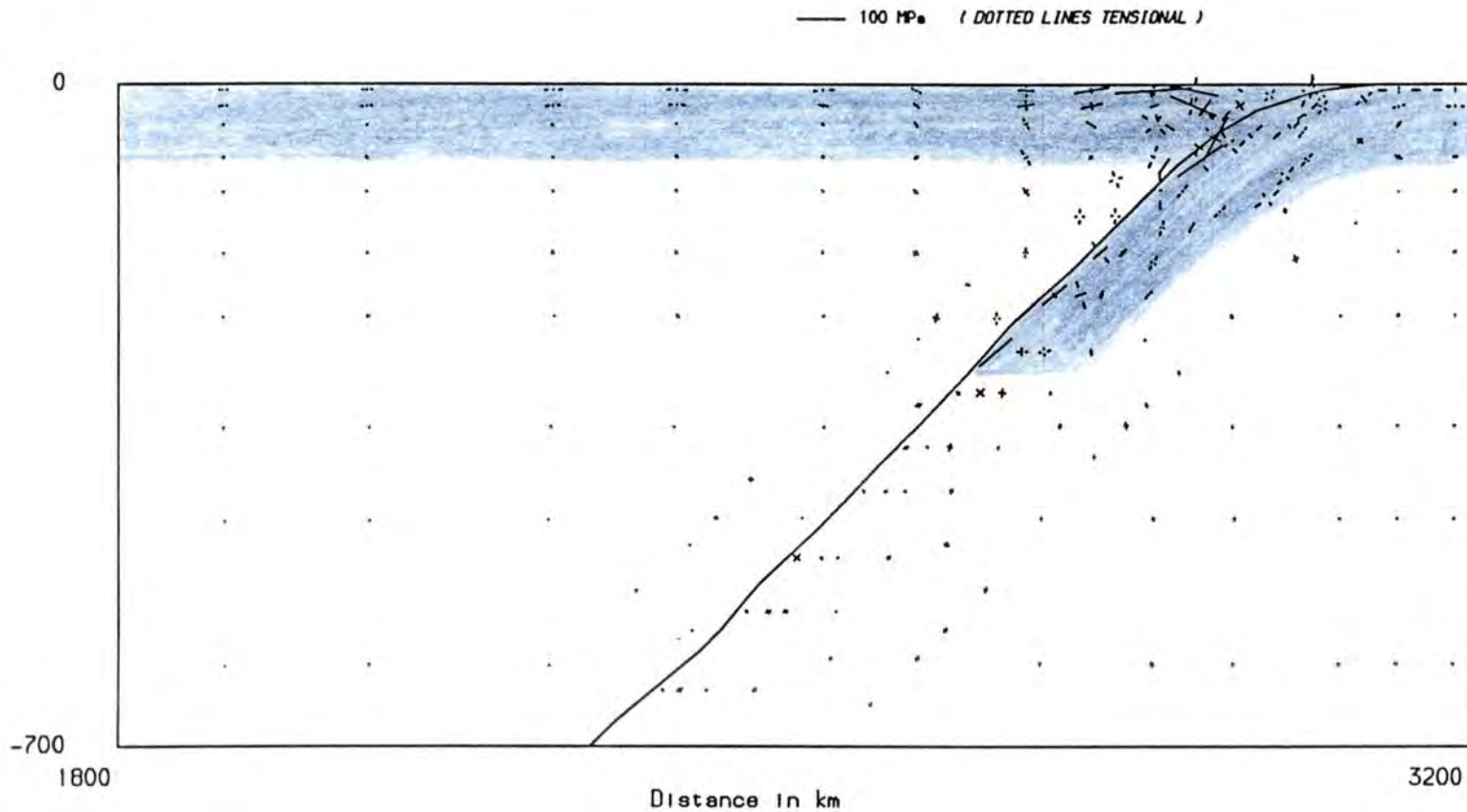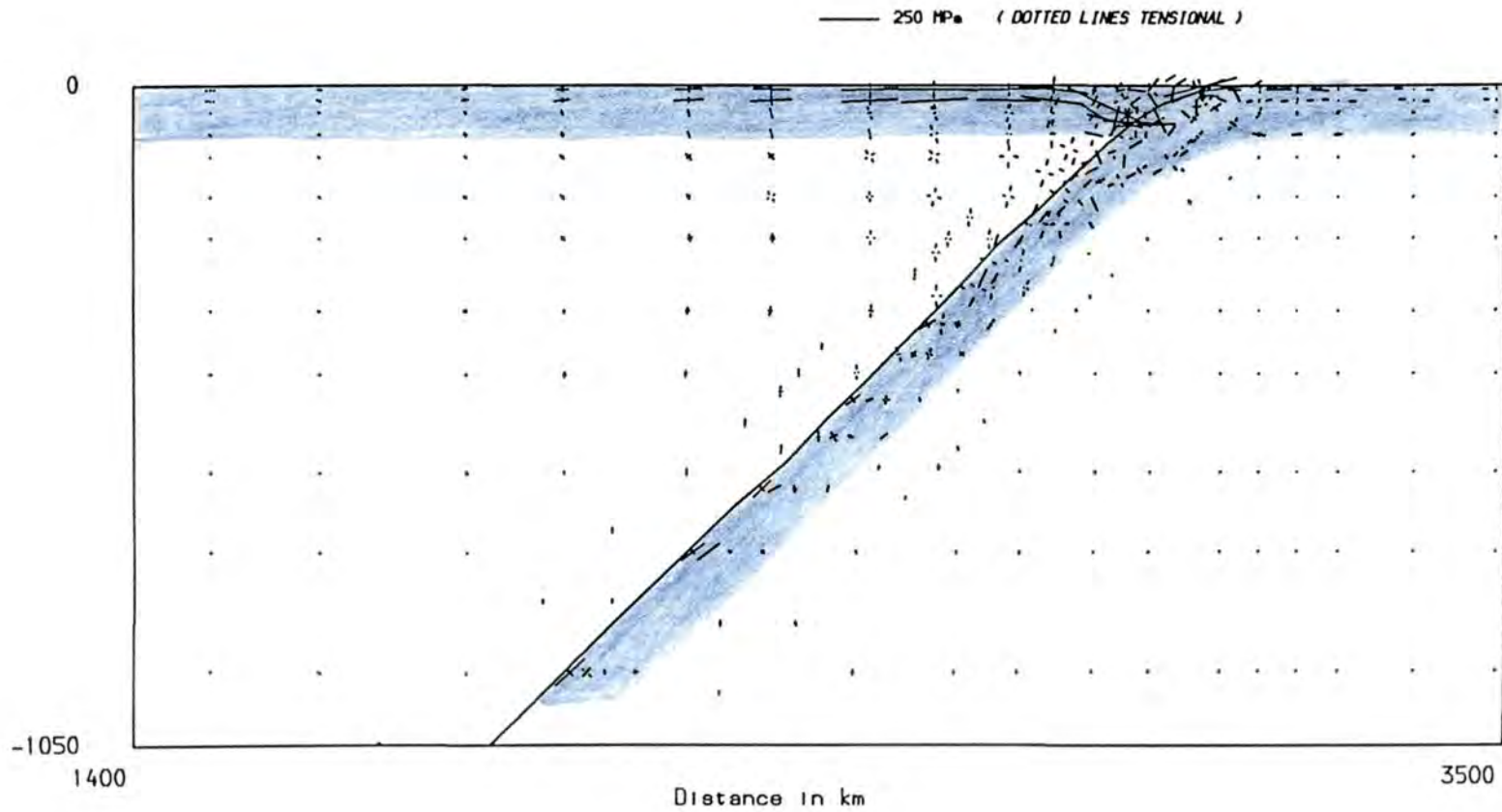
Figure 5.46   The principal stresses for the model of 1000 km penetration, lower
mantle viscosity $\mu = 10^{21}$ Pa s including the olivine-spinel transition. The solid
line denotes the position of the fault. The shading denotes the lithosphere. A
scale length of vector magnitude is given above.
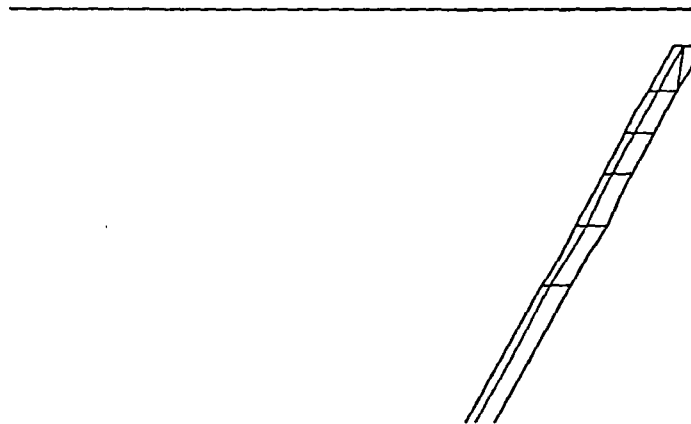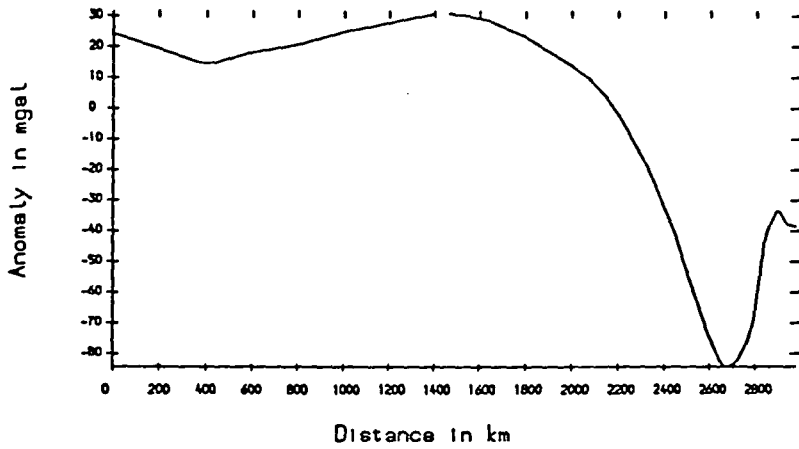
Gravity Profile

Figure 5.47   The gravity profile in mGal calculated on a plane 0.5 km above the surface of the overriding plate for the model of 1000 km penetration, lower mantle viscosity $\mu = 10^{21}$ Pa s including the olivine-spinel transition. The lower box shows the position of the density anomalies.
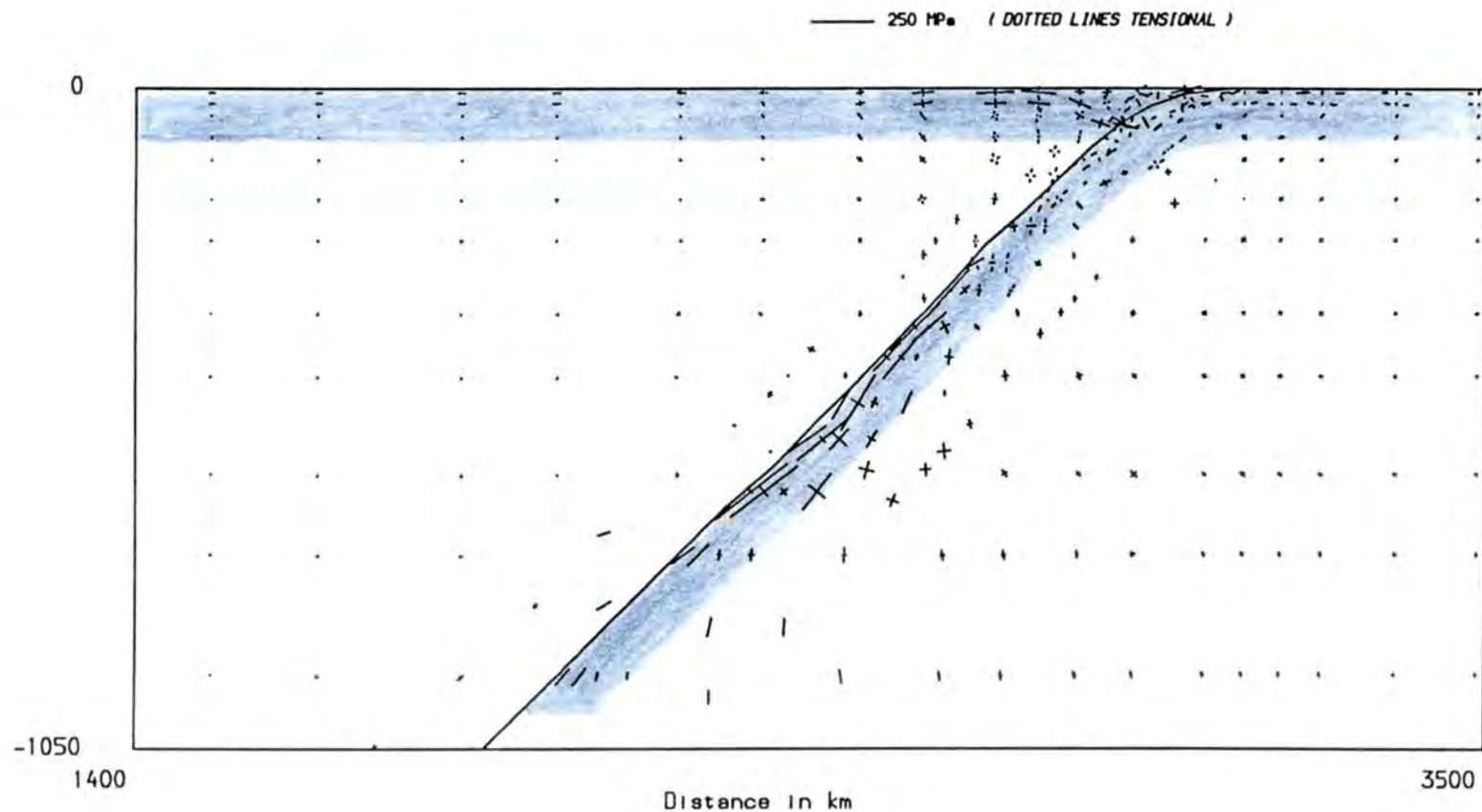
Figure 5.48   The principal stresses for the model of 1000 km penetration, lower mantle viscosity $\mu = 10^{23}$ Pa s including the olivine-spinel transition. The solid line denotes the position of the fault. The shading denotes the lithosphere. A scale length of vector magnitude is given above.
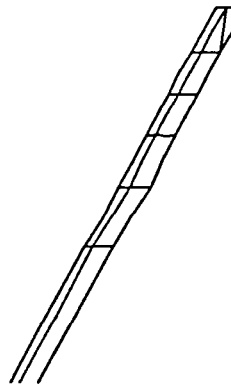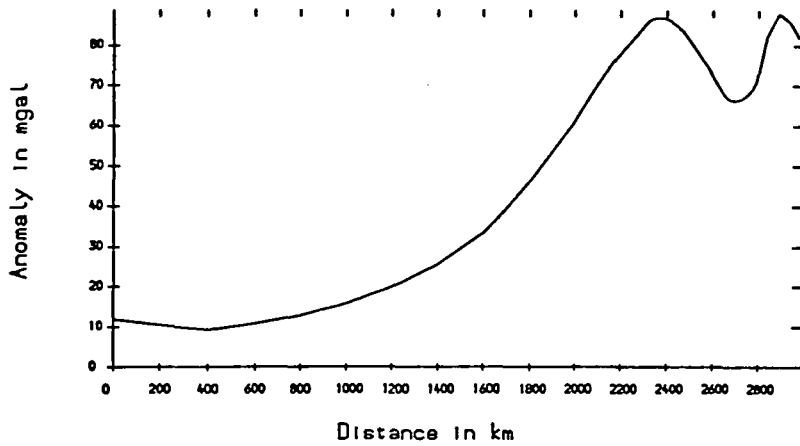
Gravity Profile

Figure 5.49   The gravity profile in mGal calculated on a plane 0.5 km above the surface of the overriding plate for the model of 1000 km penetration, lower mantle viscosity $\mu = 10^{23}$ Pa s including the olivine-spinel transition. The lower box shows the position of the density anomalies.
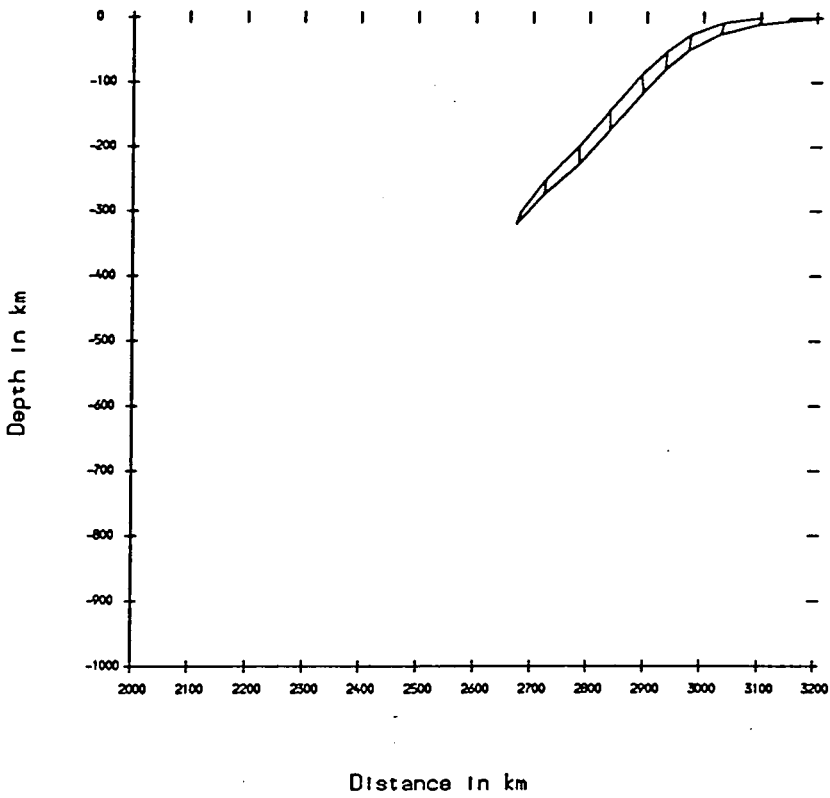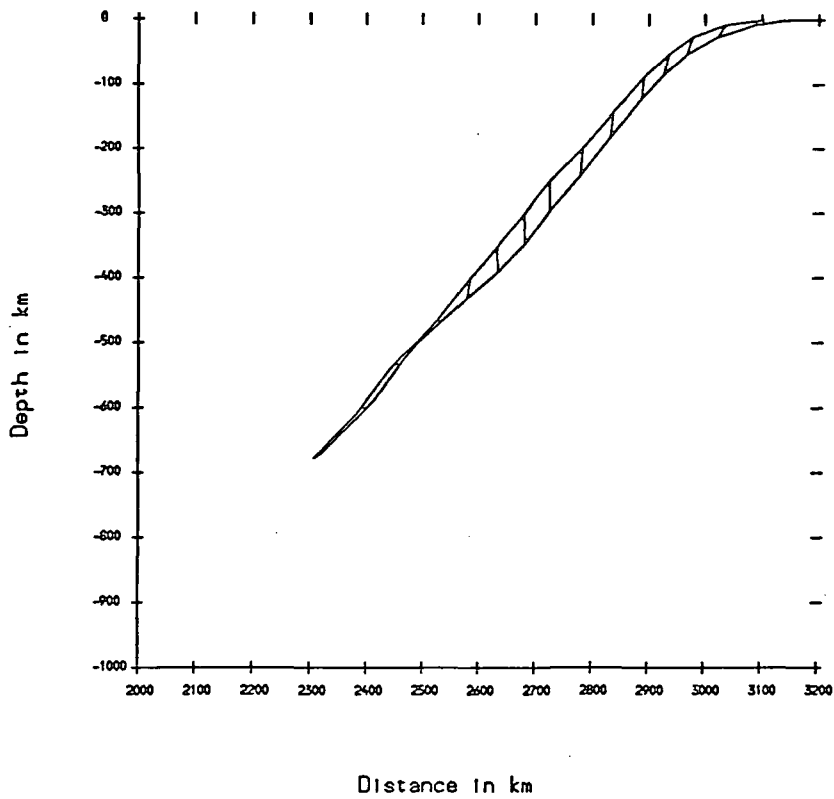
Figure 5.50   The absolute slab motion linearly extrapolated by a factor of 20
for the model of 670 km penetration, lower mantle viscosity $\mu = 10^{23}$ Pa s
including the olivine-spinel transition. The upper curve denotes the original
position of the top surface of the slab and the lower curve denotes the final
position of the top surface of the slab. The cross-lines represent displacement
vectors of the nodes.

Figure 5.51   The absolute slab motion linearly extrapolated by a factor of 20
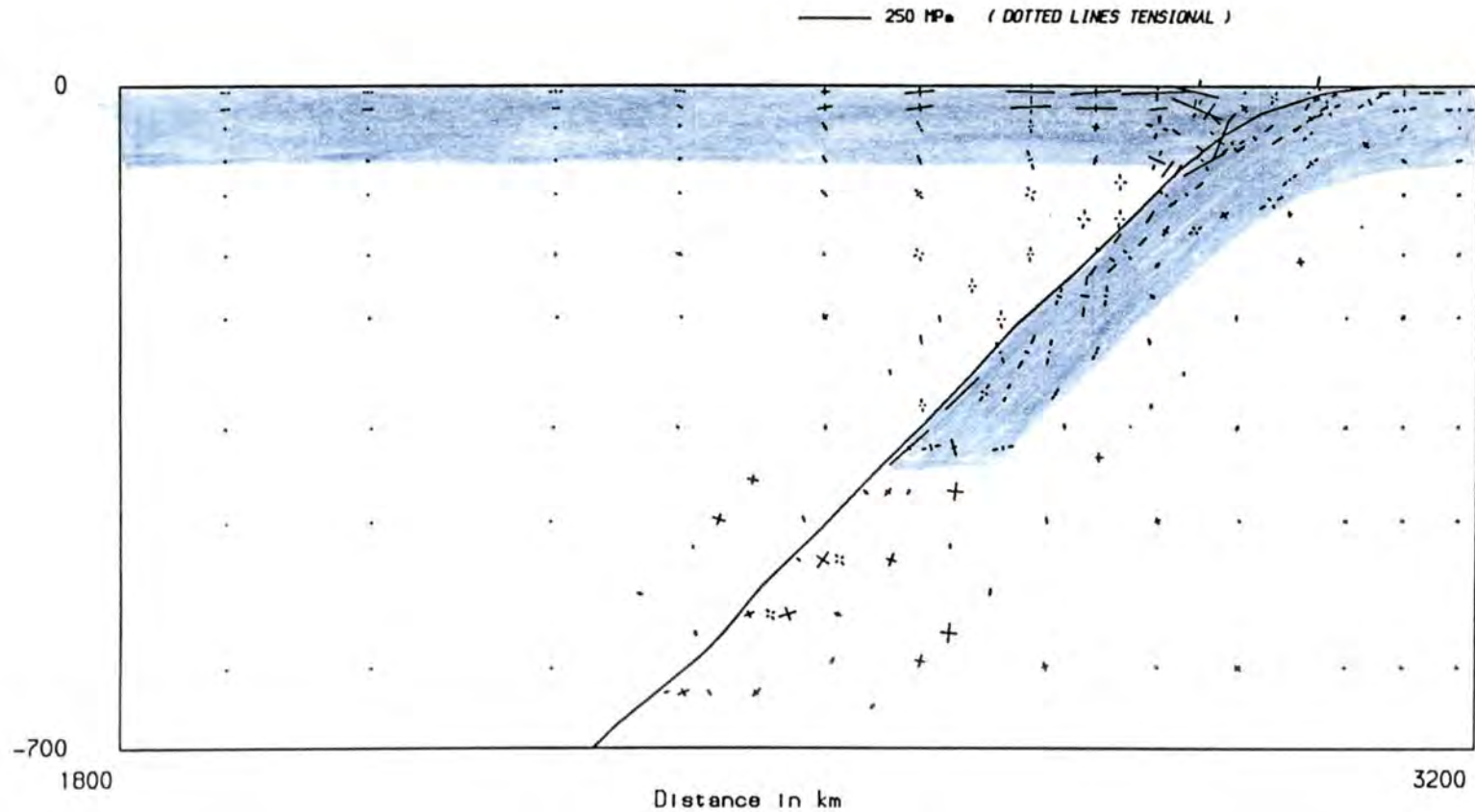for the model of 670 km penetration, lower mantle viscosity $\mu = 10^{23}$ Pa
s including the olivine-spinel transition. The lowest segment of the slab is
viscoelastic with viscosity $\mu = 10^{22}$ Pa s. The upper curve denotes the original
position of the top surface of the slab and the lower curve denotes the final
position of the top surface of the slab. The cross-lines represent displacement
vectors of the nodes.

more instructive to look at the true motion of a slab colliding with the top of the lower mantle. The diagram in figure 5.50 shows the motion of the top surface of a slab penetrating to 670 km depth with a lower mantle of viscosity 10^{23} Pa s. Virtually no penetration of the lower mantle is allowed, and so the sinking upper sections of the slab push the lower section landward. Permitting the deepest section of the slab (from $535 - 670$ km) to deform viscously, with $\mu = 10^{22}$ Pa s, results in the slab motion in figure 5.51. This shows the tendency of the slab tip to deform, migrate landwards and lay flat along the boundary. In contrast, the model in figure 5.31, with a lower mantle viscosity of 10^{22} Pa s, allows the slab to sink below the 670 km boundary.

Kincaid and Olsen (1987) demonstrated experimentally the extremely long time constant for slab material to penetrate a high viscosity lower mantle in scaled models of subduction. Thus it appears that a very high viscosity contrast may create an aggregation of slab material at the base of the upper mantle, despite the mass excess of the slab. This has virtually no observational support among the teleseismic and tomographic analyses of mantle heterogeneity and Hager (1984) argued convincingly against layers of slab material at 670 km on the basis of geoid studies. The evidence favours a viscosity contrast less than $\times 100$ at the base of the upper mantle, but it is by no means conclusive.

5.5.3   Problem Statement - Asthenosphere

In this thesis the asthenosphere is regarded as the low viscosity zone between the base of the lithosphere (90 km) and 200 km depth. The following models utilise mesh (11) for higher resolution and employ an asthenospheric viscosity of $\mu = 10^{20}$ Pa s which is a little higher than most estimates of the low viscosity layer. The time increment is reduced to 50 yrs and so 1000 time steps are implemented to give a relaxation period of 50 000 yrs. All other mesh parameters are retained identical to the previous models.

5.5.4   Discussion Of Results

The stress regime, nodal displacements, surface displacement, slab motion and gravity profile for a slab penetrating to 400 km depth are shown in figures 5.52 - 5.56 and can be compared with the equivalent non-asthenospheric model in figures 5.42 - 5.45. The tensional stresses in the subducting plate are reduced by about 30 MPa
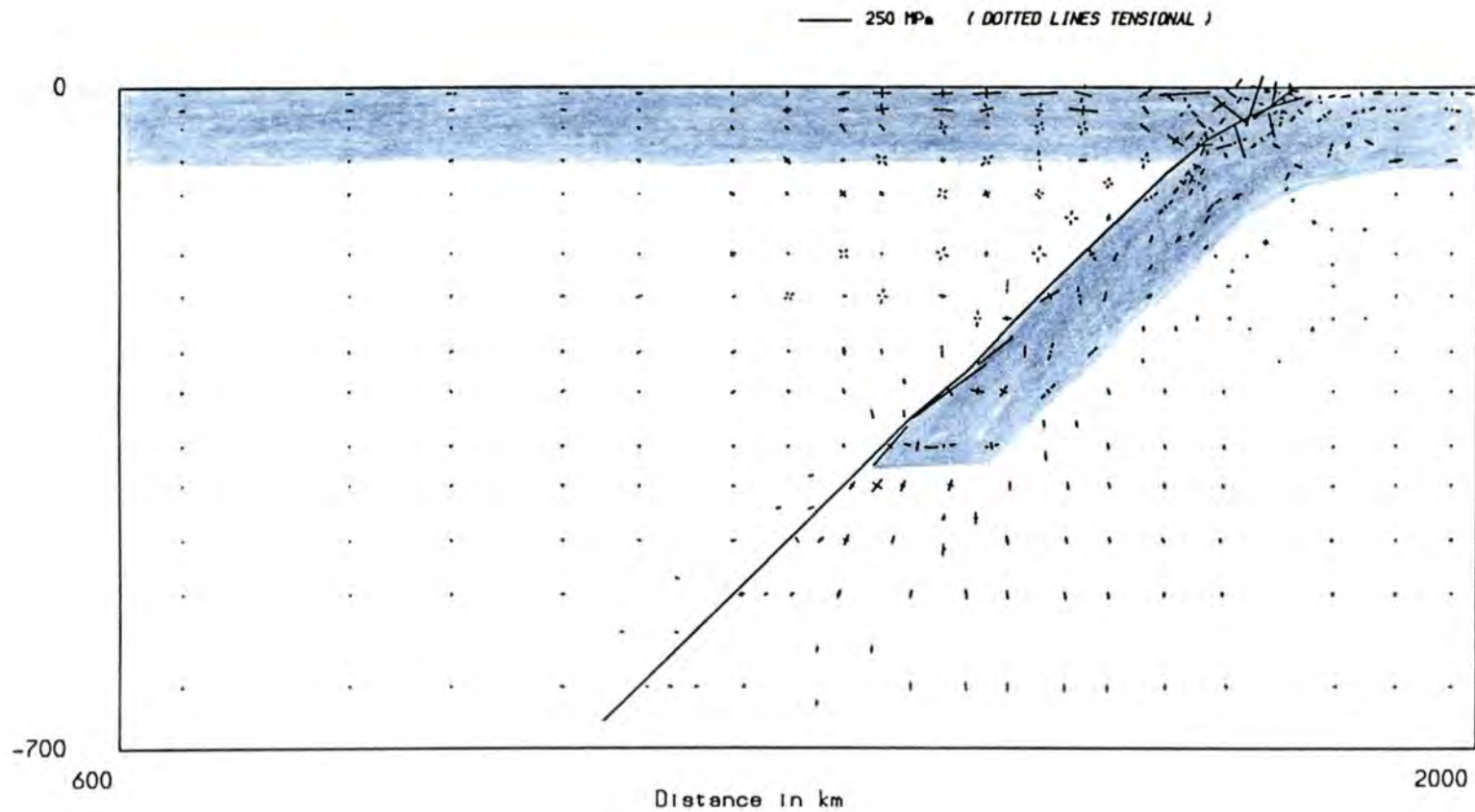
Figure 5.52 The principal stresses for the model of 400 km penetration, astheno-
sphere viscosity $\mu = 10^{20}$ Pa s including the olivine-spinel transition in mesh
(11). The solid line denotes the position of the fault. The shading denotes the
lithosphere. A scale length of vector magnitude is given above.
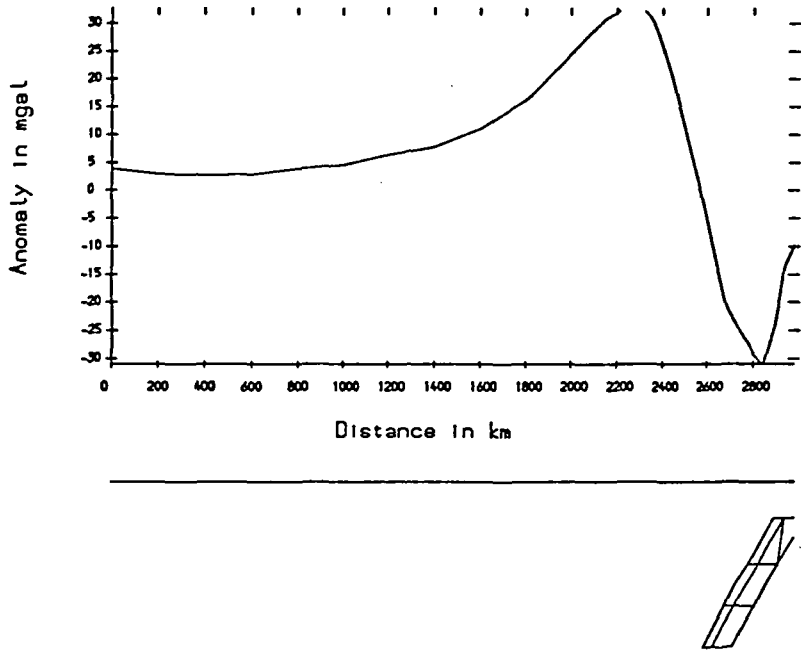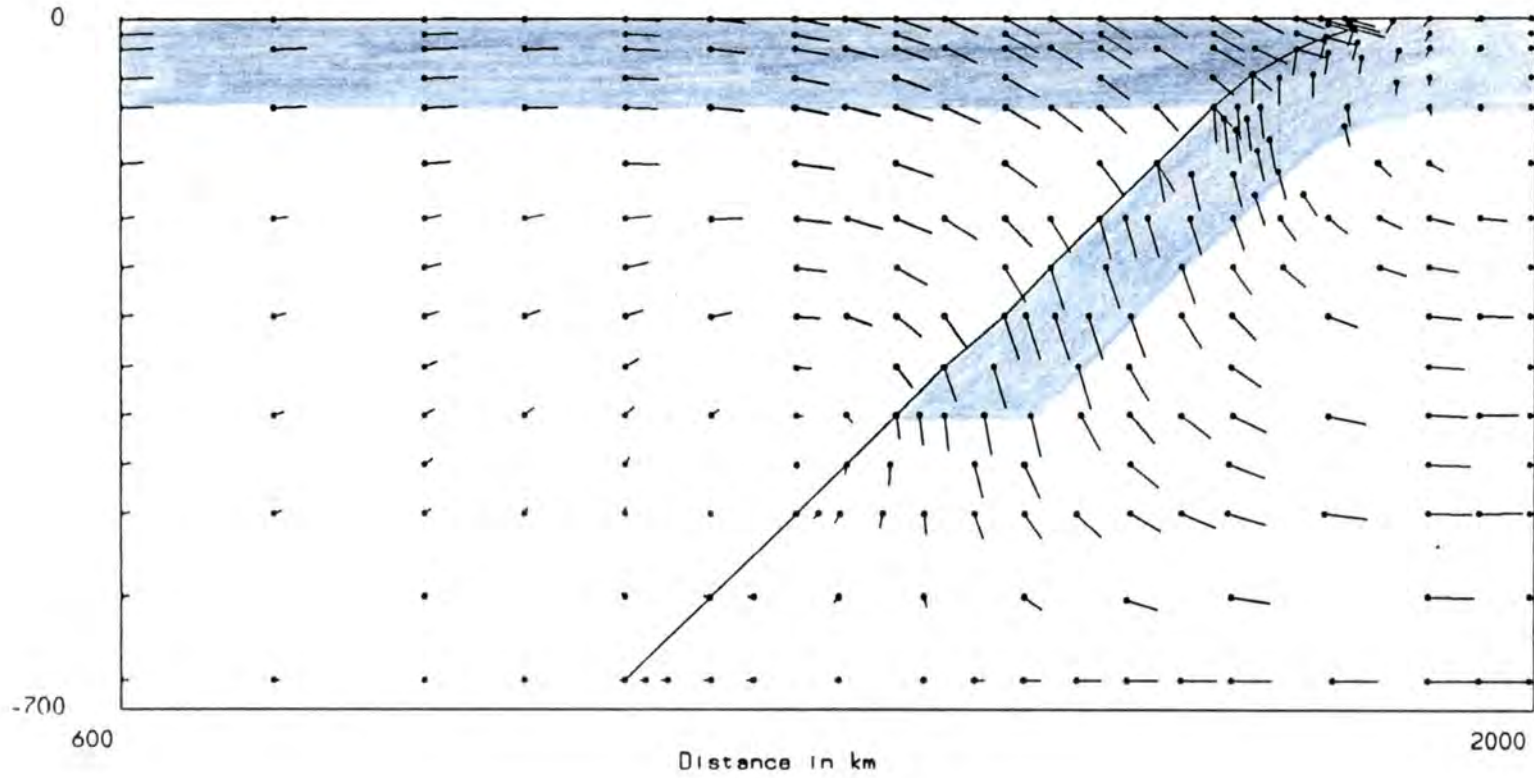
Figure 5.53 The displacement vectors for the model of 400 km penetration, asthenosphere viscosity $\mu = 10^{20}$ Pa s including the olivine-spinel transition in mesh (ɪɪ).

## Surface displacement profile (In m)
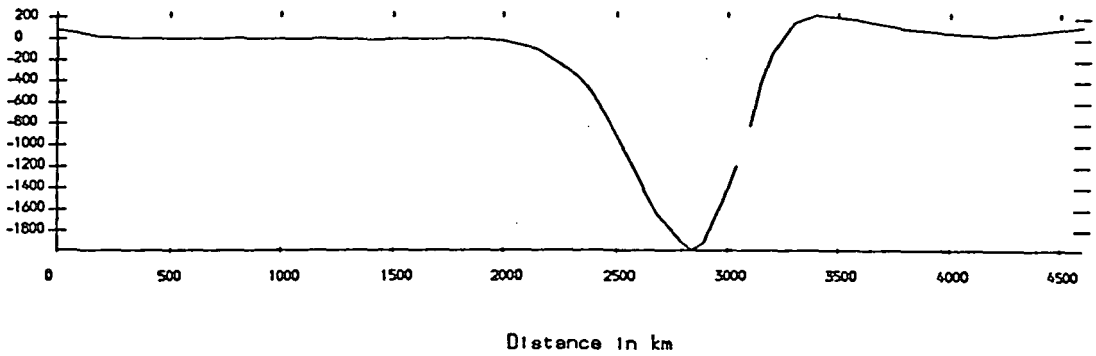

Distance in km
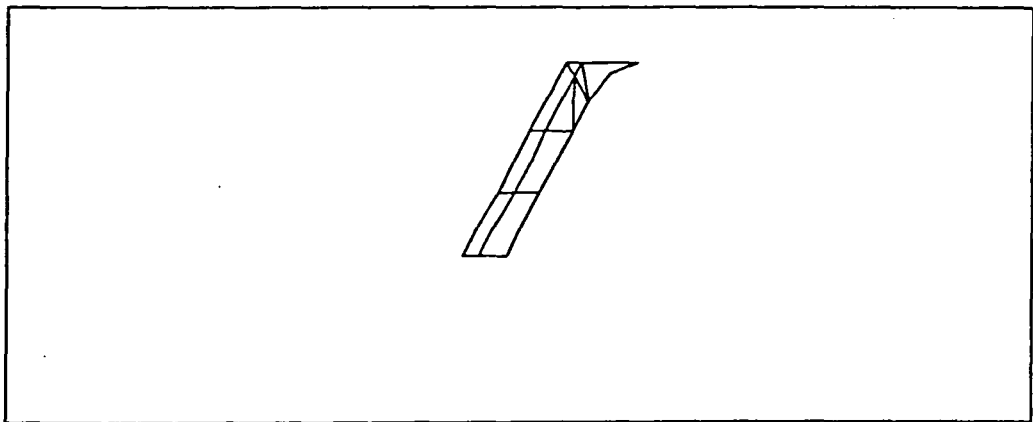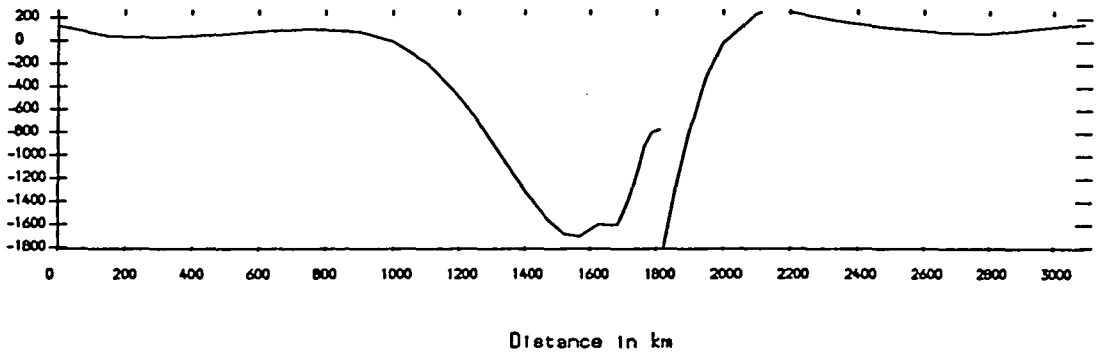
Figure 5.54   The vertical displacement of the surface for the model of 400 km penetration, asthenosphere viscosity $\mu = 10^{20}$ Pa s including the olivine-spinel transition in mesh (II). The left hand curve denotes the overriding plate, the right hand curve denotes the subducting plate. The lower box shows the relative position of the density anomalies.
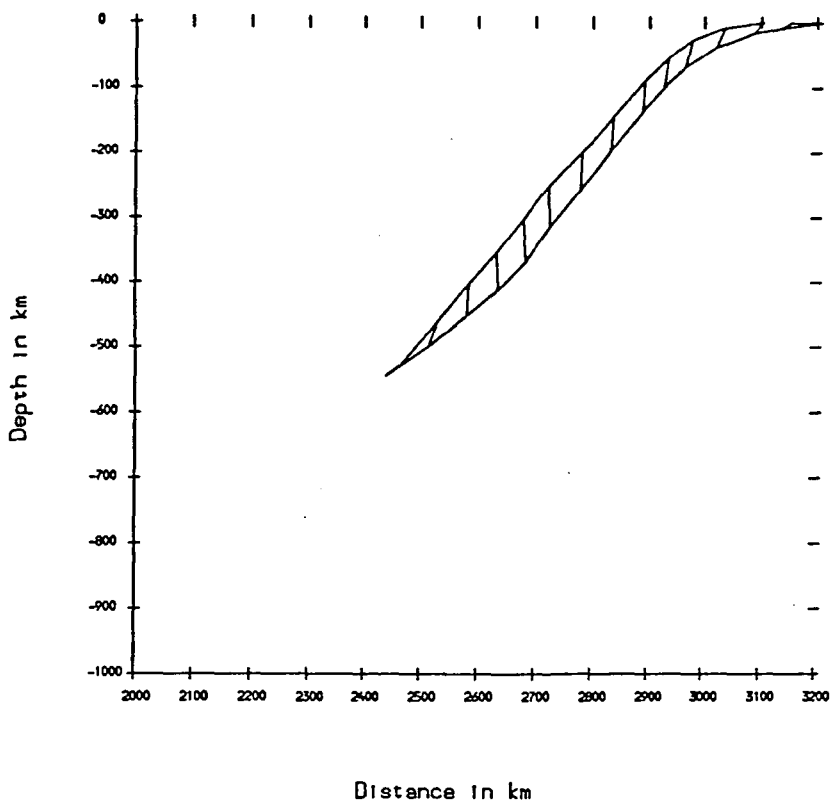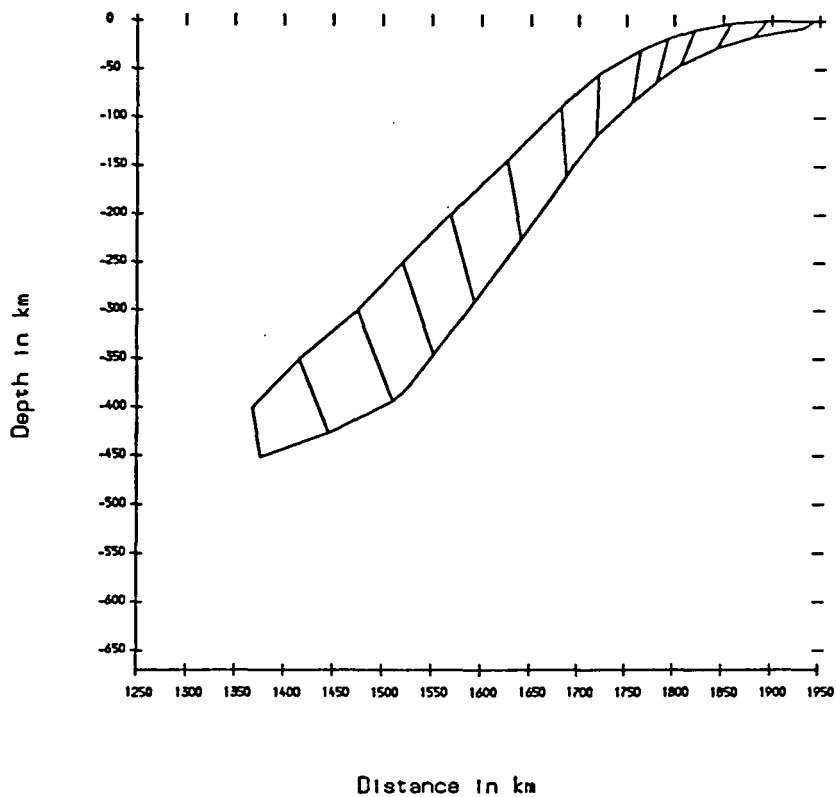
Figure 5.55 The absolute slab motion linearly extrapolated by a factor of 20 for the model of 400 km penetration, asthenosphere viscosity $\mu = 10^{20}$ Pa s including the olivine-spinel transition in mesh (n). The upper curve denotes the original position of the top surface of the slab and the lower curve denotes the final position of the top surface of the slab. The cross-lines represent displacement vectors of the nodes.
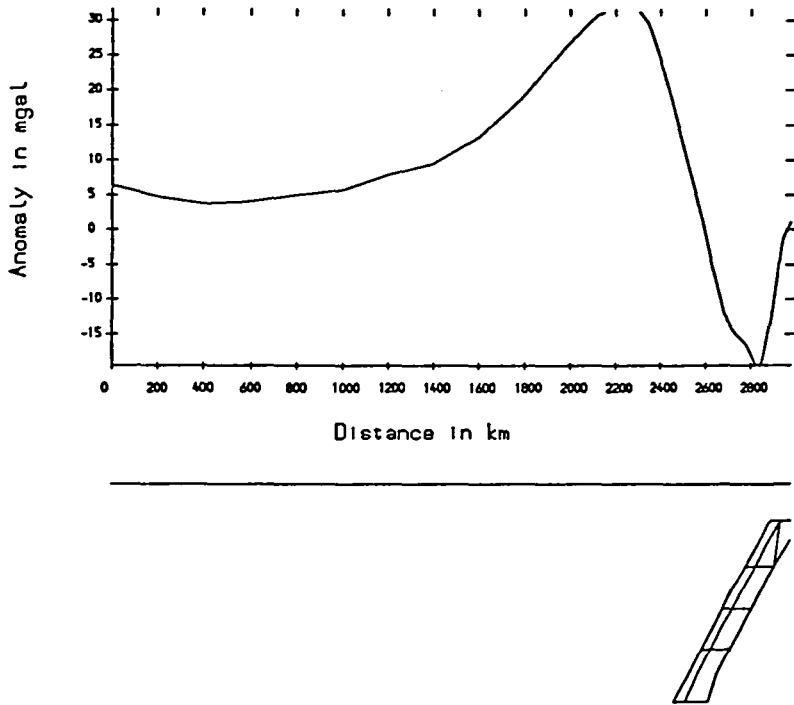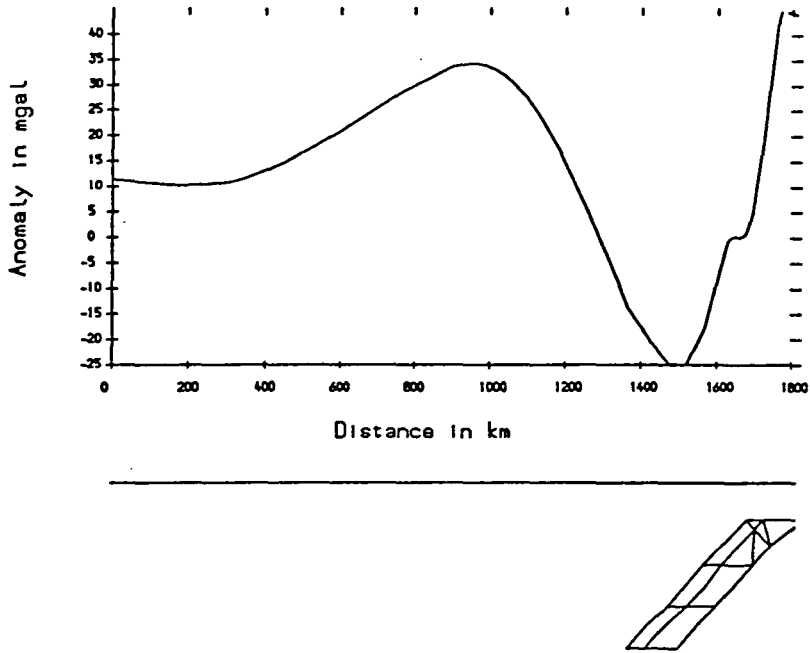
Gravity Profile

Figure 5.56 The gravity profile in mGal calculated on a plane 0.5 km above the surface of the overriding plate for the model of 400 km penetration, asthenosphere viscosity $\mu = 10^{20}$ Pa s including the olivine-spinel transition in mesh (ii). The lower box shows the position of the density anomalies.

by the introduction of the low viscosity layer. In the overriding plate the far backarc tension is much reduced from 70 MPa to 30 MPa and the compression around the arc-backarc region about 200 — 400 km from the trench increases from 90 MPa to 130 MPa. In the slab the compression near the tip has increased from 310 MPa to 430 MPa and in the upper slab the tension is uniformly reduced by about 50 MPa. The nodal displacements in figure 5.53 are given as an example, clearly showing the overriding plate being dragged into the trench and the rollback of the slab and trench creating lateral flow in the mantle. The surface displacement in figure 5.54 is very similar to the uniform upper mantle model in figure 5.43, the amplitude of depression is reduced by 100 m, and so presumably the normal stresses at the base of the lithosphere must be similar. The trench - outer rise system of the subducting plate has sharpened slightly, with the trench depth increasing from 1600 m to 1800 m. The motion of the slab has also altered (figure 5.55) compared to figure 5.44. There is much greater rotation towards the vertical causing greater bending above 100 km and below 300 km depth. The short wavelength flexure in the forearc is beginning to dominate the gravity profile in figure 5.56.

The increase in trench depth should generate greater isostatic reaction at the top of the slab and thus increase the tension in the upper slab. This does not appear to occur. The reduction in the amplitude of depression in the overriding plate should reduce the local horizontal compression in the plate, and the increase in trench rollback should increase the tension in the far backarc. This does not appear to occur. As found in the models of the previous chapter (see section 4.4) the low viscosity zone concentrates the flow into the asthenosphere (figure 5.53). Thus it appears that the lower viscosity of the asthenosphere reduces the basal drag on the overriding plate and this effect outweighs the increase in rollback resulting in a reduction in horizontal tension in the overriding plate.

5.6   Thermal Anomalies in the Backarc

5.6.1   Problem Statement

The high heat flow observed in the backarc of subduction zones has been attributed

92

to a thermal anomaly underneath the overriding plate. The origin and nature of this anomaly is not well understood but it is generally believed to be due to convective upwelling in the mantle wedge driven by the downdip motion of the slab, combined with the possibility of water release from the subducted crust. There are no direct observations of the state of the mantle and so these finite element models must rely on data derived from previous numerical simulations. Toksoz and Hsui (1978) modelled convection in the backarc which produced a thermal anomaly extending to about 300 km depth supporting about 1 km of topography at the surface. The maximum temperature anomaly (caused by raising the isotherms) proved to be about 200 K near the base of the lithosphere. Subsequent studies by Jurdy and Stefanick (1983) and Honda (1985) do not contradict these conclusions, but it is clear that the thermal anomaly is not well constrained and may vary considerably from one location to another. This finite element method cannot model thermal convection under the backarc and the generation of the thermal anomaly. So, the mechanical representation of an in-place thermal anomaly is included as a linear, vertical variation in density, temperature and viscosity.

An average density anomaly of $\Delta \rho = -8.4$ kg m^{-3} distributed over a 270 km depth range will support 1 km of submarine topography at the surface ($\Delta \rho = 2270$ kg m^{-3}). Distributing this as a linear density gradient gives the depth profile in Table 5.2 below.

Depth Range (km)	Density (kg m^{-3})	Temperature (K)
30 – 90	-14.93	150
90 – 200	-9.64	97
200 – 300	-3.11	31

Table 5.2   Vertical distribution of the backarc anomaly

The depth range represents the resolution of the elements. The equivalent temperature anomaly is evaluated from,

$$\Delta T = -\frac{\Delta \rho}{\alpha (\rho + \Delta \rho)}$$

where $\alpha = 3 \times 10^{-5}$ K^{-1} is the coefficient of thermal expansion. The full thermal anomaly is portrayed in figure 5.57 for a model of slab penetration to 400 km in mesh (ii). The equivalent temperatures calculated in Table 5.2 above are assigned to midside nodes and all other nodes are interpolated to produce a linear temperature gradient.
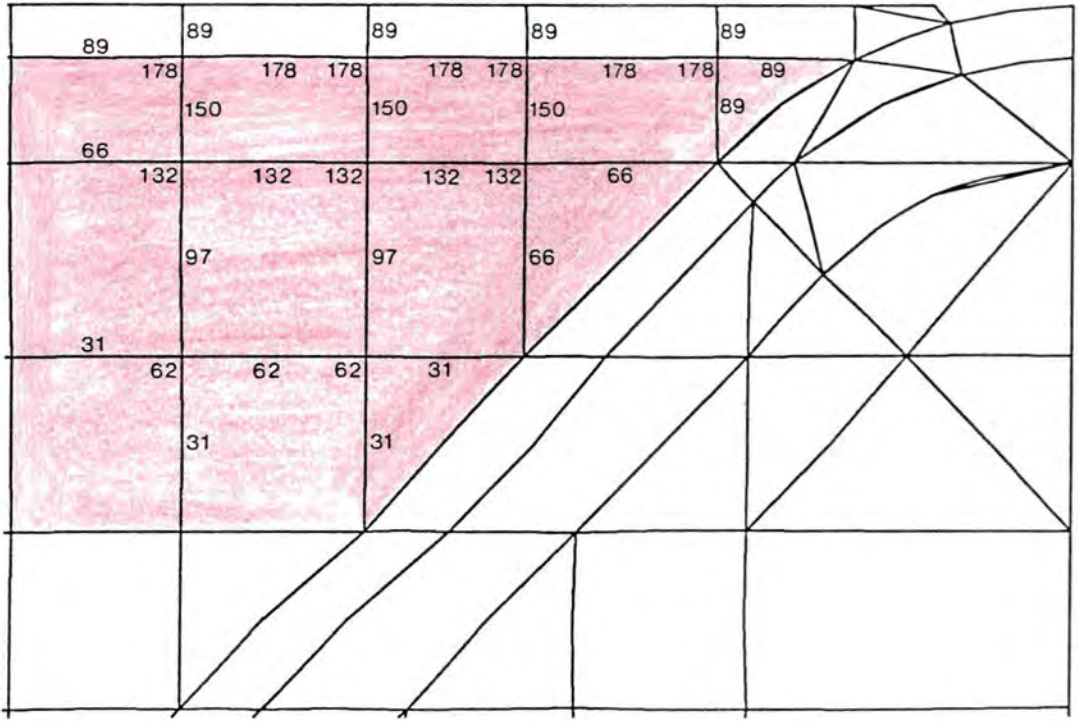
Figure 5.57   The thermal anomaly under the backarc for the model of 400 km penetration. Anomalous temperatures (in K) at the nodes are shown and the shading denotes the low viscosity zone ($\mu = 10^{20}$ Pa s).

The viscosity of the anomalous region under the backarc was reduced to $\mu = 10^{20}$ Pa s. All other parameters are identical to the final model of the previous section, including the low viscosity asthenosphere. The models have a relaxation period of 50 000 yrs.

5.6.2 Discussion of Results

To investigate the effect of the low viscosity, the temperature and density anomalies were initially omitted. The stress regime, surface displacement, slab motion and gravity profile are shown in figures 5.58 - 5.61. The overriding plate is significantly decoupled by this low viscosity wedge, resulting in a 20% decrease in the surface depression (figure 5.59) to 1350 m, and a 200 m increase in the trench depth. This has a considerable effect on the stress regime in figure 5.58. Forearc compression persists but the broad band of compression in the overriding plate is reduced in magnitude and extent (restricted to within 700 km of the trench), and the far backarc tension is increased by 20 MPa to 50 MPa. There is also a change in the slab stresses. In the depth range 90 → 200 km the top surface of the slab is much less tensional while the lower layer of elastic stresses (20 km further into the slab) retains its tension. This suggests some support for the conclusions of Sleep (1979) that double seismic zones are caused by the relaxation of the low viscosity mantle wedge which allows the slab to sag. Sadly, these models do not have sufficient resolution to study this effect in more detail. The slab motion in figure 5.60 is similar to the asthenospheric model in figure 5.55 apart from the small increase in the magnitude of the displacement vectors below 200 km depth. Thus any sagging which led to the birth of the double seismic zone is indistinguishable in this model. The motion of the slab demonstrates the control of the mantle wedge over the slab, in the absence of external flow pressures. The flexure in the forearc now dominates the gravity profile.

The density anomaly is now added to the preceding model and as figures 5.62 - 5.65 show, it has a noticeable effect. The surface depression above the anomalous region is appreciably reduced, to a maximum of 950 m. This flattening of the overriding plate leads to reduction of the previous 80 MPa surface compressions in the arc-backarc region which all but eliminates them above the anomaly. The far backarc tension and the forearc compression persist, and the slab stresses are virtually unaffected, only the trench depth and motion of the deep slab are slightly reduced. Finally the temperature
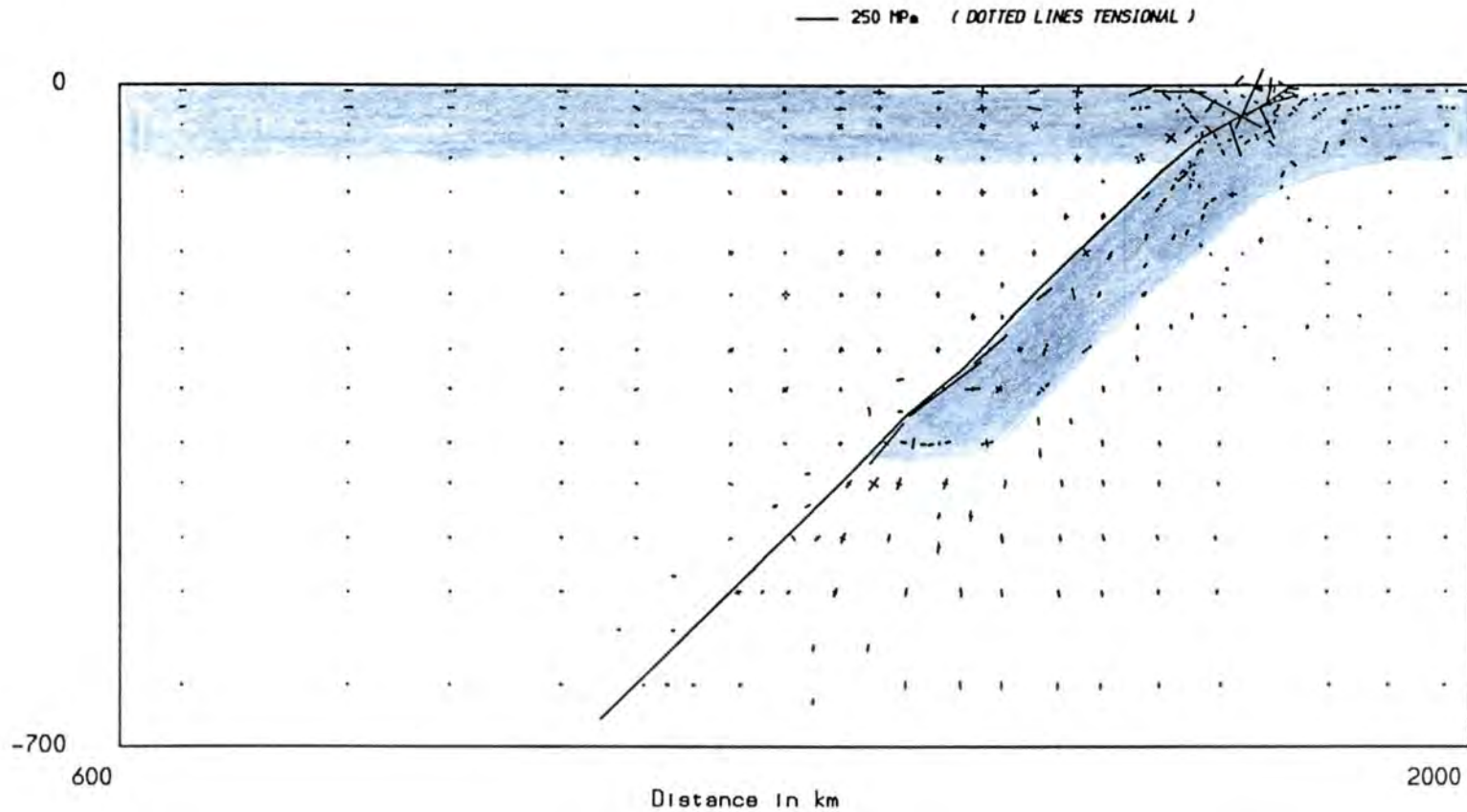
Figure 5.58   The principal stresses for the model of 400 km penetration, astheno-
sphere viscosity $\mu = 10^{20}$ Pa s including the olivine-spinel transition and the
low viscosity $\mu = 10^{20}$ Pa s of the thermal anomaly. The solid line denotes
the position of the fault. The shading denotes the lithosphere. A scale length
of vector magnitude is given above.

Surface displacement profile (in m)

Distance in km
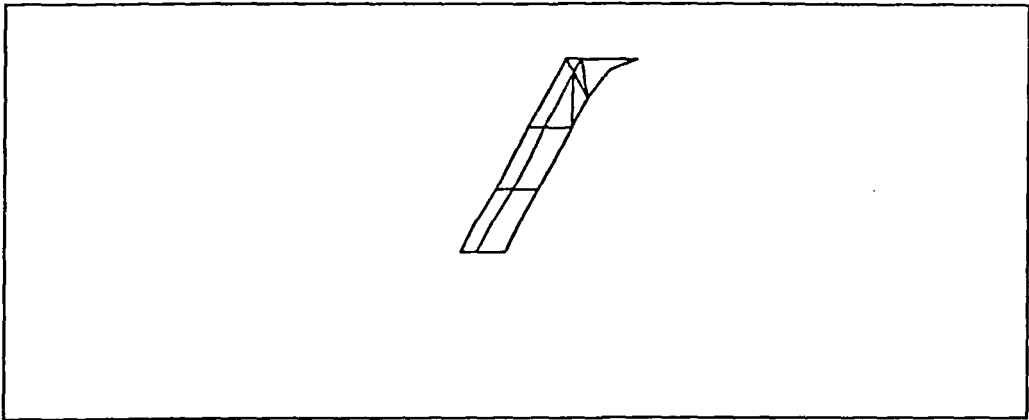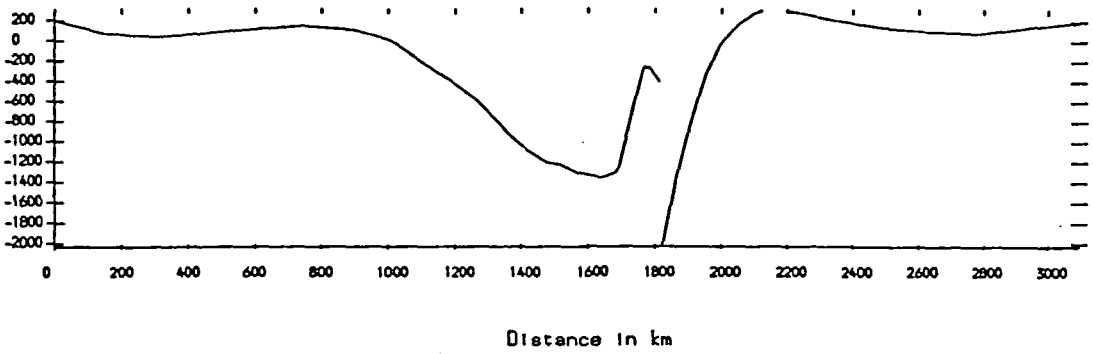
Figure 5.59   The vertical displacement of the surface for the model of 400 km penetration, asthenosphere viscosity $\mu = 10^{20}$ Pa s including the olivine-spinel transition and the low viscosity $\mu = 10^{20}$ Pa s of the thermal anomaly. The left hand curve denotes the overriding plate, the right hand curve denotes the subducting plate. The lower box shows the relative position of the density anomalies.
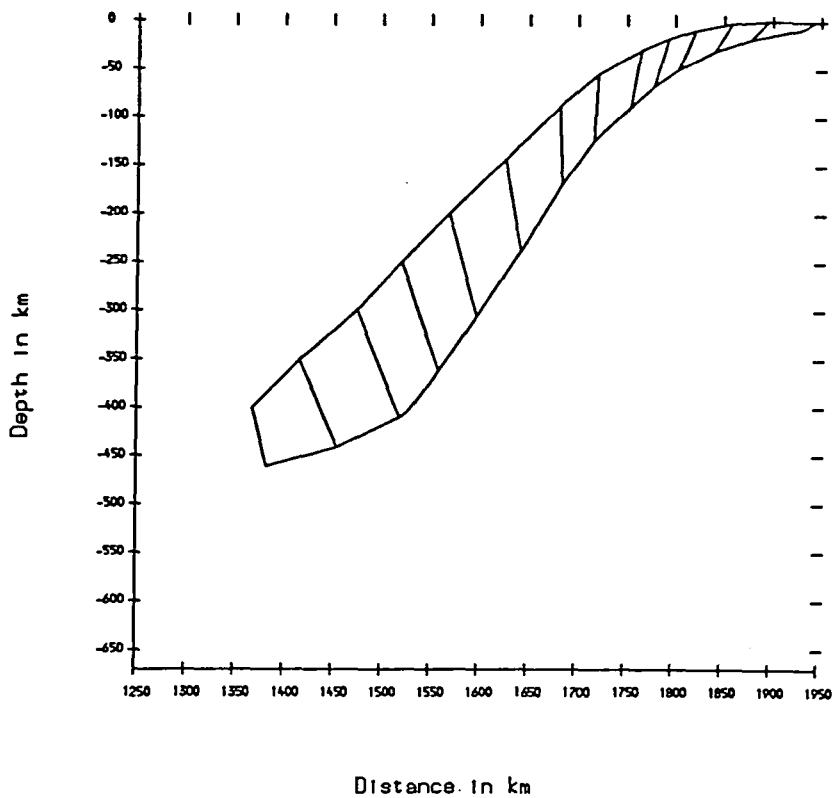
Figure 5.60   The absolute slab motion linearly extrapolated by a factor of 20
for the model of 400 km penetration, asthenosphere viscosity $\mu = 10^{20}$ Pa s
including the olivine-spinel transition and the low viscosity $\mu = 10^{20}$ Pa s of
the thermal anomaly. The upper curve denotes the original position of the
top surface of the slab and the lower curve denotes the final position of the
top surface of the slab. The cross-lines represent displacement vectors of the
nodes.
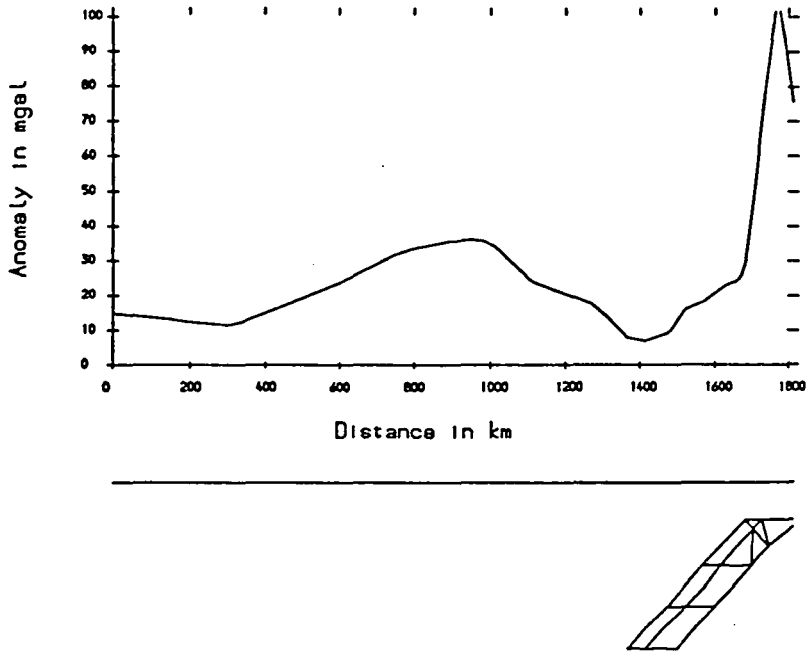
Gravity Profile

Figure 5.61   The gravity profile in mGal calculated on a plane 0.5 km above the surface of the overriding plate for the model of 400 km penetration, astheno-sphere viscosity $\mu = 10^{20}$ Pa s including the olivine-spinel transition and the low viscosity $\mu = 10^{20}$ Pa s of the thermal anomaly. The lower box shows the position of the density anomalies.
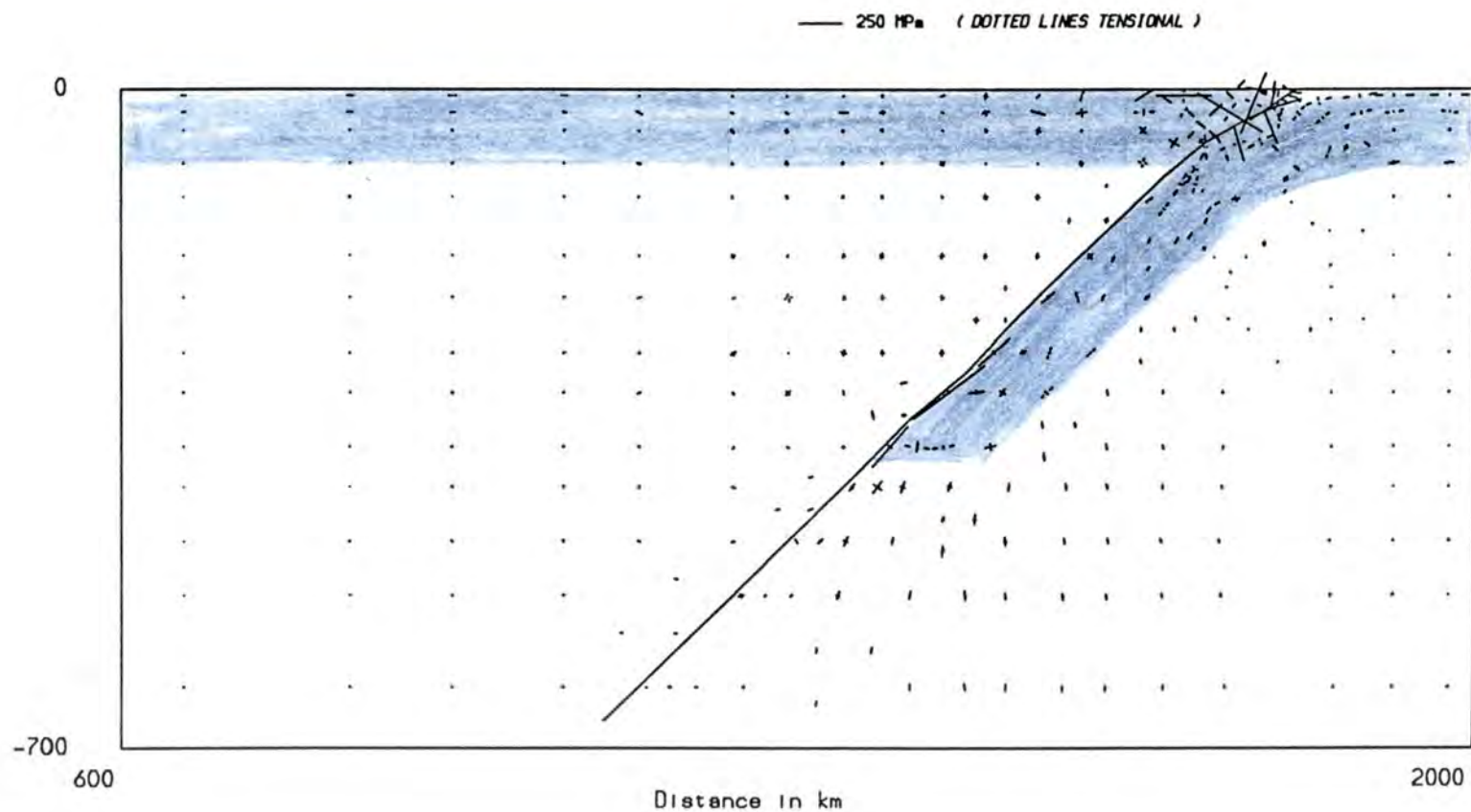
Figure 5.62　The principal stresses for the model of 400 km penetration, astheno-sphere viscosity $\mu = 10^{20}$ Pa s including the olivine-spinel transition, the low viscosity $\mu = 10^{20}$ Pa s and the density anomaly of the thermal anomaly. The solid line denotes the position of the fault. The shading denotes the lithosphere. A scale length of vector magnitude is given above.
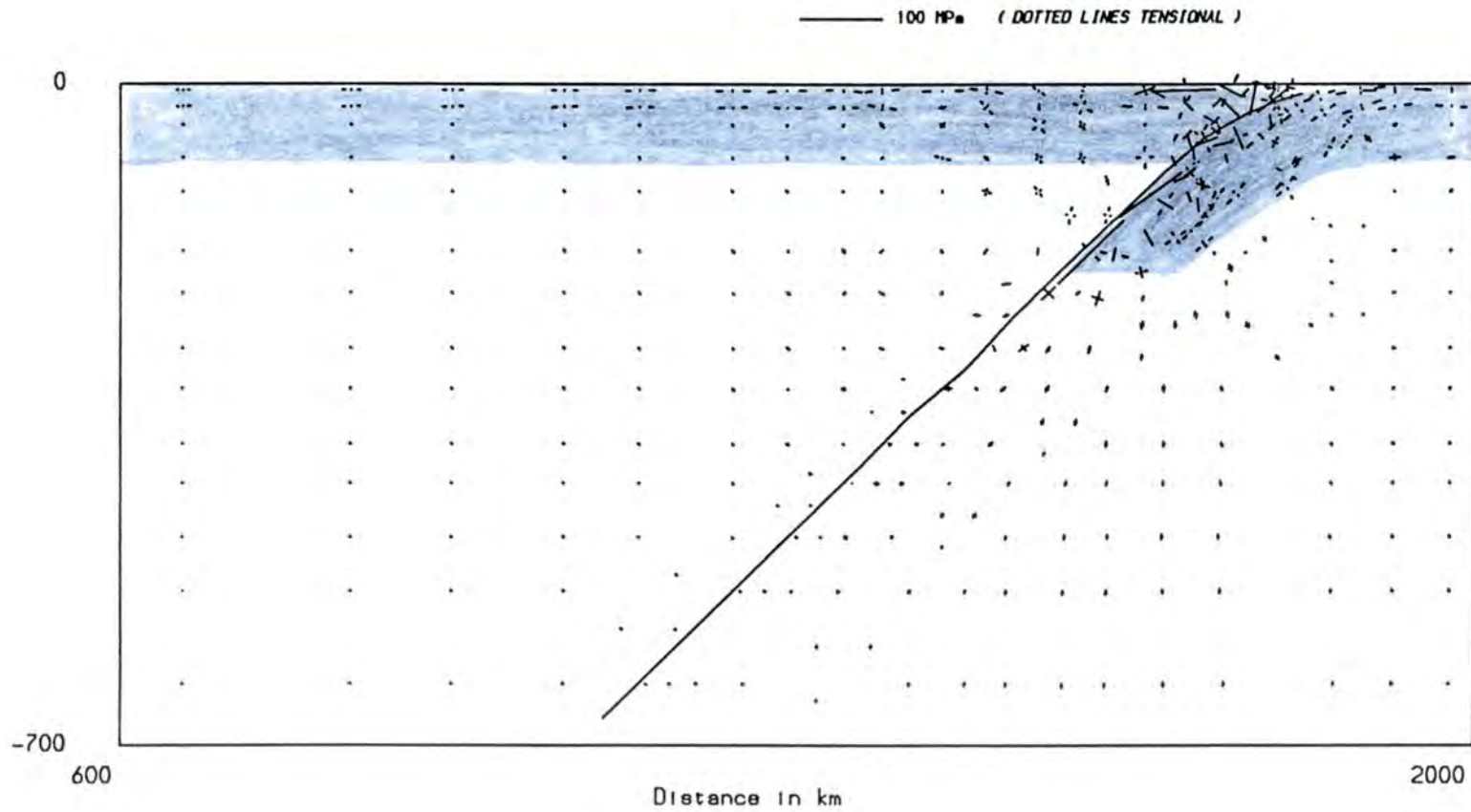
Surface displacement profile (in m)

Distance in km
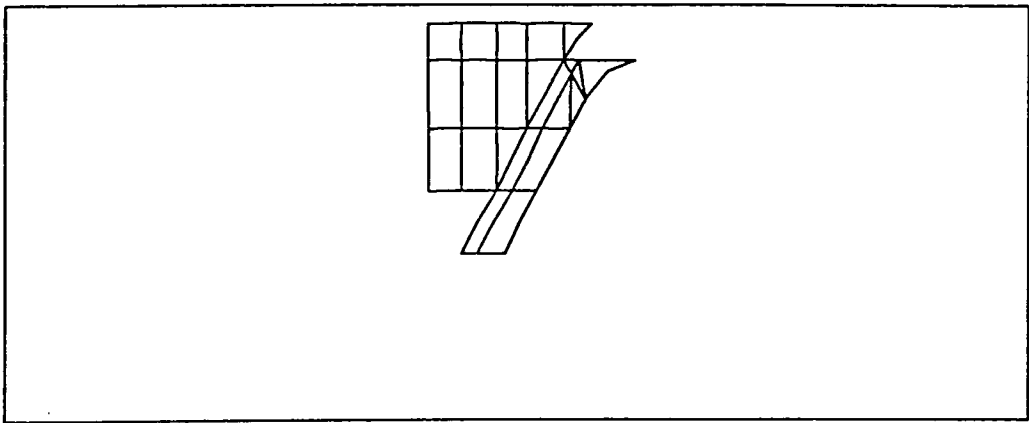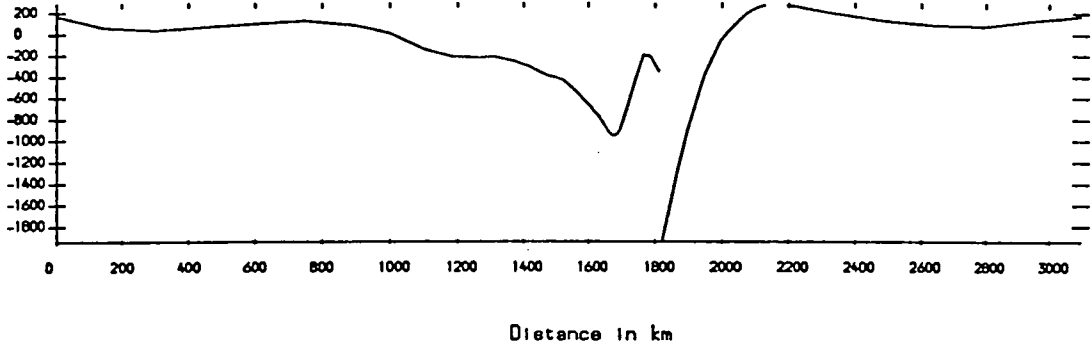
Figure 5.63   The vertical displacement of the surface for the model of 400 km penetration, asthenosphere viscosity $\mu = 10^{20}$ Pa s including the olivine-spinel transition, the low viscosity $\mu = 10^{20}$ Pa s and the density anomaly of the thermal anomaly. The left hand curve denotes the overriding plate, the right hand curve denotes the subducting plate. The lower box shows the relative position of the density anomalies.
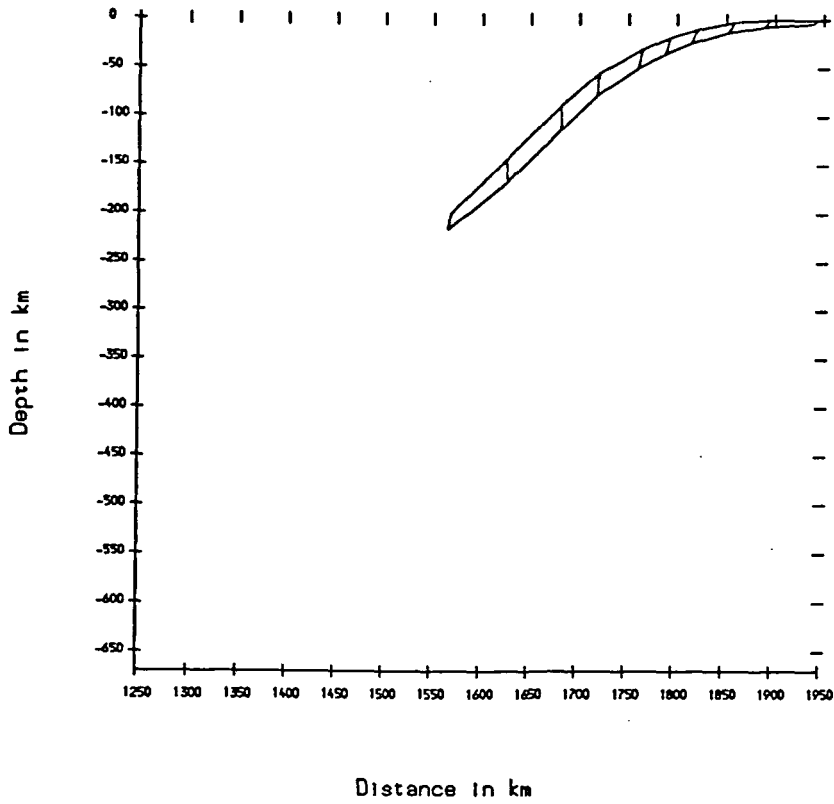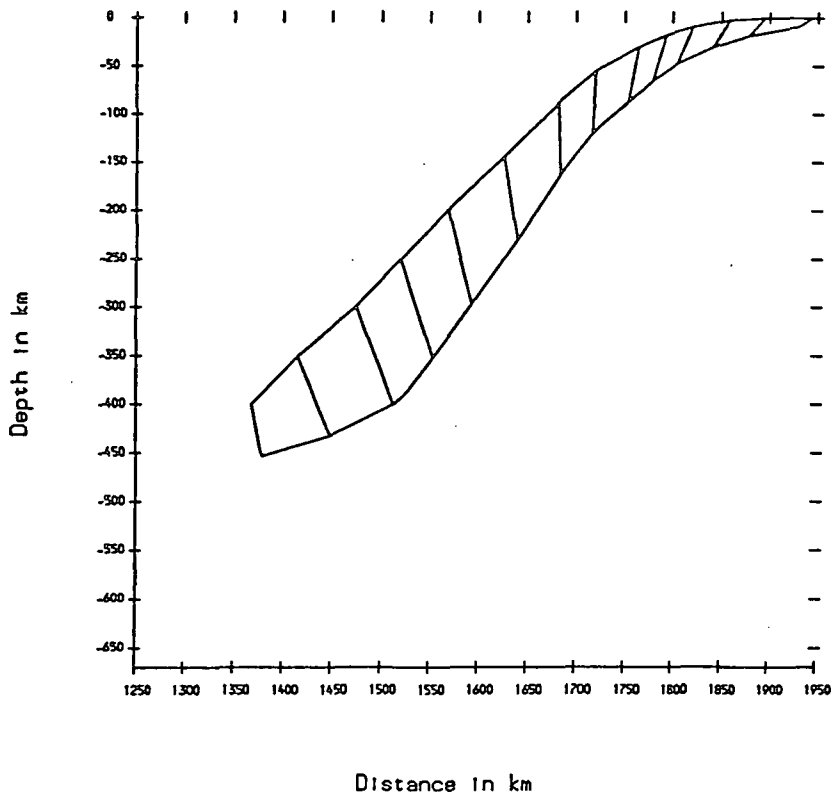
Figure 5.64 The absolute slab motion linearly extrapolated by a factor of 20 for the model of 400 km penetration, asthenosphere viscosity $\mu = 10^{20}$ Pa s including the olivine-spinel transition, the low viscosity $\mu = 10^{20}$ Pa s and the density anomaly of the thermal anomaly. The upper curve denotes the original position of the top surface of the slab and the lower curve denotes the final position of the top surface of the slab. The cross-lines represent displacement vectors of the nodes.
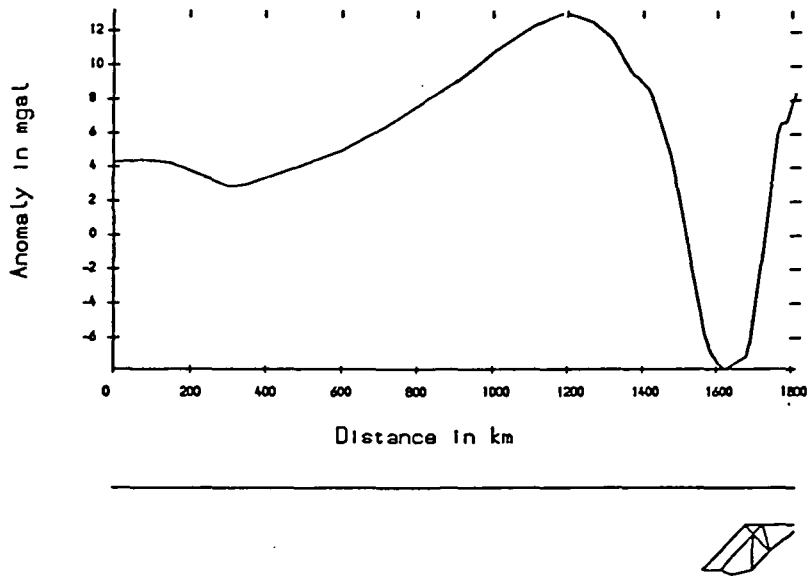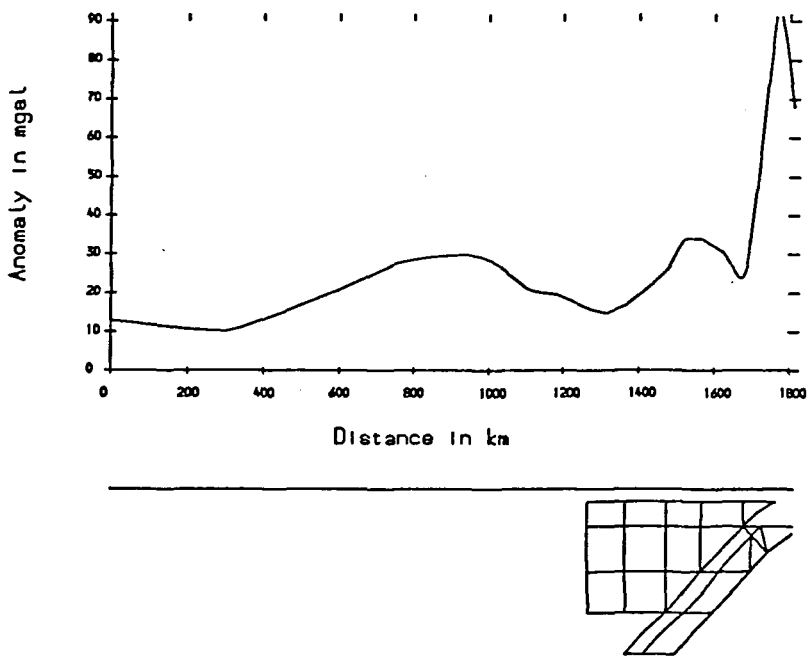
Gravity Profile

Figure 5.65   The gravity profile in mGal calculated on a plane 0.5 km above the surface of the overriding plate for the model of 400 km penetration, asthenosphere viscosity $\mu = 10^{20}$ Pa s including the olivine-spinel transition, the low viscosity $\mu = 10^{20}$ Pa s and the density anomaly of the thermal anomaly. The lower box shows the position of the density anomalies.
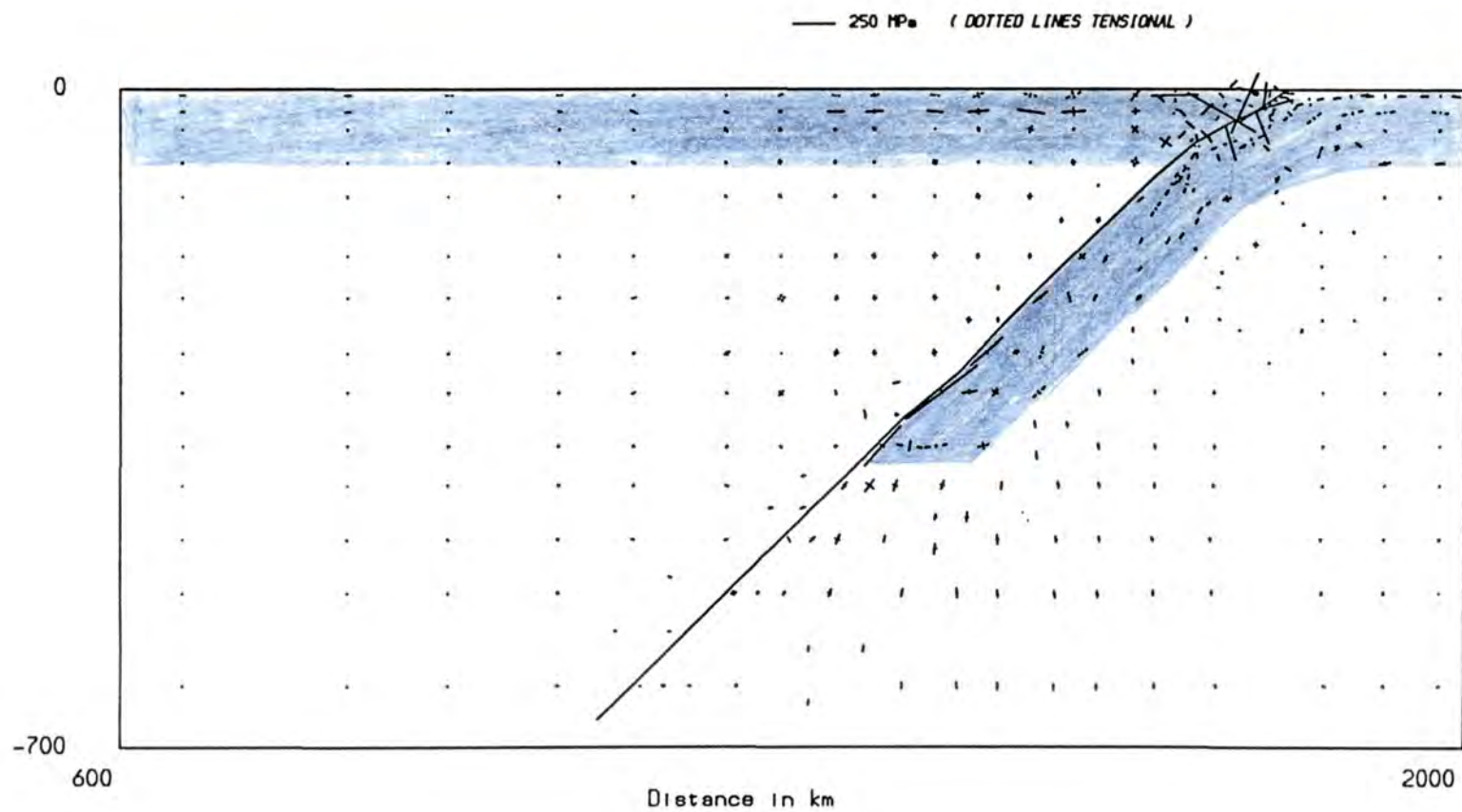
Figure 5.66 The principal stresses for the model of 400 km penetration, astheno-
sphere viscosity $\mu = 10^{20}$ Pa s including the olivine-spinel transition and the
full thermal anomaly. The solid line denotes the position of the fault. The
shading denotes the lithosphere. A scale length of vector magnitude is given
above.

Surface displacement profile (in m)

Distance in km
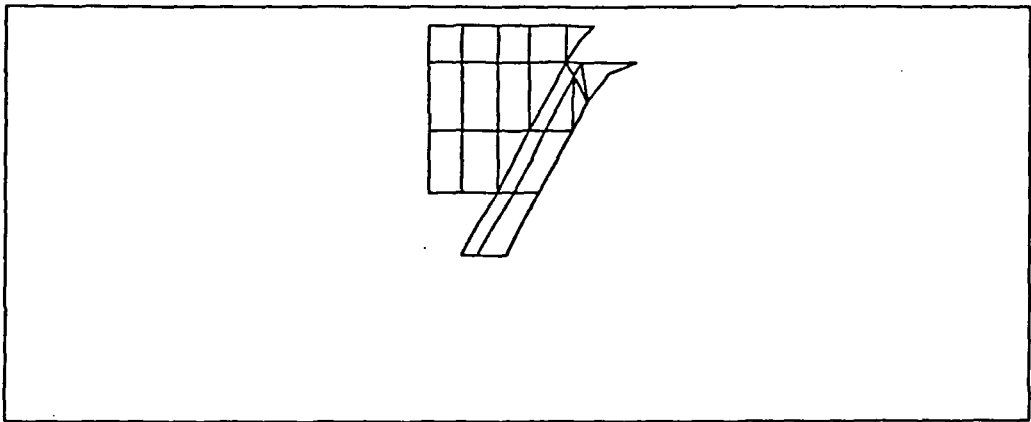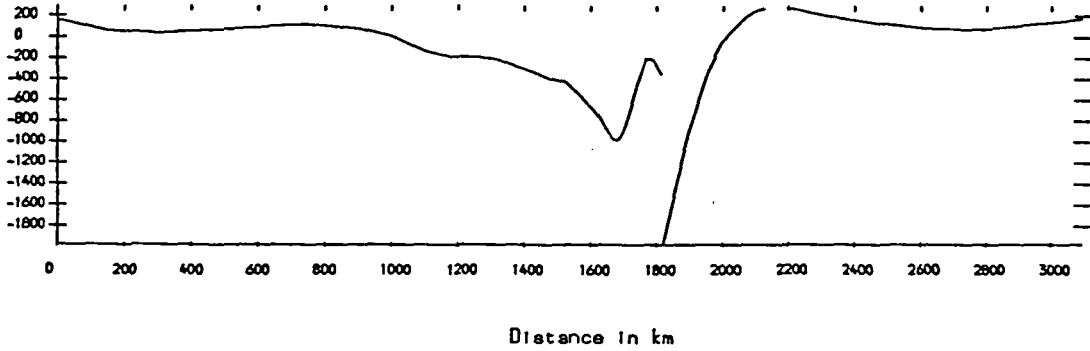
Figure 5.67   The vertical displacement of the surface for the model of 400 km penetration, asthenosphere viscosity $\mu = 10^{20}$ Pa s including the olivine-spinel transition and the full thermal anomaly. The left hand curve denotes the overriding plate, the right hand curve denotes the subducting plate. The lower box shows the relative position of the density anomalies.
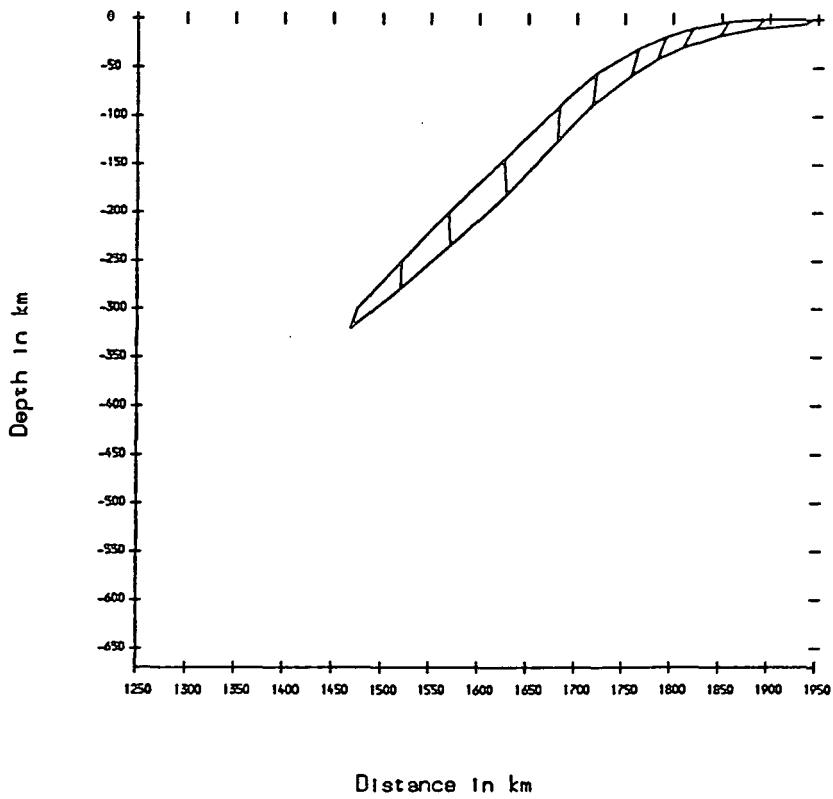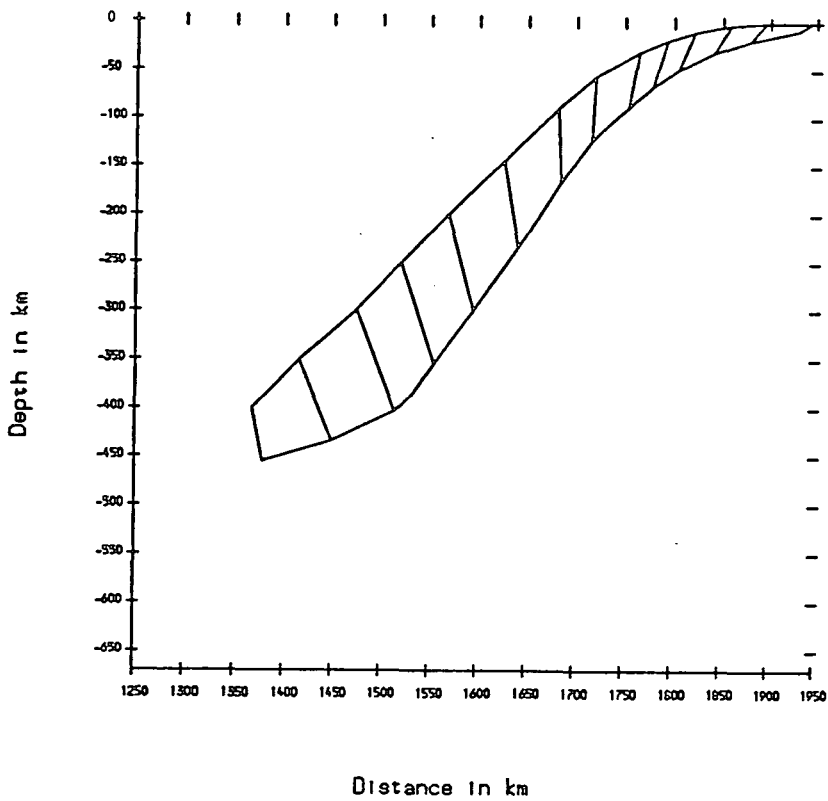
Figure 5.68   The absolute slab motion linearly extrapolated by a factor of 20 for the model of 400 km penetration, asthenosphere viscosity $\mu = 10^{20}$ Pa s including the olivine-spinel transition and the full thermal anomaly. The upper curve denotes the original position of the top surface of the slab and the lower curve denotes the final position of the top surface of the slab. The cross-lines represent displacement vectors of the nodes.
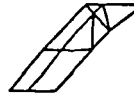
Gravity Profile

Anomaly in mgal

90
80
70
60
50
40
30
20
10
0

0   200   400   600   800   1000   1200   1400   1600   1800

Distance in km
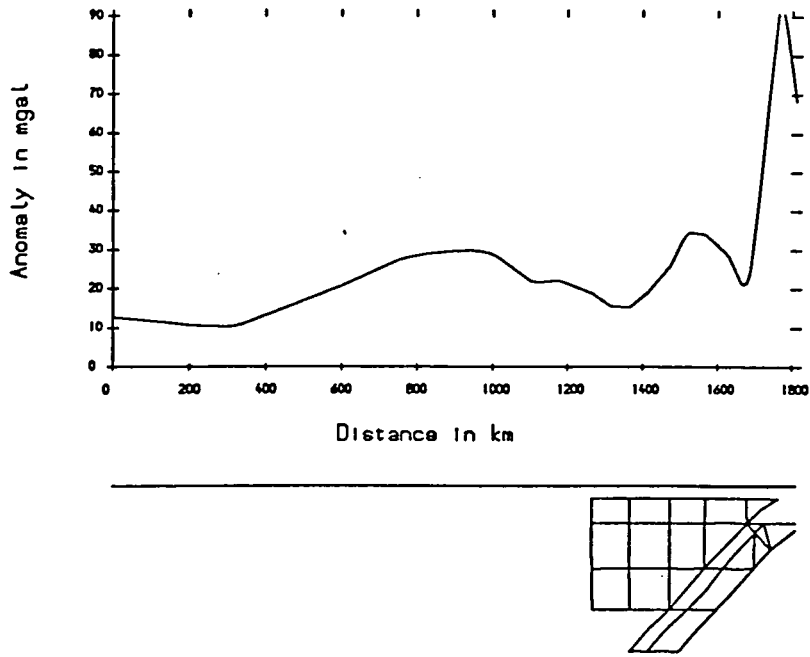
Figure 5.69 The gravity profile in mGal calculated on a plane 0.5 km above the surface of the overriding plate for the model of 400 km penetration, asthenosphere viscosity $\mu = 10^{20}$ Pa s including the olivine-spinel transition and the full thermal anomaly. The lower box shows the position of the density anomalies.

anomaly is added according to the distribution in figure 5.56, and the stress regime, surface displacement, slab motion and gravity profile are shown in figures 5.66 - 5.69. The sole change occurs in the stress field (figure 5.66). The elastic layer of the overriding plate above the anomaly has developed near-surface tensions and underlying compressions both of about 100 MPa. The remainder of the stress field is unaffected, as expected (see section 3.2).

The sequence of stress regime, surface displacement, slab motion and gravity profile in figures 5.70 - 5.73 result from the addition of a backarc thermal anomaly to a model of slab penetration to 300 km depth including a low viscosity asthenosphere. The viscosity, density and temperature anomalies each produce effects similar to the previous model, but appear to be enhanced by this shallower subduction, probably because the size of the anomaly has been overestimated. The combined effect of the viscosity and density anomaly completely eliminates the backarc depression, creating large tensions in the surface as the overriding plate is bent down sharply in the region of the arc. The temperature anomaly affects only the elastic layer, producing 100 MPa tensions above compressions as in the previous model.

A volcanic arc is assumed to contain a maximum of 10 km of crustal thickening of density $\rho = 2900$ kg m^{-3} at the surface. To simulate this isostatic load on the model of slab penetration to 400 km a normal stress of 200 MPa is applied over a width of 110 km at the surface. This is balanced on the underside of the elastic layer by equal and opposite stresses. The position of the arc is depicted by vertical vectors which represent the relative magnitude of the applied forces. The resulting stress regime in figure 5.74 depicts a 400 × 200 km area around the forearc and shows large deviatoric vertical compressions and horizontal tensions in the region of the arc.

Thus the thermal anomaly in the backarc, as implemented in these models, has a profound effect on the stress distribution at subduction zones; it generates a component of horizontal tension in the lithosphere above the anomaly and allows a double seismic zone to develop in the descending slab. The state of stress in the backarc is dependent on the relationship between viscous coupling and the thermal anomaly in the backarc. Horizontal tension is predicted despite up to 1 km depression of the overriding plate for the 400 km penetration model (figure 5.67).
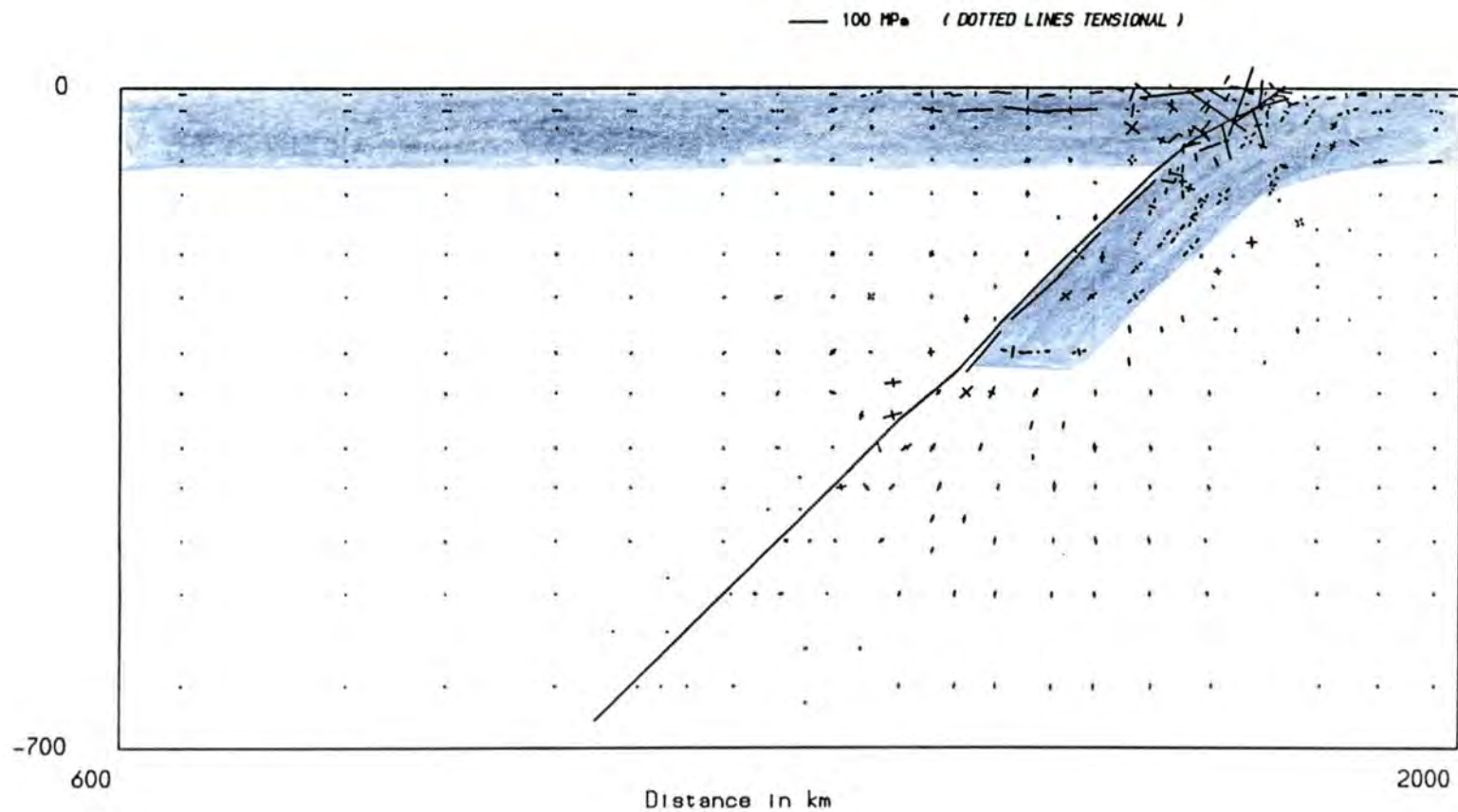
Figure 5.70   The principal stresses for the model of 300 km penetration, astheno-
sphere viscosity $\mu = 10^{20}$ Pa s and the full thermal anomaly. The solid line
denotes the position of the fault. The shading denotes the lithosphere. A scale
length of vector magnitude is given above.

Surface displacement profile (in m)

Distance in km
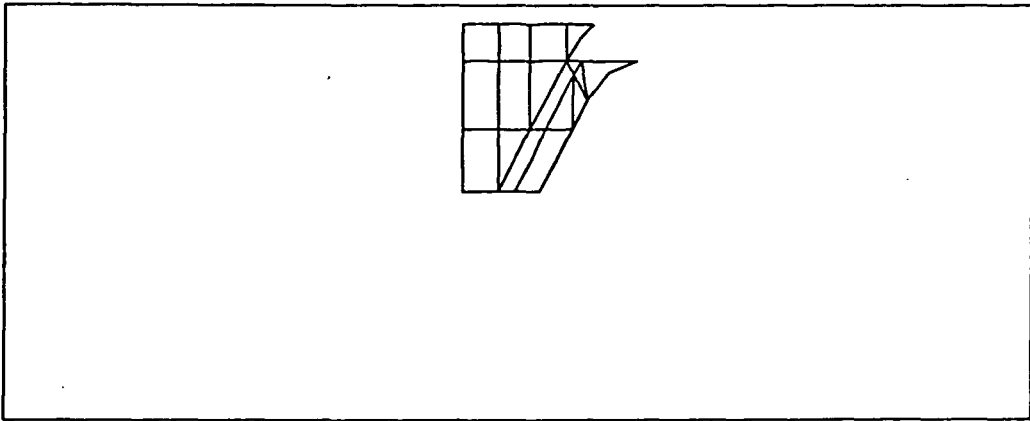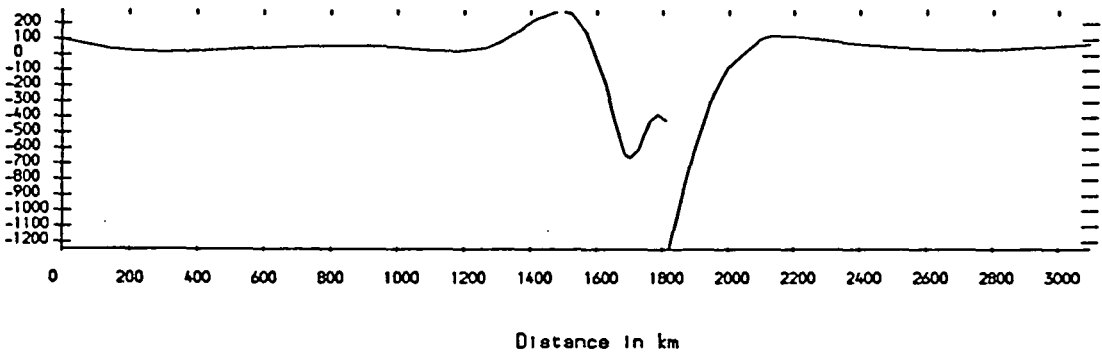
Figure 5.71   The vertical displacement of the surface for the model of 300 km pen-
etration, asthenosphere viscosity $\mu = 10^{20}$ Pa s and the full thermal anomaly.
The left hand curve denotes the overriding plate, the right hand curve denotes
the subducting plate. The lower box shows the relative position of the density
anomalies.
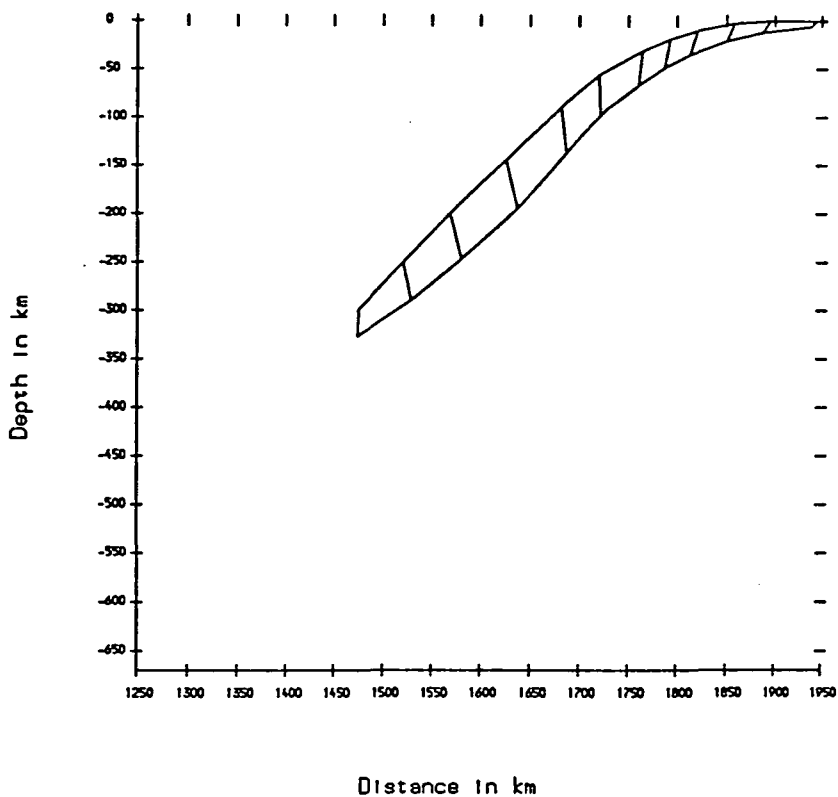
Figure 5.72   The absolute slab motion linearly extrapolated by a factor of 20 for the model of 300 km penetration, asthenosphere viscosity $\mu = 10^{20}$ Pa s and the full thermal anomaly. The upper curve denotes the original position of the top surface of the slab and the lower curve denotes the final position of the top surface of the slab. The cross-lines represent displacement vectors of the nodes.
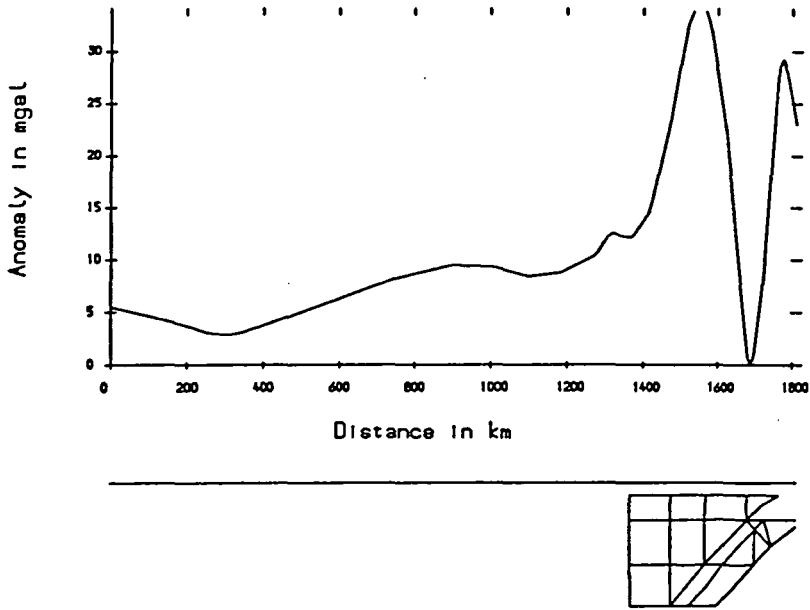
Gravity Profile

Figure 5.73 The gravity profile in mGal calculated on a plane 0.5 km above the surface of the overriding plate for the model of 300 km penetration, asthenosphere viscosity $\mu = 10^{20}$ Pa s and the full thermal anomaly. The lower box shows the position of the density anomalies.
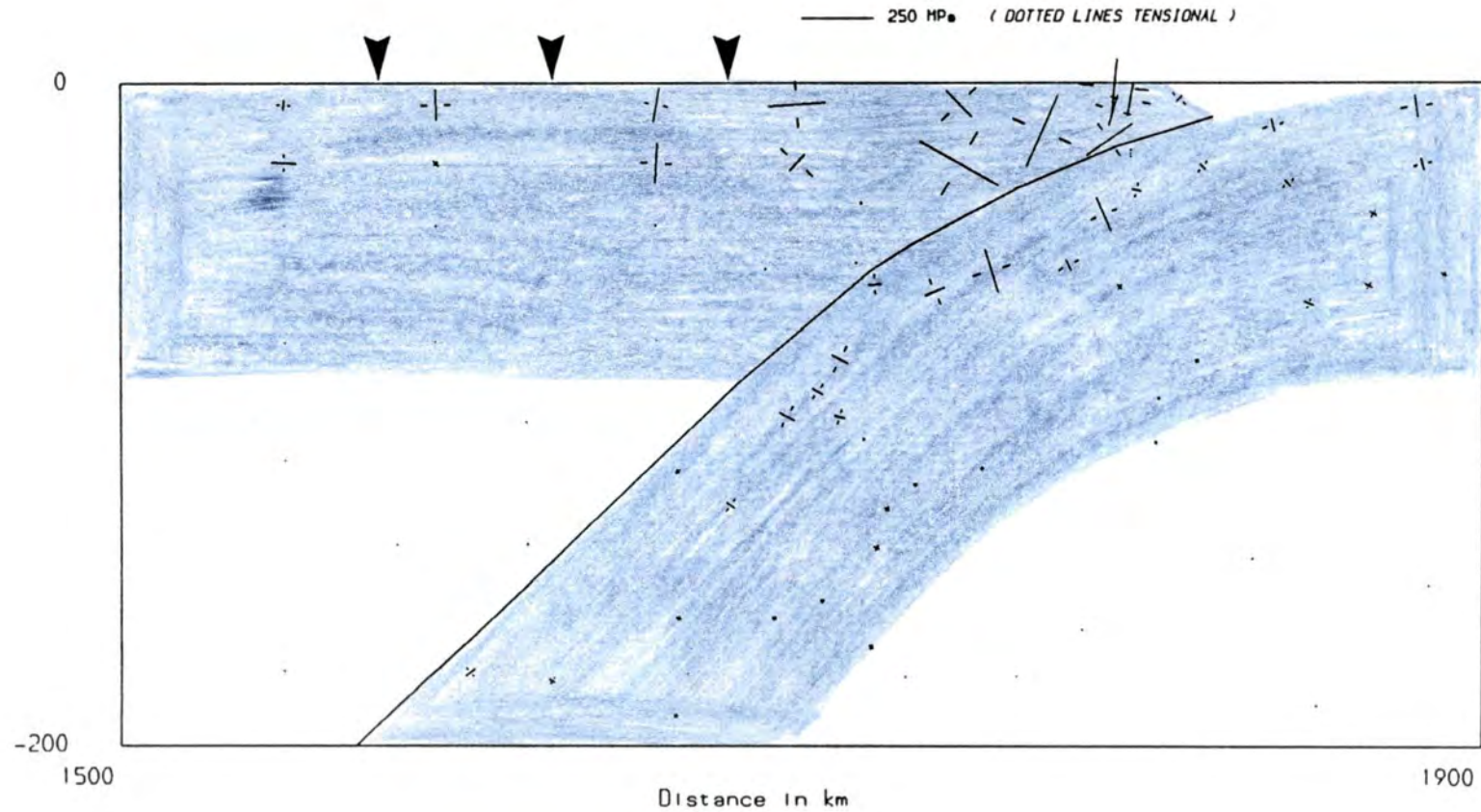
Figure 5.74 The deviatoric principal stresses for the model of 400 km penetration, asthenosphere viscosity $\mu = 10^{20}$ Pa s including the olivine-spinel transition and the full thermal anomaly. The load of the arc is designated by vertical arrows. The solid line denotes the position of the fault. The shading denotes the lithosphere. A scale length of vector magnitude is given above.

5.7 Boundary Force On The Overriding Plate

5.7.1 Problem Statement

The introductory comments of this chapter acknowledge that the boundary conditions at the far edges of the surface plates will have a strong influence over the stress regime. The boundary condition at the far edge of the subducting plate requires special consideration and will be dealt with in full in the final discussion. In all models zero horizontal motion is prescribed at this edge and this produces horizontal tension in the subducting plate and rollback of the trench and slab.

The model of slab penetration to 400 km depth from the previous section, including low viscosity asthenosphere and backarc anomaly, now has a normal stress of 20 MPa applied to the left hand edge of the overriding plate. A tension may cause the plate to retreat relative to trench motion, and a compression may cause the plate to advance seaward relative to the trench. Once again the relaxation period is 50 000 yrs.

5.7.2 Discussion of Results

A tensional tectonic stress results in the stress regime, surface displacement and slab motion in figures 5.75 - 5.77. The horizontal tension of the far backarc is increased from 30 MPa to 70 MPa and the near-surface tension above the backarc is slightly enhanced compared to figure 5.66. Most surprisingly, the stress regime of the slab is disturbed. In the upper sections of the slab the upper surface has regained its tensional character. thus eliminating the possibility of a double seismic zone developing. Applying a compressional tectonic stress produces the stress regime, surface displacement and slab motion in figures 5.78 - 5.80. The far backarc is now neutral, the tension over the backarc anomaly is almost eliminated but the underlying compression remains. The upper surface of the slab is now more compressional than figure 5.66, enhancing the double seismic zone.

The change in stress distribution of the overriding plate is explained by the surface displacement profiles in figures 5.76 and 5.78. The thrust zone at the trench causes a 'fault-like' behaviour of the plates in response to the tectonic stresses. Tension causes a normal faulting effect and the overriding plate bends down at the trench. Likewise,

96
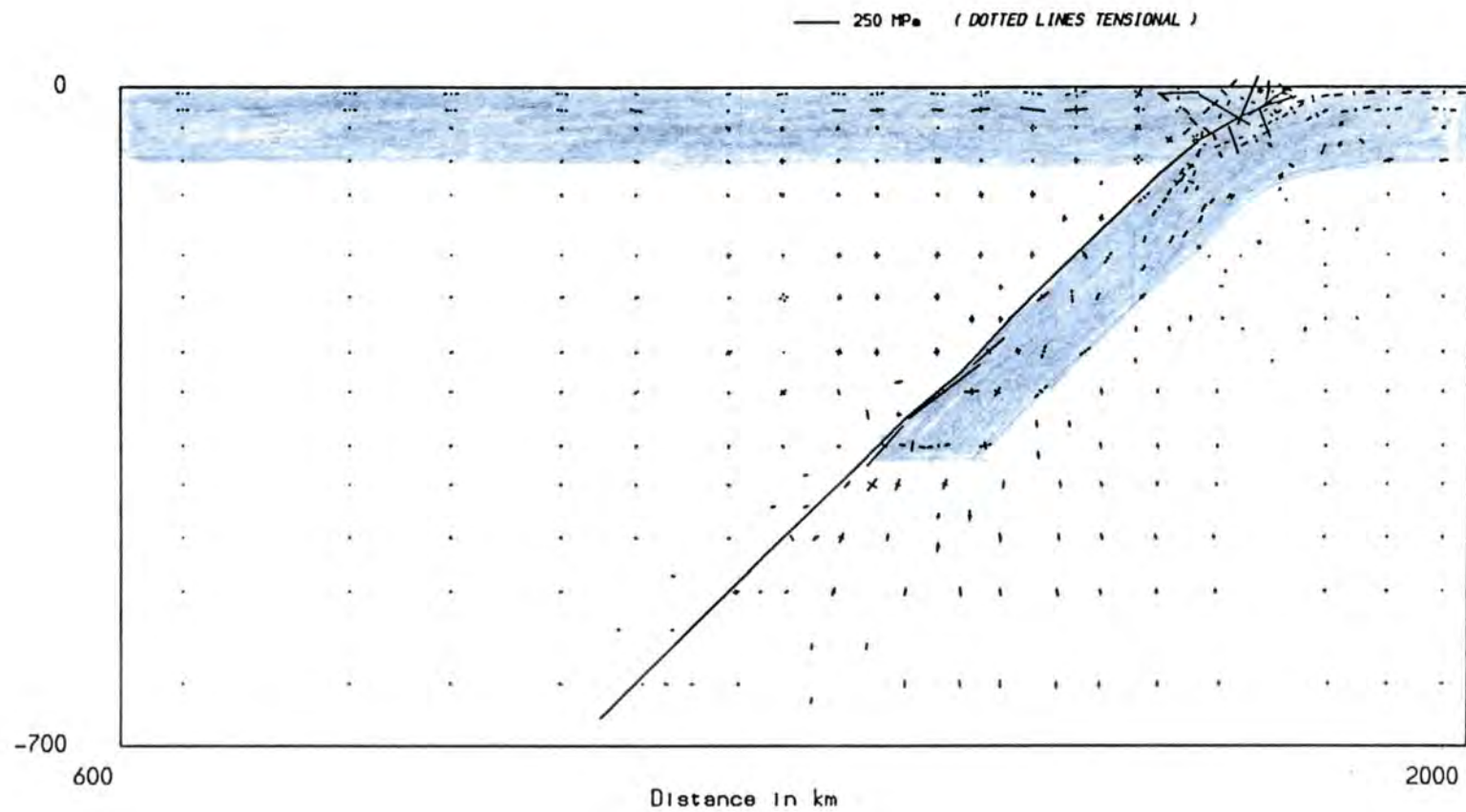
Figure 5.75   The principal stresses for the model of 400 km penetration, astheno-
sphere viscosity $\mu = 10^{20}$ Pa s including the olivine-spinel transition and the
full thermal anomaly. A 20 MPa tension is applied to the left hand edge.
The solid line denotes the position of the fault. The shading denotes the
lithosphere. A scale length of vector magnitude is given above.

Surface displacement profile (in m)

Distance in km
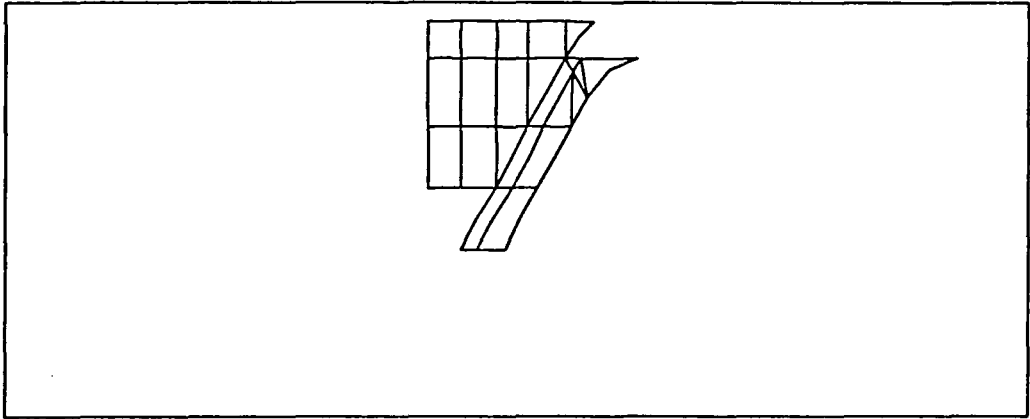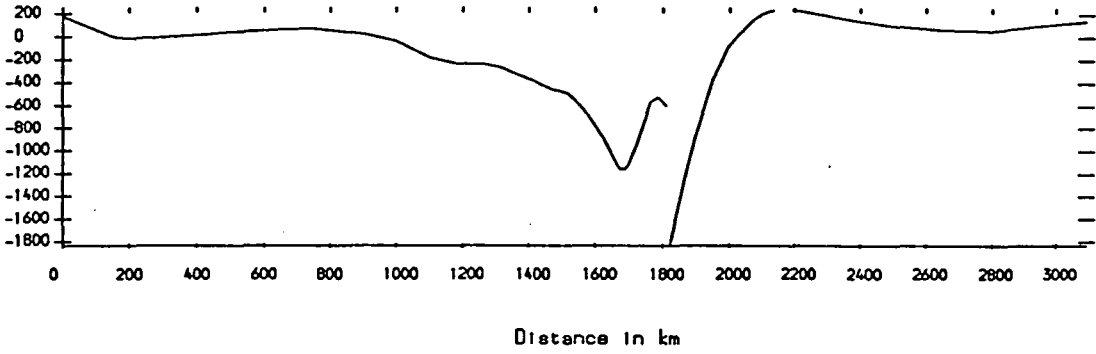
Figure 5.76   The vertical displacement of the surface for the model of 400 km penetration, asthenosphere viscosity $\mu = 10^{20}$ Pa s including the olivine-spinel transition and the full thermal anomaly. A 20 MPa tension is applied to the left hand edge. The left hand curve denotes the overriding plate, the right hand curve denotes the subducting plate. The lower box shows the relative position of the density anomalies.
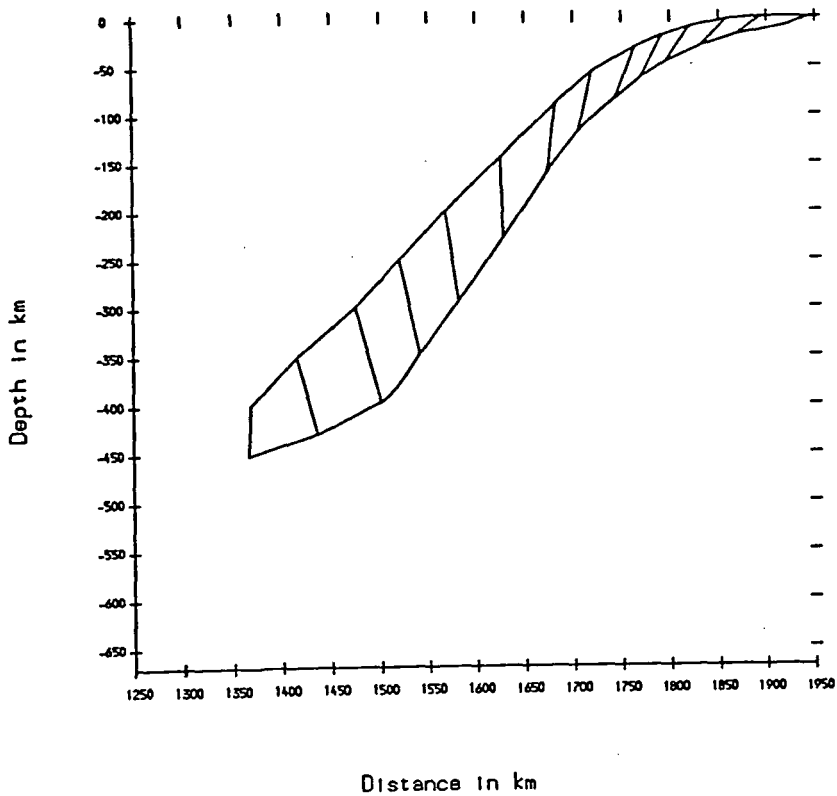
Figure 5.77   The absolute slab motion linearly extrapolated by a factor of 20
for the model of 400 km penetration, asthenosphere viscosity $\mu = 10^{20}$ Pa s
including the olivine-spinel transition and the full thermal anomaly. A 20 MPa
tension is applied to the left hand edge. The upper curve denotes the original
position of the top surface of the slab and the lower curve denotes the final
position of the top surface of the slab. The cross-lines represent displacement
vectors of the nodes.
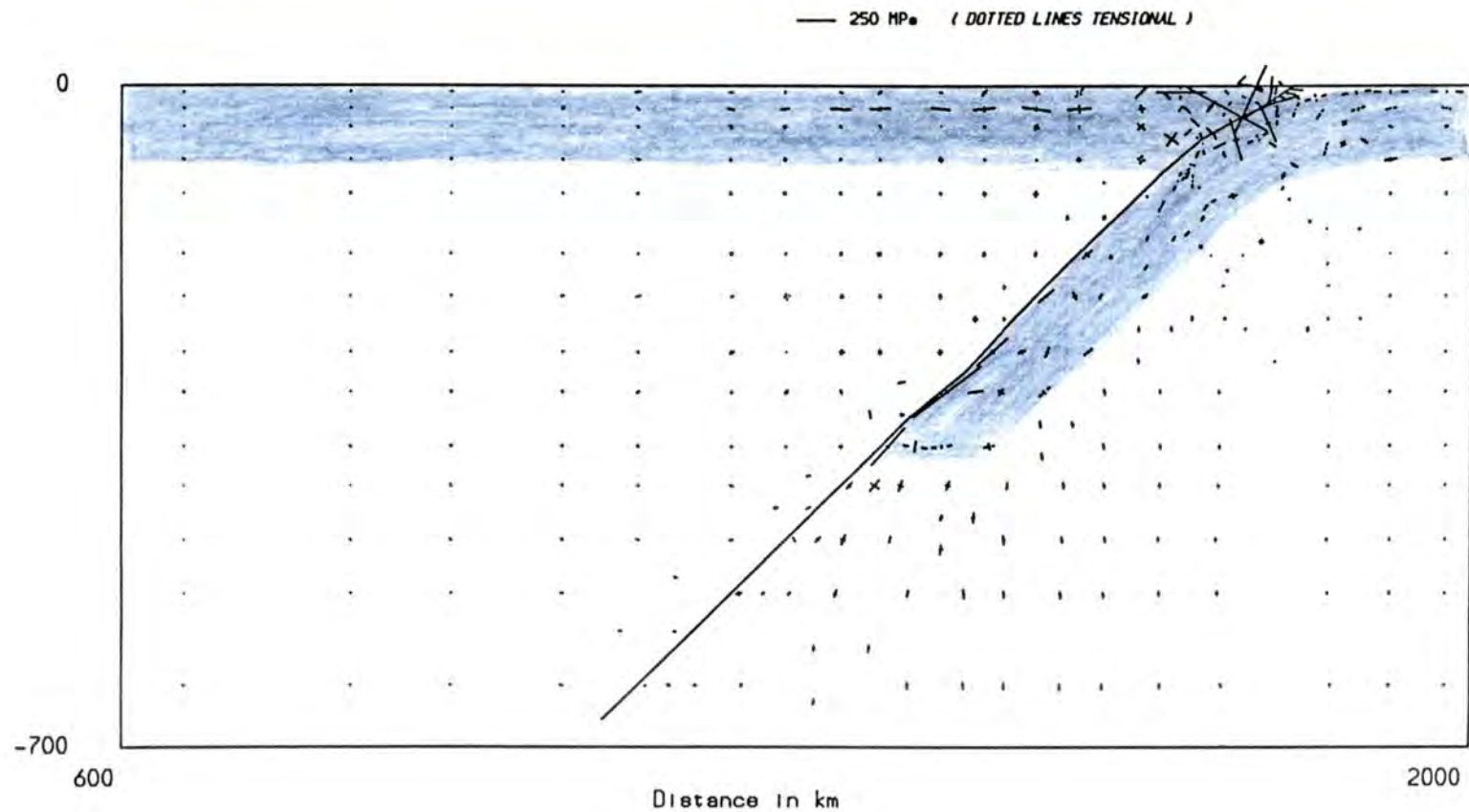
Figure 5.78 The principal stresses for the model of 400 km penetration, asthenosphere viscosity $\mu = 10^{20}$ Pa s including the olivine-spinel transition and the full thermal anomaly. A 20 MPa compression is applied to the left hand edge. The solid line denotes the position of the fault. The shading denotes the lithosphere. A scale length of vector magnitude is given above.

Surface displacement profile (in m)

Distance in km
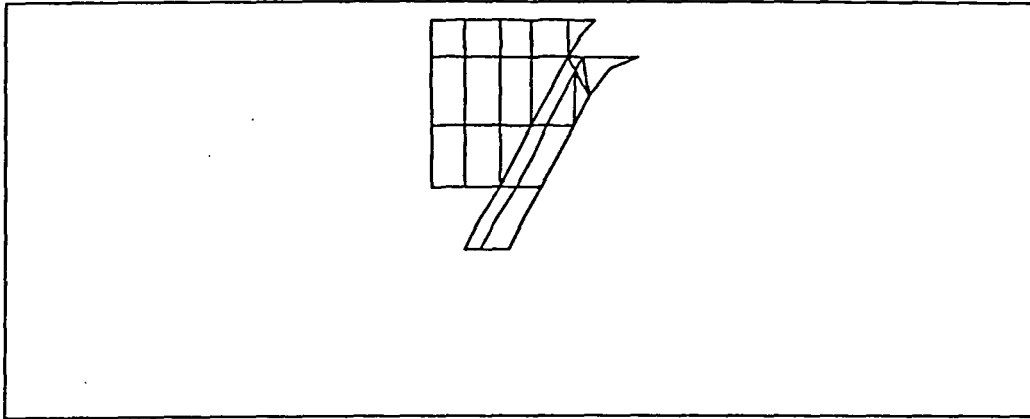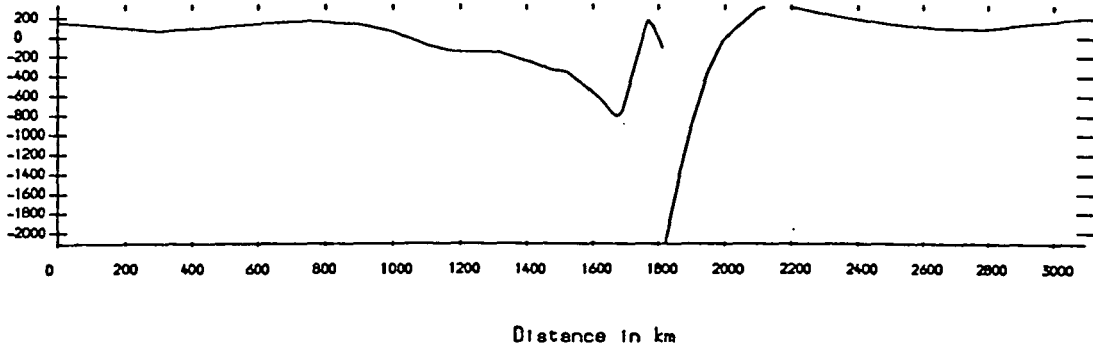
Figure 5.79   The vertical displacement of the surface for the model of 400 km penetration, asthenosphere viscosity $\mu = 10^{20}$ Pa s including the olivine-spinel transition and the full thermal anomaly. A 20 MPa compression is applied to the left hand edge. The left hand curve denotes the overriding plate, the right hand curve denotes the subducting plate. The lower box shows the relative position of the density anomalies.
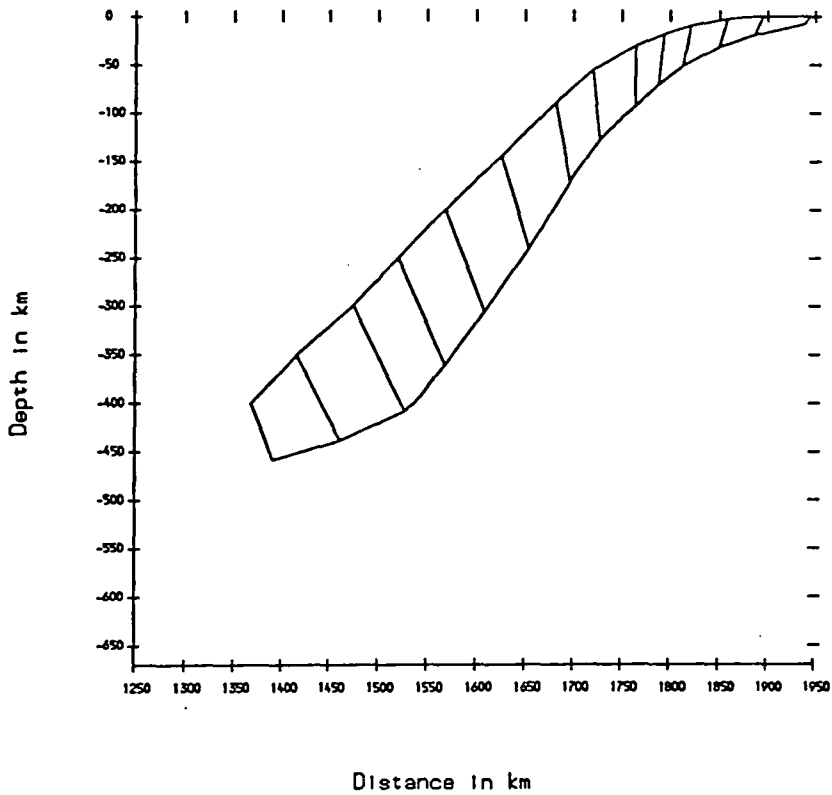
Figure 5.80   The absolute slab motion linearly extrapolated by a factor of 20 for the model of 400 km penetration, asthenosphere viscosity $\mu = 10^{20}$ Pa s including the olivine-spinel transition and the full thermal anomaly. A 20 MPa compression is applied to the left hand edge. The upper curve denotes the original position of the top surface of the slab and the lower curve denotes the final position of the top surface of the slab. The cross-lines represent displacement vectors of the nodes.
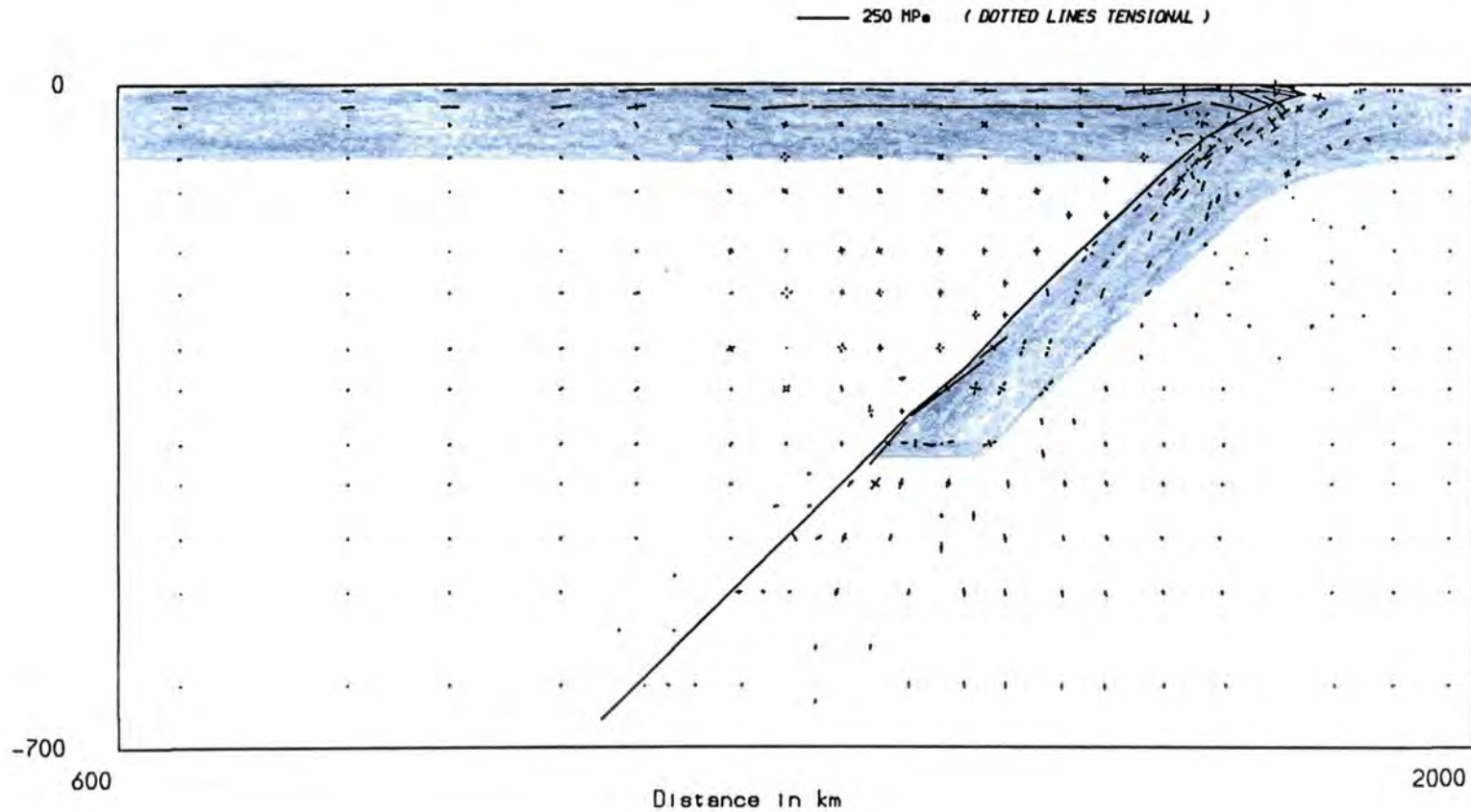
Figure 5.81   The principal stresses for the model of 400 km penetration, astheno-
sphere viscosity $\mu = 10^{20}$ Pa s including the olivine-spinel transition and the
full thermal anomaly. A 20 MPa compression is applied to the left hand edge
and the fault locked. The solid line denotes the position of the fault. The
shading denotes the lithosphere. A scale length of vector magnitude is given
above.

Surface displacement profile (in m)

Distance in km
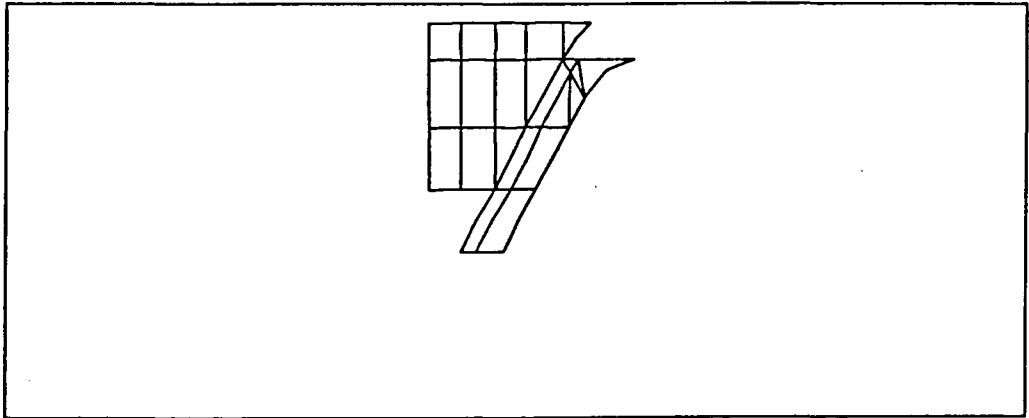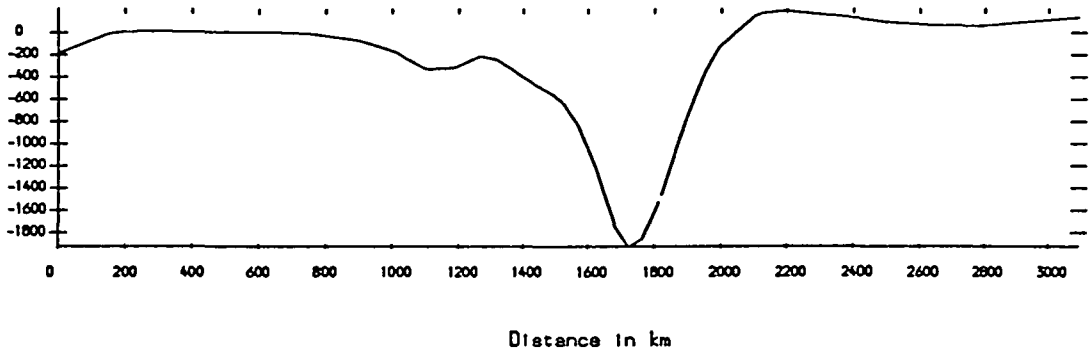
Figure 5.82   The vertical displacement of the surface for the model of 400 km penetration, asthenosphere viscosity $\mu = 10^{20}$ Pa s including the olivine-spinel transition and the full thermal anomaly. A 20 MPa compression is applied to the left hand edge and the fault locked. The left hand curve denotes the overriding plate, the right hand curve denotes the subducting plate. The lower box shows the relative position of the density anomalies.
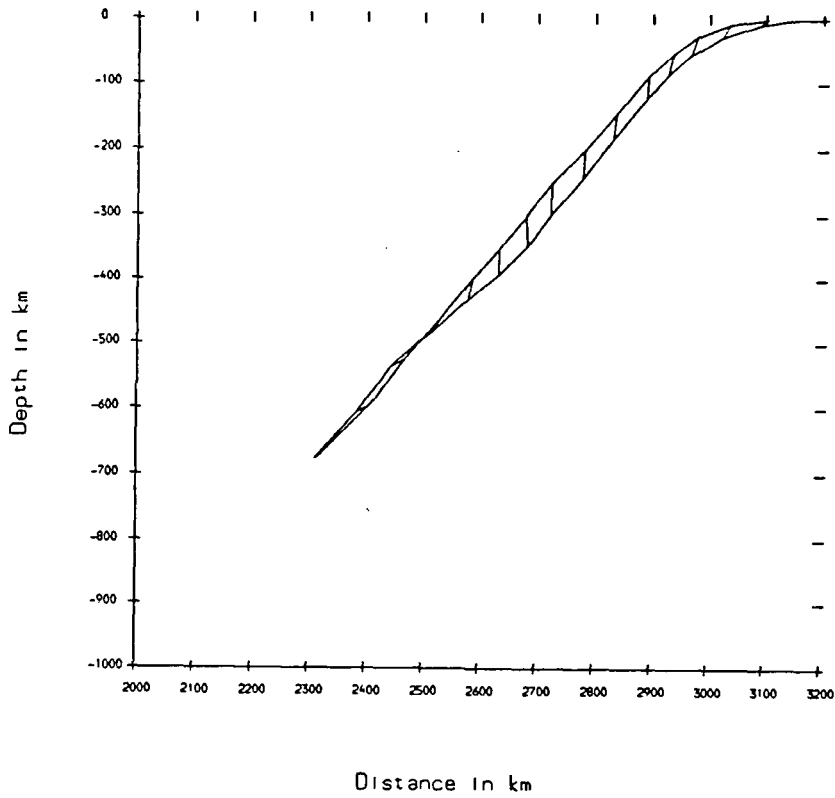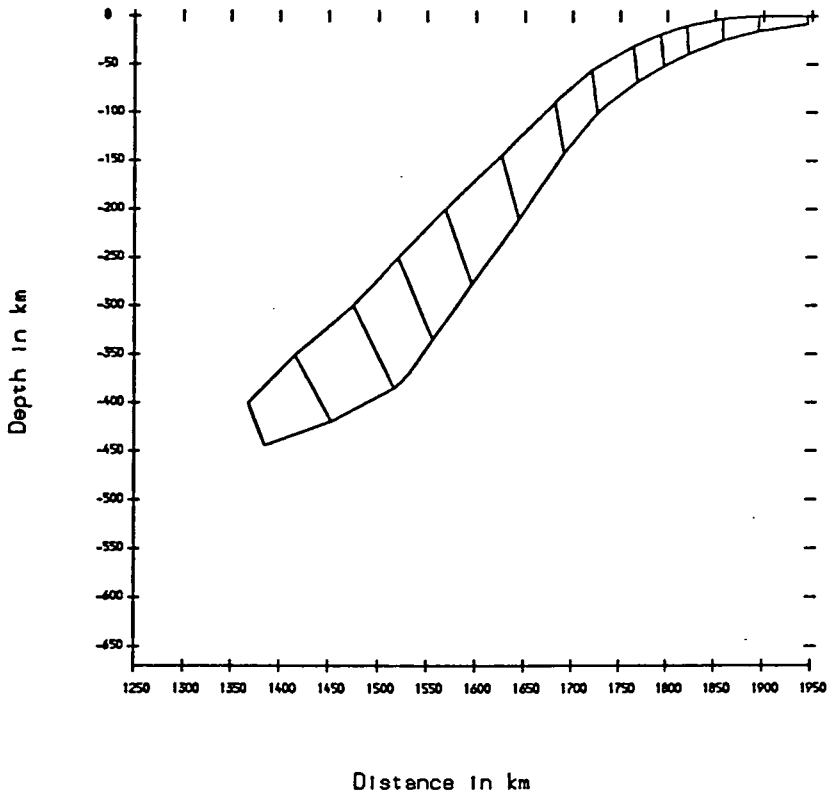
Figure 5.83   The absolute slab motion linearly extrapolated by a factor of 20 for the model of 400 km penetration, asthenosphere viscosity $\mu = 10^{20}$ Pa s including the olivine-spinel transition and the full thermal anomaly. A 20 MPa compression is applied to the left hand edge and the fault locked. The upper curve denotes the original position of the top surface of the slab and the lower curve denotes the final position of the top surface of the slab. The cross-lines represent displacement vectors of the nodes.

compression causes the leading edge of the plate to flex upwards.

The absolute motion of the subducting slab is shown in figures 5.77 and 5.80. This demonstrates how the tectonic stress influences the stress distribution of the slab. The shallow dip of the slab (in the depth range 0 — 100 km) is decreased by tension and increased by compression, as it is controlled by the coupling to the overriding plate. In turn this influences the whole trajectory of the slab motion and thus alters the slab stresses.

Compression is the most probable boundary stress since the overriding plate is quite possibly attached to a mid-ocean ridge. This is therefore the most complete general model of a subduction zone, so it is appropriate to return to the question of the behaviour of the thrust zone (see section 5.2). The stress regime, surface displacement and slab motion in figures 5.81 - 5.83 result from locking the thrust zone. Compared to figure 5.78 there is a regional horizontal compression in the overriding plate, and elimination of the double seismic zone as the descent of the plate is slightly changed.

An identical 20 MPa stress was applied to the model of slab penetration to 300 km, including the thermal anomaly and asthenosphere as in the previous section. The stress regimes show a similar behaviour to the preceding model of penetration to 400 km depth.

5.8   Limitations of the Models

The initial assumptions of the finite element models presented in this chapter demand some justification. Slab dip was chosen to be a constant 45° from the base of the lithosphere down into the lower mantle. A specific Wadati-Benioff zone profile was not modelled because of the huge variation in observed profiles from which to take an 'average', and because of the difficulty of estimating the residual bending stresses which generate the shape. No quantitative account has been attempted of the effect of variation in slab dip and thus the effects, such as depression of the overriding plate, which depend on the slab dip must be interpreted with this in mind. The upthrust of the trench was not included and this is expected to affect the stress regime of the slab and the surface plates as the isostatic reaction to the slab forces is distributed over a somewhat wider area in the models presented. This particular problem is discussed

further in the next chapter. As a consequence of slab pull trench depths up to 2 km develop, which are about 60% of the observed average trench depth. Outer rises of about 200 – 300 m amplitude are produced by the downbending at the trench and probably aided by the flow driven by rollback, but both features are very broad due to the inadequate response of the lower lithosphere.

The fault couples the mesh halves along the line of the top surface of the descending slab. The isoparametric fault element allows variation in the elastic properties of the fault with depth. Above 200 km depth the three shallowest fault elements were either shear coupled ($k_s = 10^{15}$ N m^{-1}) or shear decoupled ($k_s = 0$). The fault must be shear decoupled down to 200 km depth to allow the upper two fault elements to move freely with respect to one another. The thrust zone was either locked or unlocked, and so the models did not investigate the variation in mechanical coupling along the thrust zone. In conjunction with the angle of contact of the thrust, the mechanical coupling is expected to control the amount of compression transmitted across the fault into the overriding plate.

The mesh was density stripped to reveal the stresses more clearly. Under the plane strain approximation finite element models using full densities do not produce the lithostatic stress field (Park 1981). The actual stress field can be retrieved simply by the addition of the overburden (hydrostatic stress) to the stresses generated by the density stripped model. Unfortunately the density stripping does present a small problem for the simulation of subduction. In these models the slab is dragging neutrally buoyant lithosphere into the asthenosphere, when in reality the lithosphere just above 90 km depth is of a higher density than the adjacent asthenosphere. This could be considered as a relative upthrust which causes the slab to rotate about its centre of mass (rather than sink obliquely) pushing the slab tip seaward and the trench landwards. However, if the far edge of the subducting plate is fixed, then the slab will hinge about the trench and rollback with respect to the subducting plate. This does not overcome the problem of neutrally buoyant lithosphere arriving at the trench but it is a good approximation for short relaxation periods which do not involve large displacements.

Newtonian viscoelasticity is the rheology assigned to the mantle and this is an approximation since it does include the convective heat transport. Creep motion driven by the deviatoric stresses provides a good description of the initial flow of the viscous

fluid in response to the loads, but it cannot predict the long term behaviour. In this respect the models are considered on a 'first motion' basis. The models do not come to equilibrium but are stopped at 50 000 yrs which is convenient to prevent instability in the algorithm. However, the forces in the mantle may not be exactly balanced as is expected at a subduction zone and this may affect the final stress distribution. The equilibrium force balance between the slab body forces and the mantle resistance is discussed in the next chapter.

The most significant limitation of these models is the question of rheology. The omission of the crust is due to the low resolution of the finite element mesh, and this was discussed earlier. The models would also benefit from a non-Newtonian rheology for the lower lithosphere. High stress regions generate a large reduction in effective viscosity allowing much quicker relaxation of the stresses, but this would not affect the magnitude of the elastic stresses. The age-dependent thickness, and thus its variation along the length of the lithosphere, was not included. The mantle was considered to be uniform except for the viscosity-depth variation. A more sophisticated model should take into account the vertical and lateral variation of elastic constants and density. The end of the Wadati-Benioff zone is usually taken to be the slab tip, and in these models the slab tip influenced the slab mechanics. The exact rheology of the end of the slab is unknown and more detailed thermal modelling of this aspect is required to produce better mechanical models of the descending lithosphere.

The subducting and overriding plates were represented by uniform oceanic litho-sphere in the preceding models but the rheology is a great deal more complicated. The subducting plate decreases in age perpendicular to the strike of the trench, with a corresponding decrease in thickness of the lithosphere. Variations in thermal thickness of the lithosphere were not included in the models. In the overriding plate crustal and lithospheric thickness variations throughout the forearc-arc-backarc region contribute to the loads and strength of the plate. In addition the possibility of continental litho-sphere as the overriding plate was not investigated due to the complexity of the crustal loading and rheology of continental lithosphere.

The majority of thermoelastic effects have not been included. Apart from a very simple linear vertical temperature gradient across the lithosphere in the backarc, temperature gradients in the arc, forearc and slab have been ignored. An important ther-

moelastic stress is generated by conductive heating of descending slab. All the models were calculated under the plane strain approximation, but 3-D effects such as the spherical shell tectonics described by Yamaoka (1988) are important.

CHAPTER 6

Discussion

In this chapter the results of the models of flow in the mantle and the models of stress regime are interpreted to provide a generalised description of the two dimensional mechanics and dynamics of a convergent margin. One of the dominant themes of this thesis is the investigation of the causes of the lateral variation of the state of stress in the surface plates across the strike of convergent margins. Identifying the stress generation mechanisms should lead towards a better understanding of the origin of the driving forces of plate motion. In addition, the analysis of the deep structure of subduction should yield some insight into the evolution of subduction zones and the dynamics of subducting slabs, particularly with respect to the factors controlling the time dependence. For clarity and to avoid repetition the following discussion refers to the plots and diagrams which can be found in the previous two chapters.

6.1   The Stress Regime in the Surface Plates

The main source of tectonic stress in the surface plates at subduction zones arises from the pull of the descending slab. The forces exerted by the (non-vertical) slab are coupled to the plates by two distinct mechanisms, these are termed elastic coupling due to the physical continuity of the lithosphere through the slab bend, and viscous coupling which is due to the transmission of stress through the mantle wedge. The viscous coupling applies (predominantly) vertical forces to the base of the lithosphere whilst the elastic coupling has both a vertical and a horizontal component of the in-plate tension.

Consider this distribution of forces applied to the base of a continuum lithosphere with the thrust zone locked, as modelled in figure 5.4. The vertical forces produce an asymmetric local depression. The isostatic reaction at the surface generates vertical tension in the lithosphere which in turn produces horizontal deviatoric compression. Relaxation of the lower lithosphere leads to a concentration of the compression in the

101

upper elastic layer. Bending stresses are superimposed but are much smaller. The depression causes an overall shortening of the surface lithosphere but the fixed boundary at the right hand edge of the subducting plate restricts lateral motion and induces large horizontal tension in the subducting plate. The left hand edge is unrestrained, it is dragged seawards and viscous resistance in the asthenosphere can generate very small horizontal tensions near the left hand edge of the overriding plate. The horizontal component of the elastic coupling generates horizontal tension in the subducting plate since it acts against the fixed boundary at the right hand edge. This horizontal force is also transmitted across the thrust zone to act on the overriding plate. The left hand edge of the plate is unrestrained and so only small compressions would be produced. An additional component of regional horizontal tension in the overriding plate is created by the normal coupling at the fault which causes the leading edge of the overriding plate to follow the slab rollback. The models cannot separate the competing effects of rollback and the horizontal component of elastic coupling which are manifestations of resolving the vertical body force of the slab in the downdip direction.

Unlocking the thrust zone causes a redistribution of the stresses both locally and regionally (figure 5.8). In the immediate vicinity of the thrust the subducting plate is now under surface-parallel tension. In addition a component of regional tension is introduced into the subducting and overriding plates.

Lithosphere at the thrust zone is held out of isostatic equilibrium by the vertical pull of the slab body force. In conjunction with the isostatic reaction at the surface, horizontal compression is produced in the lithosphere as described previously (see section 5.2.2). With the fault locked the fault walls support equal and opposite shear stresses due to the compression. Unlocking the fault decouples the stresses in the plate edge either side of the fault and the plate reacts to relieve the shear stress on its edge. For the overriding plate this results in positive vertical and horizontal forces which cause slight uplift and horizontal tension in the plate. In the subducting plate negative vertical and horizontal forces are produced and this causes further depression of the edge and regional horizontal tension within the plate. The mechanism will be controlled by the angle of the thrust zone, the mechanical coupling at the fault, the angle of slab dip, and the magnitude of in-plate tension at the top of the slab.

The increase in regional tension is depicted quite clearly in figures 5.4 and 5.8,

but the stress magnitudes are complicated by the boundary conditions, the change in amplitude of the surface depression, bending stresses and rotation of the fault zone. A major limitation of the models is the spatial distribution of the isostatic reaction at the surface. The trench is not included explicitly and so the reaction to the vertical component of elastic coupling is distributed over much longer wavelengths rather than concentrated at the trench. This may affect the relative magnitude of each contribution to the regional stress.

The regional stress regime in the surface lithosphere can be interpreted to derive the origin of the plate driving forces (see section 1.3). The slab pull force drags the subducting plate into the trench. The finite element models show that horizontal tension in the subducting plate is generated by shear slip at the thrust zone in response to the vertical body forces of the slab. The trench suction force drags the overriding plate into the trench and a regional tension is similarly produced by shear slip at the thrust zone in response to the vertical body forces of the slab (Bott et al. 1988).

In resolving the slab body force downdip two equal and opposite horizontal forces are created which act on the base of the lithosphere at the top of the slab. The horizontal component of the downdip force increases the slab pull force, but is not transmitted to the overriding plate if the thrust zone is unlocked. An equal and opposite horizontal force arises from slab rollback. Since the overriding plate is coupled normally across the thrust zone it must follow the slab and trench rollback and this may generate a small regional horizontal tension in the plate.

The regional stress regime gives an indication of the driving forces but the origin of local lateral variations in stress is also of interest. Starting on the subducting plate and working landwards, the stress regimes are split into four sections, the outer trench slope, the forearc, the arc, and the backarc.

As a consequence of slab pull a trench and outer rise flexure system develops in all models (see displacement profiles e.g. figures 5.14, 5.43, 5.53). This is a much broader feature than the flexure observed at present-day margins and this is a limitation of the models (see discussion in section 5.8). Shear slip at the thrust zone causes large surface-parallel tensions in the near-surface of the outer trench slope. These tensions are predominantly due to bending (e.g. figures 5.13 and 5.42). The seismicity and geology of the outer trench slope are characterised by normal faulting and graben formation

which is usually attributed to the bending stresses of flexure caused by slab pull. The stress state of the finite element models is consistent with this interpretation.

The forearc of the overriding plate was found to be under horizontal compression in all models. Compression is generated by depression of the forearc by transmission of the vertical body forces of the slab, but may be overestimated because of the omission of the trench. In response to this downbending the leading edge of the overriding plate is flexed up over a relatively short wavelength (e.g. figure 5.43), enhanced by differential shear slip at the thrust zone. The resultant bending stresses complicate the stress regime of the forearc. However, this is a broad feature in relation to forearc tectonics. This behaviour mimics the finite element models of forearc deformation of Tharp (1985) but occurs over a much wider region with much less amplitude. This suggests that a more sophisticated rheological model of forearc deformation may produce the same phenomenon. The structural high of major forearc basins is often seeded by a basement spur but subsequent development depends on the surface processes of accretion and compressional failure (Seely 1979). Thus in the initial stages of subduction the inception of the structural high and accretionary prism may be influenced by the flexural behaviour of the leading edge.

Forearc compression persists because it is the region nearest to the top of the slab and thus the depression of the surface is greatest. Local and regional tensional stresses are not sufficient to overcome this compression. The local tension produced by the thermal anomaly under the backarc does not penetrate into the forearc, and the regional tension produced by the plate driving forces is relatively small. Westbrook et al. (1984) noted that the large negative isostatic gravity anomaly over the forearc of the Lesser Antilles indicates that the region is held down out of equilibrium by the slab. The finite element models do not have sufficient resolution nor an adequate rheology to study forearc tectonics in any detail.

The crustal thickening at the volcanic arc could not be included explicitly. Sato and Matsu'ura (1988) modelled the arc topography as a dynamically supported reaction to steady-state slip along the thrust zone. However, it is more likely that the arc assumes a more passive role as an isostatically compensated load. Thus the arc was simulated by a normal stress on the surface equivalent to the topographic load of the crustal thickening. This was counterbalanced at the base of the elastic layer by equal and opposite stresses

to simulate the underlying thickened crust and hot, buoyant magma which supports the topography. This force system produced horizontal deviatoric tension under the arc (figure 5.74) demonstrating that the load at the arc may generate tensions large enough to overcome the existing compression. This horizontal tension may be sufficient to split the crust which is already considerably weakened by the high temperature and igneous intrusions. Isolated tension at the arc is not sufficient to propagate spreading, but sustained tension in the backarc may then give birth to a spreading centre.

So the question arises, how is backarc tension produced? After a brief review of the sources of backarc stress in the finite element models other sources which have been omitted from the models are discussed. Backarc tension is often attributed to the action of the thermal anomaly in the mantle wedge above the slab. The viscoelastic rheology cannot generate the thermal anomaly, but it can model the short-term response to the normal and shear stresses induced at the base of the lithosphere by the low viscosity and buoyancy of the hot region. Thermoelastic stresses were also incorporated. The low viscosity reduces the viscous coupling resulting in a decrease in horizontal compression in the overriding plate above the anomaly (figure 5.58). The low density pushes up against the overriding plate reducing the surface depression and compression in figure 5.62 (for the case of slab penetration to 300 km the depression of the backarc is eliminated resulting in horizontal tension throughout the backarc, figures 5.70 and 5.71). A linear, vertical temperature gradient across the overriding plate produces near-surface large horizontal tension (figure 5.66). So it can be concluded that the thermal anomaly adds a component of horizontal tension in the region of the overriding plate above the anomaly. The magnitude of this tension and thus its ability to overcome compression in the backarc depends on the values of the parameters assigned to represent the anomaly.

External regional forces may influence the tectonics of the backarc and this was simulated by applying tectonic forces to the left hand edge of the overriding plate. An island arc margin would probably have a mid-ocean ridge at the far end of the plates and in this respect the compression (figure 5.78) is most realistic. However, as demonstrated earlier, subduction can transmit regional tension into an overriding plate and so the tensional tectonic force could represent hypothetical subduction at the left hand edge of the overriding plate (figure 5.75). Stress amplification in the lithosphere and the boundary conditions at the right hand edge ensure that the relatively small

tectonic force (20 MPa) dominates the stress regime of the overriding plate.

Various influences were not included, specifically the 3-D effects such as buckling. So it appears that the state of stress in the backarc is derived from a delicate balance between the competing effects of: viscous coupling, action of the thrust zone, the thermal anomaly, rollback, external tectonic forces and 3-D mechanisms. In turn these mechanisms are controlled by more fundamental parameters and many regression analyses (e.g. Jarrard 1986) attempted to ascertain the relative importance of each fundamental parameter. Problems arise when a parameter contributes via more than one mechanism. It is then impossible to distinguish the physical mechanisms which control the stress regime. It would not be profitable to attempt to derive the fundamental parameters from the finite element models.

Froidevaux et al. (1988) compared estimates of the horizontal stress due to crustal thickening at the arc with the 'average' state of stress of the overriding plate (Nakamura and Uyeda 1980). It was suggested that the difference represented compression transmitted into the backarc by mechanical coupling at the fault. However, it appears that the state of stress in the overriding plate arises from a more complex assembly of stress sources. Mechanical coupling across the thrust zone is only one of the sources, but it may be expected to play an important role in determining the magnitude of regional horizontal compression transmitted into the overriding plate.

The regional stress produced by the plate driving forces results in horizontal tension in the far backarc of the overriding plate (e.g. figures 5.13, 5.34, 5.38 and 5.42). In the scenario of a continent bounded by subduction zones, this provides a possible mechanism for rifting and other extensional tectonics which may eventually lead to continental splitting (Bott 1982b).

6.2   The Stress Regime in the Slab

In a series of papers Davies (1980, 1981, 1983) assessed the force balance of the descending lithosphere in an isoviscous mantle and estimated the stress in the slab. The conclusions were briefly commented upon in section 1.5 and the calculations will be further reviewed here. In a generalised 1-D analytical model Davies (1983) estimated the total downdip force due to the thermal anomaly of the slab to be 70×10^{12} N m^{-1}.

This is resisted by two mechanisms, at the surface by depression of the trench and overriding plate, estimated at -10×10^{12} N m^{-1}, and in the mantle by shear resistance of the viscous fluid. For the most realistic case of a mantle viscosity $\mu = 10^{21}$ Pa s, the analytical model predicts a force difference along the length of the slab of 50×10^{12} N m^{-1}, and compressions of 1300 MPa at 670 km depth. Davies (1983) pointed out that the slab could not endure these forces and would probably buckle. There is no evidence of this buckling in Wadati-Benioff zones.

The equivalent finite element models are shown in figures 5.4 and 5.8. These models produce stresses of about 180 MPa at 670 km depth which are an order of magnitude smaller than the extremely large slab stresses predicted by the analytical model of Davies above. The mass anomaly of the slab of width 90 km and penetrating to 1000 km depth with a dip of 45° and a thermal density anomaly of $\rho = 50$ kg m^{-3} is approximated by,

$$50 \times 1000\sqrt{2} \times 10^3 \times 90 \times 10^3 = 45\sqrt{2} \times 10^{11} \text{ kg m}^{-1}$$

and so the total downdip force due to the slab weight is,

$$45\sqrt{2} \times 10^{11} \times 10 \times \sin 45 = 45 \times 10^{12} \text{ N m}^{-1}$$

This is only 65% of the downdip force in the analytical model of Davies but it is not sufficient to account for the discrepancy in the predicted stresses at 670 km depth.

The force difference along the length of the slab in the finite element models can be calculated from the stress regime in figure 5.4. A generous estimate of the stress difference between the top and the base of the slab is 400 MPa. The stress is concentrated into the 30 km thick elastic layer giving a force difference along the length of the slab of 12×10^{12} N m^{-1}. This is considerably less than the total downdip force of the thermal density anomaly. The surface is depressed over a width of about 2700 km (see figure 5.5). The average depth of this depression was calculated to be 440 m which provides an upthrust of,

$$440 \times 2270 \times 9.81 \times 2700 \times 10^3 = 26 \times 10^{12} \text{ N m}^{-1}$$

This does not include the partitioning between the trench and the overriding plate; explicit inclusion of the trench will probably reduce the width over which the depression

exists. Summation of the force in the slab and the compensation at the surface does not total the body force in the slab, but as discussed in section 5.6, the models do not reach equilibrium.

The stress regimes in figures 5.4 and 5.8 show that the mantle stresses immediately adjacent to the slab are not relaxed. Above the slab both principal stresses are tensional and below it both principal stresses are compressional. This indicates a low pressure region above of magnitude $10 \rightarrow 50$ MPa, and a high pressure region below the slab of magnitude $5 \rightarrow 30$ MPa which partially support the thermal body force. Bott (1988) suggested that pressure differences in the mantle above the slab could support the slab and these pressures (ΔP) can be estimated from,

$$\Delta P = \Delta \rho \mathrm{g} T \cos \delta = 50 \times 9.81 \times 90 \times 10^3 \times \cos 45 = 31 \text{ MPa}$$

taking values from the finite element models. Values of pressure from the finite element models are in good agreement with the theoretical values suggesting that pressure differences support the slab against rotation in a self-regulating mechanism. The motion of the slab (e.g. figures 5.10, 5.15) may represent the motion from the quiescent state necessary to generate the pressure anomalies which then support the slab against further rotation as subduction progresses.

The pressures would be sustained by continuous rollback, since if rollback was prevented then inflow from under the overriding plate due to the pressure gradient would allow the slab rotate towards vertical subduction.

The finite element models have neither the correct rheology for the mantle nor the correct distribution of the upthrust at the surface. However, the models provide some understanding of the support of the slab body force. Depression of the surface plates and a small contribution from shear resistance to motion partially support the buoyancy force and consequently decrease the downdip force acting in the slab. In addition to the thermal body forces the elevated olivine-spinel phase change was included (see figure 5.13). This does not alter the basic conclusions concerning the slab support mechanism.

The distribution of stresses in the finite element models differs from the analytical solutions. The finite element models allow the slab to sink freely through a layered mantle but the analytical models assume a constant viscosity mantle with an impenetrable base at the slab tip. It is highly unlikely that the slab tip encounters an impassable

mid-mantle boundary at any given depth and so the 'free' slab tip is a more appropriate representation.

The stress distribution of the finite element models is now compared to the observed slab stress regime. Studies of earthquake focal mechanisms have proposed a typical slab stress distribution which consists of a stress minimum at about 300 km depth, below which the slab has downdip compression and above which the slab has downdip tension. The most convincing aspects of this stress regime are the position of the stress minimum and the compression in the lower slab. The stress regime in the deeply penetrating slabs (figures 5.46, 5.13, 5.48) is controlled by the viscosity contrast at 670 km depth and the isostatic reaction at the surface. The models in figures 5.13 and 5.48 approximately reproduce the observed slab stresses. However, the stresses are not sensitive to increases in viscosity contrast above ×10. The slab stress regime is complicated by the distribution of the isostatic reaction to slab pull at the surface. Observed trench depths are much greater than those produced by the finite element models (figures 5.14 and 5.30), and so the isostatic reaction of the models should be more strongly concentrated at the trench. This would increase the magnitude of the elastic coupling and consequently increase the in-plate tension near the top of the slab. The redistribution of slab stresses would be expected to increase the depth of the stress minimum and decrease the magnitude of the deep compressions.

The stress regimes in shallow penetrating slabs ($\leq$ 400 km depth) do not match the observed stress distributions. Large downdip compression (figures 5.34, 5.38) is associated with the tip and this violates the requirement of a stress minimum at 300 km depth with predominantly tension above. The compression is caused by resistance to penetration and upbending of the slab tip. Jarrard (1986) compiled the best known Wadati-Benioff zone profiles and out of 20 profiles of shallow penetrating slabs only 2 show upbending of the tip, namely New Britain and N. Sulawesi. Neither compression nor upbending are common in present-day subduction zones. The stress regime was altered by varying the geometry and rheology of the slab tip, but the large compression near the slab tip could only be eliminated by invoking aseismic extension of the slab in the upper mantle.

The dynamic reaction of the trench was omitted in all models. The inability of the finite element models to reproduce the observed slab tension could be due to

the distribution of the isostatic reaction at the surface. If more of the upthrust was concentrated at the trench then the elastic coupling would increase the magnitude of the in-plate tension at the top of the slab. The tension will be transmitted down the slab and may overcome the deeper compressions. A large trench reaction may cause the slab to 'hang' from the surface and this may alleviate the upbending of the tip which is due to the resistance to penetration in the mantle.

The finite element models could not successfully generate the stress regime in shallow penetrating slabs, but the mechanics of the slab motion imply that the trench reaction dominates the slab stresses to produce in-plate tension.

Sleep (1979) proposed that double seismic zones are generated by a low viscosity region in the mantle wedge allowing the slab to sag under its own weight. The upper surface of the slab develops compression due to bending and the lower layer retains in-plate tension because it is close to the neutral fibre. The addition of a low viscosity asthenosphere (figure 5.52) and a low viscosity thermal anomaly (figure 5.57) to the finite element models produced an increase in compression in the upper surface of the slab (compared to figure 5.42). The lower layer of in-plate tension persists. The models do not produce true double seismic zones but simply lend support to the analysis of Sleep (1979). The inadequacy of both the mantle rheology and the representation of the thermal anomaly prevent definite conclusions on the origins of double seismic zones.

6.3 The Evolution of the Subduction Zone

The continuous dynamic evolution of the slab cannot be modelled by the finite element methods employed in this thesis. However, a general framework describing the descent of the slab through the upper mantle can be assembled.

Above the transition zone the models of slab penetration to 200 km and 300 km show that the displacement of the descending lithosphere is quite small (e.g. figures 5.36, 5.40). The flow models of 300 km penetration (figure 4.33) show the slab sinking vertically and rotating towards vertical subduction at relatively small velocities. In the depth range 300 $\rightarrow$ 400 km the slab gains the body forces of the elevated olivine-spinel phase change, and this has a dramatic effect on subduction. The additional forces cause significant slab rotation towards the vertical and increase the downdip and

rollback velocities (e.g. figures 4.34, 5.44). So, for the period (say 1 Ma) over which the slab acquires higher body forces, the subduction zone may undergo a significant change in its evolution. Roecker (1985) analysed the seismotectonics of Izu-Bonin and suggested that lateral variation in the magnitude of the body forces of the elevated olivine-spinel transition was the major cause of the lateral variation in tectonics along the strike of the margin.

The next stage in the evolution of a subduction zone is collision with the 670 km discontinuity. The analysis of mantle viscosity favours a viscosity contrast of ×10 in preference to a contrast of ×100 or ×1 but is unable to give definite conclusions due to the model limitations. The increase in viscosity at the base of the upper mantle provides a resistance to the motion of the slab tip. If the slab remains rigid, this resistance to movement will be transmitted back up the slab changing the general slab motion (figure 4.35) to be realigned approximately downdip and may slightly affect the surface plates (figures 5.46, 5.13, 5.48). Alternatively, the motion in the upper mantle may remain constant but the reduction of vertical velocity in the lower mantle may cause the leading edge to deform and flow laterally (Fischer et al. 1988). The stagnation of the slab tip in the lower mantle causes a decrease in slab dip as the upper slab continues to rollback. By 'anchoring' the leading edge of the slab in the lower mantle, the strength of the slab may not be able to endure continuous rollback of its upper mantle section, but if it does a quasi- steady state subduction may ensue (Gurnis and Hager 1988). The models predict bending at 300 → 400 km depth due to the body forces of the elevated olivine-spinel transition. However, Wadati-Benioff zones are surprisingly straight at depth. Although interpretations generally average along strike which may introduce some smoothing of the profile, this is a discrepancy of the models.

In an analysis of slab dip, Jarrard (1986) proposed that dip is negatively correlated with duration of subduction. All finite element models demonstrate rotation of the slab towards vertical subduction in apparent contradiction of the observations. This may be attributed to the initial quiescent state which did not allow sustained local pressure differences in the mantle, or it may be a result of global interaction which cannot be modelled here.

Duration of subduction influences the stress field of the overriding plate as figures 5.17, 5.21, 5.25, 5.29 and 5.13 demonstrate. The width of the band of localised hori-

zontal compression in the overriding plate increases as the length of the slab increases. The models assume a constant slab dip with time which may not be realistic. As dip increases the width of the band of compression would decrease, so there is some trade-off between these competing effects.

The slowly growing band of compression which gradually encroaches into the backarc may be an important control of the stress regime and subsequent tectonics. In the absence of the local horizontal tension produced by the thermal anomaly in the mantle under the backarc, this mechanism may be responsible for the compressional tectonics of the backarc. The South American margins have very low angle slabs, no evidence of thermal activity in the mantle wedge and compressional tectonics in the overriding plate. This mechanism of viscous coupling to the surface lithosphere may be usefully applied to help explain the stress regime at these subduction zones.

CHAPTER 7

Summary and Conclusions

This thesis has presented a numerical investigation of selected aspects of the mechanics and dynamics of subduction by finite element analysis. Subduction zones pose certain rheological problems for numerical analyses. The rheology of the subducting and overriding plates and the descending slab is best approximated by an elastic-plastic-viscoelastic solid in its response to tectonic loads over geological time. In contrast, the mantle responds to loads by creep which can be numerically modelled by flow of a Newtonian viscous fluid. At the trench the surface plates are coupled along a large thrust zone which permits the subducting plate to underthrust the overriding plate. It was not possible to incorporate all three rheologies into a single finite element package and so the 2-D numerical analysis was divided between two approaches,

- Newtonian viscous flow gives a good approximation of mantle behaviour

- linear elasticity and viscoelasticity provide a good approximation of both lithospheric behaviour and the response of the thrust zone

The basic isoparametric finite element package for linear elasticity was originally developed by Waghorn (1984). Quadratic elements permit a linear strain gradient across the element and are the optimum elements for elasticity analyses (Zienkiewicz 1977). The initial strain method of Zienkiewicz et al. (1968) was implemented to provide a Newtonian viscoelastic rheology. Fault behaviour was included via the dual node concept of Mithen (1980). The isoparametric elements allow curved faults to be introduced which is important for modelling the thrust zone of subduction. This basic package was updated and improved to combine the faulting into the viscoelastic algorithm and to include the full mechanical response to a thermal anomaly.

Quadratic isoparametric elements can be used for the analysis of viscous fluids although they are not optimal. The linear elasticity package was converted to solve the Navier-Stokes equations for viscous flow by the reduced integration penalty (RIP) method following Zienkiewicz and Godbole (1975). This was further developed to allow motion of the free surface following the arbitrary Lagrange-Eulerian (ALE) method of

Hughes et al. (1978).

Chapter 4 presented models of flow in the mantle driven by motion of a slab dipping at 45°, under the assumption that subduction is controlled by the viscosity-depth profile. The lithosphere of the surface plates and the subducting slab was represented by a 90 km thick high viscosity layer. The free surface evolved over a time interval of 50 000 yrs which can be regarded as approximately instantaneous with respect to the time constant of subduction.

The models produced an asymmetric depression of the surface above the slab. The depth and width of this depression was found to be dependent on the viscosity of the lower mantle, the length and mechanical strength of the slab. Implications for slab motion inferred from the flow field constrain the viscosity contrast at the upper - lower mantle interface to be of the order ×10 rather than ×100 or ×1.

Analysis of the variation in depth of penetration of the slab shows that acquisition of the body forces of the elevated olivine-spinel transition and collision with the 670 km discontinuity are significant events in the evolution of subduction zones which may contribute to abrupt changes in tectonics.

The major limitations of the models are the rheology of the lithosphere, the omission of the thrust zone and the boundary conditions of the mesh. The flow models cannot simulate the subduction of one plate under the adjacent and thus corner flow is not generated and the surface does not evolve to reproduce the correct topography. The compensation of the body force of the slab by depression of the surface will not be accurately distributed. The boundary conditions do not permit a mass flux across the sides of the mesh and so all flow is contained within the mesh. Thus the lateral flow driven by subduction to mid-ocean ridges, which is part of the mechanism of thermal convection, is not produced by the models.

In Chapter 5 an island arc margin was modelled using the linear elasticity package. The lithosphere was represented by an elastic layer 30 km thick overlying a 60 km thick viscoelastic layer. The underlying mantle was modelled as a layered viscoelastic body and the two meshes used extended to 670 km and 1400 km depth respectively. A fault dividing the meshes into two halves was used to simulate the thrust zone. The models provide a good approximation of the surface, lithosphere and thrust zone, and of the initial flow response of the mantle. The aim of the study is to quantitatively investigate

the influence of the negative buoyancy of the slab over subduction tectonics.

The stress regime at subduction zones has been analysed for three distinct phenomena,

- the origin of the driving forces of plate motion

- the cause of lateral variations in stress state of the surface plates

- the mechanics and dynamics of the descending slab

The slab pull force drags the subducting plate into the trench and it was proposed that regional tension in the plate is generated by differential shear slip at the thrust zone in response to the vertical forces applied by the slab.

The trench suction force drags the overriding plate into the trench and it was proposed regional tension in the plate is generated also by differential shear slip at the thrust zone in response to the vertical forces applied by the slab.

The magnitude of the stress is dependent on the dip and in-plate tension in the top of the slab, and the angle and degree of mechanical coupling at the thrust zone.

The stress state of the surface plates was partitioned into five regimes. Bending of the subducting plate in response to the vertical forces applied by the slab through the slab bend region created large horizontal tension at the outer trench slope. This is consistent with the extensional tectonics observed in the region. The forearc was found to be under horizontal compression in all models. The compression arises from the vertical tension in the lithosphere created by the combination of vertical downpull of the slab and isostatic upthrust at the surface. Thus horizontal compression in the overriding plate can be generated by the vertical forces of subduction. The isostatically compensated topographic load of the volcanic arc may generate horizontal deviatoric tension in the lithosphere at the arc if the horizontal tension due to the load exceeds the local compression. The backarc shows considerable variety in stress state. A component of regional horizontal tension is produced by the plate driving forces and regional horizontal compression by locking the thrust zone. A component of local horizontal compression is produced by depression of the backarc due to viscous coupling to the sinking slab. A component of local horizontal tension is produced by an underlying thermal anomaly. The final state of stress is dependent upon a delicate balance of the stress components. However, an external regional tectonic force applied to the far edge of the overriding plate dominated the backarc. This suggests support for the theory

115

that subduction tectonics are primarily controlled by global plate interaction (Dewey 1980) rather than solely by local forces. The regional stress of the plate driving forces creates horizontal tension in the far backarc which provides a source mechanism for stress-controlled extensional tectonics (Bott 1982b).

The negative buoyancy of the slab is partially supported by depression of the surface and shear resistance of the viscous fluid. Thus the resultant downdip force within the slab is much reduced. The stress state of the slab, in response to the downdip force, is controlled by the isostatic reaction of the surface and the viscosity-depth distribution in the mantle. The mass deficit of the trench produces tension in the upper slab, and a viscosity contrast at 670 km depth causes compression in the lower slab. The models of a deeply penetrating slab reproduce the observed average stress distribution. The stress regimes of the shallower penetrating models do not fit the observations, probably because of incorrect partitioning of the isostatic reaction at the surface. A low viscosity zone above the slab leads to the development of double seismic zones.

A low pressure zone above, and high pressure zone below the slab act against the body forces to inhibit slab rotation towards vertical subduction. The pressure anomalies are maintained by continuous subduction and rollback, and act in a self-regulating mechanism to prevent large changes in dip with time and excessive torques along the length of the slab.

The limitations of the models are dominated by the inadequate rheology of the mantle and the problem of resolution which necessitated the omission of the crust. Also, the addition of a plastic rheology allowing finite strain deformation of the slab bend region would allow the dynamics of the trench to be included.

The success of this 2-D analysis is encouraging but limitations of the models leave many questions unanswered. Further work on 2-D generalised subduction zone models would profit from rheological sophistications and better resolution of the meshes. In particular non-Newtonian viscoelastic and large deformation plastic rheologies would allow the trench and slab bend regions to be included. Detailed thermal modelling of the slab to yield a better mechanical model of the slab, especially the behaviour of the slab tip, will aid analysis of the slab mechanics. Most importantly direct coupling of viscous and elastic behaviour is required, without which there will be no true dynamical

116

model of subduction.

The Computer Programs

The Linear Elasticity Finite Element Library - ISOLIB

The main algorithms of the library program ISOLIB were not significantly altered and so the program is not listed here. A full description and listing of the basic program can be found in Waghorn (1984). However, some operational changes were made to the program and these are described below.

ISOLIB was converted to FORTRAN77, structured and some additional subroutines were added which are briefly described here. In order to test the faulting algorithm subroutines to calculate the stresses and viscous strains at the fault walls were added. The implementation of Dirichlet conditions is described in section 2.3.5; this exact method is preferred over the Payne-Irons method and is included as an optional routine. Often it is necessary to make minor changes to a mesh and so a subroutine was developed which adds or deletes specific nodes, renumbers the mesh accordingly and produces a new input file. A subroutine to find the eigenvalues of the symmetric system matrix reduces the band matrix to tridiagonal form by Jacobi rotations and then employs the QL algorithm to extract the eigenvalues using the public domain routines available in NAG. Anomalous densities of the elements and deflection of isostatic boundaries contribute to the gravity field. Source code for the main calculation was kindly provided by Prof. M.H.P. Bott and included in a subroutine to calculate the 2-D gravity anomaly at the surface of the mesh. The original routine in ISOLIB to calculate the initial strain of a temperature anomaly was corrected and thermal stresses were incorporated into the viscoelastic algorithm.

The Viscous Flow Finite Element Library - ISOVISC

The library program ISOVISC was produced by converting ISOLIB as described in section 2.3.1, and hence retains many of its features. The library is accessed from a calling program ISOCALL. The input/output units are assigned as follows,

- 1   echo the mesh data

- 3   data for mesh renumbering

- 4   mesh data

o 5   data for the plotting routines

o 6   output of program status

o 7   output of solution data

o 9   graphical output

The source code listing below contains both a general operational description and definitions of major variables for each routine. The subroutines access external routines from the libraries NAG and GHOST80 for matrix manipulation and graphical output respectively, and also the MTS system routine TIME which monitors the CPU time elapsed.

```
C
C
C        The main program for the finite element library ISOVISC.
C
C        Program execution is controlled by the sequence of subroutines
C        remaining unCOMMENTed. Details of the subroutines can be found in
C        library ISOVISC.
C
C
C
C
C        Acknowledgement:   This program was developed from an original
C                           finite element library for linear elasticity
C                           written by G.D. Waghorn.
C
C
C
C
C
        IMPLICIT DOUBLE PRECISION (A-H,O-W)
        CHARACTER   TITLE(4)*8,ZUF(4)*4
        PARAMETER(IGL=880,JGL=131,KGL=66)
        COMMON /CHAR/ TITLE,ZUF
        COMMON /CONS/ NTRI,NQUAD,NINCS,NNOD,KSIZE,KSBW,NNOD2,NMAT,IDUM(4),
       +              GAMMA,PI,BETA,NST,NSI,NSEG,NODSEG,DELTAT
        COMMON /NODS/ X(IGL/2),Y(IGL/2),DISP(IGL),FORCE(IGL),
       +              XSTPOS(4,500),YSTPOS(4,500)
        COMMON /ELEM/ NODEL(8,500),NGAUSS(500),NOTEL(500),NOQEL(500),
       +              NOTCOL(500),NOQCOL(500),DIFFOP(9,500),BLIB(144,500),
       +              PRINC(16,500)
        COMMON /FORC/ NOD4S(100),NDIS4S(100),NLOAD(100),NCOM1(300),
       +              FNORM(100),FTAN(100),FNTOT(100),FTTOT(100)
        COMMON /FIXT/ DFIX(2,500),NOFIX(500),IFLAG(2,500),NFIX,NEXT,NSTOP
        COMMON /MATS/ EM(9),PM(9),TM(9),RHOM(9),ETAM(9),ETAN,ITYP(9)
        COMMON /STIF/ ELK(18,18),GLOBK(IGL,JGL)
        COMMON /STF4/ GLOBKL(IGL,KGL),FORCE0(IGL),NROPIV(IGL)
        COMMON /VISC/ DSTORE(12,900),FINIT(IGL),FOUT(IGL),AMASS(IGL)
        COMMON /VARS/ W1W2,DETJ,RHO,C2,FACT,DNXDX(8),DNXDY(8),B(4,18),
       +              BTC(18,4),NO,NGAUS,NO2,NUMEL,NSURF,IG
        COMMON /TIMS/ ELSIZE(2,500),DELT,ILOAD(IGL),TTOTAL
        COMMON /MOVE/ VPART(IGL),VMESH(IGL),APARAM(IGL),STRANS(IGL),
       +              ATRANS(IGL),DMESH(IGL),APART(IGL),AMESH(IGL),
       +              VMESH2(IGL),DMESH2(IGL),XOLD(IGL),YOLD(IGL)
        COMMON /GAPT/ S,T,SHAPE(8),DNXDS(8),DNXDT(8),TSHAPE(6,36),
       +              TDNXDS(6,36),TDNXDT(6,36),TW1W2(6,6),QSHAPE(3,72),
       +              QDNXDS(3,72),QDNXDT(3,72),QW1W2(3,9),WEITRI(12,6),
       +   WEIQAD(18,3),PLACET(12,6),PLACEQ(18,3),PLACEL(3),WEILIN(3)
C
        CALL TIME(0,1)
        CALL READ
C       CALL RENODE
        CALL PREK
C       CALL FORMK
C       CALL EIGEN
        CALL TIMSOL
C       CALL DISOUT
C       CALL STRESS
C       CALL STOUT
        CALL PAMS
C       CALL GRID
C       CALL FRAME
        CALL VELPLT
C       CALL FRAME
C       CALL VECPLT
C       CALL FRAME
C       CALL SURF
C       CALL FRAME
C       CALL DPROF
```

```
        CALL GREND
C
        CALL EXIT
        END
```

```
C
C
C        An isoparametric finite element library for solving the
C        Navier-Stokes equations in 2-D incorporating the free
C        surface of the fluid.
C
C
C        The reduced integration penalty (RIP) formulation is
C        used to generate the system matrix.
C
C        The formal derivation can be found in Hughes et al. (1978)
C
C
C
C
C
C
C
C        Array is 2600*50 for wave model
C
         SUBROUTINE READ
C
C+       ━━━━━━━━━━━━━━━━
C        Read in all information required to set up the model and echo immediately
C        to the check file attached to unit 1.
C        Major variables: X    =node x-coords       Y    =node y-coords
C                          FORCE =system force vector |F|
C                          DELTAT=time increment
C-
         IMPLICIT DOUBLE PRECISION (A-H,O-W)
         CHARACTER   TITLE(4)*8,ZUF(4)*4
         PARAMETER(IGL=880,JGL=131,KGL=66)
         COMMON /CHAR/ TITLE,ZUF
         COMMON /CONS/ NTRI,NQUAD,NINCS,NNOD,KSIZE,KSBW,NNOD2,NMAT,IDUM(4),
        +              GAMMA,PI,BETA,NST,NSI,NSEG,NODSEG,DELTAT
         COMMON /NODS/ X(IGL/2),Y(IGL/2),DISP(IGL),FORCE(IGL),
        +              XSTPOS(4,500),YSTPOS(4,500)
         COMMON /ELEM/ NODEL(8,500),NGAUSS(500),NOTEL(500),NOQEL(500),
        +              NOTCOL(500),NOQCOL(500),DIFFOP(9,500),BLIB(144,500),
        +              PRINC(16,500)
         COMMON /FORC/ NOD4S(100),NDIS4S(100),NLOAD(100),FNOD(200),
        +              FNORM(100),FTAN(100),FNTOT(100),FTTOT(100)
         COMMON /FIXT/ DFIX(2,500),NOFIX(500),IFLAG(2,500),NFIX,NEXT,NSTOP
         COMMON /MATS/ EM(9),PM(9),TM(9),RHOM(9),ETAM(9),ETAN,ITYP(9)
         COMMON /VARS/ COMB(165),NOSECT,NDIS,NDIR,IOOMX(2),IG
         COMMON /MOVE/ VPART(IGL),VMESH(IGL),APARAM(IGL),STRANG(IGL),
        +              ATRANS(IGL),DMESH(IGL),APART(IGL),AMESH(IGL),
        +              VMESH2(IGL),DMESH2(IGL),XOLD(IGL),YOLD(IGL)
C
C        *** Read title
C
         ITEST=0
         WRITE(6,10)
10       FORMAT(1H0,'Finite Element Program for free-surface flow',/
        +         '  up and running...')
         READ(4,20)TITLE
         WRITE(1,20)TITLE
20       FORMAT(4A8)
C
C        *** Read in model information
C
         READ(4,30)NNOD,NTRI,NQUAD,NMAT,NFIX,NDIR,NSEG,NSI,NST,NFS
```

```
         WRITE(1,30)NNOD,NTRI,NQUAD,NMAT,NFIX,NDIR,NSEG,NSI,NST,NFS
30       FORMAT(1115)
         NNOD2=NNOD*2
C
C        *** Read solution information
C
         READ(4,35)NINCS,GAMMA,BETA,ETAN,DELTAT
         WRITE(1,35)NINCS,GAMMA,BETA,ETAN,DELTAT
35       FORMAT(I5,4D10.4)
C
C        *** Read node numbers, coordinates and free surface parameter
C
         DO 50 INOD=1,NNOD
         READ(4,40)JNOD,X(JNOD),Y(JNOD),APARAM(2*JNOD-1),APARAM(2*JNOD)
40       FORMAT(I5,4F10.3)
C
C        *** Convert from polar to rectangular
C
         IF(NST.EQ.2) THEN
           ANG=X(JNOD)*PI/180.0
           X(JNOD)=Y(JNOD)*DSIN(ANG)
           Y(JNOD)=Y(JNOD)*DCOS(ANG)
         ENDIF
         WRITE(1,40)JNOD,X(JNOD),Y(JNOD),APARAM(2*JNOD-1),APARAM(2*JNOD)
C
C        *** Convert to metres
C
         IF(NSI.EQ.0) THEN
           X(JNOD)=X(JNOD)*1.0E3
           Y(JNOD)=Y(JNOD)*1.0E3
         ENDIF
50       CONTINUE
C
C        *** Read in material types
C
         DO 70 IMAT=1,NMAT
         READ(4,60)EM(IMAT),PM(IMAT),RHOM(IMAT),TM(IMAT),ETAM(IMAT)
         WRITE(1,60)EM(IMAT),PM(IMAT),RHOM(IMAT),TM(IMAT),ETAM(IMAT)
60       FORMAT(D10.3,2F10.3,2D10.3)
70       CONTINUE
C
C        *** Read element topologies, material types and gauss points
C
         IF(NTRI.GT.0) THEN
           DO 90 IEL=1,NTRI
           READ(4,80) JEL,(NODEL(KEL,JEL),KEL=1,6),ITYP(JEL),NGAUSS(JEL)
           WRITE(1,80) JEL,(NODEL(KEL,JEL),KEL=1,6),ITYP(JEL),NGAUSS(JEL)
80         FORMAT(9I5)
           NOTEL(IEL)=JEL
90         CONTINUE
         ENDIF
C
         IF(NQUAD.GT.0) THEN
           DO 120 IEL=1,NQUAD
           READ(4,110) JEL,(NODEL(KEL,JEL),KEL=1,8),ITYP(JEL),NGAUSS(JEL)
           WRITE(1,110)JEL,(NODEL(KEL,JEL),KEL=1,8),ITYP(JEL),NGAUSS(JEL)
110        FORMAT(1115)
           NOQEL(IEL)=JEL
120        CONTINUE
         ENDIF
C
C        *** Initialise force vector
C
```

```fortran
      CALL VECNUL(FORCE,IGL,NNOD2,ITEST)
C
C     *** Read direct nodal forces
C
      IF(NDIR.GT.0) THEN
         DO 140 I=1,NDIR
         READ(4,150)NOD4S(I),FNOD(2*I-1),FNOD(2*I)
         WRITE(1,150)NOD4S(I),FNOD(2*I-1),FNOD(2*I)
150      FORMAT(I5,2(4X,D11.4))
         IF(NST.EQ.1) THEN
            FORCE(2*NOD4S(I)-1)=FNOD(2*I-1)*2.0D00*PI*X(NOD4S(I))
            FORCE( 2*NOD4S(I) )=FNOD( 2*I )*2.0D00*PI*X(NOD4S(I))
         ELSE
            FORCE(2*NOD4S(I)-1)=FNOD(2*I-1)
            FORCE( 2*NOD4S(I) )=FNOD( 2*I )
         ENDIF
140      CONTINUE
      ENDIF
C
C     *** Read surface tractions
C
      IF(NSEG.GT.0) THEN
         NDIS=0
         DO 142 I=1,NSEG
         READ(4,150)NODSEG
         WRITE(1,150)NODSEG
         DO 143 J=1,NODSEG
         READ(4,150)NDIS4S(J),FNORM(J),FTAN(J)
         WRITE(1,150)NDIS4S(J),FNORM(J),FTAN(J)
         NLOAD(NDIS+J)=NDIS4S(J)
         FNTOT(NDIS+J)=FNORM(J)
         FTTOT(NDIS+J)=FTAN(J)
143      CONTINUE
C
C     *** For each surface, divide into NOSECT 3-node edge elements
C
         NOSECT=(NODSEG-1)/2
         CALL GLOBF
         NDIS=NDIS+NODSEG
142      CONTINUE
      ENDIF
C
C     *** Read Dirichlet conditions
C
      IF(NFIX.GT.0) THEN
         DO 170 I=1,NFIX
         READ(4,160)NOFIX(I),(IFLAG(J,I),DFIX(J,I),J=1,2)
         WRITE(1,160)NOFIX(I),(IFLAG(J,I),DFIX(J,I),J=1,2)
160      FORMAT(I5,2(I5,D10.3),F10.3)
170      CONTINUE
      ENDIF
C
      WRITE(6,190)
190   FORMAT('0READ finished')
      CALL TIME(1,1)
C
      RETURN
      END
C
C
C...............................................................
C
```

```fortran
      SUBROUTINE LSHAPE
C
C+
C     Calculate the shape functions of the 1-D edge element at the local
C     coordinate point which is supplied.
C     Major variables:  SHAPE =shape functions
C                        DNXDS, DNXDT =derivatives w.r.t. local coords
C-
      IMPLICIT DOUBLE PRECISION (A-H,O-W)
      PARAMETER(IGL=880,JGL=131,KGL=66)
      COMMON /GAPT/ S,T,SHAPE(8),DNXDS(8),DNXDT(8),PCOM(1611),
     +              PLACEL(3),WEILIN(3)
C
      SHAPE(1)=(SS-S)/2.0
      SHAPE(2)=1.0-SS
      SHAPE(3)=(SS+S)/2.0
      DNXDS(1)=S-0.5
      DNXDS(2)=-2.0*S
      DNXDS(3)=S+0.5
C
      RETURN
      END
C
C
C...............................................................
C
C
      SUBROUTINE GLOBF
C
C+
C     Calculate the contribution to the global force vector of normal
C     and tangential stresses, dividing this edge into 3-node 1-D elements.
C     Major variables:  FORCE =system force vector {F}
C                        FNORM, FTAN =supplied edge stresses
C-
      IMPLICIT DOUBLE PRECISION (A-H,O-W)
      PARAMETER(IGL=880,JGL=131,KGL=66)
      COMMON /NODS/ X(IGL/2),Y(IGL/2),DISP(IGL),FORCE(IGL),
     +              XSTPOS(4,500),YSTPOS(4,500)
      COMMON /GAPT/ S,T,SHAPE(8),DNXDS(8),DNXDT(8),PCOM(1611),
     +              PLACEL(3),WEILIN(3)
      COMMON /FORC/ NOD4S(100),NDIS4S(100),NLOAD(100),FNOD(200),
     +              FNORM(100),FTAN(100),FNTOT(100),FTTOT(100)
      COMMON /VARS/ COMR(165),NOSECT,NDIS,NDIR,NOD(3)
C
C     *** For each 1-D edge element
C
      DO 10 IS=1,NOSECT
         LNOD2=2*IS
         LNOD1=LNOD2-1
         LNOD3=LNOD2+1
         NOD(1)=NDIS4S(LNOD1)
         NOD(2)=NDIS4S(LNOD2)
         NOD(3)=NDIS4S(LNOD3)
C
C     *** Integrate the stress by 3-pt gaussian
C
         DO 20 IG=1,3
         S=PLACEL(IG)
         DS=WEILIN(IG)
```

```fortran
          CALL LSHAPE
          XPOS=0.0D00
          DXXDS=0.0D00
          DYXDS=0.0D00
          DO 30 I=1,3
            XPOS=XPOS+SHAPE(I)*X(NOD(I))
            DXXDS=DNXDS(I)*X(NOD(I)) + DXXDS
            DYXDS=DNXDS(I)*Y(NOD(I)) + DYXDS
30        CONTINUE
C
C     *** Evaluate the stresses at the gauss point
C
          IF(NST.EQ.1) THEN
            PN=( FNORM(LNOD1)*SHAPE(1)+FNORM(LNOD2)*SHAPE(2)+
     +           FNORM(LNOD3)*SHAPE(3) )*2.0D00*PI*XPOS
            PT=(  FTAN(LNOD1)*SHAPE(1)+ FTAN(LNOD2)*SHAPE(2)+
     +           FTAN(LNOD3)*SHAPE(3) )*2.0D00*PI*XPOS
          ELSE
            PN=FNORM(LNOD1)*SHAPE(1)+FNORM(LNOD2)*SHAPE(2)+
     +         FNORM(LNOD3)*SHAPE(3)
            PT= FTAN(LNOD1)*SHAPE(1)+ FTAN(LNOD2)*SHAPE(2)+
     +         FTAN(LNOD3)*SHAPE(3)
          ENDIF
          DSX=(PT*DXXDS-PN*DYXDS)
          DSY=(PN*DXXDS+PT*DYXDS)
          DO 40 I=1,3
            FORCE(2*NOD(I)-1)=SHAPE(I)*DSX*DS + FORCE(2*NOD(I)-1)
            FORCE( 2*NOD(I) )=SHAPE(I)*DSY*DS + FORCE( 2*NOD(I) )
40        CONTINUE
20      CONTINUE
10    CONTINUE
C
      RETURN
      END
C
C
C.................................................................
C
C
      SUBROUTINE FORMK
C     _____
C+
C     Calculate the global stiffness by summing contributions from each
C     element stiffness.
C     Major variables:  ELK   =element stiffness     BLIB =strain operator [B]
C                       GLOBK =system matix [K]
C-
      IMPLICIT DOUBLE PRECISION (A-H,O-W)
      PARAMETER(IGL=880,JGL=131,KGL=66)
      COMMON /CONS/ NTRI,NQUAD,NINCS,NNOD,KSIZE,KSBW,NNOD2,NMAT,IDUM(4),
     +              GAMMA,PI,BETA,NST,NSI,NSEG,NODSEG,DELTAT
      COMMON /NODS/ X(IGL/2),Y(IGL/2),DISP(IGL),FORCE(IGL),
     +              XSTPOS(4,500),YSTPOS(4,500)
      COMMON /ELEM/ NODEL(8,500),NGAUSS(500),NOTEL(500),NOQEL(500),
     +              NOTCOL(500),NOQCOL(500),DIFFOP(9,500),BLIB(144,500),
     +              PRINC(16,500)
      COMMON /MATS/ EM(9),PM(9),TM(9),RHOM(9),ETAM(9),ETAN,ITYP(9)
      COMMON /STIF/ ELK(18,18),GLOBK(IGL,JGL)
      COMMON /GAPT/ S,T,SHAPE(8),DNXDS(8),DNXDT(8),TSHAPE(6,36),
     +              TDNXDS(6,36),TDNXDT(6,36),TW1W2(6,6),QSHAPE(3,72),
```

```fortran
     +              QDNXDS(3,72),QDNXDT(3,72),QW1W2(3,9),WEITRI(12,6),
     +     WEIQAD(18,3),PLACET(12,6),PLACEQ(18,3),PLACEL(3),WEILIN(3)
      COMMON /VARS/ W1W2,DETJ,ETA,C2,FACT,DNXDX(8),DNXDY(8),B(4,18),
     +              BTC(18,4),NO,NGAUS,NO2,NUMEL,NROW,IG
C
      ITEST=0
C
C     *** Triangular element stiffness
C
      IF(NTRI.GT.0) THEN
        NO=6
        NO2=NO*2
        DO 30 IEL=1,NTRI
C
C     *** Initialise
C
          CALL MATNUL(ELK,18,18,18,18,ITEST)
          NUMEL=NOTEL(IEL)
          MAT=ITYP(NUMEL)
          ETA=ETAM(MAT)
          IF(ETA.EQ.0.0D00) THEN
            FACT=ETAN
          ELSE
            FACT=ETA*ETAN
          ENDIF
          NGAUS=NGAUSS(NUMEL)
          NROW=NOTCOL(IEL)
C
C     *** Numerically integrate
C
          DO 20 IG=1,NGAUS
            IPOS=(IG-1)*NO
            JPOS=IPOS*2
            XPOS=0.0
            YPOS=0.0
            DO 10 IV=1,NO
              NODE=NODEL(IV,NUMEL)
              SHAPE(IV)=QSHAPE(NROW,IPOS+IV)
              XPOS=XPOS+SHAPE(IV)*X(NODE)
              YPOS=YPOS+SHAPE(IV)*Y(NODE)
              DNXDS(IV)=TDNXDS(NROW,IPOS+IV)
              DNXDT(IV)=TDNXDT(NROW,IPOS+IV)
10          CONTINUE
            XSTPOS(IG,NUMEL)=XPOS
            YSTPOS(IG,NUMEL)=YPOS
            W1W2=TW1W2(NROW,IG)
            CALL BFORM
C
C     *** Store the strain rate operator
C
            DO 12 I=1,NO
              L=2*I
              K=L-1
              BLIB(JPOS+K,NUMEL)=DNXDX(I)
              BLIB(JPOS+L,NUMEL)=DNXDY(I)
12          CONTINUE
            CALL ELSTIF
20        CONTINUE
C
C     *** Load the element stiffness into the global stiffness
C
```

```
          CALL LOADK                                                  CALL BFORM
C                                                                      DO 90 I=1,NO
C                                                                        L=2*I
C     *** Evaluate the volumetric component                             K=L-1
C                                                                        BLIB(JPOS+K,NUMEL)=DNDDX(I)
      CALL MATNUL(ELK,18,18,18,18,ITEST)                                BLIB(JPOS+L,NUMEL)=DNDDY(I)
      DO 110 IG=1,3                                             90     CONTINUE
        IPOS= IG*2                                                      CALL ELSTIF
        T=PLACET(IPOS-1,3)                                      60    CONTINUE
        S=PLACET(IPOS,3)                                        C
        CALL DTSHAP                                             C
        CALL BFORM                                              C     *** Load the element stiffness
        W1W2=WEITRI(IPOS,3)                                     C
        CALL PENALT                                                    CALL LOADK
110     CONTINUE                                                70    CONTINUE
C                                                               ENDIF
      CALL LOADK                                                C
C                                                               RETURN
30    CONTINUE                                                  END
      ENDIF                                                     C
C                                                               C
C                                                               C.............................................................
C     *** Quadrilateral Elements                               C
C                                                               C
      IF(NQUAD.GT.0) THEN                                       C
        NO=8                                                    SUBROUTINE PREK
        NO2=NO*2                                                C
        NO1=NO2-1                                               C+  ==============
        DO 70 IEL=1,NQUAD                                       C
C                                                               C   Evaluate the bandwidth, gauss quadrature points, the shape
C     *** Initialise                                            C   functions and their derivatives.
C                                                               C   Major variables:   KSIZE =bandwidth
      CALL MATNUL(ELK,18,18,18,18,ITEST)                        C                      TSHAPE, DTSHAP =triangle shape fns.
      NUMEL=NOQEL(IEL)                                          C                      QSHAPE, DQSHAP =quad shape fns.
      MAT=ITYP(NUMEL)                                           C                      C  =elasticity matrix [C]
      ETA=ETAM(MAT)                                             C-
      IF(ETA.EQ.0.0D00) THEN                                        IMPLICIT DOUBLE PRECISION (A-H,O-W)
        FACT=ETAN                                                   PARAMETER(IGL=880,JGL=131,KGL=66)
      ELSE                                                          COMMON /CONS/ NTRI,NQUAD,NINCS,NNOD,KSIZE,KSBW,NNOD2,NMAT,IDUM(4),
        FACT=ETA*ETAN                                             +         GAMMA,PI,BETA,NST,NSI,NSEG,NODSEG,DELTAT
      ENDIF                                                         COMMON /ELEM/ NODEL(8,500),NGAUSS(500),NOTEL(500),NOQEL(500),
      NGAUS=NGAUSS(NUMEL)                                         +         NOTCOL(500),NOQCOL(500),DIFFOP(9,500),BLIB(144,500),
      NROW=NOQCOL(IEL)                                            +         PRINC(16,500)
C                                                                   COMMON /MATS/ EM(9),PM(9),TM(9),RHOM(9),ETAM(9),ETAN,ITYP(9)
C     *** Numerically integrate                                     COMMON /STIF/ ELK(18,18),GLOBK(IGL,JGL)
C                                                                   COMMON /GAPT/ S,T,SHAPE(8),DNDDS(8),DNDDT(8),TSHAPE(6,36),
      DO 60 IG=1,NGAUS                                            +         TDNDDS(6,36),TDNDDT(6,36),TW1W2(6,6),QSHAPE(3,72),
        IPOS=(IG-1)*NO                                            +         QDNDDS(3,72),QDNDDT(3,72),QW1W2(3,9),WEITRI(12,6),
        JPOS=IPOS*2                                               +      WEIQAD(18,3),PLACET(12,6),PLACEQ(18,3),PLACEL(3),WEILIN(3)
        XPOS=0.0                                                     COMMON /VARS/ COMS(21),B(3,18),BTC(18,4),ICOM1(5),IG
        YPOS=0.0                                                     DIMENSION NOGT(6),NOGQ(3),NOD(6)
        DO 50 IV=1,NO                                           C
          NODE=NODEL(IV,NUMEL)                                  C   *** Calculate semibandwidth from max nodal difference
          SHAPE(IV)=QSHAPE(NROW,IPOS+IV)                        C
          XPOS=XPOS+SHAPE(IV)*X(NODE)                               ITEST=0
          YPOS=YPOS+SHAPE(IV)*Y(NODE)                               MAX=0
          DNDDS(IV)=QDNDDS(NROW,IPOS+IV)                        C
          DNDDT(IV)=QDNDDT(NROW,IPOS+IV)                            IF(NTRI.GT.0) THEN
50        CONTINUE                                                    DO 30 IEL=1,NTRI
        XSTPOS(IG,NUMEL)=XPOS                                        NUMEL=NOTEL(IEL)
        YSTPOS(IG,NUMEL)=YPOS                                        DO 20 J=1,5
        W1W2=QW1W2(NROW,IG)                                            IST=J+1
                                                                      NOD1=NODEL(J,NUMEL)
```

```
              DO 10 K=IST,6
                IDIF=IABS(NOD1-NODEL(K,NUMEL))
                MAX=MAX0(IDIF,MAX)
10            CONTINUE
20          CONTINUE
30        CONTINUE
        ENDIF
C
        IF(NQUAD.GT.0) THEN
          DO 70 IEL=1,NQUAD
            NUMEL=NOQEL(IEL)
            DO 60 J=1,7
              IST=J+1
              NOD1=NODEL(J,NUMEL)
              DO 50 K=IST,8
                IDIF=IABS(NOD1-NODEL(K,NUMEL))
                MAX=MAX0(IDIF,MAX)
50            CONTINUE
60          CONTINUE
70        CONTINUE
        ENDIF
C
        KSBW=2*(MAX+1)
        KSIZE=2*KSBW-1
        IF(MAX.EQ.0)      CALL CRASH
        IF(KSIZE.GT.JGL) CALL BADLUK
C
C    *** Establish gauss points
C
        CALL GAUSSQ
C
C    *** Evaluate triangular shape fns and derivs
C
        IF(NTRI.GT.0) THEN
          NOGT(1)=6
          NOTGP=1
C
C    *** Establish the no. of sets of gauss points used in the mesh and
C    *** flag each with NOTCOL
C
          DO 150 IEL=1,NTRI
            NUMEL=NOTEL(IEL)
            NGAUS=NGAUSS(NUMEL)
            DO 130 IMP=1,NOTGP
              IF(NOGT(IMP).EQ.NGAUS) THEN
                NOTCOL(IEL)=IMP
                GOTO 150
              ENDIF
130         CONTINUE
            NOTGP=NOTGP+1
            NOGT(NOTGP)=NGAUS
            NOTCOL(IEL)=NOTGP
150       CONTINUE
C
C    *** For each set of gauss points evaluate shapes and derivs
C
          DO 230 NOP=1,NOTGP
            NGAUS=NOGT(NOP)
            DO 220 IG=1,NGAUS
              SPOS=2*IG
              TPOS=SPOS-1
              S=PLACET(SPOS,NGAUS)
              T=PLACET(TPOS,NGAUS)
              W1=WEITRI(SPOS,NGAUS)
              W2=WEITRI(TPOS,NGAUS)
              CALL TSHAFN
              CALL DTSHAP
              IPOS=(IG-1)*6
              DO 210 IV=1,6
                JPOS=IPOS+IV
                TSHAPE(NOP,JPOS)=SHAPE(IV)
                TDNXDS(NOP,JPOS)=DNXDS(IV)
                TDNXDT(NOP,JPOS)=DNXDT(IV)
210           CONTINUE
              TW1W2(NOP,IG)=W1
220         CONTINUE
230       CONTINUE
        ENDIF
C
C    *** Evaluate quadrilateral shape fns and deriv
C
        IF(NQUAD.GT.0) THEN
          NOGQ(1)=4
          NOQGP=1
          DO 190 IEL=1,NQUAD
            NUMEL=NOQEL(IEL)
            NGAUS=NGAUSS(NUMEL)
            DO 170 IMP=1,NOQGP
              IF(NOGQ(IMP).EQ.NGAUS) THEN
                NOQCOL(IEL)=IMP
                GOTO 190
              ENDIF
170         CONTINUE
            NOQGP=NOQGP+1
            NOGQ(NOQGP)=NGAUS
            NOQCOL(IEL)=NOQGP
190       CONTINUE
C
          DO 260 NOP=1,NOQGP
            NGAUS=NOGQ(NOP)
            LCOL=1
            IF(NGAUS.EQ.9) LCOL=2
            DO 250 IG=1,NGAUS
              SPOS=2*IG
              TPOS=SPOS-1
              S=PLACEQ(SPOS,LCOL)
              T=PLACEQ(TPOS,LCOL)
              W1=WEIQAD(SPOS,LCOL)
              W2=WEIQAD(TPOS,LCOL)
              CALL QSHAFN
              CALL DQSHAP
              IPOS=(IG-1)*8
              DO 240 IV=1,8
                JPOS=IPOS+IV
                QSHAPE(NOP,JPOS)=SHAPE(IV)
                QDNXDS(NOP,JPOS)=DNXDS(IV)
                QDNXDT(NOP,JPOS)=DNXDT(IV)
240           CONTINUE
              QW1W2(NOP,IG)=W1*W2
250         CONTINUE
```

```
260     CONTINUE
        ENDIF
C
270     RETURN
        END
C
C
C•••••••••••••••••••••••••••••••••••••••••••••••••••••••••••••••••••••••
C
C
        SUBROUTINE GAUSSQ
C
C       ══════════════
C+
C       Set up the gaussian integration points.
C       Major variables:  PLACET, WEITRI =gauss points and weights for triangles
C                          PLACEQ, WEIQAD =gauss points and weights for quads
C-
        IMPLICIT DOUBLE PRECISION (A-H,O-W)
        COMMON /GAPT/ COM6(1385),WEITRI(12,6),WEIQAD(18,3),PLACET(12,6),
       +              PLACEQ(18,3),PLACEL(3),WEILIN(3)
C
C       ••• Set up triangles
C
        PLACET(1,1)=0.33333333333333300
        PLACET(2,1)=PLACET(1,1)
C
        G1=0.666666666666667D0
        G2=0.166666666666667D0
        PLACET(1,3)=G1
        PLACET(2,3)=G2
        PLACET(3,3)=G2
        PLACET(4,3)=G1
        PLACET(5,3)=G2
        PLACET(6,3)=G2
C
        G1=0 600
        G2=0 200
        PLACET(1,4)=PLACET(1,1)
        PLACET(2,4)=PLACET(1,1)
        PLACET(3,4)=G1
        PLACET(4,4)=G2
        PLACET(5,4)=G2
        PLACET(6,4)=G1
        PLACET(7,4)=G2
        PLACET(8,4)=G2
C
        G1=0.816847572980459D0
        G2=0.091576213509771D0
        G3=0.108103018168070D0
        G4=0.445948490915965D0
        PLACET(1,6)=G1
        PLACET(2,6)=G2
        PLACET(3,6)=G2
        PLACET(4,6)=G1
        PLACET(5,6)=G2
        PLACET(6,6)=G2
        PLACET(7,6)=G3
        PLACET(8,6)=G4
        PLACET(9,6)=G4
        PLACET(10,6)=G3
```

```
        PLACET(11,6)=G4
        PLACET(12,6)=G4
C
C       ••• Set up quadrilaterals
C
        G1=-0.577350269189626D0
        G2=-G1
        PLACEQ(1,1)=G1
        PLACEQ(2,1)=G1
        PLACEQ(3,1)=G1
        PLACEQ(4,1)=G2
        PLACEQ(5,1)=G2
        PLACEQ(6,1)=G1
        PLACEQ(7,1)=G2
        PLACEQ(8,1)=G2
C
        G1=-0.774596669241483D0
        G2=0.0D0
        G3=-G1
        PLACEQ(1,2)=G1
        PLACEQ(2,2)=G1
        PLACEQ(3,2)=G1
        PLACEQ(4,2)=G2
        PLACEQ(5,2)=G1
        PLACEQ(6,2)=G3
        PLACEQ(7,2)=G2
        PLACEQ(8,2)=G1
        PLACEQ(9,2)=G2
        PLACEQ(10,2)=G2
        PLACEQ(11,2)=G2
        PLACEQ(12,2)=G3
        PLACEQ(13,2)=G3
        PLACEQ(14,2)=G1
        PLACEQ(15,2)=G3
        PLACEQ(16,2)=G2
        PLACEQ(17,2)=G3
        PLACEQ(18,2)=G3
C
C       ••• Set up triangle weights
C
        WEITRI(1,1)=0.5D0
        WEITRI(2,1)=0.5D0
C
        DO 10 I=1,6
          WEITRI(I,3)=.166666666666667D0
10      CONTINUE
C
        WEITRI(1,4)=-0.28125D0
        WEITRI(2,4)=WEITRI(1,4)
        DO 20 I=3,8
          WEITRI(I,4)=.260416666666667D0
20      CONTINUE
C
        DO 30 I=1,6
          WEITRI(I,6)=.549758718276609D-1
          WEITRI(I+6,6)=0.111690794839005D0
30      CONTINUE
C
C       ••• Set up quadrilateral weights
C
```

```fortran
      DO 50 I=1,8
        WEIQAD(I,1)=1.0D0
50    CONTINUE
C
      G1=0.55555555555556D0
      G2=0.8888888888889D0
      G3=G1
      WEIQAD(1,2)=G1
      WEIQAD(2,2)=G1
      WEIQAD(3,2)=G1
      WEIQAD(4,2)=G2
      WEIQAD(5,2)=G1
      WEIQAD(6,2)=G3
      WEIQAD(7,2)=G2
      WEIQAD(8,2)=G1
      WEIQAD(9,2)=G2
      WEIQAD(10,2)=G2
      WEIQAD(11,2)=G2
      WEIQAD(12,2)=G3
      WEIQAD(13,2)=G3
      WEIQAD(14,2)=G1
      WEIQAD(15,2)=G3
      WEIQAD(16,2)=G2
      WEIQAD(17,2)=G3
      WEIQAD(18,2)=G3
C
      RETURN
      END
C
C
C..........................................................................
C
C
      SUBROUTINE TSHAFN
C
C+
C   Calculate the shape functions of a triangular element
C-
      IMPLICIT DOUBLE PRECISION (A-H,O-W)
      COMMON /GAPT/ S,T,SHAPE(8),COM7(1633)
C
      P=1.0D0-S-T
      SHAPE(1)=2.0D0*S*S-S
      SHAPE(3)=2.0D0*T*T-T
      SHAPE(5)=2.0D0*P*P-P
      SHAPE(2)=4.0D0*S*T
      SHAPE(4)=4.0D0*T*P
      SHAPE(6)=4.0D0*S*P
C
      RETURN
      END
C
C
C..........................................................................
C
C
      SUBROUTINE QSHAFN
C
C+
C   Calculate the quadrilateral shape functions.
C-
```

```fortran
      IMPLICIT DOUBLE PRECISION (A-H,O-W)
      COMMON /GAPT/ S,T,SHAPE(8),COM7(1633)
C
      S2=S*2.0D0
      T2=T*2.0D0
      SS=S*S
      TT=T*T
      SST=SS*T
      STT=S*TT
      ST=S*T
C
      SHAPE(1)=(-1.0D0+ST+SS+TT-SST-STT)/4.0D0
      SHAPE(2)=(1.0D0-T-SS+SST)/2.0D0
      SHAPE(3)=(-1.0D0-ST+SS+TT-SST+STT)/4.0D0
      SHAPE(4)=(1.0D0+S-TT-STT)/2.0D0
      SHAPE(5)=(-1.0D0+ST+SS+TT+SST+STT)/4.0D0
      SHAPE(6)=(1.0D0+T-SS-SST)/2.0D0
      SHAPE(7)=(-1.0D0-ST+SS+TT+SST-STT)/4.0D0
      SHAPE(8)=(1.0D0-S-TT+STT)/2.0D0
C
      RETURN
      END
C
C
C..........................................................................
C
C
      SUBROUTINE DTSHAP
C
C+
C   Evaluate the derivatives of the triangular shape functions.
C-
      IMPLICIT DOUBLE PRECISION (A-H,O-W)
      COMMON /GAPT/ S,T,SHAPE(8),DNXDS(8),DNXDT(8),COM8(1617)
C
      T4=4.0D0*T
      S4=4.0D0*S
C
C   *** Derivatives w.r.t. s(xi)-coord
C
      DNXDS(1)=S4-1.0D0
      DNXDS(3)=0.0D0
      DNXDS(5)=S4+T4-3.0D0
      DNXDS(2)=T4
      DNXDS(4)=-T4
      DNXDS(6)=4.0D0-T4-2.0D0*S4
C
C   *** Derivatives w.r.t. t(eta)-coord
C
      DNXDT(1)=0.0D0
      DNXDT(3)=T4-1.0D0
      DNXDT(5)=S4+T4-3.0D0
      DNXDT(2)=S4
      DNXDT(4)=4.0D0-S4-2.0D0*T4
      DNXDT(6)=-S4
C
      RETURN
      END
C
C
C..........................................................................
C
C
```

```fortran
      SUBROUTINE DOSHAP
C     ==============
C+
C
C     Calculate the derivatives of the quadrilateral shape functions.
C
C-
      IMPLICIT DOUBLE PRECISION (A-H,O-W)
      COMMON /GAPT/ S,T,SHAPE(8),DNXDS(8),DNXDT(8),COMB(1617)
C
      TT=T*T
      SS=S*S
      ST=S*T
      T2=2.0D0*T
      S2=2.0D0*S
      ST2=2.0D0*ST
C
C     *** Derivatives w.r.t s(xi)-coord
C
      DNXDS(1)=(S2+T-ST2-TT)/4.0D0
      DNXDS(2)=ST-S
      DNXDS(3)=(TT-ST2-T+S2)/4.0D0
      DNXDS(4)=(1.0D0-TT)/2.0D0
      DNXDS(5)=(ST2+TT+S2+T)/4.0D0
      DNXDS(6)=-ST-S
      DNXDS(7)=(S2-T+ST2-TT)/4.0D0
      DNXDS(8)=-DNXDS(4)
C
C     *** Derivatives w.r.t. t(eta)-coord
C
      DNXDT(1)=(S+T2-SS-ST2)/4.0D0
      DNXDT(2)=(SS-1.0D0)/2.0D0
      DNXDT(3)=(T2-S+ST2-SS)/4.0D0
      DNXDT(4)=-ST-T
      DNXDT(5)=(SS+ST2+S+T2)/4.0D0
      DNXDT(6)=-DNXDT(2)
      DNXDT(7)=(T2-S+SS-ST2)/4.0D0
      DNXDT(8)=ST-T
C
      RETURN
      END
C
C
C.................................................................
C
C
      SUBROUTINE BFORM
C     ==============
C
C+
C
C     Calculate the components of the strain rate operator [B].
C     Major variables:  DNXDX, DNXDY =global derivatives
C                       DETJ =determinant of Jacobian
C-
      IMPLICIT DOUBLE PRECISION (A-H,O-W)
      DOUBLE PRECISION JAC(2,2),JACINV(2,2)
      PARAMETER(IGL=880,JGL=131,KGL=66)
      COMMON /NODS/ X(IGL/2),Y(IGL/2),DISP(IGL),FORCE(IGL),XCOM1(4000)
      COMMON /ELEM/ NODEL(8,500),NGAUSS(500),NOTEL(500),NOOEL(500),
     +              NOTOOL(500),NOOCOL(500),DIFFOP(9,500),BLIB(144,500),
     +              PRINC(16,500)
      COMMON /GAPT/ S,T,SHAPE(8),DNXDS(8),DNXDT(8),TSHAPE(6,36),
     +              TDNXDS(6,36),TDNXDT(6,36),TW1W2(6,6),OSHAPF(3,72),
```

```fortran
     +              QDNXDS(3,72),QDNXDT(3,72),QW1W2(3,9),WEITRI(12,6),
     +     WEIQAD(18,3),PLACET(12,6),PLACEQ(18,3),PLACEL(3),WEILIN(3)
      COMMON /VARS/ W1W2,DETJ,ETA,C2,FACT,DNXDX(8),DNXDY(8),B(4,18),
     +              BTC(18,4),NO,NGAUS,ICASE,NUMEL,NROW,IG
C
      ITEST=0
C
C     *** Calculate the Jacobian
C
      JAC(1,1)=0.0D0
      JAC(1,2)=0.0D0
      JAC(2,1)=0.0D0
      JAC(2,2)=0.0D0
      DO 10 INOD=1,NO
        NODE=IABS(NODEL(INOD,NUMEL))
        XNOD=X(NODE)
        YNOD=Y(NODE)
        JAC(1,1)=JAC(1,1)+DNXDS(INOD)*XNOD
        JAC(1,2)=JAC(1,2)+DNXDS(INOD)*YNOD
        JAC(2,1)=JAC(2,1)+DNXDT(INOD)*XNOD
        JAC(2,2)=JAC(2,2)+DNXDT(INOD)*YNOD
10    CONTINUE
C
C     *** Evaluate determinant and inverse
C
      DETJ=JAC(1,1)*JAC(2,2)-JAC(1,2)*JAC(2,1)
      JACINV(1,1)= JAC(2,2)/DETJ
      JACINV(1,2)=-JAC(1,2)/DETJ
      JACINV(2,1)=-JAC(2,1)/DETJ
      JACINV(2,2)= JAC(1,1)/DETJ
C
C     *** Store the inverse Jacobian
C
      IPOS=(IG-1)*4
      PRINC(IPOS+1,NUMEL)=JACINV(1,1)
      PRINC(IPOS+2,NUMEL)=JACINV(1,2)
      PRINC(IPOS+3,NUMEL)=JACINV(2,1)
      PRINC(IPOS+4,NUMEL)=JACINV(2,2)
C
C     *** Evaluate strain rate operator
C
      DO 20 I=1,NO
        DNXDX(I)=JACINV(1,1)*DNXDS(I)+JACINV(1,2)*DNXDT(I)
        DNXDY(I)=JACINV(2,1)*DNXDS(I)+JACINV(2,2)*DNXDT(I)
20    CONTINUE
C
      RETURN
      END
C
C
C.........................................................................
C
C
      SUBROUTINE ELSTIF
C     ===============
C
C+
C
C     Calculate the element stiffness.
C     Major variables:  DNXDX, DNXDY =global derivatives
C                       ETA =element viscosity    FACT =penalty parameter
C                       ELK =element stiffness
C-
```

```fortran
      IMPLICIT DOUBLE PRECISION (A-H,O-W)
      PARAMETER(IGL=880,JGL=131,KGL=66)
      COMMON /CONS/ NTRI,NQUAD,NINCS,NNOD,KSIZE,KSBW,NNOD2,NMAT,IDUM(4),
     +              GAMMA,PI,BETA,NST,NSI,NSEG,NODSEG,DELTAT
      COMMON /STIF/ ELK(18,18),GLOBK(IGL,JGL)
      COMMON /ELEM/ NODEL(8,500),NGAUSS(500),NOTEL(500),NOQEL(500),
     +              NOTOOL(500),NOCOOL(500),DIFFOP(9,500),BLIB(144,500),
     +              PRINC(16,500)
      COMMON /VARS/ W1W2,DETJ,ETA,C2,FACT,DNXDX(8),DNXDY(8),B(4,18),
     +              BTC(18,4),NO,NGAUS,ICASE,NUMEL,IROW,IG
C
C
C     ••• Initialise
C
      ITEST=0
      NO2=NO*2
      CALL MATNUL(B,4,18,4,18,ITEST)
      CALL MATNUL(BTC,18,4,18,4,ITEST)
C
C     ••• Calculate the non-zero components of  [BT][C1+C2], both shear and
C     ••• volumetric components can be integrated directly for the quads.
C
      DO 10 I=1,NO
        L=2*I
        K=L-1
        B(1,K)=DNXDX(I)
        B(2,L)=DNXDY(I)
        B(3,K)=DNXDY(I)
        B(3,L)=DNXDX(I)
C
C     ••• Check for quadrilaterals
C
        IF(NGAUS.EQ.4) THEN
C
C     ••• Check for axisymmetric
C
          IF(NST.EQ.1) THEN
            B(4,K)=SHAPE(I)/XSTPOS(IG,NUMEL)
            BTC(K,1)=B(1,K)*2.0D0*ETA  + (B(1,K)+B(4,K))*FACT
            BTC(L,1)=                         B(2,L)*FACT
            BTC(K,3)=B(3,L)*ETA
            BTC(K,4)=B(4,K)*2.0D00*ETA + (B(1,K)+B(4,K))*FACT
            BTC(K,2)=                     (B(1,K)+B(4,K))*FACT
            BTC(L,2)=B(2,L)*2.0D0*ETA  + B(2,L)*FACT
            BTC(L,3)=B(3,L)*ETA
            BTC(L,4)=                         B(2,L)*FACT
          ELSE
            BTC(K,1)=B(1,K)*2.0D0*ETA + B(1,K)*FACT
            BTC(L,1)=                  .  B(2,L)*FACT
            BTC(K,3)=B(3,K)*ETA
            BTC(K,2)=                     B(1,K)*FACT
            BTC(L,2)=B(2,L)*2.0D0*ETA + B(2,L)*FACT
            BTC(L,3)=B(3,L)*ETA
          ENDIF
        ELSE
          BTC(K,1)=B(1,K)*2.0D0*ETA
          BTC(K,3)=B(3,K)*ETA
          BTC(L,2)=B(2,L)*2.0D0*ETA
          BTC(L,3)=B(3,L)*ETA
        ENDIF
10    CONTINUE
C
C     ••• Calculate numerical integration operator
C
```

```fortran
      IF(NST.EQ.1) THEN
        DV=W1W2*DETJ*2.0D00*PI*XSTPOS(IG,NUMEL)
      ELSE
        DV=W1W2*DETJ
      ENDIF
      DIFFOP(IG,NUMEL)=DV
C
C     ••• Evaluate the element stiffness
C
      DO 40 NROW=1,NO2
        DO 30 NCOL=NROW,NO2
          DUM=0.0
          DO 20 J=1,4
            DUM=DUM+BTC(NROW,J)*B(J,NCOL)
20        CONTINUE
          ELK(NROW,NCOL)=ELK(NROW,NCOL)+DUM*DV
30      CONTINUE
40    CONTINUE
C
      RETURN
      END
C
C
C•••••••••••••••••••••••••••••••••••••••••••••••••••••••••••••••••••••••••••
C
C
      SUBROUTINE PENALT
C    ===================
C
C+
C     Calculate the penalty function contribution to the element stiffness.
C     Major variables:  FACT =penalty parameter    ELK =element stiffness
C-
      IMPLICIT DOUBLE PRECISION (A-H,O-W)
      PARAMETER(IGL=880,JGL=131,KGL=66)
      COMMON /CONS/ NTRI,NQUAD,NINCS,NNOD,KSIZE,KSBW,NNOD2,NMAT,IDUM(4),
     +              GAMMA,PI,BETA,NST,NSI,NSEG,NODSEG,DELTAT
      COMMON /STIF/ ELK(18,18),GLOBK(IGL,JGL)
      COMMON /GAPT/ S,T,SHAPE(8),DNXDS(8),DNXDT(8),TSHAPE(6,36),
     +              TDNXDS(6,36),TDNXDT(6,36),TW1W2(6,6),QSHAPE(3,72),
     +              QDNXDS(3,72),QDNXDT(3,72),QW1W2(3,9),COM2(258)
      COMMON /VARS/ W1W2,DETJ,ETA,C2,FACT,DNXDX(8),DNXDY(8),B(4,18),
     +              BTC(18,4),NO,NGAUS,NO2,NUMEL,NROW,IG
C
C     ••• Reduced integration of the volumetric component
C
      ITEST=0
C
C     ••• Initialise
C
      CALL MATNUL(B,4,18,4,18,ITEST)
      CALL MATNUL(BTC,18,4,18,4,ITEST)
C
C     ••• Calculate non-zero components of the stiffness
C
      DO 10 I=1,NO
        L=2*I
        K=2*I-1
        B(1,K)=DNXDX(I)
        B(2,L)=DNXDY(I)
        B(3,K)=DNXDY(I)
```

```fortran
          B(3,L)=DNXDX(I)
          IF(NST.EQ.5) THEN
            B(4,K)=SHAPE(I)/XSTPOS(IG*2-1,NUMEL)
            BTC(K,1)=(B(1,K)+B(4,K))*FACT
            BTC(L,1)= B(2,L)*FACT
            BTC(K,2)= BTC(K,1)
            BTC(K,4)= BTC(K,L)
            BTC(L,2)= BTC(L,1)
            BTC(L,4)= BTC(L,1)
          ELSE
            BTC(K,1)=B(1,K)*FACT
            BTC(L,1)=B(2,L)*FACT
            BTC(K,2)=B(1,K)*FACT
            BTC(L,2)=B(2,L)*FACT
          ENDIF
10     CONTINUE
C
       DV=DIFFOP(IG,NUMEL)
C
C      ... Evaluate the element stiffness
C
       DO 40 NROW=1,NO2
         DO 30 NCOL=NROW,NO2
           DUM=0.0
           DO 20 J=1,4
             DUM=DUM+BTC(NROW,J)*B(J,NCOL)
20         CONTINUE
           ELK(NROW,NCOL)=ELK(NROW,NCOL)+DUM*DV
30       CONTINUE
40     CONTINUE
C
       RETURN
       END
C
C
C*****************************************************************
C
C
       SUBROUTINE LOADK
C
C+
C      Load the element stiffness into the global stiffness matrix.
C      Major variables: ELK =element stiffness   NODEL =element nodes
C                        GLOBK =system matrix [K]
C-
       IMPLICIT DOUBLE PRECISION (A-H,O-W)
       PARAMETER(IGL=880,JGL=131,KGL=66)
       COMMON /CONS/ NTRI,NQUAD,NINCS,NNOD,KSIZE,KSBW,NNOD2,NMAT,IDUM(4),
      +              GAMMA,PI,BETA,NST,NSI,NSEG,NODSEG,DELTAT
       COMMON /STIF/ ELK(18,18),GLOBK(IGL,JGL)
       COMMON /VARS/ COMB(165),NO,NGAUS,NO2,NUMEL,NROW,IG
       COMMON /ELEM/ NODEL(8,500),NGAUSS(500),NOTEL(500),NOGEL(500),
      +              NOTCOL(500),NOGCOL(500),DIFFOP(9,500),BLIB(144,500),
      +              PRINC(16,500)
C
C      ... Fill in lower triangle of element stiffness
C
       DO 50 IFIL=1,NO2
         DO 50 JFIL=IFIL,NO2
           ELK(JFIL,IFIL)=ELK(IFIL,JFIL)
```

```fortran
50     CONTINUE
C
C      ... Load the element stiffness into the banded system matrix
C
       DO 10 I=1,NO
         ICOL=2*NODEL(I,NUMEL)-2+KSBW
         IELK=2*I-2
C
C      ... Evaluate the column number of the two dof
C
         DO 20 J=1,2
           JCOL=ICOL + J
           JELK=IELK + J
           DO 30 K=1,NO
             IROW=2*NODEL(K,NUMEL)-2
             KELK=2*K-2
C
C      ... Evaluate the row number of the two dof and reduce the column
C
             DO 40 L=1,2
               KROW=IROW + L
               KCOL=JCOL - KROW
               LELK=KELK + L
               GLOBK(KROW,KCOL)=GLOBK(KROW,KCOL)+ELK(LELK,JELK)
40           CONTINUE
30         CONTINUE
20       CONTINUE
10     CONTINUE
C
       RETURN
       END
C
C
C*****************************************************************
C
C
       SUBROUTINE BOUND2
C
C+
C      Enforce the Dirichlet boundary conditions exactly by adding each known
C      component to free nodes in the force vector.
C      Major variables: NFIX =no. of fixed dof    DFIX =known value
C                       GLOBK =system matrix [K]   FORCE =force vector |F|
C-
       IMPLICIT DOUBLE PRECISION (A-H,O-W)
       PARAMETER(IGL=880,JGL=131,KGL=66)
       COMMON /CONS/ NTRI,NQUAD,NINCS,NNOD,KSIZE,KSBW,NNOD2,NMAT,IDUM(4),
      +              GAMMA,PI,BETA,NST,NSI,NSEG,NODSEG,DELTAT
       COMMON /STIF/ ELK(18,18),GLOBK(IGL,JGL)
       COMMON /NODS/ X(IGL/2),Y(IGL/2),DISP(IGL),FORCE(IGL),XCOM1(4000)
       COMMON /FIXT/ DFIX(2,500),NOFIX(500),IFLAG(2,500),NFIX,NEXT,NSTOP
C
       IF(NFIX.EQ.0) RETURN
C
C      ... Subtract the known values from the force vector
C
       DO 10 I=1,NFIX
         DO 10 J=1,2
           K=2*NOFIX(I)+J-2
           IF(IFLAG(J,I).EQ.1) THEN
```

```
      DO 20 NOD=1,NNOD2
        JCOL=KSBW+K-NOD
        IF(JCOL.GT.0.AND.JCOL.LE.KSIZE)
     +  FORCE(NOD)=FORCE(NOD)-GLOBK(NOD,JCOL)*DFIX(J,I)
20      CONTINUE
      ENDIF
10    CONTINUE
C
C     *** Insert the exact solution
C
      DO 25 I=1,NFIX
        DO 25 J=1,2
          K=2*NOFIX(I)+J-2
          IF(IFLAG(J,I).EQ.1) THEN
            DO 30 IROW=1,NNOD2
              JCOL=KSBW+K-IROW
              IF(JCOL.GT.0.AND.JCOL.LE.KSIZE) GLOBK(IROW,JCOL)=0.0D0
30          CONTINUE
            DO 40 ICOL=1,KSIZE
              GLOBK(K,ICOL)=0.0D0
40          CONTINUE
            GLOBK(K,KSBW)=1.0D0
            FORCE(K)=DFIX(J,I)
          ENDIF
25    CONTINUE
C
      RETURN
      END
C
C
C...............................................................
C
C
C
      SUBROUTINE BODY4S
C
C+    ========
C+
C     Calculate the contributions to the global force vector for body
C     forces acting in the positive y-direction. Note that gravity is
C     1.0  for the wave-test model.
C     Major variables:  RHOM  =density of material type
C                       FORCE =force vector |F|
C-
      IMPLICIT DOUBLE PRECISION (A-H,O-W)
      PARAMETER(IGL=880,JGL=131,KGL=66)
      COMMON /CONS/ NTRI,NQUAD,NINCS,NNOD,KSIZE,KSBW,NNOD2,NMAT,IDUM(4),
     +              GAMMA,PI,BETA,NST,NSI,NSEG,NODSEG,DELTAT
      COMMON /NODS/ X(IGL/2),Y(IGL/2),DISP(IGL),FORCE(IGL),XCOM1(4000)
      COMMON /MATS/ EM(9),PM(9),TM(9),RHOM(9),ETAM(9),ETAN,ITYP(9)
      COMMON /ELEM/ NODEL(8,500),NGAUSS(500),NOTEL(500),NOQEL(500),
     +              NOTCOL(500),NOQCOL(500),DIFFOP(9,500),BLIB(144,500),
     +              PRINC(16,500)
      COMMON /GAPT/ S,T,SHAPE(8),DNXDS(8),DNXDT(8),TSHAPE(6,36),
     +              TDNXDS(6,36),TDNXDT(6,36),TW1W2(6,6),QSHAPE(3,72),
     +              QDNXDS(3,72),QDNXDT(3,72),QW1W2(3,9),WEITRI(12,6),
     +              WEIQAD(18,3),PLACET(12,6),PLACEQ(18,3),PLACEL(3),WEILIN(3)
C
      IF(NTRI.GT.0) THEN
        DO 30 IEL=1,NTRI
          NUMEL=NOTEL(IEL)
          MAT=ITYP(NUMEL)
```

```
          RHO=RHOM(MAT)
          IF(ETAM(MAT).EQ.0.0D00) THEN
            GRAV=1.0D00
          ELSE
            GRAV=9.81D00
          ENDIF
          NGAUS=NGAUSS(NUMEL)
          NROW=NOTCOL(IEL)
          FLOAD=-RHO*GRAV
C
C     *** Integrate the element weight to give the nodal forces
C
          DO 20 IG=1,NGAUS
            IPOS=(IG-1)*6
            DV=DIFFOP(IG,NUMEL)
            DO 10 INT=1,6
              SHAPE(INT)=TSHAPE(NROW,IPOS+INT)
              NOD=NODEL(INT,NUMEL)
              FORCE(2*NOD)=SHAPE(INT)*FLOAD*DV+FORCE(2*NOD)
10          CONTINUE
20        CONTINUE
30      CONTINUE
      ENDIF
C
      IF(NQUAD.GT.0) THEN
        DO 70 IEL=1,NQUAD
          NUMEL=NOQEL(IEL)
          MAT=ITYP(NUMEL)
          RHO=RHOM(MAT)
          IF(ETAM(MAT).EQ.0.0D00) THEN
            GRAV=1.0D00
          ELSE
            GRAV=9.81D00
          ENDIF
          NGAUS=NGAUSS(NUMEL)
          NROW=NOQCOL(IEL)
          FLOAD=-RHO*GRAV
          DO 60 IG=1,NGAUS
            DV=DIFFOP(IG,NUMEL)
            IPOS=(IG-1)*8
            DO 50 INT=1,8
              SHAPE(INT)=QSHAPE(NROW,IPOS+INT)
              NOD=NODEL(INT,NUMEL)
              FORCE(2*NOD)=SHAPE(INT)*FLOAD*DV+FORCE(2*NOD)
50          CONTINUE
60        CONTINUE
70      CONTINUE
      ENDIF
C
      RETURN
      END
C
C
C...............................................................
C
C
      SUBROUTINE FORMN
C
C     ========
C
C+
C     Calculate the convective operator [H] using the latest velocities,
C     and assuming the Boussinesq approx.
C     Major variables: FOUT  =convective operator [H]   RHOM  =density
```

```
C                    DISP  =current velocity solution |v|
C-
      IMPLICIT DOUBLE PRECISION (A-H,O-W)
      PARAMETER(IGL=880,JGL=131,KGL=66)
      COMMON /CONS/ NTRI,NQUAD,NINCS,NNOD,KSIZE,KSBW,NNOD2,NMAT,IDUM(4),
     +              GAMMA,PI,BETA,NST,NSI,NSEG,NODSEG,DELTAT
      COMMON /NODS/ X(IGL/2),Y(IGL/2),DISP(IGL),FORCE(IGL),XCOM1(4000)
      COMMON /MATS/ EM(9),PM(9),TM(9),RHOM(9),ETAM(9),ETAN,ITYP(9)
      COMMON /ELEM/ NODEL(8,500),NGAUSS(500),NOTEL(500),NOQEL(500),
     +              NOTCOL(500),NOQCOL(500),DIFFOP(9,500),BLIB(144,500),
     +              PRINC(16,500)
      COMMON /FIXT/ DFIX(2,500),NOFIX(500),IFLAG(2,500),NFIX,NEXT,NSTOP
      COMMON /STIF/ ELK(18,18),GLOBK(IGL,JGL)
      COMMON /VISC/ DSTORE(12,900),FINIT(IGL),FOUT(IGL),AMASS(IGL)
      COMMON /GAPT/ S,T,SHAPE(8),DNXDS(8),DNXDT(8),TSHAPE(6,36),
     +              TDNXDS(6,36),TDNXDT(6,36),TW1W2(6,6),QSHAPE(3,72),
     +              QDNXDS(3,72),QDNXDT(3,72),QW1W2(3,9),WEITRI(12,6),
     +   WEIQAD(18,3),PLACET(12,6),PLACEQ(18,3),PLACEL(3),WEILIN(3)
      COMMON /VARS/ W1W2,DETJ,RHO,C2,FACT,DNXDX(8),DNXDY(8),B(4,18),
     +              VEL(2),DVEL(2,2),COM3(66),NO,NGAUS,NO2,NUMEL,NROW,IG
C
C     ... Initialise
C
      ITEST=0
      RHO=RHOM(1)
      CALL VECNUL(FOUT,IGL,NNOD2,ITEST)
C
      IF(NQUAD.GT.0) THEN
         DO 10 IEL=1,NQUAD
           NO=8
           NO2=NO*2
           NUMEL=NOQEL(IEL)
           NGAUS=NGAUSS(NUMEL)
           NROW=NOQCOL(IEL)
           CALL MATNUL(ELK,18,18,18,18,ITEST)
           DO 20 IG=1,NGAUS
             IPOS=(IG-1)*NO
             DV=DIFFOP(IG,NUMEL)
             CALL VECNUL(VEL,2,2,ITEST)
             CALL MATNUL(DVEL,2,2,2,2,ITEST)
C
C     ... Unload the shape functions and derivatives at the gauss
C     ... point, calculate the velocity and it's derivative
C
             DO 30 NOD=1,NO
               NODE=NODEL(NOD,NUMEL)
               SHAPE(NOD)=QSHAPE(NROW,IPOS+NOD)
               DNXDX(NOD)=BLIB(IPOS*2+2*NOD-1,NUMEL)
               DNXDY(NOD)=BLIB(IPOS*2+2*NOD  ,NUMEL)
               VEL(1)=VEL(1)+SHAPE(NOD)*DISP(2*NODE-1)
               VEL(2)=VEL(2)+SHAPE(NOD)*DISP(2*NODE)
               DVEL(1,1)=DVEL(1,1)+DNXDX(NOD)*DISP(2*NODE-1)
               DVEL(1,2)=DVEL(1,2)+DNXDY(NOD)*DISP(2*NODE-1)
               DVEL(2,1)=DVEL(2,1)+DNXDX(NOD)*DISP(2*NODE)
               DVEL(2,2)=DVEL(2,2)+DNXDY(NOD)*DISP(2*NODE)
   30        CONTINUE
C
C     ... Integrate the velocity-derivative product to give the
C     ... convective operator
C
             DO 40 NOD=1,NO
               NODE=NODEL(NOD,NUMEL)
               FOUT(2*NODE-1)=FOUT(2*NODE-1)-RHO*DV*SHAPE(NOD)*
```

```
     +                      (           DVEL(1,2)*VEL(2))
               FOUT(2*NODE)=FOUT(2*NODE)-RHO*DV*SHAPE(NOD)*
     +                      (DVEL(2,1)*VEL(1)                  )
   40        CONTINUE
   20      CONTINUE
   10    CONTINUE
      ENDIF
C
      IF(NTRI.GT.0) THEN
         DO 60 IEL=1,NTRI
           NO=6
           NO2=NO*2
           NUMEL=NOTEL(IEL)
           NGAUS=NGAUSS(NUMEL)
           NROW=NOTCOL(IEL)
           CALL MATNUL(ELK,18,18,18,18,ITEST)
           DO 70 IG=1,NGAUS
             IPOS=(IG-1)*NO
             DV=DIFFOP(IG,NUMEL)
             CALL VECNUL(VEL,2,2,ITEST)
             CALL MATNUL(DVEL,2,2,2,2,ITEST)
C
C     ... Unload the shape functions and derivatives at the gauss
C     ... point, calculate the velocity and it's derivative
C
             DO 80 NOD=1,NO
               NODE=NODEL(NOD,NUMEL)
               SHAPE(NOD)=TSHAPE(NROW,IPOS+NOD)
               DNXDX(NOD)    =BLIB(IPOS*2+2*NOD-1,NUMEL)
               DNXDY(NOD)    =BLIB(IPOS*2+2*NOD  ,NUMEL)
               VEL(1)=VEL(1)+SHAPE(NOD)*DISP(2*NODE-1)
               VEL(2)=VEL(2)+SHAPE(NOD)*DISP(2*NODE)
               DVEL(1,1)=DVEL(1,1)+DNXDX(NOD)*DISP(2*NODE-1)
               DVEL(1,2)=DVEL(1,2)+DNXDY(NOD)*DISP(2*NODE-1)
               DVEL(2,1)=DVEL(2,1)+DNXDX(NOD)*DISP(2*NODE)
               DVEL(2,2)=DVEL(2,2)+DNXDY(NOD)*DISP(2*NODE)
   80        CONTINUE
C
C     ... Integrate the velocity-derivative product to give the
C     ... force increment
C
             DO 90 NOD=1,NO
               NODE=NODEL(NOD,NUMEL)
               FOUT(2*NODE-1)=FOUT(2*NODE-1)-RHO*DV*SHAPE(NOD)*
     +                      (DVEL(1,2)*VEL(2))
               FOUT(2*NODE)=FOUT(2*NODE)-RHO*DV*SHAPE(NOD)*
     +                      (DVEL(2,1)*VEL(1))
   90        CONTINUE
   70      CONTINUE
   60    CONTINUE
      ENDIF
C
C     ... Ensure Dirichlet conditions
C
      IF(NFIX.GT.0) THEN
         DO 100 I=1,NFIX
           DO 100 J=1,2
             K=2*NOFIX(I)+J-2
             IF(IFLAG(J,I).EQ.1) FOUT(K)=0.0D0
  100    CONTINUE
```

```
      ENDIF
C
C     *** Multiply each component by the stability factor
C
      DO 600 I=1,NNOD2
        FOUT(I)=FOUT(I)*GAMMA*DELTAT
600   CONTINUE
C
      RETURN
      END
C
C
C........................................................................
C
C
      SUBROUTINE TIMSOL
C     ============
C
C+
C     Evaluate the time-dependent solution to the Navier-Stokes' equations
C     using a predictor-corrector algorithm incorporating the free surface
C     of the fluid.
C     Major variables:  GLOBK =system matrix [K]     FORCE =force vector {F}
C                       DISP  =current velocity {v}
C                       AMASS =inertial term [M]     FOUT  =convective [H]
C                       DPART, VPART, APART=particle displ, vel, and acc
C                       DMESH, VMESH, AMESH=mesh displ, vel, acc
C-
      IMPLICIT DOUBLE PRECISION (A-H,O-W)
      PARAMETER(IGL=800,JGL=131,KGL=66)
      COMMON /CONS/ NTRI,NQUAD,NINCS,NNOD,KSIZE,KSBW,NNOD2,NMAT,IDUM(4),
     +              GAMMA,PI,BETA,NST,NSI,NSEG,NODSEG,DELTAT
      COMMON /NODS/ X(IGL/2),Y(IGL/2),DISP(IGL),FORCE(IGL),XCOM1(4000)
      COMMON /STIF/ ELK(18,18),GLOBK(IGL,JGL)
      COMMON /FRON/ GLOBK0(IGL,JGL)
      COMMON /STF4/ GLOBKL(IGL,KGL),FORCE0(IGL),NROPIV(IGL)
      COMMON /MATS/ EM(9),PM(9),TM(9),RHOM(9),ETAM(9),ETAN,ITYP(9)
      COMMON /ELEM/ NODEL(8,500),NGAUSS(500),NOTEL(500),NOQEL(500),
     +              NOTCOL(500),NOQCOL(500),DIFFOP(9,500),BLIB(144,500),
     +              PRINC(16,500)
      COMMON /VISC/ DSTORE(12,900),FINIT(IGL),FOUT(IGL),AMASS(IGL)
      COMMON /FIXT/ DFIX(2,500),NOFIX(500),IFLAG(2,500),NFIX,NEXT,NSTOP
      COMMON /VARS/ W1W2,DETJ,RHO,C2,FACT,DNXDX(8),DNXDY(8),B(4,18),
     +              BTC(18,4),NO,NGAUS,NO2,NUMEL,NSURF,IG
      COMMON /TIMS/ ELSIZE(2,500),DELT,NLOAD(IGL),TTOTAL
      COMMON /MOVE/ VPART(IGL),VMESH(IGL),APARAM(IGL),STRANS(IGL),
     +              ATRANS(IGL),DMESH(IGL),APART(IGL),AMESH(IGL),
     +              VMESH2(IGL),DMESH2(IGL),XOLD(IGL),YOLD(IGL)
      DIMENSION DUMMY(IGL),AMESH2(IGL)
C
      NITER=1
      ITEST=0
      DELT=0.0
      TTOTAL=0.0
      ICOMP=20
      ISURF=1
      COMM=GAMMA*DELTAT
C
C     *** Initialise
C
      CALL VECCOP(X,IGL,XOLD,IGL,NNOD,ITEST)
```

```
      CALL VECCOP(Y,IGL,YOLD,IGL,NNOD,ITEST)
      CALL VECNUL(VMESH,IGL,NNOD2,ITEST)
      CALL VECNUL(VPART,IGL,NNOD2,ITEST)
      CALL VECNUL(APART,IGL,NNOD2,ITEST)
      CALL VECNUL(DMESH,IGL,NNOD2,ITEST)
      CALL VECNUL(AMESH,IGL,NNOD2,ITEST)
      CALL VECNUL(FINIT,IGL,NNOD2,ITEST)
      CALL MATNUL(DSTORE,12,900,5,900,ITEST)
C
      DO 5 I=1,NFIX
        DO 5 J=1,2
          K=2*NOFIX(I)+J-2
          IF(IFLAG(J,I).EQ.1) VPART(K)=DFIX(J,I)
5     CONTINUE
C
C     *** Flag the Dirichlet conditions
C
      DO 8 IROW=1,NNOD2
        DUMMY(IROW)=0.0
        DO 11 I=1,NFIX
          DO 11 J=1,2
            K=2*NOFIX(I)+J-2
            IF(K.EQ.IROW.AND.IFLAG(J,I).EQ.1) DUMMY(K)=1.0
11      CONTINUE
8     CONTINUE
C
C     *** Start the time-stepping algorithm
C
      DO 20 INC=1,NINCS
C
C     *** Initialise for this increment
C
        DO 110 I=1,NNOD2
          DMESH(I)=DMESH(I)+VMESH(I)*DELTAT+
     +             (1.0-2.0*BETA)*AMESH(I)*DELTAT*DELTAT/2.0D0
          DMESH2(I)=DMESH(I)
          VMESH(I)=VMESH(I)+DELTAT*(1.0-GAMMA)*AMESH(I)
          VPART(I)=VPART(I)+DELTAT*(1.0-GAMMA)*APART(I)
110     CONTINUE
C
C     *** Start iterations for this increment
C
        DO 30 ITER=1,NITER
C
C     *** Calculate the system matrix and apply the boundary conditions
C
          CALL REMESH
C
C     *** Calculate the [L] transform matrix from the shape fns.
C
          CALL FORML
C
C     *** Calculate the time-dependent term [M] from the shape fns.
C
          CALL FORMM
C
C     *** Multiply by the stability factor
C
          DO 10 IROW=1,NNOD2
            IF(DUMMY(IROW).EQ.1.0) THEN
```

```
              FORCE(IROW)=FORCE0(IROW)                              CALL VECOOP(DISP,IGL,FINIT,IGL,NNOD2,ITEST)
              DO 13 JCOL=1,KSIZE                           C      WRITE(7,100) ITER,VELMAX,CONVER
                GLOBK(IROW,JCOL)=GLOBK0(IROW,JCOL)         100    FORMAT(' Iteration ',I2/15X,'Max Velocity ',E8.2,10X,
13            CONTINUE                                          +         'Remainder ',E7.2)
C           ELSE                                           C
C             FORCE(IROW)=FORCE0(IROW)*GAMMA*DELTAT         C    *** Smooth this solution
C             DO 12 JCOL=1,KSIZE                            C
C               GLOBK(IROW,JCOL)=GLOBK0(IROW,JCOL)*GAMMA*DELTAT     CALL SMOOTH
C12            CONTINUE                                     30     CONTINUE
C           ENDIF                                           C
10          CONTINUE                                        C    *** Form the 'constant' for the next time-increment
C                                                           C
C                                                           99     DO 60 I=1,NNOD2
C      *** Form the left-hand side of the soln 'corrector'        DMESH(I)=DMESH2(I)
C                                                                  VMESH(I)=VMESH2(I)
C           DO 15 IROW=1,NNOD2                                     AMESH(I)=AMESH2(I)
C             GLOBK(IROW,KSBW)=GLOBK(IROW,KSBW)+AMASS(IROW)        APART(I)=(DISP(I)-VPART(I))/(DELTAT*GAMMA)
C15          CONTINUE                                              VPART(I)=DISP(I)
            CALL GAURDN(GLOBK,IGL,JGL,GLOBKL,IGL,JGL,NNOD2,KSBW,   60     CONTINUE
          +            NROPIV,IGL,ITEST)                    C
C                                                           C    *** Initialise the next time-increment
C      *** Assemble the force vector, starting with the 'constant' VPART   C
C                                                           C      INCRE=INC
            CALL VECNUL(DISP,IGL,NNOD2,ITEST)              C      CALL TIMINC
            CALL VECADD(DISP,IGL,FORCE,IGL,NNOD2,ITEST)    C      GAMMA2=COMM/DELT
C           DO 80 IROW=1,NNOD2                             C      IF(GAMMA2.GE.0.5.AND.GAMMA2.LE.1.0) THEN
C             DISP(IROW)=AMASS(IROW)*VPART(IROW)           C         GAMMA=GAMMA2
C80          CONTINUE                                      C         DELTAT=DELT
C                                                           C      ELSE
C      *** Form the convective operator                    C         GAMMA=0.75
C                                                           C         IF(DELT.LT.DELTAT*10.0) THEN
C           CALL FORMN                                      C           DELTAT=DELT
C                                                           C         ELSE
C      *** Form the out-of-balance force                    C           DELTAT=DELTAT*10.0
C                                                           C         ENDIF
C           CALL VECADD(DISP,IGL,FOUT,IGL,NNOD2,ITEST)      C         DELT=0.0
C                                                           C         COMM=GAMMA*DELTAT
C      *** Solve for the corrected velocities                C      ENDIF
C                                                           C
            CALL GAUSUB(GLOBK,IGL,JGL,GLOBKL,IGL,JGL,NNOD2,KSBW,   C    *** Store the surface displacements for plotting
          +            NROPIV,IGL,DISP,IGL,ITEST)          C
C                                                                  IF(INC.EQ.ICOMP) THEN
C      *** Update the mesh movement for this iteration             DO 910 I=1,900
C                                                                    DSTORE(ISURF,I)=Y(I)
            CALL FORMS                                      910    CONTINUE
            DO 120 I=1,NNOD2                                       ICOMP=ICOMP+10
              VMESH2(I)=APARAM(I)*DISP(I)-ATRANS(I)*STRANS(I)      ISURF=ISURF+1
              AMESH2(I)=(VMESH2(I)-VMESH(I))/(DELTAT*GAMMA)        ENDIF
              DMESH2(I)=DMESH(I)+DELTAT*DELTAT*BETA*AMESH2(I)       TTOTAL=TTOTAL + DELTAT
120         CONTINUE                                       20     CONTINUE
C                                                           C
C      *** Check for convergence between successive iterations    WRITE(7,800) TTOTAL/3.16E10
C                                                           800    FORMAT('0Solution Duration',3X,F8.3,2X,'ka')
            VELMAX=0.000                                           WRITE(6,600)
            DO 49 I=1,NNOD2                                 600    FORMAT('0Time-dependent solution completed')
              VELMAX=DMAX1(VELMAX,ABS(DISP(I)))                    CALL TIME(1,1)
49          CONTINUE                                        C
            CONVER=0.0                                             RETURN
            DO 50 I=1,NNOD2                                        END
              CONVER=DMAX1(CONVER,ABS(DISP(I)-FINIT(I))/VELMAX)    C
50          CONTINUE                                        C
                                                            C..........................................................
                                                            C
```

```
C
C     SUBROUTINE FORM
C     ─────────────
C
C+
C     Calculate the lumped mass matrix [M], a diagonal matrix. The Boussinesq
C     approximation assumes that the reference material is the first quoted.
C     Major variables:  AMASS =inertial term [M]
C-
      IMPLICIT DOUBLE PRECISION (A-H,O-W)
      PARAMETER(IGL=880,JGL=131,KGL=66)
      COMMON /CONS/ NTRI,NQUAD,NINCS,NNOD,KSIZE,KSBW,NNOD2,NMAT,IDUM(4),
     +             GAMMA,PI,BETA,NST,NSI,NSEG,NODSEG,DELTAT
      COMMON /MATS/ EM(9),PM(9),TM(9),RHOM(9),ETAM(9),ETAN,ITYP(9)
      COMMON /ELEM/ NODEL(8,500),NGAUSS(500),NOTEL(500),NOQEL(500),
     +             NOTOOL(500),NOQCOL(500),DIFFOP(9,500),BLIB(144,500),
     +             PRINC(16,500)
      COMMON /FIXT/ DFIX(2,500),NOFIX(500),IFLAG(2,500),NFIX,NEXT,NSTOP
      COMMON /VISC/ DSTORE(12,900),FINIT(IGL),FOUT(IGL),AMASS(IGL)
      COMMON /GAPT/ S,T,SHAPE(8),DNXDS(8),DNXDT(8),TSHAPE(6,36),
     +             TDNXDS(6,36),TDNXDT(6,36),TW1W2(6,6),QSHAPE(3,72),
     +             QDNXDS(3,72),QDNXDT(3,72),QW1W2(3,9),WEITRI(12,6),
     +    WEIQAD(18,3),PLACET(12,6),PLACEQ(18,3),PLACEL(3),WEILIN(3)
C
C     *** Initialise
C
      ITEST=0
      RHO=RHOM(1)
      CALL VECNUL(AMASS,IGL,NNOD2,ITEST)
C
      IF(NQUAD.GT.0) THEN
         DO 10 IEL=1,NQUAD
            NO=8
            NO2=NO*2
            NUMEL=NOQEL(IEL)
            NGAUS=NGAUSS(NUMEL)
            NROW=NOQCOL(IEL)
            ELMASS=0.0
            DO 20 IG=1,NGAUS
               IPOS=(IG-1)*NO
               DV=DIFFOP(IG,NUMEL)
               SHAP=0.0
               DO 30 NOD=1,NO
                  SHAP=SHAP+QSHAPE(NROW,IPOS+NOD)
30             CONTINUE
               ELMASS=ELMASS+SHAP*RHO*DV
20          CONTINUE
            DO 40 NOD=1,NO/2
               I=NODEL(2*NOD,NUMEL)
               J=NODEL(2*NOD-1,NUMEL)
               K=2*I
               L=K-1
               M=2*J
               N=M-1
               AMASS(M)=AMASS(M) + ELMASS/36.0D0
               AMASS(N)=AMASS(N) + ELMASS/36.0D0
               AMASS(K)=AMASS(K) + ELMASS*8.0D0/36.0D0
               AMASS(L)=AMASS(L) + ELMASS*8.0D0/36.0D0
40          CONTINUE
10       CONTINUE
      ENDIF
C
      IF(NTRI.GT.0) THEN
```

```
         DO 50 IEL=1,NTRI
            NO=6
            NO2=NO*2
            NUMEL=NOTEL(IEL)
            NGAUS=NGAUSS(NUMEL)
            NROW=NOTOOL(IEL)
            ELMASS=0.0
            DO 60 IG=1,NGAUS
               IPOS=(IG-1)*NO
               DV=DIFFOP(IG,NUMEL)
               SHAP=0.0
               DO 70 NOD=1,NO
                  SHAP=SHAP+TSHAPE(NROW,IPOS+NOD)
70             CONTINUE
               ELMASS=ELMASS+SHAP*RHO*DV
60          CONTINUE
            DO 80 NOD=1,NO/2
               I=NODEL(2*NOD,NUMEL)
               K=2*I
               L=K-1
               AMASS(K)=AMASS(K) + ELMASS/3.0D0
               AMASS(L)=AMASS(L) + ELMASS/3.0D0
80          CONTINUE
50       CONTINUE
      ENDIF
C
C     *** Ensure Dirichlet conditions
C
      IF(NFIX.NE.0) THEN
         DO 90 I=1,NFIX
            DO 90 J=1,2
               K=2*NOFIX(I)+J-2
               IF(IFLAG(J,I).EQ.1) AMASS(K)=0.0D00
90       CONTINUE
      ENDIF
C
      RETURN
      END
C
C
C●●●●●●●●●●●●●●●●●●●●●●●●●●●●●●●●●●●●●●●●●●●●●●●●●●●●●●●●●●●●●●●●●●●●●●●●●●●●
C
C
      SUBROUTINE FORML
C     ─────────────
C
C
C+
C     Calculate the lumped matrix [L], a diagonal matrix.
C     Major variables:  ATRANS =translation matrix [L]
C-
      IMPLICIT DOUBLE PRECISION (A-H,O-W)
      PARAMETER(IGL=880,JGL=131,KGL=66)
      COMMON /CONS/ NTRI,NQUAD,NINCS,NNOD,KSIZE,KSBW,NNOD2,NMAT,IDUM(4),
     +             GAMMA,PI,BETA,NST,NSI,NSEG,NODSEG,DELTAT
      COMMON /ELEM/ NODEL(8,500),NGAUSS(500),NOTEL(500),NOQEL(500),
     +             NOTOOL(500),NOQCOL(500),DIFFOP(9,500),BLIB(144,500),
     +             PRINC(16,500)
      COMMON /FIXT/ DFIX(2,500),NOFIX(500),IFLAG(2,500),NFIX,NEXT,NSTOP
      COMMON /GAPT/ S,T,SHAPE(8),DNXDS(8),DNXDT(8),TSHAPE(6,36),
     +             TDNXDS(6,36),TDNXDT(6,36),TW1W2(6,6),QSHAPE(3,72),
```

```
     +            QDNXDS(3,72),QDNXDT(3,72),QW1W2(3,9),WEITRI(12,6),
     +    WEIQAD(18,3),PLACET(12,6),PLACEQ(18,3),PLACEL(3),WEILIN(3)
      COMMON /MOVE/ VPART(IGL),VMESH(IGL),APARAM(IGL),STRANS(IGL),
     +              ATRANS(IGL),DMESH(IGL),APART(IGL),AMESH(IGL),
     +              VMESH2(IGL),DMESH2(IGL),XOLD(IGL),YOLD(IGL)
C
C     ••• Initialise
C
      ITEST=0
      CALL VECNUL(ATRANS,IGL,NNOD2,ITEST)
C
      IF(NQUAD.GT.0) THEN
         DO 10 IEL=1,NQUAD
            NO=8
            NO2=NO•2
            NUMEL=NOQEL(IEL)
            NGAUS=NGAUSS(NUMEL)
            NROW=NOQQOL(IEL)
            ELMASS=0.0
            DO 20 IG=1,NGAUS
               IPOS=(IG-1)•NO
               DV=DIFFOP(IG,NUMEL)
               SHAP=0.0
               DO 30 NOD=1,NO
                  SHAP=SHAP+QSHAPE(NROW,IPOS+NOD)
30             CONTINUE
               ELMASS=ELMASS+SHAP•DV
20          CONTINUE
            DO 40 NOD=1,NO/2
               I=NODEL(2•NOD,NUMEL)
               J=NODEL(2•NOD-1,NUMEL)
               K=2•I
               L=K-1
               M=2•J
               N=M-1
               ATRANS(M)=ATRANS(M) + ELMASS/36.0D0
               ATRANS(N)=ATRANS(N) + ELMASS/36.0D0
               ATRANS(K)=ATRANS(K) + ELMASS•8.0D0/36.0D0
               ATRANS(L)=ATRANS(L) + ELMASS•8.0D0/36.0D0
40          CONTINUE
10       CONTINUE
      ENDIF
C
      IF(NTRI.GT.0) THEN
         DO 50 IEL=1,NTRI
            NO=6
            NO2=NO•2
            NUMEL=NOTEL(IEL)
            NGAUS=NGAUSS(NUMEL)
            NROW=NOTOOL(IEL)
            ELMASS=0.0
            DO 60 IG=1,NGAUS
               IPOS=(IG-1)•NO
               DV=DIFFOP(IG,NUMEL)
               SHAP=0.0
               DO 70 NOD=1,NO
                  SHAP=SHAP+TSHAPE(NROW,IPOS+NOD)
70             CONTINUE
               ELMASS=ELMASS+SHAP•DV
60          CONTINUE
```

```
               DO 80 NOD=1,NO/2
                  I=NODEL(2•NOD,NUMEL)
                  K=2•I
                  L=K-1
                  ATRANS(K)=ATRANS(K) + ELMASS/3.0D0
                  ATRANS(L)=ATRANS(L) + ELMASS/3.0D0
80             CONTINUE
50          CONTINUE
      ENDIF
C
      IF(NFIX.NE.0) THEN
         DO 90 I=1,NFIX
            DO 90 J=1,2
               K=2•NOFIX(I)+J-2
               IF(IFLAG(J,I).EQ.1) ATRANS(K)=0.0D00
90       CONTINUE
      ENDIF
C
      DO 110 I=1,NNOD2
         IF(ATRANS(I).NE.0.0D0) ATRANS(I)=1.0D0/ATRANS(I)
110   CONTINUE
C
      RETURN
      END
C
C
C••••••••••••••••••••••••••••••••••••••••••••••••••••••••••••••••••••••••
C
C
      SUBROUTINE FORMS
C
C     ════════════════
C
C+
C     Calculate the transform vector [S] from the mesh displacements
C     and particle velocities.
C     Major variables:  STRANS =transform vector [S]
C-
      IMPLICIT DOUBLE PRECISION (A-H,O-W)
      PARAMETER(IGL=680,JGL=131,KGL=66)
      COMMON /CONS/ NTRI,NQUAD,NINCS,NNOD,KSIZE,KSBW,NNOD2,NMAT,IDUM(4),
     +              GAMMA,PI,BETA,NST,NSI,NSEG,NODSEG,DELTAT
      COMMON /NODS/ X(IGL/2),Y(IGL/2),DISP(IGL),FORCE(IGL),XCOM1(4000)
      COMMON /ELEM/ NODEL(8,500),NGAUSS(500),NOTEL(500),NOQEL(500),
     +              NOTOOL(500),NOQQOL(500),DIFFOP(9,500),BLIB(144,500),
     +              PRINC(16,500)
      COMMON /FIXT/ DFIX(2,500),NOFIX(500),IFLAG(2,500),NFIX,NEXT,NSTOP
      COMMON /GAPT/ S,T,SHAPE(8),DNDXS(8),DNDXT(8),TSHAPE(6,36),
     +              TDNXDS(6,36),TDNXDT(6,36),TW1W2(6,6),QSHAPE(3,72),
     +              QDNXDS(3,72),QDNXDT(3,72),QW1W2(3,9),WEITRI(12,6),
     +    WEIQAD(18,3),PLACET(12,6),PLACEQ(18,3),PLACEL(3),WEILIN(3)
      COMMON /MOVE/ VPART(IGL),VMESH(IGL),APARAM(IGL),STRANS(IGL),
     +              ATRANS(IGL),DMESH(IGL),APART(IGL),AMESH(IGL),
     +              VMESH2(IGL),DMESH2(IGL),XOLD(IGL),YOLD(IGL)
C
C     ••• Initialise
C
      ITEST=0
      CALL VECNUL(STRANS,IGL,NNOD2,ITEST)
C
      IF(NQUAD.GT.0) THEN
```

```
      DO 10 IEL=1,NQUAD
        NO=8
        NO2=NO*2
        NUMEL=NODEL(IEL)
        NGAUS=NGAUSS(NUMEL)
        NROW=NODCOL(IEL)
        DO 20 IG=1,NGAUS
          IPOS=(IG-1)*NO
          DV=DIFFOP(IG,NUMEL)
          ALPHX=0.0
          ALPHY=0.0
          DISPX=0.0
          DISPY=0.0
          VELX=0.0
          VELY=0.0
          DDISPX=0.0
          DDISPY=0.0
          DO 30 NOD=1,NO
            NODE=NODEL(NOD,NUMEL)
            SHAPE(NOD)=QSHAPE(NROW,IPOS+NOD)
            DNXDS(NOD)=QDNXDS(NROW,IPOS+NOD)
            DNXDT(NOD)=QDNXDT(NROW,IPOS+NOD)
            ALPHX=ALPHX+SHAPE(NOD)*(1.0D0-APARAM(2*NODE))
            ALPHY=ALPHY+SHAPE(NOD)*(1.0D0-APARAM(2*NODE-1))
            DISPX=DISPX+SHAPE(NOD)*(DMESH2(2*NODE-1)+X(NODE))
            DISPY=DISPY+SHAPE(NOD)*(DMESH2(2*NODE  )+Y(NODE))
            VELX=VELX+SHAPE(NOD)*DISP(2*NODE)
            VELY=VELY+SHAPE(NOD)*DISP(2*NODE-1)
            DDISPX=DDISPX+DNXDT(NOD)*(DMESH2(2*NODE-1)+X(NODE))
            DDISPY=DDISPY+DNXDS(NOD)*(DMESH2(2*NODE  )+Y(NODE))
   30     CONTINUE
          JPOS=(IG-1)*4
          DO 40 NOD=1,NO
            NODE=NODEL(NOD,NUMEL)
            STRANS(2*NODE-1)=STRANS(2*NODE-1)+
     +                       SHAPE(NOD)*APARAM(2*NODE-1)
     +          *ALPHX*VELX*DDISPX*PRINC(JPOS+4,NUMEL)*DV
            STRANS(2*NODE  )=STRANS(2*NODE  )+
     +                       SHAPE(NOD)*APARAM(2*NODE  )
     +          *ALPHY*VELY*DDISPY*PRINC(JPOS+2,NUMEL)*DV
   40     CONTINUE
   20   CONTINUE
   10 CONTINUE
      ENDIF
C
      RETURN
      END
C
C
C.........................................................
C
C
      SUBROUTINE REMESH
C    ================
C+
C     Recalculate the system matrix from the most recent mesh displacements.
C     Major variables : DMESH2 =mesh displacements of this iteration
C                        XOLD, YOLD= x- and y-coords of reference frame
C                        GLOBK =system matrix [K]
C-
```

```
      IMPLICIT DOUBLE PRECISION (A-H,O-W)
      PARAMETER(IGL=880,JGL=131,KGL=66)
      COMMON /CONS/ NTRI,NQUAD,NINCS,NNOD,KSIZE,KSBW,NNOD2,NMAT,IDUM(4),
     +              GAMMA,PI,BETA,NST,NS1,NSEG,NODSEG,DELTAT
      COMMON /NODS/ X(IGL/2),Y(IGL/2),DISP(IGL),FORCE(IGL),XCOM1(4000)
      COMMON /MATS/ EM(9),PM(9),TM(9),RHOM(9),ETAM(9),ETAN,ITYP(9)
      COMMON /STIF/ ELK(18,18),GLOBK(IGL,JGL)
      COMMON /FRON/ GLOBK0(IGL,JGL)
      COMMON /STF4/ GLOBKL(IGL,KGL),FORCE0(IGL),NROPIV(IGL)
      COMMON /FIXT/ DFIX(2,500),NOFIX(500),IFLAG(2,500),NFIX,NEXT,NSTOP
      COMMON /MOVE/ VPART(IGL),VMESH(IGL),APARAM(IGL),STRANS(IGL),
     +              ATRANS(IGL),DMESH(IGL),APART(IGL),AMESH(IGL),
     +              VMESH2(IGL),DMESH2(IGL),XOLD(IGL),YOLD(IGL)
C
C     *** Initialise
C
      ITEST=0
      CALL MATNUL(GLOBK,IGL,JGL,NNOD2,KSIZE,ITEST)
      CALL VECNUL(FORCE,IGL,NNOD2,ITEST)
C
C     *** For the wave propagation model
C
      IF(ETAM(1).EQ.0.0D00) THEN
        ANGLE=(0.0836940854D0*TTOTAL) -4.0D0
        AFIX=3.38624670600*(1.0D0 + TANH(ANGLE))
        DO 30 NOD=1,5
          DMESH(2*NOD-1)=AFIX
   30   CONTINUE
        AFIX=0.28340882126D00*(1.0D0-TANH(ANGLE)*TANH(ANGLE))
        DO 20 I=NFIX-4,NFIX
          DFIX(1,I)=AFIX
   20   CONTINUE
      ENDIF
C
C     *** Calculate global matrix and apply b.c.
C
      CALL FORMK
      CALL BODY4S
      CALL BOUND2
C
C     *** Store the matrices at the beginning of the iteration
C
      CALL VECCOP(FORCE,IGL,FORCE0,IGL,NNOD2,ITEST)
      CALL MCOPY(GLOBK,IGL,JGL,GLOBK0,IGL,JGL,NNOD2,KSIZE,ITEST)
C
      RETURN
      END
C
C
C.........................................................
C
C
      SUBROUTINE TIMINC
C    ================
C+
C     Calculate the time increment from the Courant convection criteria.
C-
      IMPLICIT DOUBLE PRECISION (A-H,O-W)
      PARAMETER(IGL=880,JGL=131,KGL=66)
      COMMON /CONS/ NTRI,NQUAD,NINCS,NNOD,KSIZE,KSBW,NNOD2,NMAT,IDUM(4),
```

```fortran
     +               GAMMA,PI,BETA,NST,NS1,NSEG,NODSEG,DELTAT
      COMMON /NODS/ X(IGL/2),Y(IGL/2),DISP(IGL),FORCE(IGL),XCOM1(4000)
      COMMON /ELEM/ NODEL(8,500),NGAUSS(500),NOTEL(500),NOQEL(500),
     +              NOTCOL(500),NOQCOL(500),DIFFOP(9,500),BLIB(144,500),
     +              PRINC(16,500)
      COMMON /GAPT/ S,T,SHAPE(8),DNXDS(8),DNXDT(8),TSHAPE(6,36),
     +              TDNXDS(6,36),TDNXDT(6,36),TW1W2(6,6),QSHAPE(3,72),
     +              QDNXDS(3,72),QDNXDT(3,72),QW1W2(3,9),WEITRI(12,6),
     +    WEIQAD(18,3),PLACET(12,6),PLACEQ(18,3),PLACEL(3),WEILIN(3)
      COMMON /TIMS/ ELSIZE(2,500),DELT,ILOAD(IGL),TTOTAL
C
C     *** Initialise at the centre of the element
C
      DELT=1.0D30
      IF(NQUAD.GT.0) THEN
        S=0.0
        T=0.0
        CALL QSHAFN
        DO 10 IEL=1,NQUAD
          NUMEL=NOQEL(IEL)
          NO=8
          VELX=0.0D0
          VELY=0.0D0
          DO 20 NOD=1,NO
            NODE=NODEL(NOD,NUMEL)
            VELX=VELX + SHAPE(NOD)*DISP(2*NODE-1)
            VELY=VELY + SHAPE(NOD)*DISP(2*NODE  )
20        CONTINUE
          IF(VELX.EQ.0.0D0.AND.VELY.EQ.0.0D0) THEN
            DUM=1.0D30
          ELSE
            DUM=1.0D00/((DABS(VELX)/ELSIZE(1,NUMEL)) +
     +                  (DABS(VELY)/ELSIZE(2,NUMEL)))
          ENDIF
          DELT=DMIN1(DELT,DUM)
10      CONTINUE
      ENDIF
C
      IF(NTRI.GT.0) THEN
        S=1.0D00/3.0D00
        T=S
        CALL TSHAFN
        DO 30 IEL=1,NTRI
          NUMEL=NOTEL(IEL)
          NO=6
          VELX=0.0
          VELY=0.0
          DO 40 NOD=1,NO
            NODE=NODEL(NOD,NUMEL)
            VELX=VELX + SHAPE(NOD)*DISP(2*NODE-1)
            VELY=VELY + SHAPE(NOD)*DISP(2*NODE  )
40        CONTINUE
          DUM=1.0D00/((DABS(VELX)/ELSIZE(1,NUMEL)) +
     +                (DABS(VELY)/ELSIZE(2,NUMEL)))
          DELT=DMIN1(DELT,DUM)
30      CONTINUE
      ENDIF
C
      RETURN
      END
C
C
C**********************************************************************
```

```fortran
C
C
      SUBROUTINE STRESS
C     ------------------
C
C+
C     Calculate the total stress at each gauss point.
C     Major variables:  STMAX  =max absolute value of stress
C                        DISP   =current mesh velocities
C                        BLIB   =strain rate operator
C-
      IMPLICIT DOUBLE PRECISION (A-H,O-W)
      PARAMETER(IGL=880,JGL=131,KGL=66)
      COMMON /CONS/ NTRI,NQUAD,NINCS,NNOD,KSIZE,KSBW,NNOD2,NMAT,IDUM(4),
     +              STMAX,PI,BETA,NST,NS1,NSEG,NODSEG,DELTAT
      COMMON /NODS/ X(IGL/2),Y(IGL/2),DISP(IGL),FORCE(IGL),
     +              XSTPOS(4,500),YSTPOS(4,500)
      COMMON /MATS/ EM(9),PM(9),TM(9),RHOM(9),ETAM(9),ETAN,ITYP(9)
      COMMON /ELEM/ NODEL(8,500),NGAUSS(500),NOTEL(500),NOQEL(500),
     +              NOTCOL(500),NOQCOL(500),DIFFOP(9,500),BLIB(144,500),
     +              PRINC(16,500)
      COMMON /GAPT/ S,T,SHAPE(8),DUM1(16),TSHAPE(6,36),
     +              TDNXDS(6,36),TDNXDT(6,36),TW1W2(6,6),QSHAPE(3,72),
     +              QDNXDS(3,72),QDNXDT(3,72),QW1W2(3,9),WEITRI(12,6),
     +    WEIQAD(18,3),PLACET(12,6),PLACEQ(18,3),PLACEL(3),WEILIN(3)
      COMMON /VARS/ CO(2),ETA,C2,C3,DNXDX(8),DNXDY(8),Q(18),COM12(36),
     +              DNXDS(8),DNXDT(8),CO14(76),NO,NUMEL,NGAUS,MAT,NROW,IG
C
C     *** Initialise
C
      STMAX=0.0D0
      ITEST=0
C
      IF(NTRI.GT.0) THEN
        NO=6
        DO 60 IEL=1,NTRI
C
C     *** Unload the material constants and strain rate operator
C
          NUMEL=NOTEL(IEL)
          MAT=ITYP(NUMEL)
          ETA=ETAM(MAT)
          NGAUS=NGAUSS(NUMEL)
C
C     *** Retrieve the nodal velocities
C
          DO 10 J=1,6
            Q(2*J-1)=DISP(2*NODEL(J,NUMEL)-1)
            Q( 2*J )=DISP( 2*NODEL(J,NUMEL) )
10        CONTINUE
C
C     *** Unload strain rate operator at this gauss point
C
          DO 50 IG=1,3
            IPOS=(IG+2)*6
            KPOS=(IG-1)*12
            DO 30 IV=1,NO
              SHAPE(IV)=TSHAPE(1,IPOS+IV)
              L=2*IV
              K=L-1
              DNXDX(IV)=BLIB(IPOS*2 +K,NUMEL)
              DNXDY(IV)=BLIB(IPOS*2 +L,NUMEL)
30          CONTINUE
C
C     *** Evaluate the principal stresses
C
```

```
              CALL PRINCS
50         CONTINUE
60         CONTINUE
           ENDIF
C
C      ••• Quadrilateral Elements
C
           IF(NQUAD.GT.0) THEN
              NO=8
              DO 130 IEL=1,NQUAD
              NUMEL=NQOEL(IEL)
              MAT=ITYP(NUMEL)
              ETA=ETAM(MAT)
              NGAUS=NGAUSS(NUMEL)
C
C      ••• Unload the velocities
C
              DO 80 J=1,NO
                 Q(2•J-1)=DISP(2•NODEL(J,NUMEL)-1)
                 Q( 2•J )=DISP( 2•NODEL(J,NUMEL) )
80         CONTINUE
C
C      ••• Unload the strain rate operator at this gauss point
C
              DO 120 IG=1,4
                 IPOS=(IG-1)•NO
                 KPOS=IPOS•2
                 DO 100 IV=1,NO
                    JPOS=IPOS+IV
                    SHAPE(IV)=QSHAPE(1,JPOS)
                    L=2•IV
                    K=L-1
                    DNXDX(IV)=BLIB(IPOS•2 +K,NUMEL)
                    DNXDY(IV)=BLIB(IPOS•2 +L,NUMEL)
100        CONTINUE
C
C      ••• Evaluate principal stresses
C
                    CALL PRINCS
120        CONTINUE
130        CONTINUE
           ENDIF
C
           WRITE(6,150)
150    FORMAT('0Principal stresses computed')
           CALL TIME(1,1)
C
           RETURN
           END
C
C
C•••••••••••••••••••••••••••••••••••••••••••••••••••••••••••••••••••••••••••••••
C
C
           SUBROUTINE PRINCS
C
C+
C      Calculate the principal deviatoric stresses at this gauss point.
C      Major variables:  PRINCS =principal stresses
C                         DISP   =current velocities
C                         BLIB   =strain rate operator
C                         ETA    =element viscosity
C-
```

```
           IMPLICIT DOUBLE PRECISION (A-H,O-W)
           PARAMETER(IGL=880,JGL=131,KGL=66)
           COMMON /CONS/ NTRI,NQUAD,NINCS,NNOD,KSIZE,KSBW,NNOD2,NMAT,IDUM(4),
          +              STMAX,PI,BETA,NST,NSI,NSEG,NODSEG,DELTAT
           COMMON /MATS/ EM(9),PM(9),TM(9),RHOM(9),ETAM(9),ETAN,ITYP(9)
           COMMON /ELEM/ NODEL(8,500),NGAUSS(500),NOTEL(500),NQOEL(500),
          +              NOTCOL(500),NOQCOL(500),DIFFOP(9,500),BLIB(144,500),
          +              PRINC(16,500)
           COMMON /VARS/ CO(2),ETA,C2,C3,DNXDX(8),DNXDY(8),Q(18),STRN(4),
          +              STRES(4),COM1(118),NO,NUMEL,NGAUS,MAT,NROW,IG
C
C      ••• Unload properties and initialise
C
           P=PM(MAT)
           E=EM(MAT)
           INDEX=(IG-1)•4
           STRN(1)=0.0
           STRN(2)=0.0
           STRN(3)=0.0
           STRN(4)=0.0
C
C      ••• Evaluate strain rates
C
           DO 10 I=1,NO
              L=2•I
              K=L-1
              STRN(1)=STRN(1)+DNXDX(I)•Q(K)
              STRN(2)=STRN(2)+DNXDY(I)•Q(L)
              STRN(3)=STRN(3)+DNXDX(I)•Q(L)+DNXDY(I)•Q(K)
10         CONTINUE
C
C      ••• Form stresses from the strains
C
           STRES(1)=2.0D00•ETA•STRN(1)
           STRES(2)=2.0D00•ETA•STRN(2)
           STRES(3)=      ETA•STRN(3)
           STRES(4)=0.0D00
C
C      ••• Form the principal stresses
C
           IF(STRES(1).EQ.STRES(2)) THEN
              THETA=PI/4.0D0
           ELSE
              THETA=0.5D0•(DATAN(2.0D0•STRES(3)/(STRES(1)-STRES(2))))
              IF(THETA.LE.0.0) THETA=THETA+PI/2.0D0
           ENDIF
C
           PRINC(1+INDEX,NUMEL)=STRES(1)•(DCOS(THETA)•DCOS(THETA)) +
          +                    STRES(2)•(DSIN(THETA)•DSIN(THETA)) +
          +                    STRES(3)•DSIN(2.0D0•THETA)
           PRINC(2+INDEX,NUMEL)=STRES(1)+STRES(2)-PRINC(1+INDEX,NUMEL)
           PRINC(3+INDEX,NUMEL)=STRES(3)
           PRINC(4+INDEX,NUMEL)=THETA•180.0D0/PI
C
C      ••• Determine maximum stress
C
           STMAX=DMAX1(DABS(PRINC(1+INDEX,NUMEL)),
          +            DABS(PRINC(2+INDEX,NUMEL)),
          +            DABS(PRINC(3+INDEX,NUMEL)),STMAX)
C
```

```
      RETURN
      END
C
C
C••••••••••••••••••••••••••••••••••••••••••••••••••••••••••••••••••••••
C
C
      SUBROUTINE SMOOTH
C
C+    ─────────────
C     Calculate the displacement of the side nodes by averaging the
C     displacement of the adjacent corner nodes.
C     Major variables: DMESH2 =current mesh displacements
C-
      IMPLICIT DOUBLE PRECISION (A-H,O-W)
      PARAMETER(IGL=880,JGL=131,KGL=66)
      COMMON /CONS/ NTRI,NQUAD,NINCS,NNOD,KSIZE,KSBW,NNOD2,NMAT,IDUM(4),
     +              STMAX,PI,BETA,NST,NSI,NSEG,NODSEG,DELTAT
      COMMON /NODS/ X(IGL/2),Y(IGL/2),DISP(IGL),FORCE(IGL),XCOM1(4000)
      COMMON /ELEM/ NODEL(8,500),NGAUSS(500),NOTEL(500),NOQEL(500),
     +              NOTCOL(500),NOQCOL(500),DIFFOP(9,500),BLIB(144,500),
     +              PRINC(16,500)
      COMMON /MOVE/ VPART(IGL),VMESH(IGL),APARAM(IGL),STRANS(IGL),
     +              ATRANS(IGL),DMESH(IGL),APART(IGL),AMESH(IGL),
     +              VMESH2(IGL),DMESH2(IGL),XOLD(IGL),YOLD(IGL)
C
      ITEST=0
      IF(NQUAD.GT.0) THEN
        DO 10 IEL=1,NQUAD
        NUMEL=NOQEL(IEL)
        DMESH2(2*NODEL(2,NUMEL)-1)=(DMESH2(2*NODEL(1,NUMEL)-1)+
     +        DMESH2(2*NODEL(3,NUMEL)-1))/2.0D00
        DMESH2(2*NODEL(2,NUMEL)  )=(DMESH2(2*NODEL(1,NUMEL)  )+
     +        DMESH2(2*NODEL(3,NUMEL)  ))/2.0D00
        DMESH2(2*NODEL(4,NUMEL)-1)=(DMESH2(2*NODEL(3,NUMEL)-1)+
     +        DMESH2(2*NODEL(5,NUMEL)-1))/2.0D00
        DMESH2(2*NODEL(4,NUMEL)  )=(DMESH2(2*NODEL(3,NUMEL)  )+
     +        DMESH2(2*NODEL(5,NUMEL)  ))/2.0D00
        DMESH2(2*NODEL(6,NUMEL)-1)=(DMESH2(2*NODEL(5,NUMEL)-1)+
     +        DMESH2(2*NODEL(7,NUMEL)-1))/2.0D00
        DMESH2(2*NODEL(6,NUMEL)  )=(DMESH2(2*NODEL(5,NUMEL)  )+
     +        DMESH2(2*NODEL(7,NUMEL)  ))/2.0D00
        DMESH2(2*NODEL(8,NUMEL)-1)=(DMESH2(2*NODEL(7,NUMEL)-1)+
     +        DMESH2(2*NODEL(1,NUMEL)-1))/2.0D00
        DMESH2(2*NODEL(8,NUMEL)  )=(DMESH2(2*NODEL(7,NUMEL)  )+
     +        DMESH2(2*NODEL(1,NUMEL)  ))/2.0D00
10      CONTINUE
      ENDIF
C
      IF(NTRI.GT.0) THEN
        DO 20 IEL=1,NTRI
        NUMEL=NOQEL(IEL)
        DMESH2(2*NODEL(2,NUMEL)-1)=(DMESH2(2*NODEL(1,NUMEL)-1)+
     +        DMESH2(2*NODEL(3,NUMEL)-1))/2.0D00
        DMESH2(2*NODEL(2,NUMEL)  )=(DMESH2(2*NODEL(1,NUMEL)  )+
     +        DMESH2(2*NODEL(3,NUMEL)  ))/2.0D00
        DMESH2(2*NODEL(4,NUMEL)-1)=(DMESH2(2*NODEL(3,NUMEL)-1)+
     +        DMESH2(2*NODEL(5,NUMEL)-1))/2.0D00
        DMESH2(2*NODEL(4,NUMEL)  )=(DMESH2(2*NODEL(3,NUMEL)  )+
     +        DMESH2(2*NODEL(5,NUMEL)  ))/2.0D00
```

```
        DMESH2(2*NODEL(6,NUMEL)-1)=(DMESH2(2*NODEL(5,NUMEL)-1)+
     +        DMESH2(2*NODEL(1,NUMEL)-1))/2.0D00
        DMESH2(2*NODEL(6,NUMEL)  )=(DMESH2(2*NODEL(5,NUMEL)  )+
     +        DMESH2(2*NODEL(1,NUMEL)  ))/2.0D00
20      CONTINUE
      ENDIF
C
C    ••• Update mesh coordinates
C
      DO 30 I=1,NNOD
        X(I)=XOLD(I)+DMESH2(2*I-1)
        Y(I)=YOLD(I)+DMESH2(2*I  )
30    CONTINUE
C
      RETURN
      END
C
C
C••••••••••••••••••••••••••••••••••••••••••••••••••••••••••••••••••••••
C
C
      BLOCK DATA
C
C    ─────────────
C+
C     Initialise the fundamental parameters
C-
C
      IMPLICIT DOUBLE PRECISION (A-H,O-W)
      CHARACTER   TITLE(4)*8,ZUF(4)*4
      COMMON /CHAR/ TITLE,ZUF
      COMMON /CONS/ NTRI,NQUAD,NINCS,NNOD,KSIZE,KSBW,NNOD2,NMAT,IDUM(4),
     +              STMAX,PI,BETA,NST,NSI,NSEG,NODSEG,DELTAT
      COMMON /GAPT/ S,T,SHAPE(8),DNXDS(8),DNXDT(8),PCOM(1611),
     +              PLACEL(3),WEILIN(3)
C
      DATA PI /3.14159265358979300/
      DATA ZUF /'ST. ','ND. ','RD. ','TH. '/
      DATA PLACEL/.77459666924148300,0.0D0,
     +     -.77459666924148300/,
     +    WEILIN/.555555555555556D0,
     +           .888888888888889D0,
     +           .555555555555556D0/
C
      END
C
C
C••••••••••••••••••••••••••••••••••••••••••••••••••••••••••••••••••••••
C
C
      SUBROUTINE CRASH
C
C+    ─────────────
C     Check bandwidth
C-
      WRITE(7,10)
10    FORMAT(1H0,'•• RUN ABORTED ••'/'Bandwidth equals zero')
      CALL TIME(1,1)
C
      STOP
```

```
          END
C
C
C••••••••••••••••••••••••••••••••••••••••••••••••••••••••••••••••••••
C
C
      SUBROUTINE BADLUK
C       ==========
C+
C     Check bandwidth
C-
      IMPLICIT DOUBLE PRECISION (A-H,O-W)
      COMMON /CONS/ NTRI,NQUAD,NINCS,NNOD,KSIZE,KSBW,NNOD2,NMAT,IDUM(4),
     +              STMAX,PI,BETA,NST,NSI,NSEG,NODSEG,DELTAT
C
      WRITE(6,10) KSIZE
10    FORMAT(1H0,'•• RUN ABORTED ••'/
     +       'Bandwidth =',I5,', and exceeds storage space')
      CALL TIME(1,1)
C
      STOP
      END
C
C
C••••••••••••••••••••••••••••••••••••••••••••••••••••••••••••••••••••
C
C
      FUNCTION RAMAX(X,N)
C      ====================
C
C+
C     Find the maximum value of a vector
C-
C
      DIMENSION X(N)
      RAMAX=X(1)
      DO 10 IMAX=2,N
        RAMAX=AMAX1(RAMAX,X(IMAX))
10    CONTINUE
C
      RETURN
      END
C
C
C••••••••••••••••••••••••••••••••••••••••••••••••••••••••••••••••••••
C
C
      FUNCTION RAMIN(X,N)
C      ====================
C
C+
C     Find the minimum value of a vector
C-
C
      DIMENSION X(N)
      RAMIN=X(1)
      DO 10 IMIN=2,N
        RAMIN=AMIN1(RAMIN,X(IMIN))
10    CONTINUE
C
```

```
      RETURN
      END
C
C
C••••••••••••••••••••••••••••••••••••••••••••••••••••••••••••••••••••••••
C
C
      SUBROUTINE RENODE
C       ==========
C+
C     Add or delete nodes from the mesh and renumber accordingly.
C-
      IMPLICIT DOUBLE PRECISION (A-H,O-W)
      INTEGER NODE(200),NO(8)
      CHARACTER  TITLE(4)•8,ZUF(4)•4
      PARAMETER(IGL=880,JGL=131,KGL=66)
      COMMON /CHAR/ TITLE,ZUF
      COMMON /CONS/ NTRI,NQUAD,NINCS,NNOD,KSIZE,KSBW,NNOD2,NMAT,IDUM(4),
     +              GAMMA,PI,BETA,NST,NSI,NSEG,NODSEG,DELTAT
      COMMON /NODS/ X(IGL/2),Y(IGL/2),DISP(IGL),FORCE(IGL),XCOM1(4000)
      COMMON /ELEM/ NODEL(8,500),NGAUSS(500),NOTEL(500),NOQEL(500),
     +              NOTCOL(500),NOQCOL(500),DIFFOP(9,500),BLIB(144,500),
     +              PRINC(16,500)
      COMMON /FORC/ NOD4S(100),NDIS4S(100),NLOAD(100),FNOD(200),
     +              FNORM(100),FTAN(100),FNTOT(100),FTTOT(100)
      COMMON /FIXT/ DFIX(2,500),NOFIX(500),IFLAG(2,500),NFIX,NEXT,NSTOP
      COMMON /MATS/ EM(9),PM(9),TM(9),RHOM(9),ETAM(9),ETAN,ITYP(9)
      COMMON /VARS/ COMB(165),NOSECT,NDIS,NDIR,ICOMX(2),IG
C
C     ••• This routine adds or deletes nodes from the mesh writing the new
C     ••• file to unit 7. Data for the new nodes must be added separately
C
      READ(3,•)ISIGN
      READ(3,•)NNODE
      READ(3,•) (NODE(I),I=1,NNODE)
      N=NNOD+(NNODE•ISIGN)
C
      WRITE(7,1)TITLE
1     FORMAT(4A8)
      WRITE(7,2)N,NTRI,NQUAD,NMAT,NFIX,NDIR,NSEG,NSI,NST,NFS
2     FORMAT(11I5)
      WRITE(7,3)NINCS,GAMMA,VERGE,ETAN,DELTAT
3     FORMAT(I5,4D10.4)
C
      IF(NSI EQ.0) THEN
          SCALE=1.0D03
      ELSE
          SCALE=1.0D0
      ENDIF
      ICOUNT=1
C
C     ••• Update coordinate data
C
      DO 10 INOD=1,NNOD
      N=INOD
      DO 20 I=1,NNODE
        IF(INOD.GT.NODE(I)) N=N+ISIGN
20    CONTINUE
      IF(N.GT.ICOUNT) THEN
          DO 25 I=1,N-ICOUNT-1
```

```
             WRITE(7,4) ICOUNT+I,X(INOD-1)/SCALE
   25          CONTINUE
             ENDIF
             WRITE(7,4) N,X(INOD)/SCALE,Y(INOD)/SCALE
   4         FORMAT(I5,2F10.3)
             ICOUNT=N
   10      CONTINUE
           NNOD=NNOD+NNODE
   C
   C       ... Write material properties
   C
           DO 11 IMAT=1,NMAT
             WRITE(7,5)EM(IMAT),PM(IMAT),RHOM(IMAT),TM(IMAT),ETAM(IMAT)
   5         FORMAT(D10.3,2F10.3,2D10.3)
   11      CONTINUE
   C
   C       ... Write element topologies
   C
           IF(NTRI.GT.0) THEN
             DO 30 IEL=1,NTRI
               JEL=NDTEL(IEL)
               DO 40 KEL=1,6
                 NO(KEL)=NODEL(KEL,JEL)
                 DO 50 I=1,NNODE
                   IF(NODEL(KEL,JEL).GT.NODE(I))  NO(KEL)=NO(KEL)+ISIGN
   50            CONTINUE
   40          CONTINUE
               WRITE(7,2)JEL,(NO(KEL),KEL=1,6),ITYP(JEL),NGAUSS(JEL)
   30        CONTINUE
           ENDIF
   C
           IF(NQUAD.GT.0) THEN
             DO 60 IEL=1,NQUAD
               JEL=NODEL(IEL)
               DO 70 KEL=1,8
                 NO(KEL)=NODEL(KEL,JEL)
                 DO 80 I=1,NNODE
                   IF(NODEL(KEL,JEL).GT.NODE(I))  NO(KEL)=NO(KEL)+ISIGN
   80            CONTINUE
   70          CONTINUE
               WRITE(7,2)JEL,(NO(KEL),KEL=1,8),ITYP(JEL),NGAUSS(JEL)
   60        CONTINUE
           ENDIF
   C
   C       ... Direct nodal forces
   C
           IF(NDIR.GT.0) THEN
             DO 110 I=1,NDIR
               INODE=NOD4S(I)
               DO 112 K=1,NNODE
                 IF(NOD4S(I).GT.NODE(K))  INODE=INODE+ISIGN
   112          CONTINUE
               WRITE(7,6) INODE,FNOD(2*I-1),FNOD(2*I)
   6           FORMAT(I5,2(4X,D11.4))
   110       CONTINUE
           ENDIF
   C
   C       ... Surface tractions
   C
           IF(NSEG.GT.0) THEN
```

```
           DO 140 I=1,NSEG
             WRITE(7,2)NODSEG
             DO 140 J=1,NODSEG
               INODE=NDIS4S(J)
               DO 145 K=1,NNODE
                 IF(NDIS4S(J).GT.NODE(K))  INODE=INODE+ISIGN
   145          CONTINUE
               WRITE(7,6)INODE,FNORM(J),FTAN(J)
   140       CONTINUE
           ENDIF
   C
   C       ... Dirichlet conditions
   C
           IF(NFIX.GT.0) THEN
             DO 160 I=1,NFIX
               INODE=NOFIX(I)
               DO 165 J=1,NNODE
                 IF(NOFIX(I).GT.NODE(J))  INODE=INODE+ISIGN
   165          CONTINUE
               WRITE(7,7)INODE,(IFLAG(J,I),DFIX(J,I),J=1,2)
   7           FORMAT(I5,2(I5,D10.3),F10.3)
   160       CONTINUE
           ENDIF
   C
           RETURN
           END
   C
   C
   C.............................................................
   C
   C
           SUBROUTINE EIGEN
   C
   C+
   C       Extract the normalised eigenvalues.
   C       Major variables:  GLOBK =system matrix [K]
   C-
           IMPLICIT DOUBLE PRECISION (A-H,O-W)
           PARAMETER(IGL=880,JGL=131,KGL=66)
           COMMON /CONS/ NTRI,NQUAD,NINCS,NNOD,KSIZE,KSBW,NNOD2,NMAT,IDUM(4),
          +              STMAX,PI,BETA,NST,NSI,NSEG,NODSEG,DELTAT
           COMMON /STIF/ ELK(18,18),GLOBK(IGL,JGL)
           DOUBLE PRECISION DIAG(IGL),SUB(IGL)
   C
   C       ... Initialise, EPS is the smallest representable number
   C
           ITEST=0
           DUMMY=0.0D0
           EPS=X02AAF(DUMMY)
           I=0
   C
   C       ... The system matrix is scaled by [S][K][S] where [S] is a diagonal
   C       ... matrix composed of 1/SQRT of the diagonals of [K]
   C
           DO 10 KROW=1,NNOD2
             DUM=ABS(GLOBK(KROW,KSBW))
             DUM=1.0D0/SQRT(DUM)
             DO 20 KCOL=1,KSIZE
               GLOBK(KROW,KCOL)=GLOBK(KROW,KCOL)*DUM
   20        CONTINUE
```

```fortran
      DO 30 IROW=1,NNOD2
        ICOL=KROW+KSBW-IROW
        IF(ICOL.GE.1.AND.ICOL.LE.KSIZE)
     +            GLOBK(IROW,ICOL)=GLOBK(IROW,ICOL)*DUM
30    CONTINUE
C
C     *** Check unit diagonals
C
      ICHECK=NINT(GLOBK(KROW,KSBW))
      IF(ICHECK.NE.1) GOTO 99
C
C     *** Check symmetry
C
      DO 40 KCOL=1,NNOD2
        ICOL=KCOL+KSBW-KROW
        IROW=KROW+KSBW-KCOL
        IF(ICOL.GE.1.AND.ICOL.LE.KSIZE.AND.IROW.GE.1.AND.
     +                   IROW.LE.KSIZE) THEN
          IF(GLOBK(KROW,ICOL).NE.GLOBK(KCOL,IROW)) GOTO 99
        ENDIF
40    CONTINUE
10    CONTINUE
C
C     *** Decompose matrix
C
      CALL JACO(GLOBK,IGL,JGL,DIAG,IGL,SUB,IGL,NNOD2,KSBW,ITEST)
C
C     *** Extract eigenvalues
C
      CALL QLVAL(DIAG,IGL,SUB,IGL,NNOD2,EPS,ITEST)
C
C     *** Evaluate spectrum condition numbers
C
      C1=ABS(DIAG(NNOD2)/DIAG(1))
      C2=ABS(DIAG(NNOD2)/DIAG(2))
      C1=LOG10(C1)
      C2=LOG10(C2)
      WRITE(7,200)
200   FORMAT(14X,' Spectrum Condition Numbers'/24X,
     +              ' First',4X,'Second')
      WRITE(7,300) C1,C2
300   FORMAT(20X,2(5X,F5.1)//)
      CALL PRTVEC(DIAG,IGL,NNOD2,7,ITEST)
C
      WRITE(6,100)
100   FORMAT('0Eigenvalues extracted')
      CALL TIME(1,1)
C
      RETURN
C
99    WRITE(6,500)
500   FORMAT('0Incorrect system matrix detected')
      CALL TIME(1,1)
      STOP
      END
C
C
C•••••••••••••••••••••••••••••••••••••••••••••••••••••••••••••••••••••••
C
C
```

```fortran
      SUBROUTINE DISOUT
C
C------------------
C+
C     Output of nodal positions and final velocities.
C     Major variables:  DISP =current velocities
C                        X, Y =node coords
C-
C
      IMPLICIT DOUBLE PRECISION (A-H,O-W)
      CHARACTER    TITLE(4)*8,ZUF(4)*4
      PARAMETER(IGL=880,JGL=131,KGL=66)
      COMMON /CHAR/ TITLE,ZUF
      COMMON /CONS/ NTRI,NQUAD,NINCS,NNOD,KSIZE,KSBW,NNOD2,NMAT,IDUM(4),
     +              STMAX,PI,BETA,NST,NSI,NSEG,NODSEG,DELTAT
      COMMON /NODS/ X(IGL/2),Y(IGL/2),DISP(IGL),FORCE(IGL),
     +              XSTPOS(4,500),YSTPOS(4,500)
C
      WRITE(7,10)TITLE
10    FORMAT(1H0/1H ,50X,4A8/1H0,10X,'Nodal Velocities'/
     +       1H+,10X,'_____'/
     +       1H0,5X,'Node',12X,' x-coord: km',8X,' y-coord: km',8X,
     +                     ' Vel(x): m/s',10X,' Vel(y): m/s'/1H0)
C
      DO 20 IDIS=1,NNOD
        WRITE(7,30) IDIS,X(IDIS)/1.0E03,Y(IDIS)/1.0E03,DISP(2*IDIS-1),
     +              DISP(2*IDIS)
30      FORMAT(6X,I4,8X,2(3X,F10.2,7X),2(9X,1PE13.6))
20    CONTINUE
C
      WRITE(6,40)
40    FORMAT('0Velocities written')
      CALL TIME(1,1)
C
      RETURN
      END
C
C
C•••••••••••••••••••••••••••••••••••••••••••••••••••••••••••••••••••••••
C
C
      SUBROUTINE GRID
C
C------------------
C+
C     Plot the original and the final mesh configurations.
C     Major variables:  XOLD, YOLD = coords of reference frame
C                        X, Y       = coords of final mesh
C-
C
      IMPLICIT DOUBLE PRECISION (A-H,O-W)
      PARAMETER(IGL=880,JGL=131,KGL=66)
      COMMON /CONS/ NTRI,NQUAD,NINCS,NNOD,KSIZE,KSBW,NNOD2,NMAT,IDUM(4),
     +              STMAX,PI,BETA,NST,NSI,NSEG,NODSEG,DELTAT
      COMMON /NODS/ X(IGL/2),Y(IGL/2),DISP(IGL),FORCE(IGL),XCOM1(4000)
      COMMON /PLOT/ XMAX,XMIN,YMAX,YMIN,XOMAX,XOMIN,YOMAX,YOMIN,
     +              XSP,YSP,XPL(50),YPL(50)
      COMMON /ELEM/ NODEL(8,500),NGAUSS(500),NOTEL(500),NOQEL(500),
     +              NOTCOL(500),NOQCOL(500),DIFFOP(9,500),BLIB(144,500),
     +              PRINC(16,500)
      COMMON /MOVE/ VPART(IGL),VMESH(IGL),APARAM(IGL),STRANS(IGL),
     +              ATRANS(IGL),DMESH(IGL),APART(IGL),AMESH(IGL),
     +              VMESH2(IGL),DMESH2(IGL),XOLD(IGL),YOLD(IGL)
C
C     *** Initialise
C
```

```fortran
      XSP1=XSP+0.2
      CALL PSPACE(0.2,XSP1,0.1,1.0)
      CALL MAP(XMIN,XMAX,YMIN,YOMAX)
C
C     ••• Plot original mesh with a broken line
C
      CALL BROKEN(5,15,5,15)
      DO 300 NMESH=1,2
        IF(NTRI.GT.0) THEN
          DO 20 IEL=1,NTRI
            NUMEL=NOTEL(IEL)
            DO 10 I=1,6
              NOD=NODEL(I,NUMEL)
              IF(NMESH.EQ.1) THEN
                XPL(I)=XOLD(NOD)
                YPL(I)=YOLD(NOD)
              ELSE
                XPL(I)=X(NOD)
                YPL(I)=Y(NOD)
              ENDIF
10          CONTINUE
            XPL(7)=XPL(1)
            YPL(7)=YPL(1)
            CALL CURVEO(XPL,YPL,1,3)
            CALL CURVEO(XPL,YPL,3,5)
            CALL CURVEO(XPL,YPL,5,7)
20        CONTINUE
        ENDIF
C
        IF(NQUAD.GT.0) THEN
          DO 50 IEL=1,NQUAD
            NUMEL=NOQEL(IEL)
            DO 40 I=1,8
              NOD=NODEL(I,NUMEL)
              IF(NMESH.EQ.1) THEN
                XPL(I)=XOLD(NOD)
                YPL(I)=YOLD(NOD)
              ELSE
                XPL(I)=X(NOD)
                YPL(I)=Y(NOD)
              ENDIF
40          CONTINUE
            XPL(9)=XPL(1)
            YPL(9)=YPL(1)
            CALL CURVEO(XPL,YPL,1,3)
            CALL CURVEO(XPL,YPL,3,5)
            CALL CURVEO(XPL,YPL,5,7)
            CALL CURVEO(XPL,YPL,7,9)
50        CONTINUE
        ENDIF
        CALL FULL
300   CONTINUE
C
C     ••• Annotate
C
      CALL LABEL
C
      WRITE(6,90)
90    FORMAT('0Element mesh drawn')
C
```

```fortran
      RETURN
      END
C
C
C•••••••••••••••••••••••••••••••••••••••••••••••••••••••••••••••••••••••
C
C
      SUBROUTINE PAMS
C
C
C+    This routine sets up a plotting space XSP,YSP in which the
C     output is plotted. This plot space has an annotation border,
C     of 0.2 in each x-direction, 0.1 at the base and it stretches
C     to fill up the top border.
C     Major variables:  XSP, YSP =physical size of plot
C                        XMIN, XMAX, YMIN, YMAX =extremities of coords
C-
C
      IMPLICIT DOUBLE PRECISION (A-H,O-W)
      PARAMETER(IGL=880,JGL=131,KGL=66)
      COMMON /CONS/ NTRI,NQUAD,NINCS,NNOD,KSIZE,KSBW,NNOD2,NMAT,IDUM(4),
     +              STMAX,PI,BETA,NST,NSI,NSEG,NODSEG,DELTAT
      COMMON /PLOT/ XMAX,XMIN,YMAX,YMIN,XOMAX,XOMIN,YOMAX,YOMIN,
     +              XSP,YSP,XPL(50),YPL(50)
C
C     ••• Initiate plot
C
      CALL PAPER(1)
C
C     ••• Read coordinate boundaries
C
      READ(5,10)XMIN,XMAX
      READ(5,10)YMIN,YMAX
10    FORMAT(2F10.3)
C
C     ••• Read size of PSPACE
C
      READ(5,20)XSP,YSP
20    FORMAT(2F5.2)
C
C     ••• Scale
C
      IF(NSI.EQ.0) THEN
        XMIN=XMIN*1000.0
        XMAX=XMAX*1000.0
        YMIN=YMIN*1000.0
        YMAX=YMAX*1000.0
      ENDIF
C
C     ••• Calculate mapping area for the border region
C
      XSC=(XMAX-XMIN)/(XSP*10.0)
      YSC=(YMIN-YMAX)/(YSP*10.0)
      XOMIN=XMIN-XSC*2.0
      XOMAX=XMIN+(XSC*(XSP+0.2)*10.0)
      YOMIN=YMIN+YSC
      YOMAX=YMAX-(YSC*(0.9-YSP)*10.0)
C
      WRITE(6,100)
100   FORMAT('0PAMS completed')
C
```

```
      RETURN                                          100  FORMAT('0Current plot annotated')
      END                                          C
C                                                        RETURN
C                                                        END
C                                                   C
C••••••••••••••••••••••••••••••••••••••••••••••••••  C
C                                                   C••••••••••••••••••••••••••••••••••••••••••••••••••••••
C                                                   C
      SUBROUTINE LABEL                               C
C                                                        SUBROUTINE VECPLT
C        ==========                                  C
C                                                   C        ==========
C+                                                   C
C    Annotate axes of the current plot.             C+
C    Major variables:  TITLE =title of model        C    Plot the stress vectors at selected gauss points.
C-                                                   C    Major variables: XSTPOS, YSTPOS =coords of gauss points
C                                                   C                     PRINCS =stress at gauss points
      IMPLICIT DOUBLE PRECISION (A-H,O-W)           C-
      CHARACTER   TITLE*32,ZUF(4)*4                  C
      COMMON /CHAR/ TITLE,ZUF                              IMPLICIT DOUBLE PRECISION (A-H,O-W)
      COMMON /CONS/ NTRI,NQUAD,NINCS,NNOD,KSIZE,KSBW,NNOD2,NMAT,IDUM(4),  PARAMETER(IGL=800,JGL=131,KGL=66)
     +           STMAX,PI,BETA,NST,NSI,NSEG,NODSEG,DELTAT    COMMON /MATS/ EM(9),PM(9),TM(9),RHOM(9),ETAM(9),ETAN,ITYP(9)
      COMMON /PLOT/ XMAX,XMIN,YMAX,YMIN,XOMAX,XOMIN,YOMAX,YOMIN,  COMMON /CONS/ NTRI,NQUAD,NINCS,NNOD,KSIZE,KSBW,NNOD2,NMAT,IDUM(4),
     +           XSP,YSP,XPL(50),YPL(50)             +           STMAX,PI,BETA,NST,NSI,NSEG,NODSEG,DELTAT
C                                                         COMMON /VARS/ COM0(165),NO,NUMEL,NGAUS,LOOM(2),IG
      XSP1=XSP+0.4                                        COMMON /PLOT/ XMAX,XMIN,YMAX,YMIN,XOMAX,XOMIN,YOMAX,YOMIN,
      CALL CSPACE(0.0,XSP1,0.0,1.0)                  +           XSP,YSP,XVECS,YVECS,XPL(48),YPL(50)
      CALL PSPACE(0.0,XSP1,0.0,1.0)                       COMMON /ELEM/ NODEL(8,500),NGAUSS(500),NOTEL(500),NODEL(500),
      CALL MAP(XOMIN,XOMAX,YOMIN,YOMAX)             +           NOTOOL(500),NODOOL(500),DIFFOP(9,500),BLIB(144,500),
C                                                   +           PRINC(16,500)
C    ••• Plot title                                 C
C                                                        XSP1=XSP+0.2
      CALL CTRMAG(20)                                    CALL CSPACE(0.0,XSP1,0.0,1.0)
      XST=XMIN                                            CALL PSPACE(0.2,XSP1,0.1,1.0)
      YST=YMAX+(YOMAX-YMAX)*0.8                           CALL MAP(XMIN,XMAX,YMIN,YOMAX)
      CALL PLOTCS(XST,YST,TITLE)                     C
      CALL CTRMAG(15)                                C    ••• Scale the vectors to the physical size of the plot
C                                                   C
C    ••• Plot the corner coords                          XVECS=(ABS(XMAX-XMIN)/(25.0*XSP))*1.0
C                                                        YVECS=(ABS(YMAX-YMIN)/(25.0*YSP))*1.0
      IYKM=YMIN/1.0E3                                C
      XST=XMIN-(XMAX-XMIN)/20.0                           IF(NTRI.GT.0) THEN
      CALL PLOTNI(XST,YMIN,IYKM)                           DO 20 IEL=1,NTRI
C                                                             NUMEL=NOTEL(IEL)
      IYKM=YMAX/1.0E3                                          MAT=ITYP(NUMEL)
      CALL PLOTNI(XST,YMAX,IYKM)                               NGAUS=3
C                                                             CALL STPLOT
      YST=(YMIN-YMAX)*1.09                          20        CONTINUE
      IXKM=XMIN/1.0E3                               C         ENDIF
      CALL PLOTNI(XMIN,YST,IXKM)                     C
C                                                        IF(NQUAD.GT.0) THEN
      IXKM=XMAX/1.0E3                                     DO 40 IEL=1,NQUAD
      CALL PLOTNI(XMAX,YST,IXKM)                               NUMEL=NODEL(IEL)
C                                                             MAT=ITYP(NUMEL)
C    ••• Draw a border around the plot                       NGAUS=4
C                                                             CALL STPLOT
      XSP2=XSP+0.2                                   40       CONTINUE
      YSP1=YSP+0.1                                   C        ENDIF
      CALL PSPACE(0.2,XSP2,0.1,YSP1)                 C
      CALL BORDER                                    C    ••• Annotate
C                                                   C
      WRITE(6,100)
```

```
      XSP1=XSP+0.4
      CALL PSPACE(0.0,XSP1,0.0,1.0)
      CALL MAP(XOMIN,XOMAX,YOMIN,YOMAX)
      CALL CTRMAG(12)
      XST=XMAX-(XMAX-XMIN)*0.4
      YST=YMAX+(YOMAX-YMAX)*0.2
      CALL POSITN(XST,YST)
      IF(STMAX.LT.50.0E06) THEN
        XST=XST+1.0E08*XVECS/STMAX
        CALL JOIN(XST,YST)
        CALL TYPECS('  50 MPa',8)
      ELSEIF(STMAX.LT.100.0E06) THEN
        XST=XST+2.0E08*XVECS/STMAX
        CALL JOIN(XST,YST)
        CALL TYPECS(' 100 MPa',9)
      ELSE
        XST=XST+5.0E08*XVECS/STMAX
        CALL JOIN(XST,YST)
        CALL TYPECS(' 250 MPa',9)
      ENDIF
      CALL ITALIC(1)
      CALL TYPECS('     ( DOTTED LINES TENSIONAL )',30)
      CALL ITALIC(0)
      XST=XMAX-(XMAX-XMIN)*0.5
      YST=YMAX+(YOMAX-YMAX)*0.7
      CALL PLOTCS(XST,YST,'STRESS VECTORS',14)
C
C
C     *** Label
C
      CALL LABEL
C
      WRITE(6,100)
100   FORMAT('0Vectors plotted')
C
      RETURN
      END
C
C
C*******************************************************************
C
C
      SUBROUTINE STOUT
C
C     ===================
C
C+
C     Write stresses to unit 7
C     Major variables: XSTPOS, YSTPOS =coords of gauss points
C                      PRINCS =stresses at gauss points
C-
C
      IMPLICIT DOUBLE PRECISION (A-H,O-W)
      CHARACTER   TITLE(4)*8,ZUF(4)*4
      PARAMETER(IGL=880,JGL=131,KGL=66)
      COMMON /CHAR/ TITLE,ZUF
      COMMON /CONS/ NTRI,NQUAD,NINCS,NNOD,KSIZE,KSBW,NNOD2,NMAT,IDUM(4),
     +              STMAX,PI,BETA,NST,NSI,NSEG,NODSEG,DELTAT
      COMMON /NODS/ X(IGL/2),Y(IGL/2),DISP(IGL),FORCE(IGL),
     +              XSTPOS(4,500),YSTPOS(4,500)
      COMMON /ELEM/ NODEL(8,500),NGAUSS(500),NOTEL(500),NOQEL(500),
     +              NOTCOL(500),NOQCOL(500),DIFFOP(9,500),BLIB(144,500),
```
```
     +              PRINC(16,500)
C
C     *** Write title and header
C
      WRITE(7,10) TITLE
10    FORMAT('1 ',20X,4A8)
      WRITE(7,20)STMAX/1.0D06
20    FORMAT(1H0,10X,'STRESSES'/
     +       1H+,10X,'_____'/
     +       1H0,10X,'Maximum Stress =',1PD10.3,'MPa (Absolute value)'/
     +       1H0,10X,'El',5X,'x: (km)',6X,'y: (km)',7X,
     +               'Principal Stresses',9X,'Angle',6X,'Shear',//)
C
C     *** Write out triangles then quads
C
      NOEL=NTRI
      NO=3
      DO 50 IS=1,2
        IF(NOEL.GT.0) THEN
          DO 40 IEL=1,NOEL
            IF(IS.EQ.1) THEN
              NUMEL=NOTEL(IEL)
            ELSE
              NUMEL=NOQEL(IEL)
            ENDIF
            DO 30 IG=1,NO
              JPOS=(IG-1)*4
              WRITE(7,60)NUMEL,XSTPOS(IG,NUMEL),YSTPOS(IG,NUMEL),
     +                   PRINC(1+JPOS,NUMEL),PRINC(2+JPOS,NUMEL),
     +                   PRINC(4+JPOS,NUMEL),PRINC(3+JPOS,NUMEL)
60            FORMAT(8X,I3,5X,E10.3,3X,E10.3,3X,E10.3,3X,E10.3,
     +               3X,F8.3,3X,E10.3)
30          CONTINUE
40        CONTINUE
          NOEL=NQUAD
          NO=4
        ENDIF
50    CONTINUE
C
      WRITE(6,100)
100   FORMAT('0Stresses written')
      CALL TIME(1,1)
C
      RETURN
      END
C
C
C*******************************************************************
C
C
      SUBROUTINE STPLOT
C
C     ===================
C
C+
C     Plot the two stress vectors at this gauss point.
C     Major variables: XSTPOS, YSTPOS =coords of gauss points
C                      PRINCS =stress at gauss points
C-
C
      IMPLICIT DOUBLE PRECISION (A-H,O-W)
```

```
      PARAMETER(IGL=880,JGL=131,KGL=66)
      COMMON /CONS/ NTRI,NQUAD,NINCS,NNOD,KSIZE,KSBW,NNOD2,NMAT,IDUM(4),
     +              STMAX,PI,BETA,NST,NSI,NSEG,NODSEG,DELTAT
      COMMON /VARS/ COM0(165),NO,NUMEL,NGAUS,LCOM(2),IG
      COMMON /PLOT/ XMAX,XMIN,YMAX,YMIN,XOMAX,XOMIN,YOMAX,YOMIN,
     +              XSP,YSP,XVECS,YVECS,XPL(48),YPL(50)
      COMMON /NODS/ X(IGL/2),Y(IGL/2),DISP(IGL),FORCE(IGL),
     +              XSTPOS(4,500),YSTPOS(4,500)
      COMMON /ELEM/ NODEL(8,500),NGAUSS(500),NOTEL(500),NODEL(500),
     +              NOTOOL(500),NOCOOL(500),DIFFOP(9,500),BLIB(144,500),
     +              PRINC(16,500)
C
C     *** For each gauss point in this element
C
      DO 10 IG=1,NGAUS
        KPLT=1
        IPOS=(IG-1)*4
        XPOS=XSTPOS(IG,NUMEL)
        YPOS=YSTPOS(IG,NUMEL)
C
C     *** Retrieve the angles of the principal stresses
C
        IF(DABS(PRINC(4+IPOS,NUMEL)-90.0).LT.1.0E-7) THEN
          CTHETA=0.0
          STHETA=1.0
        ELSE
          TTHETA=PRINC(4+IPOS,NUMEL)*PI/180.0
          CTHETA=DCOS(TTHETA)
          STHETA=DSIN(TTHETA)
        ENDIF
C
C     *** Evaluate the end of the first vector
C
        XPLT=XPOS+(PRINC(1+IPOS,NUMEL)*CTHETA/STMAX*XVECS)
        YPLT=YPOS+(PRINC(1+IPOS,NUMEL)*STHETA/STMAX*YVECS)
        DO 30 KPLT=1,2
          CALL POSITN(XPLT,YPLT)
C
C     *** Broken line for tension
C
          IF(PRINC(KPLT+IPOS,NUMEL) GT 0.0) THEN
            XPLT1=0.4*XPOS+0.6*XPLT
            YPLT1=0.4*YPOS+0.6*YPLT
            CALL JOIN(XPLT1,YPLT1)
            XPLT1=1.6*XPOS-0.6*XPLT
            YPLT1=1.6*YPOS-0.6*YPLT
            CALL POSITN(XPLT1,YPLT1)
          ENDIF
          XPLT1=2.0*XPOS-XPLT
          YPLT1=2.0*YPOS-YPLT
          CALL JOIN (XPLT1,YPLT1)
          IF(KPLT.EQ.1) THEN
            IF(CTHETA.NE.0.0) THEN
              COP=CTHETA
              CTHETA=STHETA
              STHETA=COP
            ELSE
              STHETA=0.0
              CTHETA=1.0
            ENDIF
          ENDIF
```

```
            XPLT=XPOS-(PRINC(2+IPOS,NUMEL)*CTHETA/STMAX*XVECS)
            YPLT=YPOS+(PRINC(2+IPOS,NUMEL)*STHETA/STMAX*YVECS)
          ENDIF
30      CONTINUE
10    CONTINUE
C
      RETURN
      END
C
C
C**************************************************************************
C
C
C
      SUBROUTINE SURF
C
C     _____
C
C+
C     Plot the surface displacement profile of the final configuration.
C     Major variables: X, Y =coords of final mesh
C-
C
      IMPLICIT DOUBLE PRECISION (A-H,O-W)
      PARAMETER(IGL=880,JGL=131,KGL=66)
      COMMON /CONS/ NTRI,NQUAD,NINCS,NNOD,KSIZE,KSBW,NNOD2,NMAT,IDUM(4),
     +              STMAX,PI,BETA,NST,NSI,NSEG,NODSEG,DELTAT
      COMMON /NODS/ X(IGL/2),Y(IGL/2),DISP(IGL),FORCE(IGL),XCOM1(4000)
      COMMON /VISC/ DSTORE(12,900),FINIT(IGL),FOUT(IGL),AMASS(IGL)
      DIMENSION NN(500),XP(9,500),YDISP(9,500),XPLT(500),YPLT(500)
C
      XSTART=0.0
      XEND=0.0
      YBOT=0.0
      YTOP=0.0
      IPLT=0
C
      READ(5,200) NPLT
200   FORMAT(I5)
      DO 210 I=1,NPLT
        READ(5,200) NN(I)
210   CONTINUE
C
      CALL PSPACE(0.2,1.0,0.3,0.6)
      CALL MAP(0.0,91.0,0.0,-5.0,1.0)
      CALL SCALES
C
      DO 10 I=1,4
        DO 20 IPLT=1,NPLT
          XPLT(IPLT)=X(NN(IPLT))/1.0E03
          YPLT(IPLT)=DSTORE(I,NN(IPLT))/1.0E03
          WRITE(7,100) XPLT(IPLT),YPLT(IPLT)
100       FORMAT(2(5X,F10.3))
20      CONTINUE
        CALL CURVEO(XPLT,YPLT,1,NPLT)
10    CONTINUE
C
      CALL PSPACE(0.0,1.0,0.0,1.0)
      CALL MAP(0.0,1.0,0.0,1.0)
      CALL CTRMAG(17)
      CALL THICK(2)
      CALL PLOTCS(0.2,0.75,'Surface Displacement Profiles',29)
```

```
          CALL THICK(1)
          CALL CTRMAG(12)
          CALL PLOTCS(0.4,0.20,'Distance along profile in km',28)
          CALL CTRORI(90.0)
          CALL PLOTCS(0.10,0.35,'Surface height in km',20)
          CALL CTRORI(0.0)
C
          WRITE(6,50)
50        FORMAT('0Specified displacements plotted')
C
          RETURN
          END
C
C
C
C....................................................................................
C
C
C
          SUBROUTINE VELPLT
C         =================
C+
C         Plot the velocity vectors at the nodes.
C         Major variables:  DISP  =current velocities
C                           X, Y  =mesh coords
C-
C
          IMPLICIT DOUBLE PRECISION (A-H,O-W)
          PARAMETER(IGL=880,JGL=131,KGL=66)
          COMMON /NODS/ X(IGL/2),Y(IGL/2),DISP(IGL),FORCE(IGL),XCOM1(4000)
          COMMON /CONS/ NTRI,NQUAD,NINCS,NNOD,KSIZE,KSBW,NNOD2,NMAT,IDUM(4),
         +              STMAX,PI,BETA,NST,NSI,NSEG,NODSEG,DELTAT
          COMMON /VARS/ W1W2,DETJ,ETA,C2,FACT,DNXDX(8),DNXDY(8),B(4,18),
         +              BTC(18,4),NO,NGAUS,ICASE,NUMEL,IROW,IG
          COMMON /PLOT/ XMAX,XMIN,YMAX,YMIN,XOMAX,XOMIN,YOMAX,YOMIN,
         +              YSP,YSP,XPL(50),YPL(50)
          COMMON /ELEM/ NODEL(8,500),NGAUSS(500),NOTEL(500),NOQEL(500),
         +              NOTCOL(500),NOQCOL(500),DIFFOP(9,500),BLIB(144,500),
         +              PRINC(16,500)
          DIMENSION XPLT(50),YPLT(50),STORE(750),NULL(750),NN(50)
C
C         *** Evaluate the largest velocity vector
C
          DIMAX=0.0D0
          DO 10 I=IPLOT,NNOD
              DVEC=DSQRT(DISP(I*2-1)**2+DISP(I*2)**2)
              DIMAX=DMAX1(DVEC,DIMAX)
10        CONTINUE
C
C         *** Set up plot frame
C
          XSP1=XSP+0.20
          CALL CSPACE(0.2,XSP1,0.0,1.0)
          CALL PSPACE(0.2,XSP1,0.0,1.0)
          CALL MAP(XMIN,XMAX,YOMIN,YOMAX)
C
C         *** Plot a circle at each node
C
          CALL CTRFNT(1)
          CALL CTRMAG(7)
```
```
          CALL PTPLOT(X,Y,1,NNOD,245)
          CALL CTRMAG(15)
C
C         *** Plot the scaled velocity vectors
C
          XVECS=ABS(XMAX-XMIN)/(25.0*XSP)
          YVECS=ABS(YMAX-YMIN)/(25.0*YSP)
          SCALEX=XVECS/DIMAX
          SCALEY=YVECS/DIMAX
          CALL REDPEN
          DO 20 I=IPLOT,NNOD
              CALL POSITN(X(I),Y(I))
              XP=X(I)+(DISP(I*2-1)*SCALEX)
              YP=Y(I)+(DISP(I*2)*SCALEY)
              CALL JOIN(XP,YP)
20        CONTINUE
          CALL BLKPEN
C
C         *** Plot the displacement of the surface above the frame
C
          READ(5,200) NPLT
200       FORMAT(I5)
          DO 210 I=1,NPLT
              READ(5,200) NN(I)
210       CONTINUE
C
          DO 220 IPLT=1,NPLT
              XPLT(IPLT)=X(NN(IPLT))
              YPLT(IPLT)=Y(NN(IPLT))/1.0E03
              WRITE(7,230) XPLT(IPLT)/1.0D03,YPLT(IPLT)
230           FORMAT(2(5X,F10.3))
220       CONTINUE
C
          XSP1=XSP+0.2
          YSP1=0.1+YSP
          YSP2=YSP1+0.1
          CALL PSPACE(0.2,XSP1,YSP1,YSP2)
          CALL MAP(XMIN,XMAX,-4.0,1.0)
          CALL POSITN(XMIN,1.0)
          CALL JOIN(XMIN,-4.0)
          CALL BROKEN(20,20,10,20)
          CALL POSITN(XMIN,0.0)
          CALL JOIN(XMAX,0.0)
          CALL FULL
          CALL CURVEO(XPLT,YPLT,1,NPLT)
C
C         *** Annotate
C
          XSP1=XSP+0.4
          CALL PSPACE(0.0,XSP1,0.0,1.0)
          CALL CSPACE(0.0,XSP1,0.0,1.0)
          CALL MAP(XOMIN,XOMAX,YOMIN,YOMAX)
          CALL CTRMAG(10)
          XLABEL=XMAX - (XMAX-XMIN)*0.4
          YLABEL=YMAX + (YMAX-YMIN)*0.4
          CALL POSITN(XLABEL,YLABEL)
          XLABEL=XLABEL +15.80E-10*SCALEX
          CALL JOIN(XLABEL,YLABEL)
          CALL TYPECS(' 50 mm/yr',10)
C
C         *** Label axes
C
```

```
      CALL LABEL                                              CALL JOIN(XEND,0.1)
C                                                             CALL FULL
      WRITE(6,11)                                             YSP1=YSP1+0.16
11    FORMAT('0Velocities plotted')                          YSP2=YSP2+0.16
      RETURN                                          20   CONTINUE
      END                                             C
C                                                             CALL PSPACE(0.2,0.8,0.2,YSP1)
C                                                             CALL MAP(0.0,1.0,0.0,1.0)
C•••••••••••••••••••••••••••••••••••••••••••••••••••••••••    CALL POSITN(0.0,0.0)
C                                                             CALL JOIN(1.0,0.0)
C                                                             CALL JOIN(1.0,1.0)
      SUBROUTINE DPROF                                        CALL JOIN(0.0,1.0)
C                                                             CALL JOIN(0.0,0.0)
C     ▬▬▬▬▬▬▬▬▬▬▬▬▬▬                                 C
C                                                             CALL PSPACE(0.0,1.0,0.0,0.2)
C+                                                            CALL MAP(0.0,1.0,0.0,1.0)
C     Plot the surface profile of the travelling wave problem.    CALL CTRMAG(12)
C     Major variables:  X, Y =mesh coords                     CALL PLOTCS(0.3,0.5,'Scaled distance in reference frame',34)
C-                                                             CALL PLOTNF(0.19,0.8,XSTART,1)
      IMPLICIT DOUBLE PRECISION (A-H,O-W)                     CALL PLOTNF(0.79,0.8,60.0,1)
      PARAMETER(IGL=880,JGL=131,KGL=66)               C
      COMMON /NODS/ X(IGL/2),Y(IGL/2),DISP(IGL),FORCE(IGL),XCOM1(4000)    CALL PSPACE(0.8,1.0,0.0,1.0)
      COMMON /VISC/ DSTORE(12,900),FINIT(IGL),FOUT(IGL),AMASS(IGL)    CALL MAP(0.0,1.0,0.0,1.0)
      COMMON /MOVE/ VPART(IGL),VMESH(IGL),APARAM(IGL),STRANS(IGL),    CALL CTRMAG(15)
     +              ATRANS(IGL),DMESH(IGL),APART(IGL),AMESH(IGL),    CALL PLOTCS(0.2,0.3,'n=40',4)
     +              VMESH2(IGL),DMESH2(IGL),XOLD(IGL),YOLD(IGL)    CALL PLOTCS(0.2,0.46,'n=60',4)
      DIMENSION XPLT(350),YPLT(350),NN(350)                   CALL PLOTCS(0.2,0.62,'n=80',4)
C                                                             CALL PLOTCS(0.2,0.78,'n=100',5)
      XSTART=0.0                                      C
      XEND=0.0                                                CALL PSPACE(0.0,1.0,YSP1,1.0)
      YBOT=0.0                                                CALL MAP(0.0,1.0,0.0,1.0)
      YTOP=0.0                                                CALL CTRMAG(13)
      IPLT=0                                                  CALL THICK(2)
      YSP1=0.2                                                CALL PLOTCS(0.2,0.3,'Free-surface of the fluid at selected times',
      YSP2=0.35                                       +         43)
C                                                             CALL THICK(1)
      READ(5,100) NPLT                                C
100   FORMAT(I5)                                              CALL PSPACE(0.0,0.2,0.0,1.0)
      DO 150 I=1,NPLT                                         CALL MAP(0.0,1.0,0.0,1.0)
        READ(5,100) NN(I)                                     CALL CTRMAG(9)
150   CONTINUE                                                CALL PLOTNF(0.9,0.205,0.0,1)
C                                                             CALL PLOTNF(0.9,0.345,0.1,1)
      DO 20 ISURF=1,4                                         CALL PLOTNF(0.9,0.365,0.0,1)
        DO 10 I=1,NPLT                                        CALL PLOTNF(0.9,0.505,0.1,1)
          XPLT(I)=X(NN(I))/10.0                               CALL PLOTNF(0.9,0.525,0.0,1)
          YPLT(I)=( DSTORE(ISURF,NN(I)) - YOLD(NN(I)) )/10.0    CALL PLOTNF(0.9,0.665,0.1,1)
          WRITE(7,200) XPLT(I),YPLT(I)                        CALL PLOTNF(0.9,0.685,0.0,1)
200       FORMAT(2(5X,F10.3))                                 CALL PLOTNF(0.9,0.825,0.1,1)
          XSTART=AMIN1(XSTART,XPLT(I))                        CALL CTRMAG(12)
          XEND=AMAX1(XEND,XPLT(I))                            CALL CTRORI(90.0)
          YBOT=AMAX1(YBOT,YPLT(I))                            CALL PLOTCS(0.4,0.3,'Scaled amplitude of position of free-surface'
          YTOP=AMIN1(YTOP,YPLT(I))                   +          ,44)
10      CONTINUE                                               CALL CTRORI(0.0)
C                                                       C
      CALL PSPACE(0.2,0.8,YSP1,YSP2)                           WRITE(6,300)
      CALL MAP(XSTART,XEND,-0.005,0.1)                 300  FORMAT('0Surface displacement plotted')
      CALL CURVEO(XPLT,YPLT,1,NPLT)                    C
      CALL POSITN(XSTART,0.0)                                  RETURN
      CALL JOIN(XEND,0.0)                                      END
      CALL BROKEN(10,10,10,10)                         C
      CALL POSITN(XSTART,0.1)                          C
                                                       C•••••••••••••••••••••••••••••••••••••••••••••••••••••••••
                                                       C
```

```
C
      SUBROUTINE MCOPY(A,IA,JA,B,IB,JB,M,N,ITEST)
C     ================================================
C+
C
C     Duplicate one matrix into another
C-
C
      IMPLICIT DOUBLE PRECISION (A-H,O-W)
      DIMENSION A(IA,JA),B(IB,JB)
C
      DO 10 I=1,M
        DO 10 J=1,N
          B(I,J)=A(I,J)
10    CONTINUE
      RETURN
      END
C
C
C
C.............................................................................
C
C
      SUBROUTINE GRAVTY
C     ================
C+
C
C     Calculate the contribution to the global force vector for body forces
C     acting towards the centre of the Earth.
C     Major variables:  RHOM  =density of element
C                        X, Y =coords of nodes      FORCE =force vector {F}
C-
C
      IMPLICIT DOUBLE PRECISION (A-H,O-W)
      PARAMETER(IGL=880,JGL=131,KGL=66)
      COMMON /CONS/ NTRI,NQUAD,NINCS,NNOD,KSIZE,KSBW,NNOD2,NMAT,IDUM(4),
     +              STMAX,PI,BETA,NST,NSI,NSEG,NODSEG,DELTAT
      COMMON /NODS/ X(IGL/2),Y(IGL/2),DISP(IGL),FORCE(IGL),XSTPOS(4,500),
     +              YSTPOS(4,500)
      COMMON /MATS/ EM(9),PM(9),TM(9),RHOM(9),ETAM(9),ETAN,ITYP(9)
      COMMON /ELEM/ NODEL(8,500),NGAUSS(500),NOTEL(500),NOQEL(500),
     +              NOTCOL(500),NOQCOL(500),DIFFOP(9,500),BLIB(144,500),
     +              PRINC(16,500)
      COMMON /GAPT/ S,T,SHAPE(8),DNXDS(8),DNXDT(8),TSHAPE(6,36),
     +              TDNXDS(6,36),TDNXDT(6,36),TW1W2(6,6),QSHAPE(3,72),
     +              QDNXDS(3,72),QDNXDT(3,72),QW1W2(3,9),WEITRI(12,6),
     +      WEIQAD(18,3),PLACET(12,6),PLACEQ(18,3),PLACEL(3),WEILIN(3)
C
      IF (NTRI.NE.0) THEN
        DO 30 IEL=1,NTRI
          NUMEL=NOTEL(IEL)
          MAT=ITYP(NUMEL)
          RHO=RHOM(MAT)
          NGAUS=NGAUSS(NUMEL)
          NROW=NOTCOL(IEL)
          FLOAD= RHO*9.81
          DO 20 IG=1,NGAUS
            IPOS=(IG-1)*6
            DV=DIFFOP(IG,NUMEL)
            ANG=ATAN(XSTPOS(IG,NUMEL)/YSTPOS(IG,NUMEL))
            ZLOAD=-FLOAD*DCOS(ANG)
            XLOAD= FLOAD*DSIN(ANG)
            DO 10 INT=1,6
              SHAPE(INT)=TSHAPE(NROW,IPOS+INT)
              NOD=NODEL(INT,NUMEL)
              FORCE(2*NOD  )=SHAPE(INT)*ZLOAD*DV+FORCE(2*NOD  )
              FORCE(2*NOD-1)=SHAPE(INT)*XLOAD*DV+FORCE(2*NOD-1)
10          CONTINUE
20        CONTINUE
30      CONTINUE
      ENDIF
C
      IF(NQUAD.NE.0) THEN
        DO 70 IEL=1,NQUAD
          NUMEL=NOQEL(IEL)
          MAT=ITYP(NUMEL)
          RHO=RHOM(MAT)
          NGAUS=NGAUSS(NUMEL)
          NROW=NOQCOL(IEL)
          FLOAD= RHO*9.81
          DO 60 IG=1,NGAUS
            DV=DIFFOP(IG,NUMEL)
            IPOS=(IG-1)*8
            ANG=ATAN(XSTPOS(IG,NUMEL)/YSTPOS(IG,NUMEL))
            ALOAD=-FLOAD*DCOS(ANG)
            BLOAD=-FLOAD*DSIN(ANG)
            DO 50 INT=1,8
              SHAPE(INT)=QSHAPE(NROW,IPOS+INT)
              NOD=NODEL(INT,NUMEL)
              FORCE(2*NOD  )=SHAPE(INT)*ALOAD*DV+FORCE(2*NOD  )
              FORCE(2*NOD-1)=SHAPE(INT)*BLOAD*DV+FORCE(2*NOD-1)
50          CONTINUE
60        CONTINUE
70      CONTINUE
      ENDIF
C
      WRITE(6,90)
90    FORMAT('0Body forces applied')
      CALL TIME(1,1)
C
      RETURN
      END
```

References

Acharya H. 1981, Volcanism and aseismic slip in subduction zones, *J. Geophys. Res.* **86**, 335-344

Anderson D.L. 1987, Thermally induced phase changes, lateral heterogeneity of the mantle, continental roots and deep slab anomalies, *J. Geophys. Res.* **92**, 13968-13980

Andrews D.J., Sleep N.H. 1974, Numerical modelling of tectonic flow behind island arcs, *Geophys. J. R. astr. Soc.* **38**, 237-251

Apperson K.D., Frohlich C. 1987, The relationship between Wadati-Benioff zone geometry and P, T and B axes of intermediate and deep focus earthquakes, *J. Geophys. Res.* **92**, 13821-13831

Barlow J. 1976, Optimal stress locations in finite element models, *Int. Jour. Num. Meth. Eng.* **10**, 243-251

Batchelor G.K. 1967, *An introduction to fluid dynamics*, Cambridge University Press

Boss A.P., Sacks I.S. 1986, High spatial resolution models of time-dependent, layered mantle convection, *Geophys. J. R. astr. Soc.* **87**, 241-264

Bott M.H.P. 1976, Formation of sedimentary basins of graben type by extension of the continental crust, *Tectonophysics* **36**, 77-86

Bott M.H.P. 1982a, *The Interior of the Earth (2 ed)*, Arnold

Bott M.H.P. 1982b, Origin of the lithospheric tension causing basin formation, *Phil. Trans. R. Soc. Lond.* A **305**, 319-324

Bott M.H.P., Kusznir N.J. 1984, Origin of tectonic stress in the lithosphere, *Tectonophysics* **105**, 1-13

Bott M.H.P. 1988, Global gravity anomalies, hot spots and subduction zones, in prep.

Bott M.H.P., Waghorn G.D., Whittaker A. 1988, Plate boundary forces at subduction zones and trench-arc compression, *Tectonophysics, submitted*

Braun J., Beaumont C. 1987, Styles of continental rifting: results from dynamic models of lithospheric extension, in: Beaumont C., Tankard A.J. (eds), *Sedimentary basins and basin-forming mechanisms*, Canadian Soc. Petrol. Geol., Mem. **12** 241-258

Brookes D.A., Carlson R.L., Harry D.L., Melia P.S., Moore R.P., Rayhorn J.E., Tubb D.G. 1984, Characteristics of back-arc regions, *Tectonophysics* **102**, 1-16

118

Carlson R.L. 1981, Boundary forces and plate velocities, *Geophys. Res. Lett.* **8**, 958-961

Carlson R.L. 1983. Plate motions, boundary forces, and horizontal temperature gradients: Implications for the driving mechanism, *Tectonophysics* **99**, 149-164

Carlson R.L., Melia P.J. 1984, Subduction hinge migration, *Tectonophysics* **102**, 399-411

Cathles L.M. 1975, *The viscosity of the Earth's mantle*, Princeton Press, New Jersey

Ceuleneer G., Rabinowicz M., Monnereau M., Cazenave A., Rosemberg C. 1988, Viscosity and thickness of the sub-lithospheric low-viscosity zone: constraints from geoid and depth over oceanic swells, *Earth Planet. Sci. Lett.* **89**, 84-102

Chapman M.E., Talwani M. 1982, Geoid anomalies over deep sea trenches, *Geophys. J. R. astr. Soc.* **68**, 349-370

Chase C.G. 1979, Subduction, the geoid and lower mantle convection, *Nature* **282**, 464-468

Chase C.G., McNutt M.K. 1982, The geoid: Effect of compensated topography and uncompensated oceanic trenches, *Geophys. Res. Lett.* **9**, 29-32

Christensen U.R. 1984, Convection with pressure- and temperature-dependent non-Newtonian rheology, *Geophys. J. R. astr. Soc.* **77**, 343-384

Christensen U.R., Yuen D.A. 1984, The interaction of a subducting lithospheric slab with a chemical or phase boundary, *J. Geophys. Res.* **89**, 4389-4402

Christensen U.R., Yuen D.A. 1985, Layered convection induced by phase transitions, *J. Geophys. Res.* **90**, 10291-10300

Chung T.J. 1978, *Finite element analysis in fluid dynamics*, McGraw-Hill

Cloetingh S.A.P.L., Wortel M.J.R., Vlaar N.J. 1982, Evolution of passive continental margins and initiation of subduction zones, *Nature* **297**, 139-141

Cook R.D. 1981, *Concepts and applications of finite element analysis, (2 ed)*, John Wiley and Sons

Creager K.C., Jordan T.H. 1984, Slab penetration into the lower mantle, *J. Geophys. Res.* **89**, 3031-3050

Creager K.C., Jordan T.H. 1986, Slab penetration into the lower mantle beneath Mariana and other island arcs, *J. Geophys. Res.* **91**, 3573-3589

Crough S.T. 1975, Thermal model of oceanic lithosphere, *Nature* **256**, 388-390

Crough S.T., Jurdy D.M. 1980, Subducted lithosphere, hotspots and the geoid, *Earth Planet. Sci. Lett.* **48**, 15-22

Cserepes L., Rabinowicz M. 1985, Gravity and convection in a two layer mantle, *Earth Planet. Sci. Lett.* **76**, 193-207

Davies G.F. 1980, Mechanics of subducted lithosphere, *J. Geophys. Res.* **85**, 6304-6318

Davies G.F. 1981, Regional compensation of subducted lithosphere: effects on geoid, gravity and topography from a preliminary model, *Earth Planet. Sci. Lett.* **54**, 431-441

Davies G.F. 1983, Subduction zone stresses: constraints from mechanics and from topographic and geoid anomalies, *Tectonophysics* **99**, 85-98

Davies G.F. 1984, Geophysical and isotopic constraints on mantle convection: an interim synthesis, *J. Geophys. Res.* **89**, 6017-6040

Davies G.R., Norry M.J., Gerlach D.C., Cliff R.A. 1988, A combined chemical and Pb-Sr-Nd isotope study of the Azores and Cape Verde hot spots: the geodynamic implications, in: *Magmatism in the Ocean Basins*, eds. A. Saunders and M.J. Norry, Geol. Soc. London

Dewey J.F. 1980, Episodicity, sequence and style at convergent plate boundaries, in: Strangeway (ed.), *The Continental Crust and It's Mineral Deposits.*, Geol. Assoc. Can., Spec. Pap. **20**, 553-573

Dziewonski A.M. 1984, Mapping the lower mantle: determination of lateral heterogeneity in *P* velocity up to degree and order 6, *J. Geophys. Res.* **89**, 5929-5952

Engdahl E.R. 1975, Effects of plate structure and dilatency on relative teleseismic *P* wave residuals, *Geophys. Res. Lett.* **2**, 420-422

Fischer K.M., Jordan T.H., Creager K.C. 1988, Seismic constraints on the morphology of deep slabs, *J. Geophys. Res.* **93**, 4773-4784

Fitch T.J. 1977, In situ P-wave velocities in deep earthquake zones of the SW Pacific: evidence for a phase boundary between upper and lower mantle, in: *Island Arcs, Deep Sea Trenches, and Backarc Basins*, Ewing Ser. 1 ed. M. Talwani, W.C. Pitman, 123-136, AGU, Washington, D.C.

Forsyth D., Uyeda S. 1975, On the relative importance of the driving forces of plate motion, *Geophys. J. R. astr. Soc.* **43**, 163-200

Frank F.C. 1968, Curvature of island arcs, *Nature* **220**, 363-365

Froidevaux C., Uyeda S., Uyeshima M. 1988, Island arc tectonics, *Tectonophysics* **148**, 1-9

Fujimoto H., Tomoda Y. 1985, Lithospheric thickness anomaly near the trench and possible driving force of subduction, *Tectonophysics* **112**, 103-110

Fujita K., Kanamori H. 1981, Double seismic zones and stresses of intermediate depth earthquakes, *Geophys. J. R. astr. Soc.* **66**, 131-156

Fukao Y., Furumoto M. 1985, Hierarchy in earthquake size distribution, *Phys. Earth Planet. Inter.* **37**, 149-168

Fukao Y., Yamaoka K., Sakurai T. 1987, Spherical shell tectonics: buckling of subducted lithosphere, *Phys. Earth Planet. Inter.* **45**, 59-67

Garfunkel Z., Anderson C.A., Schubert G. 1986, Mantle circulation and lateral migration of subducted slabs, *J. Geophys. Res.* **91**, 7205-7223

Giardini D., Woodhouse J.H. 1984, Deep seismicity and modes of deformation in Tonga subduction zone, *Nature* **307**, 505-509

Goto K., Hamaguchi H., Suzuki Z. 1985, Earthquake generating stresses in a descending slab, *Tectonophysics* **112**, 111-128

Grand S.P. 1987, Tomographic inversion for shear velocity beneath the North American plate, *J. Geophys. Res.* **92**, 14065-14090

Gunn R. 1943, A qualitative study of isobaric equilibrium and gravity anomalies in the Hawaiian Islands, *J. Franklin Inst.* **236**, 373-390

Gurnis M., Hager B.H. 1988, The shape and dip of subducted slabs (abstract), *EOS Trans. Am. Geophys. Un.* **69**, 468

Hager B.H. 1978, Oceanic plate motions driven by lithospheric thickening and subducted slabs, *Nature* **276**, 156-159

Hager B.H., O'Connell R.J. 1978, Subduction zone dip angles and flow driven by plate motion, *Tectonophysics* **50**, 111-134

Hager B.H., O'Connell R.J., Raefsky A. 1983, Subduction, back-arc spreading and global mantle flow, *Tectonophysics* **99**, 165-189

Hager B.H. 1984, Subducted slabs and the geoid: constraints on mantle rheology and flow, *J. Geophys. Res.* **89**, 6003-6015

Hager B.H., Clayton R.W., Richards M.A., Comer R.P., Dziewonski A.M. 1985, Lower mantle heterogeneity, dynamic topography and the geoid, *Nature* **313**, 541-545

Hager B.H., Gurnis M. 1987, Mantle convection and the state of the Earth's interior, *Rev. Geophys.* **25**, 1277-1285

Hamaguchi H., Goto K., Suzuki Z. 1983, Double-planed structure of intermediate-depth seismic zone and thermal stress in the descending plate, *J. Phys. Earth* **31**, 329-347

Hansen U., Ebel A. 1984a, Experiments with a numerical model related to mantle convection: boundary layer behaviour of small- and large-scale flows, *Phys. Earth Planet. Inter.* **36**, 374-390

Hansen U., Ebel A. 1984b, Numerical and dynamical stability of convection cells in the Rayleigh number range $10^3 - 8.10^5$, *Annales Geophys.* **2**, 291-302

Harper J.F. 1984, Mantle flow due to internal vertical forces. *Phys. Earth Planet. Inter.* **36**, 285-290

Harper J.F. 1986, Mantle flow and plate motions, *Geophys. J. R. astr. Soc.* **87**, 155-171

Haxby W.F., Parmentier E.M. 1988, Thermal contraction and the state of stress in the oceanic lithosphere, *J. Geophys. Res.* **93**, 6419-6429

Hilde T.W.C., Sharman G.F. 1978, Fault structure of the descending plate and its influence on the subduction process, *EOS Trans. Am. Geophys. Un.* **59**, 1182

Hinton E., Scott F.C., Ricketts R.E. 1975, Local least squares stress smoothing for parabolic isoparametric elements, *Int. Jour. Num. Meth. Eng.* **9**, 235-238

Hofmann A.W., Jochum K.P., Seufert M., White W.M. 1986, Nb and Pb in oceanic basalts: new constraints on mantle convection, *Earth Planet. Sci. Lett.* **79**, 33-45

Honda S. 1985, Thermal structure beneath Tohoku, N.E. Japan - a case study for understanding the detailed thermal structure of the subduction zone, *Tectonophysics* **112**, 69-102

House L.S., Jacob K.H. 1983, Earthquakes, plate subduction and stress reversals in the Eastern Aleutian arc, *J. Geophys. Res.* **88**, 9347-9373

Hsui A.T., Toksoz M.N. 1981, Back arc spreading: trench migration, continental pull or induced convection, *Tectonophysics* **74**, 89-98

Hughes T.J.R., Liu W.K., Brooks A. 1979, Finite element analysis of incompressible viscous flows by the penalty function formulation, *J. Comp. Phys.* **30**, 1-60

Hughes T.J.R., Liu W.K., Zimmerman T. 1978, Lagrangian-Eulerian FE formulation for incompressible, viscous flows, in: *U.S.-Japan Seminar on Interdisciplinary FE Analysis*, Cornell University, Ithaca, New York, August 7-11, 1978

Ida Y. 1983, Convection in the mantle wedge above the slab and tectonic processes in subduction zones, *J. Geophys. Res.* **88**, 7449-7456

Isacks B., Oliver J., Sykes L.R. 1968, Seismology and the new global tectonics, *J. Geophys. Res.* **73**, 5855-5899

Isacks B., Molnar P. 1971, Distribution of stresses in the descending lithosphere from a global survey of focal-mechanism solutions of mantle earthquakes, *Rev. Geophys.* **9**, 103-174

Isacks B.L., Barazangi M. 1977, Geometry of the Benioff zones: internal segmentation and downwards bending of the subducted lithosphere, in: *Island Arcs, Deep Sea Trenches, and Backarc Basins*, Ewing Ser. 1 ed. M. Talwani, W.C.

Pitman, 99-114, AGU, Washington, D.C.

Jaeger J.C., Cook N.G.W. 1976, *Fundamentals of rock mechanics (2 ed)*, Chapman and Hall

Jarrard R.D. 1986, Relations among subduction parameters, *Rev. Geophys.* 24, 217-284

Jarvis G.T., Peltier W.R. 1982, Mantle convection as a boundary layer phenomenon, *Geophys. J. R. astr. Soc.* 68, 389-427

Jarvis G.T., Peltier W.R. 1986, Lateral heterogeneity in the convecting mantle, *J. Geophys. Res.* 91, 435-452

Jeanloz R., Thompson A.B. 1983, Phase transition and mantle discontinuities, *Rev. Geophys.* 21, 51-74

Jeanloz R., Morris A. 1986, Temperature distribution in the crust and mantle, *Ann. Rev. Earth Plan. Sci.* 14, 377-415

Jones G.M. 1983, Isostatic geoid anomalies over trenches and island arcs, *Tectonophysics* 99, 119-138

Jordan T.H. 1977, Lithospheric slab penetration into the lower mantle beneath the Sea of Okhotsk, *J. Geophys.* 43, 473-496

Jurdy D.M., Stefanick M. 1983, Flow models for backarc spreading, *Tectonophysics* 99, 191-206

Karner G.D. 1984, Continental tectonics- A quantitative view of the thermal and mechanical properties of the continental lithosphere in compressional and extensional stress regimes, Univ. Durham

Karner G.D. 1985, Thermally induced residual topography within oceanic lithosphere, *Nature* 318, 527-532

Kawakatsu H. 1986, Downdip tensional earthquakes beneath the Tonga arc, a double seismic zone?, *J. Geophys. Res.* 91, 6432-6440

Kawakatsu H. 1986, Double seismic zones : kinematics, *J. Geophys. Res.* 91, 4811-4825

Keen C.E. 1985, The dynamics of rifting: deformation of the lithosphere by active and passive driving forces, *Geophys. J. R. astr. Soc.* 80, 95-120

Kenyon P.M., Turcotte D.L. 1983, Convection in a two-layer mantle with a strongly temperature dependent viscosity, *J. Geophys. Res.* 88, 6403-6414

Kiechhefer R.M., Short G.G., Curray J.R., Sugiarta W., Hehuwat F. 1980, Seismic refraction studies of the Sunda Trench and fore arc basin, *J. Geophys. Res.* 85, 863-890

Kincaid C., Olson P. 1987, An experimental study of subduction and slab migration, *J. Geophys. Res.* 92, 13832-13840

Kirby S.H. 1987, Localized polymorphic phase transformations in high-pressure faults and applications to the physical mechanism of deep earthquakes, *J. Geophys. Res.* **92**, 13789-13800

Kirby S.H., Kronenberg A.K. 1987, Rheology of the lithosphere: selected topics, *Rev. Geophys.* **25**, 1219-1244

Knittle E., Jeanloz R., Smith G.L. 1985, The thermal expansion of silicate perovskite and stratification of the Earth's mantle, *Nature* **319**, 214-216

Kogan M.G. 1976, The gravity field of oceanic block ridges, *Izu. Acad. Sci. USSR Phys. Solid Earth* **12**, 710-717

Kostoglodov V. 1988, Sediment subduction: a probable key for seismicity and tectonics at active plate boundaries, *Geophys. J. R. astr. Soc.* **94**, 65-72

Kusznir N.J., Bott M.H.P. 1977, Stress concentration in the upper lithosphere caused by underlying viscoelastic creep, *Tectonophysics* **43**, 247-256

Lefevre L.V., McNally K.C. 1985, Stress distribution and subduction of aseismic ridges in the middle America subduction zone, *J. Geophys. Res.* **90**, 4495-4510

Lewis S.D., Hayes D.E. 1984, A geophysical study of the Manila trench, Luzon, Philippines, 2, fore arc basin structural and stratigraphic evolution, *J. Geophys. Res.* **89**, 9196-9214

Lister C.R.B. 1975, Gravitational drive on oceanic plates caused by thermal contraction, *Nature* **257**, 663-667

Liu L.G. 1979, On the 650 km seismic discontinuity, *Earth Planet. Sci. Lett.* **42**, 202-208

Loper D.E., Stacey F.D. 1983, The dynamical and thermal structure of deep mantle plumes, *Phys. Earth Planet. Inter.* **33**, 304-317

Loper D.E. 1984, The dynamical structures of D'' and deep plumes in a non-Newtonian mantle, *Phys. Earth Planet. Inter.* **34**, 57-67

Loper D.E. 1985, Simple model of whole mantle convection, *J. Geophys. Res.* **90**, 1809-1836

Louden K.E. 1980, The crustal and lithospheric thicknesses of the Philippine Sea as compared to the Pacific, *Earth Planet. Sci. Lett.* **50**, 275-288

Lui C-S, Sandwell D.T., Curray J.R. 1982, The negative gravity field over the 85° E ridge, *J. Geophys. Res.* **87**, 7673-7686

Malkus D.S. 1976, *Int. J. Solids Struct.* **12**, 731-738

Mareschal J-C, Kuang J. 1986, Intraplate stresses and seismicity: the role of topography and density heterogeneities, *Tectonophysics* **132**, 153-162

McAdoo D.C. 1981, Geoid anomalies in the vicinity of subduction zones, *J. Geo-*

phys. Res. **86**, 6073-6090

McAdoo D.C. 1982, On the compensation of geoid anomalies due to subducting slabs, *J. Geophys. Res.* **87**, 8684-8692

McKenzie D.P., Parker R.L. 1967, The north Pacific: an example of tectonics on a sphere, *Nature Lond.* **216**, 1276-1280

McKenzie D.P. 1969, Speculations on the consequences and causes of plate motions, *Geophys. J. R. astr. Soc.* **18**, 1-32

McKenzie D.P., Roberts J.M., Weiss N.D. 1974, Convection in the Earth's mantle: towards a numerical solution, *J. Fluid Mech.* **62**, 465-538

Melosh H.J., Raefsky A. 1980, The dynamical origin of subduction zone topography, *Geophys. J. R. astr. Soc.* **60**, 333-354

Minster J.B., Jordan T.H. 1978, Present-day plate motions, *J. Geophys. Res.* **83**, 5331-5350

Mithen D.P. 1980, *Numerical investigations into the mechanism of graben formation*, PhD thesis, Univ. of Durham

Morgan W.J. 1968, Rises, trenches, great faults, and crustal blocks, *J. Geophys. Res.* **73**, 1959-1982

Mutter J.C., Buck W.R., Zehnder C.M. 1988, Convective partial melting 1. A model for the formation of thick basaltic sequences during the initiation of spreading, *J. Geophys. Res.* **93**, 1031-1048

Nakada M., Lambeck K. 1986, Seamount loading of a compressible viscoelastic plate: an analytical solution, *J. Geodynamics* **5**, 103-110

Nakamura K., Uyeda S. 1980, Stress gradient in arc-backarc regions and plate subduction, *J. Geophys. Res.* **85**, 6419-6428

Norrie D.H., DeVries G. 1978, *An introduction to finite element analysis*, Academic Press

Oden J.T. 1982, RIP methods for stokesian flows, in: *Finite Elements in Fluids*, Vol 4, Wiley

Officer C.B., Newman W.S., Sullivan J.M., Lynch D.R. 1988, Glacial isostatic adjustment and mantle viscosity, *J. Geophys. Res.* **93**, 6397-6409

Oliver J., Isacks B. 1967, Deep earthquake zones, anomalous structures in the upper mantle, and the lithosphere, *J. Geophys. Res.* **72**, 4259-4275

Olsen P. 1984, An experimental approach to thermal convection in a two-layered mantle, *J. Geophys. Res.* **89**, 11293-11301

Park M.J.M. 1981, *Numerical analysis of deformation in the upper part of subduction zones*, PhD thesis, Univ. of Durham

Parsons B., Molnar P. 1976, The origin of outer topographic rises associated with trenches, *Geophys. J. R. astr. Soc.* 45, 707-712

Peltier W.R., Farrell W.E., Clark J.A. 1978, Glacial isostasy and relative sea level: a global finite element model, *Tectonophysics* 50, 81-110

Peltier W.R., Drummond R.A., Tushington A.M. 1986, Post-glacial rebound and transient lower mantle rheology, *Geophys. J. R. astr. Soc.* 87, 79-116

Peterson E.T., Seno T. 1984, Factors affecting seismic moment release rates in subduction zones, *J. Geophys. Res.* 89, 10233-10248

Rabinowicz M., Lago B., Froidevaux C. 1980, Thermal transfer between the continental asthenosphere and the oceanic subducting lithosphere: its effect on subcontinental convection, *J. Geophys. Res.* 85, 1839-1853

Rabinowicz M., Lago B., Souriau M. 1983, Large-scale gravity profiles across subducted plates, *Geophys. J. R. astr. Soc.* 73, 325-349

Rabinowicz M., Lago B. 1984, Large scale gravity profiles as evidence of a convective circulation, *Annales Geophys.* 2, 321-332

Rabinowicz M., Cserepes L. 1985, Gravity and convection in a two-layer mantle, *Earth Planet. Sci. Lett.* 76, 193-207

Raff A.D., Mason R.G. 1961, Magnetic survey off the west coast of North America, 40° N. latitude to 52° N. latitude, *Bull. Geol. Soc. Am.* 72, 1267-1270

Ramsay J.G. 1979, Shear zone geometry: a review, *J. Struct. Geol.* 2, 83-99

Revenaugh J., Parsons B. 1987, Dynamic topography and gravity anomalies for fluid layers whose viscosity varies exponentially with depth, *Geophys. J. R. astr. Soc.* 90, 349-368

Reyners M., Coles K.S. 1982, Fine structure of the dipping seismic zone and subduction mechanics in the Shumigan Islands, Alaska, *J. Geophys. Res.* 87, 356-366

Richards M.A., Hager B.H. 1984, Geoid anomalies in a dynamic Earth, *J. Geophys. Res.* 89, 5987-6002

Richards M.A., Hager B.H., Sleep N.H. 1987, Dynamically supported geoid highs over hotspots: observation and theory, *J. Geophys. Res.* 93, 7690-7708

Richter F.M. 1973, Dynamical models for sea floor spreading, *Rev. Geophys.* 11, 223-287

Richter F.M. 1975, Simple plate models of mantle convection, *J. Geophys. Res.* 44, 441-471

Robinson E.M., Parsons B., Daly S.F. 1987, The effect of a shallow low-viscosity zone on the apparent compenstion of mid-plate swells, *Earth Planet. Sci. Lett.* 82, 335-348

Roecker S.W. 1985, Velocity structure in Izu-Bonin seismic zone and depth of the olivine-spinel phase transition in the slab, *J. Geophys. Res.* **90**, 7771-7794

Ruff L., Kanamori H. 1980, Seismicity and the subduction process, *Phys. Earth Planet. Inter.* **23**, 240-252

Ruff L., Kanamori H. 1983, Seismic coupling and uncoupling at subduction zones, *Tectonophysics* **99**, 99-117

Sacks I.S. 1983, The subduction of young lithosphere, *J. Geophys. Res.* **88**, 3355-3366

Samowitz I.R., Forsyth D.W. 1981, Double seismic zone beneath the Mariana island arc, *J. Geophys. Res.* **86**, 7013-7021

Sato T., Matsu'ura M. 1988, A kinematic model for deformation of the lithosphere at subduction zones, *J. Geophys. Res.* **93**, 6410-6418

Schubert G., Yuen D.A., Turcotte D.L. 1975, Role of phase transitions in a dynamic mantle, *Geophys. J. R. astr. Soc.* **42**, 705-735

Sclater J.G., Francheteau J. 1970, The implications of terrestrial heat flow observations on current tectonic and geochemical models of the crust and upper mantle of the Earth, *Geophys. J. R. astr. Soc.* **20**, 509-542

Sclater J.G. 1972, Heat flow and elevation of the marginal basins of the Western Pacific, *J. Geophys. Res.* **77**, 5697-5704

Sclater J.G., Karig D., Lawver L.A., Louden K.E. 1976, Heat flow, depth and crustal thickness of the marginal basins of the South Philippine Sea, *J. Geophys. Res.* **81**, 309-318 .

Seely D.R. 1979, The evolution of structural highs bordering major forearc basins, in: *Geological and Geophysical investigations of continental margins*, eds. Watkins J.S., Montadert L., Dickerson P.W., Mem. Am. Ass. Petrol. Geol. **29**, 245-260

Segerlind L.J. 1976, *Applied finite element analysis*, John Wiley and Sons

Shiono K., Sugi N. 1985, Life of an oceanic plate: cooling time and assimilation time, *Tectonophysics* **112**, 35-50

Silver P.G., Chan W.W. 1986, Observations of body wave multipathing from broadband seismograms: evidence for lower mantle slab penetration beneath the Sea of Okhotsk, *J. Geophys. Res.* **91**, 13787-13802

Sleep N.H. 1975, Stress and flow beneath island arcs, *Geophys. J. R. astr. Soc.* **42**, 827-857

Sleep N.H. 1979, The double seismic zone in downgoing slabs and the viscosity of the mesosphere, *J. Geophys. Res.* **84**, 4565-4571

Sleep N.H. 1987, An analytical model for a mantle plume fed by a boundary layer,

Geophys. J. R. astr. Soc. **90**, 119-128

Spence G.D., Clowes R.M., Ellis R.M. 1985, Seismic structure across the subduction zone of western Canada, *J. Geophys. Res.* **90**, 6754-6772

Spence W. 1986, Evidence for the slab pull force at a subduction zone, *J. Geophys. Res.* **91**, 7225-7234

Spence W. 1987, Slab pull and seismotectonics of subducting lithosphere, *Rev. Geophys.* **25**, 55-69

Stacey F.D., Loper D.E. 1983, The thermal boundary layer interpretation of D'' and its role as a plume source, *Phys. Earth Planet. Inter.* **33**, 45-55

Stark P.B., Frohlich C. 1985, The depths of the deepest deep earthquakes, *J. Geophys. Res.* **90**, 1859-1869

Stein S., Engein J.F., Weins D.A., Speed R.C., Fujita K. 1983, Slow subduction of old lithosphere in the Lesser Antilles, *Tectonophysics* **99**, 139-148

Stevenson D.J., Turner J.S. 1977, Angle of subduction, *Nature* **270**, 334-336

Stirrup J.F., Mann A.J.S., Mather M.A., Whittington A.B. 1987, *The plant modelling system program reference manual*, CISD/CC/P732, CEGB

Suzuki S., Sasatani T., Motoya Y. 1983, Double seismic zone beneath the middle of Hokkaido, Japan, in the southwestern side of the Kurile Arc, *Tectonophysics* **96**, 59-76

Sykes L.R. 1966, The seismicity and deep structure of island arcs, *J. Geophys. Res.* **71**, 2981-3006

Tatsumi Y., Sakuyama M., Fukuyama H., Kushiro I. 1983, Generation of arc basalt magmas and thermal structure of the mantle wedge in subduction zones, *J. Geophys. Res.* **88**, 5815-5825

Taylor B., Karner G.D. 1983, On the evolution of marginal basins, *Rev. Geophys.* **21**, 1727-1741

Temam R. 1977, *Navier-Stokes Equations*, North-Holland, Amsterdam

Tharp T.M. 1985, Numerical models of subduction and forearc deformation, *Geophys. J. R. astr. Soc.* **80**, 419-437

Toksoz M.N., Hsui A.T. 1978, Numerical studies of backarc convection and the formation of marginal basins, *Tectonophysics* **50**, 177-196

Tovish A., Schubert G., Luyendyk B.P. 1978, Mantle flow pressure and the angle of subduction: non-Newtonian corner flow, *J. Geophys. Res.* **83**, 5892-5898

Turcotte D.L., McAdoo D.C., Caldwell J.G. 1978, An elastic-perfectly plastic analysis of the bending of the lithosphere at a trench, *Tectonophysics* **47**, 193-205

Uyeda S. 1982, Subduction zones: an introduction, *Tectonophysics* **81**, 133-159

Uyeda S. 1986, Facts, ideas and open problems on trench-arc-backarc systems, in: *The Origin of Arcs*, ed. F.-C. Wezel, Elsevier

Vanpé J-M 1984, Thermo-mechanical convection in a subduction zone and initiation of back-arc spreading, *Annales Geophys.* **2**, 343-352

Vassiliou M.S. 1984, The state of stress in subducting slabs as revealed by earthquakes analysed by moment tensor inversion, *Earth Planet. Sci. Lett.* **69**, 195-202

Vassiliou M.S., Hager B.H., Raefsky A. 1984, The distribution of earthquakes with depth and stress in subducting slabs, *J. Geodynamics* **1**, 11-28

Vening Meinesz F.A. 1941, Gravity over the Hawaiian Archipelago and over the Madeira area: conclusions about the Earth's crust, *Proc. X. Ned. Akad. Wetensch.* **44**, 1-12

Vine F.J., Matthews D.H. 1963, Magnetic anomalies over oceanic ridges, *Nature Lond.* **199**, 947-949

Von Huene R., Kulm L.D., Miller J. 1985, Structure of the frontal part of the Andean convergent margin, *J. Geophys. Res.* **90**, 5429-5442

Waghorn G.D. 1984, *Numerical modelling of the stress regimes at subduction zones*, PhD thesis, Univ. of Durham

Walcott R.I. 1970, Flexural rigidity, thickness and viscosity of the lithosphere, *J. Geophys. Res.* **75**, 3941-3954

Ward S.N. 1985, Small-scale mantle flows and induced lithospheric stress near island arcs, *Geophys. J. R. astr. Soc.* **81**, 409-428

Watanabe M.G., Langseth M.G., Anderson R.N. 1977, Heat flow in backarc basins of the Western Pacific, in: *Island Arcs, Deep Sea Trenches, and Backarc Basins*, Ewing Ser. 1 ed. M. Talwani, W.C. Pitman, 137-162, AGU, Washington, D.C.

Watts A.B., Cochran J.R. 1974, Gravity anomalies and flexure of the lithosphere along the Hawaiian-Emperor seamount chain, *Geophys. J. R. astr. Soc.* **38**, 119-141

Watts A.B., Talwani M. 1974, Gravity anomalies seaward of deep sea trenches and the tectonic implications, *Geophys. J. R. astr. Soc.* **36**, 57-90

Watts A.B., Bodine J.H., Steckler M.S. 1980, Observations of flexure and the state of stress in oceanic lithosphere, *J. Geophys. Res.* **85**, 6369-6376

Watts A.B. 1982, Seamounts and flexure of the lithosphere, *Nature* **297**, 182-183

Westbrook G.K., Mascle A., Biju-Duval B. 1984, Geophysics and the structure of the Lesser Antilles forearc, in: *Initial Reports of the Deep Sea Drilling Project*, Vol LXXVIII, Washington

Westbrook G.K., McCann W.R. 1986, Subduction of Atlantic lithosphere beneath the Caribbean, in: Vogt P.R., Tucholke B.E., *The Geology of North America*, Vol M, The Western North Atlantic Region: The Geological Society of America

Westbrook G.K., Brown K.M. 1986, The tectonic fabric of the Barbados Ridge accretionary complex, *Marine and Petroleum Geology*, Vol 4

Wiens D.A., Stein S. 1985, Implications of oceanic intraplate seismicity for plate stresses, driving forces and rheology, *Tectonophysics* 116, 143-162

Wiens D.A., Okal E.A. 1987, Tensional intraplate seismicity in the Eastcentral Pacific, *Phys. Earth Planet. Inter.* 49, 264-282

Willemann R.J., Davies G.F. 1982, Bending stresses in subducted lithosphere, *Geophys. J. R. astr. Soc.* 71, 215-224

Willemann R.J., Anderson C.A. 1987, Model geoid anomalies due to subduction of inextensible lithosphere, *Geophys. Res. Lett.* 14, 820-823

Woodhouse J.H., Dziewonski A.M. 1984, Mapping the upper mantle: three-dimensional modelling of Earth structure by inversion of seismic waveforms, *J. Geophys. Res.* 89, 5953-5986

Wortel R. 1982, Seismicity and rheology of subducted slabs, *Nature* 296, 553-556

Wortel R. 1986, Deep earthquakes and the thermal assimilation of subducting lithosphere, *Geophys. Res. Lett.* 13, 34-37

Wortel M.J.R., Cloetingh S.A.P.L. 1986, On the dynamics of convergent plate boundaries and stress in the lithosphere, in: *The Origin of Arcs*, ed. F.-C. Wezel, Elsevier

Yamaoka Y., Fukao Y., Kumazawa T. 1986, Spherical shell tectonics: effects of sphericity and inextensibility on the geometry of the descending lithosphere, *Rev. Geophys.* 24, 27-54

Yamaoka Y. 1988, Spherical shell tectonics: on the buckling of the lithosphere at subduction zones, *Tectonophysics* 147, 179-192

Zienkiewicz O.C., Watson M., King I.P. 1968, A numerical method of viscoelastic stress analysis, *Int. J. Mech. Sci.* 10, 807-827

Zienkiewicz O.C., Godbole P.N. 1975, Viscous, incompressible flow with special reference to non-Newtonian fluids, in: *Finite Elements in Fluids*, Vol 1, Wiley, London

Zienkiewicz O.C. 1977, *The Finite Element Method (3 ed)*, McGraw-Hill

Zindler A., Hart S. 1986, Chemical Geodynamics, *Ann. Rev. Earth Plan. Sci.* 14, 493-571